1996

Large And Medium-scale Dynamics In The Mesosphere And Lower Thermosphere Measured By Mf And Meteor Vhf Radars

Thayananthan Thayaparan

Recommended Citation

Thayaparan, Thayananthan, "Large And Medium-scale Dynamics In The Mesosphere And Lower Thermosphere Measured By Mf And Meteor Vhf Radars" (1996). *Digitized Theses*. 2627.
https://ir.lib.uwo.ca/digitizedtheses/2627

Large and medium-scale dynamics in the mesosphere and lower thermosphere measured by MF and meteor VHF radars

by

Thayananthan Thayaparan

Department of Physics

Submitted in partial fulfilment
of the requirements for the degree of
Doctor of Philosophy

Faculty of Graduate Studies
The University of Western Ontario
London, Ontario
December 1995

National Library of Canada
Acquisitions and Bibliographic Services Branch
395 Wellington Street
Ottawa, Ontario
K1A 0N4

Bibliothèque nationale du Canada
Direction des acquisitions et des services bibliographiques
395, rue Wellington
Ottawa (Ontario)
K1A 0N4

Your file Votre référence

Our file Notre référence

ISBN 0-612-09886-9

Abstract

This thesis focuses on the experimental investigation of large- and medium-scale dynamics in the 70-100 km height range measured with MF (2.219 MHz) and meteor VHF (40.68 MHz) radar systems located at London (43° N, 81° W), Ontario, Canada. The MF radar uses the spaced antenna method by means of partial reflections to determine the horizontal winds. The VHF radar determines the horizontal wind velocity by means of radio reflections from meteor trails.

The major studies in this thesis include the following: (1) development of a numerical model to simulate the spaced antenna method, (2) validation of both radars, (3) studies of the spatial and temporal characteristics of tidal and mean motions over London with the MF radar, (4) studies of the spatial and temporal characteristics of the quasi 2-day wave over London with the MF radar, (5) comparison with other similar mid-latitude ground-based radars, (6) tidal/gravity wave interactions, and (7) intercomparison between MF and meteor VHF radar measurements.

Significant findings include the following.

(1) The numerical model simulation results show that the full correlation analysis is consistent and a reliable tool for measurements of atmospheric motions.

(2) Strong observational evidence of tidal/gravity wave interactions is found over London using the MF radar system. Our observations show significant correlation between gravity waves and tides (diurnal) at certain times of the year, and the nature of the correlation is intermittent and varies with time of year. We also propose a simple model which is found to be consistent with the major features of the observed data.

(3) Our tidal studies show good and consistent agreement with other nearby studies and numerical models but with some notable exceptions. These exceptions are probably due to local effects like gravity wave interactions.

(4) The periods of the quasi 2-day wave determined from our study, both at the London and Saskatoon sites, are found to be smaller (46-47 h) than the 51-52 h period generally suggested by other northern hemisphere results. Our observations show significant correlation between the London and Saskatoon sites on the 2-day wave during time periods of strong 2-day wave activity. The results suggest that the 2-day wave is a westward propagating wave of zonal wavenumber 3, although a possible connection with the zonal wavenumber 5 is also suggested at certain times.

(5) Simultaneous comparison of winds and tides by MF and meteor VHF radars shows very good overall agreement between the two techniques. The important conclusion is "that in general and on the average and with relatively few exceptions the technique of MF spaced antenna drift measurements approximately reflect the real motions of the neutral air in the 85-94 km region, and therefore is a valuable tool in middle atmospheric research, at least for periods of greater than a few hours".

Acknowledgements

The work described in this thesis was carried out under the supervision of Dr. Wayne Hocking, using the facilities available at the Department of Physics of The University of Western Ontario. Dr. Hocking's advice, encouragement, and guidance were indispensible throughout the project. He has been an inspirational supervisor, always helpful and supportive in countless ways. It is with deep gratitude and profound respect that I acknowledge his assistance. I would also like to thank him for his prompt and careful reading of the manuscript.

Special thanks are due to Dr. John MacDougall for his review comments on numerous points of the manuscript and his helpful overall advice. I would also like to thank my advisory committee member, Dr. Jean-Pierre St. Maurice, for his comments and suggestions for improvement of this work.

I would like to thank Drs. Alan Manson and Chris Meek for providing the Saskatoon data used for comparison purposes. In particular, I am grateful to Dr. Meek's valuable correspondence. I would also like to thank Dr. William Ward for furnishing the preliminary WINDII data used for comparison purposes.

For the many insights gained from our discussions, I am grateful to my colleagues Radian Belu, Bob Stockwell, Brian Jackel, Peter Brown, Dr. Randy Kissack, and Dr. Kathy Gilbert. Special thanks should go to Brian Jackel for his IDL expertise whenever I needed it.

As many "Ph.D. Widows" know, to complete a thesis, it takes a heavy toll not only of its author, but also of his loved ones as well. I am fortunate that my wife, Yasothai, and our sons - Chayyon, two years old, and Maayon, two months - are so understanding. Yasothai's strength sustained me over the four years since our marriage. Her patience and enthusiasm have been inestimable gifts. Chayyon used to cheer me up whenever I return home late at nights after working long hours at the university, and for the past two months Maayon has faithfully made sure that I get up early the following morning. For this, I thank my wife and children. The completion of this doctorate is as joyous an event for them as it is for me; the sacrifice, theirs, as much as mine.

Special mention should be made of the rest of my family. Even from the other side of the Pacific Ocean, their spiritual encouragement was invaluable. Thanks to my father-in-law Nadarajah, mother-in-law Asokaranee, brothers-in-law Basharan and Prabaharan, sisters-in-law Dushyanthi and Anusooyai, who could not see their loved ones for nearly four years because of my commitments connected with this project. My thanks are also due to my brother-in-law Ramdev and my sister Thayanithy.

In conclusion, I whole-heartedly thank my parents for their unstinted support and encouragement throughout my entire academic career. Their generous assistance in caring for Maayon since their arrival in Canada is greatly acknowledged.

Contents

List of Figures

List of Tables

List of Appendices

Chapter 1

Introduction

This dissertation describes the analysis of data collected with the new UWO (University of Western Ontario) MF (Medium Frequency) radar and the new VHF (Very High Frequency) meteor radar located near London, Ontario, Canada, with the aim of studying the large- and medium-scale dynamics of the mesosphere and lower thermosphere. The work contained in this dissertation discusses primarily the regions of the Earth's atmosphere between 70 and 100 km above ground level. The thesis has been structured such that the introductory material relevant to individual topics is addressed at the commencement of the relevant chapter. As a result, this introduction is necessarily brief. We begin with a simple general discussion of the mean vertical structure of the atmosphere.

1.1 Vertical structure of the atmosphere

The discussion in this section mainly follows that of Hines el al. [1965], Egeland et al. [1973], Wallace and Hobbs [1977], Brasseur and Solomon [1986], Andrews et al. [1987], Kelley [1989], and Hargreaves [1992], in addition to the references given.

The static atmosphere is described by the four properties, pressure (P), density (ρ), temperature (T) and composition. Between them these properties determine much of the atmosphere's behaviour. These properties are not independent, but are related by the universal gas law which may be written in various forms. For our purposes the form $P = nkT$, where n is the number of molecules per unit volume and k is the Boltzman constant (1.38×10^{-23} J molecule^{-1} K^{-1}), is particularly useful. The quantity "n" is called the *concentration* or the *number density*, but *density* alone is often used when the sense is clear (in this case we have $P = \rho R_* T$, where R_* is the gas constant which depends on the composition of the gas (e.g., $R_* = 287$ J kg^{-1}

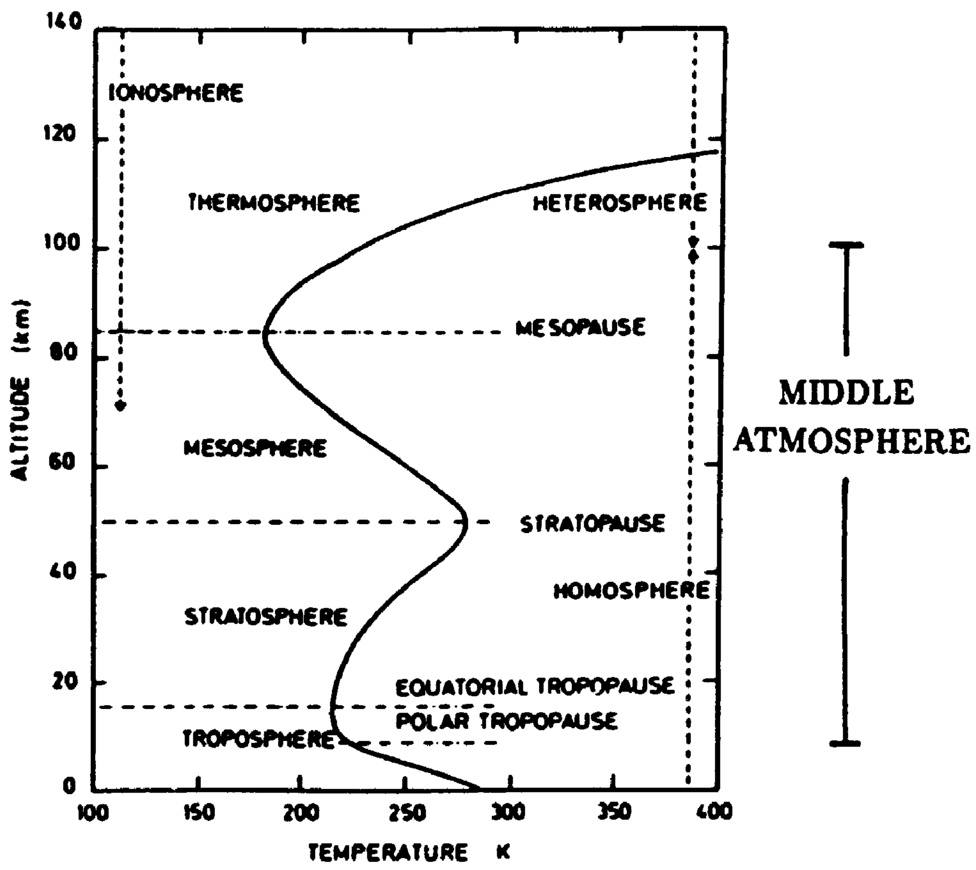

Figure 1.1: The vertical temperature structure of the Earth's atmosphere, showing the principal regions [after Brasseur and Solomon, 1986].

K^{-1} for dry air)).

The region of the atmosphere are named according to various schemes based, in particular, on temperature, composition, and state of mixing. The atmosphere shows a significant variation in its nature. The largest distinction is between neutral and ionized atmospheres, which are roughly separated by a height of around 100 km. Below this height, the atmosphere is treated as a neutral fluid, while ionized plasma plays an important role above it. These regions had long been studied independently, and it is only recently that both have been studied in parallel.

The other common way of dividing atmospheric regions is the one based on the vertical structure of atmospheric temperature. At any position on the Earth (except at near-polar latitudes in perpetual darkness during the winter), the observed change in atmospheric temperature with height has the same qualitative variation as that depicted in Figure 1.1. It is important to note that these sample profiles can only be approximate, since the temperature can vary substantially with time and location. In this system individual temperature regions are named *spheres* and the transition regions are called *pauses*. The atmosphere is classified into 4 regions of *troposphere*, *stratosphere*, *mesosphere*, and *thermosphere* in ascending order of height. These regions are separated by the *tropopause*, *stratopause*, and the *mesopause* (see Figure 1.1).

It is useful to consider just why the temperature profile follows the shape given. The temperature structure is governed by the absorption of solar radiation and re-radiation of infrared radiation at different heights, with different atmospheric species absorbing and radiating in different parts of the solar spectrum.

The troposphere (0 - $\sim$ 15 km) is the region of the atmosphere which most affects our day-to-day lives. Containing most of the atmospheric mass and energy, it is what is generally considered "the atmosphere " by non specialist in the field. The troposphere is characterized by a rather constant decrease in temperature with height. The main heat source for this region is the solar radiation absorbed by the surface of the Earth. Most ($\sim$ 70%) of the radiation reaching the surface is absorbed, and heats the surface to a temperature in the range 280-300 K. The Earth then re-radiates this heat, as a black-body spectrum, peaking in intensity at infrared wavelengths. If the atmosphere was transparent to this radiation then the temperature would fall with height at Γ_a = 9.8 K km^{-1} due to natural adiabatic cooling, where Γ_a is the dry adiabatic lapse rate (devoid of any liquid particles). This temperature gradient in the troposphere is due to the emission of long wave radiation from the Earth's surface - the temperature falling with distance from the source. However, atmospheric water vapour, carbon dioxide and other greenhouse gases absorb some of these re-emitted infrared wavelengths, and heat the atmosphere. All of these processes combine to give typical tropospheric lapse rates in the range 3-10 K km^{-1}, but usually near 6.6 K km^{-1}.

These tropospheric lapse rates are both spatially and temporally variable. If the lapse rate is in fact larger than the dry adiabatic lapse rate (Γ_a), it is called superadiabatic, and a vertically displaced parcel of air continues in its direction of motion, leading to convective instabilities. Because typical tropospheric lapse rates are $\sim$ 3-10 K km^{-1}, convective instabilities frequently arise, and it is because of this that the troposphere, literally meaning *turning sphere*, is so named. Other factors, such as surface cooling, weather storms such as thunderstorms, cyclones, hurricanes, geographical variability (land-sea-ice contrast), and so forth can not only effect the lapse rate, but also induce other dynamical features such as turbulence and gravity waves (see shortly, Section

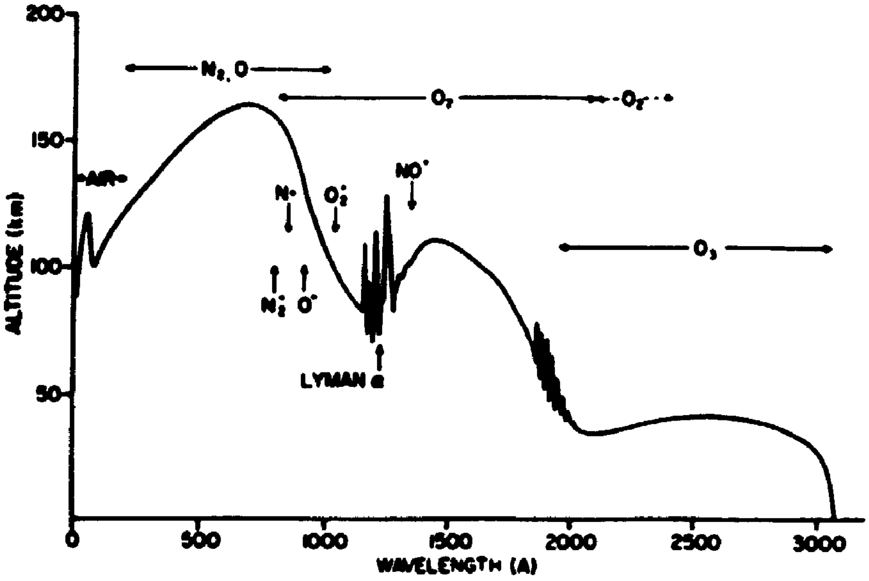

Figure 1.2: Altitude at which the intensity of solar radiation drops to $\frac{1}{e}$ of its value outside the Earth's atmosphere, for vertical incidence [After Hines et al. 1965]. 1 Angstrom (A) = 0.1 nm = 10^{-10} m.

1.3.3). All of these factors make the troposphere very dynamic, with huge amounts of energy being exchanged. The dynamics are also rather non-linear, and a variety of complex meteorological phenomena arise. In addition, absorption of infrared radiation by water vapour in the troposphere is known to provide most of the forcing for the atmospheric diurnal tides (see Section 2.3 for details).

The temperature ceases to decrease near 10-15 km, at the *tropopause*. The height of the tropopause has a clear latitudinal variation, being highest in the equatorial region and decreasing with increasing latitude. Typical tropopause heights range from 18 km near the equator to around 7 km at the poles. Above the tropopause, ozone becomes important which is the major energy input to that region of atmosphere.

It is increasing concentration of ozone with height which is responsible for the heating of the stratosphere. It has been known for more than 50 years that ozone in the atmosphere is most important to the heat budget of the stratosphere. Ozone, by its absorption of solar radiation of wavelengths in the 200-300 nm range (where 1 nm = 10^{-9} m, see Figure 1.2), provides the heat source that is responsible for the global mean increase of temperature between tropopause and the stratopause; in the absence of ozone there would be no stratosphere ! The ozone layer, through its absorption of harmful ultraviolet radiation, is also essential for the health of plant and animal life. The budget of atmospheric ozone, which involves very complex photochemical cycles depending on many trace species, both natural and man-made, is thus a major environmental concern. Thus, study of the formation, maintenance, and stability of the ozone layer is a critical aspect of middle atmospheric science. The ozone concentration peaks near stratopause heights of around 22 km [e.g., Andrews et al., 1987] so that temperature reaches its maximum of about 270 K in the stratosphere above that height (~ 50 km). The stable stratification of the air due to positive temperature gradient accounts for the origin of the name of this region. As the temperature increases with height, the stratosphere is highly stratified (hence *stratosphere*) and stable, and the large temperature gradients are responsible for large zonal winds at these heights [e.g., Andrews et al., 1987].

Above 50 km the temperature decreases with height, due to rapidly decreasing ozone concentrations. By analogy to the tropospheric situation, the height of maximum temperature near 50 km is called the *stratopause*. The subsequent atmosphere up to ~ 90 km, where the temperature abates, is called the *mesosphere* (literally "middle sphere"), and this upper level is called the *mesopause* (varies between 85-90 km). Around the mesopause, (which is the coldest place in the terrestrial environment in summer, temperatures as low as 120 K observed, e.g., Brasseur and Solomon [1984]), the atmosphere assumes very different characteristics. The exact location of the temperature minimum (the mesopause) is difficult to determine, since considerable wave-related fluctuations are superposed on the measurement [Kelley and Ulwick, 1988]. Recent observations suggest that there are two temperature minima near 86 km and 99 km, although the mechanisms responsible for the formation of double minima are not clear at present [e.g., She et al., 1993, 1995]. The region between the stratopause and mesopause is also called the (ionospheric) D-region. Figure 1.2 shows that this region is responsible for the absorption of hard ultraviolet radiation (~ 100-200 nm, which includes the Lyman-α lines) and soft X-rays (~ 0.2-0.8 nm) from the Sun (fortunate for life on Earth !). Firstly, the air now becomes slightly ionized, mainly through photoionization of various molecular species by ultraviolet radiation from the Sun (see below), and the resulting electrons form the D-region. However, the total ionization is too small to produce significant distortion to the dynamics through electromagnetic effects, so that this ionized air merely advected with the neutral air. The very weak ionization allows electrons to be used as tracers for the neutral gases. This allows radar reflections to be used to determine neutral motions.

In the past, meteorologists often designated the entire region above the tropopause as the "upper atmosphere". Only fairly recently has the term *middle atmosphere* become popular in referring to the region from the tropopause to the homopause (at approximately 100 km, see below). In this part of the atmosphere eddy processes keep the constituents well mixed and ionization plays only a minor part. Over the past 25 years, the concept of the "middle atmosphere" has grown in importance. This region was not well studied in the 60's and 70's, at least partially because most of it was too high for aircraft and balloon *in situ* measurement and too low for similar studies from rockets and satellites.

Above the mesopause the temperature increases monotonically with height. This extended region is referred to as the *thermosphere* (90-400 km). Above 100 km, ionization begins to affect the dynamics through interactions with the Earth's electric and magnetic field. In the thermosphere above 90 km the increasing molecular mean free paths lead to a gradual change from dominance of mixing by macroscopic fluid motions below 100 km to control by molecular diffusion about 120 km. At altitudes where molecular diffusion dominates, each species (in the absence of source or sinks) has an exponential decay of density with height with a scale height determined by its molecular mass. Thus less massive species increasingly dominate with height. The region of the atmosphere where eddy mixing dominates is referred to as the *homosphere*, while the molecular diffusion region is the *heterosphere*. These are separated by the *homopause*, near 100 km, which is often considered to the level where two processes are of equal importance.

The upper most part of the atmosphere is called the *exosphere* (> 400 km). Here neutral particles move along a ballistic trajectory with little probability of collision.

1.2 The ionosphere below 100 km

The ionosphere is defined as that region of the atmosphere which contains ions and electrons of sufficient concentration to affect the propagation of radio waves. The ionosphere is composed of a number of characteristic regions based upon the electron concentration profile. The ionosphere consists of three main parts; (a) the D-region situated between about 50 and 90 km, (b) the E-region continuing upwards to about 150 km, and (c) the F-region extending further to 500 km. The electron density shows an increasing trend through the ionosphere up to peak electron density of the F-region occurring at about 250 km, and then falls off gradually at greater heights. In the present section we shall consider how the different regions are produced. We shall limit the discussion to the D- and lower E-regions, because they are responsible

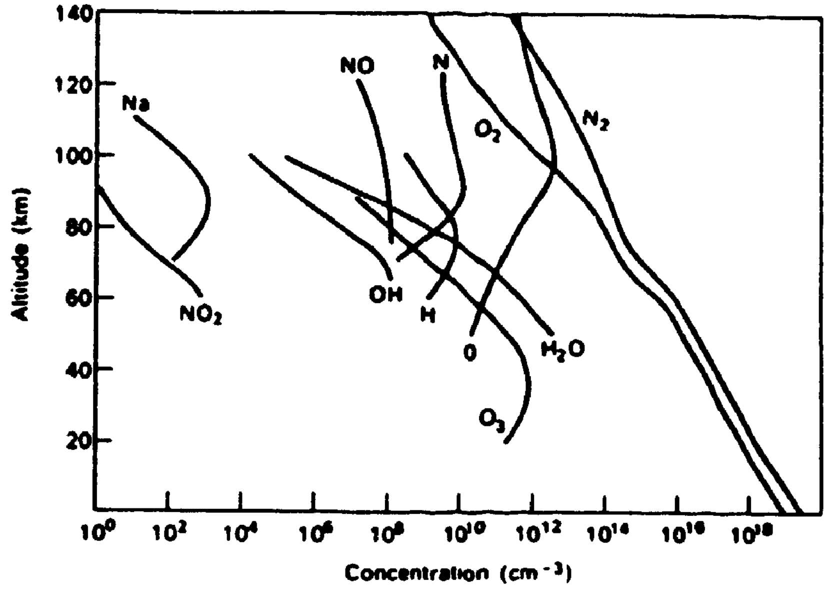

Figure 1.3: An altitude profile of the more important neutral gases of the atmosphere, which is a qualitative of their concentration rates. It is important to note, however, that these profiles are typical only, and that they do predictably vary with time of day, season, latitude and solar cycle [after McEwan and Phillips, 1975].

for partial radar reflections below 100 km. Furthermore, the work contained in this dissertation discusses primarily the regions of the Earth's atmosphere between 70 and 100 km above ground level.

The region of the atmosphere below about 100 km, which includes the D-region (~ 50-90 km) and lower E-region (~ 90-100 km) is relatively weakly ionized compared with the upper ionosphere (above 100 km) because most of the ionizing radiation from the Sun has been absorbed at these upper levels. The ionosphere is that part of the Earth's atmosphere where free electrons exist in large enough quantities to influence the propagation of radio waves. The formation of the D- and lower E-regions are dominated by the photoionization of minor constituents and has a complicated ion chemistry. The chemical reactions and concentrations of the various atmospheric species at these levels are strongly temperature dependent. Therefore, the electron density profiles in the D-region may exhibit strong diurnal, seasonal and latitudinal variations. Irregular variations produced by particle precipitation events or solar flare may occasionally enhance the electron concentrations in the D-region quite considerably.

In the D- and lower E-regions the pressure is relatively large and collisions are dominant so that the usual techniques of studying the ionosphere are not applicable. For instance, ionosonde sounding is not possible because the collision frequency exceeds the critical frequency in general, which means absorption is heavy at all frequencies. For this reason, rocket techniques have been particularly important in this region. From the point of view of radio communication, the D-region is of great importance because most of the absorption of MF and HF radio waves occurs at that layer.

The minor neutral constituents of the atmosphere represent important mechanisms in the ionization processes and chemical reactions which lead to the formation and destruction of different ions. Rocket borne mass spectrometer measurements have shown that minor constituents such as O, O_3, CO_2, NO, NO_2, H_2O and OH play an important role in the ion chemistry of this region (see also Figure 1.3). The final equilibrium state of these chemical reactions determine the electron concentrations at the various levels. Because some of these minor constituents and their ionization products have long photochemical lifetimes, their distributions in both the horizontal and vertical directions can be strongly influenced by transport processes in the atmosphere. The processes are influenced to some extent by the meteorology of the lower atmosphere, and atmospheric motion produced by the propagation of planetary waves, atmospheric tides and gravity waves (see below) through the region of interest as well as eddy and molecular diffusion.

Since the morphology of the D- and the lower E-regions can be altered by a large number of phenomena, its behaviour is less regular than that of the ionosphere at greater heights. Much of our knowledge of properties of the D- lower E-regions are obtained from rocket measurements and ground-based measurements of radio waves partially reflected from irregularities in electron density.

1.2.1 Basic structure and formation

The D-region appears to consist of three somewhat separate subregions. In the upper part, from 80 to 90 km, solar extreme ultraviolet (EUV) radiation and X-rays in the range 0.2-0.8 nm are believed to be the predominant ionization agents for most of the dominant constituent neutral gases, while the hydrogen Lyman-β line (102.6 nm), a major EUV line, can just ionize molecular oxygen. These predominant ionization agents are also believed to be the principle source of photoionization in the lower E-region.

In the height region between 70 and 80 km the principle source of photo ionization is the extremely strong Lyman-α hydrogen line (121.6 nm). The Lyman-α hydrogen line is less strongly absorbed by the major atmospheric neutral gas constituents O, O_2, N_2, and N than both shorter wavelength radiation and also some larger wavelengths, (i.e. the atmosphere has by "chance" a window in the spectrum at 121.6 nm, see Figure 1.2), and so the Lyman-α line can penetrate to considerable depths. X-rays (0.2-0.8 nm) can penetrate to heights below about 75 km, and can be important at these levels especially during solar flare conditions.

Below 70 km a tenuous ionized layer has been observed. It has been found that this layer is formed abruptly in the morning twilight period. The layer is produced by galactic cosmic rays, and this production is therefore also present during the night. During the night, however, the ionization is present in the form of negative ions. The electron layer is then produced at the time of sunrise by photo detachment of the negative ions. Hence, the electron concentration will rapidly increase in this region at Sunrise, with a subsequent decrease at sunset. The relative contribution of the galactic cosmic rays to ionization in this region increases with geomagnetic latitude and decreases with solar activity. During solar maximum the increased magnetic fields associated with the solar wind tend to screen out our galactic cosmic rays in the vicinity of the Earth. Electron precipitation can also be a significant source of ionization [e.g., Montbriand and Belrose, 1976; Chamberlain and Jacka, 1979].

The dominant primary ions in the D- and E-regions are NO^+ and O_2^+. At the higher levels N_2^+ will also formed, but is readily transformed into O_2^+ by charge transfer. Heavy metallic atomic ions such as Mg^+ and Fe^+ and small quantities of sodium, calcium and nickel of meteoric origin are also observed in the D- and lower E-regions. Rocket measurements have also shown that water vapour complexes are very important in these regions. In fact, during normal conditions in the D-region, hydrated ions are dominant. Mass 19 (H_3O^+), 37 ($H_5O_2^+$) and 55 ($H_7O_3^+$) have been observed as the most common ions.

A more detailed discussion on the production of ionization can be found in Gnanalingam and Kane [1978], Torr and Torr [1979], Thomas [1971, 1974, 1980], and Wayne [1991].

The winter anomaly

Many of the reactions in the D-region are strongly temperature dependent, so small change in temperature can have significant effects on chemical composition. The mesopause is warmer in winter than summer (see shortly, Section 1.3.3), and theory suggests that the warmer winter mesopause could result in enhanced NO^+ concentrations (with corresponding electron increases) [Offermann, 1979]. Large temperature changes can also occur in the D-region within time scales of a day or so, and these can be correlated with anomalous radio wave absorption. Theoretical results also suggest that temperature changes can dramatically affect NO densities [Reid, 1977; Koshelev, 1979].

The term "winter anomaly" usually refers to the increase in electron concentration in the 60-80 km height range during the wintertime. The increased ionization at lower height levels, where the collision frequency is high, leads to an increase in MF-HF radio wave absorption. The enhanced concentrations of NO^+ ions and corresponding increased electron production observed between 60 and 90 km on some occasions have been explained by temperature changes and downward transport of N and N_2 from upper levels by turbulent diffusion [e.g., Koshelev, 1979]. These increases in electron concentration give rise to higher than normal radio wave absorption, and occur particularly in winter, when the mesosphere is warmer which in turn is dependent on the dynamics of the mesosphere. This phenomenon is called anomalous winter absorption or simply the winter anomaly. Offermann [1979] suggested that short period (i.e. a few days) increases in absorption are correlated with increases in stratospheric temperature. Randa and Randa [1977] showed that the short period winter anomaly is highly correlated with geomagnetic activity. Koshelkov [1987] argued that the short period winter anomaly is the effects of temperature change and vertical/horizontal transport motions, which may be triggered by a period of strong turbulence in the mesosphere and thermosphere. Gregory and Manson [1970], Offerman [1979], and Kawahira [1982] attributed this phenomenon to stratospheric warmings and large amplitude planetary waves (see shortly, Section 1.3.1). Although above observations refer to short period anomalies, it is often suggested that the longer term seasonal variation is due to some kind of turbulent mixing associated with the breaking of gravity waves, planetary waves or tides, or changes in global dynamics which result in enhanced vertical/horizontal motions (see also Section 1.3.1). Clearly, there are many possible factors which can affect D-region absorption and further discussion of these is beyond the scope of this section, and is a subject for further research.

Additionally, the increase in ionization can also permit stronger reflections (which depends on electron density gradient, *not* on the total electron density) or scatterings from lower heights. This effect probably contributes in part to the descent of the minimum observing height of the UWO MF radar (at London) from approximately 80 km during the summertime (daytime) to approximately 70 km during the wintertime (daytime - usually lasting a few days).

1.3 Atmospheric waves and dynamics

Atmospheric wave motions are essential components of the general circulation in the middle atmosphere. Studies of winds and temperatures in the atmosphere have shown that there exist numerous oscillations and wave-like motions superimposed on the general atmospheric circulation, and that these waves have periods ranging from minutes to days. The systems of wave motion will be identified here are planetary waves, tidal oscillations, and (short-period) gravity waves. These waves can be classified in numerous ways, according to their physical or geometrical properties [Andrews et al., 1987]. The main classification is based on their restoring mechanisms: gravity waves due to the stratification of the atmosphere, inertio-gravity waves due to the combination of stratification and Coriolis parameter, planetary waves due to the Coriolis effect. These waves are all solutions of the Navier-Strokes equation (see equations (2.1)-(2.2)), but in each case different terms dominate. For example if we ignore the contribution due to gravity, Coriolis force, and viscosity, we end up with acoustic waves. Consideration of the gravity term only leads to gravity waves, while if we maintain the Coriolis term we deal with planetary waves.

Waves can also be distinguished on the basis of being a forced or free mode; an example of forced waves are the solar thermal tides (see Chapter 2 for details) while a free mode wave is the 2-day wave (see Chapter 6 for details). Another classification can be made according to the propagation characteristics of the waves; those that can propagate only in some general horizontal directions are said to be vertically evanescent. Another example of evanescent waves are the equatorial waves which are trapped and prevented from propagating latitudinally. Waves can also be separated into stationary and travelling wave; the former are those that maintain a fixed phase relationship with respect to the Earth [Andrews et. al., 1987].

In the following sections we will briefly discuss some of the dominant atmospheric wave motions that are common in the middle atmosphere at mid-latitudes. The basic important attributes will be discussed, and no detailed wave solutions will be presented.

1.3.1 Planetary waves

Planetary waves, also known as Rossby waves, are global in scale, with horizontal wavelengths of a few thousand kilometers: the full range of longitudes may encompass a single dominant oscillation ('zonal wavenumber 1') or a few such oscillations, while waves of somewhat smaller scale (zonal wavenumbers to 10 or 15) appear in lesser strength. Although the horizontal wavelengths are of the order of the scale of the Earth, the vertical wavelengths are relatively small (several tens of km). Planetary waves are usually classified by their zonal wavenumber, which is defined as the number of complete cycles around the globe for a given latitude (this zonal wavenumber should not be confused with the physical wavenumber which is equal to $\frac{2\pi}{\lambda}$).

Planetary waves propagate in a westward direction relative to the air stream, so that their motion may therefore be either eastward or westward relative to the ground. Depending on their period, planetary waves fall into two categories; travelling and quasi-stationary. Quasi-stationary waves are assumed to be any planetary wave with a period greater than 30 days. Notable wave periods that have been identified as corresponding to travelling planetary wave oscillations are 2, 10, and 16 days. With the possible exception of the quasi 2-day wave (in the Southern Hemisphere), the periods of these oscillations are not integral numbers of days and typically the observed periods fall in the period ranges 1.9-2.2, 4-7 and 10-20 days [e.g., Salby, 1981]. Generally it is difficult to distinguish the mean wind from the effects of quasi-stationary wave in the absence of satellite data. While radars are capable of providing long time series and therefore identifying the presence of planetary wave periodicities, they are distributed too sparsely to provide adequate information on zonal wavenumbers. On the other hand, satellites are now capable of providing good spatial coverage with marginally useful temporal information. With satellite observations the zonal wavenumbers can be easily determined [e.g., Rodgers and Prata, 1981; Rosenlof and Thomas, 1990].

Planetary waves arise due to the existence of the variation of the Coriolis force with latitude, this being greatest at the poles and and smallest at the equator. If there were no latitudinal variation of the Coriolis force, then planetary waves would degenerate into geostrophic wind, where the Coriolis force and the pressure gradient forces are in equilibrium. Planetary waves are formed by the departure of a fluid flow from geostrophic equilibrium which may be induced by instabilities in the mean zonal flow, topographical forcing and land-sea differential heating. Baroclinic and barotropic instabilities are the most relevant type of instabilities which can be expected to trigger a planetary scale disturbances [e.g., Houghton, 1977; Holton, 1979]. A barotropic instability results if the shear of a mean zonal fluid flow becomes unstable whereas a baroclinic instability results from a stably stratified mean zonal flow in the presence of a meridional temperature gradient. Planetary waves generated by instabilities have comparatively short wavelengths of several thousand kilometers (e.g., travelling wave), whereas disturbances produced by topographical forcing and land-sea differential heating must have wavelengths which are global in scale (e.g., quasi-stationary wave).

Because of their long time scales, measured in days, they appear (as on weather maps) to be deformations of the general circulation and may indeed be counted as part of it for many purposes. But they have certain properties that allow them to be isolated as separate dynamical systems. Chief amongst these, for present purposes, is their ability to propagate upward. With this goes the ability to produce wind perturbations that increase with height, and the ability to carry energy, momentum, etc. with them to the upper levels, for transfer ultimately into the background flow. Indeed, if this ability were not offset in large measure by other effects, the atmosphere above the D-region would be altered out of all recognition from the state in which we actually find it.

The principle offsetting processes results from interaction with the background flow of the general circulation at stratospheric heights. For the most part, planetary waves do not propagate vertically but remain trapped in the troposphere and stratosphere. However, the vertical propagation is possible under certain conditions. Using the β-plane approximation (where the Coriolis parameter f is set equal to $f_0 + \beta y$, where the latitudinal gradient of the Coriolis parameter $\beta = \frac{df}{dy}$ is a constant, and y is the latitude; see Houghton [1977] for more details), it can be shown that vertical propagation is only possible when

$$0 < \bar{u} < \frac{\beta}{k^2 + l^2} \tag{1.1}$$

where k and l are the zonal and meridional wavenumbers respectively. This result implies that the waves cannot propagate through the stratosphere if there are any mean winds less than zero (i.e. any westward winds). Furthermore, in the case of eastward winds, the mean winds must be less than $\frac{\beta}{k^2+l^2}$ in order for the waves to propagate, which generally means the waves cannot propagate if $\bar{u}_c \geq 40$ m/s (for mid-latitude, where $\bar{u}_c$ is the eastward critical wind velocity and is dependent on both the scale of the wave and latitude) [Charney and Drazen, 1961]. However, the penetration through eastward winds is generally allowed when the mean wind velocity is less than the critical wind velocity, $\bar{u}_c$. The strong dependence of the critical wind velocity on wavelength explains why quasi-stationary waves, with their very long horizontal wavelengths, are a regular feature of the upper mesosphere in winter [e.g., Salby, 1984; Houghton, 1986]. Although the amplitudes are largest in the stratosphere, they remain relatively large up to 80 km [e.g., Barnett and Corney, 1985] and also up to 110 km [e.g., Brown and John, 1979].

Among these consequences is some role in the production of the 'winter anomaly' of radio absorption (see also Section 1.2.1). The precise role is not yet clear, but one line of argument is that the winds produced by the waves might carry a parcel of atmosphere some hundreds of kilometres horizontally, and simultaneously several kilometres vertically, in a matter of hours or days. Important consequences might be effected in this way, particularly in the concentration of minor constituents whose variation with height is rapid. Planetary waves have also been recognized as important in their affect on the distribution of chemical species, like ozone, N_2O, N_2O_5 and NO_2 [e.g., Berggren and Labitzke, 1968; Schmidt, 1982; Solomon and Garcia, 1983]. In any event, there is a widespread hope that planetary waves will prove to be the key to the occurrence of anomalous absorption, and this hope is strengthened by a correlation of anomalous days with 'stratospheric sudden warmings' which are themselves associated with planetary waves [e.g., Andrews et al., 1987]. Current theories, primarily stemming from Matsuno [1971], suggest that tropospherically forced planetary waves play a crucial role in the dynamics of stratospheric sudden warmings (see Andrews et al. [1987] for more details).

Observational studies by Barnett and Corney [1985] show that the amplitudes of the quasi-stationary waves achieve maximum values at latitudes of 60°-70° in the winter hemisphere. Spectral analysis of stratospheric temperature data obtained with the NIMBUS 5 satellite has revealed differences between the planetary wave motions in the two hemispheres [Chapman and Peckham, 1980]. In general, they found that planetary wave activity in the middle atmosphere is at a maximum during the Northern Hemisphere winter. The Southern Hemisphere is much less disturbed by planetary activity and the maximum tended to occur during the spring. Observations also showed that the amplitudes of the travelling planetary waves are similar in both hemispheres but the quasi-stationary waves are significantly stronger in the Northern Hemisphere. This is understandable since the planetary wave activity in the Northern and Southern Hemispheres is quite different because of the differences in surface features in the two hemispheres. The quasi-stationary planetary wave amplitudes in the Southern Hemisphere are weaker because the zonal asymmetries in topography and the land-sea heat differences which force these waves are much smaller in the Southern Hemisphere than the Northern Hemisphere. Quasi-stationary waves play a principle role in the development of stratospheric warmings, which occur more frequently and with more effect in the Northern Hemisphere. Major warmings occur on average about once every other winter in the Northern Hemisphere, but have not been observed in the Southern Hemisphere. Minor warmings in the upper stratosphere occur more frequently, and in both hemispheres [e.g., Andrews et al., 1987].

A prominent class of planetary waves in the mesosphere and lower thermosphere is the quasi 2-day wave which play a significant role in the dynamics of that atmosphere. The presence of a quasi 2-day wave of zonal wavenumber 3 in the mesosphere during the summer has been reported from wind observations [e.g., Muller and Kingsley, 1974; Craig et al., 1980, 1981; Aso et al., 1980]. The quasi 2-day wave has been the subject of considerable theoretical and observational interest in recent years, and can be easily studied with modern radars [e.g., Salby, 1981]. These studies are particularly important for their relevance to the interaction between such waves and the mean flow, and have important implications for the general circulation of the middle atmosphere during the summer. It may be also important in the transport of atmospheric constituents at these heights during the summer [Plumb et al., 1987].

The quasi 2-wave appears to be asymmetric about the equator as it is present in both meridional and zonal wind components at mid- and high-latitudes in the Northern Hemisphere [e.g., Muller and Nelson, 1978] and only in the meridional wind component near the equator [e.g., Kalchenko 1987; Harris and Vincent, 1993] and primarily in the meridional component at mid-latitudes in the Southern Hemisphere [e.g., Craig et al., 1980; Craig and Elford, 1981]. The anomalous appearance of planetary wave activity in the mesosphere during the summer cannot be explained in terms of upward propagating planetary waves. The presence of strong westward winds in summer in the stratosphere should inhibit the vertical propagation of planetary waves through the middle atmosphere. This behaviour may indicate that the source of the observed planetary waves in the mesosphere during summer, and perhaps winter, resides at upper levels rather than in the lower atmosphere. While there is no conclusive evidence pointing to the source of the quasi 2-day wave observed at mesospheric heights, further observations are required in order to resolve questions about generating mechanisms and to understand better the role of the wave in the middle atmosphere. Observation of the quasi 2-day wave is one of the main objectives of this dissertation and therefore will be dealt with in more detail in Chapter 6.

1.3.2 Tidal oscillations

The tides of the atmosphere are generated in part gravitationally, both by the Sun and by the Moon, but in greater part thermally by the Sun. They are inherently global in scale, and their dominant components propagate westward to maintain a constant phase relationship with respect to the Earth so that it remains synchronized with the position of the Sun or the Moon. Tidal oscillations are generated by H_2O insolation absorption in the troposphere, O_3 insolation absorption in the stratosphere and EUV

(20-100 nm)/UV (120-200 nm) insolation absorption in the lower thermosphere, and propagate through the mesopause and into the lower thermosphere. Tides represent a major source of temperature and wind variability in the mesopause region and are also capable of generating turbulence and depositing mean momentum, heat, and constituents above 85 km. Observation of atmospheric tides is one of the other prime objectives of this dissertation and therefore will be dealt with in more detail in the following Chapter.

1.3.3 Internal gravity waves

The atmosphere contains a spectrum of waves. Any true wave must be associated with some restoring mechanisms. For acoustic waves, the restoring force arises from the compressibility of the air. These waves are longitudinal waves in which the individual particle motion is parallel to the direction of propagation and the gravitational forcing of the Earth plays no role [see e.g., Houghton, 1986]. In a stably stratified atmosphere, an air parcel displaced vertically seeks to return to equilibrium, and executes oscillations at a characteristic frequency called the Brunt-Väisälä or buoyancy frequency N. Since the atmosphere is in neutral equilibrium with respect to horizontal displacements, displacements in any oblique direction can be sustained as waves propagating within the body of the atmosphere with frequencies smaller than the buoyancy frequency. These waves are called internal gravity waves to distinguish them from surface waves (e.g., ocean waves) which may exist at a boundary separating two fluids. In the past 35 years, since the original treatment of atmospheric gravity waves by Hines [1960] and following his suggestion that many of the irregular motions in the middle atmosphere (even above 100 km) may have their origin in propagating atmospheric gravity waves, the properties of these wave have been extensively studied and empirical evidence of their occurrence and behaviour has rapidly accumulated [e.g., Witt, 1962; Gossard, 1962; Manson et al., 1974, 1975; Vincent and Ball, 1977; Miller et al., 1978; Eckermann and Vincent, 1989].

There are many mathematical methods of deriving gravity wave solutions from the Navier-stokes momentum equations, the mass continuity, and the adiabatic energy equation [see Section 2.2.1 for details], modified to the atmospheric situation with appropriate simplification. The essential feature which supports internal gravity waves is the exponential decrease of atmospheric density with height due to hydrostatic balance in the vertical; that is balance between gravity acting downwards and buoyancy acting upwards on fluid parcel. As these are the only external forces required to derive the gravity wave motion, other force terms in the Navier-Stokes equations are usually dropped to simplify the derivation. Indeed, when some of the other force terms are included (e.g., Coriolis force), they produce only secondary changes to the wave motion. It serves no purpose to replicate such derivations here, and we shall merely quote the important results, appropriately referenced where necessary. Mathematical manipulation leads to a dispersion relation for gravity waves of the following form [e.g., Gossard and Hookes, 1975]

$$m^2 = k_h^2\left(\frac{N^2 - \omega^2}{\omega^2 - f^2}\right) - \frac{1}{4H_p^2} + \frac{\omega^2}{C_s^2} \tag{1.2}$$

where

$$k_h^2 = k^2 + l^2 \tag{1.3}$$

$$N^2 = \frac{g}{T}\left(\frac{dT}{dz} + \frac{g}{C_p}\right) \tag{1.4}$$

$$\omega = \sigma - k\bar{U} - l\bar{V} \tag{1.5}$$

$$f \approx \frac{4\pi}{24 \text{ hours}} \sin\theta \tag{1.6}$$

where m is vertical wavenumber, k_h is the horizontal wavenumber, k is the zonal wave number, l is the meridional wave number, N is the Brunt-Väisälä frequency (typically in the 5-10 minutes range below 100 km), f is the Coriolis or inertial frequency, H_p is the density scale height, C_s is the speed of sound, T is the background temperature, g is the gravitational acceleration, C_p is the atmospheric specific heat at constant pressure, θ is the latitude, ω is the intrinsic frequency (the frequency which would be seen by an observer moving with the background flow), σ is the ground-based wave frequency (as measured from a fixed position on the ground, not including the effects of the background flow), and $\bar{U}$ (zonal) and $\bar{V}$ (meridional) are the mean background winds.

In the middle atmosphere the last term on the right hand side of equation (1.2) is negligible, and H_p is only significant for waves with vertical wavelength ($\frac{2\pi}{m}$) larger than about 40 km. Therefore, the first term in equation (1.2) is adequate for most purposes, and gives real solutions when $f^2 < \omega^2 < N^2$, where f and N define lower and upper bounds respectively on the intrinsic wave frequency ω. The requirement $\omega^2 > f^2$ is particularly important for atmospheric tides (see Section 2.2.3). Thus f varies from zero at the equator to $\frac{2\pi}{12\text{ hours}}$ at the poles (see equation (1.6)). Hence, internal gravity waves with periods shorter than 12 h can propagate anywhere, but for longer periods, internal gravity waves propagate vertically in regions increasingly confined to the vicinity of the equator. At latitude 43°, as in our case over London, internal gravity waves with periods less than 17.6 h can propagate vertically anywhere.

A number of polarization relations also result, which relate wave induced fluctuations of various fluid parameters. The following equations serve as useful approximations to the polarization relations. These are not exact, and more precise relations can be found elsewhere [e.g., Hines, 1960; Gossard and Hookes, 1975]. The 3-dimensional velocity fluctuations (u', v', w') are related by

$$v' = \imath \frac{f}{\omega} u' \tag{1.7}$$

and

$$w' = -\frac{k}{m} u' \tag{1.8}$$

where $\imath$ is the imaginary unit such that $\imath^2 = -1$. This describes the velocity polarization of the wave. Nevertheless, these approximations are often useful because they are extremely simple, yet still apply fairly accurately over a wide range of frequencies. They are particularly good at frequencies of more than 3 times the Brunt-väisälä frequency. In general, the wave polarization is elliptical. As $\omega \rightarrow f$ the polarization becomes circular and as $\omega \rightarrow N$ it becomes linear (i.e. for high frequency waves). However, one must incorporate m and k to understand the full 3-dimensional structure of the gravity wave. Note that gravity waves are almost transverse wave motions, even though small compressional components of the wave motion produce longitudinal behaviour.

The gravity waves have the curious property that the phase velocity (i.e. $\frac{\omega}{m}$) and group velocity (i.e. $\frac{\partial \omega}{\partial m}$) are perpendicular to each other. It can be shown (after some manipulations) from equation (1.2) that a downward phase velocity ($m < 0$) is associated with upward group velocity and hence upward energy propagation, and vice versa (see also Section 2.4). For upward energy propagation ($m < 0$) the wind vector rotates clockwise (seen from above) with increasing height in the Northern Hemisphere and anti-clockwise with increasing height in the Southern Hemisphere.

These simple relations are really all that is needed to give a picture of the physical nature of a gravity wave. There are many more polarization that relate other perturbation quantities, such as temperature T', pressure p', and density ρ' [see e.g., Gossard and Hookes, 1975], yet these variations result from the vertical adiabatic displacement of air parcels by the wave, and can be understood by considering the w' fluctuations. Further discussion of wave polarization and dispersion is given by Hines [1960], Gossard and Hookes [1975], and Andrews et al. [1987], yet one should remember that most of the discussion revolves around equations (1.2)-(1.8).

The only certain natural sources of these waves in the upper atmosphere are provided by the auroral electrojets and particle precipitation, and perhaps, on one occasion each, by an eclipse and by an earthquake, while nuclear detonations in the troposphere and at higher elevations have provided man-made sources. Tidal oscillations within the upper atmosphere may act, through non-linear processes, both to generate gravity waves locally and to transfer energy within pre-existent gravity wave spectrum. There is reason to believe that meteorological sources in the troposphere provide the bulk of the spectrum observed in the middle and upper atmosphere - sources such as severe weather such as thunderstorms [e.g., Davies and Jones, 1972], jet streams, airflow over irregular or unevenly heated topographic features [e.g., Mastrantonio et al., 1976], tropical cyclones, hurricanes and typhoons [e.g., Hung, 1977], tornadoes [e.g., Hung et al., 1978], thermal convective instabilities [e.g., Röttger, 1980]. Generation of waves by non-linear processes such as non-linear interaction between tides and gravity waves [e.g., Sidi and Teitelbaum, 1978], wave-wave interaction [e.g., Bretherton, 1969], is a more complex problem. Isolation of sources in individual cases, and identification of their statistical distribution by type, season, and geographical position, constitute outstanding problems in the study of these waves. Clearly, almost any process which can produce instabilities in the atmosphere with periods greater than the Brunt-Väisälä frequency are a likely source of internal gravity waves.

Whatever the sources, internal gravity waves play an important role in the observed dynamical processes in the mesosphere and lower thermosphere. On horizontal scales of a few hundreds of kilometres and less (e.g., 10-300 km), and vertical scales of less than a few tens of kilometres (e.g., 5-50 km), the main dynamical motions in the mesosphere and lower thermosphere are those due to gravity waves (and turbulence). It is also generally believed that gravity waves are the main cause of wind and temperature fluctuations (of the order 1 to 30 m/s) with periods of a few hours and less, down to a few minutes. Their strongest members occur at somewhat longer periods, typically 1 to 3 h, where they begin to overlap higher-order tidal harmonics (though the latter are not normally in evidence above the "noise" imposed by the former). It should be noted here that gravity waves may be taken to have a short-period cut-off at the Brunt-väisälä period, lying in the range 4 to 6 min in the D- and E- regions. Individual waves propagate with vertical phase speeds of 1 to 20 m/s and horizontal phase speeds of 20 to 100 m/s, more or less.

Not all waves generated in the lower atmosphere can propagate to upper levels. The spectrum of gravity waves that reaches the upper levels from regions low in the atmosphere is often a (filtered) fraction of the spectrum that is launched. Gravity waves generated in the troposphere appear to have a rather broad two-dimensional spectrum of phase speeds that includes meridional propagating waves as well as zonally propagating waves that move both eastward and westward relative to the mean flow. Thus, during all seasons at least some gravity waves can propagate through the middle atmosphere without encountering critical levels (i.e. where the horizontal phase speed of a gravity wave equals the local mean wind). Note that at critical levels the intrinsic frequency (or speed) of the wave will approach to zero (i.e. $\omega \rightarrow 0$, see equation (1.5)). Observations indicate that in extratropical latitudes the vertical flux of gravity wave activity is greater in the winter than in the summer. This seasonal dependence is probably due primarily to variations in the strength of tropospheric sources. In addition, there is an important seasonal dependence of the wave activity is due to selective transmission caused by the presence of mean wind critical levels. During the summer (winter), waves that are westward (eastward) relative to the mean flow are selectively filtered out so that there is a net upward transfer of eastward (westward) momentum (also see Chapter 5).

As discussed above, the background flow of the general circulation, and the background temperature distribution that drives it, usually account for the gross features of the filtering process. However, perturbations caused by planetary waves and tidal oscillations can be equally effective in certain circumstances because their relatively long time-scales make them appear to be part of the 'background', as that background is viewed by the short-period gravity waves. It seems that planetary waves in the middle atmosphere are effective in varying the filtering of gravity waves at mid- and high-latitudes, at least in wintertime [e.g., Hines, 1972].

When ω (the intrinsic phase speed of the wave) becomes small near the critical levels, the wave is more sensitive to dissipative processes. In such regions the wave will begin to deposit much of its energy and momentum into the mean background flow [e.g., Hines and Reddy, 1967; Reid and Vincent, 1987]. Therefore, as the waves propagate upward through the stratosphere and mesosphere, they continuously dissipate energy and make important contributions to momentum and turbulence budgets at all altitudes. In addition, the turbulence generated by the breaking gravity waves strongly influences the transport and distributions of long-lived chemical species such as NO [e.g., Forbes et al., 1991]. In fact, gravity waves probably represent the most important means of momentum coupling in the middle atmosphere.

For many years, the mean state of the mesosphere, as measured experimentally, could not be adequately modelled. Experiments showed that it departs significantly from radiative equilibrium. This departure is now directly attributed to the effect of gravity waves in the mesosphere. That gravity wave dissipation could make a large contribution to the state of the mesosphere was initially proposed by Houghton [1978] while the mathematical ideas were developed by Lindzen [1981]. These ideas were then incorporated into general circulation models, and the results were at last found to agree with experimental observations [e.g., Matsuno, 1982; Dunkerton, 1982; Holton and Zhu, 1984]. The deposition of momentum and energy transported by gravity waves largely induce the mean zonal and meridional circulation, and thus temperature distribution, as well as the turbulent diffusion of heat and constituents, in the mesosphere [e.g., Lindzen, 1981; Matsuno, 1982; Holton, 1982; Garcia and Solomon, 1985] and in the stratosphere [e.g., Miyahara et al., 1986]. It is also now strongly believed that the seasonal variation of ozone in the mesosphere is controlled mainly by propagating gravity waves, and this can be explained as follows.

Observations show that near the mesopause the seasonal variation of ozone is characterized by a strong maximum at the spring equinox, a secondary maximum at the autumn equinox, and minimum at the solstices [e.g., Thomas and Barth, 1984]. These seasonal changes are almost certainty not due to chemistry alone. Ozone photochemistry is temperature sensitive and in the absence of other variations, the largest mesospheric abundances would be associated with the coldest temperatures. This would imply a maximum ozone density in summer, when the mesopause temperature is coldest at mid- and high-latitudes, not in the spring as observations show. Thus, the observed distribution must be dynamically controlled. At mid-latitudes, middle atmospheric zonal winds are eastward in winter, absorbing all eastward propagating gravity waves before they reach the 80 km level, but allowing propagation of westward propagating waves to the mesosphere, where they can break and produce diffusion. In summer the zonal winds are reversed so that only the eastward propagating waves reach the mesosphere [e.g., Lindzen , 1981]. During the equinoctial seasons the zonal winds tend to be weakly eastward in the stratosphere and weakly westward in the mesosphere. Under these conditions only the high phase speed portion of the gravity wave spectrum can propagate to the mesopause region. Further, filtering by the mean zonal winds affects the altitude at which wave breaking occurs [e.g., Lindzen, 1981]. The background zonal wind speed at the breaking altitude also influences the intensity of the diffusion produced by breaking waves. The overall result is substantially reduced diffusion near the equinoxes as compared to solstice (by about a factor of 5 at 80 km) through both the filtering and background wind effects [e.g., Garcia and Solomon, 1985]. This reduced vertical transport at the equinox in the mesosphere can have two important effects. First, the downward flux of atomic oxygen below the 80 km level would be reduced. This fact, combined with the more or less steady downward diffusion from the thermosphere, would lead to a build up of atomic oxygen near the mesopause. Second, there would be a reduced upward transport of water vapour from the lower mesosphere. The former effect would tend to increase the rate of ozone concentration, and the latter would tend to reduce the amount of OH available for catalytic destruction of ozone. This implies that the transport of mesospheric chemical constituents is controlled mainly by the gravity wave breaking process [e.g., Thomas and Barth, 1984].

Another perplexing observation for early researchers was the relatively hot polar winter mesopause and cold polar summer mesopause (the latter gives the coldest temperature observed anywhere in the atmosphere (see Figture 1.1)), and this can be explained as follows. In radiative equilibrium the pressure gradient force driving a north-south flow from the summer to winter pole, is converted by a Coriolis force into a purely zonal flow so as to conserve angular momentum. This zonal flow also experiences a Coriolis force which opposes the original pressure gradient force, resulting in a net zero meridional flow. However, gravity waves are absorbed at or near critical levels, (where the local horizontal wind speed equals their horizontal phase speed), so that the only gravity waves reaching the mesosphere from below are expected to have phase speeds outside the range of horizontal wind speeds occurring in the underlying stratosphere. Thus, when winter eastward winds are present in the stratosphere we can anticipate that gravity waves with a range of westward phase speeds will occur in the mesosphere and break there. Conversely, when summer westward winds are present in the stratosphere, gravity waves with eastward phase speeds would be expected to appear, and break, in the mesosphere. In winter, the breaking gravity waves with westward phase speed will exert a westward force (i.e. through driven westward acceleration) on the eastward jet, and hence tend to close it off; similarly, the breaking gravity waves in summer will tend close off the westward jet. [e.g., Houghton, 1978; Andrews et al., 1987]. This reduction in zonal flow causes an imbalance of forces in the north-south direction, and this thereby produces a net meridional flow. This meridional flow then produces subsidence (and therefore heating) over the winter pole, and rising motions (and therefore cooling) over the summer poles. As a result, the temperatures in the upper atmosphere are also substantially altered relative to their radiative situation, and one dramatic result of note is the phenomenon of the polar summer mesopause becoming much colder than even the winter polar mesopause. [e.g., Dunkerton, 1978; Barnett and Corney, 1985].

1.4 Observational techniques

Most of the direct velocity measurements in the middle atmosphere have been made *in situ* by rocket soundings and remotely from the ground using several radar methods, operating in a variety of frequency range. These includes partial reflection drift method, meteor radars, and so called MST (Mesosphere-Stratosphere-Troposphere) radars.

In the partial reflection drift technique, a triangular array of receivers is usually used to determine the drift velocities of ionized irregularities that partially reflect the radar signal. Only bulk horizontal (and vertical) motions can be sensed with this technique, and measurements are limited to the middle and upper mesosphere and lower thermosphere. Meteor radars are Doppler radars that measure line of sight velocities using returns from ionized meteor trials in the mesopause region. These radars are thus particularly appropriate for studying means winds and global scale oscillations (e.g., planetary waves and tides). A more detailed discussion of these radars can be found in Chapters 3 and 7.

The MST technique utilizes very-high frequency (VHF) radars (wavelengths of the order of a few meters) in Doppler mode to determine the drift velocities of backscattering elements whose nature depends on the region being scanned. The echoes received by such radars from the troposphere and lower stratosphere are caused by refractive index variations due to density fluctuations associated with neutral atmosphere (clear air) turbulence. In the mesosphere the echoes are produced by scattering due to fluctuations in free electron density associated with turbulence. With the MST technique it is possible to obtain 3-dimensional velocity fields. MST radars have limited horizontal coverage but can produce data with high temporal and vertical resolution in a given locality. They are thus particularly appropriate for studying high frequency components of the motion fields, such as gravity waves and tides.

MST radars cannot provide information on the temperature fluctuations associated with atmospheric motions. Such information can be provided by ground-based lidar sounding. Lidars designed to detect the Rayleigh backscatter from air molecules can yield density profiles in the altitude range of 30-100 km. From these soundings the temperature profile can be computed. Other types of lidars can be used to provide profiles of ozone, aerosols, and other trace constituents in the middle atmosphere.

1.5 Motivation and scope of the thesis

During the past 30 years substantial advances have been made in our understanding of the dynamics, physics, and chemistry of the middle atmosphere. Much of the observational and theoretical research that has led to this progress was stimulated by fears that human activities might adversely affect the ozone layer. A considerable body of evidence supports the view that stratospheric ozone has decreased substantially over the past few decades as a result of the action of trace gases, mainly chlorofluorocarbons (CFC's) [e.g., Watson et al., 1988; Scientific Assessment of Stratospheric Ozone (SASO), 1989]. These gases can have a significant impact on ozone, either directly through photochemistry or indirectly by changing the radiative budget and hence the temperature and chemistry. Ozone absorbs ultraviolet (UV) insolation, accounting for the basic structure of the stratosphere, in which temperature increases with altitude from the tropopause to the stratopause, and shields the biosphere from potentially harmful effects. The magnitude and sign of changes in the ozone layer is govern primarily by changes in the lower stratosphere where most of the ozone resides. In this altitude range, chemistry, dynamics (i.e. atmospheric wave motions such as planetary waves, atmospheric tidal waves, and gravity waves), and radiation play equally important roles, so that these processes and interactions need to be represented as accurately as possible.

Recent numerical model studies by Roble and Dickinson [1989] show that changes in the distributions of certain trace gases may influence the temperature profile in the lower, middle, and upper atmospheres. The results especially show that variations in lower atmospheric concentrations of CO_2 and CH_4 have an important influence on the global mean thermal and compositional structure of the mesosphere and thermosphere. These results indicate that the mesosphere and thermosphere temperatures will cool by about 10 K and 50 K respectively as the CO_2 and CH_4 doubled. These regions are heated by similar amounts when the trace gas mixing ratios are halved. These results clearly show that global change from trace gas increases is not confined to the lower atmosphere alone but also extends into the mesosphere, thermosphere, and ionospheric regions. Thus, the lower atmosphere strongly influences the physics and chemistry of the middle atmosphere in a variety of ways; i.e an understanding of the properties of this lower region requires in turn some degree of understanding of the properties of the rest of the atmosphere, for the region cannot be treated in isolation.

It is now well established from Sections 1.2 and 1.3 (and Chapter 2 - atmospheric tides) that planetary waves, atmospheric tidal waves, and gravity waves play a significant role in the dynamics of the middle atmosphere. The general circulation of the middle atmosphere is to a large degree controlled dynamically by atmospheric wave motions that originate in the troposphere (and stratosphere - e.g., semidiurnal tide). In this way, atmospheric waves act as a coupling mechanism transporting energy, momentum, and constituents from the lower atmosphere to the middle and upper atmospheres. Coupling between the troposphere, stratosphere, and mesosphere has received considerable attention during the last decade.

Middle atmosphere ozone loss affects the atmospheric tides, since these are mainly driven by absorption of solar ultraviolet (UV) by ozone (see also Section 2.3). The observed distribution of tidal waves at any level in the mesosphere or lower thermosphere depends both on the ozone (source) distribution in the stratosphere and on the propagation characteristics of the atmosphere between the level of observation and the source region. Changes in tidal wave amplitudes and distributions in the stratosphere due to anomalies in the source (ozone) strength, clearly may have substantial impact on the circulation of the mesosphere and lower thermosphere. Therefore, long term changes in the amount and distribution of ozone will cause concomitant changes in the character of the atmospheric tides. Generally, a decrease of stratospheric ozone reduces the amplitudes of the upward propagating tides throughout the atmosphere. Tidal amplitudes are small in the upper stratosphere where most of the forcing occurs, but they exert considerable influence in the mesosphere and lower thermosphere, through momentum and energy deposition and modulation of gravity wave propagation. Thus the upward propagating tides act to couple lower atmosphere trace gases perturbations to the middle atmosphere. All these factors distinctly indicate that any signature of ozone depletion in the stratosphere (and also "global warming") is expected to be seen in the mesosphere and lower thermosphere. Thus, continued monitoring of this region, through the observation of tidal waves and its characteristics, is essential. Observation of such tidal waves and their interactions with gravity waves is one of the major themes of this dissertation.

As already mentioned, but worth repeating, while the ozone layer in the stratosphere absorbs most of the 200-300 nm UV, the upper mesosphere is responsible for the absorption of hard UV ($\sim$ 100-200 nm) and soft X-rays from the Sun. These radiation bands are more energetic than those absorbed by ozone, and would cause quick death to most life on Earth. Their absorption is important for high altitude aircraft. For this reason alone, study of this region is very important.

This dissertation is divided into nine main chapters. Chapter 2 highlights some important advances made in the study of middle atmosphere tides in the last 10 years. The objective of this chapter is not to derive classical tidal theory, but to reiterate some of the simplifying assumptions used in developing an analytical solution and to state the equations and terminology which define the foundation from which the rest of this dissertation is developed. Specific attention is given to the variability of tides, as it arises due to tidal-gravity wave interactions, non-linear interactions, and non-migrating tides. The basic radar equations (fundamentals), the qualitative synopsis of the basic echoing mechanisms, the data analysis technique of the new UWO MF radar system, and a numerical model of the spaced antenna method (an important technique used in this work) are described in Chapter 3. The numerical model simulates the volume scatter conditions assumed by the Full Correlation Analysis (FCA) method. This model is used to investigate some of the biases reported in the use of the FCA. Chapter 4 reports measurements of climatologies of the tides and winds made with a UWO MF radar system. The observed results are compared with the recent numerical and empirical models, and with other similar mid-latitude ground-based radars. Chapter 5 reports observational evidence of tidal-gravity wave interactions using the UWO MF radar. We also propose a simple model which is found to be consistent with the major features of the observed data. Chapter 6 reports measurements of the quasi 2-day wave made with a UWO MF radar system. The observed results are simultaneously compared with the similar MF radar system located at Saskatoon. Chapter 7 describes the new VHF meteor radar system and the data analysis method. We also present the observed results of the meteor distribution as a function of height, time, etc. Chapter 8 reports another important study of the simultaneous observation of winds and tides by MF and meteor radars, where the two sets of equipments were only 400 meters apart. These results are used to investigate some of the biases reported in the spaced antenna method and therefore determine whether the spaced antenna drift measurements reflect the real motions of the neutral air in the mesosphere and lower thermosphere. Finally, Chapter 9 contains conclusions, comments and possibilities of future extended work.

Chapter 2

Atmospheric tides

2.1 Introduction and history

Atmospheric motions whose periods are integral fractions of the solar or lunar day (*diurnal* refers to a period of one day - 24 hours, *semidiurnal* refers to a period of half a day - 12 hours, *terdiurnal* refers to a period of one third of a day - 8 hours, etc.) are called atmospheric tidal oscillations. Atmospheric tidal oscillations are produced in two very different ways; (a) the gravitational forces of the Moon and Sun, and (b) the thermal action of the Sun. Both the Sun and the Moon exert periodic external forces upon the Earth's atmosphere. In the case of the Moon these forces are wholly gravitational, except for the minute heating effect from the reflected radiation at full Moon. The Sun, however exerts, a strong thermal effect and a much weaker gravitational effect. The Earth's atmosphere will respond to these forces in a manner analogous to forced mechanical vibrations. Throughout nearly two centuries these tides, thermal and gravitational, have been extensively discussed in the literature of science, although they are very minor phenomenon at ground level. We shall begin with a review of the history of the study of tides in which the center of attention was the source of the semidiurnal pressure variation. When Kelvin proposed his hypothesis (resonance theory, see below), the existence of the ozone layer, the primary source of the semidiurnal tide, was unknown. This discussion will be followed by a review of our present knowledge and theoretical understanding on atmospheric tides.

The discussion in the following subsections (2.1.1-2.1.7) mainly follows that of Lindzen and Chapman [1969], Chapman and Lindzen [1970], Beer [1974], and Lindzen [1967, 1974, 1990], in addition to the references given.

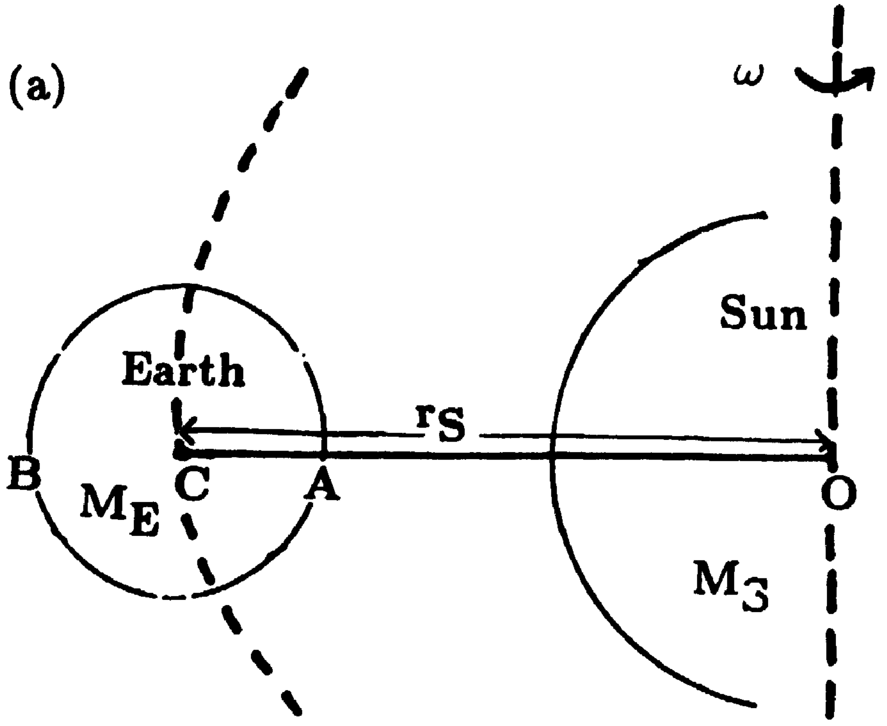

The total centrifugal force at C = $M_E r_S \omega^2$

Total gravitational attraction force at C = $\frac{GM_EM_S}{r_S^2}$

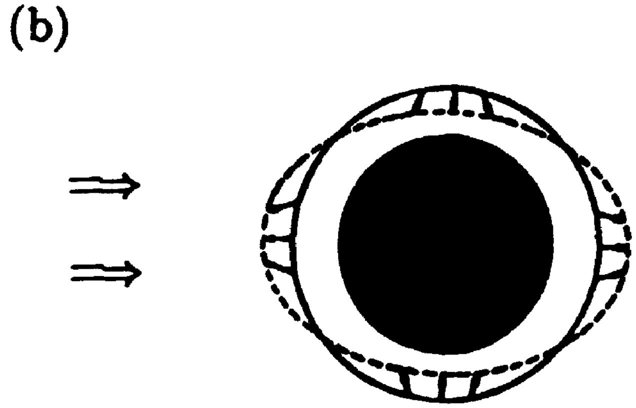

Figure 2.1: (a) Schematic of the gravitational attraction and the centrifugal forces on the Earth by the Sun. (b) The resultants of the gravitational and centrifugal forces. See the text for more details.

2.1.1 Gravitational excitation of tides

(1) Why do tides exist at all ? What periods do we expect ?

The first tides that were observed by man were ocean tides whose cause was correctly attributed to the Moon and Sun. Ocean tides, with rise and fall of the water twice daily on most open ocean coasts, have been known and described for over two thousand years. In contrast to ocean tides, atmospheric tides were not observed until the invention of the barometer by Torricelli [ca. 1643]. The connection of the tides with the Moon seems to have been first recognized and recorded as far back as available records go [Hyde, 1947; Cassen, 1959]. The true explanation of the dominance of the semidiurnal component of the ocean tides was first indicated by Newton [1687]. The semidiurnal component of the ocean tides are a consequence of the lunar and solar gravitational forces acting in accordance with Newton's laws of mechanics. Briefly, tidal forcing depends not only on the average gravitational force exerted by either the Sun or Moon, but also on the relative variation of this force over the diameter of the Earth (Figure 2.1). The latter factor gives a substantial advantage to the Moon. As an example, the solar gravitational semidiurnal tide can be explained in an approximate way as follows:

Consider the Sun as an immovable mass m_S, with center O, around which the Earth, of mass m_E and center C at distance r_S, revolves with the angular velocity ω. Then, the total centrifugal force acting at C on the Earth equals $m_E\omega^2 r_S$ and the total gravitational attraction force acting at C on the Earth equals $\frac{Gm_S m_E}{r_S^2}$.

Figure 2.1a shows that the gravitational attraction force is greater and the centrifugal force is less at A than at C, so that there is a distribution of unbalanced upward force directed sunwards (obliquely to the vertical near A). On the opposite side of the Earth, B, the gravitational attraction force is less and the centrifugal force is greater at B than at C, so that there is a distribution of unbalanced force obliquely outward there also (near B). From the perspective of the Earth, both unbalanced forces act vertically outwards at A and B. The result is that bulges in the atmosphere tend to form on the sides toward the Sun and away from the Sun while depressions tend to form between the bulges (Figure 2.1b). Therefore, in a single period (24 hours) while the Earth rotates beneath, these bulges and depressions constitute waves (the semidiurnal tides) which travel around the Earth each day. Particles free to move, like those of ocean and air, are pushed outward twice. The water surface tends to become spheroid as in Figure 2.1b. In a similar fashion, although less simply, an analogous lunar gravitational semidiurnal tide can be explained. The lunar gravitational tide is 2.37 times larger than the solar gravitational one; thus the 'Moon governs the gravitational tide'. The two components are superimposed at times of full and new Moon and are out of phase at the intervening lunar phases. Therefore, the amplitudes are greatest at full Moon and new Moon. Amplitudes of both the lunar and solar components in the free ocean should be largest at the tropics and least at high latitude.

Owing to the rotation of the Earth, the tidal force at any point in the sea or air continually changes; thus 'the tide is a dynamical phenomenon'. During the 18th century and later, Newton's successors developed his dynamical astronomy of the solar system, and succeeded in explaining the planetary motions in almost every details. They began also to develop the theory of the tides, a task in which Laplace [1799-1830] took a leading role. The subject of Laplace's tidal theory will be discussed later in this chapter.

(2) Ocean tides are always 12 hour period - why can atmosphere can sustain other periods (e.g., 24, 12, 8,...hours) ?

2.1.2 The barometric pressure variation and the possible relevance of thermal heating

The tides can be gauged by measuring the changing height of the water surface. The air tides cannot be measured in this way because the atmosphere has no such clearly defined boundaries. The alternative is to use a barometer at the bottom of the aerial ocean. The vertical accelerations of the air are so small that the barometer effectively measures the weight of the overlying air. To detect the atmospheric tide, records of sea level atmospheric pressure must be averaged over long periods in order to eliminate the large pressure changes associated with weather and to separate the lunar and solar effects. An above-average barometer reading implies a high tide of air whereas the low tide produces a low barometer reading [Beer, 1974].

Newton realized that the tidal forces must affect the atmosphere as well as the oceans, but thought that the atmosphere tides would be too small to be observed. Given the amount of data available in northern Europe in the 17 th century, he was certainly correct. The situation is demonstrated in Figure 2.2, which shows time series for surface pressure at both Potsdam (52° N - mid-latitude) and Batavia (6° S - low-latitude) during November 1919 [Bartels, 1928]. By analogy with the ocean tides one would expect a rise and fall of the barometer with a lunar semidiurnal period. Clearly, in the tropics (at Batavia) the barometer does show a marked semidiurnal variations (synoptic scale pressure perturbations are very small). In the mid-latitude, on the

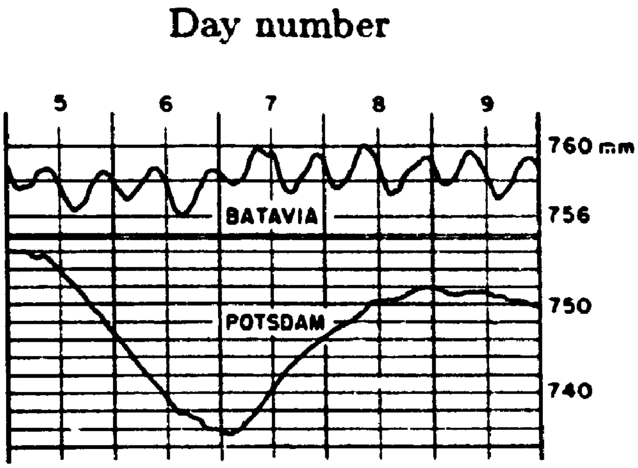

Figure 2.2: Barometric variations at Batavia (6° S) and Potsdam (52° N) during November 1919. After Bartels [1928].

other hand, whatever tiny tide might exist is swamped by large irregular variations, associated with weather changes; that is, planetary waves dominate at mid-latitudes. These observations revealed that the lunar semidiurnal tide which is gravitational in origin are extremely small; somewhat less than 10 Pa (0.1 mb), compared with the observed semidiurnal tide which is considerably larger, about 1.5×10^2 Pa (1.5 mb).

We shall see later, however, that these atmospheric surface pressure tides are primarily driven by heating effects of the Sun rather than by the gravitational effects of either Sun or Moon, and the equatorial barometers show this solar semidiurnal variation (see Figure 2.2). Laplace [1799] was already aware of this observational fact and he quite properly concluded that the atmospheric tide was due to the thermal action of the Sun. As the heating effect of the Sun has a 24-hour periodicity one would expect the solar diurnal tide to dominate. This is not what would be expected. This discrepancy will be dealt with in the following subsections.

(3) Why is the semidiurnal surface pressure oscillation stronger and more regular than the diurnal oscillation (Figure 2.2) ?

2.1.3 Kelvin's resonance theory

Lord Kelvin [1882] recognized the paradoxical character of these early observations, and he consequently attributed the solar semidiurnal tide not to gravitational effects at all, but to thermal excitation of the atmosphere through absorption of solar radiation. The essence of the paradox is as follows: Gravitational tides are semidiurnal due to the intrinsic semidiurnal character of the forcing (Section 2.1.1); if, however, atmospheric tides are thermally forced, then one would expect a predominantly diurnal periodicity to dominate (because the Sun appears every 24 hours). Why then is the response still predominantly semidiurnal ?

Historically there have been many attempts to explain the dominance of the semidiurnal tide in terms of the resonance theory. However, development of this idea in a quantitatively satisfactory manner proved to be elusive and difficult. Kelvin put forward the hypothesis that the atmosphere had a suitable free oscillation with a period very near to 12 hours. This resonance hypothesis dominated thinking on atmospheric tides for almost seventy years [Margules, 1890, 1892, 1893; Rayleigh, 1890]. Theoretical work centered on the search for the atmospheric free oscillation. Margules [1890] showed that an atmosphere with an equivalent depth of 7.85 km would produce a free oscillation with a period near to 12 hours. The physical and mathematical meaning of 'atmospheric equivalent depth' will be explained when we turn to the theory of atmospheric tides. The atmospheric equivalent depth depends on its thermal structure. In the late 19 th century, this structure was largely unknown and most of the theoretical works were mainly based on using crude and unrealistic (in view of today's knowledge) assumptions.

2.1.4 More realistic atmospheric models

Lamb [1910, 1916] made an important extension of Laplace theory of waves in an isothermal atmosphere. He investigated the matter more systematically and found that for either an isothermal basic state wherein density variations occur isothermally (Laplace's case), or for an atmosphere with a basic state with an adiabatic lapse rate, the equivalent depth was very nearly resonant. Lamb also showed that when the basic state temperature varied linearly with height, but not adiabatically, the atmosphere had an infinite number of equivalent depths - thus greatly increasing the possibilities for resonance. However, the impression persisted widely for over twenty years that for any type of atmosphere there is one value of atmospheric equivalent depth. Another suggestion due to Lamb was that the solar semidiurnal tide might indeed be gravitationally forced. His point was that such forcing would require such a degree of resonance to produce the observed tide that it would actually distinguish between the solar semidiurnal period (12 hours) and the lunar semidiurnal period (12 hr 26 min). Lamb, himself, noted at least two problems with this suggestion. First, of course, was the intrinsic unlikelihood of the atmosphere being so highly tuned. The second reason was that the phase of the observed surface pressure tide led rather than lagged the phase of the Sun. This was opposite to what calculations showed. Chapman [1924] argued that the resonance theory might still be correct if thermal forcing was of the same magnitude as gravitational forcing. With this rather coarse fix, the resonance theory was largely accepted for the next eight years. This situation changed dramatically with the work of Taylor and Pekeris.

2.1.5 Doubts about resonance theory

Whipple [1918] and Taylor [1932] were led to doubt the validity of the resonance hypothesis, despite the strength of the general arguments in its favour. Taylor noted that an atmosphere with an equivalent depth h should propagate small-scale atmospheric disturbances, such as would be generated by explosions, earthquakes, etc., at a speed $\sqrt{gh}$. Using data from the Krakatoa volcanic eruption of 1883, he showed that the atmospheric pulse travelled at a speed of 319 m/s, corresponding to $h = 10.4$ km, a value markedly too far from 7.85 km to produce resonance nearly equal to 12 hours. As realized later in 1936, Taylor returned to the Lamb's earlier result and proved its validity (though more rigorously) that the atmosphere might have several equivalent depths [Taylor, 1936]. This allowed some hope for the, by now much modified, Kelvin resonance hypothesis. This hope received an immense boost from the work of Pekeris [1937].

2.1.6 Temperature distribution and renewed hope in the resonance theory

Pekeris examined a variety of complicated basic states in order to see what distribution of temperature would support an equivalent depth of 7.85 km. The distribution he found was one where the temperature decreased with height as observed in the troposphere; above the tropopause ($\sim$ 12 km) the temperature increased with height to a high value (350° K) near 50 km, and then decreased upwards to a low value. It should be noted that in the mid-1930s we had no direct measurements of upper atmosphere temperature. This was in agreement with the temperature distribution proposed by Martyn and Pulley [1936], on the basis of then recent meteor and anomalous sound data. It was a remarkable achievement that Pekeris had deduced the atmosphere's complete thermal structure from tidal data at the Earth's surface, simply by assuming resonance. He showed that the atmosphere could oscillate in ways corresponding to two equivalent depths of 10.4 km and 7.85 km, subject to certain condition. For the next fifteen years following Pekeris's remarkable work, most research on this subject was devoted to the refinement and interpretation of Pekeris's work [e.g., Weekes and Wilkes, 1947]. Subsequent global analyses of this research were comprehensively reviewed in a monograph by Wilkes [1949]. However, once more accurate upper atmospheric temperature determinations became available, the atmosphere was seen to no longer have a second equivalent depth, and it was also clear that the magnification of the solar semidiurnal tide was no longer sufficient to account for the observed semidiurnal tide on the basis of any realistic combination of gravitational excitation and excitation due to the upward diffusion of the daily variation of surface temperature [Jacchia and Kopal, 1951]. With the demise of the resonance theory, the search began for additional thermal sources.

2.1.7 Abandonment of the resonance theory and emergence of thermally generating tides

Even though various resurgences of the resonance theory appear from time to time [Covez, 1971] it is most probable that atmospheric thermal sources are able to explain the amplitude of the solar semidiurnal tide. According to this viewpoint we would consider the diurnal tide as being suppressed, rather than the simidiurnal tide as enhanced. Although most of the Sun's radiation is absorbed by the Earth's surface, about 10 percent is absorbed directly by the atmosphere, and this appeared a likely source of excitation. Siebert [1961] pointed out that insolation absorption by water vapour in the troposphere could account for one third of the observed semidiurnal surface pressure oscillation. This was far more than could be accounted for by gravitational excitation or surface heating. Shortly afterwards Butler and Small [1963] showed that heating by ozone absorption in the region of 50 km could account for the remaining two-thirds of the surface semidiurnal oscillation.

At this juncture one is forced to return to the original question that was put by Lord Kelvin in 1882: Why is the semidiurnal oscillation stronger than the diurnal one ? The situation had become more complicated with the increased data available by the mid-1960s. Observational and theoretical interest in atmospheric tides continued over the next ten years. A comprehensive review was undertaken by Chapman and Lindzen [1970]. Lindzen [1967, 1968] carried out theoretical calculations for the atmospheric tides, and we will provide satisfactory answers for the observed features in the following section.

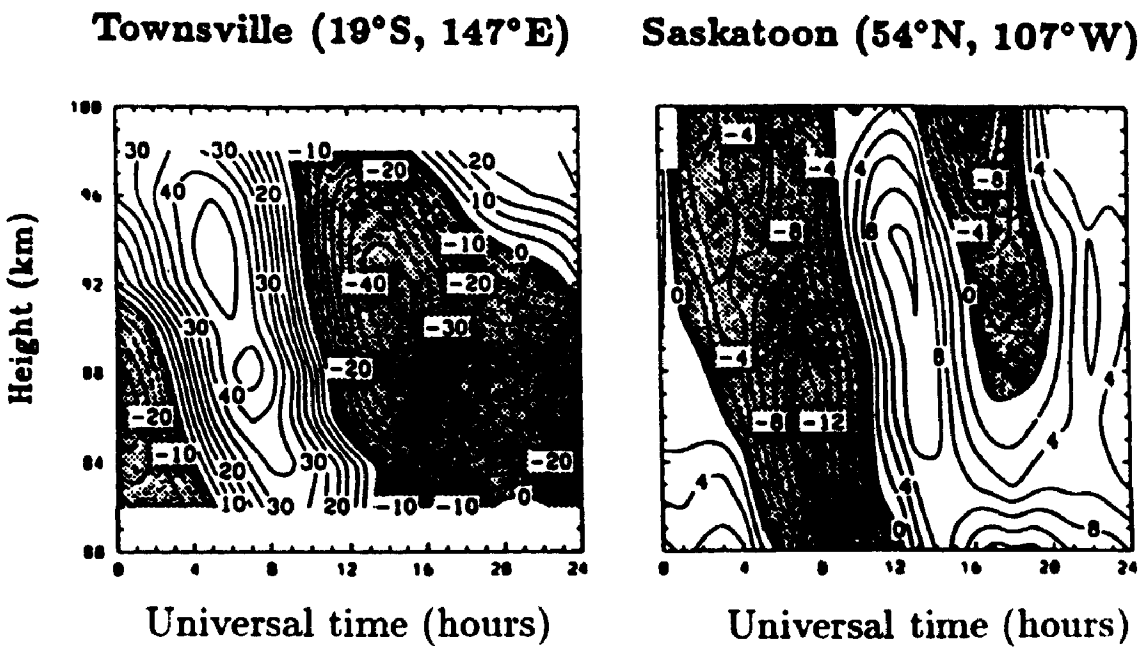

Figure 2.3: Height-local time contours depicting average northward winds during the period March 18-27, 1979, over Townsville, Australia (19° S, 147° E) and Saskatoon, Canada (52° N, 107° W), as measured by the spaced antenna method [after Forbes, 1993].

In summary, atmospheric tides are excited not only by the gravitational forces of the Moon and Sun but also by the diurnal periodicity of the solar heating. These thermally driven atmospheric tides are several orders of magnitude larger than gravitationally induced tidal motions in the atmosphere, in marked contrast to the situation in the oceans where the gravitational tide predominates.

Figure 2.3 illustrates height/local time contours representing average meridional wind patterns between 80 and 100 km over Townsville, Australia (19° S, 147° E) and Saskatoon, Canada (52° N, 107° W) during the period March 18-27, 1979. Note first of all that the character is mainly diurnal over Townsville (24 hour harmonic dominates), and mainly semidiurnal over Saskatoon (12 hour harmonic dominates).

The questions we wish to focus on are:

(4) Why is the semidiurnal oscillation dominant in the upper atmosphere at mid-high latitudes (Figure 2.3) ?

(5) Why is the diurnal oscillation dominant in the upper atmosphere at low latitudes (Figure 2.3) ?

(6) Why is that phase progression is downwards (i.e. the wind contours tilt to the

left in Figure 2.3) ? And, given that there are no significant heat sources at these heights, why is it that these tidal oscillations assume such a prominent role in the meteorology of the mesosphere and lower thermosphere ?

2.2 Quantitative theory of atmospheric tides

Atmospheric tides are global scale oscillations in temperature, wind, density and pressure at periods which are subharmonics of a solar or lunar day. Tides are classified according to their propagation with respect to the Earth's surface; we thus have migrating and non-migrating tides.

By migrating tides we mean tides which are fixed in phase to local time; i.e., tides which follow the apparent motion of the Sun or Moon. Migrating tides are due to the gravitational attraction of the atmosphere by the Moon and the Sun, as well as solar heating of the atmosphere [e.g., Lindzen, 1974; Grove, 1976]. The gravitational effects of the Moon and Sun are in general much weaker than the thermal effects. There is virtually no way of isolating solar gravitational tides from solar thermal tides in the data. Lunar tides, with their different period, are distinguishable. The solar heating is differential due to the spherical shape of the Earth, and therefore creates thermodynamic imbalance. The solar thermal tidal oscillations result as the atmosphere attempts to return to thermodynamic equilibrium. These tidal oscillations must propagate westward with respect to the Earth's surface in order to maintain a fixed phase relationship with their driving force.

Non-migrating tides, on the other hand, do not follow the apparent motion of the Sun. Non-migrating tides are associated with local topography and geographically fixed tropospheric heat sources. Non-migrating tides are of no relevance to this classical tidal theory and hence will not be considered further in the following subsection. We will return to this subject in Sections 2.2.3 and 2.5.

The theory of atmospheric tides has two main parts. The first is the study of the sources of periodic excitation; this includes a detailed consideration of atmospheric composition and chemistry, the solar spectrum, molecular absorption, radiative transfer, turbulent transfer, and other topics. The second is the calculation of the atmospheric response to the excitation. This could in principle concern all the problems involved in the general circulation of the entire atmosphere, including non-adiabatic, orographic, non-linear, hydromagnetic, complex wave-wave interactions, and other types of process. It is not possible to be so comprehensive in this review, and we shall here concern ourselves with topics relevant to the middle atmosphere.

2.2.1 Classical tidal theory

The theory of tidal oscillations has been known for many years and can be found in numerous references [Wilkes, 1949; Chapman, 1951; Kertz, 1957; Seibert, 1961; Craig, 1965; Lindzen, 1967; Chapman and Lindzen, 1970; Lindzen, 1974, 1990; Beer, 1974; Kato, 1980; Forbes, 1984; Andrews et al., 1987; Volland, 1988]. The objective of this section is not to derive classical tidal theory, but to reiterate some of the simplifying assumptions used in developing an analytical solution and to state the equations and terminology which define the foundation from which the rest of this dissertation is developed. We begin by describing the equations for the atmospheric response to arbitrary excitations - invoking numerous assumptions and approximations. The equations and discussion in this section mainly follow Chapman and Lindzen [1970], Lindzen [1974, 1990], Beer [1974], Holton [1975], Andrews et al. [1987], Volland [1988], and Forbes [1993], in addition to the references given.

Assumptions, approximations and equations

The main assumptions used in tidal theory are listed below.

1. The motion of the atmosphere may be described by the Navier-Stokes equations for a compressible gas. It is convenient to express these equations in spherical coordinates for a frame of reference rotating with the Earth.

2. The atmosphere is a perfect gas, $p = \rho R_* T$, where p, ρ, T, and R_* denote the pressure, density, temperature (Kelvin), and gas constant. This is nearly true up to $\sim$ 90 km. $R_* = 287.1$ J kg^{-1} K^{-1} at the ground, 287.8 J kg^{-1} K^{-1} at 100 km, 316.0 J kg^{-1} K^{-1} at 200 km - 10% error is introduced.

3. The atmosphere is thin compared with Earth's radius. Thus, expressing the distance from the Earth's center as $r = a + z$, where a = radius of the Earth, and z = distance from Earth's surface. We neglect terms in our equations whose order is $(\frac{z}{a})$.

4. The gravitational acceleration, g, is treated as constant; at $z = 100$ km the error is only 3%. This implies that the error involved within the lower and middle atmosphere is only a few percent.

5. We neglect the component of the Earth's rotation vector parallel to the Earth's surface; this assumption appears to be valid for oscillations of planetary scales, and tidal periods (very much more than the Brunt-Väisälä period) [Phillips, 1968].

6. The atmosphere is taken to be in hydrostatic equilibrium. This implies that vertical accelerations are small compared with $g = 9.8 \text{ ms}^{-2}$, so that $\frac{\partial p}{\partial z} = -\rho g$ [Yanowitch, 1966]. Only the vertical pressure gradient and the gravitational acceleration are retained in the vertical equation of motion. This is an excellent approximation for long-period and large-scale motions (e.g., tides). Acoustic waves are eliminated by this approximation.

7. The Earth is assumed to be sphere; the Earth's ellipticity is ignored.

None of the above approximations seems to constitute serious limitations on atmospheric tidal theory. The following are more significant approximations.

8. The Earth's topography is ignored; land-sea distribution, mountain ranges, etc. The Earth's surface is assumed to be a smoothed rigid sphere where the vertical velocity w is zero. The consequence is that the distribution of radiation absorbing gas is independent of longitude.

At this point our equations are the following:

$$\rho(\frac{\partial u}{\partial t} + \vec{u}\cdot\nabla u + \frac{wu}{a} - uv\frac{\cot\theta}{a} + 2\omega v\cos\theta) = -\frac{1}{a\sin\theta}\frac{\partial p}{\partial\phi} - \frac{\rho}{a\sin\theta}\frac{\partial\Omega}{\partial\phi} - F_\phi \quad (2.1)$$

$$\rho(\frac{\partial v}{\partial t} + \vec{u}\cdot\nabla v + \frac{wv}{a} - u^2\frac{\cot\theta}{a} - 2\omega u\cos\theta) = -\frac{1}{a}\frac{\partial p}{\partial\theta} - \frac{\rho}{a}\frac{\partial\Omega}{\partial\theta} - F_\theta \quad (2.2)$$

$$\frac{\partial p}{\partial z} = -\rho\frac{\partial\Omega}{\partial z} \quad (2.3)$$

$$\frac{\partial\rho}{\partial t} + \vec{u}\cdot\nabla\rho + \rho\nabla\cdot\vec{u} = 0 \quad (2.4)$$

$$\rho c_V\frac{dT}{dt} = R_*T\frac{d\rho}{dt} + J - C \quad (2.5)$$

$$p = \rho R_*T \quad (2.6)$$

where:

$$\vec{u}\cdot\nabla = \frac{v}{a}\frac{\partial}{\partial\theta} + \frac{u}{a\,\sin\,\theta}\frac{\partial}{\partial\phi} + w\frac{\partial}{\partial z}; \qquad\qquad \vec{u} = (u, v, w)$$

$$\nabla\cdot\vec{u} = \frac{1}{a\,\sin\,\theta}\frac{\partial}{\partial\theta}(v\,\sin\,\theta) + \frac{1}{a\,\sin\,\theta}\frac{\partial u}{\partial\phi} + \frac{\partial w}{\partial z}$$

$$\frac{d}{dt} = \frac{\partial}{\partial t} + \vec{u}\cdot\nabla$$

where

θ = colatitude
ϕ = longitude
t = time
u = eastward velocity
v = northward velocity
w = vertical velocity
T = temperature
p = pressure

ρ = density
Ω = gravitational potential
ω = Earth's rotation rate
R_* = gas constant
c_V = heat capacity at constant volume
F_θ = frictional force in θ direction
F_ϕ = frictional force in ϕ direction
J = thermotidal heating
C = heat diffusion and radiative cooling

Here (2.1) and (2.2) are the equations for eastward and northward momentum (Navier-Stokes equations in spherical coordinates for a frame of reference rotating with the Earth) respectively; (2.3) is the hydrostatic pressure relation; (2.4) is the continuity equation; (2.5) is the thermodynamic energy equation; (2.6) is the perfect gas law. We next adapt the following approximations, which are significant simplifications.

9. Dissipative processes such as molecular and turbulent viscosity and conductivity, ion drag, and infrared radiative transfer are ignored; F_θ, F_ϕ and C are neglected.
10. Tidal oscillations are considered as linearizable perturbations on a mean flow:

$$\begin{bmatrix} u \\ v \\ w \\ T \\ p \\ \rho \end{bmatrix} = \underset{\substack{\text{mean}\\ \text{fields}}}{\begin{bmatrix} u_0 \\ v_0 \\ w_0 \\ T_0 \\ p_0 \\ \rho_0 \end{bmatrix}} + \underset{\substack{\text{tidal}\\ \text{oscillations}}}{\begin{bmatrix} u' \\ v' \\ w' \\ \delta T \\ \delta p \\ \delta\rho \end{bmatrix}} \tag{2.7}$$

Now Ω is considered to be of the form: $\Omega = \Omega_0(z) + \Omega'(\theta, \phi, z, t)$, where Ω' is a tidal forcing (potential due to the Sun and Moon). By 'linearizable' we mean that we may neglect quadratic and higher order terms in the tidal perturbations.

11. We assume that the atmospheric basic state is at rest. This implies that the zonal, meridional, and vertical prevailing winds are zero and the basic state of the atmosphere (i.e. $p_0(z)$, $\rho_0(z)$ and $T_0(z)$) are independent of latitude and longitude.

Having made all the above assumptions and/or approximations, we are left with a basic state where:

$$\frac{\partial p_0}{\partial z} = -\rho_0 g \tag{2.8}$$

$$p_0 = \rho_0 R_* T_0 \tag{2.9}$$

From equations (2.8) and (2.9) we then obtain:

$$p_0 = p_0(0) e^{-x} \tag{2.10}$$

$$\rho_0 = \frac{p_0}{gH} \tag{2.11}$$

where: T_0 is the basic temperature distribution.

$$H = \frac{R_* T_0}{g} \tag{2.12}$$

$$x = \int_0^z \frac{dz}{H} \tag{2.13}$$

H is known as the local scale height while x is the height in the scale heights. We now investigate the equations based on the above approximations/assumptions. The equations (2.1)-(2.6) may be written as perturbation equations, so that we then have:

$$\frac{\partial u'}{\partial t} + 2\omega v' \cos\theta = -\frac{1}{a \sin\theta} \frac{\partial}{\partial \phi}\left(\frac{\delta p}{\rho_0} + \Omega'\right) \tag{2.14}$$

$$\frac{\partial v'}{\partial t} - 2\omega u' \cos\theta = -\frac{1}{a} \frac{\partial}{\partial \theta}\left(\frac{\delta p}{\rho_0} + \Omega'\right) \tag{2.15}$$

$$\frac{\partial \delta p}{\partial z} = -g\delta\rho - \rho_0 \frac{\partial \Omega'}{\partial z} \qquad (2.16)$$

$$\frac{d\rho}{dt} + \rho_0 \chi = 0 \qquad (2.17)$$

$$c_V \frac{dT}{dt} = \frac{R_* T_0}{\rho_0}\frac{d\rho}{dt} + J' \qquad (2.18)$$

$$\frac{\delta p}{p_0} = \frac{\delta \rho}{\rho_0} + \frac{\delta T}{T_0} \qquad (2.19)$$

where: $\chi = \nabla \cdot \vec{u}'$ and $\vec{u}' = (u', v', w')$

Our aim is reduce equations (2.14)-(2.19) to a single equation in a single unknown. First we eliminate δT using (2.19). (2.18) becomes:

$$\frac{dp}{dt} = \gamma g H \frac{d\rho}{dt} + \rho_0(\gamma - 1)J' \qquad (2.20)$$

where: $\gamma = \frac{c_P}{c_V}$ and $c_P = R_* + c_V$.

In tidal theory we are generally concerned with perturbations which are periodic in time and longitude. Assume the perturbations to consist of longitudinally propagating waves of zonal wavenumber s and frequency σ. Then using the form of complex quantities we have:

$$e^{i(s\phi - \sigma t)}; \qquad \frac{\partial}{\partial t} \rightarrow -i\sigma; \qquad \frac{\partial}{\partial \phi} \rightarrow is \qquad (2.21)$$

where: $\tau = \frac{2\pi}{\sigma}$; τ (expressed in solar or lunar day/s) is the period of the wave oscillation, and $s = 0, \pm 1, \pm 2$, etc. is the integer which determines the integral number of oscillations around a circle of latitude. This $(s\phi - \sigma t)$ form for the phase is chosen so that positive values for σ correspond to eastward propagating waves and negative values to westward propagating waves (i.e. the real part of (2.21) is $\cos(s\phi - \sigma t)$ and the crest of the wave occurs when $\phi = \sigma t/s$).

Using (2.21) we may solve for (2.14) and (2.15) for u' and v':

$$u' = \frac{i\sigma}{4a^2\omega^2(f^2 - \cos^2\theta)}\left(\frac{\partial}{\partial \theta} + \frac{s\cot\theta}{f}\right)\left(\frac{\delta p}{\rho_0} + \Omega'\right) \qquad (2.22)$$

$$v' = \frac{-\sigma}{4a^2\omega^2(f^2-\cos^2\theta)}\left(\frac{\cos\theta}{f}\frac{\partial}{\partial\theta} + \frac{s}{\sin\theta}\right)\left(\frac{\delta p}{\rho_0} + \Omega'\right) \tag{2.23}$$

where: $f = \frac{\sigma}{2\omega}$.

Equations (2.22) and (2.23) appear to suggest that u' and v' become infinite when $f = \pm\cos\theta$. However, this condition is never reached in reality. Now u' and v' enter the remaining equations only through the velocity divergence, $\chi = \nabla \cdot \vec{u}'$, which now can be written, using (2.22) and (2.23):

$$\chi = \frac{\imath\sigma}{4a^2\omega^2}F\left(\frac{\delta p}{\rho_0} + \Omega'\right) + \frac{\partial w'}{\partial z} \tag{2.24}$$

where:

$$F = \frac{1}{\sin\theta}\frac{\partial}{\partial\theta}\left(\frac{\sin\theta}{f^2-\cos^2\theta}\frac{\partial}{\partial\theta}\right) - \frac{1}{f^2-\cos^2\theta}\left(\frac{s}{f}\frac{f^2+\cos^2\theta}{f^2-\cos^2\theta} + \frac{s^2}{\sin^2\theta}\right) \tag{2.25}$$

Now the remaining equations (2.16), (2.17), (2.20), and (2.24) are four equations in four unknowns, δp, χ, $\delta\rho$ and w. As it turns out, the most convenient variable to solve for is:

$$G = -\frac{1}{\gamma p_0}\frac{dp}{dt} \tag{2.26}$$

After some manipulations, one obtains a single equation for G alone.

$$H\frac{\partial^2 G}{\partial z^2} + \left(\frac{dH}{dz} - 1\right)\frac{\partial G}{\partial z} = \frac{g}{4a^2\omega^2}F\left[\left(\frac{dH}{dz} + \kappa\right)G - \frac{\kappa J}{\gamma g H}\right] \tag{2.27}$$

where: $\kappa = \frac{\gamma-1}{\gamma}$. This may be solved by the method of separation of variables. We assume that:

$$G(\theta, z) = \sum_n L_n(z)\Theta_n(\theta) \tag{2.28}$$

and, moreover, that the set $\{\Theta_n\}$ is complete for $0 \leq \theta \leq \pi$. Then J may be expanded in terms of the function Θ_n as:

$$J(\theta, z) = \sum_n J_n(z)\Theta_n(\theta) \tag{2.29}$$

Substituting (2.28) and (2.29) into (2.27) yields the following set of two equations for Θ_n and L_n:

$$F(\Theta_n) = -\frac{4a^2\omega^2}{gh_n}\Theta_n \tag{2.30}$$

and:

$$H\frac{\partial^2 L_n}{\partial z^2} + \left(\frac{dH}{dz} - 1\right)\frac{\partial L_n}{\partial z} + \frac{1}{h_n}\left(\frac{dH}{dz} + \kappa\right)L_n = \frac{\kappa}{\gamma g H h_n}J_n \tag{2.31}$$

where, $\epsilon_n = \frac{4a^2\omega^2}{gh_n}$ is the separation constant. Laplace [1799, 1825] first derived equation (2.30), which is therefore called Laplace's tidal equation. His work was fundamental in concept and in his honour some of the terminology is based on his original work. The boundary conditions on $\{\Theta_n\}$ are that they be bounded at the poles (i.e., at $\theta = 0, \pi$). It defines an eigenfunction-eigenvalue problem, where the eigenfunctions are known as Hough functions, and the eigenvalues are expressed in terms of h_n. Historically h_n is referred to as the "equivalent depth". This nomenclature originates from the first appearance of equation (2.30) in connection with the ocean tide problem where h is the ocean depth [Taylor, 1936]. The full solution associated with a given Hough function is called a Hough mode.

Equation (2.31) is an inhomogeneous equation which, given two boundary conditions, has a unique vertical structure for a given Hough mode. Equation (2.31) is often called the vertical structure equation. We will now examine solutions to the vertical structure equation and Laplace's tidal equation which are coupled through the equivalent depth, h_n.

2.2.2 Vertical structure equation

We follow the common practice of reducing (2.31) to canonical form by a change of variables. Letting $x = \frac{z}{H}$ and $L_n = e^{x/2}y_n$, then (2.31) becomes:

$$\frac{\partial^2 y_n}{\partial x^2} + \left[\frac{1}{h_n}\left(\kappa H + \frac{dH}{dx}\right) - \frac{1}{4}\right]y_n = \frac{\kappa J_n}{\gamma g h_n}e^{-x/2} \tag{2.32}$$

The solution of (2.32) requires two boundary conditions: (1) lower boundary condition; (2) upper boundary condition. Given our assumption of a smooth spherical Earth, the lower boundary condition requires that $w = 0$ at $x = z = 0$. After some manipulations, this implies that at $x = 0$:

$$\frac{dy_n}{dx} + \left(\frac{H}{h_n} - \frac{1}{2}\right)y_n = \frac{i\sigma}{\gamma g h_n}\Omega_n \tag{2.33}$$

Details of the above expression can be found in Chapman and Lindzen [1970], and Lindzen [1974].

For the upper boundary condition one generally requires bounded and radiative conditions. For the general solution of this differential equation in an isothermal atmosphere, where $H = constant$, (2.32) becomes:

$$\frac{\partial^2 y_n}{\partial x^2} + \alpha^2 y_n = F(x) \tag{2.34}$$

where:

$$\alpha^2 = \frac{\kappa H}{h_n} - \frac{1}{4} \tag{2.35}$$

and:

$$F(x) = \frac{\kappa J_n}{\gamma g h_n} e^{-x/2} \tag{2.36}$$

Now we shall examine the two cases where (I) $F(x) \neq 0$ (forced solution) (II) $F(x) = 0$ (free solution).

(I) 'FORCED' SOLUTION

(a) "Evanescent" or "Trapped Wave": When $F(x) \neq 0$. there are two possibilities; (1) $h_n < 0$ or (2) $h_n > 4\kappa H$, then $\alpha^2 < 0$. The form of the solution is:

$$y_n \sim Ae^{\beta x} + Be^{-\beta x} \tag{2.37}$$

where:

$$\beta = \sqrt{\frac{1}{4} - \frac{\kappa H}{h_n}} < \frac{1}{2} \tag{2.38}$$

For the upper boundary condition one generally requires that the kinetic energy density shall remains bounded as $z \to \infty$. This in turn, requires that $y_n(x)$ remains bounded as $x \to \infty$. This implies that a bounded solution above the source region:

$$y_n \sim e^{-\beta x} \tag{2.39}$$

In this case waves are referred to as evanescent or trapped since the wave oscillations are more or less confined to the region of excitation. The vertical energy propagation is inhibited and amplitudes will decay with height.

(b) "Propagating" Wave: When $F(x) \neq 0$, and $0 < h_n < 4\kappa H$, then $\alpha^2 > 0$. The form of the solution is:

$$y_n \sim Ce^{i\alpha x} + De^{-i\alpha x} \tag{2.40}$$

where

$$\alpha^2 = \frac{\kappa H}{h_n} - \frac{1}{4} \tag{2.41}$$

In this case y_n is bounded for any choice of C and D. The term $e^{i\alpha x}$ is associated with upward propagation of energy and $e^{-i\alpha x}$ downward propagation of energy. Thus $D = 0$ if there is no energy sources at $x = \infty$ (there will be no incoming energy from infinity). It is generally referred to as radiation condition ($C_{gx} > 0$) at $x = \infty$ implies:

$$y_n \sim e^{\pm i|\alpha|x} \tag{2.42}$$

where (+, -) corresponds to (westward, eastward) propagating waves (see also Section 2.4). In this case solutions are oscillatory (roughly sinusoidal) in the vertical. This is the so-called propagating solution, where the wave propagates away from the source region. The vertical propagation of energy is possible and amplitudes will grow exponentially with height. We use the radiation conditions in our calculations. However, as shown later, it is not always applicable. In particular, it is possible for viscosity and conductivity, both of which increase as $1/\rho$ to cause reflections of tides at great altitudes if α is very small.

(II) 'FREE' SOLUTION

Resonance theory

At this stage it becomes possible to try and determine whether the gravitational forcing (Ω) or the thermal forcing (J) is the dominant mechanism responsible for the tides actually observed in the Earth's atmosphere. To do this, we draw upon an analogy with the theory of mechanical oscillations which informs us that a system has a set of free oscillations. If the period of the forcing matches the free period then there will be a resonant amplification of the system [Beer, 1974].

Rather than find free periods, we shall find the equivalent depths for which (2.32) has analytic solutions subject to the boundary condition (2.33) with $\Omega_n = 0$ and the radiation condition with $J_n = 0$. If this equivalent depth matches one of the equivalent depths obtained from the eigenvalues of Laplace's tidal equation, which is independent of the driving mechanism, then that particular mode will be amplified.

For realistic atmosphere and hydrostatic waves, the atmosphere has only one equivalent depth, 10.4 km (see history). If h_n is equal to the equivalent depth of the atmosphere, then we have a resonance.

When $F(x) = 0$, the only nontrivial solution satisfying boundedness and $w = 0$ at $z = 0$ is :

$$y_n \sim e^{(\kappa - 1/2)x} \tag{2.43}$$

and

$$h_n = \frac{H}{1 - \kappa} \tag{2.44}$$

Incidently, it can be easily shown that the equivalent depth of an isothermal atmosphere is $h = \gamma H = 10.5$ km, where $\gamma = 1.4$ and $H \sim 7.5$ km (corresponding to $T_0 = 256$ K). This free (unforced) solution corresponds to a resonant response of the atmosphere. Note that the above solution implies

$$u \sim e^{\kappa x} \tag{2.45}$$

corresponding to energy (ρu^2) decay away from the surface while velocity and other wave fields increase exponentially (by a factor of 40 from the surface to 100 km). These waves are sometimes called 'Lamb' or 'edge' waves. Furthermore, for $h_n = 10.5$ km, α^2 is negative, implying a vertical flux of energy out of the atmosphere ($w = 0$) and no phase change with height. Without dissipation, such free oscillations would continue indefinitely without forcing [Lindzen and Blake, 1972].

2.2.3 Laplace tidal equation: Nomenclature and classification of modes

Solving equation (2.30) is a technical task which we will skip over (details may be found in Chapman and Lindzen, 1970]). However, we should note that all information about geometry and rotation is contained in h_n. Laplace's tidal equation (2.30) is often written as follows to emphasize the explicit dependences on s, σ and ϵ_n:

$$F_{s,\sigma}(\Theta_n^{s,\sigma}) = \epsilon_n^{s,\sigma}\Theta_n^{s,\sigma} \tag{2.46}$$

For each choice of s and σ, there exists a set of ϵ_n and Θ_n which satisfy (2.46). The ϵ_n^s and σ are generally related parametrically for a given s in diagrams like the one shown in Figure 2.4 for $s = 1$ (diagrams for $s = 2$ and $s = 3$ are very similar to Figure 2.4, and are not shown here, but can be found in Volland [1988]). Two families of curves are evident for either eastward-propagating ($\frac{\sigma}{s} > 0$) or westward-propagating ($\frac{\sigma}{s} < 0$) solutions. These are sometimes referred to as "Class I" or "Solutions of the First

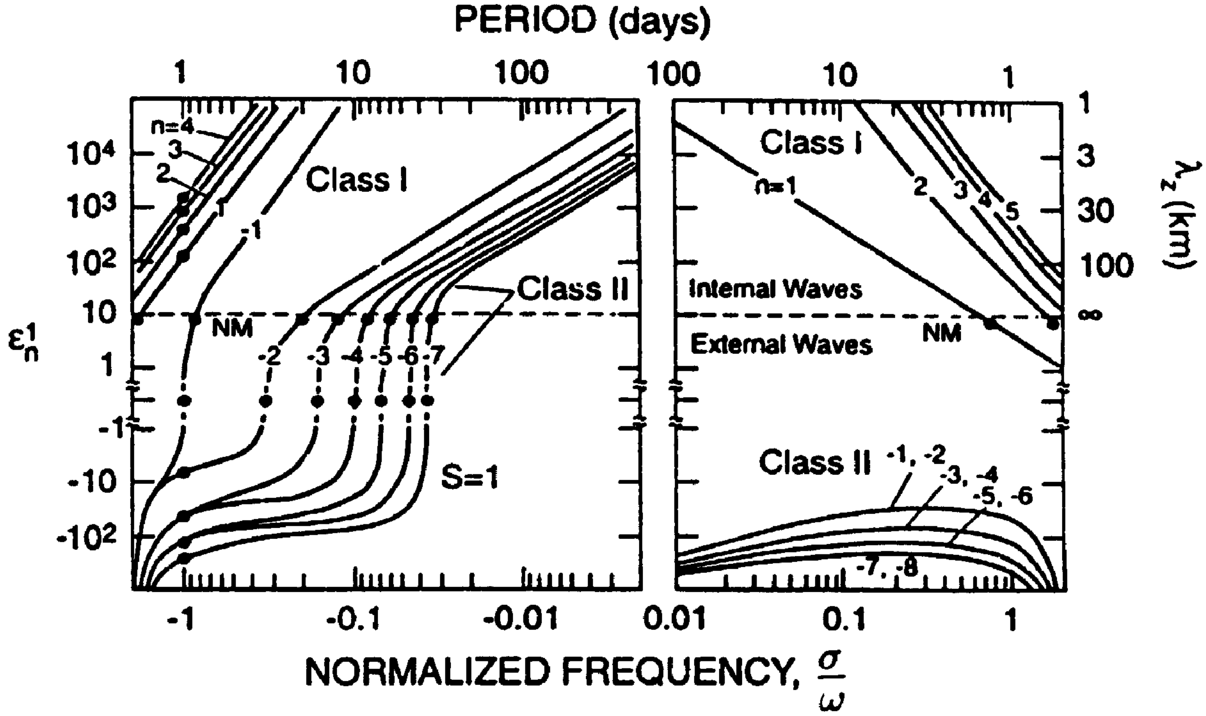

Figure 2.4: Eigenvalues ϵ_n^s of wave modes of zonal wavenumber $s = 1$ vs normalized frequency $\frac{\sigma}{\omega}$. Waves with positive (negative) frequencies propagate to the east (west). The dots corresponding to $\epsilon_n^1 = 0$ denote the so-called Rossby-Haurwitz waves. The dots corresponding to "NM" refer to the normal modes ($\epsilon \approx 8.4$). The vertical series of dots at $\frac{\sigma}{\omega} = -1.0$ define the ϵ_n^1 for the diurnal tide. The eastward propagating gravity-type (Class I) modes are 'Kelvin waves'. Figure and caption adapted from Volland [1988].

Kind" and "Class II" or "Solutions of the Second Kind". A more common usage is to refer to the first class as "gravity modes" and the second class as "Rossby", "rotational" or "planetary wave" modes. There are energy partitioning and other properties which differ between these two classes of solutions [Longuet-Higgins, 1968], but we will no concern ourselves with these issues. The remainder of this section will mainly use the terms "gravity" and "Rossby" to distinguish the wave types.

We note from Figure 2.4 some general features and properties. For instance, gravity (Class I) modes always have $\epsilon_n > 0$, whether they are westward-propagating or eastward-propagating. On the other hand, Rossby (Class II) modes only possess $\epsilon_n > 0$ for westward-propagating waves; in all other cases the Rossby modes have $\epsilon_n < 0$. From the expression for α^2 in (2.34), for negative or sufficiently small ϵ_n (or large h_n) the vertical structures are "trapped" or "evanescent", whereas for $\epsilon_n > 100$ solutions are propagating with vertical wavelengths less than 100 km. Note that the (1,-1) mode in Figure 2.4 belongs to the Rossby mode Class for $\epsilon_n^1 < 10$ but joins the Gravity mode family of curves for $\epsilon_n^1 > 10$. This is so called mixed Rossby-gravity wave. This mode exists for higher wavenumber as well. The eastward-propagating ($\sigma > 0$) gravity modes in Figure 2.4 are referred to as Kelvin waves.

The collection of all Θ_n are eigenfunctions of Laplace tidal equation, and are called Hough functions in honour of the individual who pioneered their numerical computation [Hough, 1897, 1898]. Either the ϵ_n or the h_n (where $\epsilon_n = \frac{4\omega^2 a^2}{g h_n} \approx \frac{88\mathrm{km}}{\mathrm{h_n}}$) are referred to as eigenvalues of the system. Each eigenfunction/eigenvalue pair constitutes a "mode". It is common to refer to a particular mode as the Θ_n^s mode or just the (s, n) mode [Flattery, 1967]. A common nomenclature in identifying modes is to explicitly express s, the zonal wavenumber (i.e., the integral number of oscillations in 24 hour), and n, the meridional index or mode number (so-named since it provides information on the number of latitudinal nodes and symmetry characterizing Θ_n). The zonal wave number $s = 1$ is a westward propagating mode with a single sinusoid longitudinal structure. The $s = 1$ diurnal mode is called the *migrating* mode because the phase structure is constant with the phase of the Sun progressing westward around the Earth. All other zonal wavenumbers for the diurnal tide are called *non-migrating* modes. The effects of non-migrating modes on the migrating tidal modes will be discussed in more detail in Section 2.5. Positive values of n represent propagating modes (or gravity modes) which transport energy vertically. Negative values of n represent evanescent modes (or rotational or trapped modes) which do not freely propagate energy vertically and whose amplitude decays exponentially away from the height of excitation.

The semidiurnal symmetric gravitational modes are thus (2,2), (2,4),..., and antisymmetric (about the equator) propagating modes are (2,3), (2,5),.... For diurnal tides the corresponding symmetric and antisymmetric modes are (1,1), (1,3),..., and (1,2), (1,4),.... The symmetric and antisymmetric diurnal evanescent modes are designated by (1,-2), (1,-4),..., and (1,-1), (1,-3). As an example, the (1,-2) diurnal mode referred to as the "first symmetric trapped diurnal tide" and the (1,1) mode as the "first symmetric propagating diurnal tide".

Note also from Figure 2.4 that the (1,-2) can assume other periods; at the free mode value of $\epsilon_n = 8.4$ km ($h_n = 10.5$ km) for a 256 K isothermal atmosphere, the (1,-2) mode would represent the "5-day wave" ($\frac{\sigma}{\omega} \approx -0.20$). The above experience in locating the "5-day wave" alludes to two possible ways in which diagrams like Figure 2.4 can be utilized. For forced modes we generally know the frequency of forcing, σ; by drawing a vertical line at $\frac{\sigma}{\omega}$ on Figure 2.4, the points of intersection define the ϵ_n^1 values corresponding to the modes which comprise the response at that frequency. This provides information on the vertical structure of the forced response. The points of intersection corresponding to the diurnal tide ($\frac{\sigma}{\omega} = -1.0$) are indicated in Figure 2.4. We see that the response consists of a mixture of trapped ((1,-1), (1,-2),....) and propagating ((1,1), (1,2),....) modes, the latter with vertical wavelengths between 15 and 50 km. This means that some localized heating in the lower atmosphere will result in (a) several modes which propagate to higher levels, and (b) a response partially contained at the levels of excitation (The e-folding distance of the latter will depend on the value of ϵ_n). The degree to which the response falls into either of these categories is determined by how well the horizontal and vertical structures of these modes matches that of the forcing. Examination of the analog of Figure 2.4 for $s = 2$ (not shown here) would show the semidiurnal response ($\frac{\sigma}{\omega} = -2.0$) to consist only of propagating modes (ϵ_n); Rossby modes at frequencies higher than 2ω do not exist.

For free (unforced) modes, we know that $\epsilon_n = 8.4$ for an isothermal atmosphere at 256 K. In Figure 2.4 the horizontal line defines the free or normal modes that exists for $s = 1$. Looking down from the points of intersection (labelled "NM"), we can then infer the frequencies or periods of the normal modes. For $s = 1$, these occur approximately at periods of 28 hours, 5 days, 8 days, and 12 days, and so on. According to our present nomenclature, we may refer to the last three of these, respectively, as the (1,-2), (1,-3), and (1,-4) westward-propagating Rossby modes of zonal wavenumber one. The 28-hour mode is a mixed Rossby-gravity mode, and is designated (1,-1). At periods of order 1 day or less, this mode behaves like a Rossby mode; at longer periods, it is gravity-like (i.e. propagating) in its character. Similarly,

Wave	(s,n)	h_n (km)	λ_z (km)	Additional Descriptors
Diurnal tide	(1,1)	0.6906	27.9	Gravity: first symmetric propagating
Diurnal tide	(1,2)	0.2384	15.9	Gravity: first asymmetric propagating
Diurnal tide	(1,3)	0.1203	11.2	Gravity: second symmetric propagating
Diurnal tide	(1,-1)	803.3560		Rotational: first asymmetric trapped
Diurnal tide	(1,-2)	-12.2703		Rotational: first symmetric trapped
Diurnal tide	(1,-4)	-1.7581		Rotational: second symmetric trapped
Semidiurnal tide	(2,2)	7.8519	311.0	Gravity: first symmetric propagating
Semidiurnal tide	(2,3)	3.6665	81.4	Gravity: first asymmetric propagating
Semidiurnal tide	(2,4)	2.1098	53.8	Gravity: second symmetric propagating
Semidiurnal tide	(2,5)	1.3671	41.0	Gravity: second asymmetric propagating
Semidiurnal tide	(2,6)	0.9565	33.4	Gravity: third symmetric propagating

Table 2.1: Nomenclatures and other data for various common westward propagating waves in the middle and upper atmosphere. The column (s,n) indicates the nomenclature used in the present work, and in Volland [1988] and Chapman and Lindzen [1970]. The columns indicate the equivalent depth for each mode [Chapman and Lindzen, 1970], h_n, propagating-mode vertical wavelengths λ_z for an isothermal atmosphere at 256 K, and further descriptors pertaining to the wave. Note that many of the values of λ_z in the real atmosphere vary significantly from the isothermal values given below, especially above and below the mesopause where the dT/dz term in equation (2.48) (also see equation (2.47)) plays an important role.

if one examines the $s = 3$ family of curves (not shown here), we would find that the mixed Rossby-gravity normal mode for $s = 3$ occurs close to $\frac{\sigma}{\omega} = 0.5$, corresponding to the "2-day wave". The characteristic of the 2-day wave will be discussed in Chapter 6.

Equivalent depth (h_n) and Vertical wavelength (λ_z)

Table 2.1 lists some of the more common westward-propagating modes and their nomenclatures, with approximate values of h_n and corresponding vertical wavelength (λ_z) in an isothermal atmosphere calculated from:

$$\lambda_z = \frac{2\pi}{o} = \frac{2\pi H}{\sqrt{\frac{\kappa H}{h_n} - \frac{1}{4}}} \text{ or } \frac{2\pi}{\sqrt{\frac{N^2}{g h_n} - \frac{1}{4H^2}}} \tag{2.47}$$

where, N is the Brunt-Väisälä frequency.

In a non-isothermal atmosphere, the definition of α^2 in (2.34) is as follows:

$$\alpha^2 = \frac{\kappa H + dH/dx}{h_n} - \frac{1}{4} \tag{2.48}$$

The present nomenclature is consistent with that of Volland [1988] and Chapman and Lindzen [1970]. It should be emphasized that these estimates are for the idealized (as defined in Section (2.2.1)) atmosphere and that vertical wavelengths of the propagating tides in the atmosphere may be affected by many factors, including mean winds and dissipation, departure from hydrostatic equilibrium, surface topography, etc. In this nomenclature a mode is symmetric about the equator if $(n + s)$ is even (odd) and antisymmetric if $(n + s)$ is odd (even) for gravity (Rossby) solutions. The mixed Rossby-gravity modes obey the Rossby mode symmetry conditions. For symmetric modes Θ_n (and hence all variables δp, $\delta \rho$, δT, w, and u) are mirror images with respect to the equator, whereas v is antisymmetric; for antisymmetric modes v is symmetric and the other variables change sign at the equatorial node.

The solar semidiurnal thermal tide

For the solar semidiurnal tide, $s = 2$ and $f = \sigma/2\omega = 1$. The Hough functions, Θ_n, for the semidiurnal tide are shown in Figure 2.5a. The tidal oscillations in the atmosphere can be resolved into two orthogonal components; one in the N/S or meridional plane and the other in the E/W or zonal plane. The relative amplitude of the zonal and meridional components of the various tidal modes is shown in Figures 2.5b and 2.5c by the latitudinal velocity expansion functions U_n and V_n defined by the equations (2.22) and (2.23). The zonal and meridional components have phase differences which results in a rotating wind vector with time. The time varying combined wind vector rotates in a clockwise direction (as seen from above) in the Northern Hemisphere where the meridional component generally leads the zonal component in phase. A reversal of sign of the meridional component in the Southern Hemisphere implies a 180° change in phase; hence the wind vector rotates in an anticlockwise direction. In addition, there may exist regions where the tidal oscillations vary in their sense of rotation from one latitude to another, being elliptically polarized at one latitude and passing through linear polarizations (N/S and E/W) at certain latitudes where nodes exist in the expansion functions [Blamont and Teitelbaum, 1968]. The superposing of a number of tidal modes may result in interference effects which can produce a height variation in the sense of rotation of the combined wind vector even at single latitude. It is important to notice that the semidiurnal velocity expansion functions tend to maximize at middle to high latitudes, increasingly so as the meridional index, n, of the mode increases.

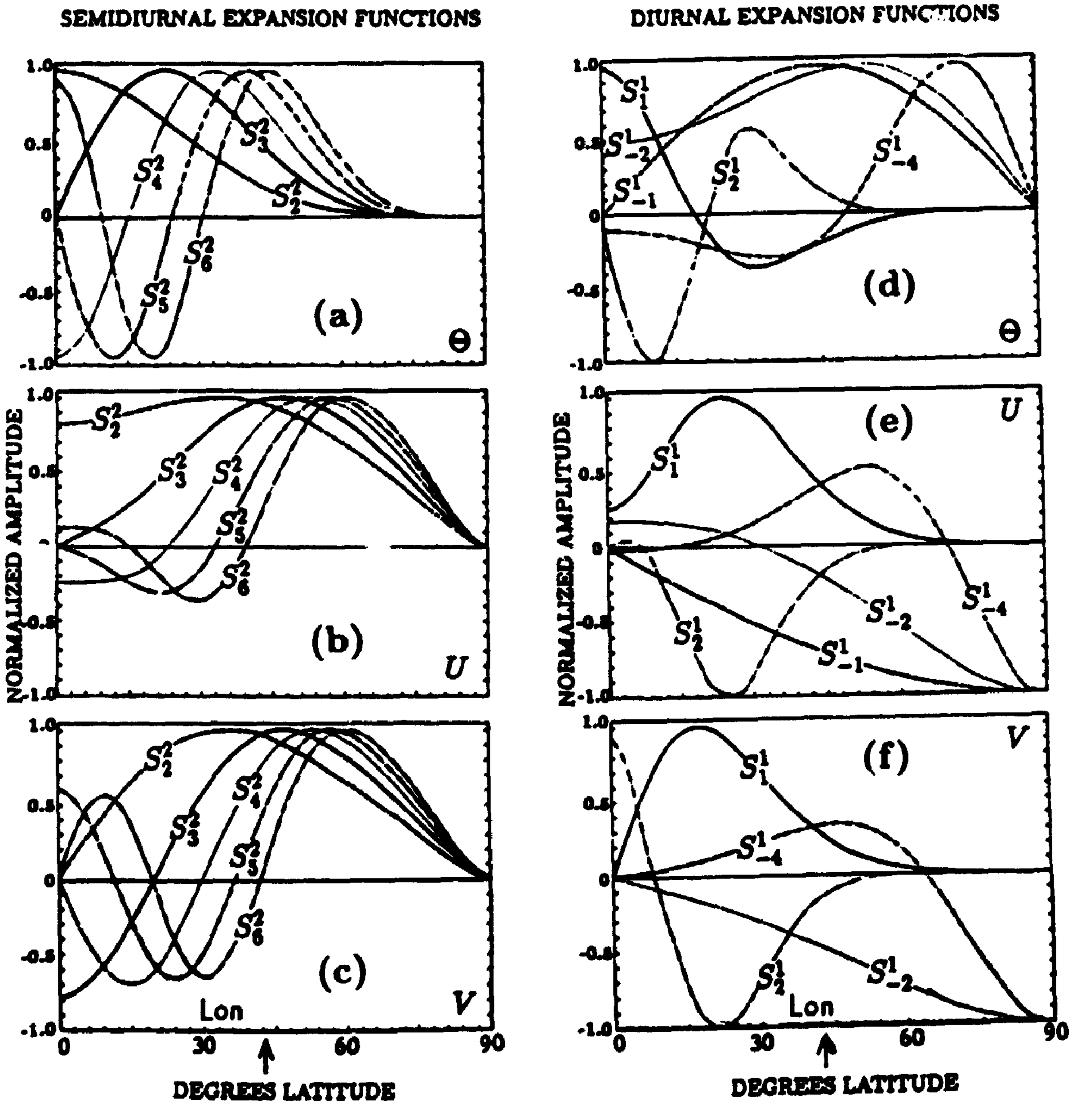

Figure 2.5: Normalized expansion functions for the solar semidiurnal and diurnal tides. Top: Hough function. Middle: eastward wind expansion function. Bottom: northward wind expansion function. After Forbes [1982a].

The equivalent depths for the semidiurnal tide are all positive, all modes are of the gravity wave class, and are shown in Table 2.1. The thermal forcing for diurnal and semidiurnal tides is also shown in Figures 2.6 and 2.7 (both the vertical and latitudinal distributions of excitation). Note that the dominant mode, (2,2), resembles the latitude structure of the forcing and has an equivalent depth, $h_n = 7.85$ km. For this equivalent depth, the quantity α^2 (or $\frac{N^2}{gh_n} \approx \frac{1}{4H^2}$) in (2.47) is almost zero through most of the atmosphere. This implies that the (2,2) mode is associated with extremely long vertical wavelengths ($\sim$ 150 km). Because of its long vertical wavelength, the (2,2) mode not only receives the most of the semidiurnal excitation, but also responds with particular efficiency since all the main excitations below 100 km acts in phase (this will be discussed in more detail in the following section). The latter results from the fact that the excitation going into the (2,2) mode is determined by the overall global distribution of excitation, which is insensitive to local regional variations. The (2,2) mode can be trapped in regions of decreasing temperature such as the mesosphere, where the $\frac{dH}{dz}$ term in equation (2.32) becomes sufficiently large and negative to make the wave evanescent. Butler and small [1963] and Lindzen [1968] showed that ozone is considerably more important than H_2O vapour in exciting semidiurnal oscillations. This is because ozone excitation occurs over a greater depth than H_2O vapour excitation, and at higher altitudes. These facts immediately explain the strength and regularity of the observational features of the solar semidiurnal surface pressure oscillation (see Figure 2.2). However, the larger local variations in heating will primarily excite the higher order modes, less efficient Hough modes, which are not evanescent in the mesosphere, so that these become increasingly important at high altitudes and latitudes.

The solar diurnal thermal tide

For the solar diurnal tide, $s = 1$ and $f = \sigma/2\omega = 1/2$. The Hough functions, Θ_n, and the associated velocity expansion functions U_n and V_n are shown in Figure 2.5d,e,f. The situation for the diurnal tide is very different to that for the semidiurnal tide. For the diurnal tide, note the relative concentration of Θ_n, U_n, and V_n at low latitudes for the propagating modes and high latitudes for the trapped modes. The propagating modes are also more oscillatory with latitude in character. *This provides the first hint of why wind observations around the mesopause should appear predominantly diurnal in character at low latitudes, and more semidiurnal in character at middle to high latitude (Figure 2.3).*

Over half of the globe (poleward of ±30° latitude), 24 hours is longer than the local pendulum day (the period corresponding to the local Coriolis or inertial parameter is $\approx \frac{12}{\sin\theta}$hours, where θ is the latitude, also see Section 1.3.3 and equation (1.6)), and under these circumstances a 24 hour oscillation is incapable of propagating vertically. Therefore, we see two distinct sets of eigenfunctions for the diurnal tide. One is concentrated in latitudes poleward of 30° latitude with negative equivalent depths and one is concentrated equatorward of 30° with small positive equivalent depths. The existence of negative equivalent depths has already been discussed in Section 2.2.2 and represent a particular class of oscillations with a unique latitudinal structure. If we look at equation (2.32) we see that negative h_n's are associated with vertical trapping while sufficiently small positive h_n's are associated with vertical propagation. Because of this, it turns out that 80% of the diurnal forcing goes into physically trapped modes, near the levels of excitation, which are unable to propagate to the ground. These trapped diurnal modes were discovered independently by Lindzen [1966] and Kato [1966]. It is important to notice that the small positive h_n's are associated with large α^2 (see equation 2.47), and this, in turn, implies that the modes associated with positive $h_n's$ will propagate vertically with short wavelengths (see Table (2.1)).

In contrast to the semidiurnal tide, no single diurnal mode bears much resemblance to the latitude structure of the Hough mode forcing, though (1,-2) mode comes closer than any other mode. However, (1,-2) mode, in contrast to (2,2) mode, is not associated with a preferential atmospheric response. The results from Lindzen [1967] showed that although the (1,-2) mode receives significant excitation (but not as great as the (2,2) mode), the (1,1) mode plays a major role in the surface pressure oscillation. In addition, Lindzen showed that H_2O (near the ground) is a larger contributor than ozone (far above the ground) to the modes with negative h_n's. Notice that the (1,-2) mode has a negative equivalent depth and energy in this mode cannot propagate vertically. This trapping becomes increasingly great for the modes (1,-4) and (1,-6). It is interesting to note, however, that even for the propagating modes, H_2O is the largest contributor to the surface pressure oscillation. This is due to the short vertical wavelengths associated with these modes. This will further be discussed in the following subsection.

2.3 Forcing of atmospheric tides

Atmospheric tides represent an obvious example of "forced" atmospheric waves for which we know the wave periods quite well. Lunar tides are of course determined by the period of the Moon's apparent rotation around the Earth. Here we will be mainly

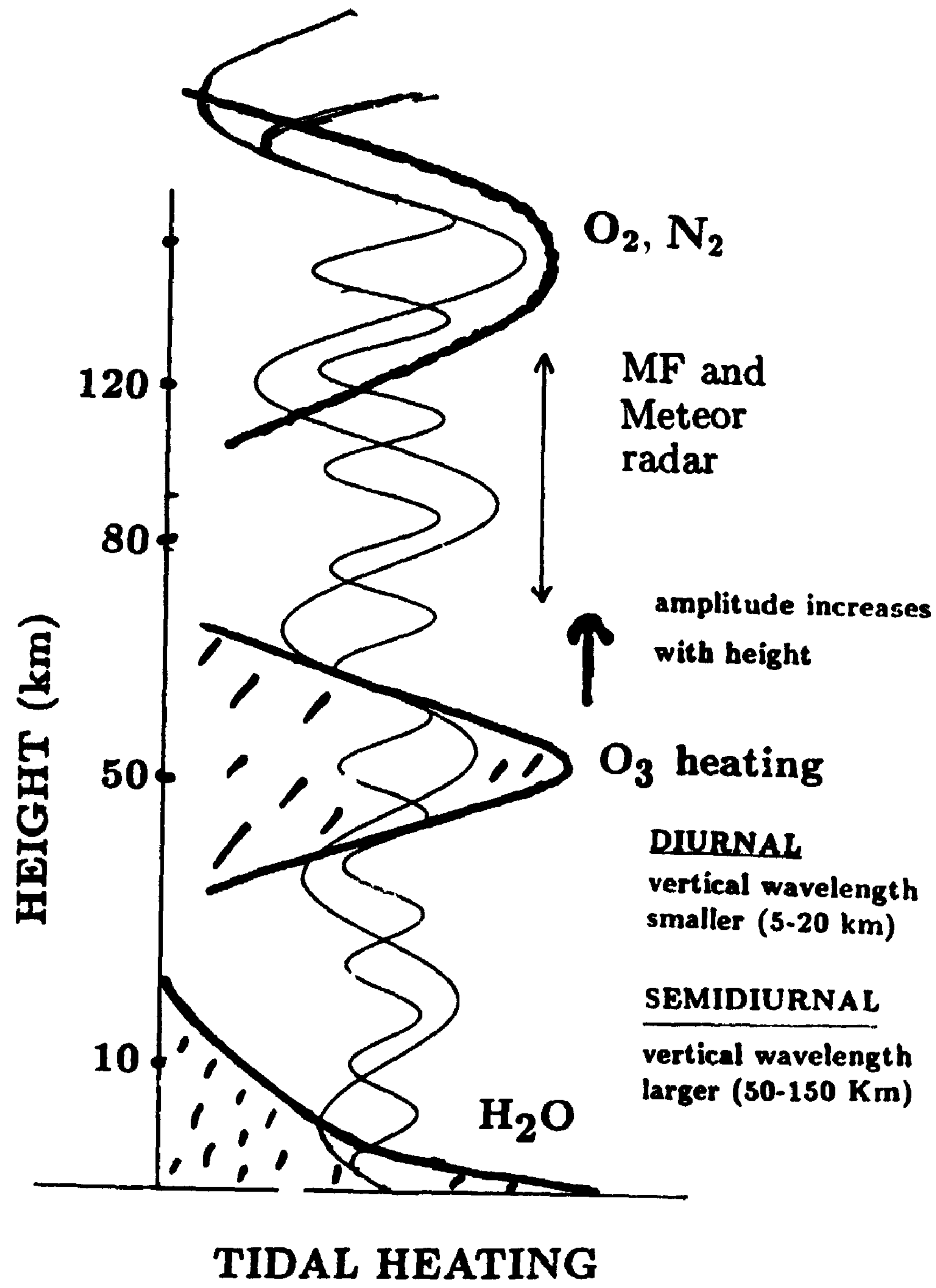

Figure 2.6: Schematic of vertical variation of tidal heating.

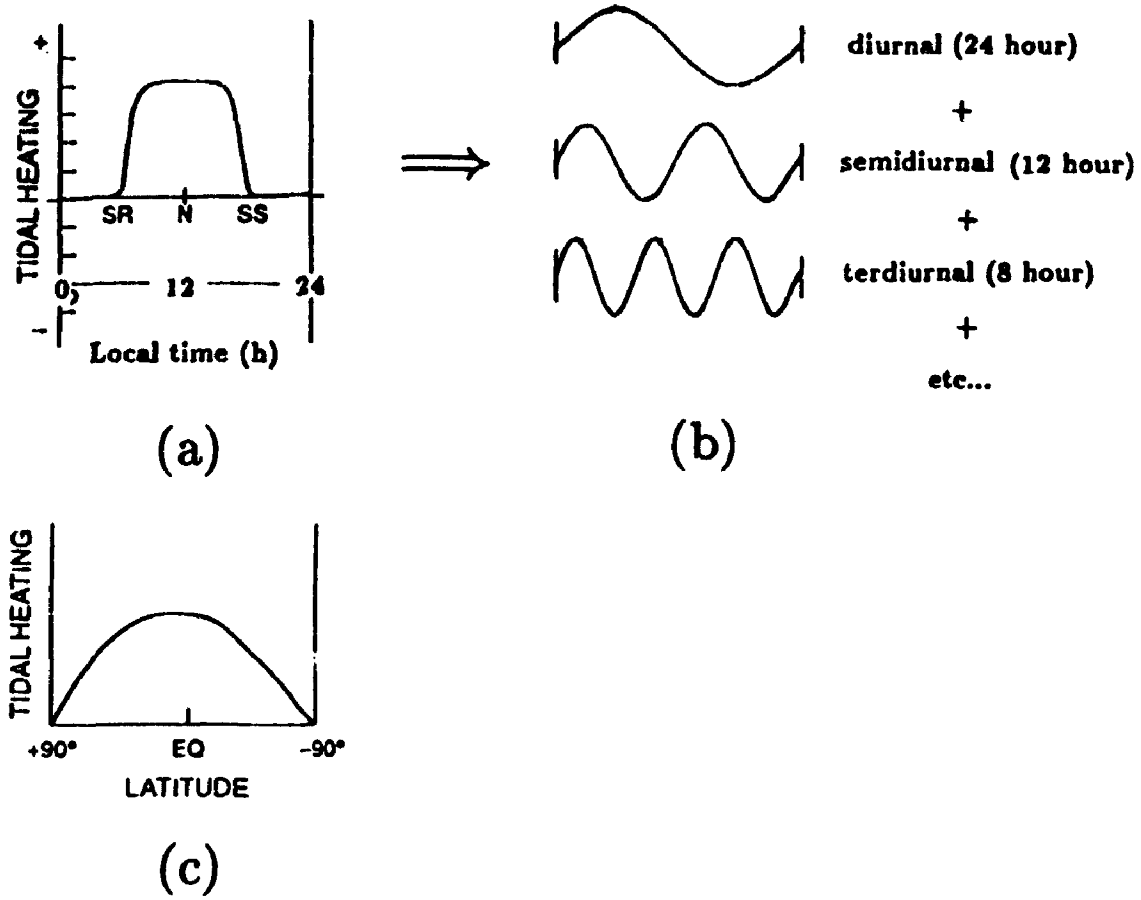

Figure 2.7: Schematic of diurnal (top) and latitudinal (bottom) variations of tidal heating.

concerned with solar or thermally-forced tides, which are excited by the periodic absorption of solar radiation connected with the apparent motion of the Sun around the Earth. Although most insolation is absorbed at the ground, a significant amount is absorbed in the upper atmosphere. Figure 2.6 is a schematic of the main points. The atmospheric solar tides are generated primarily by the daily cycle of heating and cooling, the mechanism being the absorption of various parts of the solar spectrum (solar electromagnetic radiation) in the atmosphere. Absorption of infrared radiation by water vapour in the troposphere, ultraviolet by ozone in the stratosphere, and absorption of EUV (20-100 nm)/UV (120-200 nm) by major atmospheric constituents (e.g., O_2 and N_2) in the lower thermosphere are known to provide most of the forcing for the atmospheric solar tides (Figure 2.6). Note that the region around the mesopause, where most meteor and MF radar measurements provide wind data (see Figure 2.6) is in a region of "no excitation".

Figure 2.6 shows that the ozone excitation is distributed over a very considerable depth, ~ 40 km, of the atmosphere. The H_2O vapour excitation, on the other hand, is distributed over a depth of ~ 18 km or less. Our previous discussions show that the vertical structure of the tide is generally oscillatory as a function of height. In addition, the propagating diurnal tide generally has fairly short vertical wavelengths (see Table 2.1), whilst the propagating semidiurnal tide has very long vertical wavelengths. If the vertical wavelength is comparable with, or less than, the depth of the atmosphere in which most of the forcing occurs, then waves excited at one level can destructively interfere with waves excited at another level [Bulter and Small, 1963; Lindzen, 1968]. As a result, the ozone layer is very good at forcing a semidiurnal tide, but the fact that the vertical wavelength of the propagating diurnal tide is less than the depth of the ozone heating layer means that this layer is very poor at forcing a diurnal tide. On the other hand, the H_2O heating layer is less than the vertical wavelengths of both the propagating diurnal and semidiurnal tides, so this layer forces both periods moderately well.

The other point to notice is that the day-night variation of absorbed radiation (and hence solar heating) might look something like that shown in Figure 2.7a, at any given height in mid-latitudes. The possibility of tidal periods less than 24 h comes about because the heating cycle is more nearly in the form of square-wave than sinusoidal and is therefore rich in harmonics. A Fourier analysis of this curve include a steady component, a diurnal component (with a 24 h period), a semidiurnal component (with a 12 h period), a somewhat smaller terdiurnal component (with a 8 h period) and so on. The response of the atmosphere to this heating can likewise be decomposed into a steady part, diurnal, semidiurnal, terdiurnal and higher frequency oscillations (Figure 2.7b). Each of these harmonic components possess a height-latitude distribution (we are ignoring longitude dependences for the moment). Near the height of maximum heating, the latitudinal distribution for a given harmonic might look something like Figure 2.7c (i.e. maximum at low latitudes and minimum at the poles, in concert with the solar zenith angle influence) [Lindzen, 1968]. *These facts explain why the atmosphere sustains 24, 12, 8,.. periods.*

The above discussion explains why the solar diurnal surface pressure oscillation is relatively weak - namely inefficiency of response due to trapping and interference. It also explains why it is more irregular than the semidiurnal surface pressure oscillation - the oscillation consists in several modes, each of which is sensitive to relatively local regional variations in excitation, temperature, etc. After almost a century, Kelvin's question seems satisfactorily answered; however, as we shall see later, numerous other problems remain in atmospheric tides.

2.4 Group and phase velocity

Let us now return to our "propagating" solution to the vertical structure equation at the beginning in Section 2.2.2. If $0 < h_n < 4\kappa H$, then $\alpha^2 > 0$ and form of the solution (2.40) consists of an upgoing and downgoing wave. Imposition of a "radiation" condition at the top of our domain determines which term in (2.40) to retain. The radiation condition demands that at sufficiently high latitudes the energy is upgoing, i.e., the vertical group velocity is positive, or $C_{gx} > 0$. To derive this condition, note that since

$$\alpha_n^2 = \frac{\kappa H}{h_n} - \frac{1}{4} = \frac{\kappa H g \epsilon_n}{(2\omega a)^2} - \frac{1}{4} \tag{2.49}$$

then

$$C_{gx} = \frac{\partial \sigma}{\partial \alpha} = \pm 2\alpha \frac{\partial \sigma}{\partial \epsilon} / \frac{\partial \alpha^2}{\partial \epsilon} = \pm \alpha \frac{8\omega^2 a^2}{\kappa g H} \frac{\partial \sigma}{\partial \epsilon} \tag{2.50}$$

[Andrews et al., 1987, p. 164]. The choice of sign in front of α must be consistent with that in (2.42). From Figure 2.4, we see that $\frac{\partial \sigma}{\partial \epsilon} > 0$ for westward-propagating waves and $\frac{\partial \sigma}{\partial \epsilon} < 0$ for eastward-propagating waves. Therefore, to maintain $C_{gx} > 0$, in (2.50) we must choose $+\alpha$ for westward propagating waves and $-\alpha$ for eastward-propagating waves.

Now, let us see what this implies in terms of phase progression in height and longitude. Our solution for propagating modes is of the form

$$e^{i(s\phi \pm \alpha x - \sigma t)} \tag{2.51}$$

The equation $s\phi \pm \alpha x - \sigma t = K$ defines the line of constant phase, e.g., the crest of the oscillation if $K = 0$. At a fixed ϕ, $\pm \alpha x - \sigma t = K'$, where x is a height and K' is another constant. Therefore, for either westward-propagating $(\sigma < 0, +\alpha)$ or eastward-propagating $(\sigma > 0, -\alpha)$ waves we have $x = \frac{\sigma}{\pm\alpha} t + K''$, i.e., downward phase progression as time increases (we see now why the downward phase progressions characterizing Figure 2.3 are consistent with a wave source at lower heights, i.e., O_3 and H_2O insolation absorption, and upward progression through the mesopause.). Continuing, for a fixed t we have $s\phi \pm \alpha x = K'$ or $x = -\frac{s}{\alpha}\phi + K''$ $(x = +\frac{s}{\alpha}\phi + K'')$ implying westward (eastward) phase tilt for westward (eastward) propagating waves. Therefore, westward (eastward) phase tilt for westward (eastward) propagating waves is consistent with downward phase progression and upward energy propagation. These are important features to look for in observational data to verify theoretical interpretation.

Observations of tidal winds in the 80-100 km height range usually show a downward phase progression corresponding to an upward propagation of energy. It is probable that tides generated by sources in the thermosphere transport energy downwards but this is rarely observed as the amplitudes will decrease with increasing density according to $\rho^{-1/2}$, where ρ is the atmospheric density. Upward propagating tidal modes will grow approximately according to $\rho^{-1/2}$ until heights where appreciable damping takes place. The increase in amplitude with height is a direct consequence of the conservation of energy. If the amplitude of the wave is represented by A_0 then the kinetic energy density is given by $\frac{\rho A_0^2}{2}$ which remains constant. In the real atmosphere ρ decreases almost exponentially with height so that the amplitude also has an exponential variation. However, the inclusion of any dissipation (e.g., viscosity and thermal conductivity) terms in the linear problem will tend to suppress this amplitude growth at sufficiently great height. Significant damping of upward propagating tides usually occurs at 100-160 km and modes with shorter vertical wavelengths ($\leq$ 30 km) will be strongly damped above 100 km [Forbes and Hagan, 1982]. Because of its long vertical wavelength ($\geq$ 150 km) the (2,2) mode is considerably less attenuated and may penetrate into the the thermosphere [Groves, 1983].

2.5 The variability of tides

The amplitude and phase structure of the tidal winds frequently exhibits pronounce variability in the 80-100 km height range, both seasonally and from day to day [e.g., Bernard, 1981; Lu and Fritts, 1993]. Bernard [1981] showed that variations with periods of a few days are often observed. Specifically, he noticed that tidal fluctuations longer than a 6 day period are correlated between Garchy (47° N) and Kiruna (68° N) while shorter period fluctuations are not correlated. After some theoretical development, Bernard suggested that long period (greater than a few days $\sim$ 6 days) variations are related to variations of the global-scale tidal excitation source (e.g., ozone and water vapour distribution) or of propagation conditions (e.g., changes in zonal winds) in the middle atmosphere, whereas short time (less than a few days $\sim$ 5 days) fluctuations may be due to local perturbations. However, the causes of the observed short-term variations in tidal amplitudes and phases are not yet fully explained in terms of production mechanisms, although there are a number of plausible explanations The difficulty in specifying the mechanisms producing short time variations is probably due to the existence of several such mechanisms acting both together and separately.

Forbes [1984] suggests that seasonal tidal characteristics are more strongly associated with variations in the thermotidal forcing than coupling effects due to asymmetric mean meridional temperature gradients and zonal winds. For the diurnal tide, it would seem plausible that considerable spatial and temporal variability might be present in the tropospheric thermotidal forcing due to H_2O insolation absorption and that these would be reflected at all tropical latitudes. Forbes [1984] pointed out that the influences of the background structure can be eliminated as a source of short-term variability of the diurnal tide due to their exceptionally large phase speed compared to the zonal mean winds. However, measurable effects on a seasonal time scale might result from latitudinally asymmetric mean winds. For the semidiurnal tide in the mesosphere and lower thermosphere, it seems less plausible to ascribe its short-term variability to thermotidal forcing variability by ozone [Forbes and Garrett, 1978; Bernard 1981]. However, Forbes [1984] suggests that day to day measurements of mesospheric ozone concentrations are needed to definitely ascertain the relative importance of this source of variability for the semidiurnal tide. He also pointed out that the influence of mode coupling (see below) in generating high order semidiurnal harmonics is weaker and this source of daily variability plays only a secondary role for many of the large day to day tidal fluctuations which are observed. Forbes [1984] emphasized that the short term variations can occur in the semidiurnal tide due to the interference between several tidal modes, where comparatively small changes in one modal component can result in significant variation of the total tidal amplitude and phase.

The degree of interaction between atmospheric gravity waves and tides is an issue which is of great importance in middle atmosphere studies in recent years. It is especially important with regard to short-term tidal variability and has been numerically studied by many workers [e.g., Walterscheid, 1981; Forbes et al., 1991; Miyahara and Forbes 1991, 1992; Miyahara et al., 1993; Mclandress and Ward, 1994]. Walterscheid [1981] was the first to propose a possible connection of this modulation with gravity waves and thus demonstrated theoretically how tidal-gravity wave interactions can modulate the tidal amplitudes. Walterscheid [1981] offered a plausible alternative mechanism to generate local short-term fluctuations near the semidiurnal period. He presented quantitative time dependent calculations to show that an imposed (i.e. by thermotidal forcing) semidiurnal wave can modulate the momentum deposition of gravity waves into the mean flow and, hence, introduce a secondary oscillation near the semidiurnal frequency. The amplitude of the secondary oscillation would depend on the phase velocities, magnitudes, etc., of the gravity waves and, hence, would be quite variable from day to day. Recently, observational evidence of tidal-gravity wave interactions has been found by Fritts and Vincent [1987], Reid et al. [1988], Fritts and Yuan [1989], and Wang and Fritts [1993]. This study is one of the main objectives of this dissertation and will be dealt with in more detail in Chapter 5.

Manson [1982, 1990] showed that 9.7 hour and 16 hour period waves are frequently observed over Saskatoon (52° N), and suggested that these waves are generated by non-linear interactions between the semidiurnal tide and the well known 2-day planetary wave. Recently, Cevolani and Kingsley [1992] showed a possible non-linear coupling processes between tidal and planetary waves over Bologna (45.5° N). They also showed that such interactions would account for the presence of subsidiary peaks close to the semidiurnal period mainly in the 10-16 h band. Teitelbaum and Vial [1991] showed theoretically that many observations can be explained by non-linear interactions between tides and planetary waves having periods corresponding to those of the observed tidal amplitude modulations. These non-linear interactions generate secondary waves whose frequencies are the sum and difference of frequencies of the primary waves. These two waves beat with the tide, modulating its amplitude with the planetary wave period. They also showed that a non-linear interaction between the 2-day wave and the semidiurnal tide can generate waves with period near 9.6 and 16 hours. The observations also revealed that these two waves and the 2-day wave, and furthermore that the 2-day wave has a large amplitude in comparison with tidal amplitudes are simultaneously present over Garchy (47° N) [Teitelbaum and Vial, 1991]. These results indicate that in these cases the tidal amplitude modulations can be explained by non-linear interactions between tides and planetary waves which takes place in the upper mesosphere and lower thermosphere. Another numerical study of Teitelbaum et al. [1989] suggested that a secondary 24 oscillation could be partially generated in addition to the terdiurnal tide by the non-linear interaction of the diurnal and semidiurnal tides. For the 24 hour secondary wave, the results suggest that it can be partly responsible for the observed variability of the diurnal tide especially in the middle and high latitude winter. This phenomenon was observed by Fellous et al. [1975] in their early work on tides. This also supports the existence of these non-linear interactions.

The existence of one or two amplitude minima associated with a phase shift in the vertical profiles of the diurnal and semidiurnal tides are frequently observed in the upper mesosphere and lower thermosphere. The importance of this phenomenon for interpretation of the atmospheric tides in terms of modes has been shown by different authors [e.g., Fellous et al., 1974, 1975; Stenning et al., 1978; Tsuda et al., 1983; Vial et al., 1984]. Fellous et al. [1975] proposed an explanation using empirical models of mode superposition or interference patterns due to mode reflection. Tsuda [1983] also proposed an empirical model of mode superposition. Vial et al. [1984] tudied the possible causes of this phenomenon with a more sophisticated model than previously used. Their study was based on observations made by the French meteor radars [e.g., Fellous et al., 1974]. Among the different possible explanations, Vial et al. [1984] suggested that partial reflections of certain tidal modes (by steep temperature gradients in the lower thermosphere) may explain the main features of this phenomenon, particularly when two such structures (amplitude minimum associated with a phase shift) are simultaneously observed. However for the semidiurnal tide, they suggested that a mode superposition can also explain the phenomenon although its characteristics may be different.

As mentioned in the previous subsections, the diurnal tide consists not only the migrating tide but also the non-migrating tide. Relatively few studies have been performed to ascertain the presence of non-migrating tides [e.g., Fukuo et al., 1980; Bernard, 1981; Kato et al., 1982; Forbes and Groves, 1987; Kato, 1989; Yagai, 1989; Tsuda and Kato, 1989; Leiberman, 1991; Miyahara et al., 1993; Williams, 1994], which would give rise to longitudinal differences in tidal structures. It is known, theoretically, that the effect of longitudinal variation in the distribution of insolation absorption produces not only a component following the Sun (migrating mode), but also other components which do not move synchronously with the Sun; this would lead to the excitation of non-migrating modes with longitudinal phase velocities different from the apparent velocity of the Sun around the Earth. Tropospheric water vapour has significant longitudinal variations [Newell et al., 1972; Chelton et al., 1981] which could create possible excitation of non-migrating modes.

Evidence of longitudinal differences in phase of up to 1.5 hour had been reported by Glass at al. [1975]. Since his excitation model revealed little evidence of longitudinal variations in ozone heating, Bernard [1981] examines the possible role of longitudinal variations in background atmospheric conditions in producing such effects. He found that the primary (migrating) semidiurnal modes interact with the background structure (e.g., winds and irregularities in the middle atmosphere) to produce non-migrating modes as large as 50% of the primary tidal amplitudes, resulting in phase differences of the order of 1 hour in local time over 60°-120° differences in longitude. Forbes and Groves [1987] showed that longitudinal variations in diurnal insolation absorption by tropospheric water can account for longitudinal variations of at least ±12 – 15% of the total diurnal amplitude at low-latitude (0^o-20^o) between 80-100 km and are thus non-negligible at this height range. Phase variations about ±0.75 h also occur. The simulation study of Miyahara et al. [1993] also suggest that the non-migrating diurnal tides have significant amplitudes in the lower thermosphere.

The heating of the surface in the presence of land-sea contrasts and topography, and the heating of the atmosphere in the presence of large scale regional cloudiness may also excite non-migrating tides [e.g., Haurwitz, 1965; Haurwitz and Cowley, 1973; Tokioka and Yagai, 1987; Tsuda and Kato, 1989]. Haurwitz [1965] and Haurwitz and Cowley [1973] showed larger surface diurnal surface pressure oscillation over land areas than over ocean areas and attributed it to non-migrating modes. Wallace and Tadd [1974] pointed out that diurnal tides vary with topography and generally possess much shorter vertical wavelength than those expected from classical tidal theory [e.g., Lindzen, 1974]. Tsuda and Kato [1989] have also clearly shown the importance of land-sea difference in heating to understand the enhanced tides on land. The difference is also found to produce the very short vertical wavelength of tides in the stratosphere. It is also possible to explain why non-migrating tides often exceed migrating tides below 30 km [Tsuda and Kato, 1989].

There remain inconsistencies between characteristics of the diurnal tidal wind oscillation as observed between 80 and 100 km [e.g., Aso and Vincent, 1982; Hirota et al., 1983; Vincent et al., 1988] and those represented in theoretical calculations [e.g., Forbes, 1982]. Observations at the geographically conjugate stations at Adelaide (35^o S) and Kyoto (35^o N) [Aso and Vincent, 1982; Vincent et al., 1988] and Townsville (19^o S) and Arecibo (18^o N) [Hirota et al., 1983] were used to study hemispheric differences in the behavior of the solar diurnal and semidiurnal tides. Comparisons of the tidal amplitude and phase parameters show that there are distinct hemispheric asymmetries, particularly for the diurnal tide. This presents a serious problem for tidal studies. Since non-migrating tides are excited differently between hemispheres due to different topographies (e.g., inhomogeneities of water vapour distribution), it is possible for these tides to play a role to produce such asymmetries even at meteor heights [Kato, 1989; Vial, 1989; Forbes and Groves, 1987].

The above discussion on the non-migrating tides strongly suggest that if the non-migrating tides have large amplitude in the atmosphere, tidal studies which are done at a single location and analyzed by the harmonic analysis are contaminated by non-migrating tides, and care must be paid to compare the results with the numerical calculations, which usually consist of migrating tides only.

The diurnal tide is usually much larger in amplitude in the southern hemisphere (e.g., Adelaide, 35° S) than in the Northern Hemisphere (e.g., Kyoto, 35° N) and it exhibits a height structure which indicates a relatively larger contribution from the propagating (1,1) mode in the Southern Hemisphere than in the Northern Hemisphere [Vincent et al., 1988]. Comparisons with recent theoretical work suggest that while some of these differences may be due to hemispheric differences in forcing and/or to interactions between the tide and the background winds in the middle atmosphere [e.g., Forbes, 1982], it is also possible that they indicate weaker turbulent induced damping of the (1,1) mode in the southern hemisphere. Indeed, the difference in land-sea distributions between the two hemispheres could be expected to lead to a difference in wave generated turbulence in the upper mesosphere. Because of the great sensitivity of the diurnal tide to this turbulence [Lindzen, 1981; Forbes and Hagan, 1988], we could expect that it would be more strongly dissipated in the Northern Hemisphere, where gravity wave activity is supposed to be more important. This explanation must be further developed, but it does show the need for a better knowledge of eddy diffusion on a global scale [Vial, 1989].

2.6 Numerical model results

The classical theory of atmospheric tides, though highly idealized (linearized perturbations on a static, inviscid atmosphere), has successfully explained many major observational features of atmospheric tides. Nevertheless, it is not surprising that discrepancies are also to be found between observations and the classical theory. Theoretical studies of middle atmosphere tidal phenomena, particularly at upper levels ($\geq$ 70 km) require investigation of a number of processes beyond those considered in classical tidal theory, including molecular and eddy diffusion of heat and momentum, Newtonian cooling, electrodynamic forces, meridional temperature gradients, composition variations, interactions with background winds, wave-wave interactions and other types of process [Forbes, 1984]. This section will present important numerical progress made in the last few years.

In Section 2.2.2 we discussed the eigenfunction-eigenvalue problem corresponding to forced and free atmospheric oscillations in an isothermal, dissipationless atmosphere. By definition "separability" existed, so that each mode possessed its own vertical structure (indeed, use of the term "mode" implies separability). Separability of height and latitude dependences also exists in a non-isothermal atmosphere, and additionally for special treatments of height-dependent dissipation [Lindzen and McKenzie,

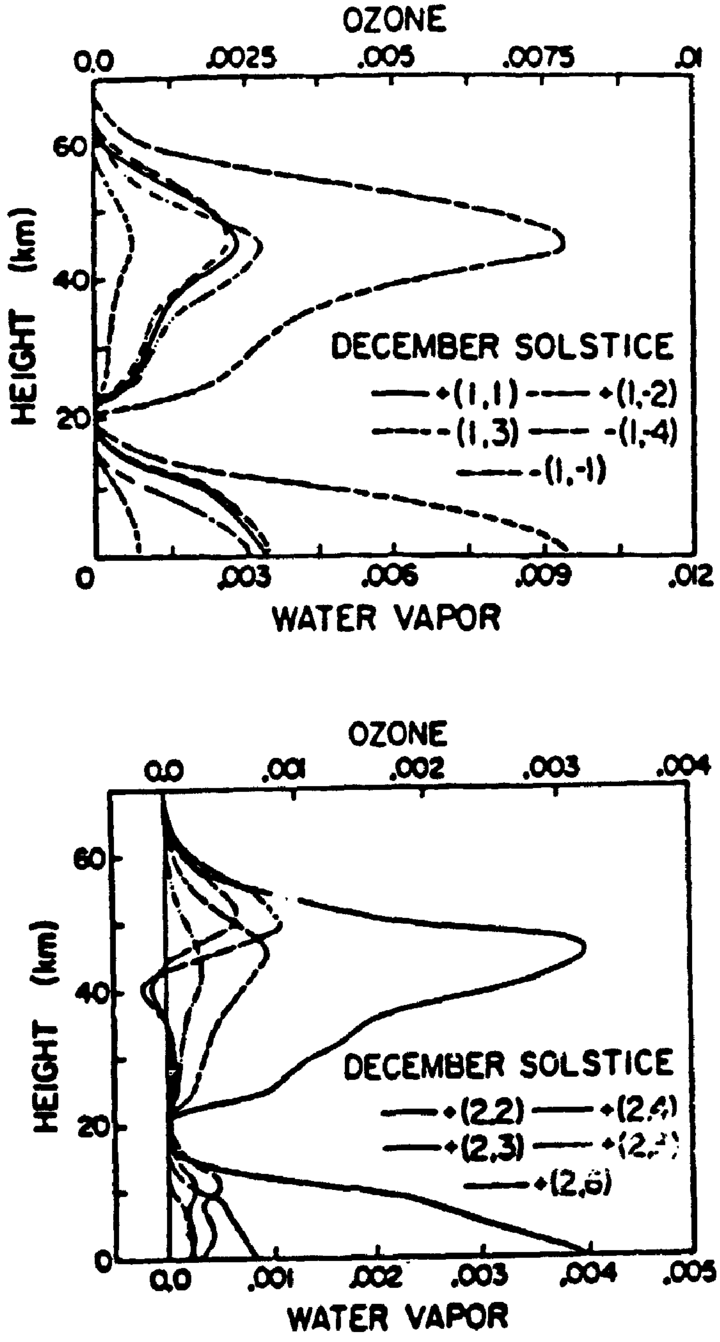

Figure 2.8: Vertical profiles of (top) diurnal and (bottom) semidiurnal heating, $e^{-x/2}J_n$, where $x = -ln\frac{p}{p_0}$, due to insolation absorption by ozone and water vapour, corresponding to various solar tidal modes. The units are J kg^{-1} sec^{-1}. Adapted from Forbes and Garrett [1978].

1967; Lindzen, 1970]. However, in the joint presence of latitude-dependent rotation and vertical diffusion of heat and momentum, or in the presence of latitude dependent mean winds, the equations for an oscillation with specified frequency and zonal wavenumber are nonseparable. First of all, this necessitates a numerical approach to the problem; secondly, strictly speaking, this precludes reference to "modes", particularly in the mesosphere and lower thermosphere. However, it is commonplace to use modal terminology nonetheless, as many observed features of prominent oscillations exhibit characteristics very similar to what would be expected on the basis of "classical" theory. In fact, it is commonplace to decompose the diurnal forcing in numerical models into Hough modes to facilitate interpretation of the results (as in Figure 2.8), even though the solution is nonseparable . We will now briefly review some of these numerical models.

There are basically three types of numerical models which take into account dissipation, mean winds, and other processes which have developed in recent years to simulate middle atmospheric tides. The hierarchy of numerical tidal models in early years has been reviewed by Forbes and Garrett [1979]. The first genre neglect eddy and molecular dissipation, but include mean winds and meridional temperature gradients, Newtonian cooling, and perhaps a Rayleigh friction (linear damping) term to filter out small-scale noise or to facilitate application of upper boundary conditions. Dispensing with diffusion allows one to derive a single second-order partial differential equation in height and latitude for the perturbation geopotential. The first such numerical simulation model was that of Lindzen and Hong [1974], who treated the semidiurnal tide in an inviscid atmosphere but with a meridional temperature gradient and associated mean zonal wind. They solved the geopotential equation for the semidiurnal tide using a finite difference methods. They successfully resolved some of the discrepancies between classical tidal theory and observational evidence; e.g. (1) the semidiurnal tidal oscillation near 100 km in middle latitudes is often dominated by the (2,4) component [Murphy, 1969; Spizzichino, 1973; Amayenc, and Reddy, 1972] while classical theory predicted a dominant (2,2) mode, and (2) no phase reversal of the horizontal wind is found near 30 km [Harris et al., 1962; Reed, 1967] although there is some evidence for one near 50 km [Reed, 1967]. The calculations of Lindzen and Hong [1974] showed that effects related to the mean winds could account for the observed dominance of the (2,4) component and for the high elevation of the phase reversal during the summer. Following this first study, several other simulations of the semidiurnal tide in the middle atmosphere were made on the basis of improved parameterization of the background atmosphere and thermal excitation [Walterscheid and Venkateswaran 1979 a,b; Walterscheid et al., 1980].

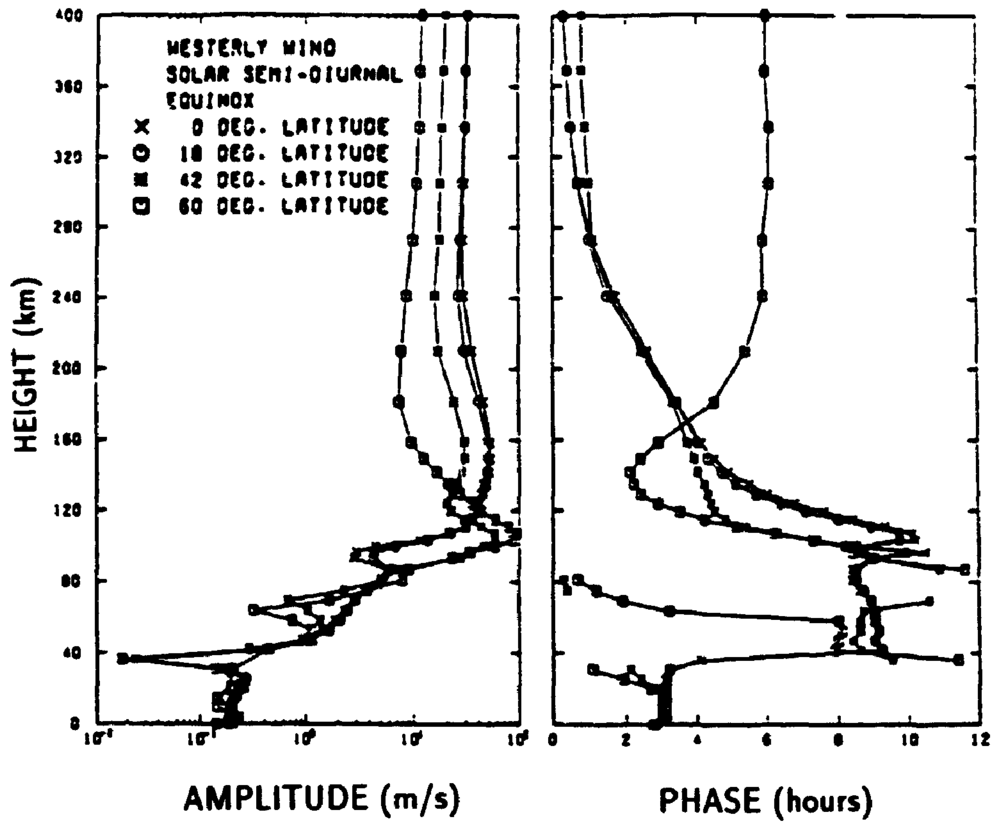

Figure 2.9: Amplitude (left) and phase (right) for solar semidiurnal eastward wind at 0°, ±18°, ±42°, and ±60° latitude for December solstice conditions. After Forbes [1982b].

Previously, a particular Hough mode is the heating function gives rise to only one mode in u', v', w', T' etc. However, with these non-separable equations, a particular heating mode produces u', v' etc fluctuation in several modes. This is called "mode coupling".

In the context of the solution of these nonseparable equations, the terminology of "mode coupling" has arisen. This refers to the generation of tidal modes (determined through an orthogonal expansion of the calculated response) which are not forced directly by thermal excitation, but which arise because of the non-separability of the governing equation. For instance, if only the (2,2) mode is excited in these models, the response at say 90 km consists of many modes (e.g., (2,2), (2,3), (2,4), (2,5) and (2,6)) due to the di[illegible]ing effects of the mean wind distribution. In the above models the (2,4) mode appears to receive about equal contributions from direct thermal forcing and mode coupling via the (2,2)-mean wind interactions which tend to add in phase. On the other hand, for the (2,3) mode the effect of mode coupling is to interfere with

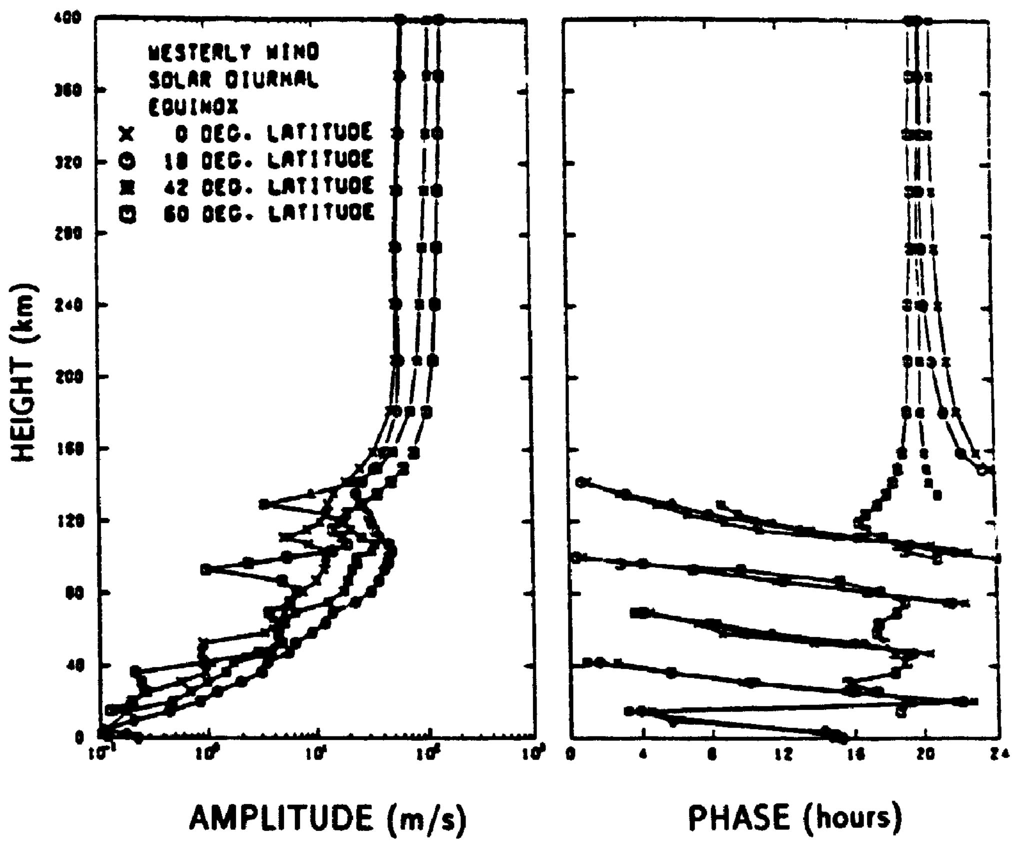

Figure 2.10: Same as Figure 2.9, except for the solar diurnal tide. After Forbes [1982a].

the directly forced component and thereby reduce the (2,3) response above the level of ozone heating. In the case of (2,5), excitation appears to arise almost exclusively due to direct thermal forcing (mode coupling is weak).

At the next hierarchical level of modeling pertaining to atmospheric tides, Forbes [1982a,b] included eddy and molecular diffusion of momentum and heat so as to properly address the structural modification of tides in the 80-150 km region and their penetration to higher altitudes. This required numerical solution of the four coupled partial differential equations in the three velocity components and temperature, as opposed to a single equation for the geopotential as in the above studies. Forbes [1982a,b] provided explicit simulations from the surface to 400 km for the solar diurnal, solar semidiurnal, and lunar semidiurnal tides due to realistic thermal and gravitational forcing; he also normalized the thermospheric extensions of solar semidiurnal modes above 80 km for use in the fitting, extrapolation and interpolation of observational data [Forbes and Hagan, 1982].

Illustrations of amplitude and phase vertical structures for the solar semidiurnal and diurnal tides from the Forbes [1982a,b] model are shown in Figures 2.9 and 2.10, respectively. In Figure 2.9, note the relatively long vertical wavelength characterizing the response below 50 km; this is consistent with most of the heating going into the long wavelength (2,2) mode (Figure 2.8, Table 2.1); above about 50 km, the wavelength decreases, due to the increased presence of short wavelength modes induced by "mode coupling" due to the strong mesospheric jets. The region between 70 and 90 km is a region of evanescence for the (2,2) mode, due to the combined effects of its large h_n and the negative temperature gradient (cf equations (2.34) and (2.28)). However, in this region the higher-order modes (2,3) and (2,4) are growing exponentially with height, and soon begin to dominate the solution in the lower thermosphere. The region between 90 and 120 km is mostly dominated by the (2,4) mode with some (2,5) and (2,2). However, as molecular viscosity begins to dominate in the 120 -150 km region, these shorter vertical wavelength modes (2,5), (2,4) (see Table 2.1) are more susceptible to dissipation, and the longer wavelength modes (2,2) begin to dominate at higher altitudes. In the upper thermosphere, molecular diffusion of heat and momentum is so efficient that it is difficult to maintain vertical shears in the wind and temperature fields, and the tidal fields asymptote to constant values above about 200 km.

The situation is similar for the diurnal tide, illustrated in Figure 2.10. Note that at high latitudes (60° in Figure 2.10) the phase is more or less constant with height, consistent with the dominance of trapped modes whose maxima are at high latitudes (see Figure 2.5). At low latitudes the solution is dominated by the (1,1) mode, with a vertical wavelength of order 30 km (see Table 2.1).

Except for the pioneering analytical work of Lindzen [1972], a relatively small number of numerical studies have been devoted to the diurnal tide in contrast to the semidiurnal tide. One can mention Forbes [1982a] who made numerical simulations of the diurnal tide below 100 km using an 'Equivalent Gravity Wave' (EGW) formalism [Forbes and Hagan, 1979] for computational convenience, and Miyahara [1978, 1881, 1984] who, in the course of his calculations of tide mean flow interaction, used simulations of the diurnal tide. Unfortunately, specific results concerning diurnal tides were not extensively presented. The diurnal tide is more difficult to simulate numerically than the semidiurnal for several reasons: normally, rapid variation of the (1,1) mode with latitude, the great sensitivity of this mode to turbulent diffusivity at the mesopause level, and the existence of a critical latitude near 30°, which can lead to numerical problems in the course of the calculations [Vial, 1989].

The past few years have seen the emergence of studies devoted to the action of dissipation and background atmosphere on the diurnal tide structure [Vial, 1986; Vial and Teitelbaum, 1984; Aso et al., 1987; Forbes and Hagan, 1988]. More recent studies by Forbes and Hagan [1988] and Vial [1986] address the diurnal tide, and utilize a Rayleigh friction (linear damping) term to parameterize turbulent diffusion of momentum. In a few words, the primary effects of dissipation are to produce an amplitude peak in the vicinity of 90 km, an increase in the vertical wavelength with height from 80 to 100 km, and a broadening of the tidal structure to higher latitudes. Forbes and Hagan [1988] interpret this latter result as a coupling into the first symmetric and antisymmetric evanescent modes (1,-2) and (1,-1) as the (1,1) mode is damped.

The presence of mean winds during the solstices were found to introduce significant asymmetries in the amplitude and phase of the first symmetric (1,1) diurnal tide about the equator. Summer amplitudes are larger than the winter ones. These were interpreted as being due to the mode coupling in which tidal modes are generated through the orthogonal expansion of the calculated responses. The asymmetric propagating mode (1,2) and the vertically trapped (1,-1) mode were found to be coupled [Forbes and Hagan, 1988] and this explained the observed short vertical wavelength of the diurnal tide in the mid-latitudes. The theoretical calculations for the low latitudes show that an westward (eastward) mean zonal wind can induce a local increase (decrease) in the amplitude of the (1,1) tidal mode [Lindzen, 1972; Vial, 1986].

All previous numerical simulations are normally confined to solstice or equinox conditions. However, the recent hierarchical level of modelling pertaining to monthly simulations of the semidiurnal tide in the 80-100 km have been performed by Forbes and Vial [1989]. These calculations benefit from new tidal heating rates, improved background winds, temperature, pressure, and dissipation rates. Some of the main characteristics of the observed semidiurnal tide in this range at middle and high latitudes are reproduced in this simulation: larger amplitudes in the winter months than in summer months, and the bi-modal behaviour of the phase with summer-like and winter-like months separated by a quick transition around the two equinoxes. The phase transition is also more rapid in the spring, consistent with observations. Semidiurnal amplitudes are generally smaller and the phases more seasonally symmetric at middle and low latitudes, as compared with the tidal structures above about 50° latitude. The wavelengths are also longer in summer than in winter, at least below 95 km (whereas in July and August the simulations exhibit some discrepancies above this altitude), similar to the observational data. The main conclusion to be drawn here is that we are now in a good position to fully understand the seasonal-latitudinal structure of the semidiurnal tide on a global basis. Furthermore, it is the first time that hemispheric asymmetrics have been taken into account in tidal modelling. The next step will be to produce similar such simulations for the diurnal tide, which, however, is considerably complicated by dissipation effects which may involve more realistically parameterization of the influences of gravity waves and the seasonal-latitudinal dependences of their sources [Forbes and Hagan, 1988].

2.7 Concluding comments

This chapter reviews some important progress made in the study of middle atmosphere tides in the past 10 years. Specific attention is given to the variability of tides, as it arises due to tidal-gravity wave interactions, non-linear interactions, and non-migrating tides. This chapter also sets forth the terminology (e.g., mode, vertical wavelength, zonal wavenumber, phase, etc.) which define the foundation from which the rest of this dissertation is developed.

In conclusion, it is now well established that atmospheric tides play an important role in the dynamics and chemistry of the middle atmosphere. The remaining chapters comprise the body of the research work.

Chapter 3

Radar, data analysis technique, and radar model

3.1 The atmospheric refractive index

Basically, all radar echoes arise from scattering or reflection from inhomogeneities in the atmospheric dielectric constant ϵ or index of refraction n [Woodman and Guillen, 1974]. The dielectric constant of free space is ϵ_0 ($\approx 8.854 \times 10^{-12}$ Fm^{-1}). A relative dielectric constant can be defined by

$$\epsilon_r = \frac{\epsilon}{\epsilon_0} \tag{3.1}$$

and the refractive index n is related to this dielectric constant by

$$n = \sqrt{\mu_r \epsilon_r} \tag{3.2}$$

where the relative permeability μ_r of air is approximately unity [Bean and Dutton, 1968].

As in the case of optics, n is defined as

$$n = \frac{c}{v} \tag{3.3}$$

where c is the speed of light in free space and v is the velocity of the radio wave in the air. Macroscopic (relative to the radar wavelength) changes of n in space cause reflection or refraction, and microscopic changes cause scattering.

In the neutral atmosphere (un-ionized ionosphere), and for radio waves ranging from HF through UHF (i.e. for metre and centimetre and radio waves), the (generalized) potential refractive index gradient (i.e. $M = \frac{dn}{dz}$, where z is the height above ground,

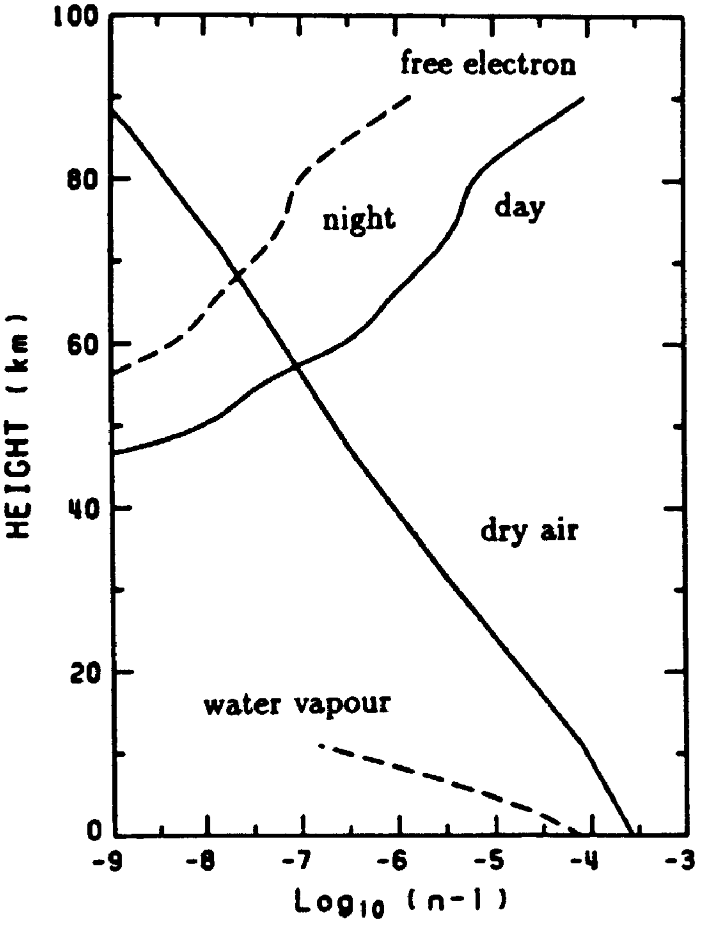

Figure 3.1: Typical altitude profiles of the wet, dry and ionization (free electron) terms which determine the radio refractive index of the atmosphere [after, Sato, 1989]. The pressure and temperature are taken from U.S. standard atmosphere (1976). The saturation pressure is used for the water vapour. The electron density (from 50 MHz radar frequency) is adopted from Mechtly et al. [1972].

see Hocking [1985] for detailed information) in the troposphere is given by [Tartarski, 1961]

$$M_t = \frac{-77.6 \times 10^{-6}}{T^2} P[1 + \frac{15500}{T} q][\frac{dT}{dz} + \Gamma_a - \frac{7800}{(1 + \frac{15500}{T} q)} \frac{dq}{dz}] \qquad (3.4)$$

where P is the atmospheric pressure (millibars), T is the temperature (degrees Celsius), Γ_a is the adiabatic lapse rate, $q = \frac{e}{1.62P}$ is the specific humidity, and e is the water vapour pressure (millibars). In the stratosphere (where q is normally neglected)

$$M_s = -77.6 \times 10^{-6} \frac{P\omega_B^2}{gT} \qquad (3.5)$$

[e.g., Gage et al., 1985] Notice that M_s is actually dependent on the Brunt-Väisälä angular frequency ω_B, since $\frac{dT}{dz} + \Gamma_a = \frac{T\omega_B^2}{g}$, where g is the gravitational acceleration. In the mesosphere, i.e. for the ionized atmosphere (dominated by electron density), the potential refractive index gradient can be written as [Hocking, 1985]

$$M_m = \frac{\partial n}{\partial N}[N\frac{\omega_B^2}{g} - \frac{dN}{dz} + \frac{N}{\rho}\frac{d\rho}{dz}] \qquad (3.6)$$

where N is the electron density, and ρ is the neutral density. The radio index of refraction is given approximately by [Gage and Balsley, 1980]

$$n - 1 = \frac{3.73 \times 10^{-1} e}{T^2} + \frac{77.6 \times 10^{-6} P}{T} - \frac{N_e}{2N_c} \qquad (3.7)$$

where P is the atmospheric pressure (millibars), e is the partial pressure of the water vapour, T is the absolute temperature (degrees Kelvin), N_e is the number density of electrons (m^{-3}), and N_c is the critical plasma density. The first two terms on the right hand side contain the contributions to the radio refractive index due to bound electrons inherent in density fluctuations of water vapour and dry air, respectively. The third term expresses the contribution due to the presence of free electrons. The first term is sometimes referred to as the "wet" term, and dominates in the lower troposphere due to the (often) large concentration of water vapour. The second term is the "dry" term, and dominates between the mid-troposphere (5 km or so) and the stratosphere (~ 50 km), where the effects of ionization begin to becomes significant. The third term is the "ionization" term, which is usually negligible below 50 km, but becomes the major contribution factor above this level, where the electron density increases rapidly with height. The ionization term exhibits a diurnal variation, as a result of the ionization produced during the day and the recombination occurring at night. The height dependence of each of these term is illustrated in Figure 3.1.

It should be noted here that the equation (3.7) is generally valid at VHF. Because of the collision dominated D-region, the equation (3.7) is generally not valid at MF, and becomes a rather complicated expression [e.g., Dyson and Newbery, 1982].

3.2 The radar equation: fundamentals

"Radar" stands for radio detection and ranging. This section briefly discuss the relation between transmitted and received powers, called the radar equation, for different situations which concern observations with an atmospheric radar. The objective of this section is not to derive exact radar equation, but to describe the very basic technical assumptions and principles and also to understand the differences between each techniques. The discussion in this section mainly follows that of Röttger and Liu [1978], Gage and Balsley [1980], Röttger [1980], Hocking and Röttger [1983], Green and Gage [1985], Gage et al. [1985], and Sato [1989], in addition to the references given.

3.2.1 The hard target

Here we consider a generalized radar equation which can be used for any antennas (dishes and arrays) and either scattering or reflection. Suppose a radar transmitter has an antenna gain G_t which is fed by the transmitter with power P_t. The power P_i (watts) on the target of cross-sectional area σ located at distance r is given by

$$P_i = \frac{P_t G_t}{4\pi r^2}\sigma \tag{3.8}$$

The power received at the radar antenna, assuming a monostatic radar system, is then given by

$$P_r = \frac{P_i A_e L}{4\pi r^2} \tag{3.9}$$

where A_e is the effective area of the antenna and L is the loss factor represents various attenuation of the received signal due to antenna, transmission line, connectors,..., etc. Combining equations (3.8) and (3.9), we obtain

$$P_r = \frac{P_t G_t A_e L}{(4\pi r^2)^2}\sigma \tag{3.10}$$

This equation gives the received echo power from a given target by a radar, and hence is called the radar equation. At the operating radar wavelength λ, it can be shown that A_e and G_t are related by

$$A_e = G_t \frac{\lambda^2}{4\pi} \tag{3.11}$$

so that equation (3.10) reduced to

$$P_r = \frac{P_t A_e^2 L}{4\pi \lambda^2 r^4}\sigma \tag{3.12}$$

This equation gives the basis for radar system design of choosing appropriate transmitter power P_t and effective antenna area A_e for a given target with a scattering cross-section σ at a range r.

3.2.2 Distributed targets

The radar equation above applies to a single target. If there are more than one target within the radar beam one must take into account the contribution from each scatterer. If all scatterers are uncorrelated and randomly distributed, the total received echo power is the algebraic sum of the echo power from individual scatterers. In this case, the σ term in the equation (3.12) is simply replaced by $\sum \sigma$. If the scatterers are uniformly but randomly distributed in some volume V, σ increases linearly with V. In this case, it is useful to define the volume reflectivity η_{tur}, so that

$$\eta_{tur} = \frac{d\sigma}{dV} \tag{3.13}$$

where V is defined by the spatial resolution of the radar. Notice that η has a dimension of m^{-1}. For uniformly distributed scatterers, V is given by

$$V = \pi(\frac{r\theta_{\frac{1}{2}}}{2})^2 \Delta r \tag{3.14}$$

where $\theta_{\frac{1}{2}}$ is the half-power beamwidth of the radar polar diagram, and Δr (= $\frac{c\Delta t}{2}$, where Δt is the pulse width) is the range resolution of the radar. It is assumed that $r \gg$ radar volume$^{1/3}$, i.e. all of the development here assumes operation in the far zone of the antenna beam.

It can be shown that G_t and $\theta_{\frac{1}{2}}$ are related by [Probert-Jones, 1962]

$$G_t = (\frac{\pi a}{\theta_{\frac{1}{2}}})^2 \tag{3.15}$$

where a is a non-dimensional constant accounting for the non-uniform antenna illumination, and normally close to unity. Combining equations (3.11), (3.14) and (3.15), the radar equation (3.12) can be written for the distributed targets as

$$P_r = \frac{\pi}{64} \frac{P_t A_e a^2 L \Delta r}{r^2} \eta \tag{3.16}$$

[e.g., Gage and Balsley, 1980] There are many interesting features for the uniformly distributed targets. First, the backscatterd power, P_r, is proportional to $\frac{1}{r^2}$, not to $\frac{1}{r^4}$ as in the case for a hard target. Secondly, P_r linearly depends on the effective antenna aperture A_e, whereas P_r is proportional to A_e^2 in the case for a hard target.

Thirdly, P_r is independent of the probing radar wavelength. These properties makes the power aperture product P_tA_e a good indication of the sensitivity of the radar. Finally, P_r linearly depends on the term Δr, which does not appear in the case for a hard target. This means that any attempt to improve the range resolution of an atmospheric radar would be made at the expense of reduced sensitivity.

The above situation can also be applied to the incoherent (thermal) scattering (see Section (3.3.4)) due to free electrons in the ionosphere observed with sufficiently large frequencies (about 1 GHz). The volume reflectivity (generally at VHF) for incoherent scattering is, with some simplification given by

$$\eta_{incoh} = \frac{N_e \sigma_e}{2} \tag{3.17}$$

[e.g., Gage and Balsley, 1980] where N_e is the number density of electrons and $\sigma_e \approx 10^{-28}$ m^{-2} is the backscattering cross-section of an electron. The received power is proportional to the electron density in the case incoherent scattering.

3.2.3 Specular targets

In the previous section we considered two extreme cases of a single target and uniformly distributed targets. In this section we consider the case of specular targets, which occur when reflection occurs from an extended horizontal layer whose refractive index differs slightly from its surrounding. This occurrence is termed as Fresnel (or partial) reflection. This may be treated as a planar mirror with reflectivity ρ for incident electric field [Friend, 1949]. The radar equation for this case is easily found because we consider the case of one-way transmission from the antenna to the image of the receiving antenna located, at a distance $2r$, as it would appear when reflected in the reflecting layer. The P_r is thus given by

$$P_r = \frac{P_t G_t A_e L}{4\pi (2r)^2} \mid \rho \mid^2 = \frac{P_t A_e^2 L}{4\lambda^2 r^2} \mid \rho \mid^2 \tag{3.18}$$

[e.g., Röttger and Liu, 1978; Gage and Green, 1978] where $\mid \rho \mid^2$ is the power reflection coefficient which depends on the reflectivity structure in the volume of the atmosphere being observed. Comparison of this equation with equations (3.12) and (3.16) reveals that although P_r is proportional to $\frac{1}{r^2}$ as in the case for distributed targets, it is proportional to $\frac{A_e^2}{\lambda^2}$ as in the case for a hard target. Another important aspect of the Fresnel reflection is its aspect sensitivity, (also termed as specularity), i.e. P_r falls off rapidly as a function of zenith angle [e.g., Röttger, 1980]. The above equation assumes that the antenna beam is directed perpendicular to the horizontal layer, for which P_r takes its maximum value.

In the case of Fresnel scatter, the above equation is given by

$$P_r = \frac{P_t A_e^2 L \Delta r}{4\lambda^2 r^2} \mid \rho \mid^2 \tag{3.19}$$

[e.g., Hocking and Röttger, 1983]. It is noteworthy here that the P_r is proportional to Δr, in contrast to Fresnel reflection [i.e., no Δr dependence, see equation (3.18)]. That is, if the backscattered power is due to a single thin layer, there is no Δr dependence. In contrast, a volume filling, horizontally layered structure comprised of many thin, stable partially reflecting layers which are randomly distributed in the vertical can be expected to add incoherently to give a Δr dependence on the backscattered power (see Hocking and Röttger [1983] for more details).

Another important application of this kind is the reflection from meteor trails which appear in the 80-100 km height range. A meteor trial is a strong localized ionization produced along the path of a meteor caused by the frictional heating when it penetrates into the earth's atmosphere. The radar equation in this case is given by (see Chapter 7, equation (7.13))

$$P_r = k \frac{P_t A_e^2 L}{\lambda r^3} q^2 \sigma_e \tag{3.20}$$

where k is a constant, q (electron/metre) is a line density, and σ_e is the scattering cross-section of an electron. It is noteworthy that P_r is proportional to $\frac{1}{r^3}$ which lies between the cases of a hard target and distributed targets. A more detailed discussion of meteors can be found in Chapter 7.

Finally, it should be noted that all information about the scattering processes are lumped in the scattering cross-section σ (equations (3.12), (3.17) and (3.20)), volume reflectivity η (equation (3.16)), and power reflection coefficient $\mid \rho \mid^2$ (equations (3.18) and (3.19)) terms. The detail discussion of these terms is beyond the scope of this section but can be found in the respective references given.

3.2.4 The range of the target

Ranging, or measurement of the distance to a target, is an important feature of a radar. In our case, the ranging is made by measuring the time delay of the received signal with respect to the transmitted signal.

As long as the refractive index n satisfies the condition $\mid n - 1 \mid \ll 1$ along all of the radio wave path, the speed of the radio wave can be well approximated by that in free space (see equation (3.3); the error in this approximation is given by equation (3.7)). However, on occasions above 95 km during certain atmospheric conditions, the virtual height may be somewhat greater than the real height of scatter at 2MHz [e.g., Namboothiri et al., 1993]. This is because the electron density becomes sufficiently large that the group velocity of radio pulses at frequencies near and below 2 MHz becomes somewhat less than the speed of the light. This can be explained as follows.

Virtual height

Virtual height is an important concept in radio physics. Suppose that a radio signal, say a short pulse, is transmitted vertically from the ground and reflected from the ionosphere. If the time of flight t to the ionosphere and back is measured, an apparent, or virtual, height h' of the reflecting layer may be found; $h' = \frac{ct}{2}$, where c is the speed of the light. The velocity of the pulse, or wave packet, is the group velocity u_g. If h_r is the real height of reflection we therefore have

$$h' = \frac{ct}{2} = c\int_0^{h_r} \frac{dh}{u_g} = \int_0^{h_r} n_g dh \tag{3.21}$$

where n_g is the group refractive index. If we assume that the effects of the earth's magnetic field and of collisions are small, we may write for the phase refractive index

$$n = (1 - \frac{N_e}{N_c})^{1/2} \tag{3.22}$$

where N_e is the number density of electrons (m^{-3}), and N_c is the critical plasma density. It should be noted here that the third term in equation (3.7) gives an approximation, valid only when $N_c \gg N_e$. The critical electron density N_e thus determines the condition where the total reflection occurs in the ionosphere. It is given in MKS units by

$$N_e = \frac{4\pi^2 \epsilon_0 m_e}{e^2} f^2 = 1.24 \times 10^{-2} f^2 \tag{3.23}$$

where ϵ_0 is the dielectric constant in free space, m_e and e are the mass and the charge of an electron, respectively, and f is the radar frequency [e.g., Stix, 1962]. It is then easy to show that

$$n_g = \frac{\partial}{\partial \omega}(\omega n) = n^{-1} \tag{3.24}$$

and we find for the virtual height

$$h' = \int_0^{h_r} \frac{dh}{n} \tag{3.25}$$

The virtual height is thus always greater than the real height (because $n \leq 1$, $n_g > 1$) and regions where n is small, for example near the (total) reflection level, will make important contributions to h'. Therefore group retardation arises whenever the background electron density approaches the critical plasma density. In general, however, in the lower and middle atmosphere (below about 100 km) $| n - 1 | < 10^{-3}$ as shown in Figure 3.1, so that the error is negligible for most practical applications.

Note that our assumptions that we can ignore the earth's magnetic field and collisions are not actually valid at 2 MHz.

Range and range resolution

Usually the MST radars and incoherent scatter radars (VHF/HF/MF) apply the conventional pulse modulation technique, i.e a short pulse is transmitted as shown in the sketch of Figure 3.2a, and the backscattered echo from a range r (or altitude z) is received after time t_R. Sampling the received echoes as function of time then allows evaluation of the echoes from different ranges. That is, assuming $n = 1$ the range of a stationary target is given by

$$r = \frac{ct_R}{2} \tag{3.26}$$

where c is the speed of the light in vacuum and t_R is the time of the round trip for a radar pulse between the transmission and reception. Figure 3.2a schematically shows a time-height chart between the range and round trip time interval for a radar echo. For example, the returns from the range r_1 can be sampled by receiving the signal returns after the time t_1, where $t_1 = \frac{2r_1}{c}$ (see Figure 3.2a).

In general the pulse shape is assumed to be rectangular, but in real applications the pulse shape is typically either Gaussian, triangular or smoothed trapezoidal. If the radar target is a thin reflecting surface (e.g., discrete, single or hard target scattering), the shape of the received pulse is the replica of the transmitted pulse. Now assume that many scatterers fill all ranges along the radar beam (e.g., soft target or volume scattering). Figure 3.2b shows schematically the transmission and reception of a purely rectangular pulse with a width Δt. It is then obvious from the figure that echoes from the range between $r_1 - \frac{c\Delta t}{2}$ and r_1 reach the receiver simultaneously at t_1, and those from r_1 to $r_1 + \frac{c\Delta t}{2}$ are received at $t_1 + \Delta t$. In total, the sampling volume extends from $r_1 - \frac{c\Delta t}{2}$ to $r_1 + \frac{c\Delta t}{2}$ which corresponds to a thickness of $c\Delta t$. The right panel in Figure 3.2b shows that the weighting function of the sampling volume has a triangular distribution partly overlapping the weighting function of the adjacent upper and lower sampling volumes. Therefore the range resolution Δr is given by

$$\Delta r = \frac{c\Delta t}{2} \tag{3.27}$$

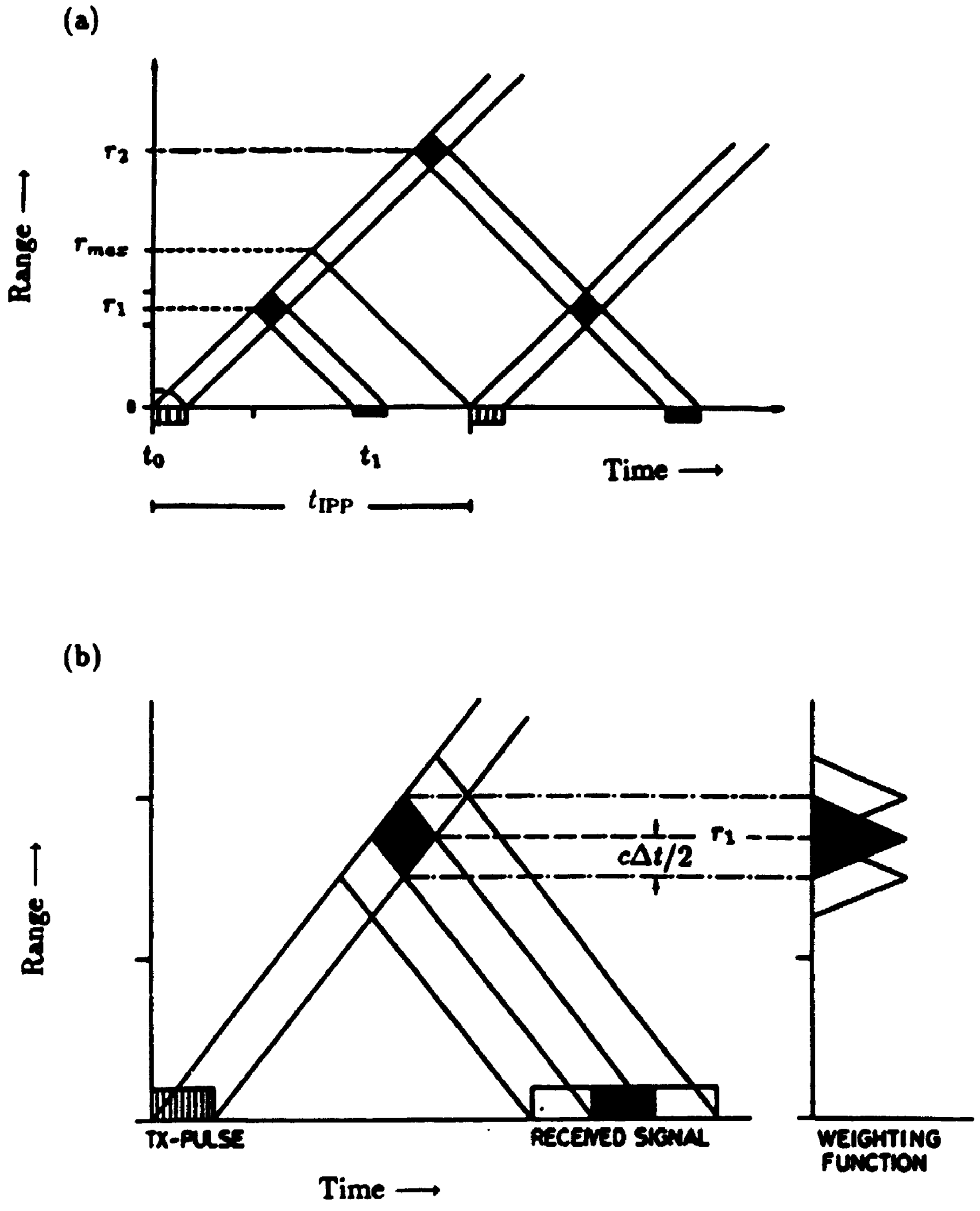

Figure 3.2: (a) Range-time chart explaining the main features of pulse transmission and reception from a volume target. The solid lines correspond to propagation of transmitted and received radio waves. The dashed-dot lines show a second-time-around echoes due to ionospheric scattering (see text for details). (b) Range-time chart and sampling weight when a rectangular pulse is transmitted (see text for details).

which corresponds to the half-power of the weighting function. In reality, the returned profile is a convolution between pulse and layer and in any detail calculation this should be borne in mind [e.g., Hocking and Röttger, 1983].

The equation (3.27) suggests the range resolution can be improved by reducing the pulse duration. Unfortunately, however, this is a conflicting relation between the pulse length (Δt) and its band-width (ΔB), i.e. $\Delta B \propto \frac{1}{\Delta t}$. Since signal-to-noise power increases with decreasing ΔB (because the noise power $P_n = kT\Delta B$, where k is the Boltzmann constant, and T is the noise temperature represents all kind of noise sources, such as resistors, sky noise, etc.), we obtain SNR $\propto \frac{1}{\Delta B} \propto \Delta t$. For the case of distributed targets (see Section 3.2.2), the equation (3.16) shows that the received echo power P_r is proportional to Δr (i.e. proportional to Δt), which represents the number of scatterers in the range cell. The SNR thus becomes proportional to Δt^2, setting a severe restriction in improving the range resolution.

Choice of inter pulse period

The interval t_{IPP} between the successive pulse transmissions is called Inter Pulse Period (IPP), and the corresponding frequency (f_{PRF}) is called the Pulse Repetition Frequency (PRF), i.e. $f_{\text{PRF}} = \frac{1}{t_{\text{IPP}}}$. The duty cycle ($D$) is defined as

$$D = \frac{\Delta t}{t_{\text{IPP}}} \tag{3.28}$$

The average transmitter power (P_a) over one inter pulse period is the product of the duty cycle and the transmitter peak pulse power (P_p), i.e. $P_a = DP_p$. Therefore $D = \frac{P_a}{P_p} = \frac{\Delta t}{t_{\text{IPP}}}$. In practice the peak power of a pulsed system is much higher than the average power. These relationships show that the SNR is linearly dependent on the average transmitted power in the IPP. Therefore, in order to increase the SNR, the IPP should be as short as possible when the pulse length and peak transmitter power are fixed. On the other hand, a sufficient length of time must elapse after a pulse is transmitted in order to receive all of the radar echoes before the transmission of the next pulse. Thus, the IPP is determined primarily by the longest range at which targets are expected. Because in normal radar operations the pulse repetition frequency is kept constant, i.e. the transmitted pulse train is periodic, the pulse repetition can introduce "range aliasing". This ambiguity is depicted in Figure 3.2a. The choice of IPP (or PRF) will be further discussed in the following section.

3.2.5 Range aliasing

If the IPP is too short, echo signals from some targets might arrive after the transmission of the next pulse, as indicated by the dot-dashed lines in Figure 3.2a. These echoes from a range greater than $\frac{ct_{IPP}}{2}$ are received during the same time that as echoes from targets nearer than $\frac{ct_{IPP}}{2}$ return echoes from the next pulse. That is, on the reception of pulse 2 from range r_1 (i.e. $r_1 = \frac{ct_1}{2}$) there is a superposed contribution due to pulse 1 from range r_2 (i.e. $r_2 = \frac{c(t_1+t_{IPP})}{2}$, also see Figure 3.2a). Higher order range aliasing can still occur from ranges $r_n = \frac{c(t_1+nt_{IPP})}{2}$, where n is an integer and $n \geq 2$. This ambiguity in the ranging is called a "range aliasing". Because these undesired echo contributions return from separate scatter volumes, the echo signals are uncorrelated but their power still accumulates in the same receiver range gate. If no special arrangement (e.g., pulse-coding, frequency changes or non-periodic t_{IPP}) are made, the maximum unambiguous range is $r_{max} = \frac{ct_{IPP}}{2}$.

<u>The UWO MF radar</u>: The UWO MF radar uses a pulse repetition frequency (PRF) of 60 Hz (i.e. $t_{IPP} = 16.67$ ms). The half-width of the optimum pulse length is ~ 20 μs, thereby giving a range resolution of ~ 3 km. The transmitter duty cycle is $\sim 0.12\%$. The maximum unambiguous range of the MF radar is $r_{max} = \frac{ct_{IPP}}{2} = 2500$ km. However, on the reception of pulse 2, echoes scattered from the ionosphere (e.g., ~ 250 km - F2 region) arising from multiple reflections due to pulse 1 may contribute in the same receiver range gate. The echo scattered from 250 km corresponds to 1.667 ms ($= \frac{2 \times 250 \text{ km}}{c}$) round trip time. Therefore, the echo scattered from 250 km due to pulse 1, after 10 'hops' (i.e. 10 multiple reflections between ionosphere and ground), will be superposed with the echo scattered from 0 km due to pulse 2. Similarly echo scattered from 251 km due to pulse 1, after 10 hops, will be superposed with the echo scattered from ~ 10 km due to pulse 2,......, and the echo scattered from 260 km due to pulse 1, after 10 hops, will be superposed with the echo scattered from ~ 100 km due to pulse 2.

The normal ionospheric echoes are much weaker than the clear air echoes and have much a broader spectral distribution. Therefore, they may instead act as a white noise added to the normal cosmic noise. Although range aliased ionospheric echoes increase the noise level, depending on the electron density, they do not present a large problem with our MF system. Continuous observations over the past three years show that only during a few occasions ($< 1\%$) there were weak ionospheric echoes observed below 60 km during the night time. Since there are no echoes (i.e. $< 1\%$) observed below 60 km we concluded that there are no problems arising from multiple hops in the 0-60 km range, and so it seems unlikely that there were any effects in the

70-100 km range either. A more detailed description of the MF system is contained in Section 3.4.3.

The VHF meteor radar: The half-width of the optimum pulse length used with the VHF meteor radar is $\sim 13.33\ \mu s$, thereby resulting a range resolution of ~ 2 km. A pulse repetition frequency (PRF) of 1100 Hz (i.e. IPP = 0.91 ms) was used in the beginning of the operation (from July 1994 to December 1994) and later (From January 1995) increased to 2143 Hz (i.e. IPP = 0.47 ms) in order to increase the meteor rate (see Chapter 7 for more details). Thus, the transmitter duty cycle was $\sim 1.47\%$ in the beginning of the operation and later increased to $\sim 2.86\%$. It is noteworthy here that the PRF of 2143 Hz is carefully chosen so that there is no ambiguity in the ranging, and this can be explained as follows.

The maximum unambiguous range of the VHF meteor radar is $r_{max} = \frac{cIPP}{2} \sim 70$ km. Therefore, on the reception of pulse 1 from 70 km there is also a contribution to the signal due to pulse 2 being scattered from 0 km. Similarly, on the reception of pulse 1 from 80 km there is also a contribution to the signal due to pulse 2 being scattered from 10 km,..., and on the reception of pulse 1 from 110 km there also is a contribution to the signal due to pulse 2 being scattered from 40 km. However, there is evidence that meteors seldom occur below 78 km or above 110 km altitude (at the radar wavelength of 7.375 m, employed in this study). Therefore, taking 78 and 130 km (maximum range recorded in our analysis procedure, see Chapter 7 for more details) as being limits to the heights of meteors, unambiguous meteor echoes could be detected in this range. In addition, our meteor detection algorithm tests whether the meteor echo is characterized by a rapid initial rise in amplitude, followed by small amplitude fluctuations. It turns out that the maximum amplitude of the meteor echo is reached frequently within $\frac{1}{10}$ s, and it was decided to use this value as a reliable time limit in the meteor detection procedure. This process successfully rejected aircraft, E-region echoes (e.g., sporadic E) and possible turbulent scatter. A more detailed description of the VHF meteor system is contained in Chapter 7.2.1.

3.3 Scattering and reflection mechanisms

The nature of the scattering and reflection mechanisms that give rise to the MST radar echoes from the clear air has been a subject of investigation for many years. The understanding of these mechanisms is essential for the correct interpretation of the data, which carry information about winds, waves, turbulence and stability in the atmosphere. In order to explain qualitatively the relevant MST radar observations, two different basic echoing mechanisms are required, namely scattering and reflection. Volume scattering from isotropic or anisotropic turbulence, and partial reflections from horizontally stratified, sharp refractive index gradients are believed to be the main contributors to the radar echoes. In general, it is most likely that combined effects from all these mechanisms produce the observed data [e.g., Lesicar and Hocking, 1992]. This section describes a qualitative synopsis of the basic echoing mechanisms that give rise to backscattering from the clear atmosphere. The discussion in this section mainly follows that of Röttger [1980], Balsley and Gage [1980], Gage and Balsley [1980], Hocking and Röttger [1983], Doviak and Zrnic [1984], Gage et al. [1985], Röttger and Larsen [1990], and Gage [1990], in addition to the references given.

3.3.1 Turbulent scatter, Fresnel scatter and Fresnel reflection

Figure 3.3 contains a sketch of the pertinent atmospheric structure. The occurrence of echoes from the clear atmosphere requires structure in the medium at the scale of half wavelength of the probing radio wave. The principle scattering mechanism widely believed to cause a majority of the clear air echoes observed by MST radars is called "turbulent scatter" or "Bragg scatter". The turbulent scatter can be isotropic or anisotropic. In the case of isotropic turbulent scattering, the mechanism requires active turbulence mixing of a gradient in the refractive index profile. Echoes showing no apparent aspect sensitivity are expected to be of this type. Anisotropic turbulent scattering also requires active turbulent mixing of a gradient in the refractive index profile, but the correlation scales which characterize the turbulence is different. For a stable atmosphere this usually means that the correlation distance is much less in the vertical than in the horizontal. The anisotropy in the turbulence field implies an angular dependence in the echo magnitude, i.e. causing an aspect sensitivity.

The process is called "Fresnel reflection" if a single, isolated sharp refractive index gradient with large horizontal distance (comparable to a 'Fresnel zone') exists in the vertical direction. Fresnel reflection produces a sharp peak in the vertical power profile which rapidly decreases as the zenith angle is increased. This process is also called "partial reflection", because only a fraction of the incident power is reflected. Fresnel reflection is called "specular reflection" if the horizontal surface of the discontinuity is assumed to be very smooth, and is called "diffuse reflection" if the discontinuity is assumed to be corrugated or somewhat rough [e.g., Röttger, 1980]. The Fresnel reflection mechanisms appears to contribute to radar echoes both from the lower

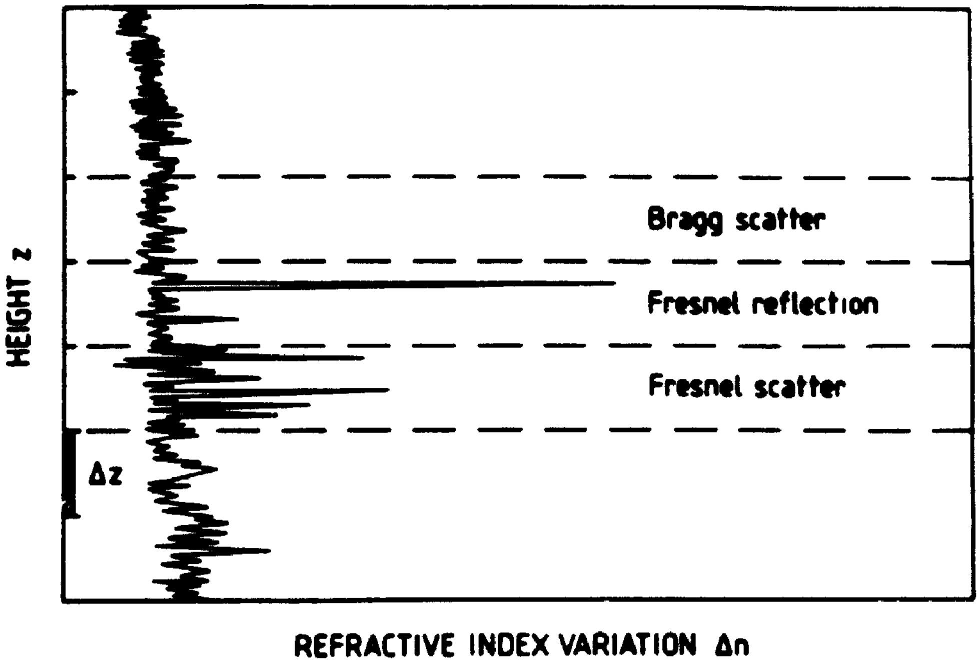

Figure 3.3: Schematic depiction of the spatial variations Δn of the refractive index in the vertical direction. The range gate is indicated by Δz. Depending on the structure of n within the range Δz, the different processes of "turbulent scatter", "Fresnel reflection" and "Fresnel scatter" can occur. The abscissa n can also be interpreted as the relative horizontal extend of constant refractive index surfaces for the different processes. Turbulent scatter occurs at every range where the variation in n is similar to the variation in the indicated range Δz. Thermal electron density fluctuations, which cause incoherent (thermal) scatter, are much weaker than the indicated variations of n [after Röttger, 1989].

neutral atmosphere and the ionosphere, especially at vertical incidence for long wavelengths radars. Observations in the lower neutral atmosphere with VHF radars has offered considerable evidence for the importance of Fresnel reflections from stable, horizontally-layered structure in the troposphere and stratosphere [e.g., Gage and Green 1978; Röttger and Liu, 1978; Fuku et al., 1978; Röttger and Vincent, 1978] and in the mesosphere [e.g., Fukuo et al., 1979, Lesicar and Hocking, 1992]. Reflection from meteor trails has long been used to determine the neutral wind motions (and possibly turbulence) in the upper mesosphere. This mechanism is also considered as a Fresnel or specular reflection process [Grossi et al., 1972] which yields usable data in the 80-100 km height range on radar systems with MST capability. This will be further discussed in Section 7.1.5.

The process is called "Fresnel scatter" if collections of isolated sharp gradients (instead of a single isolated sharp gradient) of the refractive index exist in the vertical direction. These sharp refractive index gradients are still randomly distributed in the vertical direction, but have a large correlation distance in the horizontal direction. This is an intermediate structure, and is more likely an example of realistic atmospheric structure. Fresnel scatter has many of the features of Fresnel reflection and can be thought to be comprised of the incoherent sum of partial reflections from many thin layers. It also has much in common with anisotropic turbulence.

The Fresnel scatter and Fresnel reflection are most likely in the longer radar wavelengths (i.e. in the low VHF or higher band). The Fresnel scatter and Fresnel reflection terms have been introduced because the horizontal correlation distance of the discontinuities is longer than the radar wavelength but of the order of the Fresnel zone (see Section 7.1.5). Transition to (anisotropic) turbulence scatter takes place for correlation distances much smaller than a fraction of the Fresnel zone. The Fresnel zones of typical VHF and UHF radars are always smaller than the region illuminated by the radar beam, (typically in the troposphere and stratosphere). Thus, the beamwidth limiting effect has not to be considered [Liu and Yeh, 1980]. It is perceived from Figure 3.3 that the definition of Fresnel scatter and Fresnel reflection depend, in some sense, on the radar height resolution; that is, Fresnel reflection is more likely to be observed with good (fine) height resolution, and Fresnel scatter with coarse height resolution (also see equation (3.18)).

The schematic view of atmospheric structure contained in Figure 3.3 is obviously an idealized abstraction of the refractivity structure of the real atmosphere. However, the observed echoes are usually a combination of the scattering/reflection processes summarized above, although one mechanism may dominate at any given time depending on the relative contributions of humidity, temperature, and free electron density (see equation (3.7)). The complexities of the real atmosphere lead to many effects that are a challenge to model theoretically. While much progress has been made in this subject in recent years, issues that have not been adequately addressed remain, and further discussion of these is beyond the scope of this section.

3.3.2 Volume scattering

A (MF) radar detects radar echoes (energy) scattered from within a medium when spatial variations or irregularities are present. This is quite different from the action of an ionosonde (which depends on the gradual bending of the ray within a medium of gradually varying refractive index) or of a radar for detecting a hard target (where the echo comes from a discrete surface).

Whether ionized or not, the atmosphere contains irregularities of many different sizes, and we may imagine that at each boundary a small fraction of the incident energy is scattered in all directions. Signals scattered from irregularities spaced by half a wavelength will reinforce in the direction back to the radar and thus, despite the weakness of each scattering, they can add up to a single signal strong enough to be detected. It is not necessary for the scattering structures to be regularly spaced; a radar of wavelength λ will effectively select the spatial component of scale $\frac{\lambda}{2}$, ignoring of others. Instead of a discrete echo, volume scattering produces a continuous, noise-like return which has to gated to select the signal from each range.

The process of volume scattering is essentially one of partial reflection from the refractive index discontinuities due to the irregularities (see Section 3.3.1). The value of the partial reflection method is that it enables the ionosphere to be observed in a near continuous manner over the height range 60-100 km. This is difficult to achieve otherwise, particularly at middle and high latitudes, because the electron density is too small to be detected with ionosondes and satellites cannot remain in orbit so low down. Likewise incoherent radars cannot be used: even with a powerful incoherent scatter radar long integration is needed, since the electron densities are usually between 10^8 and 10^9 m^{-3} in the 70-90 km height range.

3.3.3 Coherence

The term "coherent" and "incoherent" are somewhat loosely applied here. What coherence really means is the stability of the medium - i.e. how quickly it changes

- in relation to the radar's ability to resolve those changes. All fluids are in reality partly coherent, and there will be some 'coherence time' (between zero and infinity) for each situation. Thus, one radar system might be able to receive echoes from a scattering region so rapidly that little change occurs between successive echoes, while with another there might be a large variation between the arrival of one echo and the next. If the coherence is high, successive echoes (or echo samples, depending on the details of the technique) have very similar amplitude and phase, and thus may be added coherently, so improving sensitivity. If incoherent, successive returns are unrelated in amplitude and phase, and may be added only in terms of their powers. This also improves the sensitivity, but to a lesser extent.

By convention, radars detecting the thermal fluctuations of the medium, where the coherence time is relatively short, have been called 'incoherent' (probably caused by scatter), while those using structures within the medium which tend to vary more slowly, are called 'coherent' (probably caused by reflection or refraction) [e.g., Doviak and Zrnic]. But it is worth remembering that in each case the coherence time may be one of the most important measurements to be made, and to do this the radar must in fact bridge the gap between coherence and incoherence.

3.3.4 Coherent and incoherent scatter

While it is large (macroscopic) changes in n that are responsible for refraction or total reflection, it is small scale changes of n in the atmosphere that are responsible for radar scattering and partial reflection. Statistical fluctuations of the electron density due to random thermal motion of electrons and ions can be strong enough in the ionosphere to cause detectable scattering. This process is called incoherent scattering because scattered wave from individual electrons are random in phase, so that they add up incoherently. Received power is then proportional to the number of electrons illuminated by the radar. Because the antenna has to be large relative to the radio wavelength, incoherent scatter radar produces a narrow beam and achieves far better spatial resolution. The principal disadvantage is that an incoherent radar has to work with a very weak signal. It therefore requires a transmitter of high power, a large antenna, and the most sensitive receiver and sophisticated data processing available, all of which add up to a major facility and considerable expense.

Fluctuations due to atmospheric turbulence are generally assumed to be the major source of scattering in the lower and middle atmosphere. This process is often called coherent scattering, in contrast to the incoherent scattering in the ionosphere. The main difference of the coherent scattering from the incoherent scattering is that fluctuation of n is caused by macroscopic motion of air parcels, each of which contains a large number of electrons and/or molecules which contribute to the scattered electric field coherently in phase. Unlike incoherent scatter, where the scattered echo power is proportional to the number density of free electrons, the scattered echo power in coherent scattering is roughly proportional to the square of the number density of scatterers (see equations (3.18), (3.19) and (3.20)), although note that the scattering efficiency of each scatterer depends in part on the mean electron and density gradient.) This substantial enhancement in the echo power makes the design of MST radars much simpler and relatively less expensive than incoherent scatter radars.

3.4 Data analysis technique

Over the past 30 years, ground-based atmospheric radars have played an ever increasing role in the study of the lower and middle atmosphere dynamics. Background wind, turbulence and waves in the mesosphere, stratosphere, and troposphere (thus the generic name of MST radars) can now be studied with fine height and temporal resolution. Numerous developments in the transmitter and receiving systems as well as in signal analysis and data processing techniques supported by the advent of more powerful and affordable microcomputers have turned those radars into state of the art facilities for probing the clear atmosphere.

Generally, at least two radar techniques have been used to measure winds, as well as other parameters in the lower and middle atmosphere: Doppler radar and Spaced Antenna (SA) systems. We will briefly review the former technique, but will concentrate more on the spaced antenna technique and its general characteristics since it is by this method that the bulk of the data for this thesis were collected.

Both techniques derive their information from radar echoes from irregularities in the refractive index of the atmosphere. These irregularities arise from fluctuations in temperature, humidity, and pressure in the troposphere-stratosphere and in electron density in the mesosphere (see Section 3.1). In both regions, echoing mechanisms can involve turbulence scattering as well as Fresnel reflection and Fresnel scatter from stratified structures (see Section 3.3).

The Doppler technique makes use of one or more narrow beams pointed in different directions. For practical reasons, such as antenna size, it is usually applied at very high frequencies (VHF; 30-300 MHz) with some exception, e.g., Hocking [1983] has reported Doppler measurements at MF with the large Adelaide array. The Doppler shift measured in each beam direction provides the corresponding radial velocity, a projection of the background wind vector along the beam line of sight. It is customary to use a vertical beam and two or more non-colinear oblique beam directions in order to resolve the 3-dimensional wind vector. Doppler radars which sequentially switch one beam from one position to another are often called Doppler Beam Swinging (DBS) systems.

SA methods relate to systems that use multiple non-colinear receiving antennas. SA is a generic term which includes different analysis techniques: similar fades, Full Correlation Analysis (FCA) techniques, etc. To derive atmospheric motion, the similar fades method makes use of the time series at the separate receiving antennas. The time delays for maximum cross correlation between the received signals provide the so-called "apparent velocity" [Mitra, 1949]. Because the apparent velocity will lead to velocities that are too large if random changes are associated with the atmospheric motion [Briggs, 1984], a more sophisticated technique, called the full correlation analysis, is usually preferred. Designed by Briggs et al., [1950] and later improved by Phillips and Spencer [1955] and refined by Fedor [1967] and Gregory et al., [1979], the FCA method takes into account anisometric patterns and changes in the diffraction pattern structure but assumes that the spatial and temporal variations have the same functional form, usually Gaussian. The FCA method derives the so-called "true velocity" as well as information on the diffraction pattern from the both the mean auto-correlation and cross-correlation. Briggs [1984] provides the most recent and straightforward FCA review to date. Originally designed for ionospheric E and F region studies [Briggs, 1968], the FCA method has also been applied to the D-region [Briggs, 1977], and extensively used in the mesosphere at medium and high frequencies (MF: 1-3 MHz, HF: 3-30 MHz) [Hocking, 1989]. The SA technique has also been successfully implemented at VHF to sound the neutral lower atmosphere and detect tropospheric and stratospheric winds [Röttger and Vincent, 1978; Vincent and Röttger, 1980; Röttger, 1981; Vincent et al., 1987].

Briggs [1980] has reviewed both the advantages and disadvantages of the SA technique and the Doppler technique. He also shows that, for the case that all scatterers in the radar volume move with the same horizontal velocity, and have zero vertical velocity, then both methods must derive their information from the amplitudes and phases of the radar returns from different angles and must provide similar information about scattering irregularities, provided that the measurements are made at the same radio frequency and the same radio wave scatterers are involved. Therefore the choice between the two techniques cannot be made on theoretical grounds, but rather on practical considerations. The main difference between the SA technique and the Doppler technique lies in the direction of the radar beams. The SA technique uses vertically directed beams, whilst the Doppler technique uses beams tilted off-vertical to obtain horizontal wind velocity components plus a vertical beam to obtain vertical winds.

3.4.1 The similar fades technique

A variety of techniques have been devised to utilize the temporal variations of radio echo fading observed at several closely spaced aerials. The basic technique is to observe, using spaced receivers, the fading of radio signals which have either been reflected from the atmosphere (or ionosphere) or transmitted through it. If the spacing is smaller than the correlation distance of the fading it is likely that each receiver will record a similar fading pattern but with a small time displacement superimposed, as in Figure 3.4a. The simple interpretation is that a region of irregularities is moving bodily across the observation site. Knowing the geometry of the receiving network, it is then not difficult to deduce the speed and direction of the ionospheric motion.

Most of the methods derive from the basic methods of 'similar fades' proposed by Mitra [1949]. Mitra assumed that, on the average, the contours of constant amplitude of the diffraction pattern at the ground were circular and that the observed fading of the pattern at the ground was due solely to the horizontal motion of the pattern across the receivers. "Velocities" were determined from the vector distances between pairs of receivers, divided by the time shifts between the fading records. The apparent velocity of the ground diffraction pattern across a pair of sensors i and j, can be determined as follows. Apparent velocity vectors, V'_{ij} along the direction between the pairs of receivers i and j, can be determined directly from the observational data by

$$V'_{ij} = \frac{d_{ij}}{\tau'_{ij}} \tag{3.29}$$

where d_{ij} is the distance between sensors and τ'_{ij} is the time lag for maximum cross correlation between records for that pair of sensors.

To take a simple case, let the receivers from a right-angled triangle as in Figure 3.4b. Then the time differences t_1 and t_2 give 'apparent velocities' V'_x and V'_y in the x and y directions:

$$V'_x = \frac{R_1R_3}{t_2} \tag{3.30}$$

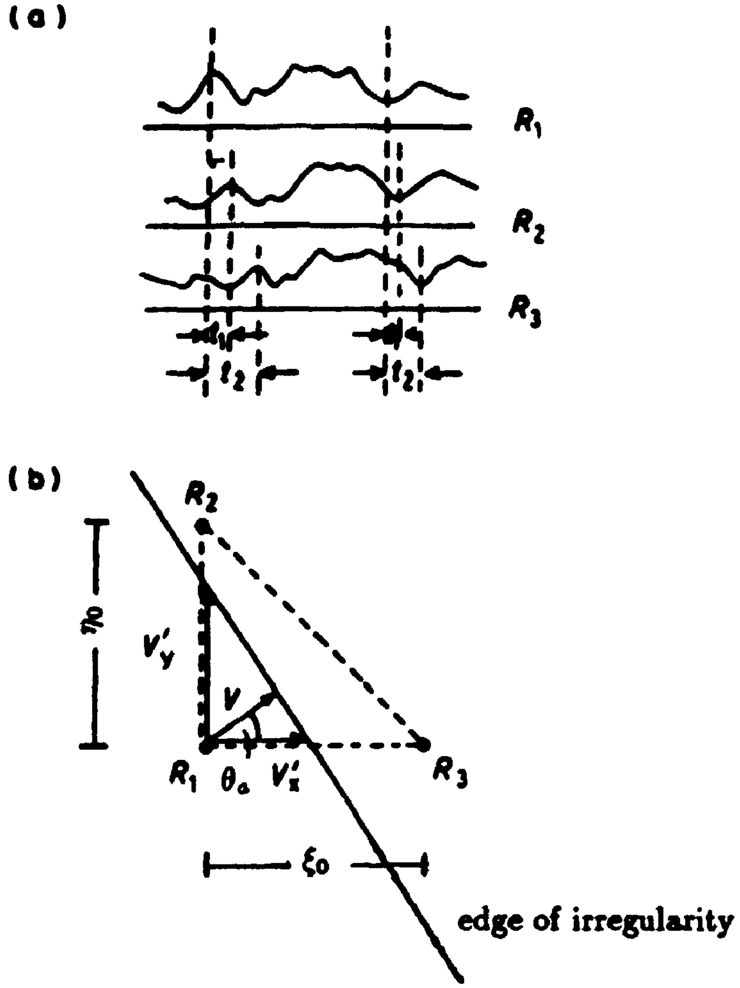

Figure 3.4: (a) The spaced antenna method for observing the movement of a diffraction pattern of irregularities over the ground. (b) Relation between true and apparent velocities (see text for details).

$$V_y' = \frac{R_1 R_2}{t_1} \tag{3.31}$$

From Figure 3.4b it is seen that

$$\frac{1}{V_a^2} = \frac{1}{(V_x')^2} + \frac{1}{(V_y')^2} \tag{3.32}$$

and hence

$$V_a = \frac{V_x' V_y'}{[(V_x')^2 + (V_y')^2]^{\frac{1}{2}}} \tag{3.33}$$

also,

$$\theta_a = \tan^{-1}(\frac{V_x'}{V_y'}) \tag{3.34}$$

Note that V_x' and V_y' are not velocity components in the usual sense.

If the contours of the ground diffraction pattern were on the average circular, and if there were no random changes, the true speed and direction of motion of the pattern would be described by the "apparent" velocity vector; this situation is actually a special case. If an isometric pattern is subject to random changes, the diffraction of the motion is unaffected, but the true velocity of drift is less than that determined by V_a. When the pattern evolves with time and is systematically elongated in one direction (anisometric), assessment of the pattern requires a more rigorous treatment, usually known as full correlation analysis (FCA).

3.4.2 Full correlation analysis

The failure of the similar fades technique to account for the effects of random changes and pattern anisometry led to the development of the "Full Correlation Analysis" (FCA). With advances in computing power, this method has gained more popularity and is the subject of the rest of this section, which closely follows Briggs [1984]. FCA begins by first considering the two-dimensional cross correlation $\rho(\xi,\eta)$ of a random pattern described by the function $f(x,y)$:

$$\rho(\xi,\eta) = \frac{<(f(x,y) - <f>)\cdot(f^*(x+\xi, y+\eta) - <f>)>}{<(f(x,y) - <f>)\cdot(f^*(x,y) - <f>)>^2} \tag{3.35}$$

where ξ and η are the spatial shifts in the x and y directions, $< .... >$ indicate averages and the asterisk denotes a complex conjugate. The function f may represent either a complex amplitude of the reflected signal, in which case the correlation function will contain a phase angle, or the modulus of this amplitude, in which case the correlation function will be real. Usually the data are adjusted so that $<f>= 0$, and we will assume this here. If the 2-dimensional function (i.e. $f(x,y)$) is random and isotropic then the cross correlation function $\rho(\xi,\eta) = constant$ forms a set of concentric circles. Mathematically, a function of a general quadratic from is usually adequate to describe the spatial correlation functions $\rho(\xi,\eta)$. Therefore $\rho(\xi,\eta)$ is only dependent on the radial displacement from the origin and we may write,

$$\rho(\xi,\eta) = \rho(A\xi^2 + B\eta^2) \tag{3.36}$$

If however, a systematic stretch is applied to the random 2-dimensional function, $\rho(\xi,\eta)$ becomes a set of concentric ellipses which may be described by,

$$\rho(\xi,\eta) = \rho(A\xi^2 + B\eta^2 + 2H\xi\eta) \tag{3.37}$$

When the function evolves with time but shows no systematic movement, a 3-dimensional $\rho(\xi,\eta)$ may be drawn with axes of ξ, η and τ. In this coordinate system, surfaces of constant correlation will form concentric ellipsoids aligned with the τ axis. Now the $\rho(\xi,\eta)$ may be described by

$$\rho(\xi,\eta,\tau) = \rho(A\xi^2 + B\eta^2 + K\tau^2 + 2H\xi\eta) \tag{3.38}$$

Note that there cannot be terms in $\xi\tau$ and $\eta\tau$ since these would lead to a tilt of the ellipsoidal correlation surfaces with respect to the τ axis. The form (3.38) implies that the temporal auto-correlation function which would be obtained from a single sensor at a fixed point in the pattern is given by

$$\rho(0,0,\tau) = \rho(K\tau^2) \tag{3.39}$$

Similarly, at a fixed time in any direction in space (say x direction) a spatial auto-correlation is given by

$$\rho(\xi,0,0) = \rho(A\xi^2) \tag{3.40}$$

Therefore, it is important to note that we have assumed that the temporal auto-correlation function and the spatial auto-correlation function have the same functional form. This assumption forms the basis of the FCA technique.

We can now consider, a diffraction pattern moving across the receivers with velocity V in a direction ϕ, as measured in a clockwise direction from the y-axis. The motion of the pattern can be introduced into the formulation by considering an observer in a frame of reference which moves with the pattern. The coordinates of this frame of reference are represented by the primed quantities (x',y',t), so that the pattern can now be represented by $f(x',y',t)$ and the associated correlation function is given by

$$\rho(\xi',\eta',\tau) = \rho(A\xi'^2 + B\eta'^2 + K\tau^2 + 2H\xi'\eta') \tag{3.41}$$

Note that terms of the form $\xi' \tau$ and $\eta' \tau$ do not appear in this equation, as the ellipsoids are not tilted with respect to the t-axis for a stationary pattern. To this observer, the observed fading will result only from random changes within the pattern. The moving and stationary frames of reference are related by,

$$x = x' + Vt \sin \phi = x' + V_x t \tag{3.42}$$

$$y = y' + Vt \cos \phi = y' + V_y t \tag{3.43}$$

where $V_x = V \sin \phi$ and $V_y = V \cos \phi$ are the components of the steady drift motion of the pattern. Therefore,

$$\xi = \xi' + V_x t \tag{3.44}$$

and

$$\eta = \eta' + V_y t \tag{3.45}$$

substituting these transformations in equation (3.13), we obtain

$$\rho(\xi, \eta, \tau) = \rho(A(\xi - V_x \tau)^2 + B(\eta - V_y \tau)^2 + K\tau^2 + 2H(\xi - V_x \tau)(\eta - V_y \tau)) \tag{3.46}$$

which has the form,

$$\rho(\xi, \eta, \tau) = \rho(A\xi^2 + B\eta^2 + C\tau^2 + 2F\xi\tau + 2G\eta\tau + 2H\xi\eta) \tag{3.47}$$

Equations (3.46) and (3.47) are basic equations used in FCA, and coefficients A, B, C, F, G, and H completely describe the spatial-temporal cross-correlation function of any anisometric, randomly changing moving pattern. All these coefficients can be evaluated experimentally and used to derive the components of the corrected velocity V, called the "true velocity". We will now discuss how the individual coefficients can be derived.

If we want to measure velocity, or any other feature of a 2-dimensional pattern, a minimum of three sensors is required. We consider an array of three sensors, arranged at the points of a right-angled triangle such as depicted in Figure 3.4b, located at (0,0), $(\xi_0, 0)$, and $(0, \eta_0)$. First consider the cross-correlation for two of the receivers, aligned along the x-axis (see Figure 3.4b) and spatially separated by a distance ξ_0. We find that equation (3.47) reduces to

$$\rho(\xi_0, 0, \tau) = \rho(A\xi_0^2 + C\tau^2 + 2F\xi_0\tau) \tag{3.48}$$

To find the maximum, we set $\frac{\partial \rho(\xi_0, 0, \tau)}{\partial \tau} = 0$, which gives,

$$\tau_x' = -\frac{F}{C}\xi_0 \tag{3.49}$$

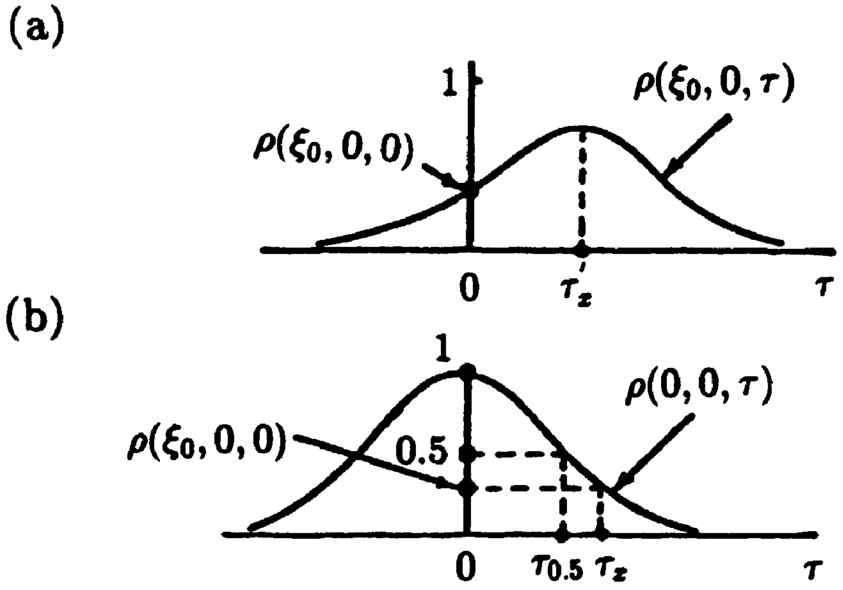

Figure 3.5: (a) Cross-correlation across two receivers separated by a distance ξ_0, and (b) Auto-correlation for a single receiver, as a function of time τ.

Similarly, if we consider the two receivers along the y-axis, we find that:

$$\tau_y' = -\frac{G}{C}\eta_0 \tag{3.50}$$

The lags τ_x' and τ_y' can be easily calculated. To proceed further we make use of the auto-correlation function. In theory, the observed auto-correlation functions for all the receivers should be the same. However, because of noise and other errors of a statistical nature, fluctuations may occur in the individual auto-correlation function. Therefore, in practice the mean of the three auto-correlations is computed and used in the analysis. The temporal auto-correlation is found from equation (3.47), which gives

$$\rho(0,0,\tau) = \rho(C\tau^2) \tag{3.51}$$

We now use the basic assumption that both the spatial and temporal functions have the same functional form, and find the time shift (τ_x) at which the auto-correlation function has the same value as the value of cross-correlation between two sensors at zero lag (i.e. $\rho(\xi_0,0,0)$) (see Figure 3.5). So, mathematically, (τ_x) satisfies the equation

$$\rho(0,0,\tau_x) = \rho(\xi_0,0,0) \tag{3.52}$$

Using equations (3.52) and (3.47), we get

$$\rho(C\tau_x^2) = \rho(A\xi_0^2) \tag{3.53}$$

and so

$$\frac{A}{C} = \frac{\tau_x^2}{\xi_0^2} \tag{3.54}$$

Similarly, we can find the time shift, with the pair of sensors along the y-axis,

$$\frac{B}{C} = \frac{\tau_y^2}{\eta_0^2} \tag{3.55}$$

and the pair of sensors situated at $(\xi_0, 0)$ and $(0, \eta_0)$,

$$\frac{H}{C} = \frac{\tau_{xy}^2}{2\xi_0\eta_0} - \frac{A\xi_0}{2C\eta_0} - \frac{B\eta_0}{2C\xi_0} \tag{3.56}$$

The value of $\frac{H}{C}$ can be found from this equation since the ratio $\frac{A}{C}$ and $\frac{B}{C}$ have already been found. τ_x^2, τ_y^2, and τ_{xy}^2 can be easily calculated. Thus the five ratios, $\frac{A}{C}$, $\frac{B}{C}$, $\frac{F}{C}$, $\frac{G}{C}$, and $\frac{H}{C}$ can be derived from the auto- and cross-correlation functions from the three spaced sensors. Only C (the scale) is required to fully describe the actual form of $\rho(\xi, \eta, \tau)$. Recall that this is the same as the functional form of the observed average auto-correlation function $\rho(0, 0, \tau)$ and is therefore known from equation (3.51). Using equation (3.51), define $\tau_{0.5}$ is the time for the mean auto-correlation to fall to 0.5. Therefore,

$$\rho(0, 0, \tau_{0.5}) = \rho(C\tau_{0.5}^2) = 0.5 \tag{3.57}$$

Finally, the cross correlation function $\rho(\xi, \eta, \tau)$ (equation (3.47)) is fully described by the coefficients A, B, C, F, G and H, and these can be used to evaluate the true velocity of the pattern and other useful information.

It should be emphasized here that the case of three sensors which form a right-angled triangle is not the optimum configuration in practice. In practice, an equilateral triangle (as in our case) is preferred (although any spatial arrangement of sensors can be used), as this symmetrical arrangement is less likely to produce a bias in directional determinations.

True velocity

The components of the mean velocities, V_x and V_y, can be found by equating the coefficients of $\xi\tau$ and $\eta\tau$ in equations (3.46) and (3.47). This gives

$$AV_x + HV_y = -F \tag{3.58}$$

and

$$BV_y + HV_x = -G \tag{3.59}$$

By dividing both equations through by C, we have a pair of linear equations, in which the coefficients $\frac{A}{C}$, $\frac{B}{C}$, $\frac{F}{C}$, $\frac{G}{C}$, and $\frac{H}{C}$ are known. These equations now can be solved for V_x and V_y. The magnitude and direction ϕ of the mean velocity are therefore given by

$$\mid V \mid^2 = V_x^2 + V_y^2 \tag{3.60}$$

and

$$\phi = \tan^{-1}(\frac{V_x}{V_y}) \tag{3.61}$$

The velocity V is termed the "true velocity" to distinguish it from the previously estimated (see Section 3.4.1) "apparent velocity" V_a. The true velocity has been corrected for fading due to random changes in the pattern form and also for spatial anisometry (i.e. contours are systematically elongated in a particular direction) of the pattern. The true and apparent velocities, V and V_a respectively, determined from the ground diffraction pattern, are finally halved to account for the 'point source effect' [e.g., Felgate, 1970]. These velocities are then representative of the motion of the ionospheric irregularities and not the velocity of the diffraction pattern over the ground. In the case where the pattern is isometric and has no change, the apparent and the true velocity will be equivalent. Otherwise the true velocity is always smaller than the apparent velocity.

Estimation of spatial properties of the pattern

The scale and degree of anisometry of the pattern are of interest and useful quantities to estimate. The spatial correlation function (equation (3.47) with $\tau = 0$) is

$$\rho(\xi, \eta, 0) = \rho(A\xi^2 + B\eta^2 + 2H\xi\eta) \tag{3.62}$$

The spatial correlation shows that contours of equal correlation are given by

$$\rho(A\xi^2 + B\eta^2 + 2H\xi\eta) = constant \tag{3.63}$$

The "characteristic ellipse" is usually defined as a particular ellipse for which $\rho = 0.5$, so that

$$\rho(A\xi^2 + B\eta^2 + 2H\xi\eta) = 0.5 \tag{3.64}$$

The time lag, $\tau_{0.5}$, for which the auto-correlation function for a stationary observer falls to 0.5 is given by (setting $\xi = \eta = 0$ and $\tau = \tau_{0.5}$ in equation (3.47))

$$\rho(0, 0, \tau_{0.5}) = \rho(C\tau_{0.5}^2) = 0.5 \tag{3.65}$$

Comparing equations (3.64) and (3.65) we obtain

$$\rho(A\xi^2 + B\eta^2 + 2H\xi\eta) = C\tau_{0.5}^2 \tag{3.66}$$

This is the general equation for the characteristic ellipse in the (ξ, η) coordinate system, while in the (ξ'', η'') coordinate system the equation is

$$\frac{\xi''^2}{a^2} + \frac{\eta''^2}{b^2} = 1 \tag{3.67}$$

where a is the semi-minor axis, b is the semi-major axis, and the axial ratio is $r = \frac{b}{a}$. The transformation between the coordinate systems is affected by rotating the axes through an angle θ so that the η axis lies in the same plane as the major axis of the characteristic ellipse (i.e. on the η'' axis). These two coordinate systems are related by

$$\xi = \xi'' \cos\theta + \eta'' \sin\theta \tag{3.68}$$

and

$$\eta = \eta'' \cos\theta - \xi'' \sin\theta \tag{3.69}$$

Substituting equations (3.68) and (3.69) in equation (3.66), and identification of coefficients with equation (3.67) leads to the following relations

$$\tan 2\theta = \frac{2H}{B - A} \tag{3.70}$$

$$a^2 = \frac{C\tau_{0.5}^2}{A\cos^2\theta + B\sin^2\theta - H\sin 2\theta} \tag{3.71}$$

$$b^2 = \frac{C\tau_{0.5}^2}{A\sin^2\theta + B\cos^2\theta + H\sin 2\theta} \tag{3.72}$$

Eliminating θ between these three equation gives

$$r^2 = \frac{b^2}{a^2} = \frac{(A+B) + (4H^2 + (A-B)^2)^{\frac{1}{2}}}{(A+B) - (4H^2 + (A-B)^2)^{\frac{1}{2}}} \tag{3.73}$$

where the axial ratio is chosen such that $r > 1$. Equations (3.71) and (3.72) can also be written in the form

$$a^2 = \frac{2C\tau_{0.5}^2}{(A+B) + (4H^2 + (A-B)^2)^{\frac{1}{2}}} \tag{3.74}$$

$$b^2 = \frac{2C\tau_{0.5}^2}{(A+B) - (4H^2 + (A-B)^2)^{\frac{1}{2}}} \tag{3.75}$$

The parameters r, a, b, and θ of the characteristic ellipse can be determined since the coefficients A, B, and H are known. Therefore the scale and degree of anisometry of the pattern can be studied. It should be re-emphasized here that we have assumed that the temporal and spatial correlation have the same shape in our calculation.

Estimation of random changes in the pattern

The random changes in the pattern can be estimated as follows. An observer who moves with the pattern will only observe changes in the pattern due to the temporal random changes or evolution of the pattern. These changes can be described by the temporal auto-correlation function of data recorded by such a moving observer. From equation (3.41) this auto-correlation function is of the form

$$\rho(0,0,\tau) = \rho(K\tau^2) \tag{3.76}$$

The "mean life time" or "time-scale", $T_{0.5}$, of the irregularities which cause the diffraction pattern to change randomly, can be defined as the time lag for which the auto-correlation function for the observer moving with the pattern falls to 0.5. Setting $\xi' = \eta' = 0$ in equation (3.76) gives,

$$\rho(0,0,T_{0.5}) = \rho(KT_{0.5}^2) = 0.5 \tag{3.77}$$

Thus $T_{0.5}$ is the "characteristic fading time" with the effects of the mean drift removed. We now have two quantities which describe a fading time: the time $\tau_{0.5}$ for the auto-correlation function to fall to 0.5 for a stationary observer, and the time $T_{0.5}$, for the auto-correlation function to fall to 0.5 for an observer moving with the pattern. Comparing equations (3.65) and (3.77), we obtain

$$T_{0.5} = \tau_{0.5}(\frac{C}{K})^{\frac{1}{2}} \tag{3.78}$$

The coefficient $\frac{C}{K}$ can be obtained by comparing terms of τ^2 in equations (3.46) and (3.47). This gives

$$AV_x^2 + BV_y^2 + K + 2HV_xV_y = C \tag{3.79}$$

Historically, the random changes associated with the pattern were described by a "random velocity", V_c. The velocity V_c is defined as the ratio of the "irregularity size" to the "irregularity lifetime". for an observer moving with the pattern. Since the pattern may in general be anisometric, V_c will have different values in different directions because the pattern scale will be different in different directions. The value of V_c in the direction of bulk motion of the pattern has special significance, and is written as $(V_c)_V$. The subscript V denotes quantities measured in the direction of the drift. Therefore,

$$(V_c)_V = \frac{d_{0.5}}{T_{0.5}} \tag{3.80}$$

is defined as the component of V_c in the direction of motion, where $d_{0.5}$ is separation, in the direction of motion, where the spatial correlation function falls to 0.5. If d is the distance in the direction of motion (i.e. in the direction of velocity V), then

$$\frac{\xi}{V_x} = \frac{\eta}{V_y} = \frac{d}{V} \tag{3.81}$$

Substituting ξ and η in the spatial correlation function given by equation (3.62), we obtain

$$\rho(d) = \rho[(AV_x^2 + BV_y^2 + 2HV_xV_y)\frac{d^2}{V^2}] \tag{3.82}$$

The "characteristic size" of the irregularity, defined as $d_{0.5}$, is obtained when $\rho(d) = 0.5$, hence equation (3.82) becomes

$$\rho[(AV_x^2 + BV_y^2 + 2HV_xV_y)\frac{d_{0.5}^2}{V^2}] = 0.5 \tag{3.83}$$

Comparing this equation with equation (3.77) which was used to define $T_{0.5}$ we obtain

$$(AV_x^2 + BV_y^2 + 2HV_xV_y)\frac{d_{0.5}^2}{V^2} = KT_{0.5}^2 \tag{3.84}$$

Using $V^2 = V_x^2 + V_y^2$ and equation (3.84), equation (3.80) then becomes

$$(V_c)_V^2 = \frac{d_{0.5}^2}{T_{0.5}^2} = \frac{K(V_x^2 + V_y^2)}{AV_x^2 + BV_y^2 + 2HV_xV_y} \tag{3.85}$$

The value of $(V_c)_V$ can be found from this equation since V_x, V_y, $\frac{A}{K}$, $\frac{B}{K}$, and $\frac{H}{K}$ are known. The dimensionless ratio

$$\frac{(V_c)_V^2}{V^2} = \frac{K}{AV_x^2 + BV_y^2 + 2HV_xV_y} \tag{3.86}$$

can be regarded as a measure of the relative importance of the random changes compared with bulk motion in producing fading at a fixed receiver. If this parameter is zero, then the fading observed is totally due to the bulk motion of the pattern, whereas, if it is infinite, the fading is due to random changes in the pattern. That is, the bigger the ratio, the more importance are the random changes.

3.4.3 The UWO MF radar

The full correlation analysis procedure described in the preceding section was used to analyse D-region drift observation from London, Ontario, Canada (43° N, 81° W). The University of Western Ontario (UWO) MF radar was established in November 1992. The MF radar operates at a frequency of 2.219 MHz and transmits 20 kW of peak power. The configuration for the three antennas is an equilateral triangle with a spacing of 225 m. Table 3.1 gives the radar system parameters. During the data

Operating frequency	2.219 MHz
Half-power half-beamwidth	20 degrees
Antenna spacing	225 m
Pulse repetition frequency	60 Hz
Coherent integration	32
Peak power output	20 kW
Duty cycle	0.12%
Height resolution	3 km
Height range	49-142 km

Table 3.1: Radar system parameters.

acquisition phase, the computer stores a time series of the complex signal amplitude (i.e. in-phase and quadrature components) from each of the three spaced receivers. The transmitter is pulsed at 60 Hz and the received signals are coherently averaged over 32 pulses. This gives an effective sampling interval of 0.533 s. The noise levels is reduced by coherent integration of the complex data in the drift program, which increases the SNR by a factor N in power, where N is the number of contiguous points in the integration. The half-power half-width of the optimum pulse length is approximately 20 μs, thereby resulting in a range resolution of approximately 3 km (see Section 3.2.4 details on range resolution). The transmitter duty cycle is approximately 0.12%. The complex auto- and cross-correlations functions obtained with 512 point time series are parameterized to obtain true velocity estimates using the full correlation analysis discussed in Section 3.4.2. The apparent velocity is also computed using the method discussed in Section 3.4.1. Records are 4.55 min in length and start at 5 min intervals.

In addition to application of the FCA, the vertical drift velocity is also measured using the complex amplitude data, from the phase of the auto-correlation function at a single receiving antenna. A vertical wind velocity will produce a Doppler shifted spectrum of the signal received at a ground based receiver. The auto-correlation function of the complex amplitude of the backscattered signal is determined from the Fourier transform of the Doppler shifted spectrum. Using the Shift Theorem, it is expected that frequency shifts in the spectrum will result in a change in the derivative of phase in the the auto-correlation function. The greater the time shift, the greater the change in rate of change of phase with frequency. The rate of change of phase with time is related to the vertical velocity by

$$V_z = -\frac{\lambda}{4\pi}\frac{d\phi}{d\tau} \qquad (3.87)$$

where V_z is the vertical wind velocity and λ is the wavelength of the transmitted wave. Therefore, the vertical drift velocity is obtained from the slope of the phase versus time delay near zero time delay. Since the half-power half-width of the receiving beam at London is ±20°, the reflected signal will also contain contributions from scatterers at off-zenith angles [e.g., Hocking, 1986, 1989]. Hence it can be expected that the observed changes in phase of the auto-correlation function are due to in some part to the horizontal motions of the drift irregularities. The vertical velocities obtained by this method are not generally valid unless a narrow beam is used, or perhaps very long term averages are used.

Since November 1992 the UWO MF radar has been used to measure horizontal winds with the spaced antenna method in the D-region. Data are sampled at virtual heights of 49-142 km, although we only use data below about 100 km (virtual height) in this thesis. Vertical winds are also measured, but will not be discussed in this dissertation.

3.4.4 Data rejection criteria

The results of the full correlation analysis were tested before extensive application, in order to determine the reliability of the drift velocity. It is usually found that some records and/or results are rejected, either because of inadequacy of the data itself (e.g., weak echo), or because the data does not appear to satisfy the assumptions of the analysis. The following criteria have been found satisfactory for data relating to mesospheric winds observed at London at a frequency of 2.219 MHz. The data and/or results are rejected if any of the following conditions occur:

1. The mean return signal is either very weak or alternatively so strong that the receivers are saturated. The signal sampled by a receiver is digitized to 64 levels, ranging from 0 to 63. The record is rejected if the mean signal did not lie in the region between 3 to 60. This limits should exclude records where the receiver output is essentially zero, due to the noise signal only, or at saturation levels, for most of the time. The data is also rejected if the standard deviation of the signal level is $\leq 2\%$ of the mean signal level. This occurs when the signal strength remains nearly constant during the data acquisition; e.g., shallow or no fading of the signal, or the receivers become saturated (20%) and with equipment failure (occurrence $\ll 1\%$).

2. The signal-to-noise ratio is less than -6 dB. The noise levels is reduced by coherent integration (over a set of 32 contiguous data points) of the complex data during the data acquisition and this improves the signal-to-noise ratio by a factor 32 in power. When, after averaging, the signal-to-noise ratio drops below - 6 dB, the data is rejected. Reflected signal strengths are usually too weak from heights below 73 km but this situation varies regularly with the day and season and irregularly with ionospheric disturbances. During strong Polar-Cap Absorption (PCA) events, reflections from the D- and E-regions may disappear completely for several days. The occurrence of poor signal-to-noise is largely a function of height, being virtually 100% at heights below 73 km, and only a few percent at heights above 82 km.

3. The mean auto-correlation function has not fallen to at least 0.5 by the maximum number of lags calculated. This condition will occur if the fading is extremely slow (greater than 10 s - occurrence $2 - 6\%$).

4. The cross-correlation maxima have not been found within the number of lags calculated (occurrence $1 - 2\%$). This usually indicates that the main peak of the corresponding cross-correlation function is subdued. This effect can occur if the pattern scale is less than the antenna spacing, such that the correlation between the time series recorded by the antenna is small.

5. The cross-correlation functions are oscillatory; in this case is impossible to determine unambiguously the necessary time shifts for the analysis (occurrence $1 - 2\%$).

6. The reliability of the time shifts τ', of the maxima of the cross-correlation functions, can be determined by calculating the sum of these time shifts around a closed path (that is the data taken in pairs around the triangle of antennas). Theoretically, the sum of the time shifts for each of the cross-correlation maxima should be equal to zero. Due to random fluctuations, this rarely occurs and the data are rejected if the normalized time discrepancy, defined by

$$NTD = \frac{|\sum \tau'|}{\sum |\tau'|} \tag{3.88}$$

   [Meek et al., 1979, May, 1988] is greater than 0.3 (occurrence $10 - 15\%$).

7. The quantity of V_c^2 estimated in FCA is negative, i.e. the natural random change parameter, V_c, is imaginary. An imaginary V_c seems to occur occasionally when V_c^2 is close to zero but negative. This probably indicates very little natural

fading and the apparent velocity can be used in place of true velocity. This anomaly may also result from statistical fluctuation introduced by the analysis (which makes V_c^2 slightly negative). Hocking [1986] has shown, using spectral widths, that this statistical fluctuations can be substantial, even when there are no significant fluctuating velocities of the scatterers, and that the experimental widths can either be greater or less (i.e. $V_c^2 < 0$ or $V_c^2 > 0$) than those due purely to beam-broadening. In practice the apparent velocity, if it seemed reliable, was used in place of the true velocity (occurrence 10 – 20%).

8. If the calculated pattern parameters indicate hyperbolic instead of elliptical contours. Rejection thus occurs if $H^2 < AB$.

9. Polynomial fits to the cross-correlation functions break down at any stage during the analysis. In order to determine τ (i.e. τ_x, τ_y, and τ_{xy}) and τ' (i.e. τ_x', τ_y') from the correlation functions, polynomials fits to the cross-correlation functions were used. In some cases, the shape of the correlation function is not adequately described by the polynomial fits and the procedure breaks down.

10. The apparent and true velocities are significantly different in amplitude or in directions. Data are rejected if:

$$V_a \geq 3V_t \quad \text{or} \tag{3.89}$$

$$V_a \leq \frac{2V_t}{3} \quad \text{or} \tag{3.90}$$

$$\mid \phi_t - \phi_a \mid \geq 40^\circ \tag{3.91}$$

These criteria are not difficult to apply with the fast modern computer speeds, and they do not normally result in excessive rejection rates. The most important of these criterions are (2), (3), and (6).

3.5 A numerical model of the spaced antenna method

The spaced antenna method (SA) has proved to be an important and relatively inexpensive radar technique for making measurements of atmospheric wind velocities and other parameters. This section examines the reliability and accuracies of various parameters which can be measured with this method, based on correlation techniques which were discussed in the previous section. We have developed a simple computer model to simulate the SA method, appropriate to the UWO MF system, in order to understand the spaced antenna technique and the full correlation analysis. Model data were used for the estimation. Our analysis shows that SA winds yield values very similar to the original input model wind velocities.

There are also other various numerical models developed to simulate the SA method [e.g., Meek and Reid, 1984; Kudeki et al., 1993; Sürücü et al., 1995; Holdsworth and Reid, 1995], and further discussion of these is beyond the scope of this section (although some results are discussed in Section 8.1).

Model description

The model is based on the volume scattering (from point scatterers) situation, whereby signal returns are assumed to arise from radar refractive index irregularities distributed randomly throughout the volume illuminated by the radar. The model incorporates the effects of transmitter, scatterers, and receiver polar diagrams, and vertical wind fluctuations (representing the effects of turbulence). In this model the radar volume (illuminated by the transmitted radar pulse) is enclosed within a $32 \times 32 \times 3$ km^3 volume, throughout which a number of scatterers are initially randomly positioned. The volume from which information is received by the SA system can be approximately determined from the effective pulse width (equivalent to height resolution) and the beamwidth of the polar diagram of the radar. The input model half-power half-width of the polar diagram is 9° and the height resolution is 3 km. After initial tests, 100 scatterers was found to be a suitable number, since more scatterers did not significantly change the results and took a large amount of computing time. If the half-power half-width of the radar polar diagram is $\sim 9^\circ$ this scenario means that there are up to 50 scattering points observed within the radar volume at any given time. These scatterers represent regions of refractive index irregularities. The temporal sampling occurred at 0.2 s time intervals, for a total of 600 samples. This made the total length of the time series 120 s (2 min), to obtain horizontal wind estimate. The Table 3.2 gives the model radar system parameters. The parameters are based on typical conditions expected at 80 km. The initial scattering positions are obtained by generating random 3-dimensional positions within the $32 \times 32 \times 3$ km^3 volume. At each sampling time the complex signal returns from each scatterer are added. The amplitude of the signal returns are based on the combined polar diagram of the radar (transmitter and receiver) and scatterers (backscattered polar diagram of the scatterers), i.e. received amplitude $\propto e^{\frac{-\theta}{\theta_T}} e^{\frac{-\theta}{\theta_R}}$, where θ_T and θ_R are the half-power half-width of the transmitter and receiver polar diagrams respectively, and θ is the half-width of the scattering polar diagram of the scatterers. After each

Operating frequency	2.219 MHz
Antenna beamwidth	9 degrees
Antenna spacing	150 m
Sampling interval	0.2 s
Height	80 km
Scattering volume	$32 \times 32 \times 3$ km^{-3}
Model input velocity	70.7 m/s
Model input direction	45 degrees

Table 3.2: Model radar system parameters.

sampling time the scattering positions are updated, based on the specified values of the background wind and turbulent motions. That is, the positions of the scatterers are updated according to the equation, $\vec{r}_i = \vec{r}_i + (\vec{V} + \vec{V}_{tur}(\vec{r}_i))\Delta t$, where $\vec{V}$ is the background wind velocity, $\vec{V}_{tur}(\vec{r}_i)$ is the turbulent motion velocity at the position of the ith scatterer, and Δt is the sampling interval. It should also be noted that the simulation calculates the the contribution from each scatterer, i.e. taking into account the transmitter-scatterer-receiver distance, and is not an approximation. The input model wind velocity and direction are 70.7 m/s and 45^o from eastwards, i.e. both the zonal and meridional components have the same wind velocity magnitude of 50 m/s. The configuration for the three receiving antennas is an equilateral triangle with a spacing of 150 m. The transmitter is placed at the centre of the 32×32 km^2 array; i.e. the system is monostatic.

Finally, the complex auto- and cross-correlations functions obtained with 600 point time series are parameterized to obtain true velocity estimates using the full correlation analysis discussed in Section 3.4.2. The apparent velocity is also computed using the method discussed in Section 3.4.1.

3.5.1 Time series generation

A typical example of the complex time series showing the in-phase (real) and quadrature (imaginary) components for the three spatially separated receivers obtained using the model MF simulation parameters is shown in Figure 3.6. The time series show considerable resemblance as the antenna separation (150 m) is of the order of the radar wavelength (135 m). On the other hand, it is also noted that the time series show little resemblance as the antenna separation is increased to 400 m (not shown).

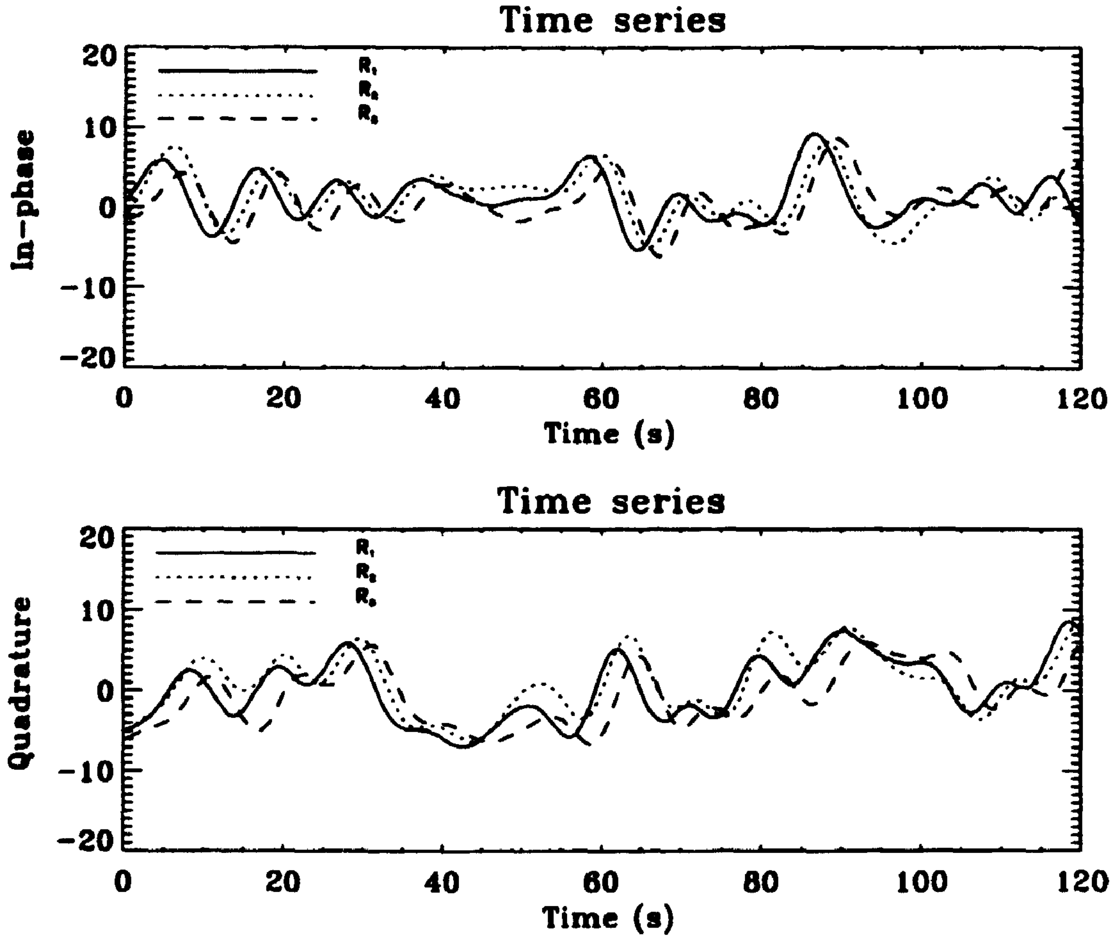

Figure 3.6: A typical complex time series measured by three spatially receivers obtained using the MF simulation parameters.

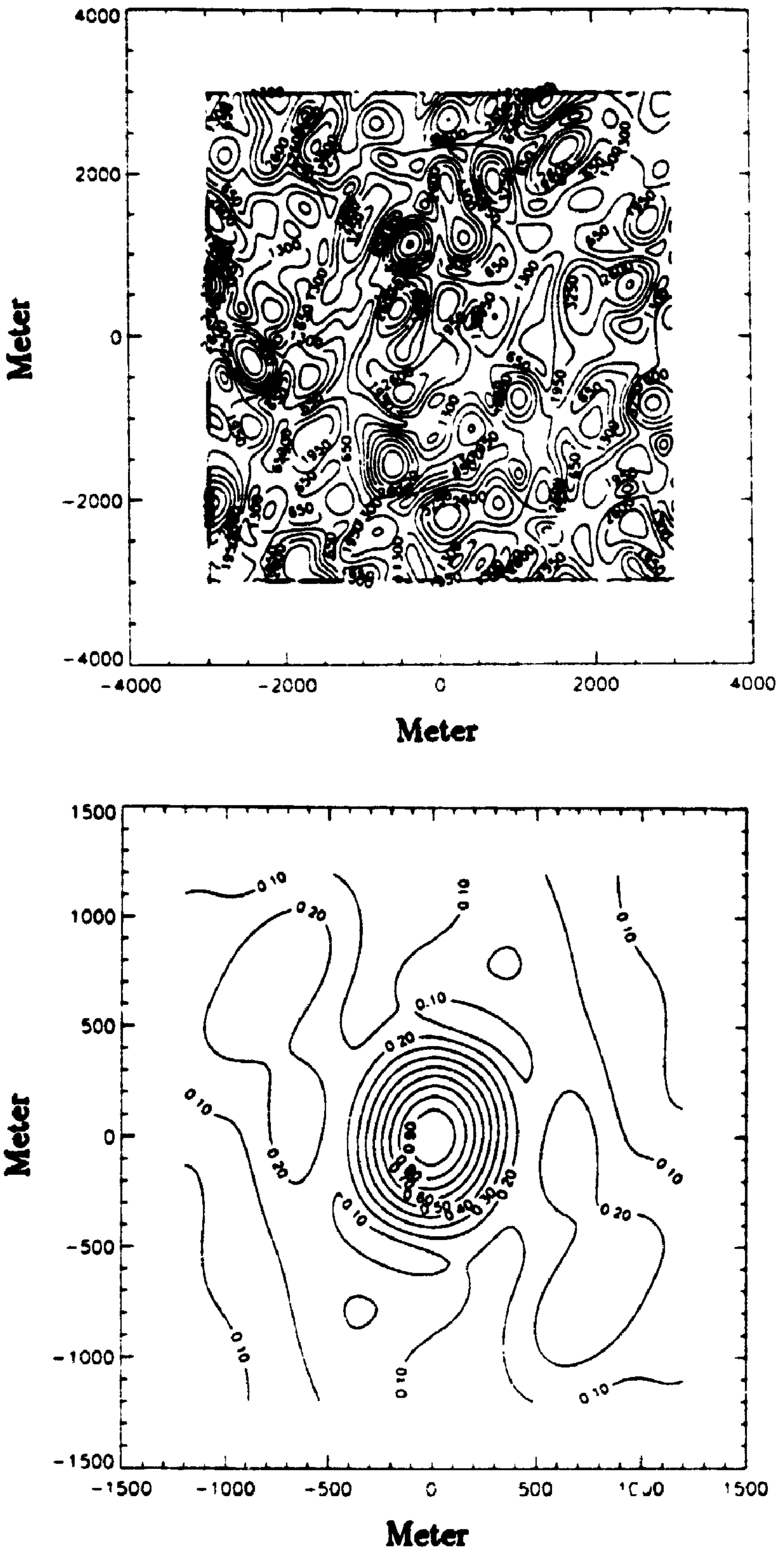

Figure 3.7: Description of an evolving diffraction pattern (top) and its family of surfaces on the ground (bottom). The resulting pattern has been sampled using a 200 by 200 array of receiving antennas with 30 m spacing.

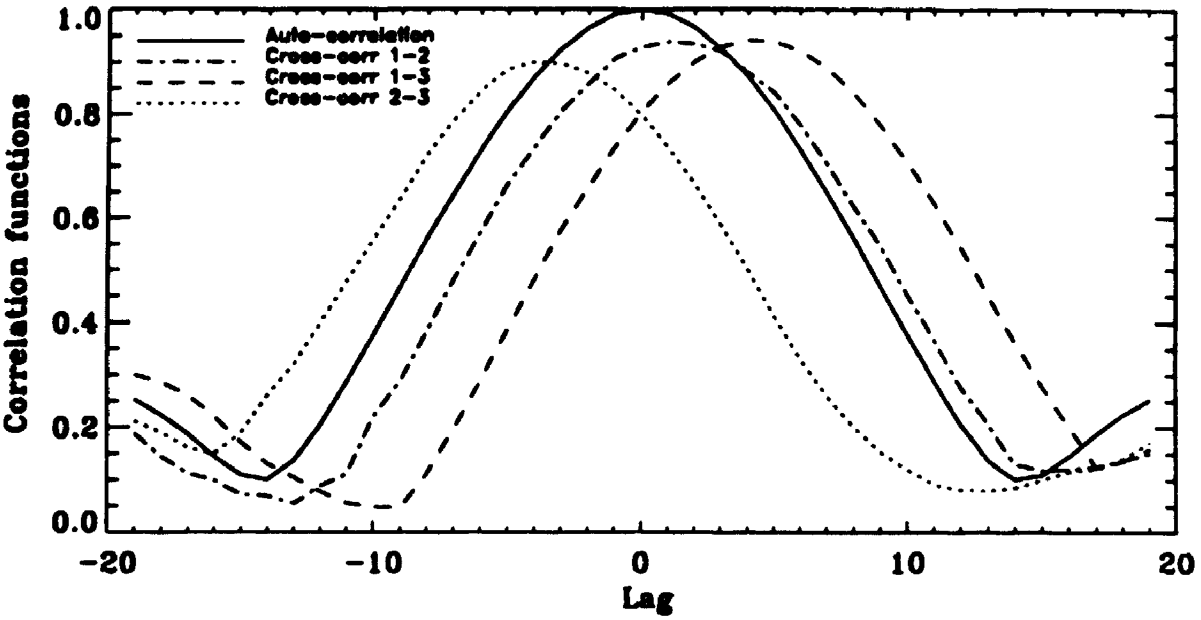

Figure 3.8: The auto- and cross-correlation functions for the time series collected by the three spatially separated receivers which is shown in Figure 3.7.

The time series generated by the model exhibit fading characteristics very similar to those exhibited in experimental data. The model-generated data illustrated here exhibit two distinct advantages over the experimental time-series. The first advantage is that the model generated data are free from the effects of noise, and the second advantage is that the model generated data are free from the effects of phase differences introduced by the receivers or through the use of different cable lengths.

3.5.2 The ground diffraction pattern

The production of useful images of the ground diffraction pattern requires a large array of receiving antennas covering an area greater than the mean scale pattern scale, and with antenna spacings considerably shorter than the mean pattern scale. The production of these images allows the application of the spatial correlation technique [e.g., Briggs, 1968]. The production of such images is also especially important for the determination of the mechanisms responsible for the radio wave backscatter, and the verification of the assumptions made by the FCA and about the behaviour of the ground diffraction pattern and the spatial-temporal correlation function. Figure 3.7 shows the description of an evolving diffraction pattern (left panel) and its family of surfaces on the ground (right panel), with a model input wind velocity of 70.7 m/s and a maximum vertical wind velocity fluctuation of 3 m/s. The resulting pattern has been sampled using a 200 by 200 array of receiving antennas with 30 m spacing.

3.5.3 Apparent and true velocities

In order to verify that the model is performing as expected a number of different analyses have been applied. These analyses have been used to check that the model input parameters are recoverable, thereby also verifying the analyses in the process. The "apparent" velocity (V_a) and direction (D_a) are estimated using the similar fades technique detailed in Section 3.4.1. The "true" velocity (V_t) and direction (D_t) are estimated using the FCA technique detailed in Section 3.4.2 which includes corrections for the effects of random changes and isometry in the diffraction pattern, and is therefore generally considered the better velocity estimate of the actual (model) velocity. Figure 3.8 shows the auto-correlation function and the cross-correlation functions between the three receivers for the time series exhibited in Figure 3.6.

Figure 3.9 illustrates apparent and true wind velocities as a function of turbulent motion ν_{tur}. These results are obtained over 5 different random seed numbers; i.e. repeating the measurements five times. The symbol " $*$ " denotes the average value and the (random) error bars indicate the standard deviations of the distributions. It is clearly apparent that when $\nu_{tur} \rightarrow 0$ or small (< 6 m/s), $V_a \approx V_t$ suggesting that the atmospheric refractive index irregularities move with the background wind. On the other hand, when $\nu_{tur} > 6$ m/s, the apparent wind velocity increases with increasing turbulent motion. The true wind velocity accurately estimates the magnitude of the model input wind velocity V_{mod}, although there is a slight tendency for V_t to overestimate V_{mod} for larger value of ν_{tur}. These effects are a direct consequence of the turbulent motions and FCA is compensating correctly for the effects of turbulent fading.

Figure 3.10 illustrates the apparent and true directions as a function of turbulent motion ν_{tur}. The apparent and true directions accurately reproduce the model wind velocity direction and there is a slight tendency for a small directional error in the direction for larger value of ν_{tur}.

Although we have not included examples here, we have also considered different scenarios such as combination of small input model velocities (e.g., 10, 30 m/s) and

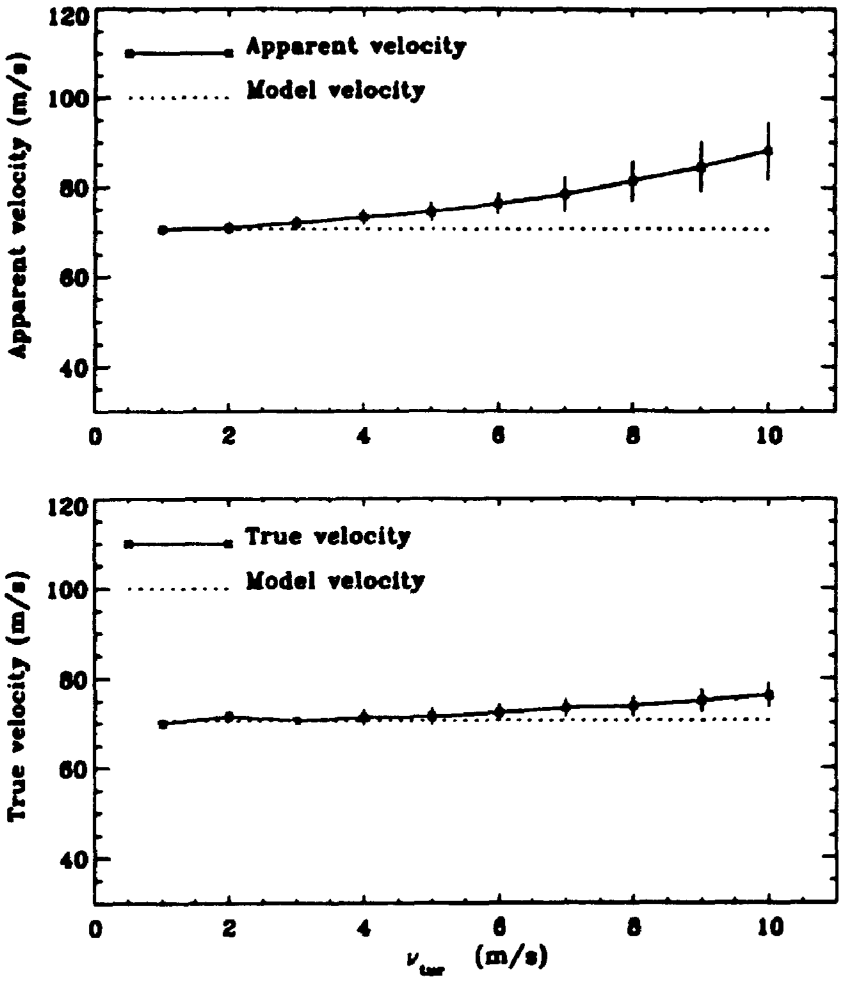

Figure 3.9: The top plot shows the comparison between horizontal model wind velocity and apparent wind velocity. The bottom plot shows the comparison between horizontal model wind velocity and true wind velocity. The symbol " * " denotes the average value and the error bars denote the standard deviation of the distribution (over 5 different random seed numbers). ν_{tur} is a maximum fluctuating vertical wind velocity and represents the effects of turbulence.

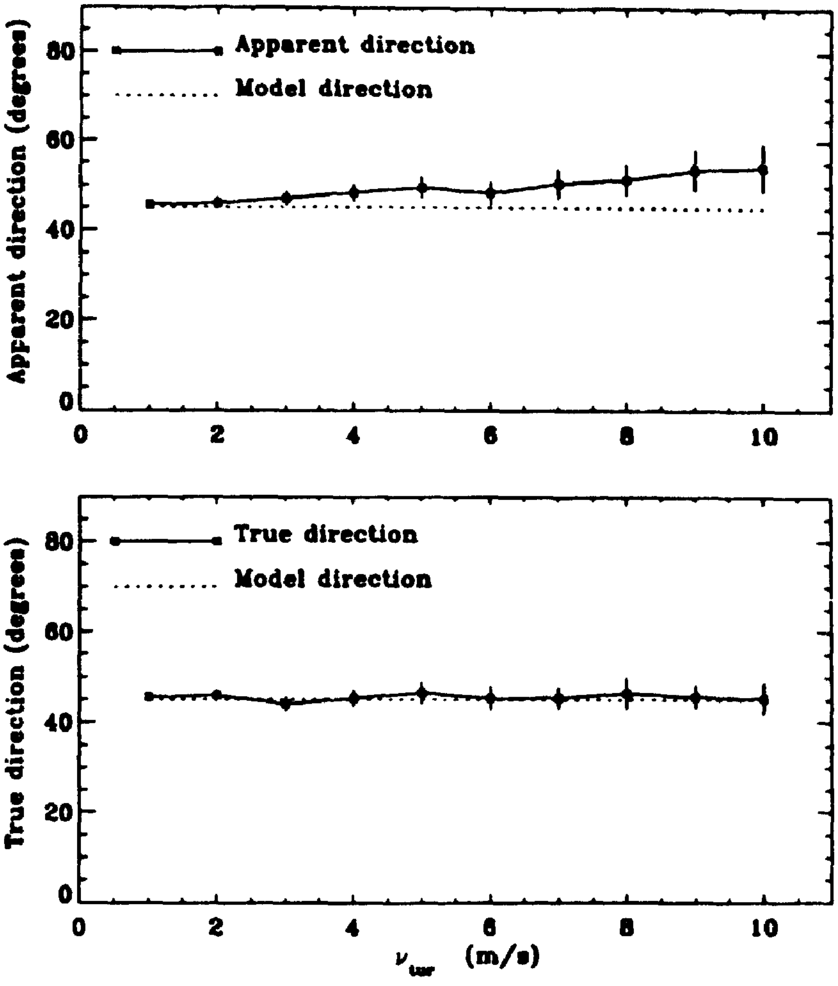

Figure 3.10: The top plot shows the comparison between horizontal model wind direction and apparent wind direction. The bottom plot shows the comparison between horizontal model wind direction and true wind direction. The symbol " $*$ " denotes the average value and the error bars denote the standard deviation of the distribution (over 5 different random seed numbers). ν_{tur} is a maximum fluctuating vertical wind velocity and represents the effects of turbulence.

different vertical wind fluctuations (e.g., 3, 6 m/s) in search of biases in the true velocity estimation. We noted there is a slight tendency for the true velocity to overestimate the input model velocity for larger value of turbulent motion (> 6 m/s) but errors are usually less than 5%.

3.5.4 The triangle size effect

The triangle size effect was first described by Golley and Rossiter [1970]. Golley and Rossiter [1970] presented a comparison between wind values measured with various antenna spacings, finding that "true" velocity tended to increase with antenna spacing, approaching a limiting value supposedly equal to the actual wind velocity. The limiting value was obtained when the antenna spacing was approximately equal to the pattern scale. Various causes of the effect have been suggested, such as antenna coupling [Fedor and Plywaski, 1972], and random noise [e.g., Meek, 1990], and even errors in the assumptions involved with FCA, but no cause has yet been unambiguously isolated.

Figure 3.11 illustrates the apparent and true wind velocities as a function of antenna spacing. The antenna spacing was varied systematically from 50 m to 390 m in steps of 20 m. A maximum vertical wind velocity fluctuation of 3 m/s was used in this case. It is clearly apparent that the true wind velocity remains unchanged with increasing antenna spacing up to 250 m and gets larger with increasing antenna spacing from 250 to 400 m, while the apparent wind velocity remains unchanged with increasing antenna spacing (showing independence of the antenna spacing). Figure 3.12 illustrates the variation of the true and apparent directions as a function of antenna spacing. The values of the true and apparent directions show little variation with the antenna spacing, and suggest that both true and apparent directions are good estimates of the direction of wind for all antenna spacing.

These results suggest that the true velocity wind deduced is a (weak) function of the antenna spacing, and an optimum spacing must be chosen before applying the method. The optimum configuration for the three antennas is an equilateral triangle [e.g., Golley and Rossiter, 1970] with a spacing such that the cross-correlation between the antenna pairs at zero lag is of the order of 0.5. If the correlation is appreciably higher than this value (antennas too close) the "true" velocity tends to be small. On the other hand, if the correlation is too small (antennas too part apart) the analysis frequently breaks down.

Figure 3.13 shows a average plot of $\frac{1}{\xi_{0.5}}$ and its uncertainty as a function of beamwidth

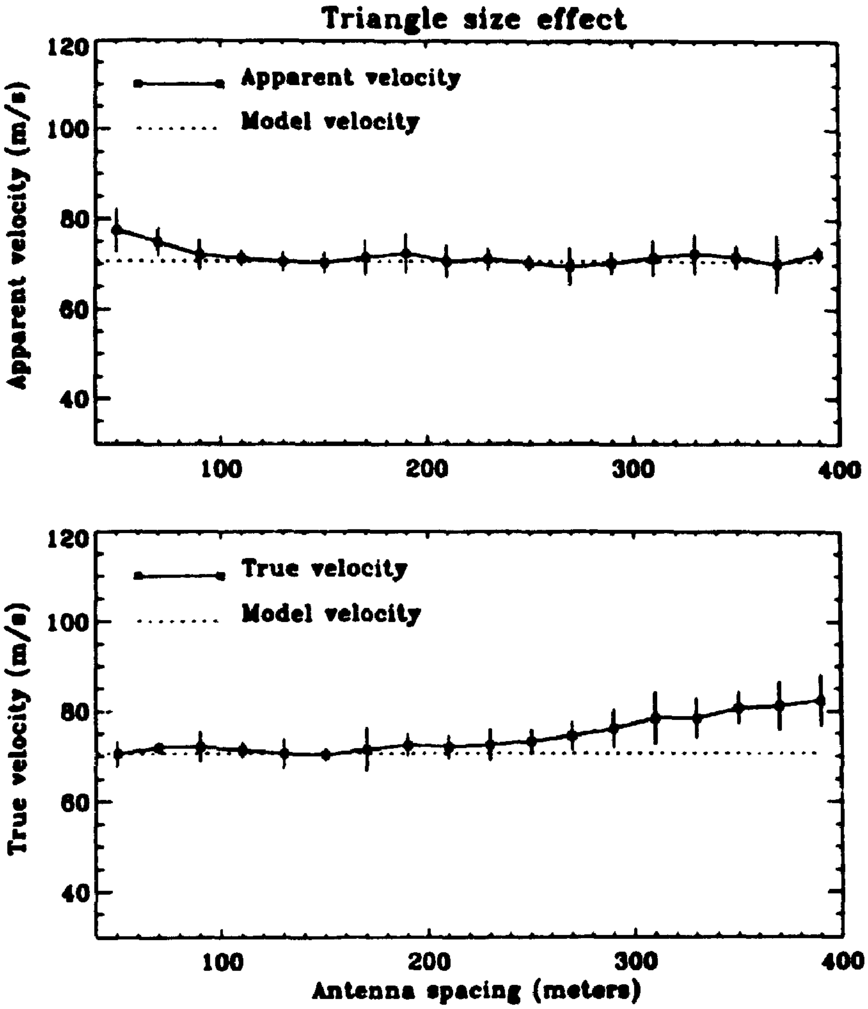

Figure 3.11: The top plot shows the variation of the apparent wind velocity with increasing antenna spacing. The bottom plot shows the variation of the true wind velocity with increasing antenna spacing. The antenna spacing was varied systematically from 50 m to 390 m in steps of 20 m. A maximum vertical wind velocity fluctuation of 3 m/s was used in this case. The symbol "*" denotes the average value and the error bars denote the standard deviation of the distribution (over 5 different random seed numbers).

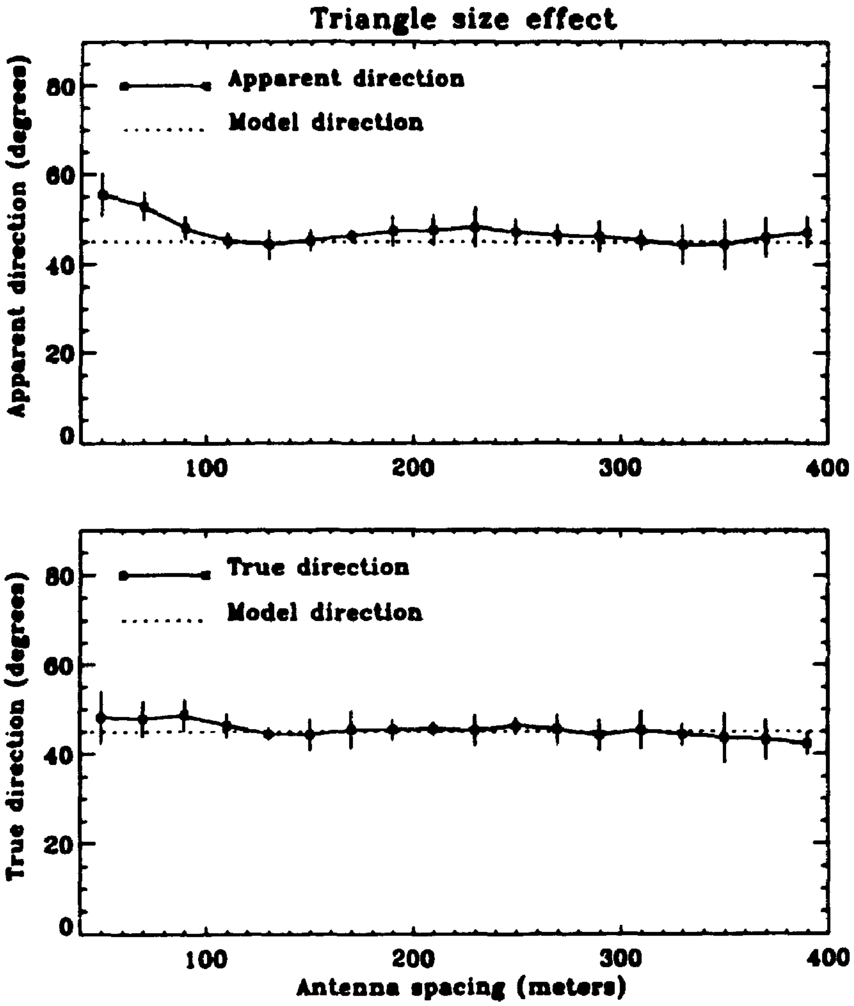

Figure 3.12: The top plot shows the variation of the apparent wind direction with increasing antenna spacing. The bottom plot shows the variation of the true wind direction with increasing antenna spacing. The antenna spacing was varied systematically from 50 m to 390 m in steps of 20 m. A maximum vertical wind velocity fluctuation of 3 m/s was used in this case. The symbol "*" denotes the average value and the error bars denote the standard deviation of the distribution (over 5 different random seed numbers).

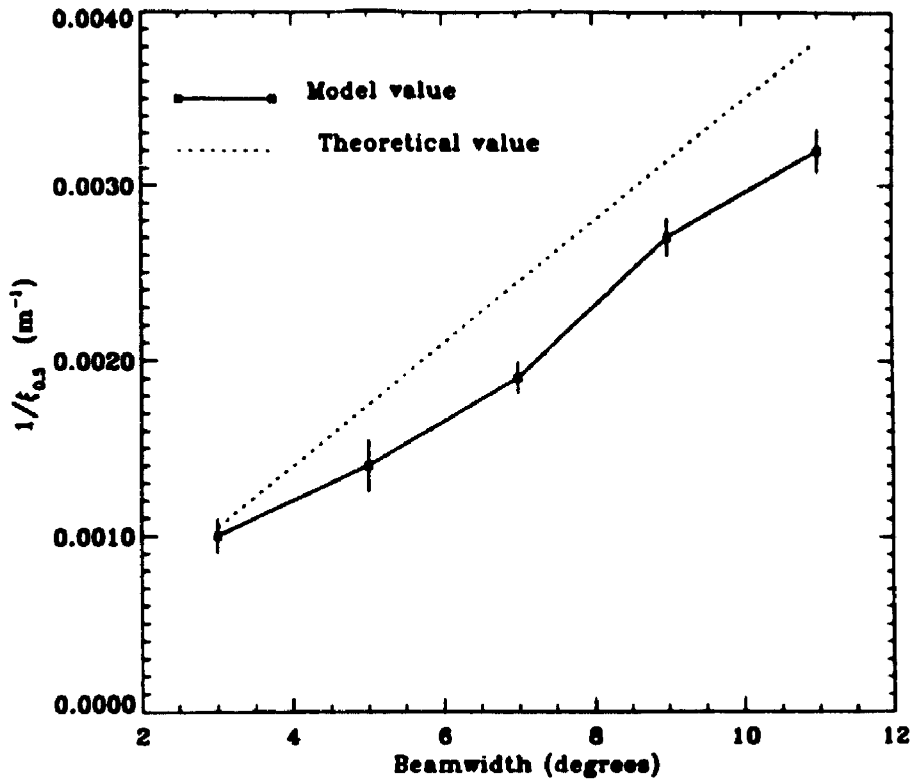

Figure 3.13: Average plot of $\frac{1}{\xi_{0.5}}$ and its standard deviation as a function of beamwidth ($\frac{1}{e}$), where $\xi_{0.5}$ is the spatial lag at which the modulus of the complex auto-correlation function falls to 0.5. The dotted line indicating the theoretical value (see text for details).

($\frac{1}{e}$ power half-width), where $\xi_{0.5}$ is the spatial lag at which the modulus of the complex auto-correlation function falls to 0.5. The dotted line indicating the theoretical value, and the respective relationship is given by

$$\xi_{0.5} \simeq \frac{15.0}{\theta_{eff}} \tag{3.92}$$

where θ_{eff} is the e^{-1} half-width of the effective radar polar diagram. Although this is not an exact relationship, it is a good approximation [e.g., Lesicar and Hocking, 1992]. This figure suggest that the saturation effect is an artifact of the model, due to the limited region of the sky which is permitted to contain scatterers.

3.5.5 Conclusion

A simple model has been developed to simulate the SA method. Our results show that the SA measurements at MF produce a reliable means of estimation of wind velocity in the D-region, when using partial reflections. The results reveal that the true velocity provides an excellent estimate of the model input wind velocity for all magnitudes of model turbulent motions at least under the assumption made in our model (i.e. volume scatter from point scatterers). It is also noted that there is a slight tendency for the true velocity to overestimate the model velocity for larger value of turbulent motion but the errors are usually less than 5%. On the other hand, the magnitude of the apparent velocity increases with increasing model turbulent motions. Both apparent and true directions accurately estimate the model direction although there is a slight tendency for a small directional error in the direction for larger values of turbulent motion. Our results also suggest that the true velocity gets larger with increasing antenna spacing, i.e. triangle size effect, and an optimum spacing must be chosen before applying the method.

In general, it can be concluded that although individual SA wind measurements yield values very similar to the original input model wind velocities, it should be interpreted with care. True wind velocity and direction are better when the turbulent motions are small (less than 6 m/s). However, long term averages (e.g., hourly values) of data collected by the spaced antenna system should provide excellent measurements of mean winds and tides and other full correlation parameters. This work therefore validated the use of the spaced antenna derived results which are subsequently used in this thesis.

Chapter 4

Mean winds and tides during 1992-1994

4.1 Introduction

Atmospheric solar tides in the atmosphere have been observed routinely for many years and have been the subject of many experimental and theoretical investigations. The theoretical understanding and historical resume of advances in atmospheric tidal theory are contained in (amongst others) Chapman and Lindzen [1970], Lindzen and Hong [1974] and Vial [1989]. In the middle atmosphere, tides are among the most regular conspicuous dynamical phenomena, and play an important role in the dynamics and energy budget of the lower thermosphere [Teitelbaum and Vial, 1991; Groves and Forbes, 1984, 1985]. Atmospheric tides are global scale oscillations in temperature, wind, density and pressure at periods which are harmonics of a solar or lunar day. Here we will mainly be concerned with solar or thermally forced tides, which are excited by the periodic absorption of solar radiation connected with the apparent motion of the Sun around the Earth. Absorption of infrared radiation by water vapour in the troposphere and absorption of ultraviolet radiation by ozone in the atmosphere are known to provide most of the forcing for the solar atmospheric tides. The tidal amplitude grows with height due to the effect of decreasing background atmospheric density with height and becomes a significant wave component in the middle atmosphere. Extensive observational studies of the winds and tides in the mesosphere and lower thermosphere have been made with MF (Medium Frequency) radars using the SA (Spaced Antenna) technique [e.g., Manson and Meek, 1985, 1986; Fleming et al., 1988]. Tidal components observed in this region sometimes indicate inherent variability from day-to-day as well as variation on seasonal and yearly time scales. Atmospheric tides are also observed to be non-uniform with longitude and latitude [Kato, 1989].

We report measurements of climatologies of the tides and mean winds made with a new UWO MF radar located near London, Ontario, Canada. In the following section, the MF radar system and data analysis methods are described. Section 4.3 gives the monthly mean winds and these are compared with the empirical CIRA-86 model [Fleming et al., 1988]. Sections 4.4 and 4.5 present the mean seasonal behavior of the amplitude and phase of the semidiurnal and diurnal tides over London as a function of height. The semidiurnal tides are compared with a model due to Forbes and Vial [1989] and the diurnal tides are qualitatively compared with a model due to Forbes and Hagan [1988]. In Section 4.6 we compare our tidal results with three other ground based radars. These radars are the MF radars using the SA technique at Saskatoon (52° N, 107° W) and Urbana (40° N, 88° W), and the meteor wind radar at Durham (43° N, 71° W). Our comparisons will be based to some extent on the data presented by Manson et al. [1989]. The conclusions of this study are presented in Section 4.7.

The Saskatoon data used for our comparisons were recorded in the same time period [Manson, private communication], whilst the Urbana data were recorded in 1991-1992 [Franke and Thorsen, 1993], and the Durham data in 1978-84 [Manson et al., 1989], so these comparisons may not be ideal. More detailed comparisons using data from the same time period have yet to be performed, but nevertheless the current comparisons are sufficient to validate our system and at the same time make some interesting comparisons between the different sites.

4.2 The London MF radar system and data analysis methods

A new UWO MF radar which uses the SA technique was established at London in November 1992. The MF radar operates at a frequency of 2.219 MHz and transmits 20 kW of peak power at a duty cycle of 0.12%. Table 3.1 gives the radar system parameters.

Since November 1992 the radar has been used to measure horizontal winds with the spaced antenna method in the 49-142 km height range. Vertical winds are also measured, but will not be discussed in this paper. Wind measurements are made at time intervals of 5 min and at 3 km height intervals, although the vertical pulse length is closer to 4-5 km. The configuration for the three antennas is an equilateral triangle with a spacing of 225 m. The complex auto- and cross-correlation functions

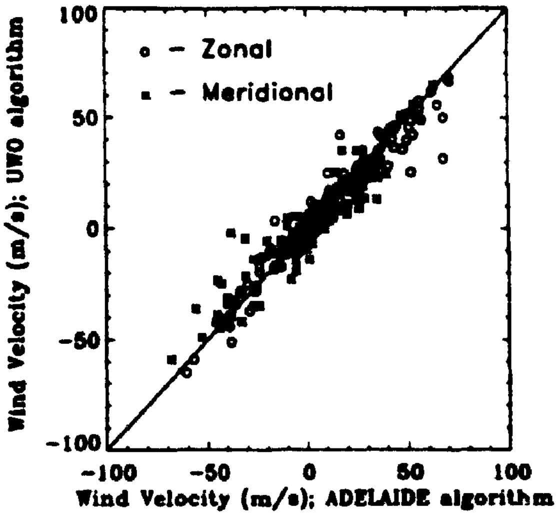

Figure 4.1: A scatter plot between the wind velocities deduced by the UWO spaced antenna FCA algorithm and by the spaced antenna FCA algorithm used in Adelaide, Australia, where each program has been applied to the same data sets.

obtained with 512 point time series are parameterized to obtain true velocity estimates using Full Correlation Analysis (FCA) [Briggs et al., 1950; Meek, 1980; Briggs, 1984; Hocking et al., 1989]. Records are 4.55 min in length and start at 5 min intervals. Using a twenty-four month continuous set of data from November 1992 to October 1994, studies of the mean winds, atmospheric tides and tidal-gravity wave coupling have been made. We will concentrate on the region 79-103 km, because we believe the data to be most reliable in this height region. This point will be elaborated upon shortly.

As part of our system development, new software code was developed so that the FCA analysis could be applied in real time on the Zenith 386 personal computer which controls the system (This has subsequently been upgraded to a DX 66 MHz 486 system). Therefore our first procedure was to validate the new code. The best way to test for possible biases in wind estimates by a given spaced antenna FCA algorithm is by comparisons with other commonly used and accepted algorithms. We collected a series of sets of raw data at different times of the year and deduced the wind velocities by two different spaced antenna FCA algorithms. Figure 4.1 shows a

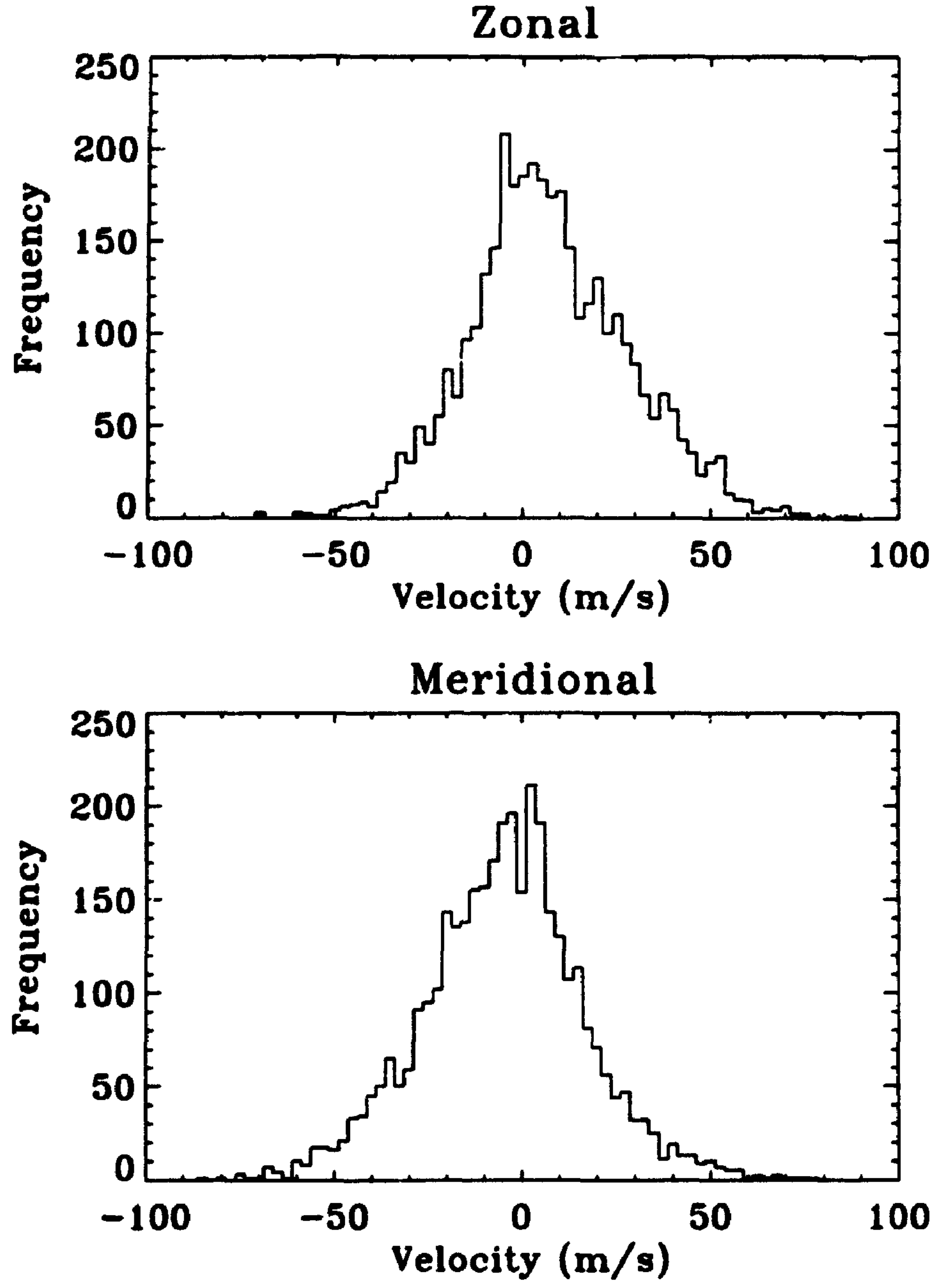

Figure 4.2: The upper panel shows the velocity histogram (binsize = 2.5 m/s) of the zonal wind and the lower panel shows the velocity histogram of the meridional wind at 91 km in February 1993.

scatter plot between the wind velocities deduced by the UWO spaced antenna FCA algorithm and by the spaced antenna FCA algorithm used in Adelaide, Australia [e.g., Ball, 1981; Briggs, 1984], which is in its third decade of operation. The best fit line suggests good agreement and it is concluded that the UWO spaced antenna FCA algorithm provides reliable estimates of the neutral air motion. Figure 4.2 shows one example of velocity histograms which was produced from one month of observation - in this case, February, 1993. These histograms were generally approximately normally distributed (to first approximation), but visual inspection showed that there were on occasion some unacceptably large velocities which fell outside the bell shape of the histogram; they are usually referred to as "outliers". Outliers are more likely to be spurious noise than real data. If we want to accept outliers we should examine each individually to determine likely relevance. Since we are only interested in tides, it is not unreasonable to reject outliers. Nevertheless these were not large in number and could easily be rejected in any subsequent analysis procedures; in general the majority of data points show a very acceptable distribution.

In our analysis procedure, we have used the hourly averaged mean winds (centered about the half-hour) at each height of observation in the analysis. There is considerable theoretical and experimental evidence that wind variations in the mesosphere and lower thermosphere result from the superposition of a prevailing wind, two-day oscillations, various tidal components (and gravity waves). Therefore, we used two day groups of data, stepped by one day (e.g., 1-2, 2-3, 3-4, ...). We then routinely fit and analyze the data using classical harmonic analysis techniques with mean, 48, 24, 12 and 8 hour components [e.g., Manson and Meek, 1985; Manson et al., 1989]. A typical comparison of the original measurements and the tidal fit for the zonal wind is given in Figure 4.3. When there were short breaks in the data, these were simply omitted from the least-squares fitting routine without seriously affecting the results. A fit is only performed if at least 16 different hours are represented in the two day data set for a given height. Note that less than 10% of all available data have less than 30 hours per two day data set. Data were also rejected if the errors in the parameters produced by the fitting procedure were unacceptably larger. Thus, a substantial proportion of these 10% are reliable. We therefore believe that we have suitably rejected any data which might bias our conclusions. We also compared our fitting procedure for the tides with the Saskatoon fitting procedure (Meek, private communication) and Adelaide fitting procedure (hourly mean winds are weighted by the errors, Ball [1981]) performed on the London data set. Both amplitudes and phases have shown excellent agreement: the correlation coefficients for the amplitudes and phases are $\sim$ 0.94 and $\sim$ 0.98 respectively. Fitting procedures have also been applied to 24-hour

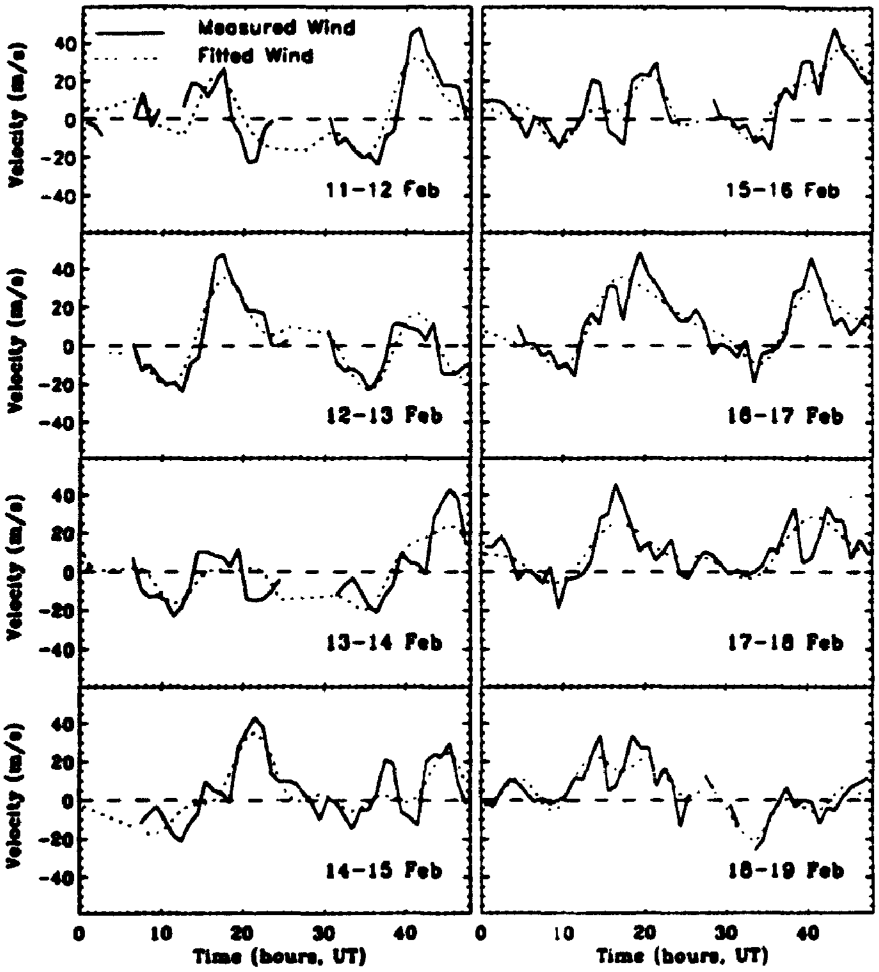

Figure 4.3: Hourly means and tidal fits for the zonal wind at 91 km, eight successive days from 11-18 February 1993.

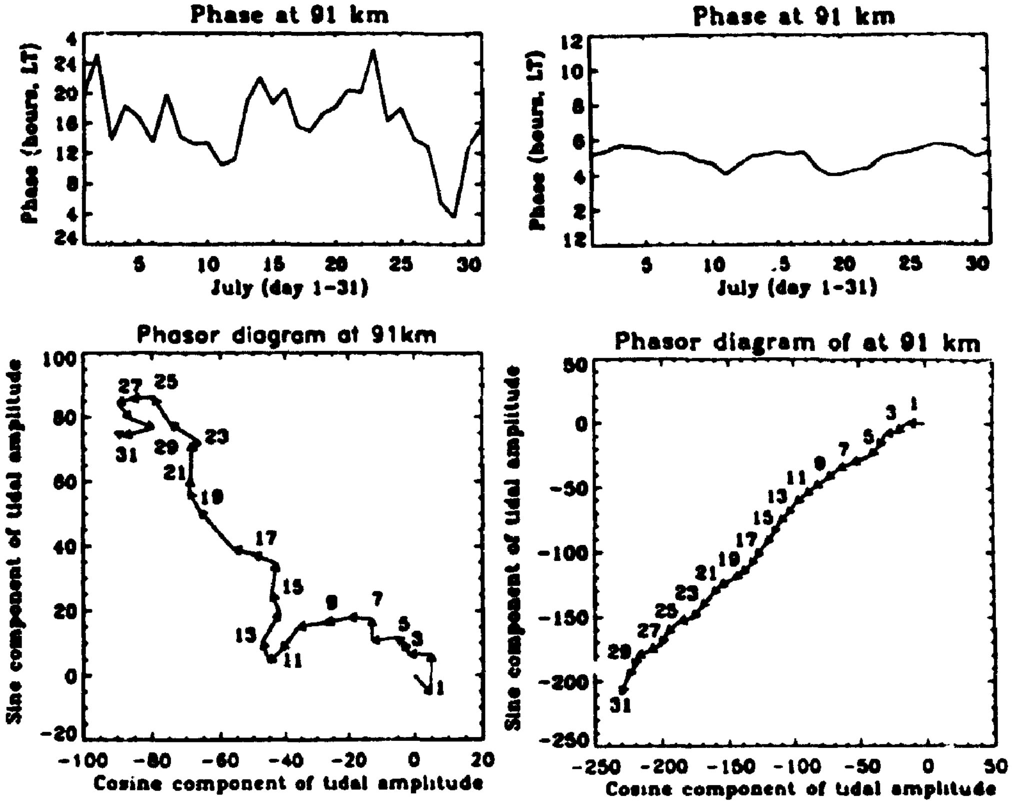

Figure 4.4: Phase and phasor diagrams of the meridional component of the diurnal and semidiurnal tides at 91 km in July 1993.

data sets, with 24 and 12 hour components; in general the overall results were the same as for the two-day fits, but in this paper we will only use the 48-hour data sets.

The graphs in Figure 4.3 illustrate the accuracy of our fitting procedures by showing the tidal fits over 8 successive days at 91 km in February 1993. In Figure 4.4 we also illustrate the phase variations of the diurnal and semidiurnal components by using both phase plots and a phasor diagram-type format. The phase and phasor diagram of the meridional semidiurnal tide in July shows moderate day-to-day variability of the tidal components and indicates that the phase of the tide does not remain constant over a month. However, it does show a tendency to fluctuate around a fairly well-defined mean phase. On the other hand, the phase and phasor diagram of the meridional diurnal tide shows substantial day-to-day variability. Observations made at London often show large changes in both amplitude and phase of the diurnal tide from one day to the next. While the day-to-day variability of the diurnal tide at mid-latitude is a prevalent feature of the mesospheric winds observed in London, the semidiurnal tide, by comparison, exhibits relatively more constant phase, although amplitudes can be variable. The causes of the observed short term variations (of the order of 3 days) in tidal amplitudes and phases are not well understood, although a number of plausible explanations have been proposed by Forbes [1985], Bernard [1981] and Vial et al. [1985] (also see Section 2.5).

Throughout the discussion of the results the following convention is used to describe the wind components. When a wind vector is resolved into geographic coordinates, a positive wind amplitude refers to a wind directed towards the east or north (eastward or northward) for zonal or meridional components respectively. The phase of the zonal component is defined as the local time in hours after midnight at which the maximum eastward wind velocity occurs and the phase of the meridional component is defined as the time of maximum northward wind velocity. Throughout this work we used vector averaging of the daily means for the diurnal and semidiurnal tides. It should be also noted that the results presented here are plotted in terms of virtual heights. Generally the virtual height and the true height are similar up to about 95 km, but there is evidence that the radar echoes received near and above 100 km are affected by some degree of group retardation (also see Section 3.2.4). Namboorthi et al. [1993] demonstra[illegible] the effects of group retardation on 2.2 MHz received echoes at Saskatoon, and suggested that the summer noon time virtual heights are similar to the International Reference Ionosphere (IRI) model, but during the winter time the IRI virtual heights are considerably lower than the observed heights. It was also demonstrated that during the winter for both solar maximum and minimum the tidal and wind data are valid up to 111 km without any correction, but in the solar minimum summer season heights falls to 97 km, and the corresponding solar maximum height falls as low as 95 km. In 1992-93 the transition from solar maximum to minimum was underway. In order to ensure that our data are not seriously affected by group retardation and E-region effects, we have limited our data to heights below 103 km. We have greatest confidence in our data for heights below 95 km, but show the data between 95 km and 103 km for completeness.

4.3 Mean winds

This section presents measurements of the mean circulation in the mesosphere, and compares them with the CIRA-86 empirical zonal wind model for the Northern Hemisphere for 40° N and 50° N. Note that the comparison may not be ideal because our latitude (43° N) is neither 40° N nor 50° N. Figure 4.5 illustrates time-height contours representing average prevailing zonal and meridional wind patterns for the first 24 months of observations at London, Ontario. The general form of the plots are somewhat similar, but there are also significant differences. In general, the meridional winds are relatively much more variable than the zonal winds, and the magnitude of the zonal component of the prevailing wind in the upper mesosphere is larger than the meridional component.

In the late spring and summer months, from mid-March to August the zonal flow over London is westward at heights below 86 km, reversing to an eastward flow above this height. The change over from the winter to summer circulation commences during March-April and the summer to winter circulation commences during late August-September. Note that the seasonal changes show a sudden transition during the fall and a more gradual transition during the spring. Meridional flow is essentially northward below 80 km, but reversing to southward flow above this height during the May-August months. It is interesting to note that the largest meridional winds were observed during December below 80 km, when speeds of 10 ms^{-1} were measured.

In the fall and winter, from September to March, the zonal flow is strongly eastward at most heights, being of maximum amplitude in the 76-82 km height range and decreasing with increasing height. The meridional flow is northward below 80 km, but there is evidence of reversal at heights above 80 km during the winter time (November-March).

The amplitudes of the zonal winds are in good agreement with the model below 86 km during late spring months, during the summer and early fall months (April-September). However, during late fall months, during the winter and early spring months (October-March) the model winds are typically 2-3 times as large as the observed values over virtually the entire height range. The model values appear to be consistently larger than those actually observed. Significant differences above 86 km have also been noted in comparisons between the CIRA-86 empirical model and the other similar radars [e.g., Manson et al., 1991; Franke and Thorsen, 1993]. Manson et al. [1991] compared meteor and MF radar zonal winds with CIRA-86 and found the model values to be consistent, especially in the 90-95 km height range during

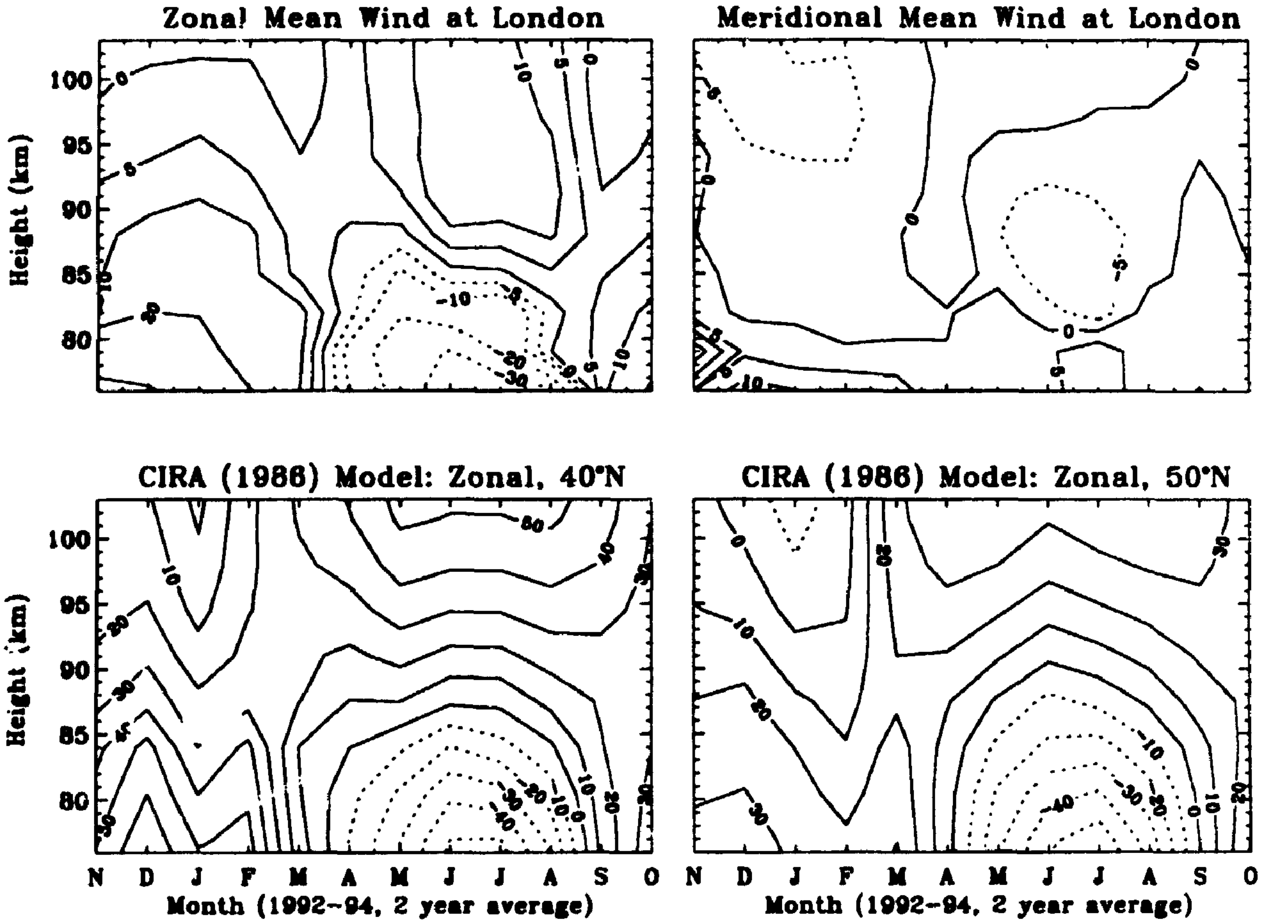
Zonal Mean Wind at London

Meridional Mean Wind at London

CIRA (1986) Model: Zonal, 40°N

CIRA (1986) Model: Zonal, 50°N

Figure 4.5: Contours of zonal and meridional mean winds at London in ms^{-1} constructed from a year of continuous data, and zonally averaged zonal monthly mean winds from the empirical model of Fleming et al. [1988] over a comparable time period. Periods of westward and southward flows are denoted by dashed lines. Note that time marks on the abscissa indicate the middle of the month. Data above 95 km will suffer group retardation, and should be treated with caution - see Section 4.2.

the spring. It should be also noted that the summer comparisons may be somewhat contaminated by daytime group retardation above 95 km.

4.4 Semidiurnal tide

This section and the following section present observations of the tidal winds over London during 1992-1994. The diurnal and semidiurnal tides are discussed separately and compared with recent tidal wind models. The semidiurnal tides are compared with the recent tidal wind model of Forbes and Vial [1989] and the diurnal tides are qualitatively compared with the Forbes and Hagan [1988] numerical model. General tidal characteristics are briefly compared with other mid-latitude radar observations [Manson et al., 1989]. More detailed comparisons are further presented in Section 4.6. The data from 1992-94 were classified into winter (December, January and February), spring (March, April and May), summer (June, July and August) and fall (September, October and November). The seasonal tidal averages and associated error bars of the London data and the model data are estimated by taking a vector average of the monthly mean tides. The model results are sampled at heights corresponding to those of the radar data.

4.4.1 Semidiurnal amplitudes

Figures 4.6-4.9 present the mean behavior as a function of height of the amplitude and phase profiles of the semidiurnal tides over London, together with the results of a tidal numerical computer model. To begin, we will discuss only our data - comparison with the model and other mid-latitude stations will be left until later in the text.

The zonal and the meridional semidiurnal tides have similar amplitudes at most of the heights in all seasons. In general the amplitudes are < 10 ms^{-1}; the amplitudes are seldom more than 10 ms^{-1} and show gradual change with season. The winter and fall amplitudes show very moderate increase with height, whilst in summer the amplitudes of both the meridional and zonal tides seem to decrease in the 79-82 km height range and then reach a broad maximum at about 91 km (±3 km). In spring above 82 km the amplitudes of the semidiurnal tides show an approximately linear increase with height and become constant above 91 km.

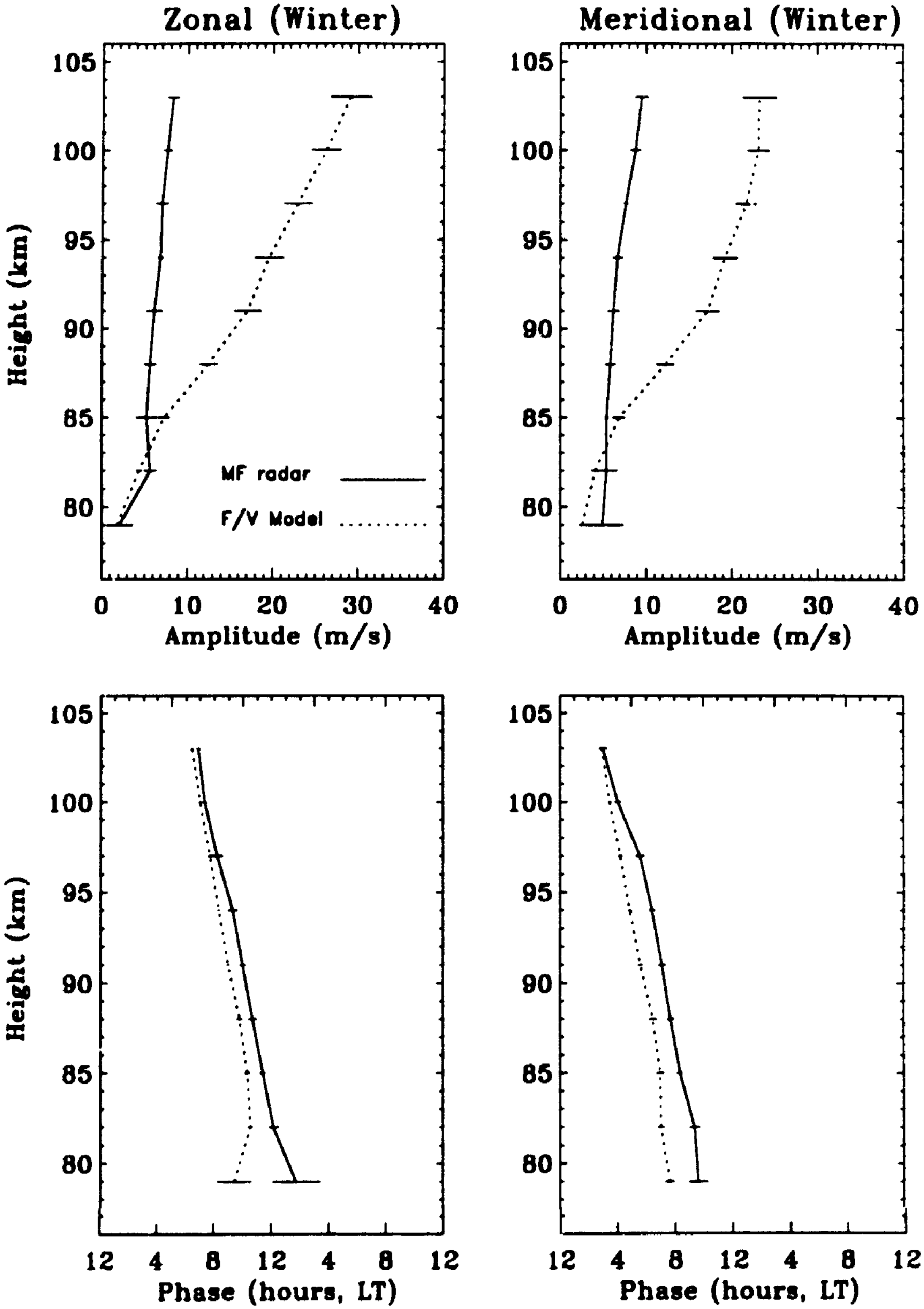

Figure 4.6: Height profiles of the amplitude and phase of the zonal and meridional wind components for the semidiurnal tide during the winter in 1992 – 94 at London, compared with the Forbes and Vial [1989] model data. Data are averaged over three months (December, January and February) and the horizontal lines show the monthly variability within the season.

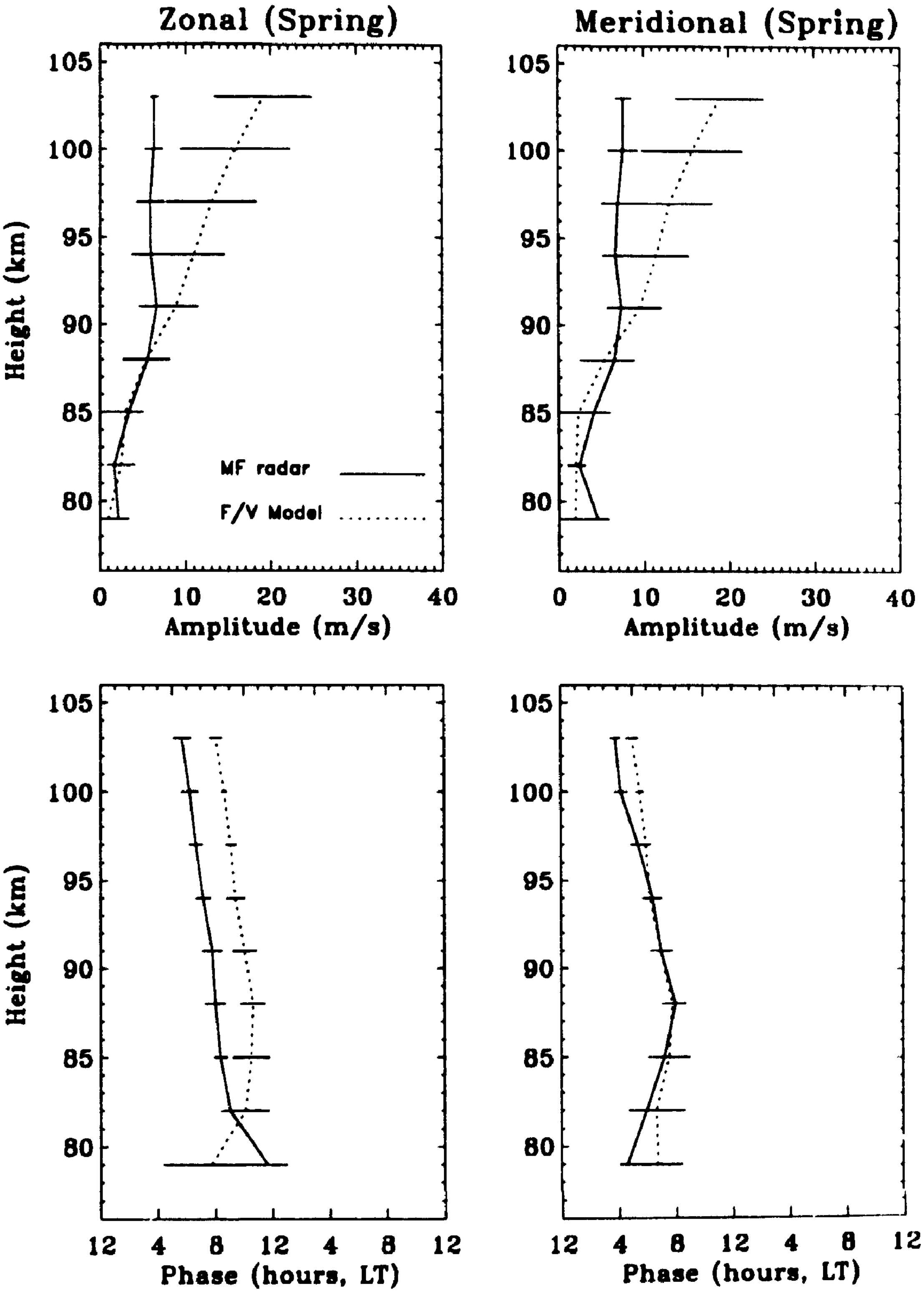

Figure 4.7: Height profiles of the amplitude and phase of the zonal and meridional wind components for the semidiurnal tide during the spring in 1993 – 94 at London, compared with the Forbes and Vial [1989] model data. Data are averaged over three months (March, April and May) and the horizontal lines show the monthly variability within the season. Data above 95 km will suffer group retardation, and should be treated with caution - see Section 4.2.

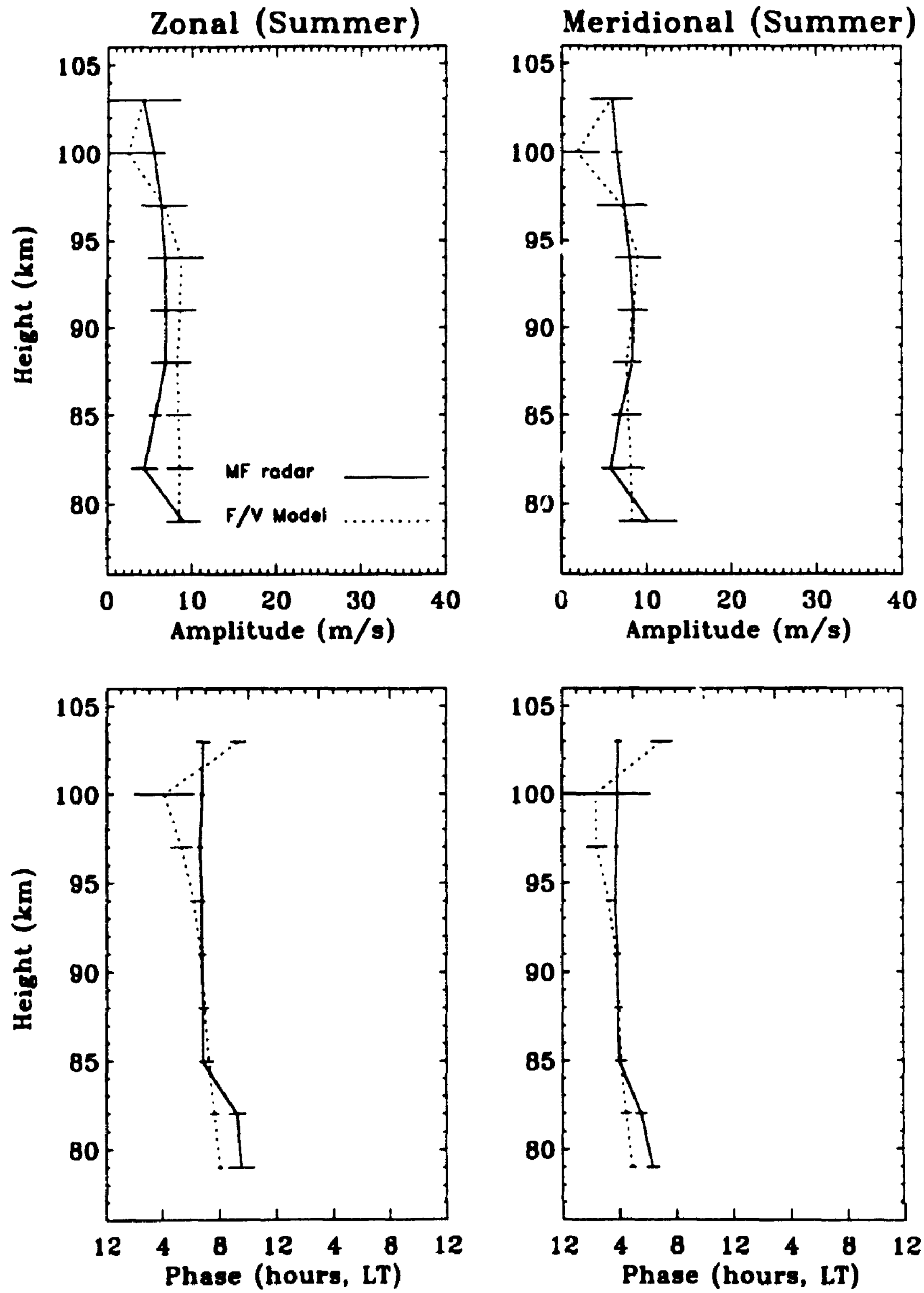

Figure 4.8: Height profiles of the amplitude and phase of the zonal and meridional wind components for the semidiurnal tide during the summer in 1993 – 94 at London, compared with the Forbes and Vial [1989] model data. Data are averaged over three months (June, July and August) and the horizontal lines show the monthly variability within the season. Data above 95 km will suffer group retardation, and should be treated with caution - see Section 4.2.

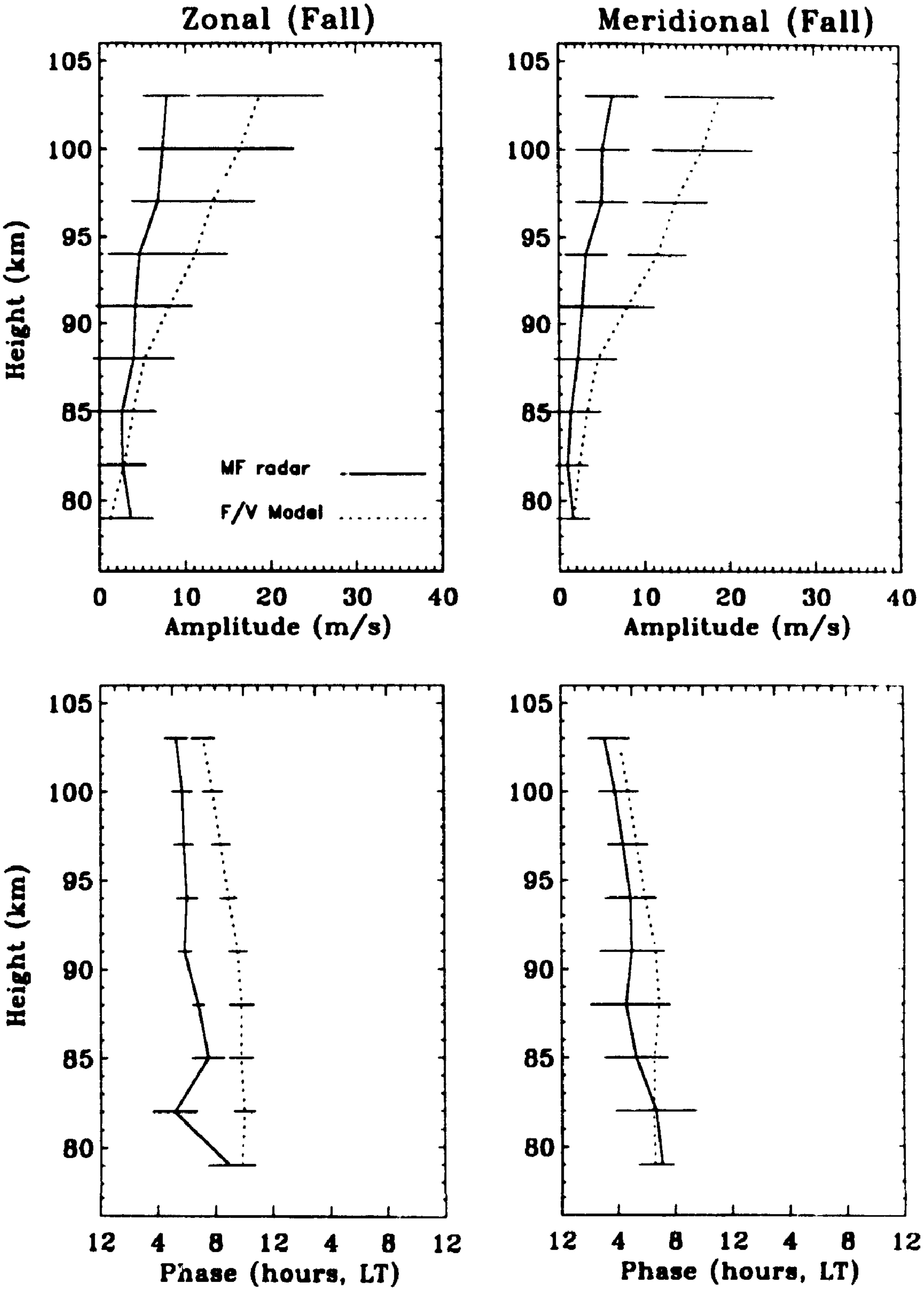

Figure 4.9: Height profiles of the amplitude and phase of the zonal and meridional wind components for the semidiurnal tide during the Fall in 1993 – 94 at London, compared with the Forbes and Vial [1989] model data. Data are averaged over three months (September, October and November) and the horizontal lines show the monthly variability within the season. Data above 95 km will suffer group retardation, and should be treated with caution - see Section 4.2.

	Zonal (km)	Meridional (km)
Winter	40 ± 5	43 ± 5
Spring	48 ± 7	32 ± 4 (below 88 km)
		43 ± 3 (above 88 km)
Summer	26 ± 5 (below 85 km)	30 ± 5 (below 85 km)
	Evanescent (above 85 km)	Evanescent (above 85 km)
Fall	100 ± 10	70 ± 15

Table 4.1: Seasonal mean vertical wavelengths λ_z for the semidiurnal tide.

4.4.2 Semidiurnal phases

The phases of the zonal and meridional components of the semidiurnal tide generally show the form of a propagating tide, with the meridional component leading the zonal by $\sim$ 3 h and phase propagating downwards. This suggests that the directions of the tidal winds at London (as is true generally in the Northern Hemisphere) rotate clockwise with the meridional component leading the zonal by approximately 90°.

Figure 4.6 demonstrates that the semidiurnal phase profiles are very linear (decrease monotonically with height) in the 79-103 km height range during the winter. This linearity can also be observed during the spring (Figure 4.7). The stability of this phase structure is indicated by the very small error bars on the seasonal averages. There is a seasonal variation of vertical wavelength with the shortest values being estimated to be $\sim$ 30-50 km during the winter and spring, whilst the longest values tend towards infinite during the summer (above 85 km) and are $\sim$ 70-100 km during the fall. The seasonal mean vertical wavelength values (λ_z) are given for each season in Table 4.2.

It is possible that the shorter wavelengths may be due to the joint presence of the (2,4), (2,5) and (2,6) modes and the longer wavelengths due to the (2,2) and (2,3) modes [Forbes 1982b]. We note in particular that there is a hint of very short summer wavelengths ($\sim$ 25-30 km) below 85 km and then a sudden transition to near evanescence (probably due to the (2,2) symmetric mode) of both the zonal and meridional components above this height. Because of its long vertical wavelength, the (2,2) mode is considerably less attenuated and may penetrate into the thermosphere [Groves, 1983]. The large amplitude and normalization factors for the (2,2) eigenfunctions also suggest this mode should be strong over London. During the solstitial months of June and December, it is also noted that the amplitudes and phases appear to be much the same as the seasonal averages.

Manson et al. [1989] summarized and compared semidiurnal and diurnal tidal characteristics observed from mid-latitude (40°-55°) radar measurements and we briefly compare the general characteristics with the London observation. General characteristics are: short vertical wavelengths during the winter ($\leq$ 50 km), long wavelengths above 80 km ($\geq$ 100 km) and short wavelengths below 80 km ($\leq$ 50 km) during the summer, rapid phase transitions between these states, small amplitudes during the summer ($\sim$ 5-10 ms^{-1}) and large amplitudes during the winter ($\sim$ 10-35 ms^{-1}). It is clear that these characteristics are observed over London except the winter amplitudes which are generally small over London.

4.4.3 Comparisons with a numerical model

Recent semidiurnal tidal model predictions from Forbes and Vial [1989] are also shown on Figures 4.6-4.9, and these are compared with tidal wind data from London. We begin by drawing attention to the relatively excellent agreement in phase between the observation and the model, and also the excellent overall agreement in amplitude and phase in some periods of the year. In particular, both amplitude and phase profiles show excellent agreement with the model during the summer time although the sudden phase transition seen in the model at around 100 km is not observed in the data. It is worthwhile to note here that the summer differences might be because the radar echoes received near and above 100 km may be affected by daytime group retardation. In spring, summer and fall the agreement for the amplitude profiles below 91 km is also excellent, and in summer the good agreement extends up to 103 km (Figure 4.8).

Despite some excellent agreement, as noted above, there are also some discrepancies between the model and the data. For example, although the observed amplitudes below 85 km approximate the generally small model tidal amplitudes, the approximately linear increase in amplitude which takes place above 85 km in the model is not observed in the data. Comparisons between model results and observations show that model amplitudes are significantly stronger than observed amplitudes at the higher altitudes except during the summer, probably because dissipation is not adequately accounted for in the high order modes of the model [Vial, 1994]. It should be also noted that the large error bars for the model during the fall and spring are due to very rapid transitions between summer-like and winter-like months. This behaviour is generally not seen at London, where the changes in the semidiurnal tidal phase tend to be gradual throughout the year. This will be discussed further in relation to Figures 4.13 and 4.14 later in the text.

4.5 Diurnal tide

4.5.1 Diurnal amplitudes

Figures 4.10 and 4.11 present the mean behavior as a function of height of the amplitude and phase of the diurnal tides over London during 1992-94. Unlike the semidiurnal tide, the amplitude of the zonal diurnal tide is in general larger (often up to 100%) than the meridional diurnal tide at most heights during all seasons, although this may not be true above 94 km during the winter. The dominance of the zonal diurnal tide can be anticipated from the Hough velocity expansion functions and their normalizing factors [Forbes, 1982a]. The zonal-meridional difference is especially pronounced during the summer at many heights and during the winter below 88 km.

Generally the amplitudes of the zonal tides during the summer are greater than those in the winter except between 85-88 km. In summer the amplitudes of the zonal tides are ~ 10 ms^{-1} except below 82 km and the amplitudes of the meridional tides are $\sim$ 3-5 ms^{-1} except below 82 km. The amplitudes of the meridional tides during the winter are $\sim$ 4-8 ms^{-1}, $70-100\%$ greater than summer above 88 km. One noticeable feature of the zonal tide during the winter is that the amplitudes show an approximately linear decay with height above 85 km: in the 85-103 km height range the amplitude decreases from ~ 13 ms^{-1} to ~ 1 ms^{-1}. Another interesting feature is that the zonal amplitudes reach a broad minimum during the summer and peak during the winter at about 85 km.

In spring and fall the amplitudes of both the zonal and meridional diurnal tides increase with height and reach a broad maximum at around 88 km and then decrease with height. The maximum amplitudes of the zonal tides during the spring and fall are ~ 10 ms^{-1} and ~ 8 ms^{-1} respectively, while the amplitudes of the meridional tides are ~ 6 ms^{-1} and ~ 5 ms^{-1} respectively. Above 94 km the amplitudes are generally small (less than 5 ms^{-1}) during the spring and fall.

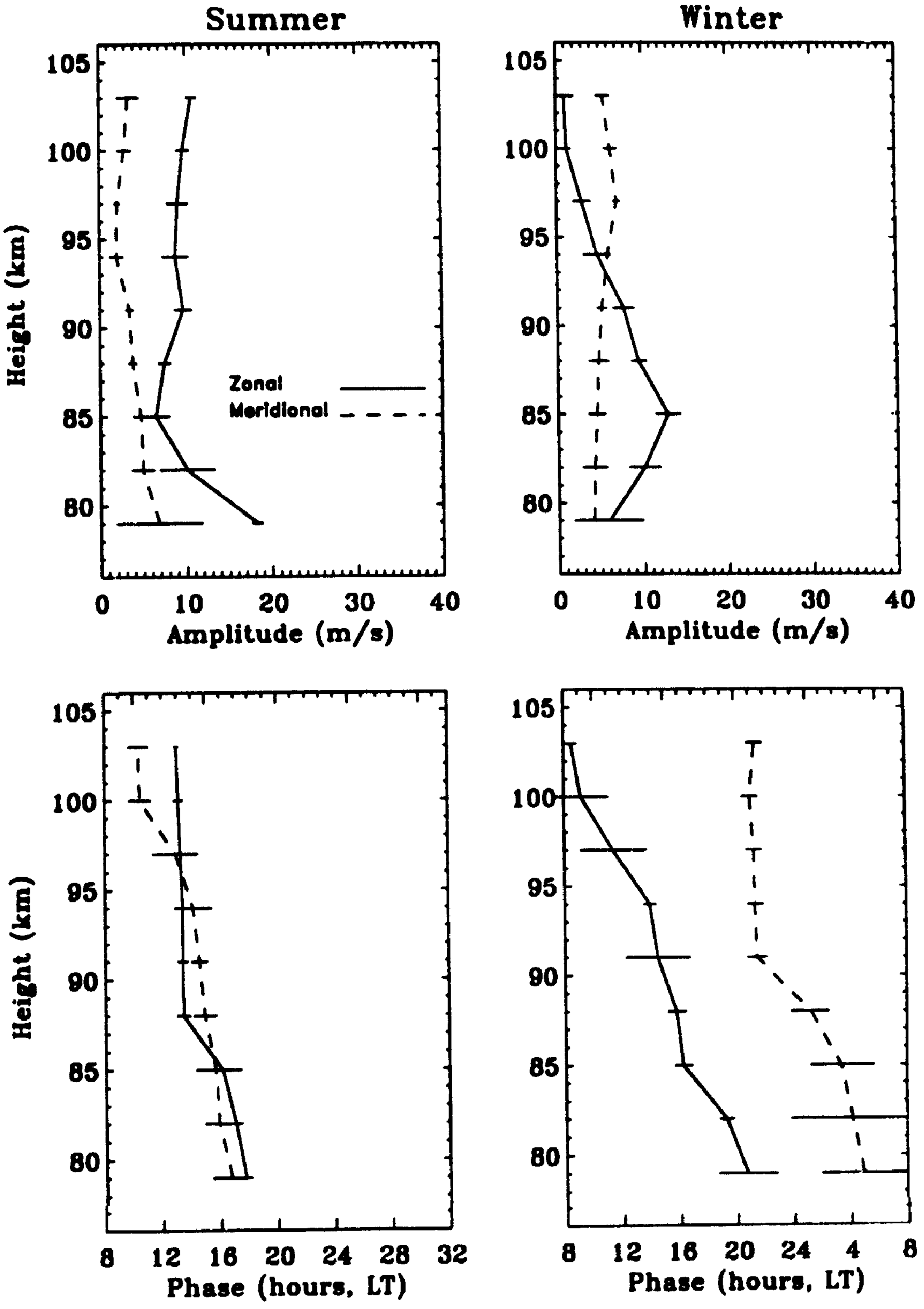

Figure 4.10: Height profiles of the amplitude and phase of the zonal and meridional wind components for the diurnal tide during the summer (June, July and August) in 1993 – 94 and during the winter (December, January and February) in 1992 – 94 at London. Data are averaged over three months and the horizontal lines show the monthly variability within the season. Data above 95 km will suffer group retardation, and should be treated with caution - see Section 4.2.

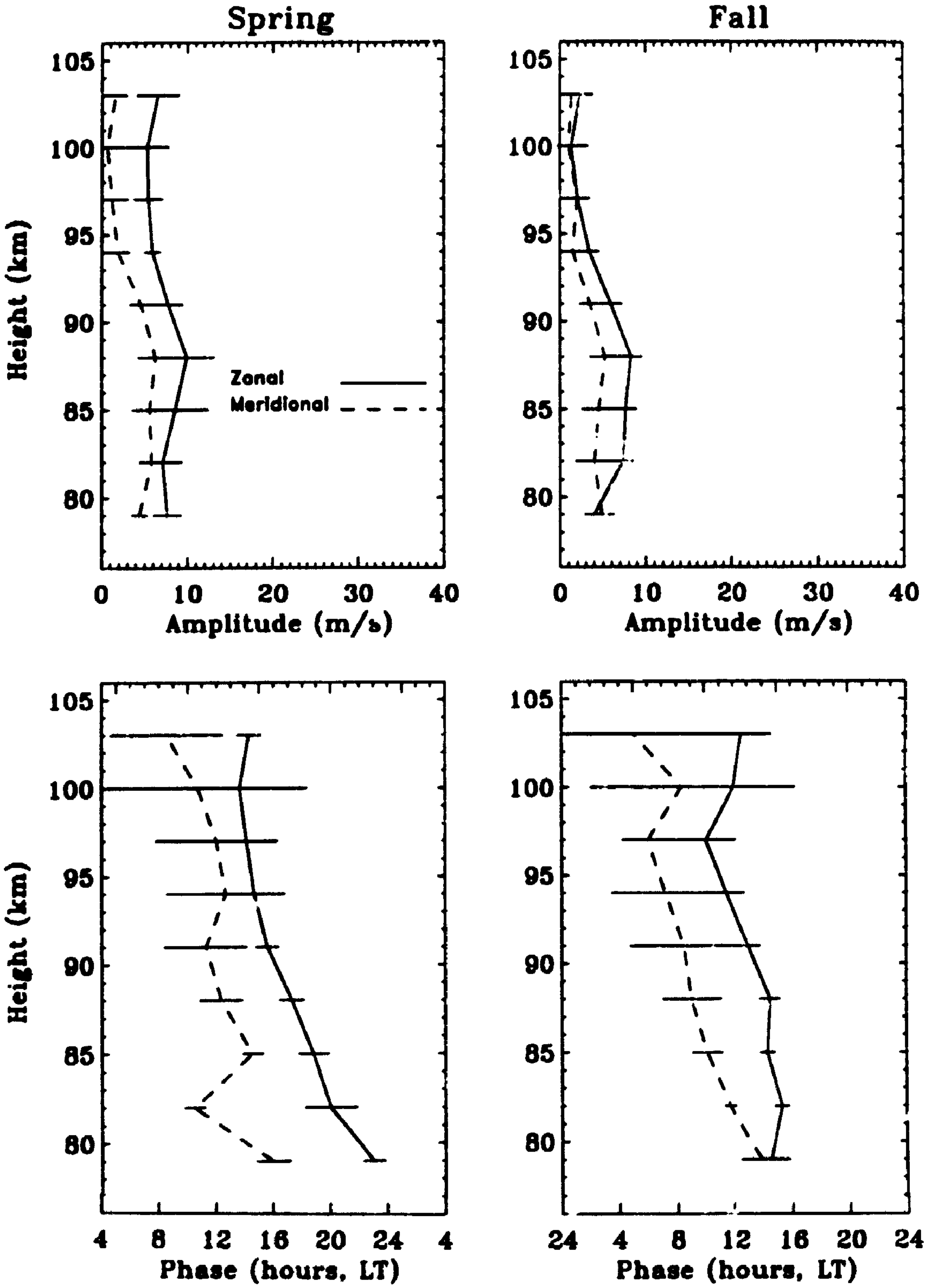

Figure 4.11: Height profiles of the amplitude and phase of the zonal and meridional wind components for the diurnal tide during the spring (March, April and May) and fall (September, October and November) in 1993 – 94 at London. Data are averaged over three months and the horizontal lines show the monthly variability within the season. Data above 95 km will suffer group retardation, and should be treated with caution - see Section 4.2.

	Zonal (km)	Meridional (km)
Winter	48 ± 7	38 ± 5 (below 91 km) Evanescent (above 91 km)
Spring	66 ± 8	76 ± 15
Summer	52 ± 5 (below 88 km) Evanescent (above 88 km)	90 ± 7
Fall	100 ± 10 (below 97 km)	64 ± 6

Table 4.2: Seasonal mean vertical wavelengths λ_z for the diurnal tide.

4.5.2 Diurnal phases

The phases of the diurnal tides are generally less organized and show larger variability than the semidiurnal tides, but some characteristics can be observed. Unlike the semidiurnal tide, the large error bars on the seasonal averages demonstrate instability of the phase structure. In general downward phase-propagation of the tides (as inferred by the negative phase gradients i.e. earlier phases at upper heights) are observed during all seasons. On occasions the phase profiles of the diurnal tide are almost constant with height suggesting the presence of evanescent or long vertical wavelength behaviour. Figure 4.10 highlights the phase transition at 88 km from propagating wave structure to near evanescent behaviour in the zonal component during the summer. This tendency can also be seen in the meridional phase profiles during the winter. The meridional phase profiles typically undergo a smooth change of ~ 6 h between 79-103 km with the earlier phase occurring at greater heights during the summer. Similar behaviour is also apparent for the zonal phase profiles during the winter, where a change in phase of ~ 12 h occur. The vertical wavelengths are generally short (~ 35-50 km) during the winter and long (90-∞ km) during the summer. A summary of the seasonal mean vertical wavelength (λ_z) values are given in Table 4.3.

It is also interesting to note that the phase of the zonal component leads that of the meridional component by ~ 8-12 h at many heights, indicating anti-clockwise rotation of the wind vector during the winter. However, in summer the rotation of the wind vector is clockwise with the meridional component leading the zonal component by ~ 0-2 h below 85 km, anti-clockwise with the zonal leading the meridional component by ~ 0-2 h between 85-94 km, and again clockwise with the meridional component leading the zonal component by ~ 0-3 h above 94 km.

In spring and fall abrupt changes with height in the phase of the meridional component are clearly apparent and suggest that mode superposition or interference may be occurring: the strong phase gradients which suggest vertical wavelengths of less than 10 km are probably not to be interpreted as a wave. These may be caused by the joint presence of two or more modes or by tidal reflections taking place due to large temperature or density gradients [Vial et al., 1985]. The vertical wavelengths are ~ 60-100 km. The phase of the meridional component generally leads that of the zonal component by ~ 3-8 h at many heights, indicating clockwise rotation of the wind vector during the spring. A similar change of rotation of the wind vector with height is also apparent during the fall.

Most vertical structure variations of the diurnal tide at mid-latitudes are due to superposition of the (1,1) and (1,-2) modes [Forbes, 1982a; Forbes, 1984; Forbes and Hagan, 1988]. The propagation characteristics of the first symmetric or (1,1) tidal mode have been investigated numerically by Forbes and Hagan [1988] for a background atmosphere characterized by zonally averaged mean winds, meridional temperature gradients, and mechanical and thermal dissipation. That numerical model predicts a well-defined amplitude peak in the vicinity of 90 km, an increase in the vertical wavelengths with height from 80 to 100 km, small amplitudes ($\leq$ 10 ms^{-1}) near 43° in latitude, and larger amplitudes during the summer than during the winter. It also predicts that the winter phases tend to lead the summer phases for the zonal component and the summer phases tend to lead the winter phases for the meridional component. These model characteristics are remarkably consistent with the behaviour of the diurnal tide over London observation. Despite this excellent agreement, the model fails to predict the observed amplitude minimum during the summer near 85 km.

We briefly compare the behaviour of the diurnal tide over London with Manson et al. [1989]. General characteristics are weaker seasonal variations, a tendency for longer vertical wavelengths during the summer, a tendency for shorter wavelengths during the winter, and generally small amplitudes with summer amplitudes often exceeding winter values. These characteristics are generally evident and observed over London, except for the long wavelengths which are observed for the meridional component in the data during the winter above 91 km.

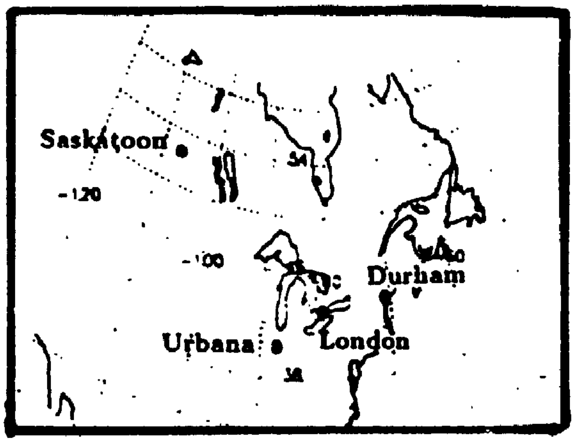

Figure 4.12: Geographical locations of London (43° N, 81° W), Urbana (40° N, 88° W), Saskatoon (52° N, 107° W) and Durham (43° N, 71° W).

4.6 Comparison of tides with other MF radars

In this section we will compare our data with measurements from stations at Saskatoon [Manson, private communication], Urbana and Durham [Manson et al., 1989]. The geographical locations of these sites are illustrated in Figure 4.12. Figure 4.13 illustrates the monthly averages of the semidiurnal amplitude and phase at 91 km and Figure 4.14 illustrates the monthly averages of the diurnal amplitude and phase at 91 km over London, and these are compared with results from the three other similar mid-latitude radars. Monthly tidal averages are estimated by taking a vector average of the daily mean fits at the London site. As noted earlier, it should be borne in mind that the overall comparison of results during different years may not be ideal because of the interannual variability of the tide. However, note that the Saskatoon data are observed during the same time period of observation, so that in some ways the comparisons with the Saskatoon data are the most interesting. In addition, different methods of data reduction (e.g., Durham site) and data analysis (e.g., Urbana site) have been used at different sites. It is desirable that a common method of data reduction be used when the results from two or more sites are compared. We intend to perform such comparisons in the future, but nevertheless for the time being we still feel that the comparisons shown here make useful contributions to a description of the morphology of atmospheric tides.

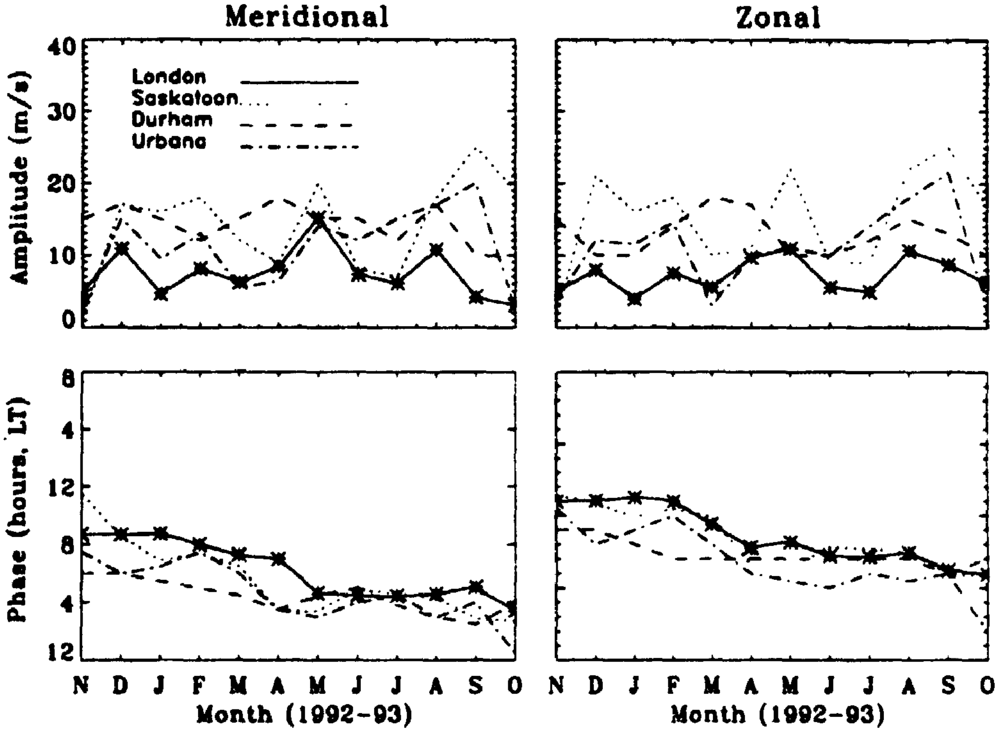

Figure 4.13: Comparison of monthly averages of amplitude and phase at 91 km of the meridional and zonal semidiurnal tides at London, Saskatoon, Urbana and Durham. Note that time marks on the abscissa indicate the middle of a month.

4.6.1 Semidiurnal tide

Semidiurnal phase comparisons

We begin by drawing attention to the relatively good overall agreement in phase between all sites for the semidiurnal component. An especially notable feature of the London and Saskatoon sites is that both the zonal and meridional semidiurnal tidal components show good agreement in phase at the two sites during the solstitial months of June and December, although the amplitudes are generally larger at Saskatoon. In addition, the meridional components have the same amplitude at the June solstice. Generally the phases for the semidiurnal tide are seen to be constant for several months around the solstices, and the change from one state to another takes place around the equinoxes. The period of almost constant phase around June lasts longer than the period of constant phases around December for the meridional component, whilst for the zonal component the December phases are constant for a longer period than the phases around June. We also note that there is a dramatic change in phase of the zonal component from October to November, and this is evident at London, Urbana and Saskatoon.

As noted, the phases of the meridional and zonal semidiurnal tides are broadly similar at the four sites, although agreement is clearly not perfect in some months. The meridional component at London in April is one example. Differences in phase are typically 0-4 h, and there is no consistent phase relationship apparent among the sites. These second order differences may be due to mode superposition or tidal-gravity wave interactions, which differ at different sites. This point will be discussed in more detail shortly. At all four sites, the meridional component leads the zonal component by $\sim$ 3 h, indicating clockwise rotation of the wind vector (looking from above).

Semidiurnal amplitude comparisons

The amplitudes of the semidiurnal tides at London (both meridional and zonal) appear to be significantly smaller ($50 - 100\%$) than those of the other three sites during the same month of the year. We note however that our values (below 91 km) show excellent agreement with the model data of Forbes and Vial [1989], as already discussed. The amplitude is seldom more than 10 ms^{-1} and shows gradual change with season. Whilst these amplitudes are small throughout much of the year when compared with other sites, the amplitudes observed in March-May and October-November coincide remarkably with similar values at the Urbana site. This excellent agreement was observed for both meridional and zonal components. Amplitude values of the meridional component in April-July and the zonal component in certain months also coincide with similar values at the Saskatoon site (same time period of observation). Relatively great day-to-day variability of the amplitudes and phases were observed in these months (March-July) and this may be important; tidal variations on time scales substantially less than one month may be important to consider when making these comparisons. London and Urbana are separated by only 3° in latitude and 7° in longitude, so simultaneous observations made at London and Urbana may in the future be possible and allow us to resolve some of the causes of these variations. Nevertheless the good agreement of phase, and the excellent agreement of amplitudes with Urbana in March, April, May, October and November makes us feel that the instrument is operating properly, and any differences with other sites are of true geophysical origin.

Interactions between gravity waves and tides have received considerable attention during recent years. This problem is particularly important with regard to tidal variability and has been discussed in the following section; we surmise that such interactions may explain at least some of the differences between the tides at the four sites under discussion. The variability due to this effect may well be substantially local and random. Walterscheid [1981] proposed a possible connection with gravity waves and thus demonstrated theoretically how tides can modulate the momentum deposited by gravity waves in the course of their interactions with the mean wind. Our observations show significant correlation between gravity waves and tides at certain times of the year, and a more detailed discussion can be found in the following chapter. It is possible that the reduced tidal amplitudes at London may relate to such interactions. The rather unique location of the London radar, in a region surrounded by the 'Great Lakes', may in some way explain some of the pecularities found there. We note that Forbes and Vial [1989] numerical model does not predict a reduction in amplitudes near 43° N in latitude.

4.6.2 Diurnal tide

Diurnal phase comparisons

Figure 4.14 shows the monthly averages of the diurnal amplitude and phase at 91 km at the four radars. One outstanding feature seen from the figure is that for the London and Saskatoon sites, the zonal diurnal tidal components show good agreement in phase during the solstitial months, and good agreement is also found between

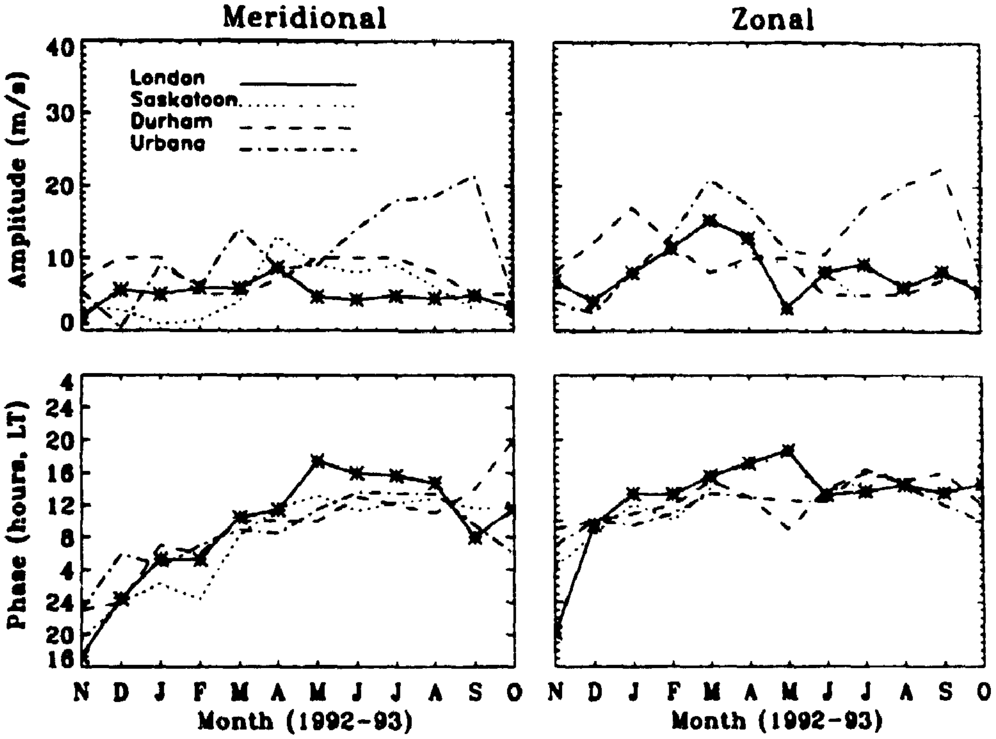

Figure 4.14: Comparison of monthly averages of amplitude and phase at 91 km of the meridional and zonal diurnal tides at London, Saskatoon, Urbana and Durham. Note that time marks on the abscissa indicate the middle of a month.

the meridional components during the December solstice. There is also excellent agreement in amplitudes for the zonal component at the December and June solstices, and this will be discussed in more detail shortly.

The good agreement for the solsticial months has been noted above, but in fact it is clear that the phase of the zonal component generally shows good agreement at all sites in most months. Remarkably good agreement is clearly apparent between the London and Saskatoon sites throughout the year, and this agreement is no doubt helped by the fact that observations were made at the same time. Unlike the semidiurnal phase, the phase of the diurnal tide shows substantial changes with season, particularly for the meridional component. The phases of meridional component at all four sites differ by ~ 0-4 h from January to April and differ by ~ 6-9 h from October to December. However, we note in Figure 4.10 that the summer diurnal tide shows a sudden phase transition, and an amplitude minimum near 85 km, which may well be due to reflection of a tide. This makes the phase very sensitive to height. Indeed, if similar reflection occur at other locations from marginally different heights, the phase at one height could show considerable sensitivity and therefore variability. We intend to address this further

Another interesting observation is the clear differences in the phase in May-August at the London site relative to the other sites, but again we note that these observations were made in different years except for the Saskatoon data. We also wish to note that London is a region close to the 'Great Lakes' area, and is often subject to strong tropospheric convective activity in these months. Although speculation at this stage, we note that this area could be a strong source of gravity waves which may propagate up and interact with the tide in these months. It is also possible that non-migrating tides play a role to produce such variabilities at these heights [Kato, 1989]. We intend to pursue this further, but we do generally feel that all the differences discussed are geophysical or temporal in origin.

Like the semidiurnal tide, there is no apparent uniform phase variation as a function of longitude across the sites. At all four sites, the meridional component leads the zonal component, indicating clockwise rotation of the wind vector.

Diurnal amplitude comparisons

It is significant to note that the amplitude time series of the zonal diurnal tides are almost similar in shape and magnitude at London and Urbana in October-February. Good agreement can also be observed between London and Saskatoon in certain months. However, large variation of the amplitude (~ 10 ms^{-1}) is also apparent among the sites during other months. Similar large variation also applies to the meridional components. The amplitudes of the meridional component during October-April are comparable (variations are 0-5 ms^{-1}) among the sites. The amplitudes remain constant at ~ 5 ms^{-1} during May-September at the London site, and this constant amplitude behaviour is also observed during May-July at the Saskatoon and Durham sites. Very large amplitudes (~ 20 ms^{-1}) are observed over Urbana in the same months. Constant amplitudes are also observed in December-March at London with amplitudes of ~ 6 ms^{-1}. The comparisons between the London and Sakatoon sites show that the zonal diurnal tide is considerably stronger in London than in Saskatoon, except in May. Furthermore, the meridional diurnal tide is significantly weaker in April-August at London than at Saskatoon, whilst the converse is true from December to March.

4.7 Conclusion

We have begun analysis of data recorded with a 2 MHz MF radar at London, Ontario. In general, the amplitude of the zonal component of the prevailing wind is much larger than the meridional component. The mesospheric circulation pattern for the zonal component is predominantly westward in summer and eastward in winter, at heights below 86 km, which is characteristics of a mesospheric monsoonal type circulation. The zonal component of the prevailing wind is particularly weak during the equinoxes as is expected due to the zonal flow reversal in equinoctial months. Above 91 km, the zonal component of the prevailing wind is predominantly eastward in all seasons. The mesospheric circulation pattern for the meridional component is northward in all seasons below 80 km. Above 94 km, there is evidence of northward flow in summer and southward flow in winter. Our zonal mean winds show generally good agreement with the empirical model due to CIRA-86 below 86 km. Significant differences above 86 km have been noted in comparisons between the CIRA-86 empirical model and other similar mid-latitude radars, and the same is true for us.

The zonal and meridional semidiurnal tides have similar amplitudes at most heights in all seasons. The semidiurnal tide generally exhibits evanescent or long vertical wavelength structure during the summer and fall. We also note that there is a hint of short wavelengths below 85 km during the summer. During the winter and spring, strong phase gradients equivalent to wavelengths of 30-50 km are observed. The comparisons of semidiurnal tides with the tidal model of Forbes and Vial [1989] show very good agreement in phase, although some differences do exist in amplitude.

The amplitude of the observed zonal diurnal tide is generally larger than the meridional component. The vertical wavelengths are generally short (~ 35-50 km) during the winter and long (~ 90-∞ km) during the summer, but this is not always true. The evanescent or long vertical wavelength structure is also observed above 91 km during the winter for the meridional component and relatively short wavelengths are observed during the summer below 88 km. A qualitative comparisons of diurnal tides with the numerical model due to Forbes and Hagan [1988] also show very good agreement. The only difference is that the model predicts an amplitude peak in the vicinity of 90 km, but our observations show that the amplitude peak does not occur during the summer, although it certainly exists in other seasons.

Comparisons of tidal data with sites at similar latitudes show reasonable agreement, but again some disparities are also noted. We have shown that these differences are of a geophysical nature, and illustrated that a great deal still needs to be learnt about atmospheric tides. We feel that tidal-gravity wave interaction may well be at the heart of this variability. The proximity of London to the Great Lakes area, which is an area prone to intense convection and therefore a possibly important source of gravity waves, may be a significant factor. The observed variability of the tides among similar mid-latitude radars sets forth the motivation to investigate tidal-gravity wave interactions, and the observational evidence of such interactions over London will be discussed in the following chapter.

Finally, in order to study the complete nature of atmospheric tides at mid-latitudes, it is necessary to continue these investigations. Coordination and intercomparisons on a international scale are particularly important.

Chapter 5

Observational evidence of tidal-gravity wave interactions

5.1 Introduction

It is well known that atmospheric solar tides and gravity waves play a significant role in the dynamics of the middle atmosphere [Lindzen, 1981; Geller, 1983]. Tidal and gravity wave amplitudes grow with height due to the effect of decreasing background atmospheric density, and eventually can become large enough to induce nonlinear interactions and breaking in the mesosphere and lower thermosphere.

However, our understanding of the complex interactions among atmospheric waves (e.g., gravity/tidal/planetary waves) remains limited. Tidal-gravity wave coupling represents one such interaction which has received considerable attention, and which can be studied with modern radars. These studies are particularly important with regard to short-term tidal variability, which is frequently observed in the mesosphere and lower thermosphere [Bernard, 1981; Lu and Fritts, 1993].

Walterscheid [1981] was the first to propose a possible connection of this modulation with gravity waves and thus demonstrated theoretically how tidal-gravity wave interactions can significantly modulate the tidal amplitudes. Such interactions can produce some wave-stress contribution to the zonal mean circulation [Miyahara et al., 1993; McLandress and Ward, 1994] and affect the spatial/temporal distribution of turbulent intensity. It should be noted that such a mutual interaction might also produce a local time variation in eddy diffusivity, which in turn may possibly impact the distributions of long-lived species (e.g., O, O_3, OH and NO) in the mesosphere and lower thermosphere. The potential importance of this problem has not yet received adequate study [Forbes et al., 1991]. It has also been shown theoretically that gravity wave stresses modified by the diurnal tide can produce significant tides having other frequencies than the primary (e.g., the semidiurnal and terdiurnal tides) in this region [Forbes et al., 1991; Miyahara and Forbes, 1991].

Recently, observational evidence of tidal-gravity wave interactions has been found by Fritts and Vincent [1987] over Adelaide, and is further substantiated by Wang and Fritts [1991] on the basis of winds measured by the Poker Flat radar system. These studies showed that the tidal amplitudes may be modulated by upward propagating gravity waves. Such tidal-gravity wave interactions were also noted by Reid et al. [1988] and Fritts and Yuan [1989], but were not addressed in detail.

In this chapter, we present analysis of radar data for different seasons which indicate that tidal-gravity wave interactions do occur and furthermore suggests that the nature of the interaction varies with time of year. As such this study is an advancement of previous work in which only a single time period was examined [Fritts and Vincent, 1987; Wang and Fritts, 1991]. Our study contributes additional geographic and seasonal data and includes continuous observations over fairly long collection periods. In the following section, data collection methods are briefly described. Section 5.3 discusses the data analysis procedures and results. A proposed model of this tidal-gravity wave interaction is presented in Section 5.4. The discussions and conclusions of this study are presented in Sections 5.5 and 5.6 respectively.

5.2 Data collection

A new MF (2.219 MHz) radar which uses the SA technique was established at London in November 1992. Peak power is 20 kW and the duty cycle is 0.12%. The pulse repetition frequency is 60 Hz with 32 point coherent integration. Since November 1992 the radar has been used to measure horizontal winds with the spaced antenna method in the height range 60-100 km, with wind measurements being made at time intervals of 5 min and at 3 km height intervals. The configuration for the three antennas is an equilateral triangle with a spacing of 225 m, and the complex auto- and cross-correlation functions obtained with 512 point time series are parameterized to obtain true velocity estimates using Full Correlation Analysis (FCA) [e.g., Briggs, 1984; Hocking et al., 1989]. We will concentrate on the 85-94 km height range.

5.3 Data analysis and results

We have examined 4 day data sets from November 1992 to October 1993, and three examples of tidal-gravity wave interactions observed during different times of the year are presented - specifically data collected in 1993 from 26 February to 1 March (winter), 15-18 July (summer) and 12-15 August (summer). We have adopted a 4 day fit because this is long enough to give reasonable significance to our results yet short enough to give reasonable sensitivity during periods of large tidal activity. It should be noted that 53 – 63% of the total available wind data were accepted in the 85-94 km height range using FCA acceptance criteria during these periods of time [e.g., Briggs, 1984; Hocking et al., 1989]. The other data were rejected due to either poor signal to noise ratio or various stringent rejection criteria (see Section 3.4.4). Generally the data were distributed fairly evenly throughout each period, ensuring no bias due to sampling problems. The average number of wind estimates during daytime (0700-1800 hrs) and nighttime (1800-0700 hrs) hours in the 85-94 km height range are 51% and 49% of the total possible number of records which could have been recorded from 26 February to 1 March respectively. These values are 54% (0600-2100 hrs) and 46% (2100-0600 hrs) during 15-18 July, and are 52% (0630-2030 hrs) and 48% (2030-0630 hrs) during 12-15 August.

In our analysis procedure, the data for 4 days in each month were analyzed using classical harmonic analysis techniques with mean, 48, 24, 12 and 8 hour components. We then obtained means and variances of wind fluctuations in 2-hour intervals, and compared these to the tidal oscillations. We will assume, as is normally done, that these residual oscillations are due to gravity waves. The graphs in Figure 5.1 illustrate our fitting and analysis procedures at 94 km from 26 February to 1 March (winter). A median filter has been applied to the data, so that outlier points lying outside of the 95% significance level were rejected in each 2 hour interval when estimating gravity wave variance.

The sequence of diagram shown in Figure 5.1 are ordered in the following way. First, the raw data, two hourly means with a 3 point running mean, and tidal fits for the zonal component are shown on the left side of the panel. The 48 and 8 hour components are not shown in Figure 5.1c due to their comparatively small amplitudes. The non-tidal component, gravity wave variance of the residuals (zonal component only), and its 3 point running mean are shown on the right side of the panel. A similar example showing gravity wave variances as a function of time at 91 km during 15-18 July (summer) is illustrated in Figure 5.2 (similar to Figures 5.1c and 5.1f).

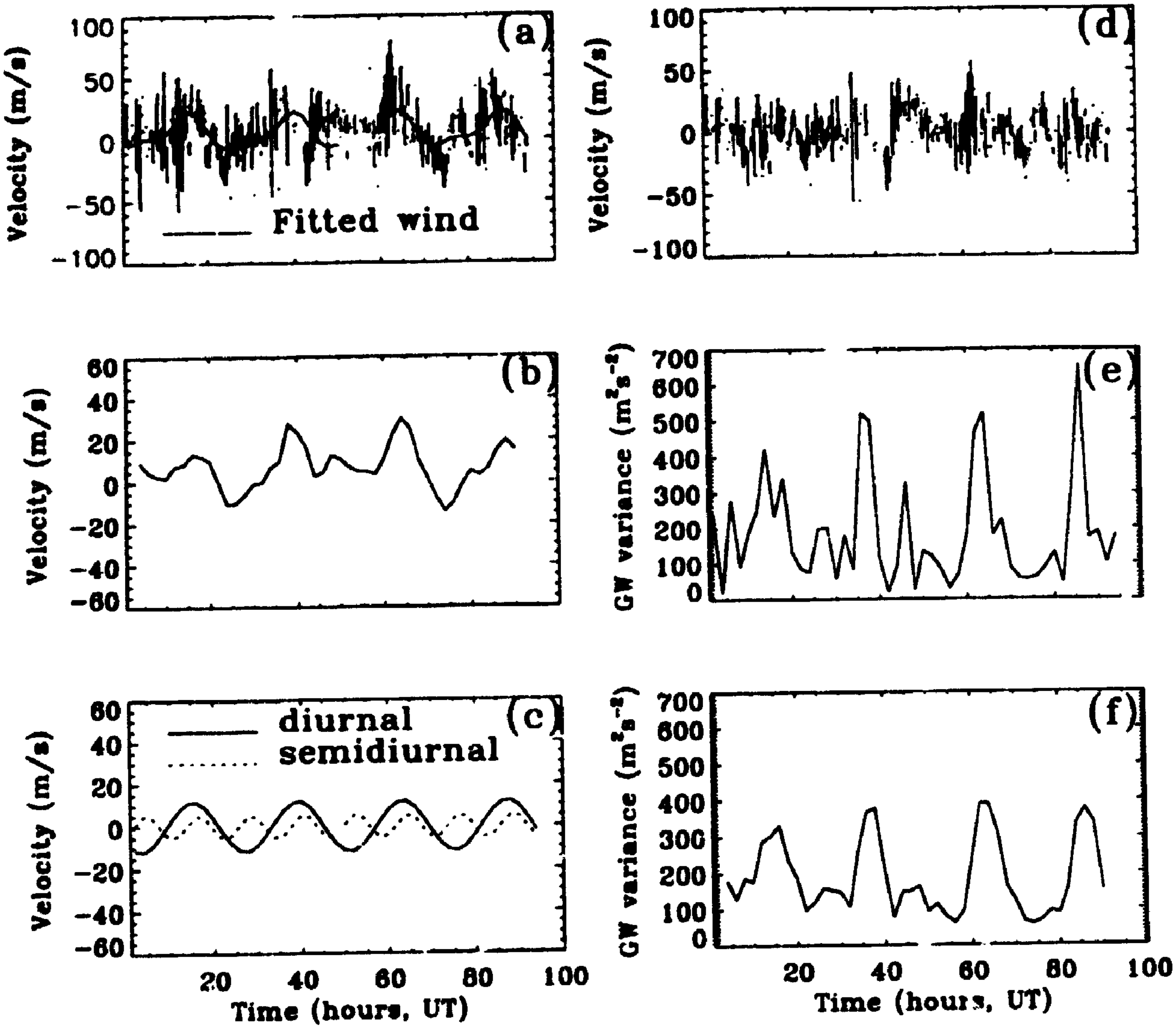

Figure 5.1: Tidal fitting and analysis procedures: The raw data, two hourly means with a 3 point running mean and tidal fits for the zonal component at 94 km from 26 February to 1 March (winter) are shown on the panels a, b, c. The non-tidal component, the gravity wave variance and its 3 point running mean are shown on the panels d, e, f.

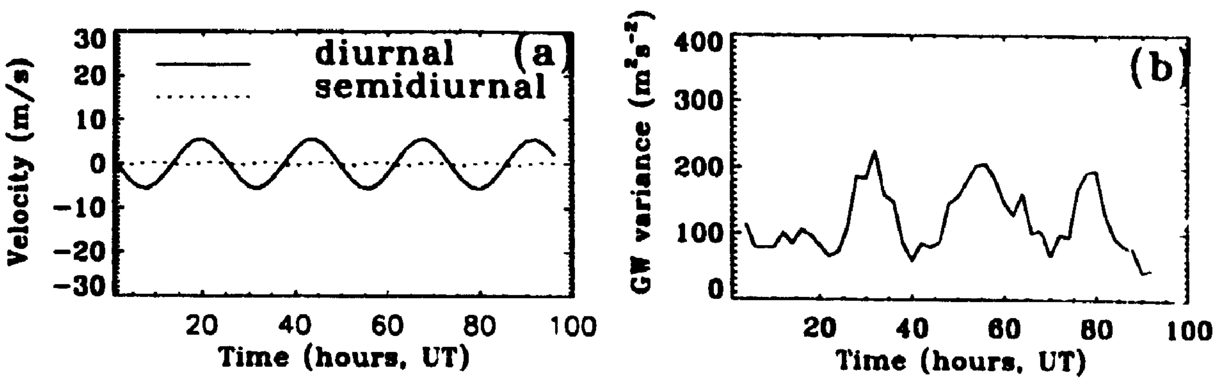

Figure 5.2: As in Figures 5.1c and 5.1f, but during 15-18 July (summer) at 91 km.

Figure 5.3a illustrates the cross-correlation between the zonal diurnal tides and gravity waves during February-March. A significant correlation between the gravity wave variance and the amplitude of the diurnal tidal motion is apparent for the zonal component. It occurs in phase at all four adjacent heights between 85-94 km, with similar correlation values. The correlation values are ~ 0.55 and the time lags for maximum correlation are found to occur between 0 and 2 hours. These data reveal that the diurnal variability of the gravity wave variance occurred with a high degree of consistency over a number of heights on this occasion. Figure 5.3b illustrates the cross-correlation between zonal diurnal tides and gravity waves during 15-18 July. A clear tendency for good correlations is also evident for the zonal component in these data. The phase of the correlation shows good agreement at all four adjacent heights between 85-94 km with correlation values of ~ 0.4-0.6. The time lags for maximum correlation occur in this case between 8 and 14 hours. This remarkable occurrence of diurnal variations shows up particularly well in the mean square velocities, and the plots of this parameter as a function of time are shown in Figures 5.1f and 5.2b. These features of the data strongly suggest that gravity wave motions may affect, and/or be affected by, daily variations of diurnal tides in that region at certain times of the year.

On the other hand, the correlation values for the meridional component were smaller at all heights and the maximum values did not show the same time lag at different heights (not shown). We emphasize that in this study we will concentrate on only the clearest examples of tidal-gravity wave coupling; other, more tentative cases will be ignored, although we may return and re-analyze these less clear examples in the

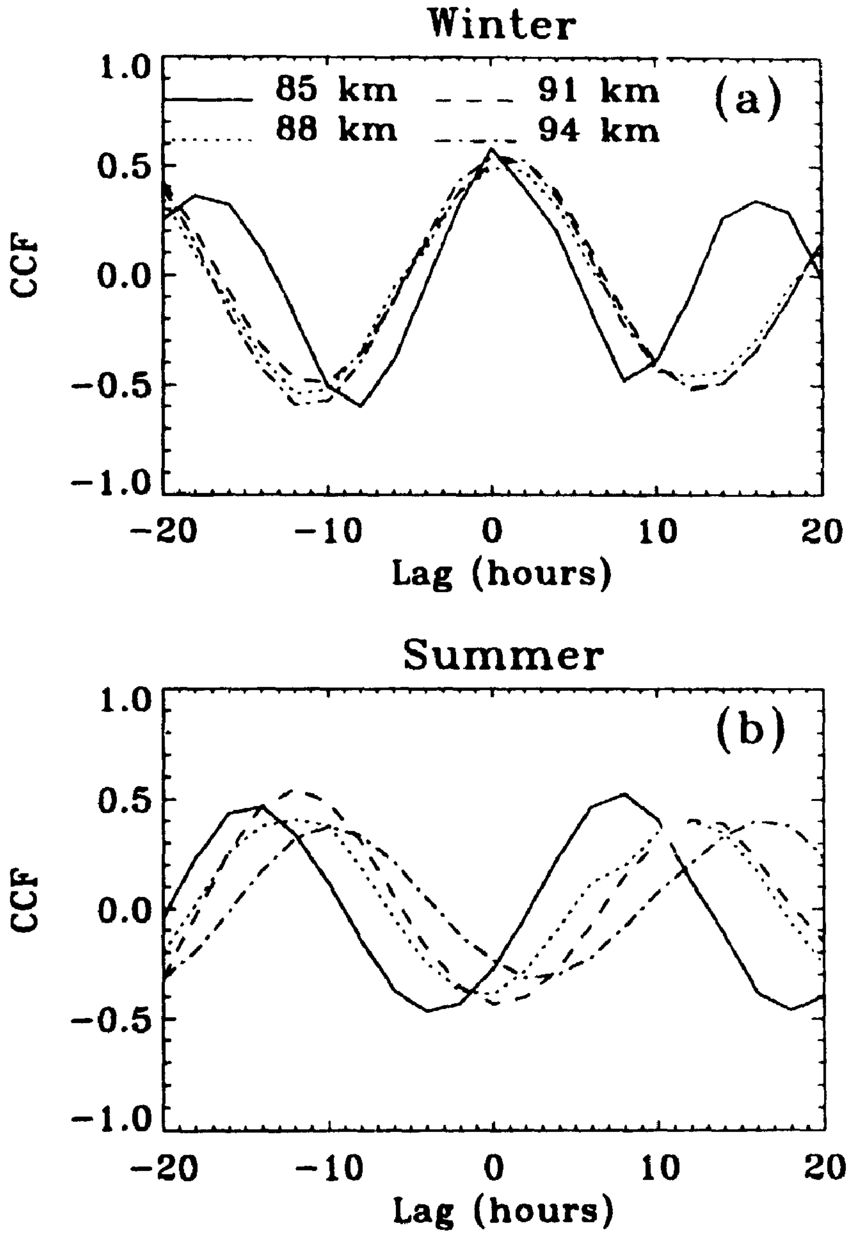

Figure 5.3: Cross-correlation between zonal diurnal tides and gravity wave variances in the 85-94 km height region a) from 26 February to 1 March 1993 (winter) and b) during 15-18 July (summer).

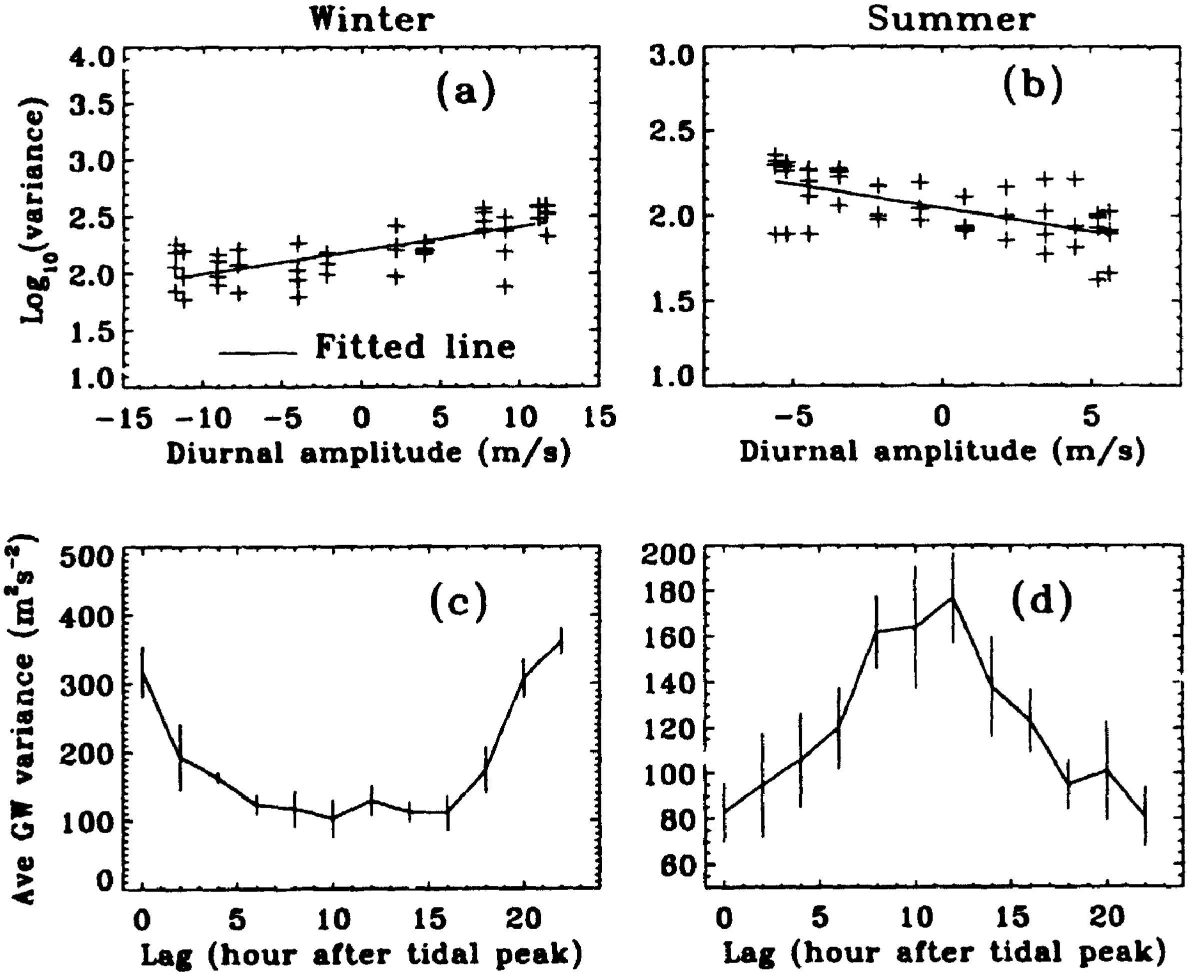

Figure 5.4: Scatter plots between the amplitude of the zonal diurnal tidal motion and the smoothed gravity wave variance a) from 26 February to 1 March and b) during 15-18 July 1993. Using the diurnal tide as a reference, superposed epochs of the gravity wave variance are shown in c and d.

future work. Our purpose here is to use our most convincing data to demonstrate that these interactions do occur.

We have also created scatter plots between the smoothed gravity wave variances and the zonal tides, and these are illustrated in Figures 5.4a and 5.4b. The solid lines show the least-squares best fit. The linear correlation coefficient at 94 km for the February data is positive with a value of 0.73 and the 95% confidence limits are 0.46 and 0.87. The average value of the correlation coefficient in the 85-94 km height range is 0.62 and the confidence limits are 0.29 and 0.82. For the July data the linear correlation coefficient at 91 km alone is negative with the value of -0.62 and the confidence limits are -0.29 and -0.82. The average value of the correlation coefficient in the 85-94 km range is -0.50 and the confidence limits are -0.12 and -0.75. It can be seen that especially for the February data (winter), the zonal component of the gravity wave variance shows a clear tendency for larger values to occur when the zonal diurnal tidal wind is largest. In contrast, the July data (summer) shows the opposite tendency with largest values associated with most negative tidal winds. These differences are discussed in our model below. Using the diurnal tide as a reference, superposed epoch analysis of the variance is presented in Figures 5.4c and 5.4d. Note that the zero time lag is taken to be the maximum amplitude of the zonal diurnal tidal motion. The maximum values of the gravity wave variances occur around 11.00 a.m. local time (daytime) for the February data but for the July data the maximum values occur around 3.00 a.m. local time (nighttime). This behaviour is also seen to be present in Figures 5.1f and 5.2b as well. It is noteworthy that the average acceptance rates of wind estimates within ±4 hours of the maximum of the gravity wave variance in the 85-94 km height range are 58% and 59% for the February and July data respectively. This again shows that the observed correlation is not biased towards decreasing number of data points.

The tidal-gravity wave interactions identified here are not observed at all times of the year, and an example in which there is no significant correlation is shown in Figure 5.5 (during 12-15 August). We also found no apparent correlation between semidiurnal tides and gravity waves over London during our observation period (not shown). This may be due to the larger amplitude of the diurnal tide as compared with the semidiurnal tide (see Figures 5.1c and 5.2a).

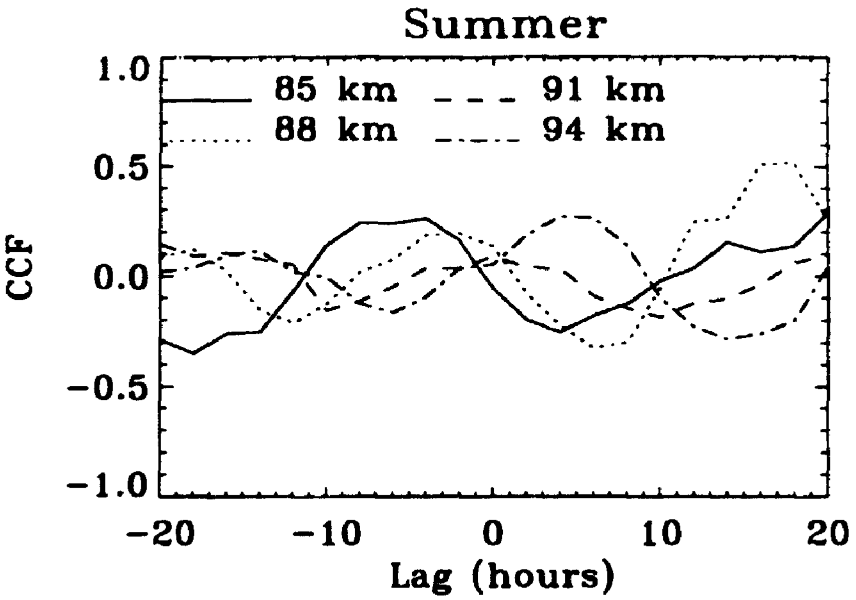

Figure 5.5: As in Figure 5.3, but during 12-15 August.

5.4 Proposed explanation of observations

Figure 5.6 illustrates one proposal to explain these observations. It is based on the work of Fritts and Vincent [1987] and Walterscheid [1981]. The essential fact which forms the basis of the model is that gravity wave amplitudes cannot exceed $u' = | \bar{u} - c |$, where $\bar{u}$ is the background wind (means + tidal components) and c is the horizontal phase speed of the gravity waves. Waves with greater amplitudes than $|\bar{u}-c|$ are convectively unstable and begin to dissipate.

When the wind profile (mean + tide) is as shown in Figure 5.6b (winter situation), westward propagating gravity waves can propagate up to 90 km with little dissipation. However, 12 hours later the situation is as in Figure 5.6c, and the mean wind at 90 km is substantially westward. Thus $| \bar{u} - c |$ is generally small, and the waves are forced to dissipate below 90 km, reducing the wave energy which reaches the higher altitudes.

Note that this scenario predicts that gravity waves in winter will be strongest when the 90 km tidal winds are eastward. In summer, the mean winds are opposite in direction so that the reverse is true, and gravity waves will be strongest at 90 km when the tidal winds are westward. Both these predictions are borne out in the observations.

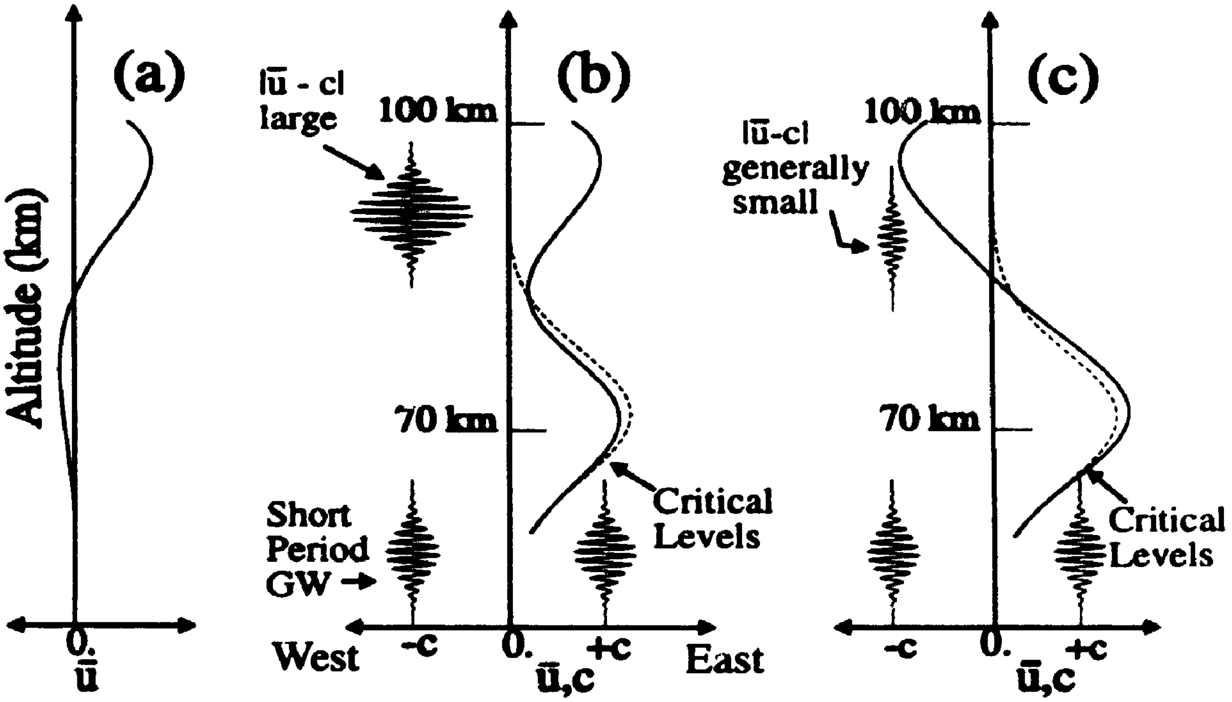

Figure 5.6: (a) Illustration of a typical height profile of the diurnal tide at one particular time of day. (b) The mean wind for a typical winter situation (broken line) is shown superposed with the tide, giving the solid line, where the phase of the tide is the same as that given in (a). Eastward propagating waves strike a critical level below 70 km, whilst westward propagating ones may grow uninhibited (at least until instability is achieved), since $|\bar{u}-c|$ is large. (c) As for part (b), but this time 12 hours later, when the phase of the tide has changed by 180°. Eastward propagating waves still strike critical levels, but westward propagating ones are severely damped because $|\bar{u}-c|$ is generally small, thus restricting the amplitudes to which the gravity waves can reach at 90 km altitude.

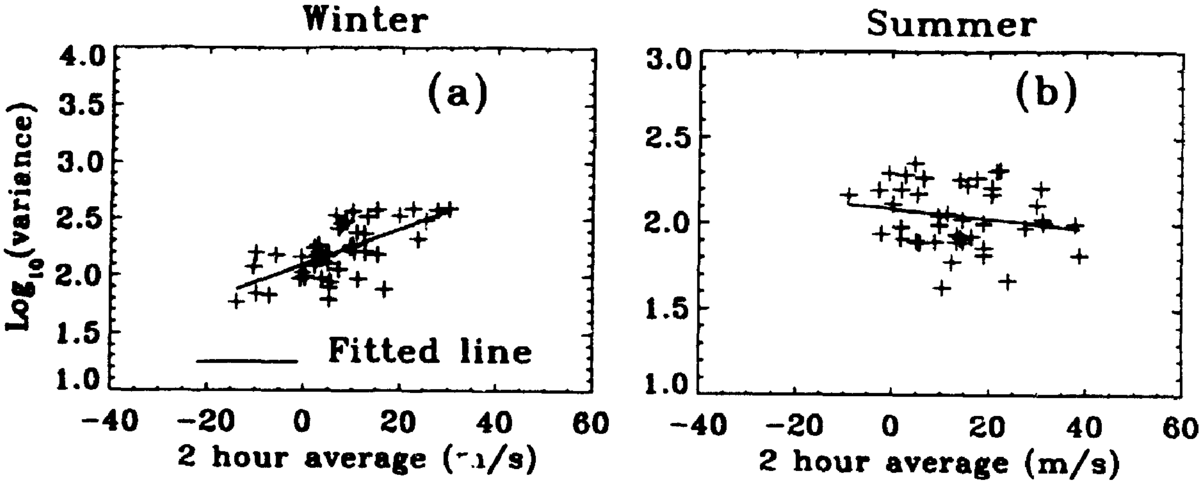

Figure 5.7: Scatter plots between the smoothed two hourly mean and the smoothed gravity wave variance a) from 26 February to 1 March and b) during 15-18 July.

It is also important to note that large amplitude waves can act to accelerate the flow as they break, so that the breaking gravity waves will also alter the tidal amplitudes.

The interaction model described here represents an interaction between the bulk flow (where the bulk flow is assumed to be the sum of steady and tidal components) and waves, rather than a true non-linear interaction. Therefore one might expect an even better correlation if a scatter plot is performed between the 2 hour mean winds and the gravity wave variances. However, tests of this hypothesis showed in fact much worse correlation (see Figure 5.7). Note, however, that the fitted lines have a similar tendency to those in Figures 5.4a and 5.4b. We do not yet understand why these plots show poorer correlation than do those for just the 24 hour tide. A more elaborate theoretical analysis is obviously required in order to understand what factors other than those discussed above are important in the interaction of gravity waves and tidal components, although we can make some suggestions. The importance of other long period waves with short vertical wavelengths in the process is one possible candidate to explain this worsened correlation, as is the relative importance of local and non-local effects on the tide.

Consider a longer period waves (periods $\geq$ 6 hours) with a short vertical wavelength, and for simplicity consider a short period gravity wave propagating through the wind field created by this longer period wave (see Figure 5.8). Then because of the short vertical wavelength of the long period wave, the altitude regions in which $u' > | \bar{u} - c |$ is valid may be too short to allow the short period wave to properly relax back to

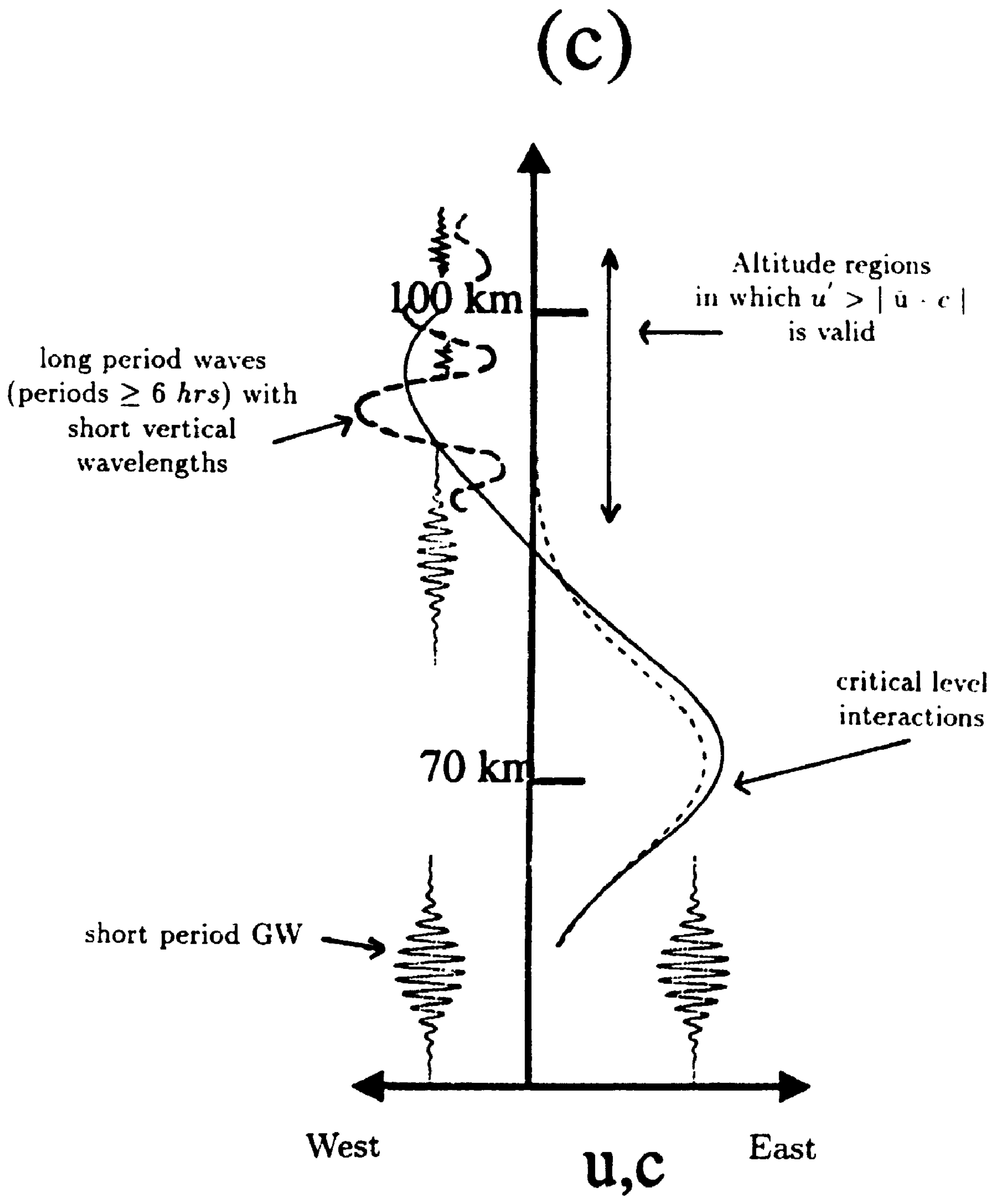

Figure 5.8: As in Figures 5.6c, but superposed with a longer period waves (periods $\geq$ 6 hours) with a short vertical wavelength. See the text for details.

the unsaturated state - the shorter period waves may in fact "tunnel through". Thus such long period wave might contribute to the 2 hourly means, but not substantially alter the short period wave variance. The existence of such long period waves in addition to the tide might then worsen the correlation. On the other hand, the data may imply that the interaction is a truly non-linear one and is not in fact described by Figure 5.6.

We recognize that our model may not be complete, and more detailed studies of a theoretical nature are needed to investigate other likely causes, but these are beyond the scope of this thesis.

5.5 Discussion

Our long period observational results strongly suggest that tidal (diurnal)-gravity wave interactions can occur over London, Canada at certain times of the year. The observed intermittency is an expected feature, given the day-to-day variability in the gravity wave sources and background wind fields. Such interactions may be an important source of short-term tidal variability in the mesosphere and lower thermosphere. These observations showed that propagating gravity waves with periods of less than 2 hours can significantly modulate the tidal amplitudes, and the reverse is also true. Numerical studies of such phenomena [e.g., Walterscheid, 1981] have also shown such interactions.

We surmise that such mutual interactions may explain at least some of the differences observed in tidal amplitudes and phases from mid-latitude ground based radars. The previous chapter has shown that zonal tidal amplitudes over London at times are suppressed compared with other sites [see Chapter 4], and we believe that this is an indication of tidal variability and may relate to tidal-gravity wave interactions. Numerical models also show that the zonal tidal amplitude can be significantly reduced ($\sim$ 8 ms^{-1} at 43° N) by momentum deposition due to gravity waves and the phase differences are less than one hour when the mutual interaction between the tides and the gravity waves exists at altitudes greater than 80 km [Miyahara and Forbes, 1991, 1992]. Our observations show that the zonal diurnal amplitude is reduced by $\sim$ 3-6 ms^{-1} compared to the mean value of that month in the 88-94 km height range during 15-18 July. For the February data the amplitude is reduced by $\sim$ 2 ms^{-1} in the 85-94 km height range. Overall phase differences are less than one hour compared to the mean of the month, in accord with these modeling studies.

5.6 Conclusion

As a result of our observations, a simple tidal-gravity wave interaction model has been proposed and the major features of the observed data are found to be consistent with the model. The nature of the interaction which varies with time of year supports the model quite nicely.

The observational evidence presented here indicates that tidal-gravity wave interactions play a major role in middle atmosphere large and small scale variability and also provides some important insights into the dynamics in the mesosphere and lower thermosphere. The observations of these interactions are important, regardless of the frequency of occurrence, and will stimulate further observations and modelling work in this area. More detailed analysis of such interactions are essential in order to improve our understanding of the dynamics on these regions.

Chapter 6

The quasi 2-day wave

6.1 Introduction

It is well known that atmospheric long-period waves play a significant role in the dynamics of the middle atmosphere. Long-period waves have been observed routinely in the middle atmosphere for many years. The quasi 2-day wave represents one such long-period wave which has received considerable theoretical and observational interest in recent years, and which can be easily studied with modern radars. These studies are particularly important for their relevance to the interaction between such waves and the mean flow, and have important implications for the general circulation of the middle atmosphere during the summer. It may be also important in the transport of atmospheric constituents at these heights during the summer [Plumb et al., 1987].

The quasi 2-day wave (hereafter referred to as the 2-day wave) is a global-scale oscillation in the middle atmosphere (in the 50-100 km height region) which has frequently been observed in both the Northern and Southern Hemispheres by radar, rocket, and satellite techniques for over 20 years, but there is still no definite universally accepted explanation as regards its generating mechanisms and its role in the middle atmosphere. A 2-day wave in the zonal and meridional winds in the mesosphere and lower thermosphere was first described by Muller (1972) from meteor wind observations, and then it was studied subsequently by many workers. Extensive observational studies of the 2-day wave in the mesosphere and lower thermosphere have been made using both meteor and partial reflection radar observations [Ka[illegible]nko and Bulgakov, 1973; Muller and Kingsley, 1974; Muller and Nelson, 1978; Kingsley et al., 1978; Massebeuf et al., 1981; Clark, 1975, 1983, 1989; Clark et al., 1993; Manson et al., 1978, 1882, 1987; Ito et al., 1984; Manson and Meek, 1987; Stening et al., 1978; Salby and

Roper, 1980; Craig et al., 1980; Craig and Elford, 1981; Craig et al., 1983; Aso et al., 1980; Plumb et al., 1987; Tsuda et al., 1988; Harris, 1993, Randel, 1993]. All these observational results were for the 2-day wave at mid-latitudes.

Observations of the 2-day wave were also extended to high-latitudes [e.g., Phillips, 1989; Williams and Avery, 1992], low-latitudes, as well as equatorial regions [Kalchanko and Bulgakov, 1973; Coy, 1979; Kalchanko, 1987; Reddi et al., 1988; Harris and Vincent, 1993; Fritts and Isler, 1994]. Rocket observations have indicated the possible existence of a 2-day wave in the winds near the equatorial stratopause [Coy, 1979; Reddi et al., 1988]. Satellite temperature observations have also been reported in the upper stratosphere and mesosphere [Rodger and Prata, 1981; Burks and Leovy, 1986]. These satellite observations give a clear global picture of the wave structure.

6.1.1 Seasonal variations

Most observations suggest that the 2-day wave is a late summer phenomenon in the middle atmosphere, mainly at low- and mid-latitudes, reaching its maximum amplitude in late July/early August in the Northern Hemisphere and in late January/early February in the Southern Hemisphere [e.g., Kingsley et al., 1978; Craig and Elford, 1981; Clark, 1983, 1989; Plumb et al., 1987; Clark et al., 1993; Harris, 1993]. A subsidiary weak maximum is often observed in the autumn or winter [e.g., Muller and Nelson, 1978; Craig and Elford, 1981; Ito et al., 1984; Harris, 1993], but at other times of the year the oscillation is usually either weak (because amplitudes are indistinguishable from noise) or non-existent, depending on the locality [Rodgers and Prata, 1981]. In general, radar observations in the Northern Hemisphere indicate the presence of a 2-day wave in all seasons, although maximum amplitudes occur in the months of July/August [e.g., Kingsley et al., 1978; Manson et al., 1981, 1982, 1987; Clark, 1983, 1989; Tsuda et al., 1988]. Clark [1983] showed that 2-day oscillations have steady amplitudes of 10-15 m/s in both zonal and meridional components in all seasons, except for a winter minimum. Salby and Roper [1983] also showed the presence of 2-day wave over Atlanta (34° N, 84° W) in all seasons, but in contrast to other observations they appeared to find a maximum amplitude in autumn and a minimum amplitude in summer. Outside the equatorial regions, at mid- and high-latitudes, the amplitude of the 2-day oscillation typically reaches an annual maximum approximately a month after the summer solstice, when total wind speeds can easily exceed those due to the atmospheric tides alone.

At equatorial regions the 2-day wave has been observed throughout the whole year, and has two maxima which correspond in time to the occurrence of the oscillation at mid-latitude in each hemisphere [e.g., Kalchenko and Bulgakov, 1973; Kalchenko, 1987; Harris and Vincent, 1993]. Radar observations in the equatorial middle atmosphere in recent years by Harris and Vincent [1993] show that the wave amplitudes are especially large about one month after the solstices, in July/August and January/February, at times coincident with large 2-day wave events in the summer mesosphere at extratropical latitudes. Radar observations at low-latitudes, over Hawaii (22° N, 160° W), [Fritts and Isler, 1994] show that the 2-day wave exhibits considerable seasonal and interannual variation. They found narrow amplitude peaks occurring during February and broader maxima occurring during July and August.

6.1.2 Latitudinal dependence

Simultaneous radar observations of the 2-day wave in the months of July and August in the Northern and Southern Hemispheres indicate that a significant cross-equatorial leakage of the wave from the summer to the winter hemisphere [Craig et al., 1983]. They found that the 2-day oscillation was evident in both the Sheffield (53° N) and Townsville (19° S) data, but not in Adelaide (35° S) data. In a similar study, Tsuda et al. [1988] made simultaneous observations at Kyoto (35° N, 136° E) and Adelaide (35° S, 138° E) during January 1984, which are located at geographically conjugate points in the Northern and Southern Hemispheres. The wave amplitudes at Adelaide were 30-35 m/s and 15-20 m/s for the meridional and zonal components, respectively, and the former is roughly four times larger than the Kyoto results. Comparative observations clearly show that the phases between the two hemispheres are in phase for the meridional component, and out of phase for the zonal component, implying antisymmetry of the 2-day wave between the Northern and Southern Hemispheres. This comparison also suggests that the 2-day wave is not confined to the summer hemisphere, but has a global structure extended over both hemispheres.

Satellite temperature measurements over a 4 year period show that the wave has largest amplitude in the mesosphere at low-latitudes in the local summer hemisphere and has a markedly asymmetric meridional structure. The maximum temperature oscillations are found near 20° S, with the wave structure extending from near 50° S in the summer hemisphere to about 20° N latitude in the winter hemisphere [Rodgers and Prata, 1981].

6.1.3 Meridional and zonal components

Most radar observations show that 2-day oscillations typically maximize in the meridional component rather than the zonal component at mid-latitudes with maximum amplitudes usually attained at heights between 80 and 95 km [e.g., Vincent, 1984; Craig et al., 1980; Craig et al., 1981; Clark, 1989; Clark et al., 1993; Tsuda et al., 1988; Ito et al., 1984]. In general, the meridional component is larger by a factor of 2-3 than the zonal component at mid-latitudes.

The 2-day wave observed in the equatorial middle atmosphere by meteor and partial reflection radars showed that the oscillation is particularly strong in the meridional component, and seems to be present almost continuously with time in the 80-100 km height region, although some intermittency is evident [Kalchenko, 1987; Harris and Vincent, 1993].

There are only a few observations of the 2-day wave in winds at low-latitudes [Coy, 1979; Reddi et al., 1988; Kalchenko, 1988; Fritts and Isler, 1994]. An examination of daily meteorological rocket data at Kwajalein (9° N, 168° E) showed that a 2-day oscillation in the stratosphere to be present only in the meridional component but not in the zonal component [Coy, 1979]. In contrast, the stratospheric and mesospheric wind data obtained from rocket launches over Trivandrun (8.5° N, 76.8° E (different longitude from Kwajalein) showed that the 2-day oscillation is present in both the zonal and meridional components, and also the amplitude in the zonal component is found to be larger than that of meridional component at certain altitudes [Reddi et al., 1988]. Radar observations over Hawaii show that the meridional values are comparable to or exceed the zonal values in all seasons [Fritts and Isler, 1994]. Satellite temperature measurements show that the 2-day oscillation maximizes just after the summer solstice and that the largest amplitudes occur at a height of 70 km [Rodgers and Prata, 1981].

6.1.4 Hemisphere differences

While there are a number of clear similarities between the Northern and Southern Hemisphere observations, there are also a number of consistent differences; in particular, the period is typically longer at northern latitudes while the maximum wave amplitudes are usually larger in the Southern Hemisphere.

Amplitude

Both ground-based and satellite observations show that amplitudes in the meridional component are larger in the Southern Hemisphere, being up to a factor of two larger than those found in the Northern Hemisphere [e.g., Rodgers and Prata, 1981; Vincent, 1984; Plumb et al., 1987, Tsuda et al., 1988; Clark, 1983, 1989; Clark et al., 1993; Ito et al., 1984]. Typical mean maximum amplitudes in the meridional component are ~ 30-40 m/s but short-term amplitudes of 50-100 m/s are common in the Southern Hemisphere [e.g., Craig et al., 1980; Craig and Elford, 1981; Phillips, 1989]. In contrast, mean maximum amplitudes near 20-30 m/s are typical in the Northern Hemisphere [e.g., Vincent, 1984; Rodgers and Prata, 1981; Tsuda et al., 1988; Clark, 1983, 1989; Clark et al., 1993]. The duration of all such events ranges from several days to intervals in excess of month.

Very large amplitudes of 45-60 m/s are reported in the equatorial middle atmosphere by radar observations [Harris and Vincent, 1993; Kalchenko,1987]. Radar observations at low-latitudes show maximum amplitude values of ±30 m/s are common in the mesosphere and lower thermosphere [Fritts and Vincent, 1994]. Rocket observations show amplitudes as large as 30 m/s are seen in the meridional component near the stratopause (~ 50 km), and similar amplitudes also occur in the mesosphere [Reddi., et al., 1988]. There is little evidence of the wave below about 40 km. Phillips [1989] showed that 2-day oscillations of 10-15 m/s in the meridional component are a regular feature of the high-latitude Southern Hemisphere summer. Further investigations are therefore required to see if the differences in amplitudes are due to hemispheric or latitudinal differences of both.

Period

In addition to amplitude differences, another apparent difference between the hemispheres in their respective summers is the wave period. Different observers report somewhat different periods in the range 43-53 h [e.g., Craig and Elford, 1981; Kalchanko, 1987; Massebeuf et al., 1981; Salby and Roper, 1980; Cevolani et al., 1983: Tsuda et al., 1988]. In the Southern Summer Hemisphere the dominant wave period seems consistently to be fairly close to 48 ± 3 h [e.g., Craig et al., 1980; Craig and Elford, 1981; Phillips, 1989; Poole, 1990; Harris, 1993], whereas in the Northern Summer Hemisphere the period seems to be 51 ± 2 h [e.g., Muller, 1972; Glass et al., 1975; Muller and Nelson, 1978; kingsley et al., 1978; Stenning et al., 1978; Manson et al., 1978; Salby and Roper, 1980; Tsuda et al., 1988]. Meteor wind observations at Kyoto (35° N, 136° E) for three years (1983-85) showed that the period of the quasi 2-day wave ranges from 52 to 55 h in summer, and becomes as short as 46 to 48 h in autumn in 1983 and 1984. The change in the wave period seems to coincide with a decrease in the amplitude of the zonal mean wind. They also showed that year-by-year variations of the dominant periods and amplitudes are relatively large [Tsuda et al., 1988].

Radar observations of the 2-day wave in the equatorial middle atmosphere show a shift in wave period from near 50 h in July/August to 48 h in January/February, when the largest amplitudes (up to 45 m/s) are observed [Harris and Vincent, 1993]. In other similar studies, wave periods other than 48 h have also been discovered. For example, wave periods from near 44 h in July/August (1981) to 52 h in July (1971) have been observed [Kalchenko, 1987].

Radar observations at low-latitudes show that the 2-day wave period is well defined near 48 h during February (Southern Hemisphere summer conditions) but the periods are less clearly defined and are in the range 44-51 h during July and August. Radar observations at high-latitudes in recent years showed that the wave period is fairly close to 48 ± 1 h [Phillips, 1989]. In a similar study at high latitudes using radar observations at Pokar Flat, Alaska (65° N, 147° W), Williams and Avery [1992] found that the 2-day period in the mesosphere migrates from 51 h during the summer to 47 h during the autumn.

The satellite temperature measurements of the stratosphere and mesosphere during January-February 1979 reveal that the wave period is near 49.92 ± 1.92 h at low-latitudes. These periods and error estimates were established from the original spectra (not averaged) for which the resolution was 0.037 per day [Burks and Leovy, 1986].

It is possible that these differences are due to hemispheric differences in the wave forcing and/or propagation conditions in the middle atmosphere. Furthermore, more precise measurements of the wave period are required if the source of the wave is to be determined.

6.1.5 Phase and vertical wavelength

In the Southern Hemisphere there are also suggestions of a locking of the phase with local time and to the same local time every year [Craig and Elford, 1981; Poole, 1990; Harris, 1993]. That is, during the time interval of maximum wave amplitude there is a tendency for the 2-day wave to have maximum wind speeds at the same local time from summer to summer. The period is normally observed to be (within experimental error) exactly 48 h. Craig and Elford [1981] found, after 9 years of observation between 1966 and 1975, that the time of maximum meridional wind at a height of 90 km occurred just after local noon, and this again seems to have been the case in 1980 [Craig et al., 1980]. Vincent [1994] suggests that subsequent observations are in agreement with these earlier results. Harris [1993] reported, after 12 summers from 1980 to 1991, that the phase (in local time) was found to vary from year to year, cycle to cycle. Although the phase locking was not precise, there was a tendency for the the maximum meridional and zonal winds of the quasi 2-day wave to occur between 1200 (midday) and 1600 h local time every year. Poole [1990] reported that the phase of the meridional wind in three successive years (1987-89) was stationary near local midnight (±3 h).

In the Northern Hemisphere, Clark [1989] showed that the phase is much more coherent during the late summer, but throughout the year the maximum meridional winds of the 2-day wave prefer to occur near 1500 h local time. The preferred phase values indicate some solar influence on the 2-day wave, possibly through interaction with the solar tides.

Both radar and satellite observations show that the wave is almost evanescent in the vertical and very long vertical wavelengths (> 150 km) are found in radar observations at mid-latitudes [Craig et al., 1980; Craig and Elford, 1981; Rodgers and Prata, 1981; Ito et al., 1984; Clark, 1989; Tsuda et al., 1988; Harris, 1993]. Vertical wavelengths of over 100 km are usual although shorter vertical wavelengths of 50-70 km are inferred at low-latitudes and equatorial middle atmosphere [Craig et al., 1980; Reddi et al., 1988; Harris and Vincent, 1993]. As would be expected from the thermal wind equation, temperature variations associated with the quasi 2-day wave are rather small, having a peak-to-peak amplitude about 1.0 K and little phase change with height [Rodgers and Prata, 1981].

6.1.6 Theoretical and numerical considerations

Simultaneous meteor wind measurements at Garchy (47° N, 3° E) and Obninsk (56° N, 36° E), led Glass et al. [1975] to propose that the 2-day wave was a westward-propagating Rossby-gravity (3,3) normal mode (nomenclature, see Section 2.2.3). This proposal was further substantiated by simultaneous observations of the 2-day wave by various investigators. Most observations in the Southern and Northern Hemispheres suggest that the 2-day wave is consistent with a westward propagating wave of zonal wave number 3 [Muller and Nelson, 1978; Craig et al., 1980; Phillips, 1989;

Poole, 1990; Clark et al., 1993]. This is also supported by satellite temperature observations [Rodgers and Prata, 1981]. On the other hand, a determination over the relatively long baseline between Sheffield (England) and Durham (U.S.A.) has firmly indicated a value for the zonal wavenumber of 2 [Clark, 1983]. Three-station observations of the long period oscillation show that the zonal wavenumber can have values from 2 to 4 for different wave periods ranging from 36 to 60 h [Cevolani et al., 1983]. Recently, Randal [1993] shows evidence that the 2-day wave can have zonal wavenumbers 3-4 with periods near 2 days. A zonal wavenumber 5 was also reported by Kalchenko [1987]. The theoretical understanding, numerical simulations, and resume of advances in 2-day wave studies are contained in (amongst others) Salby [1981], Hunt [1981], Plumb [1983], Pfister [1985], and Hagan et al., [1993].

One interpretation put forward to explain the existence of the wave is that it is a manifestation of the Rossby-gravity (3,3) normal mode forced by the lower atmosphere [Salby and Roper, 1980; Salby, 1981]. Salby [1981] attributed the excitation source of the wave to the characteristic unsteadiness of the tropospheric flow, or tropospheric "noise". He considered that the absence of an appropriate steady forcing indicated that the atmosphere had preferred or natural responses, as indicated by the presence of the 2-day and other waves. Salby [1981] theoretically studied the 2-day wave and showed that the third Rossby-gravity mode has magnified responses very near 53 h (2.2 days for solstice condition) in the presence of realistic numerical simulations of mean wind and temperature structures. He found enhanced vertical growth of amplitude at mesospheric heights in the summer hemisphere, where the winds are moderately eastward relative to the wave and the associated mesospheric temperature gradient is equatorward. In the winter hemisphere the strong westward winds and the polewards temperature gradient act in the opposite sense and therefore suppress the 2-day wave. The results indicate that the meridional wind component in this region maximizes near the equator and dominates the wind field up to mid-latitudes. He also found enhanced vertical growth across the equator and into the winter hemisphere at mesospheric heights. While Salby's theory explains many of the observed features of the 2-day wave, it still has to explain the different hemispheric response in amplitude and in wave period.

A second interpretation to explain the 2-day wave is that it is forced due to an instability in the summer jet and will occur when the eastward shear in the mesosphere is in excess of 6 $ms^{-1}km^{-1}$ [Plumb, 1983], but again a zonal wavenumber 3 is predicted. Plumb suggested that such conditions support baroclinic growth of these waves. His results were based on a one-dimensional stability analysis. Shears of this magnitude are consistent with observations. He also reported that associated wave periods are primarily determined by the strength of the jet. This implies a larger peak velocity is associated with a shorter period. The apparent difference in period between the northern and southern summer mesospheres would imply a corresponding difference in the jet velocities in their respective summers. The growth time also depends on jet curvature so that differences in the height structure of the summer jet may account for differences in the wave amplitudes observed between hemispheres. With the seasonal decay of the westward jet in late summer, the flow will be stabilized and the 2-day wave would then collapse [Plumb, 1981]. Plumb et al. [1987] also examined the importance of the 2-day wave in accelerating the mean zonal circulation, and concluded that such events have a substantial, if temporary, impact on the prevailing circulation in the upper mesosphere and may be important in the transport of constituents at these heights during the summer. Transport by the 2-day wave may be the most effective latitudinal transport process in the summer mesosphere.

Pfister [1985] extended the stability analyses to two-dimensions, and again found peaks in the unstable wave growth at zonal wavenumbers 2-4, with periods of 1.4-3 days. He pointed out that the wave growth peak at zonal wavenumber 3 with a period close to 2 days is a good match for the observed 2-day wave phenomenon, but the calculated temperature structures have their maximum amplitude at 40°-60° latitude, contrary to the observed maximum near 20°. His results also indicate the inability of the model to account fully for the fact that the 2-day planetary wave phenomenon is most frequently observed in the mesosphere.

Recently, Hagan et al. [1993] performed a series of numerical experiments for summer conditions (particularly for January month) in the Southern Hemisphere using a linearized spectral model which includes realistic means and dissipation. The results provide further evidence that the 2-day wave observed in the upper mesosphere may be a signature of the westward propagating, zonal wavenumber 3 mixed Rossby-gravity mode [Salby, 1981]. Hagan et al. [1993] showed that a combination of weak eastward winds in the winter hemisphere and a reversal of the westward jet at lower thermospheric heights in the summer hemisphere lead to the strong increase in the calculated upper mesospheric meridional amplitudes at tropical to middle summer latitudes. These results are consistent with the 2-day wave regularly observed during the January-February summer months [e.g., Harris and Vincent, 1993]. These results also suggest that the horizontal and vertical structure of the 2-day wave is very sensitive to changes in the upper stratospheric and mesospheric zonal mean winds assumed in the calculations. They found that the resonance of the 2-day wave response was dependent upon the details of the background wind fields employed in their calculations. They recovered a resonant response at a period of 55.5 h (2.3 days) which is comparable to the resonance period (2.2 days) reported by Salby [1981]. When they include the Smith [1985] Northern Hemisphere winds in the zonal mean wind fields, they recovered a pronounced response at 46.8 h (1.95 days). A subsidiary weak maxima also found in the response of the latter calculation near periods of 52.8 h (2.2 days). These results are consistent with the observations made at equatorial and mid-latitude during the January-February summer months (near 48 h period) when the 2-day wave amplitudes maximize, and during the July-August winter months (50-52 h period) when the amplitude becomes weak [e.g., Harris, 1993; Harris and Vincent, 1993].

Clearly the 2-day wave is a substantial feature in the mesosphere and lower thermosphere which deserves further investigations. While there is no conclusive evidence pointing to the source of the 2-day wave observed at mesospheric heights, aforementioned theoretical understandings and major conclusions continue to be qualitatively consistent with recent observational results. Further observations are required in order to resolve questions about the generating mechanism as well as to understand better the role of the wave in the middle atmosphere.

6.2 The 2-day wave over London

This section reports on the observation of the 2-day wave in the mesosphere and lower thermosphere with our radar. Winds in the mesosphere and lower thermosphere over London have been regularly monitored since the radar became operational in November 1992. The results of the winds and tides during the two years of operation have already discussed in Chapter 4. The present study of the 2-day wave is based on data collected during the years 1993 and 1994. Missing hourly averages were replaced by Gaussian distributed random noises with a variance matching that of the data itself. The results of the present study bring out certain new aspects of the 2-day wave at mid-latitude in the Northern Hemisphere which were not reported earlier. Our study also contributes additional mid-latitude geographic data which should aid in developing a better picture of the 2-day wave.

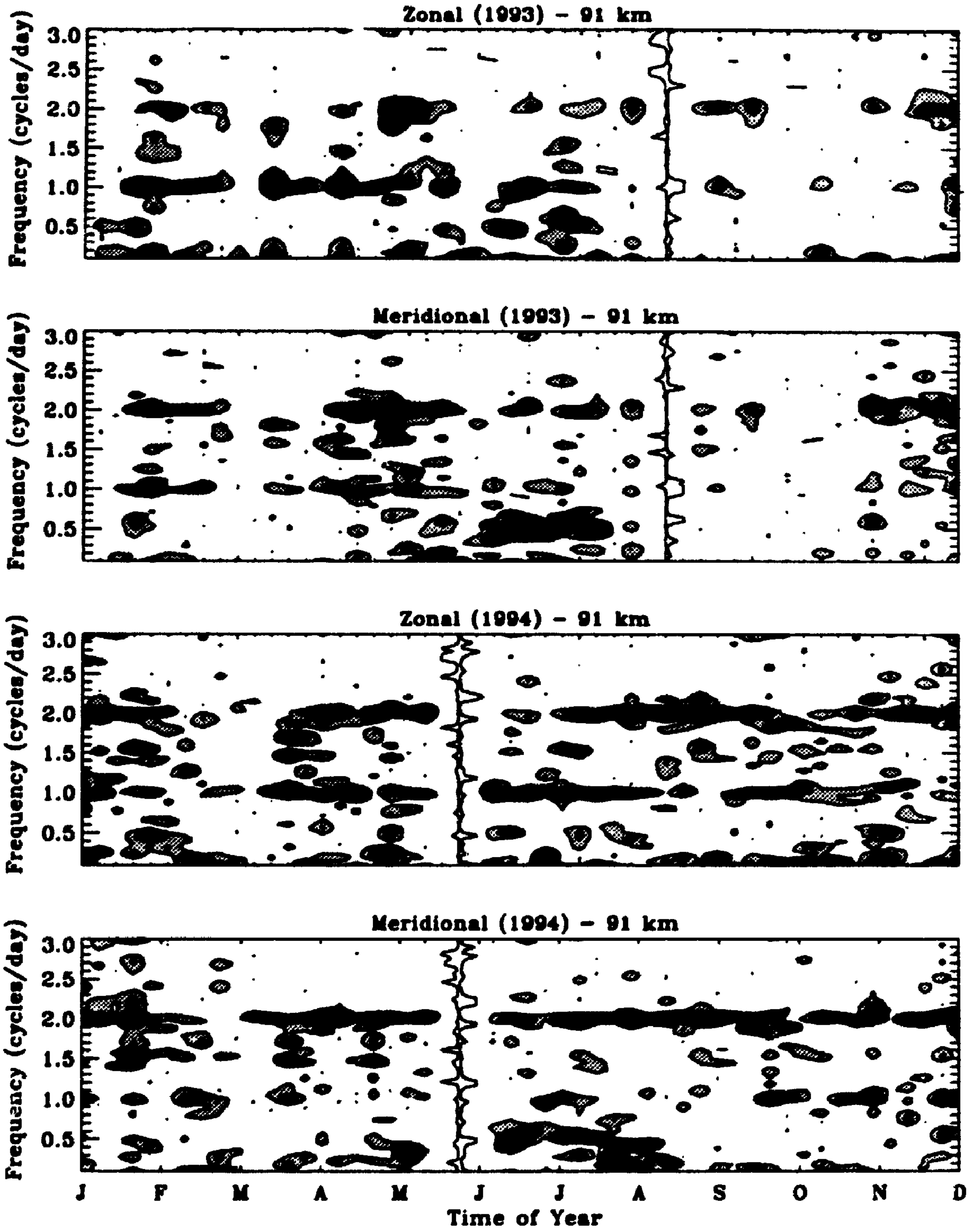

Figure 6.1: Moving Power spectra for the zonal and meridional wind components at 91 km in 1993 and 1994. A 14 day sliding window has been used, with a step of 7 days. We attained a frequency resolution of 0.036 cpd by oversampling in frequency space. The tick marks on the time axis are at the beginning and end of the months (see the text for more details).

6.2.1 Power spectra

A power spectrum is a convenient way to summarize the variance associated with each frequency interval in the wind field, and also provides a way to obtain the relative strengths of the 2-day wave, its harmonics and the atmospheric tides, as a function of frequency. One drawback of the power spectrum is that it produces the the time-averaged spectrum only. This is adequate for stationary time series in which the characteristics of the time series do not change with time. In the geophysical data, however, the stationary time series is an unrealized idealization. In order to study non-stationary phenomena, the time series can be broken into short time segments and each segment can be used to produce individual power spectral estimates using a discrete Fourier transform, which can then be grouped together to give the final spectral features of the time series. This method makes the basic assumption that the time series in each segment is stationary. If each time series segments are shorter than the coherence time of the phenomena then stationary can be assumed without loss of generality. In practice, this is at the cost of frequency resolution, since the frequency resolution depends on the length of the time series. Figure 6.1 shows the moving short term power spectra for the zonal and meridional components at 91 km in 1993 and 1994. Time segments of 14 days have been used, with steps of 7 days between each segment. In this figure we attained a frequency resolution of 0.036 cpd by oversampling in frequency space. The advantage of this oversampling technique is that it produces an image with a striking contrast without loss of generality. The Hamming window has been applied in each time segment. The life time of the 2-day wave event is typically 48 days over London, so that the assumption of stationary becomes quite tenuous, but nevertheless short segments of 14 days can still produce vital information from the moving power spectra.

Figure 6.1 shows the signal strength in the wind variance as a function of frequency and time. We confine our attention here to periods from 120 h (0.2 cpd) down to 8 h (3 cpd) in this figure although higher frequency components were also calculated. The maximum power spectral densities have been artificially limited (cut-off) at a certain peak value so that relative changes of intensity in time and frequency are preserved by the grey code assignments. Similar features are found throughout the height range from 82 to 97 km, although the precise time of maximum power may vary. Clearly there are several distinct and significant features in the figure. The notable feature of this plot is the variability of the 2-day wave at frequency of 0.5 cpd. The diurnal and semidiurnal atmospheric tides are also evident at frequencies of 1 and 2 cpd. Here we focus on the spectra at frequencies around 0.5 cpd which corresponds to

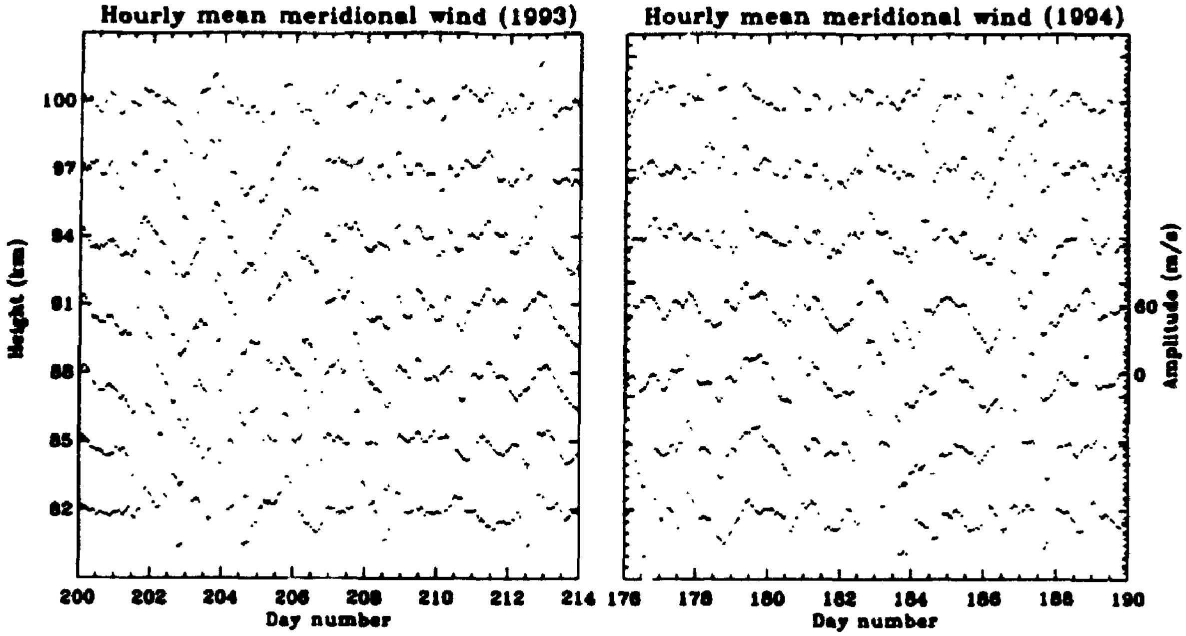

Figure 6.2: Hourly mean meridional winds in the 82-100 km height range from daynumber 200 to daynumber 214 of years 1993 and 1994, showing the 2-day wave. The values have been smoothed with a 3-h running mean in order to reduce the noise level of the data. The amplitude scale is indicated on the right hand side.

periods near 48 h. The 2-day wave is normally evident in summer months, although there is a relatively large year-to-year variation in amplitudes and wave periods. One striking feature is the increased power in the meridional component relative to the zonal component during the summer. The 2-day oscillation is well established in the meridional component during this period. The power spectra at frequency around 0.5 cpd give an impression of two strong "burst" of the 2-day wave activity. The first event occurs just after the summer solstice (late June), and the second event occurs in the latter part of July. It is clear in this figure that strong signal strength of the 2-day wave during the summer months is spread over a frequency band but is confined within the band-pass of 0.35 to 0.65 cpd (37 h to 69 h).

The dominance of the 2-day wave periodicity is also clearly evident in the hourly mean meridional winds. As an example, Figure 6.2 shows the hourly mean meridional winds in the 82-100 km height range of years 1993 and 1994. The values are slightly smoothed by a 3-h running mean in order to reduce the noise level in the data. Note

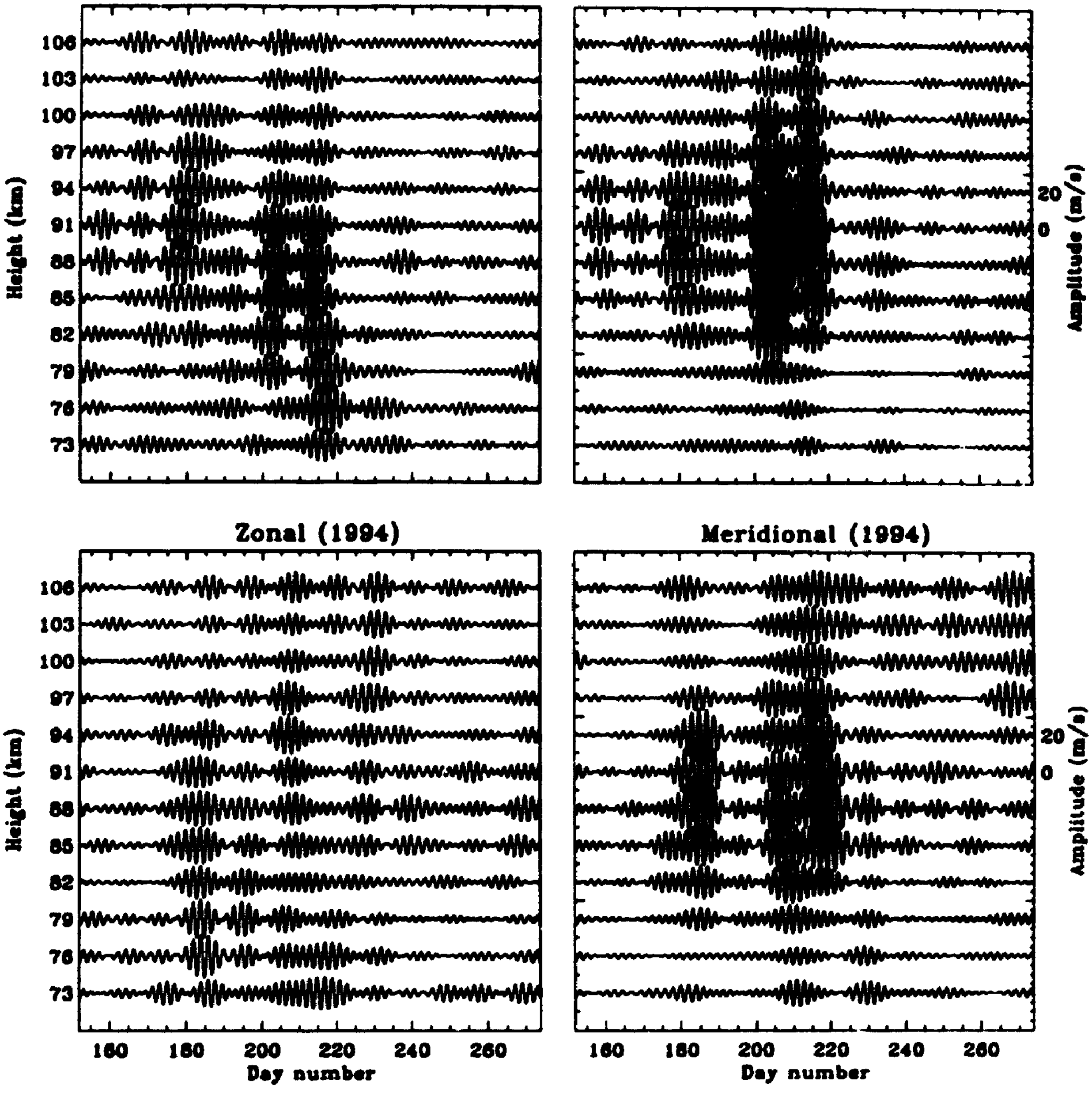

Figure 6.3: Zonal (left) and meridional (right) components of the winds observed in the 73-106 km height range from daynumber 152 to daynumber 270 in 1993 and 1994. Data have been band-pass filtered to retain only periods between 35 and 70 h. The amplitude scale is indicated on the right hand side. All times (days) are in UT; the first observation is at 0000 UT on the daynumber 152.

that the units used to display the time are daynumbers. The corresponding time segments shown in the figure are the daynumbers when the wave was at maximum amplitude. The characteristics of the 2-day wave are discussed in more detail in the following sections.

To illustrate the main features of the 2-day wave in 1993 and 1994, the data were subjected to a band-pass filter with cutoff periods of 35 h and 70 h. Thus the tides and short period gravity waves are removed by this band-pass filtering. Figure 6.3 shows the resulting filtered wind for the zonal and meridional components in the 73-106 km height range for a 100-day interval commencing 1 June. In general the 2-day oscillation is stronger in 1993 than in 1994, thereby showing an interannual variation. It is apparent that the wave is transient in nature, but the most noticeable features are the enhancements or "bursts" in the meridional oscillations for both years, with maximum amplitudes in the 25-30 m/s range. Similar behaviour is also evident for the zonal component in 1993 with maximum amplitudes of about 15-20 m/s. The initial burst starting around day 175 in 1993 and lasts for 4 cycles, and then diminishes abruptly. The second burst starting around day 200, somewhat stronger than the initial one, and lasted for 7-8 cycles, and seemed to die out completely by daynumber 225. Similar bursts are clear in 1994 too and even more remarkably, the onsets of the bursts are at similar dates for those in 1993. High temporal and spatial coherence is evident for those intervals of large amplitude. The wave amplitudes appeared to grow with height, reaching maximum amplitudes at heights of 91 and 88 km in 1993 and 1994 respectively, and to slowly decay above this heights. The zonal components in both years were smaller than the meridional components. It is also noticeable that there is a moderate phase tilt with height in both the zonal and meridional oscillations in 1993 and 1994; i.e., the wind maximum occurs at earlier times with increasing height indicating downward phase propagation (i.e, upward energy propagation) with a vertical wavelength in excess of 100 km. The amplitude decay indicates absorption of energy at heights above 91 km. A more detail discussion of phase and vertical wavelength will be given in Section 6.2.6.

6.2.2 More detailed analysis methods

The observed 2-day wave is maximum somewhat after the summer solstice, perhaps indicating a particularly effective forcing agent present at this time. If this is correct then a more precise measurements of the wave period is required, so that it may give a better clue to the source of the wave. To determine the precise period of the 2-day oscillation, we used a complex demodulation method in our study which is very sensitive to the frequency variations within the time series [e.g., Harris, 1993; Harris and Vincent, 1993]. We then compare this method to the values deduced from a harmonic analysis method. It should be emphasized that we have used both the complex demodulation and harmonic analysis methods to investigate the period of the 2-day wave but we have only used the harmonic analysis method to estimate the amplitudes and phases of the 2-day wave. The advantage and disadvantage of these methods will be discussed in the following sections.

Complex demodulation

The complex demodulation method effectively investigates one frequency range at a time [e.g., Tukey, 1961; Bloomfield, 1976; Brillinger and krishnaiah, 1983]. The basic idea can be explained as follows. If ω_0 ($\omega_0 = 2\pi f_0$, f_0 being the frequency closest to the frequency of interest) is known a priori, we can study the time-dependent behaviour of the time series by shifting ('beating') its frequency down to zero. This beating is easily accomplished by multiplying the raw time series by $exp(-\imath\omega_0 t)$. The resultant complex time series is then low-pass filtered about the zero frequency, thus demodulating the original time series around the frequency of f_0 (demodulation frequency). It should be noted that the amplitude spectrum of the complex demodulated time series is just a shifted version of the original time series spectrum. The phase gradient, i.e., the rate of change of the phase of the complex demodulated time series, is a measure of the "local" frequency difference from the demodulation frequency, i.e., $f - f_0 = \frac{1}{2\pi}\frac{d\Phi}{dt}$. Thus, if a time series contains a harmonic component with the frequency f we can detect the presence of this component by plotting the phase, Φ, as a function of time, t. This plot is approximately linear (not shown), and we can get an precise estimate of the dominant period of the 2-day wave as function of time. We performed several tests by varying the demodulation frequency, and it turns out that the period determined in this manner is independent of the demodulation frequency as long as the strong signal remains within the band-pass. A 48 h demodulation period was used in this study. The effective band-pass used was 42 to 54 h for the 48 h demodulation period in this study, which allows amplitude variations on time scales greater than 7 days. We have used a spectral window of equal weighting except for the end values, which have only half the weighting. This gave enough tapering to avoid spurious ringing and other effects in the filtered data [Forbes, 1988; Bloomfield, 1976; Bracewell, 1978].

The amplitude of the 48 h complex demodulated time series for both the zonal and meridional wind components are shown in Figure 6.4 from June to September for

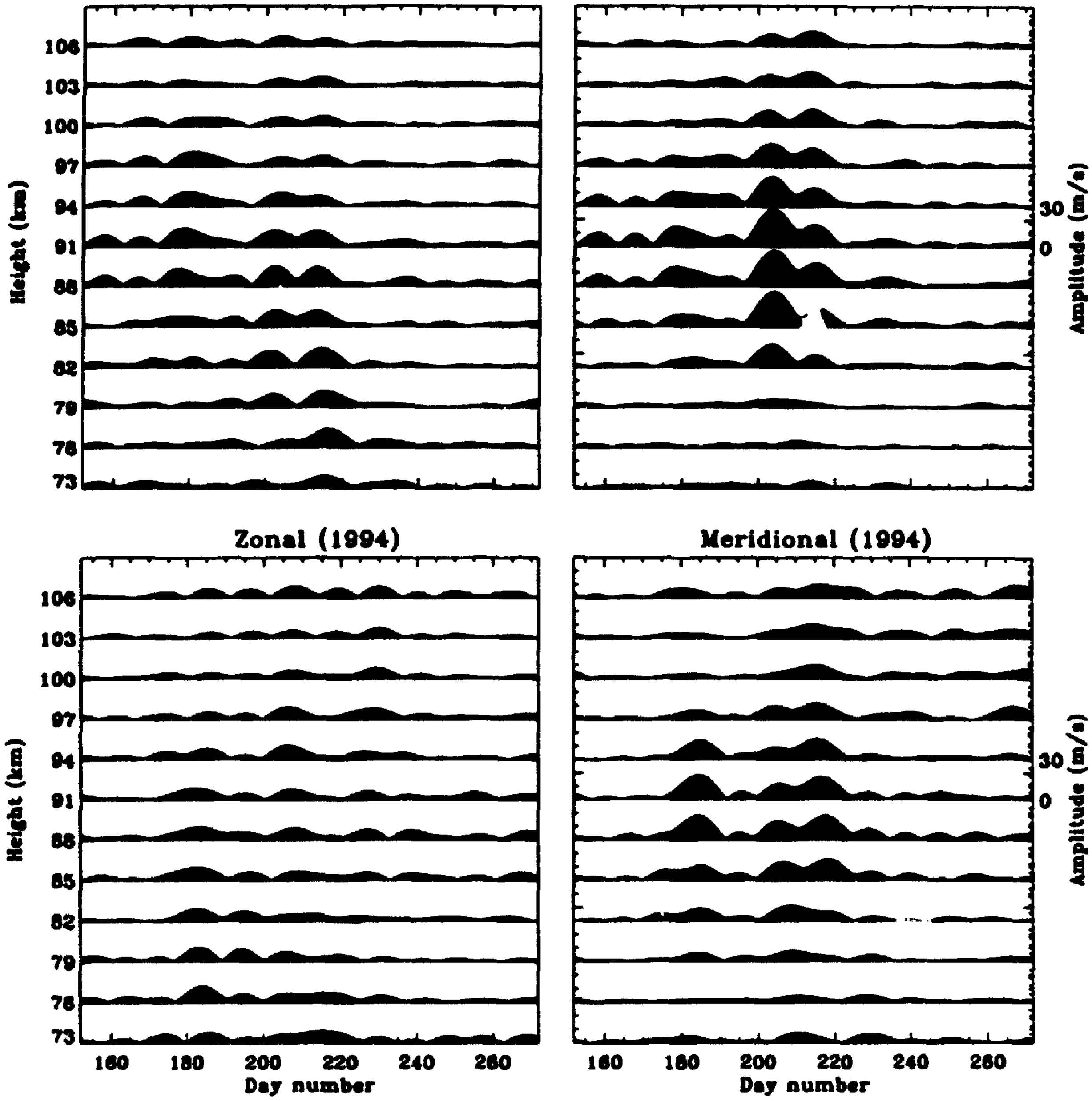

Figure 6.4: The amplitue of the zonal (left) and meridional (right) components of the 2-day wave from a complex demodulation procedure in the 73-106 km height range from daynumber 152 to daynumber 270 in 1993 and 1994. The effective band-pass used was 42 to 54 h for the 48 h demodulation period. The amplitude scale is indicated on the right hand side. All times (days) are in UT; the first observation is at 0000 UT on the daynumber 152.

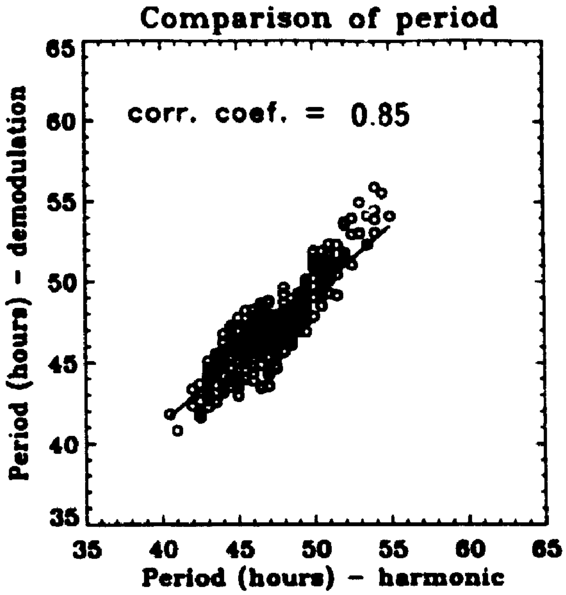

Figure 6.5: A scatter plot between the periods deduced by the complex demodulation method and by the harmonic analysis method from all heights for both the zonal and meridional components from daynumber 160 to daynumber 220 for the years 1993 and 1994. The periods of the 2-day wave were only taken into account when the demodulation amplitudes of the 2-day wave are greater than 8 m/s (see the text for more details).

the years 1993 and 1994. The maximum values are no larger than 30 m/s in the meridional components. The amplitude of the complex demodulation of the time series is a measure of the amplitude of the dominant frequency within the band-pass around the demodulation frequency. These demodulated amplitudes are smaller than the real amplitudes because the demodulated amplitudes come from a smaller bandwidth. Therefore demodulated amplitudes will not be used as an estimate of the amplitude of the 2-day wave beyond this section; nevertheless, the recurrence of the 2-day wave is clearly apparent in the meridional components. The real amplitudes are estimated from unfiltered real-valued time series using the harmonic analysis method, and the results will be discussed in Section 6.2.4.

Harmonic analysis

In a similar study, we used a harmonic analysis method to get an estimate of the dominant period of the 2-day wave. As one can be seen from Figure 6.1, various tidal components (24, 12, and 8 h) were superimposed on the 2-day wave, as expected in

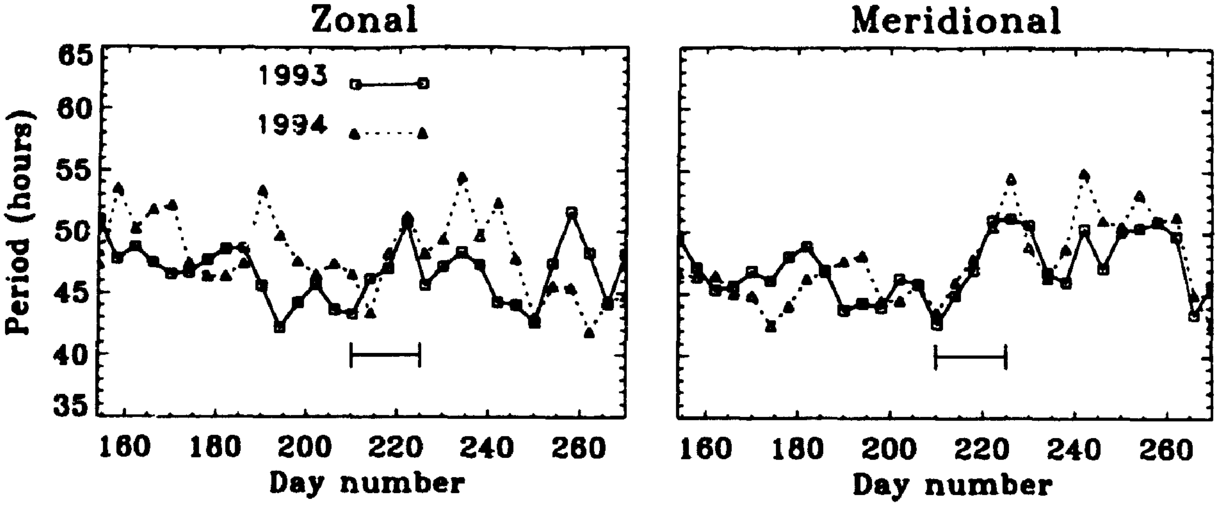

Figure 6.6: The variation of the period as a function of time in 4 day intervals at 91 km for the zonal (left) meridional (right) components from daynumber 160 to daynumber 270 for the years 1993 and 1994. All times (days) are in UT; the first observation is at 0000 UT on the daynumber 160.

view of previous observations [Chapter 4]. Because of the presence of these strong tidal components the data for each height were analyzed with a least-squares fitting process to find the mean amplitude and phase of the 2-day wave as well as the period which best fitted the observations. We used four day groups of data set, stepped by one day (e.g., 1-4, 2-5, 3-6,....). We adapted a 4-day fit because this is long enough to give reasonable significance to our results yet short enough to give reasonable sensitivity during periods of large 2-day activity. The zonal (u) and meridional (v) wind components were represented as a function of time (t) by

$$u(t), v(t) = a_0 + \sum_{i=1}^{i=4} a_i \sin(\frac{2\pi}{T_i}t + \Phi_i)$$

where a_0 is the prevailing mean wind and a_i and Φ_i give the mean amplitude and phase for the 8 h ($i = 1$), 12 h ($i = 2$), and 24 h ($i = 3$) tidal components. The wave period T_4 was varied systematically from 40 h to 60 h in steps of 0.5 h in order to provide maximum sensitivity to amplitude variations. The analysis was carried out for both zonal and meridional components at all heights between 79-106 km. We have adapted the harmonic analysis method to estimate the amplitude and phase of the 2-day wave, and the results are discussed in Sections 6.2.4 and 6.2.5.

6.2.3 Period

Figure 6.5 shows a scatter plot between the periods deduced by the complex demodulation method and by the harmonic analysis method from all heights for both the zonal and meridional components from daynumber 160 to daynumber 220 for the years 1993 and 1994. The periods of the 2-day wave were only taken into account when the demodulation amplitudes of the 2-day wave are greater than 8 m/s, which is considered as a reasonable cutoff value after several tests. It can be seen from Figures 6.2 and 6.3 that this cutoff value is large enough to reduce the effects of noise, yet small enough to allow data to be accepted for both years of 1993 and 1994. The best fit line suggests good agreement: the correlation coefficient is ~ 0.85. When the cutoff value for the demodulation amplitude is increased to 12 m/s the correlation coefficient is ~ 0.92, but it restricts a substantial proportion of the reliable data. It is then concluded that both methods provide reliable estimates of the periods.

Figure 6.6 illustrates the variation of the period determined from the complex demodulation method at 91 km with time, i.e., from daynumber 160 to daynumber 260 averaged in 4 day bins. In general different periods are evident in the 43-55 h period range. Periods seem to be frequently larger in 1994 than in 1993 for the zonal component, while periods take somewhat similar values in both years for the meridional component except at certain days. One noticeable feature is that the periods are very similar from daynumber 210 to daynumber 225 in both years for the zonal and meridional components, which seem to coincide with the maximum enhancement or "burst" in the amplitude of the 2-day wave activity.

Figure 6.7 shows the period as a function of height and time which can be compared with the amplitudes in Figure 6.4. The contour plots only illustrate the period-height variation from daynumber 170 to daynumber 227, where the demodulation amplitudes of the 2-day wave are generally larger than 8 m/s (see also Figure 6.2). Outside this time range, the estimated periods are generally less reliable owing to the comparatively small wave amplitude. In general, the periods in the zonal component are relatively more variable than the meridional component. For the zonal component it can be seen that the period is 48 h above 85 km from daynumber 170 to daynumber 180 in 1993. The period then shows gradual decrease with daynumber and reaches a constant value in the 44-46 h range up to daynumber 220 and then makes a sudden shift to a larger value of 52-54 h. In 1994 the period shows a constant value of 46-48 h below 85 km. In the 85-100 km height range the period migrates from 52 h to a constant value of 46 h during the daynumbers 170-185 and reaches again to 48-52 h from daynumber 185 to daynumber 205. The period then attains a constant value

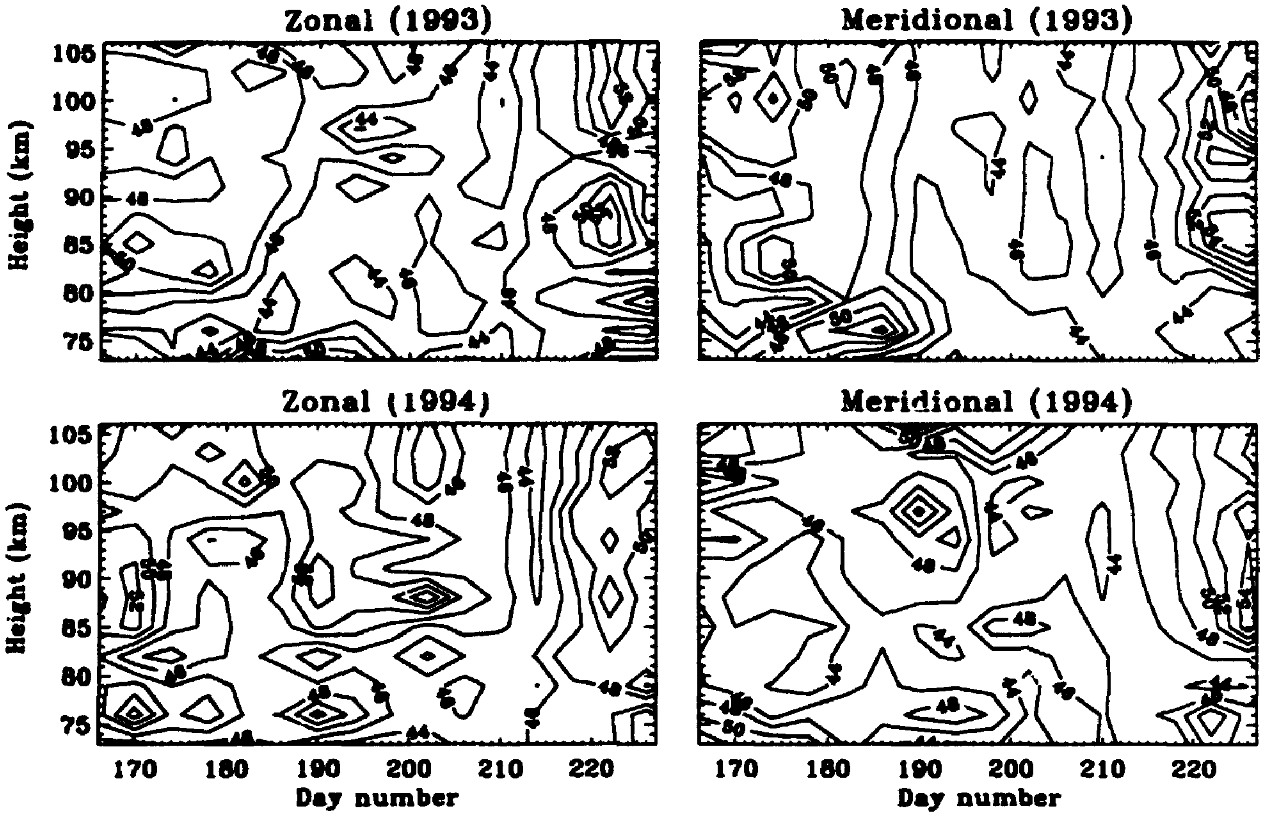

Figure 6.7: The variation of the period as a function of height and time for the zonal (left) meridional (right) components from daynumber 170 to daynumber 227 for the years 1993 and 1994. All times (days) are in UT; the first observation is at 0000 UT on the daynumber 160 (see the text for more details).

of 46 h during the daynumbers 205-215 and finally migrates to 50-52 h. The period for the zonal component in 1994 is more variable than in 1993, and this may be due to small amplitudes in 1994. For the meridional component the periods are firmly placed in the 44-48 h period range at most of the heights from daynumber 170 to daynumber 220 in both years although periods of 50 h are apparent at certain heights in 1993.

It can be seen in Figures 6.6 and 6.7 that the 2-wave occurs most frequently in the 44-48 h period range when the amplitudes are associated with larger values. In order to determine some form of mean period consideration must be made of the averaging process. Figure 6.8 shows the height variations of the mean period during the summer. In this case the periods were only taken into account when the demodulation amplitudes of the 2-day wave are greater than 8 m/s. It clearly suggests that the dominant 2-day wave activity occurs most frequently near a period

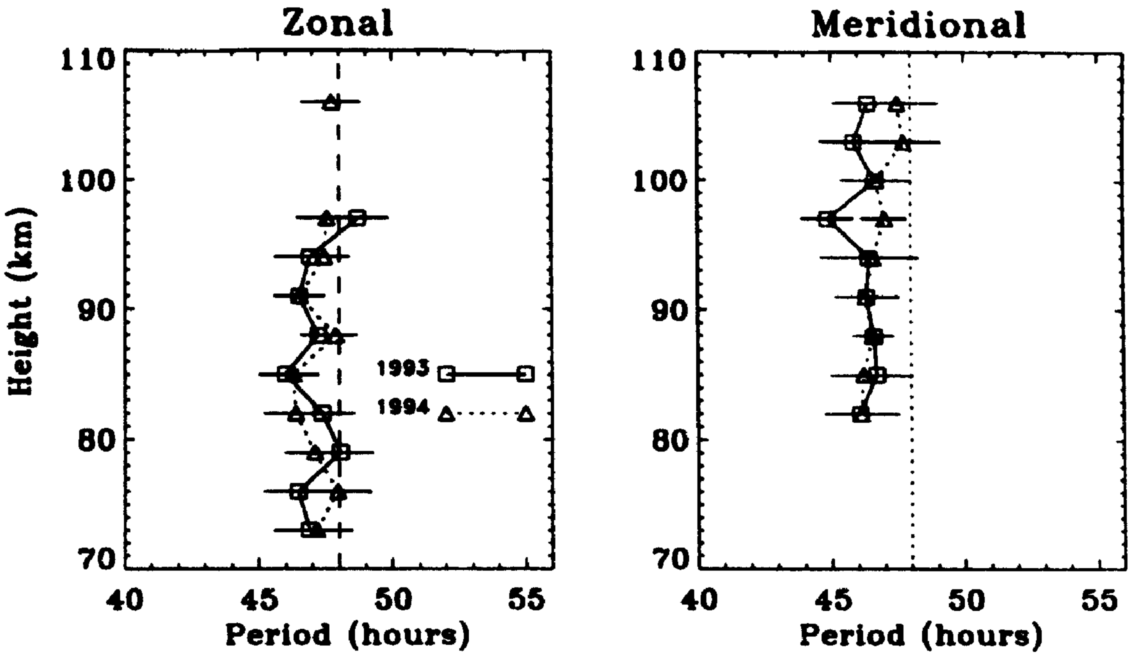

Figure 6.8: The height variation of the mean period during the summer for the zonal (left) meridional (right) for the years 1993 and 1994 (see the text for more details).

of 46 to 47 h, with some heights showing a tendency towards a period of 48 h. The mean period over all heights is 47.1 ± 1.3 h for the zonal component and 46.2 ± 1.4 h for the meridional component in 1993. These values are 46.2 ± 1.4 h for the zonal component and 46.7 ± 1.3 h for the meridional component in 1994. The mean periods are consistent even if the cutoff demodulation amplitude of the 2-[illegible] wave is increased to 12 m/s. Similar results were obtained using different demodulation frequencies.

To further confirm that the periods determined are independent of the method we used, the periods were calculated using both the complex demodulation and harmonic analysis methods, and the results are illustrated as histograms in Figure 6.9 from all heights for both the zonal and meridional components in 1993 and 1994. Only data for times when the amplitudes were greater than 8 m/s have been used in the compilation of the period distributions in order to avoid any erroneous broadening due to noise. The histograms clearly confirm that the mean period is near a period of 46 h to 47 h by both methods. This shows an excellent agreement, and we conclude that the period determination is at worst only mildly dependent on either method.

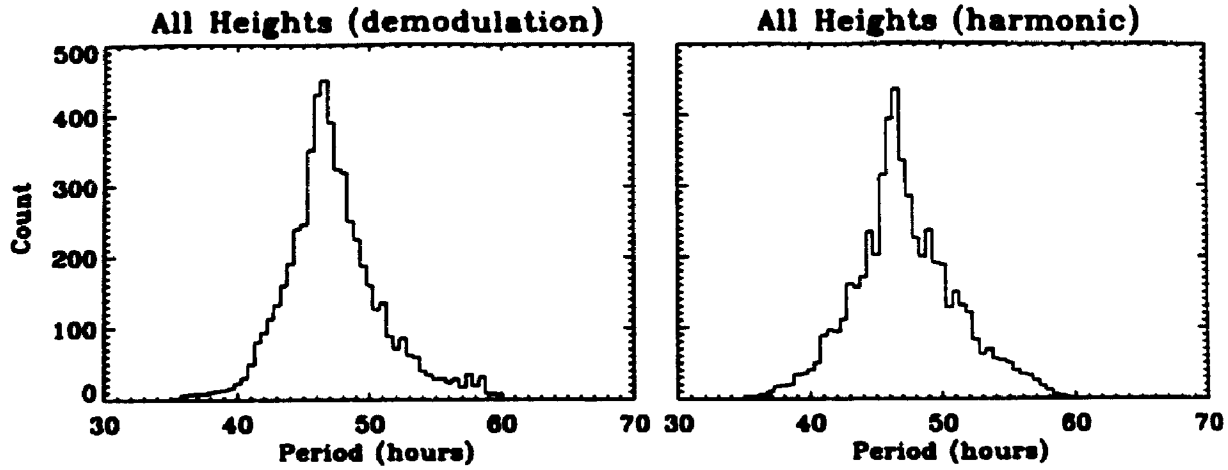

Figure 6.9: Period histograms for all heights for the zonal and meridional components in 1993 and 1994 deduced by the complex demodulation method (left) and by the harmonic analysis method (right).

6.2.4 Amplitude

A complex demodulation method can be used to give an estimate of the amplitude of the 2-day wave as a function time. It has the advantage of producing a time series with a data point for every data point in the original time series. However, this method does not produce a real-valued time series from which perturbation wind velocities can be obtained. It turns out that the demodulated amplitudes can be underestimated and the phases can be erroneous. Therefore a complex demodulation method is not suited for the studies of amplitudes and phases of the 2-day wave. We used the harmonic analysis method which was described in Section 6.2.2 for the estimation of the amplitudes and phases.

To determine whether, and to what extend the 2-day oscillation occurred at times other than mid-summer, a harmonic analysis was carried out throughout the year at London during the years 1993-1994. Figure 6.10 shows the daily amplitudes of the 2-day wave at 91 km for both the zonal and meridional components for the years 1993 and 1994 smoothed by a 4-day running mean. It is apparent from this figure that although the amplitude tends to be larger during the mid-summer, there is also much 2-day wave activity during other times of the year and it is variable from year-to-year. One noticeable feature is a strong 2-day wave activity during the spring near the daynumber 120 (late April), lasting for 6 days in the meridional component for the

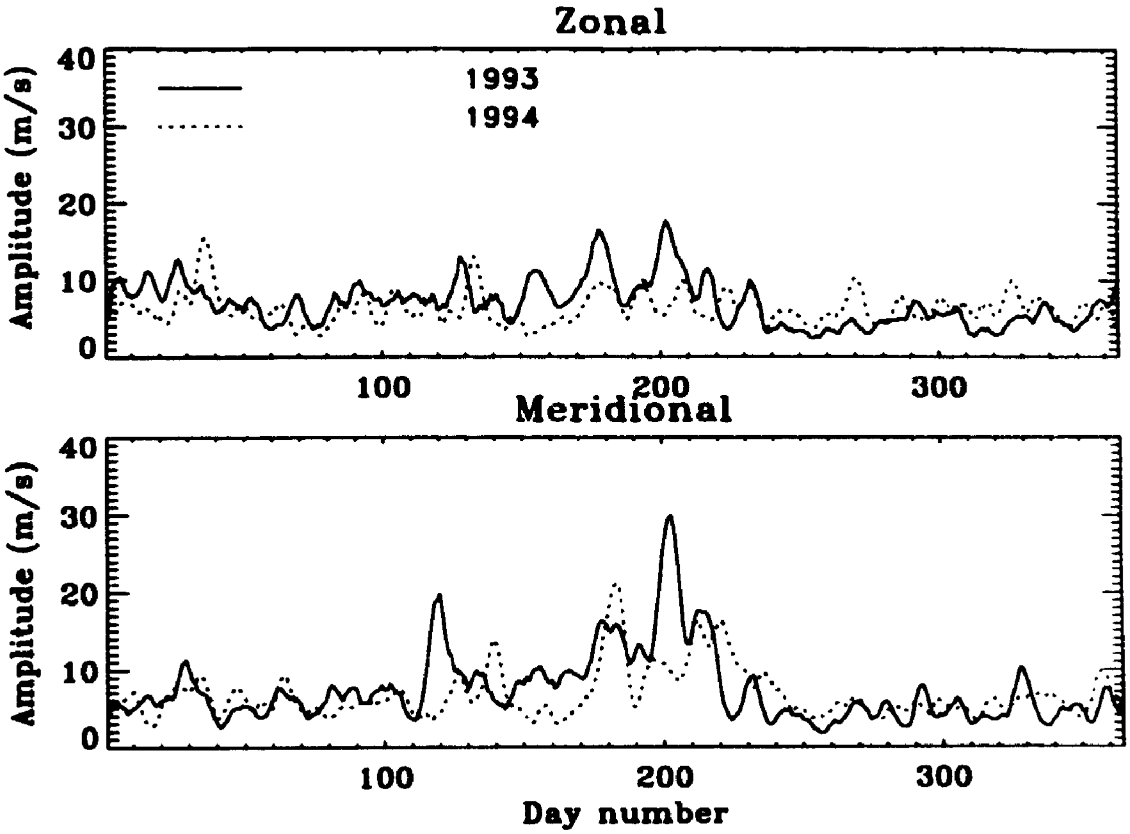

Figure 6.10: Daily amplitudes of the 2-day wave at 91 for the zonal and meridional components in 1993 and 1994. All times (days) are in UT; the first observation is at 0000 UT on the daynumber 1.

year 1993. The amplitudes attained are as large as 20 m/s, about 70% of the summer peak, during this period of time. We also note in particular that a hint of similar behaviour in 1994, but with a relatively weaker amplitude of 15 m/s, is observed near the daynumber 140 (late May) for the meridional component. It is clear that the summer amplification is generally confined to the space of about 48 days. The rest of the discussion will be focused between daynumber 172 and daynumber 220.

The 4 day mean amplitudes obtained from arithmetic and vector average of the daily values are illustrated together in Figure 6.11 for both the zonal and meridional components in 1993 and 1994. The 2-day oscillation is well established particularly in the meridional component from daynumber 175 to daynumber 220. The small differences between the arithmetic and vector averages during the pronounced 2-day wave activity indicate phase coherence during this period of time. It is clear that the amplitude of the the 2-day wave seems to vary with time. The two pronounced 2-day wave activity peaks occur particularly in the meridional component during

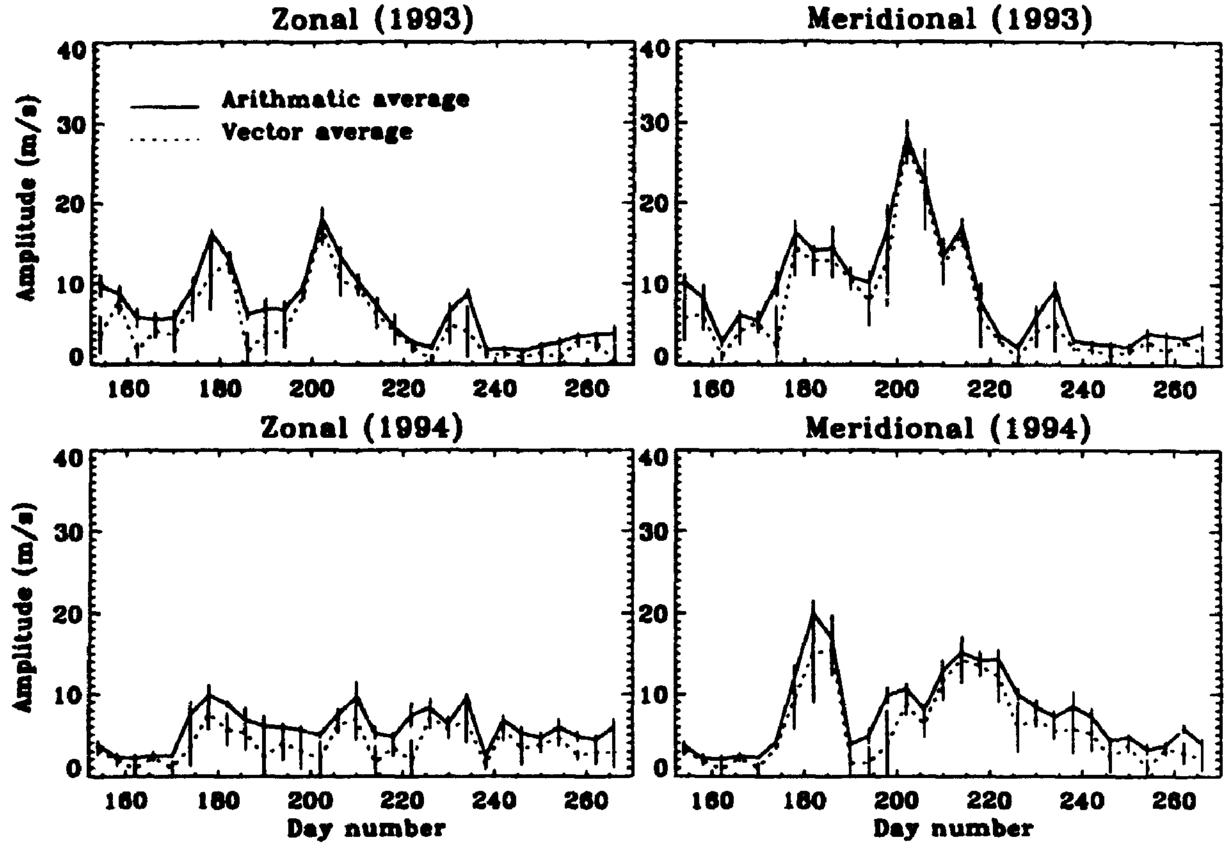

Figure 6.11: The 4 day mean amplitues obtained from arithmatic and vector average of the daily values for the zonal (left) and meridional (right) components from daynumber 152 to daynumber 270 in 1993 and 1994.

this period of time, following which rapid decays set in and abruptly diminishes the amplitudes (also see Figure 6.10). The decrease in amplitude after the pronounced 2-day wave activity is noticeably more abrupt in 1993 than in 1994. It is interesting to note that the first pronounced 2-day wave activity occurs around the daynumber 180 (end of June) in both years, and relatively stronger second pronounced 2-day activity occurs near daynumber 202 in 1993, and it seems to occur 2 weeks later, i.e. near the daynumber 216, in 1994. Another noticeable feature is that the second pronounced period of 2-day activity is two times stronger than the first pronounced 2-day activity in 1993, whereas the second pronounced 2-day activity is 25% weaker than the first pronounced activity in 1994. The zonal components show similar behaviour with smaller amplitudes in 1993, but not in 1994. Maximum amplitude values of 30 and 20 m/s are observed in 1993 and 1994 respectively for the meridional component. For the zonal component the respective amplitude values are 20 and 10 m/s in 1993 and

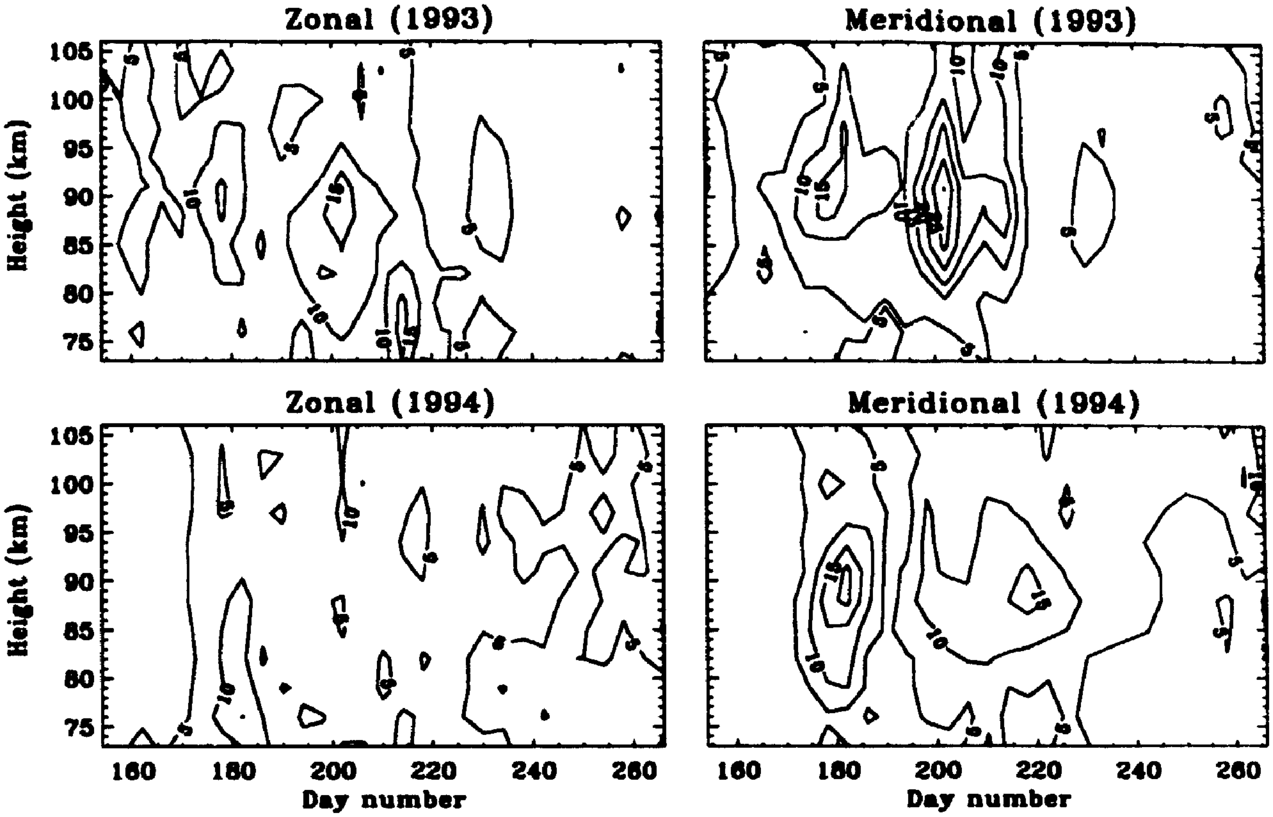

Figure 6.12: The variation of the amplitude as a function of height and time for the zonal (left) meridional (right) components fror. daynumber 152 to daynumber 270 for the years 1993 and 1994. All times (days) are in UT; the first observation is at 0000 UT on the daynumber 152 (see the text for more details).

1994.

The bursts of 2-day wave activity are also illustrated as height-time contour plots in Figure 6.12. These contours show the general background amplitudes during the period of observation, and also show year-to-year differences.

The data from daynumber 170 to daynumber 227 have been grouped into 4-day data set. The averages and associated error bars are estimated by taking a vector average of the daily values. Figures 6.13 presents the 4 day mean behaviour as a function of height of the amplitude and phase of both the zonal and meridional components of the 2-day wave in 1993. The same is presented in Figure 6.14 but for the year 1994. The meridional amplitudes are large, exhibiting strong variation with height in both years. This behaviour is also evident for the zonal component in 1993. In contrast, the zonal component in 1994 exhibit little variation with height. The wave amplitude

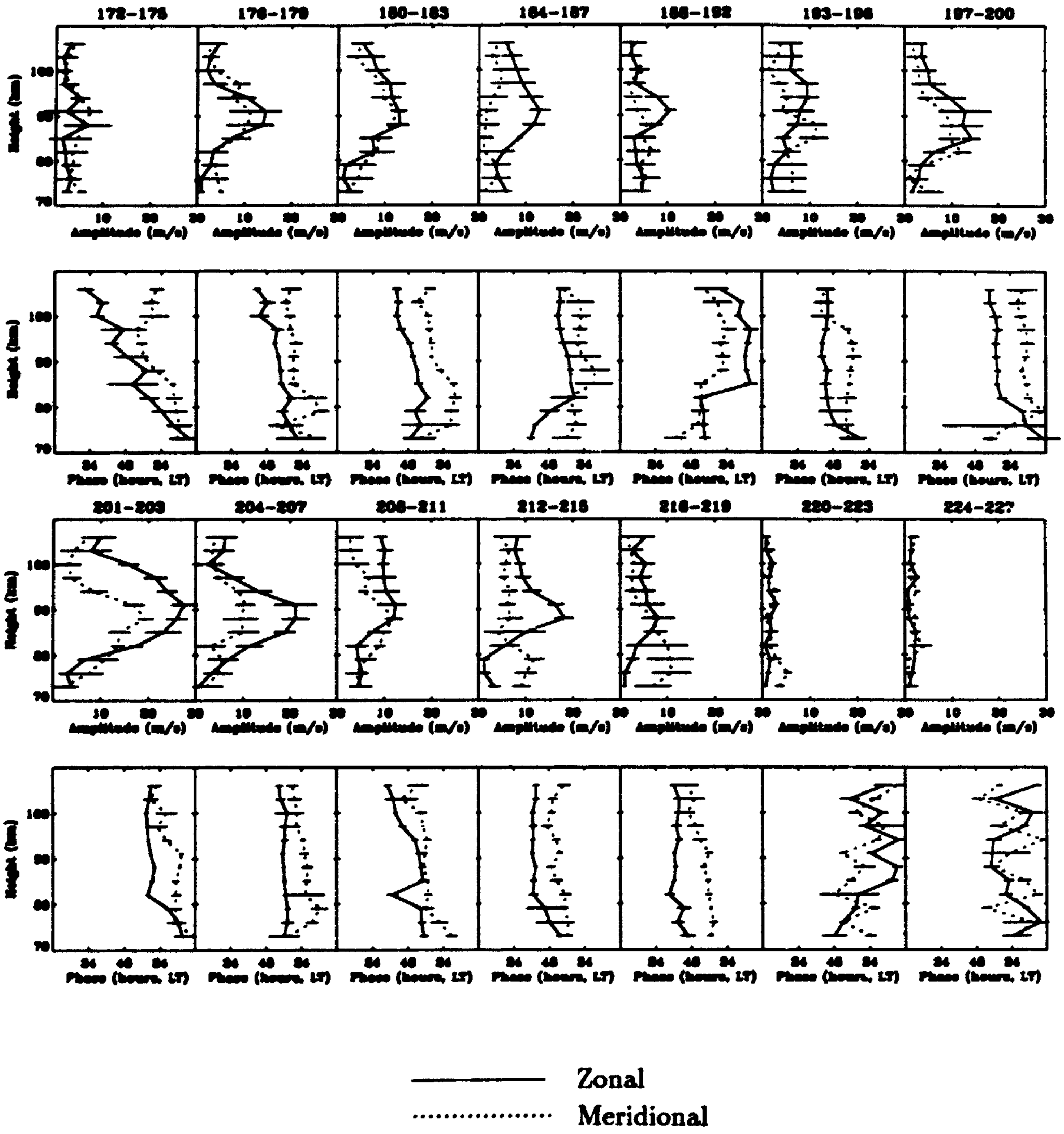

Figure 6.13: Height profiles of the 4 day mean (vector) amplitude and phase of the zonal and meridional components for the 2-day wave in 1993. The phase of the 2-day wave was obtained by determining the local time (LT) of the maximum eastward and northward winds. The phase is estimated relative to 0000 LT on January of 1993 (see the text for more details).

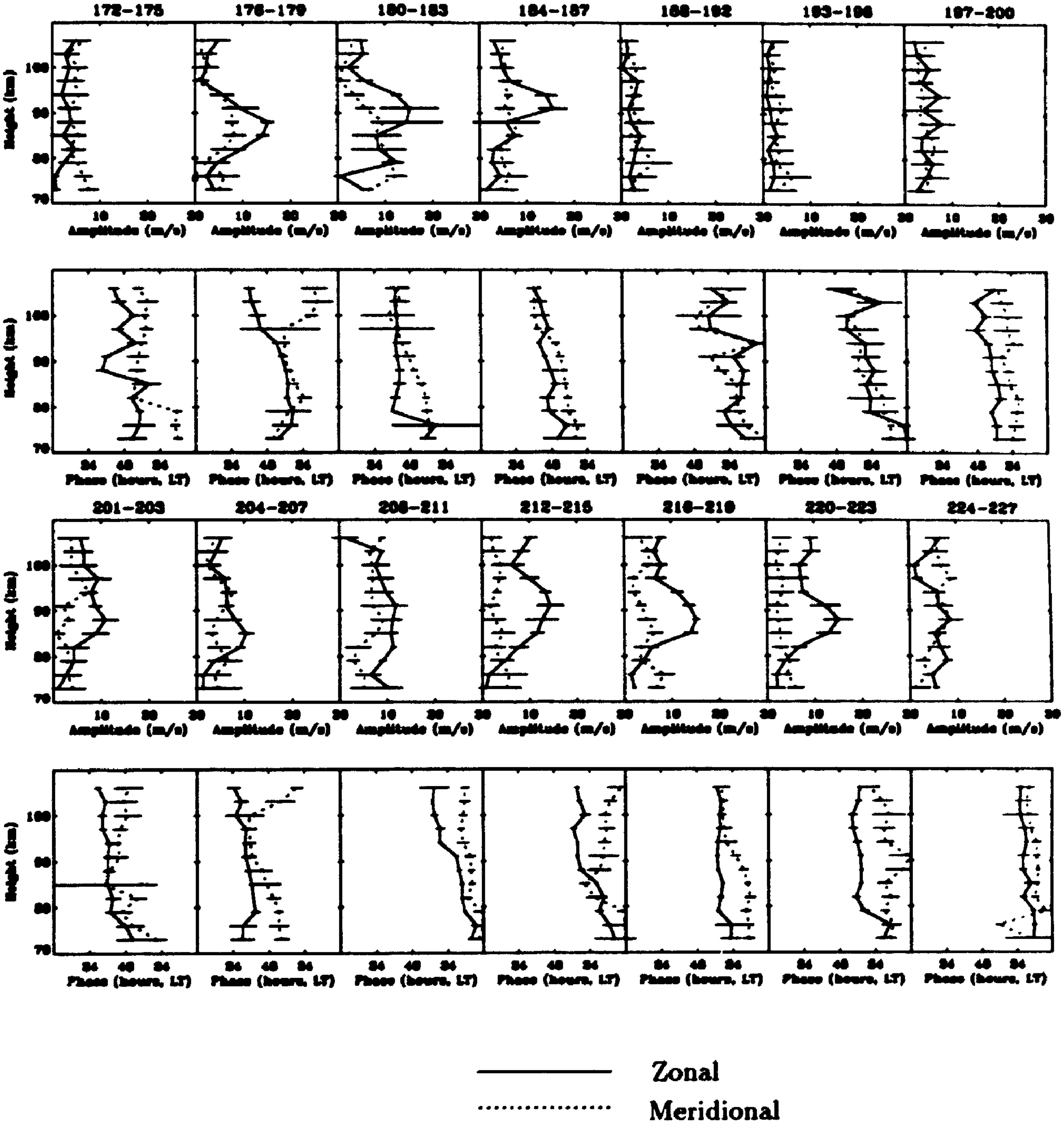

Figure 6.14: Height profiles of the 4 day mean (vector) amplitude and phase of the zonal and meridional components for the 2-day wave in 1994. The phase of the 2-day wave was obtained by determining the local time (LT) of the maximum eastward and northward winds. The phase is estimated relative to 0000 LT on January of 1994 (see the text for more details).

maximizes near 91 km in 1993 and near 88 km in 1994, and then slowly decrease with further increase with height. The first enhancement in amplitudes occurs during the daynumbers 176-187, and relatively stronger second enhancement in amplitudes occurs during the daynumbers 197-207 for both the zonal and meridional components in 1993. In 1994 similar behaviour is only observed in the meridional component, the first enhancement in amplitudes occurs during the daynumbers 176-187, in contrast, relatively weaker second enhancement in amplitudes occurs during the daynumbers 212-223.

6.2.5 Phase

The phase is illustrated on the same Figures 6.13 and 6.14, below each amplitude plot, as a function of altitude in the same fashion as for the amplitudes. The phase of the 2-day wave was obtained by determining the local time of the maximum eastward and northward winds. On a scale from 0 to 48 hours, in which zero hours was taken to be midnight on each odd day number of the year.

Note that in this study we assumed the 2-day wave period was exactly by 48 h, which is different from the dominant periods, 46-47 h (see Figures 6.7 and 6.9), frequently observed over London. However, after a number of tests we found that the error in the daily phase obtained from 4-day harmonic fit with assuming 48 h period is less than 0.5 h. It is also found that the error is less than the natural variation of the 2-day wave oscillation. Therefore, it is concluded that the phase estimates from a 4 days of data are reasonably correct, within the error bars of the data, as long as the period is fairly close to 48 h [e.g., Reddi et al., 1988; Clark, 1993; Harris and Vincent, 1993].

In the Northern and Southern Hemispheres there are suggestions of a locking of the phase with local time during the period of 2-day wave activity. Therefore daily phase values over all heights from daynumber 172 to daynumber 227 were formed into histograms to visually determine the range of most likely phases. The reliability of the phase histograms can be improved if the phase estimates associated with the small amplitudes are ignored (the same principal as estimating period, see section 6.2.3). Figure 6.15 illustrates how the phase histograms change with increasing cutoff level of the amplitude for both the zonal and meridional components in 1993 and 1994. In general the most frequent phases are spread from 1000 h LT to 1700 h LT (especially for higher amplitude data), centered on 1300 h LT in 1993 and 1200 h LT in 1994 for the meridional component. For the zonal component the phases

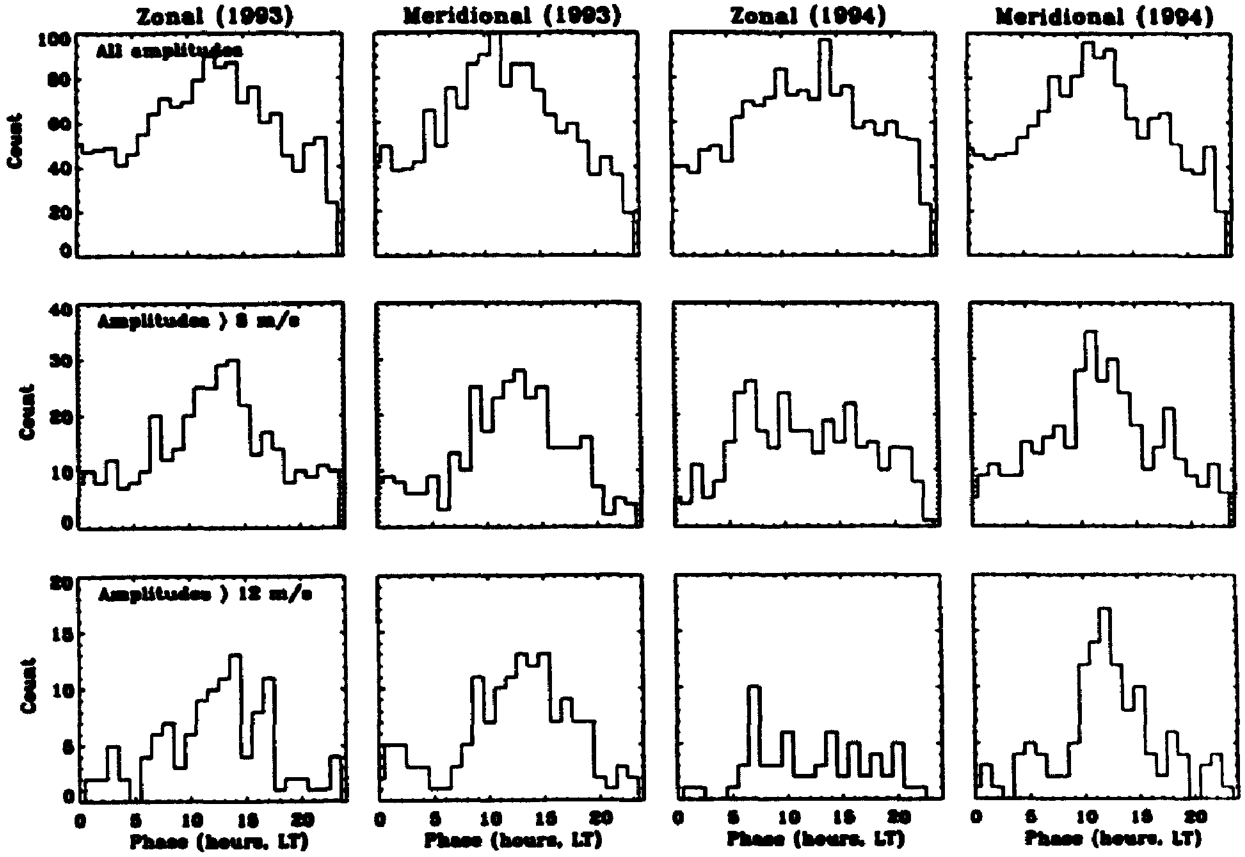

Figure 6.15: Variation in phase histogram with cutoff value over all heights from daynumber 172 to daynumber 227 in 1993 and 1994 for the zonal and meridional components (see the text for more details).

are spread from 1000 h LT to 1700 h LT, centered on 1300 h LT in 1993, whereas in 1994 the zonal amplitudes are small (as shown in Figure 6.3) so that the phase determinations are of dubious quality, reflecting more random phases. These random phases would be expected to have a uniform distribution, and therefore they increase the floor level of the histograms. That the waves with the larger amplitudes tend to have phases in the 1000-1700 h LT range is also evident in Figures 6.13 and 6.14. These results give an impression that the 2-day wave has a large vertical wavelength over london, and this will be discussed in the following section. The mean phases over all heights are ~ 12.5 ± 1.4 h and ~ 12.3 ± 1.3 h h LT for the zonal and meridional components respectively in 1993. In 1994 the respective values are ~ 12.1 ± 1.6 h and ~ 12.2 ± 1.2 h for the zonal and meridional component. The average was computed over all heights using data only from the daynumber 152 to daynumber 227 when the 2-day wave was greater than 8 m/s. The results strongly suggest locking of the phase to local noon near 1200 h LT, becoming more discernable as the amplitude cutoff is increased. This indicates that the 2-day wave has the same preferential phase, during intervals of large wave amplitude, from year to year, a phase first suggested by Craig and Elford [1981] in the Southern Hemisphere. The mean preferred phase values also indicate some solar influence on the 2-day wave possibly through interaction with the solar tides.

Figures 6.13 and 6.14 suggest that the meridional component generally leads the zonal component by anywhere from 0 to 14 h most of the time. On occasions the phase difference between the wind components exceeds even 20 h (e.g., during the daynumbers 180-183, and 197-200 in 1993).

6.2.6 Vertical wavelength

The vertical wavelength is measured by the rate of change of the phase with height. it is noticeable in Figure 6.13 and 6.14 that there is an appreciable phase change with height of the zonal and meridional oscillations. The phases of the zonal components are generally less organized and show larger variability than the meridional component, but some characteristics can be observed from these figures. In general, the time of maximum eastward and northward winds occurred at earlier times at the higher altitudes, implying a downward phase and upward energy propagation. On several occasions the phase profiles are almost constant with height suggesting the presence of evanescent or long vertical wavelength behaviour. This behaviour is most frequently observed during the time periods of strong enhancement of the 2-day wave activity, (see particularly above 80 km (associated with large amplitudes) during the daynumbers 180-187, 193-207 and 212-219 in 1993 (Figure 6.13), and during the daynumbers 180-183, 204-207 and 212-223 in 1994 (Figure 6.14)). When the amplitudes are large, the wave is more likely to become non-linear. We also observe experimentally, that for large amplitude the phase is more likely to be constant, implying that the wave period is close to 48 h and there is a long vertical wavelength. Long vertical wavelengths of over 150 km are estimated during these periods, although shorter vertical wavelengths of 60-80 km are observed at other times (e.g., during the daynumbers 176-179 and 208-211 in 1993, and during the daynumbers 184-187 and 208-211 in 1994).

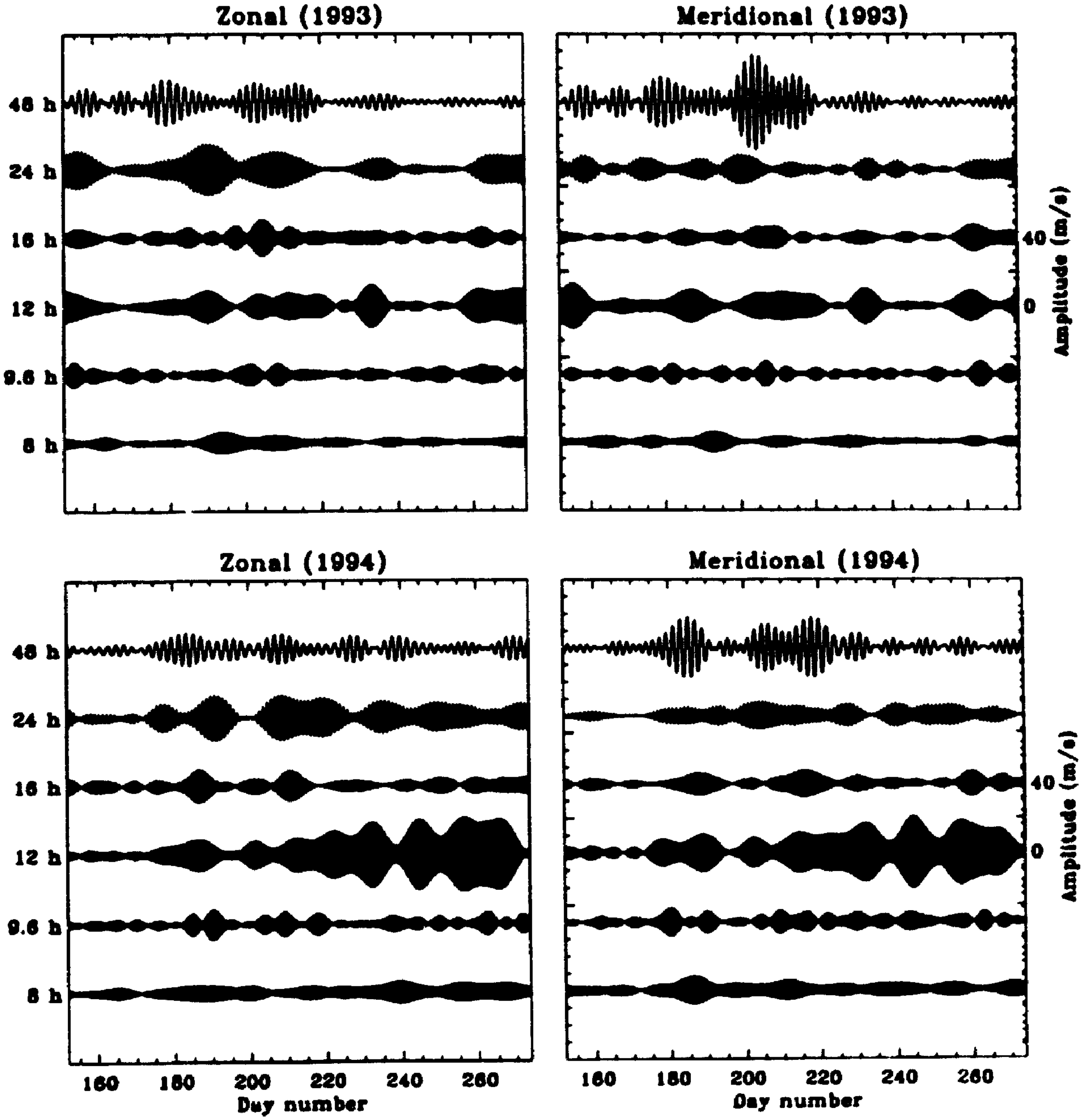

Figure 6.16: The relationship between the 2-day wave and the tidal components obtained from the resultant filtered wind for the zonal (left) and meridional (right) components at 91 km from daynumber 152 to daynumber 270 in 1993 and 1994. The band-pass used were 42-54 h, 22-26 h, 15-17 h, 11.4-12.6 h, 9.1-10.1 h, and 7.8-8.2 h for the central periods of 48 h, 24 h, 16h, 12 h, and 9.6 h respectively. The amplitude scale is indicated on the right hand side. All times (days) are in UT; the first observation is at 0000 UT on the daynumber 152 (see the text for more details).

6.2.7 Comparisons with the tides

The temporal relationship between the tides and the 2-day wave and its harmonics can be qualitatively examined by looking at the respective wave amplitudes as a function of time. In the Northern and Southern Hemispheres there are suggestions of a non-linear interaction between the 2-day wave and the solar tides [Manson et al., 1982; Manson and Meek, 1990; Teitelbaum and Vial, 1991]. These authors suggested that a non-linear interaction between the 2-day wave and one of the solar tides could produce a sum or differences term at a period of 16 h. A 16 h wind component could arise as a harmonic of the non-linear 2-day wave, but in this case a weaker 9.6 h wave should also be present.

For convenience the band-pass filtering method was employed for the present comparisons. This is sufficient for the comparisons in this section. Figure 6.16 shows the relationship between the 2-day wave and the tidal components obtained from the resultant filtered wind for the zonal and meridional components at 91 km for the years 1993 and 1994. The band-pass used were 42-54 h, 22-26 h, 15-17 h, 11.4-12.6 h, 9.1-10.1 h, and 7.8-8.2 h for the central periods of 48 h, 24 h, 16 h, 12 h, 9.6 h, and 8 h respectively. The band-pass used for the wind components is small enough to reduce the energy contributions due to noise and yet large enough to increase the coherence time of the filtered winds.

The figure shows a slight tendency for the amplitude of the diurnal tide to be diminished (< 5 m/s) during the time of large 2-day wave amplitude particularly in the meridional component for the years 1993 and 1994 (e.g., during the daynumbers 175-185 and 200-210 in 1993 for the meridional component, and during the daynumbers 178-188 in 1994 for the zonal component). It can be seen that diurnal tide increases in strength (attains values as large as 10-15 m/s) in the zonal component during this period of time. The semidiurnal amplitude generally attains in excess of ~ 10-15 m/s in the zonal and meridional components for the years 1993 and 1994 when the 2-day wave amplitude is large. One noticeable feature is that whenever a distinct peak occurs in the 2-day wave, it exists in the semidiural amplitude too. In 1994 the semidiurnal amplitude begins to increase in strength about the day 210 as the 2-day wave begins to die out completely. Closer inspection shows that the amplitude peak in the the 16 h component occurs just after the peak in the 48 h component. The amplitude values attain ~ 7-10 m/s during this period of time. A weaker 9.6 h component is also visually present in the figure but hard to discern any definite peaks. No obvious relationship is seen between the terdiurnal tide and the 2-day wave.

6.2.8 Conclusion

The observations at London show very clearly the existence of the 2-day wave during the late June-early August months, and the presence of the 2-day wave at other times of the year in 1993 and 1994 is also evident, although with lesser amplitudes. A subsidiary maximum of about 70% of the summer peak, appears during the late April-May months. The amplitudes of the meridional components (20-30 m/s) are generally larger than the zonal component (15-18 m/s), and maximize between 88-91 km in both years. Strong year to year variation was found for both the zonal and meridional components, but it is clear that the summer amplification is generally confined to a duration of about 48 days.

The period of the 2-day wave was determined at all heights by the complex demodulation method. The mean periods are found to be $\sim$ 47.1 $\pm$ 1.3 h for the zonal component and $\sim$ 46.2 $\pm$ 1.4 h for the meridional component in 1993. These values are $\sim$ 46.2$\pm$1.4 h and $\sim$ 46.7$\pm$1.3 h for the zonal meridional components respectively in 1994. Variations with height were of the order of $\pm$1 h. These values are shown to be consistent with the values obtained from the harmonic analysis method. The periods determined from the present study are found to be smaller than the 51-52 h period generally suggested by the Northern Hemisphere results.

The mean phases during intervals of larger amplitudes tend to have phases in the afternoon quadrant between 1000 h LT and 1700 h LT for both the zonal and meridional components for the years 1993 and 1994, although the number of occurrences of larger amplitudes are fewer in the zonal component. The mean phase (i.e. time of maximum) over all heights were found to be $\sim$ 12.5 $\pm$ 1.4 h and $\sim$ 12.3 $\pm$ 1.3 h for the zonal and meridional components respectively in 1993 (assuming the 2-day wave period was as exactly 48 h). In 1994 the respective values are $\sim$ 12.1 $\pm$ 1.6 h and $\sim$ 12.2 $\pm$ 1.2 h for the zonal and meridional components. These values are estimated when the amplitudes are greater than 8 m/s. These results strongly indicate that the 2-day wave prefers to peak near 1200 h LT during intervals of large wave amplitude, suggesting some solar influence on the 2-day wave, possibly through interaction with the solar tides. No obvious phase locking was apparent for small amplitudes in both components. Generally the meridional component leads the zonal component by 1-14 h most of the time. But it was frequently found that the phase relationship between the wind components are nearly 12-14 h during the time intervals of strong 2-day wave activity in the 88-94 km height range, suggesting the wave components are close to being in-quadrature.

The estimated vertical wavelengths are generally greater than 150 km when the wave amplitudes are larger, but smaller vertical wavelengths of 60-80 km are also estimated at certain times of the observation.

The temporal relationship between the 2-day wave and the diurnal tide shows that the amplitude of the diurnal tide diminish in the meridional component and increase in the zonal component during time periods of strong 2-day wave activity. On the other hand, the semidiurnal amplitude maximizes whenever the 2-day wave attains its peak amplitude. The observations indicate that the 16 h component maximizes just after the peak of the 2-day wave amplitude, and a weak 9.6 h component is also present during the same time. No correspondence can be seen between the 2-day wave and the terdiurnal tide.

Finally, in order to study the complete nature of the 2-day wave at mid-latitudes, it is imperative to continue these investigations. Further observations are required in order to resolve questions about the generating mechanism as well as to understand better the role of the wave in the middle atmosphere.

6.3 Simultaneous observations of the 2-day wave at London and Saskatoon during 1993-1994

This section describes the characteristic behaviours of the 2-day oscillation observed simultaneously by the MF radars located at London and Saskatoon in 1993 and 1994. This study mainly focuses on comparison performed at 91 km which is associated with the maximum amplitude peak of the 2-day wave activity at both sites. Missing hourly averages were replaced by Gaussian distributed random noises with a variance matching that of the data itself.

6.3.1 Amplitude

Figure 6.17 shows the daily amplitudes of the 2-day wave for both the zonal and meridional components in 1993 and 1994. In our analysis procedure, we used a harmonic analysis method to get an estimate of the amplitude of the 2-day wave. There is considerable theoretical and experimental evidence that the various tidal components (plus gravity waves) are superimposed on the 2-day wave [e.g., Manson and Meek, 1985; Manson et al., 1989]. Therefore, we used 4-day groups of data, stepped by one day (e.g., 1-4, 2-5, 3-6,....). We adopted a 4-day fit because this is long enough to give reasonable significance to our results yet short enough to give reasonable sensitivity during periods of large 2-day activity [see also Figure 6.17]. The zonal (u) and meridional (v) wind components were represented as a function of time (t) by

$$u(t), v(t) = a_0 + \sum_{i=1}^{i=4} a_i \sin(\frac{2\pi}{T_i} t + \Phi_i)$$

where a_0 is the prevailing mean wind and a_i and Φ_i give the mean amplitude and phase for the 8 h (i=1), 12 h (i=2), and 24 h (i=3) tidal components. The wave period T_4 was varied systematically from 40 h to 60 h in steps of 0.5 h in order to provide maximum sensitivity to amplitude variations. For each data interval the daily 2-day wave amplitude chosen was the one with the period which produced maximum response, and these are illustrated in Figure 6.17 and the corresponding periods representing the best fits to the data are illustrated in Figure 6.18. The values are smoothed with a 4-day running mean. The analysis was carried out for both the zonal and meridional components of years 1993 and 1994. Note that the units used to display the time series is daynumbers. Figure 6.17 clearly illustrates that the 2-day wave activity is mainly confined during the summer months (from daynumber 170 to daynumber 230). However, these observations also indicate the presence of the 2-day

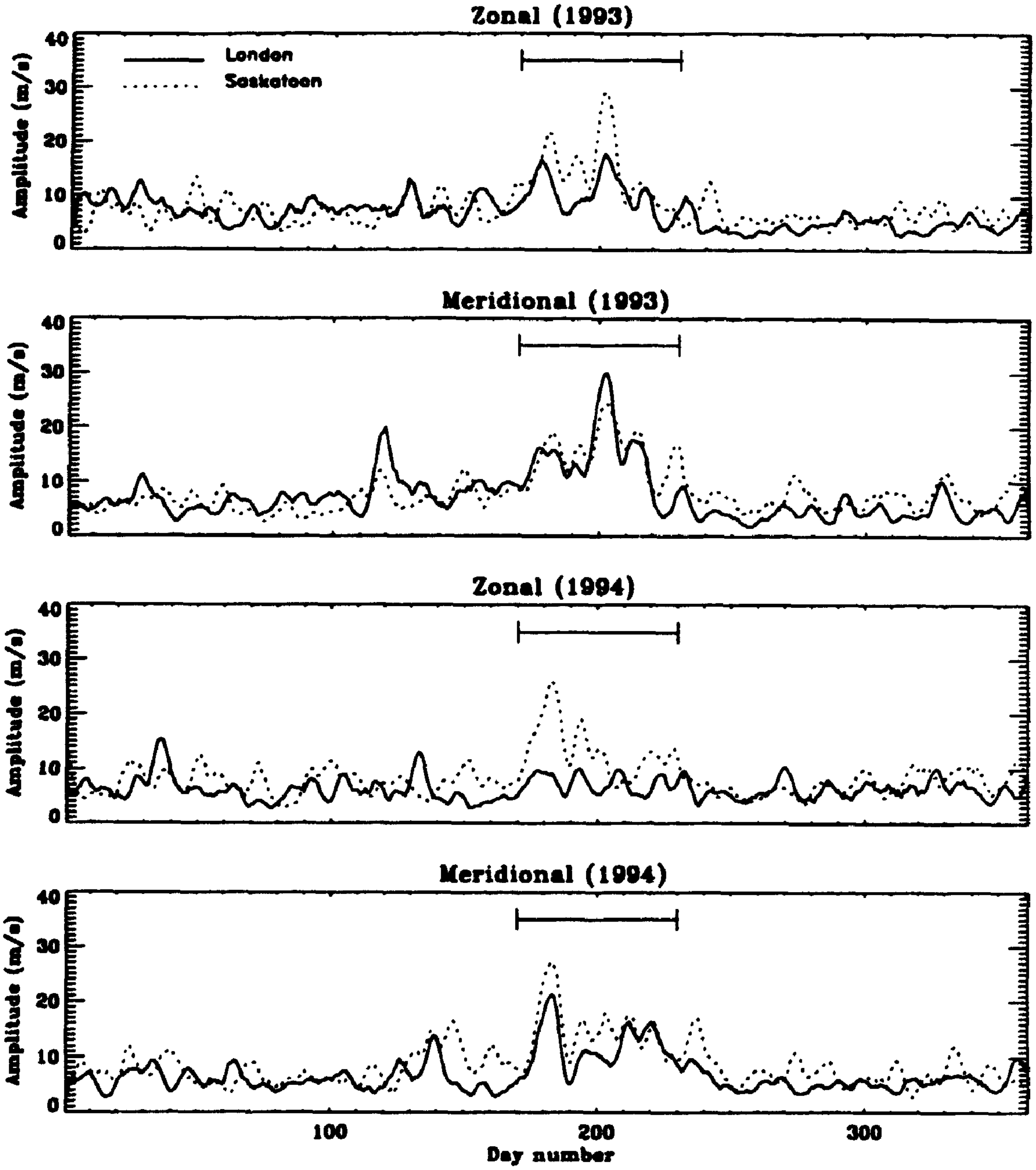

Figure 6.17: Daily amplitudes of the 2-day wave at 91 km in London and Saskatoon for the zonal and meridional components in 1993 and 1994. All times (days) are in UT; the first observation is at 0000 UT on the daynumber 1. See the text for more details.

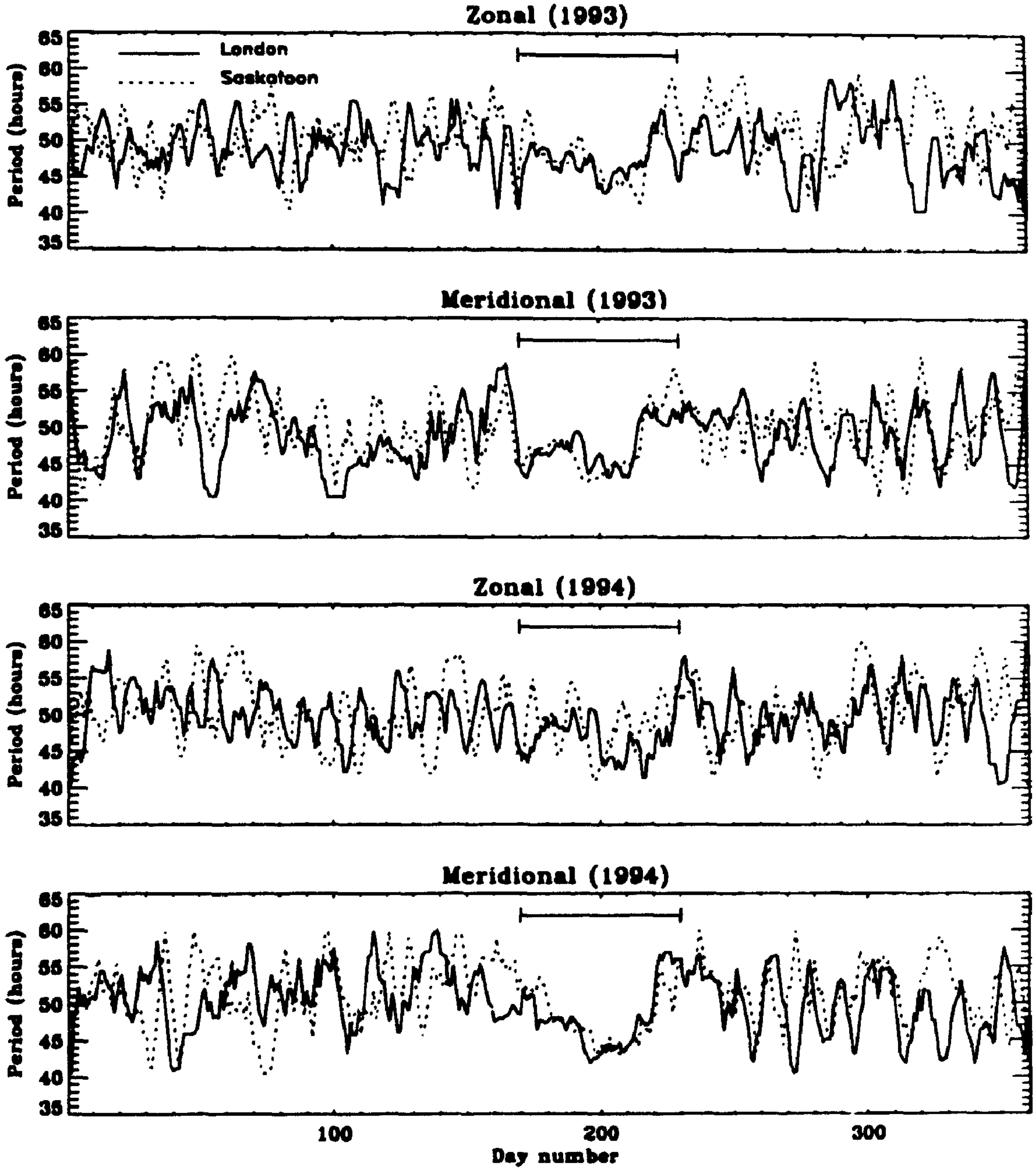

Figure 6.18: Daily periods of the 2-day wave at 91 km in London and Saskatoon for the zonal and meridional components in 1993 and 1994. All times (days) are in UT; the first observation is at 0000 UT on the daynumber 1. See the text for more details.

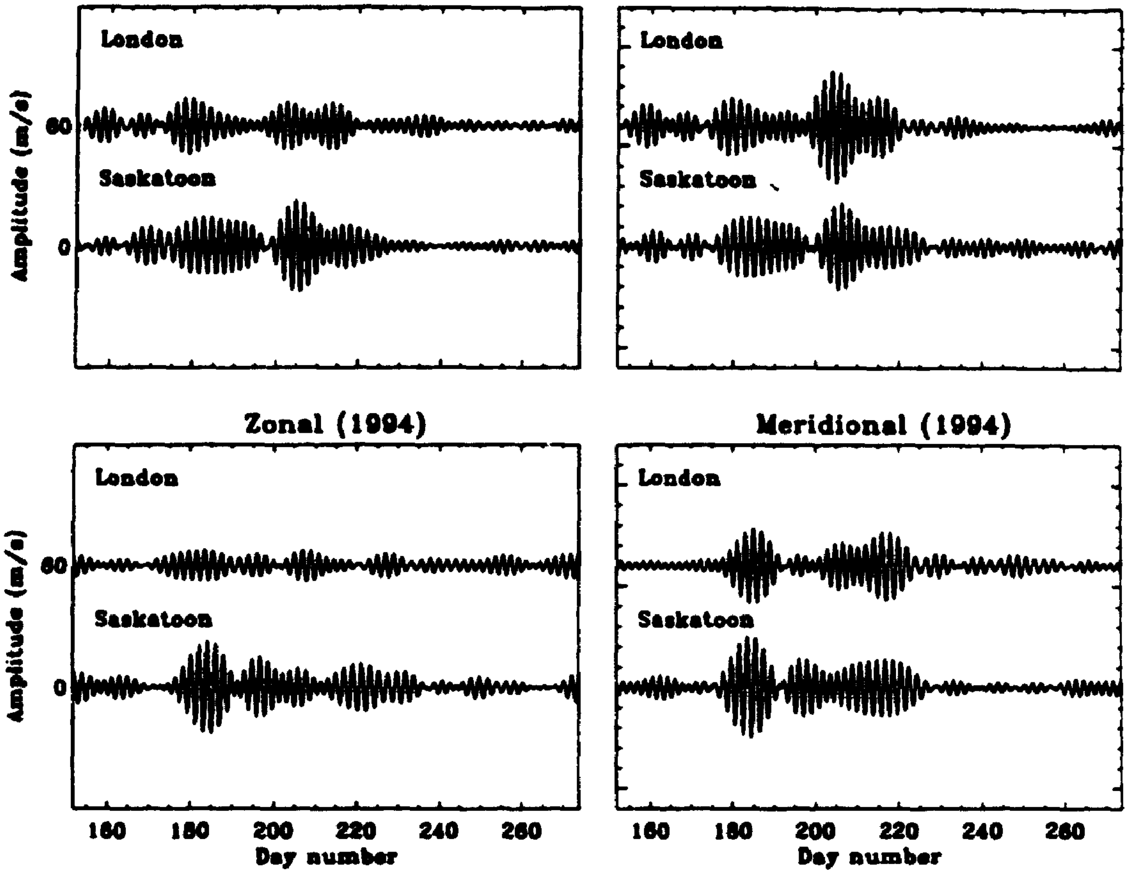

Figure 6.19: Zonal (left) and meridional (right) components of the winds observed at 91 km in London and Saskatoon from daynumber 152 to daynumber 270 in 1993 and 1994. Data have been band-pass filtered to retain only periods between 42 and 54 h. All times (days) are in UT; the first observation is at 0000 UT on the daynumber 152.

wave more weakly at other times of the year. One noticeable feature is a pronounced maximum during the daynumbers 110-120, particularly in the meridional components of the London data. Similar behaviour is also evident in the Saskatoon data during the daynumbers 125-145. Figure 6.18 shows that generally the periods are relatively less variable during the summer months (i.e. from daynumber 170 to daynumber 230) than other times of the year. It should be emphasized here that outside the summer months the estimated periods are generally less reliable owing to the comparatively small wave amplitude (also see Section 6.2.3).

Generally the amplitudes of the 2-day oscillation maximize in the meridional component rather than the zonal component over London in both years. In contrast, the amplitudes of the 2-day oscillation over Saskatoon maximize in the zonal component in 1993 and maximize in the meridional component in 1994. We also note that the 2-day oscillation in the zonal component is larger by a factor of 2-3 in Saskatoon than in London during the mid-summer amplitude oscillations, while the meridional component shows comparable amplitudes in both sites. Maximum amplitude values of ~ 20-30 m/s are observed in the meridional component. For the zonal component the maximum values attain ~ 15-18 m/s over London but very large amplitudes of 30 m/s are also observed over Saskatoon particularly in 1993.

The dominance of the 2-day periodicity is also clearly evident in the filtered time series shown in Figure 6.19. Note that the corresponding time segment shown in this figure is from daynumber 152 to daynumber 270. The data at the two sites were subjected to a band-pass filter with cutoff periods of 40 and 60 h. Figure 6.19 shows quite distinctly that the time variations of the occurrence of the 2-day wave are very similar at London and Saskatoon. It is apparent that the wave is transient in nature with the largest event taking the form of a pulse or burst starting around daynumber 175 and lasting till daynumber 220. Two pronounced 2-day activity intervals occur, particularly in the meridional component during this period of time at both sites for the years 1993 and 1994. The initial burst started around day 175-177 at both sites for the years 1993 and 1994. The second burst starting around day 200 in 1993, and starting around day 194-196 in 1994 at both sites.

6.3.2 Period

Our observations at the two sites reveal that the 2-day oscillation is very strong after the summer solstice, suggesting a particularly effective forcing agent at this period of time. Therefore, a more accurate measurement of the wave period will be helpful in

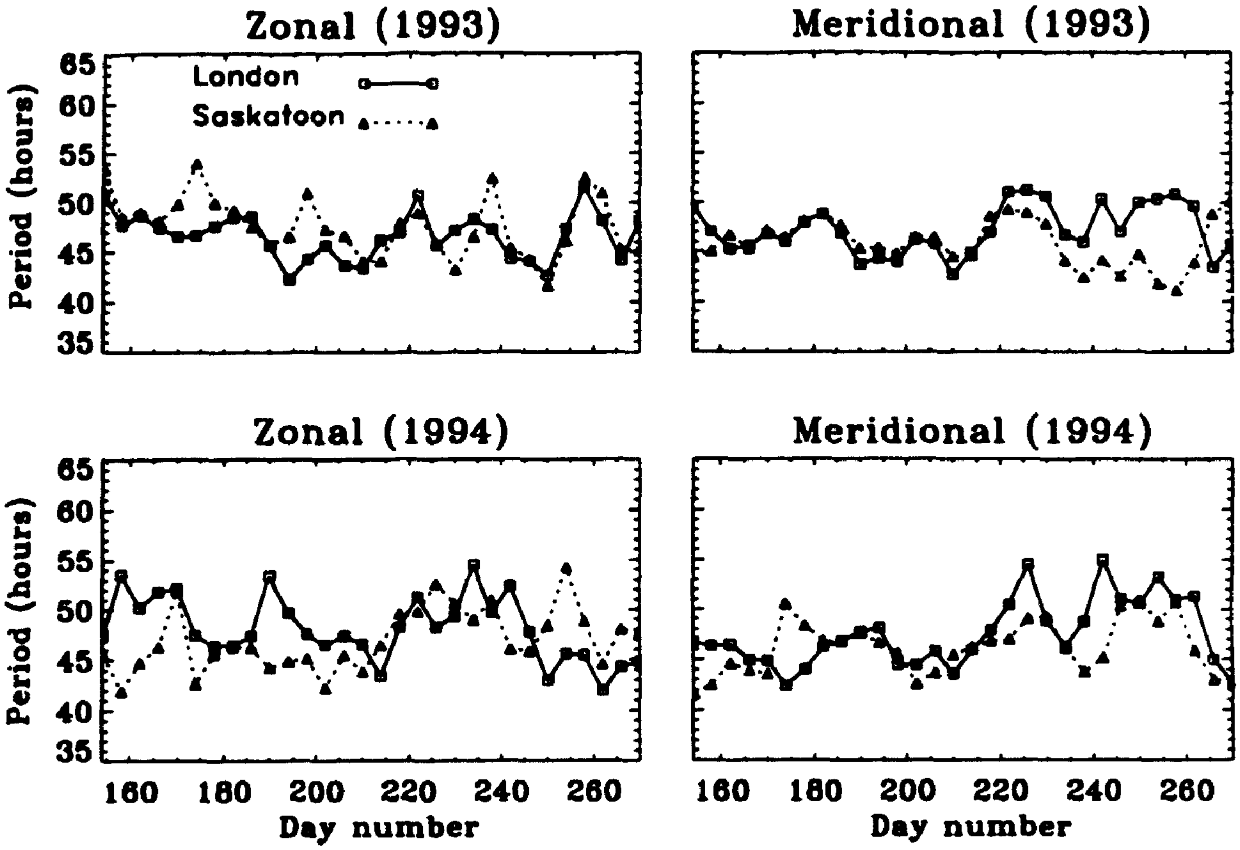

Figure 6.20: The variation of the period as a function of time in 4 day intervals at 91 km for the zonal (left) meridional (right) components in London and Saskatoon from daynumber 152 to daynumber 270 for the years 1993 and 1994. All times (days) are in UT; the first observation is at 0000 UT on the daynumber 1.

determining likely sources of the wave. We have used a complex demodulation method in the present study, which is very sensitive to the frequency variations within the time series, to determine the precise period of the 2-day oscillation (Harris, 1993, for more details see Section 6.2.2). The effective band-pass used was 42 h to 54 h for the 48 h demodulation period in this study. The periods have been estimated from the demodulating of the full time series, from daynumber 152 to daynumber 273 (from June 1 to September 30), in order to allow a large enough bandwidth and number of degrees of freedom. This band-pass allows amplitude variations with the time scales larger than 7 days.

Figure 6.20 shows the variation of the period as a function of time in 4 day intervals, which can be compared with the amplitudes in Figure 6.19. Generally the periods are between 42 h and 54 h. We draw the attention to the relatively excellent agreement in period between the two sites from daynumber 180 to daynumber 220 particularly for the meridional component in both years, which seems to coincide with the enhancement or "burst" in the amplitude of the 2-day wave. The period differs significantly for the zonal component during this period at certain times. This may be due to the small amplitudes observed over London. One interesting feature is that the periods are in the 46-49 h range during the daynumbers 175-191 for both the zonal and meridional components in both years, which coincides with the first event of "burst" in the amplitude of the 2-day activity. The periods then migrate to 43-47 h range during the daynumbers 201-216 for both components, which seems to coincide with the second event of "burst" in the amplitude of the 2-day activity. The mean periods during the bursts of the 2-day activity are 47.1 ± 1.3 h and 47.3 ± 1.2 h for the zonal component at the London and Saskatoon sites respectively, while the respective mean periods are 46.2 ± 1.4 h and 46.8 ± 1.6 h for the meridional component at the London and Saskatoon sites in 1993. In 1994 the mean period values are 47.2 ± 0.9 h and 47.0 ± 1.2 h for the zonal component at the London and Saskatoon sites respectively, and the respective values are 46.7 ± 1.2 h and 46.1 ± 1.7 h for the meridional component at the London and Saskatoon sites. It should be noted that the period of the 2-day wave was only taken into account when the wave had a demodulated amplitude greater than 8 m/s. After a number of tests it turns out that the results of the mean periods are more consistent when the cutoff amplitude is increased (e.g., 15 m/s) or the demodulation period is changed (e.g., 44 h). All these results strongly suggest that the enhancement or burst of the 2-day activity occurs most frequently near a period of 46.5 h. The periods determined in the present study are found to be smaller than the 51-52 h period generally suggested by the Northern Hemisphere results [e.g., Muller, 1972; Glass et al., 1975; Nelson and Muller, 1978; Kingsley et al., 1978; Stenning et al., 1978; Manson et al., 1978; Salby and Roper, 1980].

6.3.3 Amplitude spectra

Figures 6.17 and 6.19 clearly illustrate that, in each year, there are two strong bursts of the 2-day wave activity and they seem to die out abruptly after 7-10 cycles in each burst of the activity. Therefore we will concentrate on only the time periods associated with the large amplitude of the 2-day wave activity. The first event occurs simultaneously at both sites specifically from daynumber 175 to daynumber 191, and the second event occurs simultaneously from daynumber 201 to daynumber 216 in 1993. In 1994 the first event occurs simultaneously from daynumber 175 to daynumber 191 (same time period as in 1993), and the second event occurs simultaneously from

First event

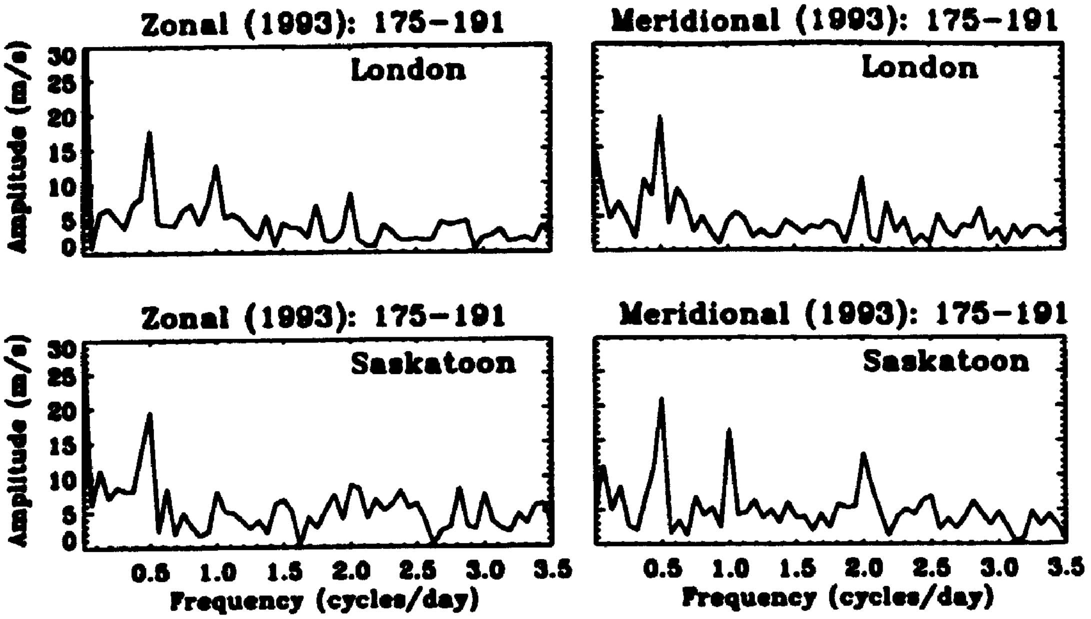

Second event

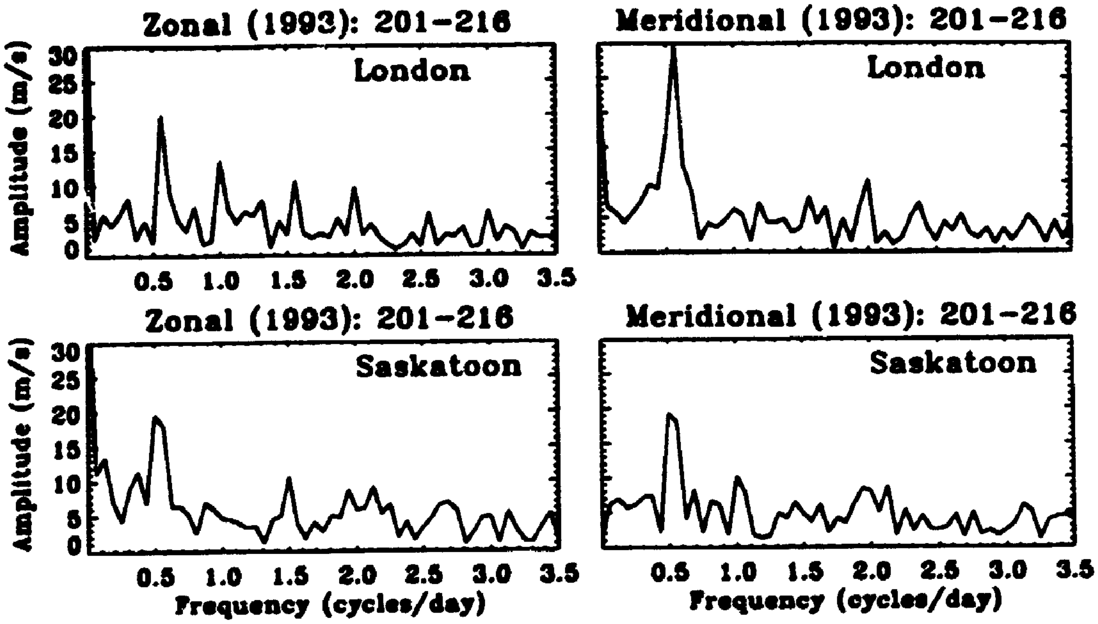

Figure 6.21: Amplitude spectra for the two burst events at 91 km for the zonal (left) and meridional (right) components in London and Saskatoon in 1993. Note that the ordinates of the resultant amplitude spectra have dimensions of m/s since the original amplitudes have been multiplied by a normalization constant which has the dimension Hz (see the text for more details).

First event

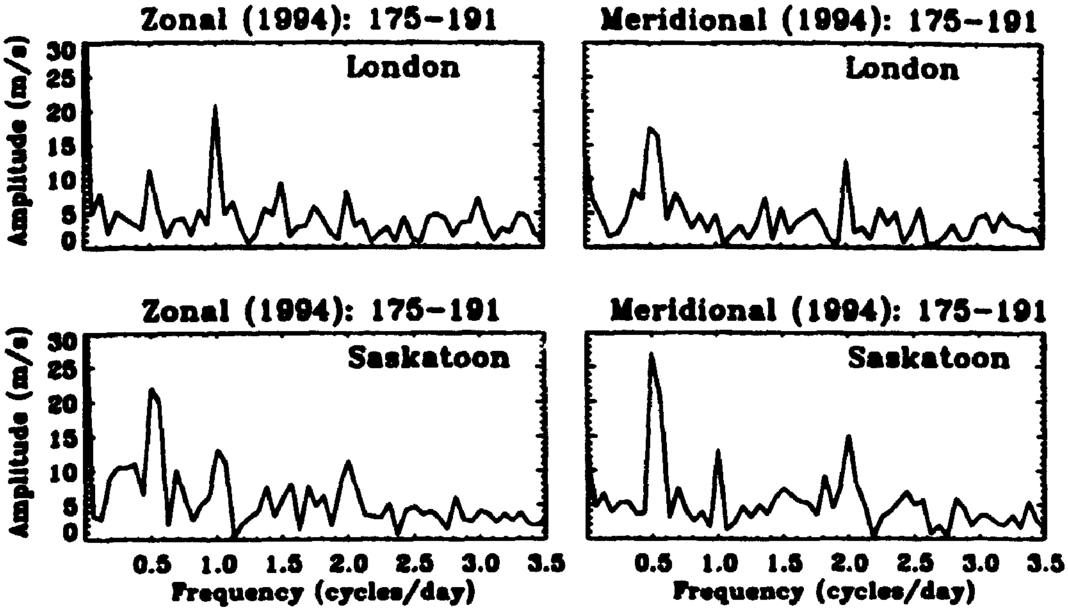

Second event

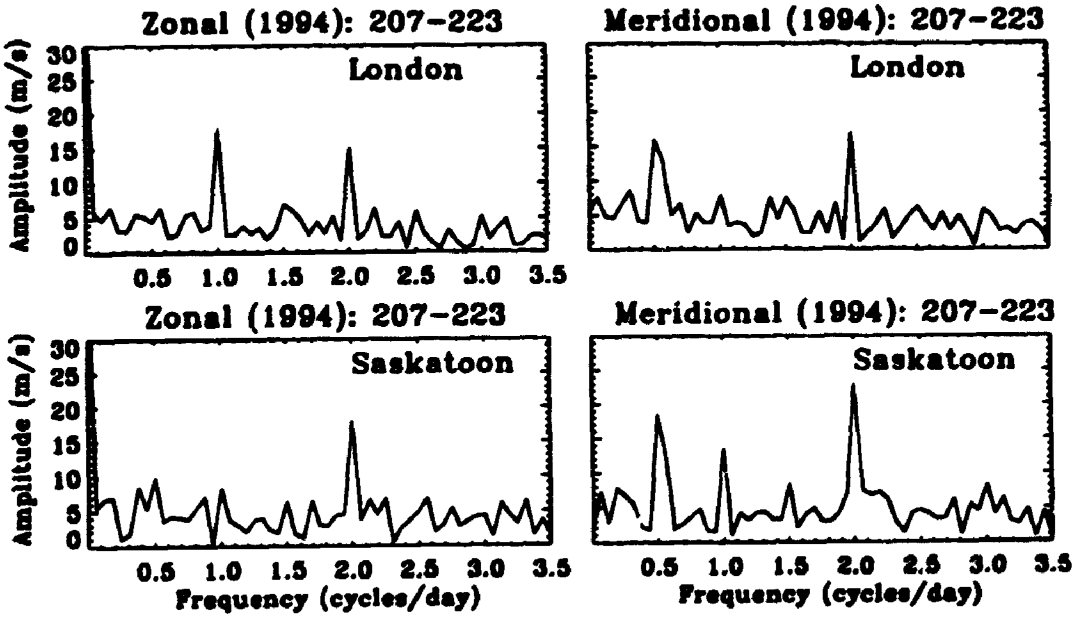

Figure 6.22: Amplitude spectra for the two burst events at 91 km for the zonal (left) and meridional (right) components in London and Saskatoon in 1994. Note that the ordinates of the resultant amplitude spectra have dimensions of m/s since the original amplitudes have been multiplied by a normalization constant which has the dimension Hz (see the text for more details).

daynumber 207 to daynumber 222. It should be noted that 90 – 95% of the total available hourly mean data were accepted at both sites during these period of time for the years 1993 and 1994.

Figures 6.21 and 6.22 show amplitude spectra for the two burst events discussed above, both for the years 1993 and 1994. Note that the ordinates of the resultant amplitude spectra have dimensions of m/s since the original amplitudes have been multiplied by a normalization constant which has dimension of Hz. This allows one to compare qualitatively the relative amplitude variation of the 2-day wave with the tidal components (e.g., 24, 12, and 8 h components) as well as with other long period oscillations (e.g., 9.6 and 16 h components). The maximum amplitude values obtained from this figure are in good agreement with the values estimated by the harmonic analysis method (compare with Figure 6.17). This Figure shows that the amplitude of the diurnal tide is significantly reduced (< 5 m/s) during the time of largest amplitude of the 2-day wave at the London site, while the amplitude values as large as 10-20 m/s are observed at the Saskatoon site in the meridional component of years 1993 and 1994. The semidiurnal tide generally attains in excess of $\sim$ 10-15 m/s during this period of time in the meridional component at both sites of years 1993 and 1994. In contrast, for the zonal component the amplitude of the diurnal tide generally attains $\sim$ 10-20 m/s at London site, and the amplitude values are significantly reduced (< 7 m/s) at the Saskatoon site in both years except from daynumber 175 to daynumber 190 in 1994. From daynumber 175 to daynumber 190 in 1994 for the zonal component the amplitude of the diurnal tide is larger (attains as large as 20 m/s) by a factor of 2 than the 2-day wave at the London site, while at the Saskatoon site the amplitude of the 2-day wave is larger ($\sim$ 20 m/s) by a factor of 2 than the diurnal tide.

From Figures 6.17-6.22 as well as in the results obtained for years 1993 and 1994, many similarities appear between the sets of data at the two sites. The time variation of the 2-day oscillations also suggests that the characteristic behaviour is similar at both sites. Therefore we used two methods, the cross correlation and cross spectrum, between the sites to achieve more quantitative results.

6.3.4 Cross-correlation

The cross-correlation method studies the variation of the cross-correlation coefficients versus the time shift experienced by one set of data compared with the other set of data. If this coefficient varies quasi-sinusoidally versus time, the period of the curve will show the period of the dominant motion present in both records. The time shift

First event

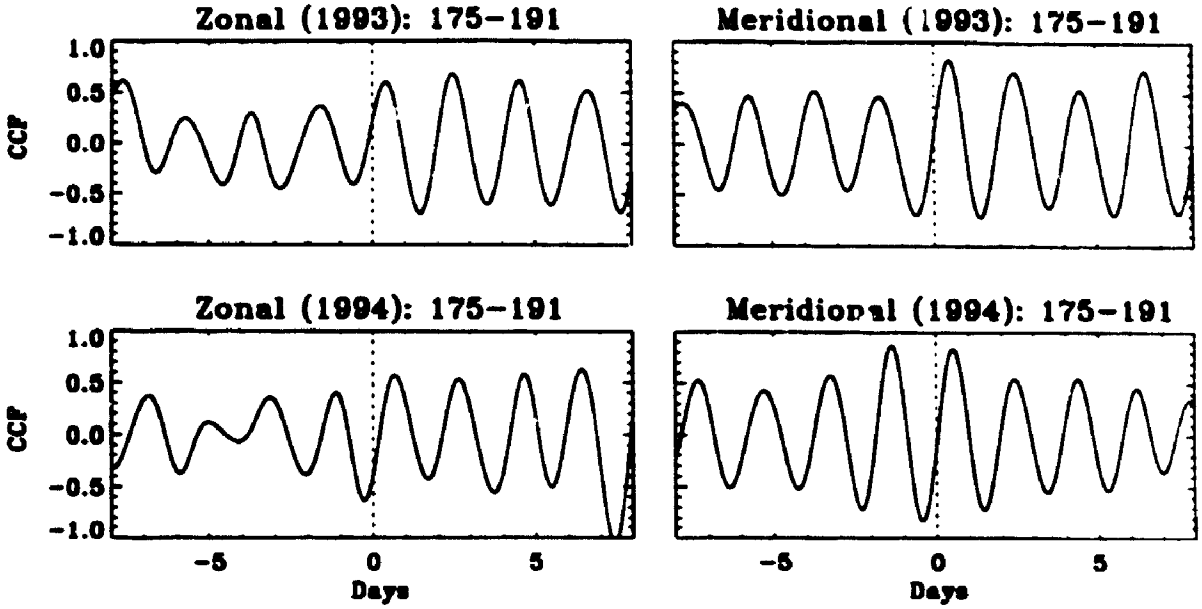

Zonal (1993): 175–191

Meridional (1993): 175–191

Zonal (1994): 175–191

Meridional (1994): 175–191

Second event

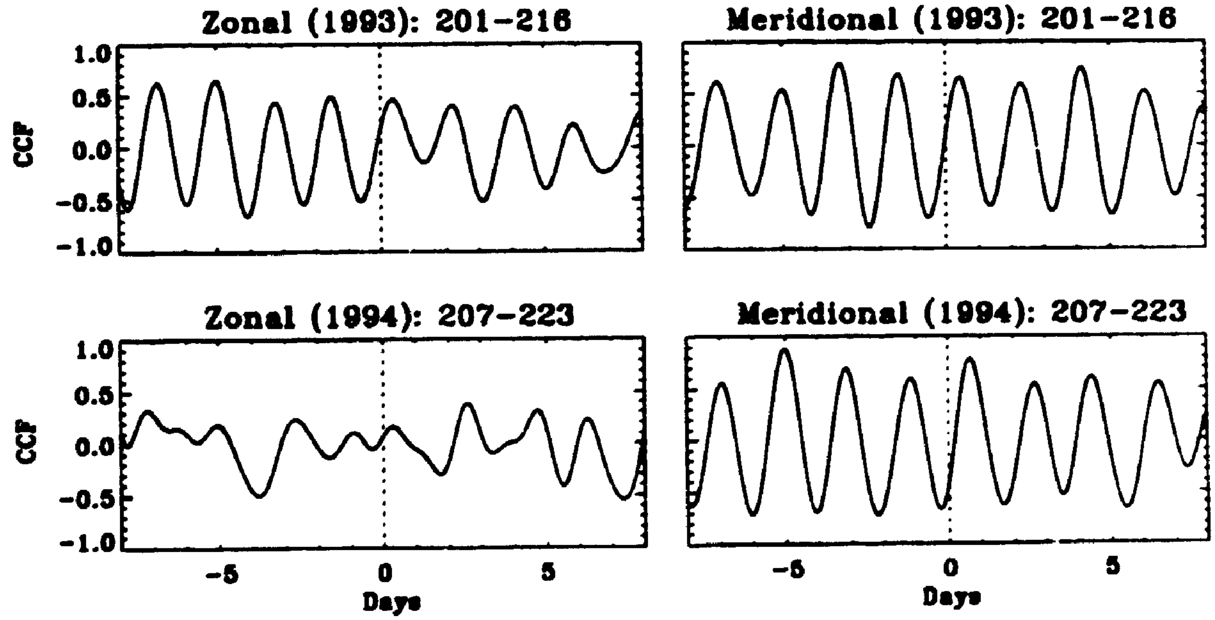

Zonal (1993): 201–216

Meridional (1993): 201–216

Zonal (1994): 207–223

Meridional (1994): 207–223

Figure 6.23: Cross-correlation between the data obtained at London and Saskatoon for the zonal (left) and meridional (right) components in 1993 and 1994 for the two burst events. Universal time has been used.

between the origin and the time when this coefficient reaches its maximum value is equal to the phase shift of the wave between both sites.

In our analysis procedure, the original hourly mean data were subjected to a low-pass filtering with the cutoff period of 30 h. Thus the tides and gravity waves are removed by this low-pass filtering. Figure 6.23 illustrates the cross-correlation between the data obtained at the London and Saskatoon sites for both the zonal and meridional components in 1993 and 1994. This figure shows quite distinctly that the same periodic motion is measured at both sites. The calculations reveal that the periods of the 2-day wave are near 46.8 ± 0.8 h and 46.4 ± 0.9 h in 1993 and 46.5 ± 1.1 h and 46.2 ± 0.8 h in 1994 for the zonal and meridional components respectively. These values are consistent with the values estimated by the complex demodulation method (see Section 6.3.2).

A significant correlation between the 2 sites is clearly apparent in Figure 6.23 for the 2-day wave particularly in the meridional component. The cross-correlation values are of $\sim$ 0.75-0.88 in both years. These results reveal that the enhancement of the 2-day wave activity occurred with a high degree of consistency between the two sites during this period of time. On the other hand, the cross-correlation values for the zonal component are comparatively smaller, with values of $\sim$ 0.5 except from daynumber 207 to daynumber 222 in 1994. The plot of the correlation function from daynumber 207 to daynumber 222 in 1994 for the zonal component yield quantitative evidence that there was no correlation between both sets of data, showing either that there were motions with quite different periods or that there were no significant periodic motions at both sites. The latter possibility agrees with Figure 6.19.

The time lags for maximum correlation are found to occur between 10 h and 11 h for the meridional component in 1993. The respective value is 12-16 h for the meridional component in 1994. For the zonal component the time lags for maximum correlation occur between 9 h and 10 h in 1993, and occur near 16 h in 1994. The physical significance of these results will be discussed in the following section.

6.3.5 Cross-spectrum

The cross-spectrum method gives not only information about the dominant periodicity simultaneously observed at two sites, but also sets out quantitatively the values of amplitude, period, and phase difference of every present motion. The main purpose of this method in this present study is to estimate the precise time differences between the two sites in order to estimate the zonal wave number of the travelling westward

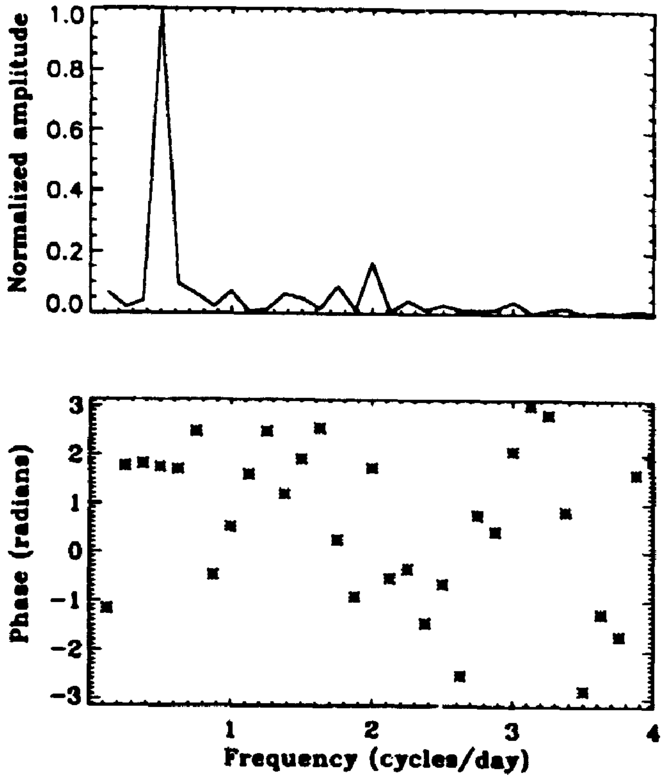

Figure 6.24: Normalized cross-spectrum of the meridional wind component between London and Saskatoon from daynumber 183 to daynumber 190 in 1994. The phase is the number of radians by which London leads Saskatoon. Universal time has been used.

wave.

The zonal wave number of the 2-day wave can be estimated by simultaneous comparisons of its phase at two sites situated at similar latitudes but separated in longitude. If we interpret the phase differences at the two sites as the effect of a westward propagating wave then we can calculate its zonal number from the apparent phase speed by using the relationship, $k = \frac{360}{T}\frac{\Delta T}{\Delta d}$ [e.g., Muller and Nelson, 1978], where k is the zonal wavenumber, T is the wave period, ΔT is the time difference between the two sites, universal time has been used for both sites), and Δd is the longitudinal difference between the observational sites in degrees. It has already been shown in the previous sections that a 2-day wave period of 46.5 h is typical at both sites during the time period of strong 2-day wave activity. It is desirable for the two sites to simultaneously sample the same cycle, i.e., to be within 120° of longitude of each other, because the wave structure may be different for each cycle as they circle the globe.

Interval (daynumbers)	Zonal (h)	Meridional (h)
175-182	8.8	10.4
183-190	10.9	9.3
191-198	-	9.7
199-206	6.4	10.1
207-214	12.7	13.5
215-222	-	11.5
Average	9.7 ± 1.4	10.8 ± 0.6

Table 6.1: The phase relationship of the 2-day wave components between London and Saskatoon in 1993. The table show the number of hours by which London leads Saskatoon.

The satellite temperature observations clearly show that each of the three cycles of the wavenumber 3 pattern differ [Rodgers and Prata, 1981]. A zonal wavenumber of 3 means that a wave will have 3 cycles circling the globe. The geographical separation of London and Saskatoon is 9° in latitude and 26° in longitude. On the other hand, the closer the sites the smaller the phase difference and hence the larger the relative error in its estimate. As an example, for an error of 1 h in each phase estimate, the difference will produce an error of $\sim$ 0.3 in the zonal wavenumber. If the 2-day wave is assumed to be due to a westward propagating wave with a zonal wavenumber 3, and also assuming there is no phase change with latitude, then the 2-day wave at London should lead that at Saskatoon by $\sim$ 10 h, i.e., the appearance of the wave moves from the east to the west.

Another approach is to use the phase of the cross-spectrum of the two wind time series. This method yields a measure of the average phase difference of the time series. Let us check whether such a motion could account for the experimental zonal wave number 3. We have examined 6 intervals of 8 day data sets from daynumber 175 to daynumber 222. One example, from daynumber 183 to daynumber 190 for the meridional component in 1994, of the normalized cross-spectrum between the two sites is shown in Figure 6.24. We have adapted a 8-day data set because Figure 6.19 suggests that this is long enough to give reasonable significance to our results, and will also allow us to create a reliable error estimate for the cross-spectral phase. Figure 6.24 shows distinctly that the 2-day oscillation is the dominant feature of the

Interval (daynumbers)	Zonal (h)	Meridional (h)
175-182	16.2	7.3
183-190	16.5	12.7
191-198	-	-
Average	16.4 ± 0.2	10.0 ± 2.7
199-206	-	17.4
207-214	-	15.2
215-222	-	17.8
Average	-	16.8 ± 0.8

Table 6.2: The phase relationship of the 2-day wave components between London and Saskatoon in 1994. The table show the number of hours by which London leads Saskatoon.

cross-spectrum during this period of time, that is, whenever a distinct peak in the spectrum appears in the London data, it exists at Saskatoon too. Similar behaviour is frequently observed during other periods of time. These results further confirm that from daynumber 175 to daynumber 222, the same periodic motions are simultaneously detected over London and Saskatoon. Tables 6.1 and 6.2 give the apparent phase lag between the two sites for 6 independent periods in 1993 and 1994 respectively. The results show that the London site leads the Saskatoon site by ~ 9.70 ± 1.36 h and ~ 10.75 ± 0.63 h for the zonal and meridional components respectively in 1993. The corresponding zonal wavenumbers are 2.89 ± 0.40 and 3.20 ± 0.19 for the zonal and meridional components. For the year 1994 we divided the data into 2 sets of data, i.e. from daynumber 175 to daynumber 198 and from daynumber 199 to daynumber 222, because of a significant increase in the estimation of the time lag (see also Table 6.2). It turns out that the London site leads the Saskatoon site by ~ 10.00 ± 2.70 h during the first half of the time period (175-198), and by ~ 16.80 ± 0.81 h during the second half of the time period (199-222) for the meridional component. The corresponding zonal wavenumbers are 2.98 ± 0.80 and 5.00 ± 0.24. For the zonal component the London leads the Saskatoon by ~ 16.35 ± 0.15 h during the first half of the time period (175-198), and the values are not shown during the second half of the time period in Table 6.2 because the amplitudes of the cross spectra are very small so that

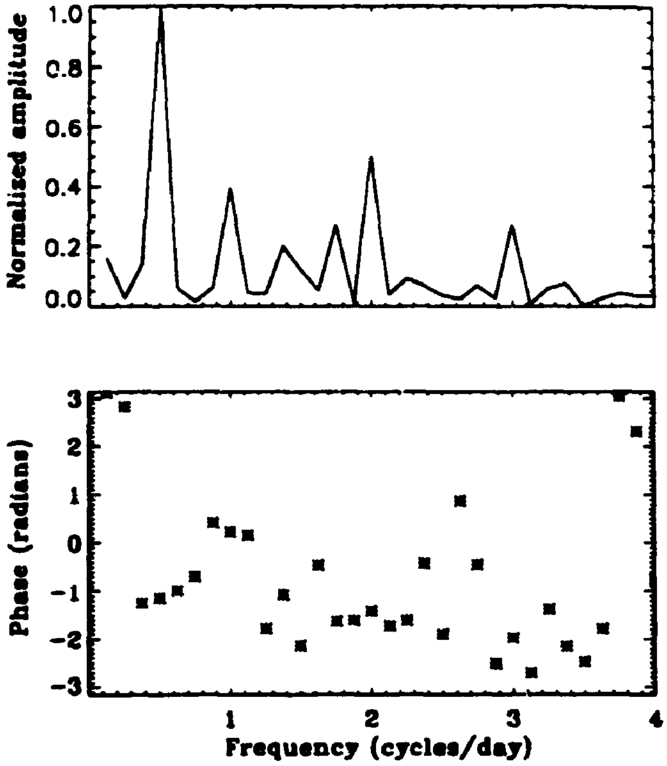

Figure 6.25: Normalized cross-spectrum of the zonal and meridional wind components for London from daynumber 183 to daynumber 190 in 1994. The phase is the number of radians by which London leads Saskatoon.

the phase determinations are of dubious quality. It should be emphasized that the values for the zonal component during the first half of the time period in 1994 should also be treated with caution, since relatively small amplitudes are associated with the cross-spectrum.

The zonal wavenumber was also calculated from a smoothed cross-spectrum in order to increase the number of degrees of freedom of the estimator. This was achieved by applying a 3 point running mean to the separate complex amplitude spectra prior to computing the cross-spectrum. But the results show there is little difference between the results from the raw and the smoothed cross-spectra. We wish to note that the estimated phase lags are consistent with the values obtained from the cross-correlation method in the previous section (see Figure 6.23 and the respective text in Section 6.3.4). A notable feature in the two sites data is the presence of a systematic phase difference, ~ 10 h within the error bars, between the oscillations at London and Saskatoon respectively. It thus appears that the 2-day oscillation is a westward

Interval (daynumbers)	London (h)	Saskatoon (h)
175-182	11.7	10.0
183-190	11.9	13.8
191-198	-	15.7
199-206	17.4	14.2
207-214	9.5	15.5
215-222	-	9.2
Average	12.6 ± 1.7	13.1 ± 1.1

Table 6.3: The phase relationship of the 2-day wave wind components at each site in 1993. The table show the number of hours by which the meridional leads the zonal component.

propagating wave of zonal wavenumber 3, which is consistent with the previous observations in the Northern Summer Hemisphere, but a possible connection with a zonal wavenumber 5 is also observed at certain times. The zonal wavenumber 5 was also reported by Kalchenko [1987]. More comparisons of this kind should be done in order to study these waves.

The phase relationship between the wind components, i.e. the zonal and meridional components, are estimated by using the cross-spectrum method, in a similar fashion to the phase relationship obtained between the sites. An example of the cross spectrum of the winds at London is illustrated in Figure 6.25. Tables 6.3 and 6.4 give the phase relationship between the zonal and meridional components at each sites in 1993 and 1994 respectively. The results show that the meridional component leads the zonal component by $\sim$ 12.62 ± 1.68 h and $\sim$ 13.07 ± 1.14 h at the London and Saskatoon sites respectively in 1993. These values are $\sim$ 10.15 ± 1.85 h and $\sim$ 13.64 ± 0.68 h at the London and Saskatoon sites respectively in 1994. The results of the London site in 1994 should be considered with caution due to small amplitudes in the cross-spectra as noted earlier. These results strongly suggest that the components of the 2-day wave were very close to 90^o during the period of strong 2-day wave activity.

Interval (daynumbers)	London (h)	Saskatoon (h)
175-182	-	14.4
183-190	8.3	12.8
191-198	-	15.3
199-206	12.0	11.5
207-214	-	-
215-222	-	13.9
Average	10.2 ± 1.9	13.6 ± 0.7

Table 6.4: The phase relationship of the 2-day wave wind components at each site in 1994. The table show the number of hours by which the meridional leads the zonal component. Universal time has been used.

6.3.6 Conclusion

Simultaneous observations between the London and Saskatoon sites have shown the existence of the 2-day wave during the late June-early August months, although these observations indicate the presence of the 2-day wave at other times of the year in 1993 and 1994. A subsidiary maximum of about 70% of the summer peak, appears during the late April-May months. The amplitudes of the meridional components (20-30 m/s) are generally larger than the zonal component (15-18 m/s) at the London site in both years. In contrast, at the Saskatoon site the amplitudes of the zonal components ($\sim$ 30 m/s) are larger than the meridional component ($\sim$ 25 m/s) in 1993, but in 1994 both the zonal and meridional components have somewhat comparable amplitudes (25-30 m/s). The amplitude variations with latitude suggest that the amplitude maximizes at low latitudes. It is still not clear whether the meridional amplitude is larger at London than at Saskatoon, although the zonal amplitudes at Saskatoon is larger by a factor of 2-3 than at London. Amplitudes vary from year to year but it is clear that the summer amplification is generally confined to a duration of about 50 days.

The period of the 2-day wave was determined by the complex demodulation method. The period of the wave is found to change with time. The mean periods during the bursts of the 2-day activity are 47.1 ± 1.3 h and 47.3 ± 1.2 h for the zonal component at the London and Saskatoon sites respectively, while the respective mean periods are 46.2 ± 1.4 h and 46.8 ± 1.6 h for the meridional component at the London and Saskatoon sites in 1993. In 1994 the mean period values are 47.2±0.9 h and 47.0±1.2 h for the zonal component at the London and Saskatoon sites respectively, and the respective values are 46.7±1.2 h and 46.1±1.7 h for the meridional component at the London and Saskatoon sites. We note that statistically these periods are not different, which we expect if they are the same wave. It should be noted that the period of the 2-day wave was only taken into account when the wave had a demodulated amplitude greater than 8 m/s. These values are shown to be consistent with the values obtained from the cross-correlation method. The periods determined from the present study are found to be smaller than the 51-52 h period generally suggested by other Northern Hemisphere results.

A striking similarity appears between the 2-day waves at London and Saskatoon. Our observations show significant correlation between the two sites of the 2-day wave during time periods of strong 2-day activity. The cross-correlation coefficient values are found to be between 0.75 and 0.88, particularly in the meridional component in 1993 and 1994.

Our results strongly suggest that the 2-day wave is a westward propagating Rossby-gravity wave of zonal wavenumber 3, assuming the phase difference to be due solely to the difference in longitude. A possible connection with the zonal wavenumber 5 is suggested at one time (early August) in 1994. These results are independently determined by the cross-spectrum and cross-correlation methods. More comparisons should be done in order to study these waves, and also to confirm our measurements.

The phase relationship between the zonal and meridional components was studied at the London and Saskatoon sites using the cross-spectrum method. It was found that the meridional component leads the zonal component by ~ 12-13 h, strongly suggesting the wave components are nearly in quadrature.

Finally, in order to study the complete nature of the 2-day wave at mid-latitudes, it is imperative to continue these investigations. Coordination and intercomparisons are required in order to resolve questions about the generating mechanism as well as to understand better the role of the wave in the middle atmosphere.

Chapter 7

A new VHF interferometer meteor radar

7.1 Introduction

What is a meteor ?

The word "meteor" is derived from the Greek "Meteoros" meaning "things up in the air" or "raised beyond". The upper atmosphere of the Earth is continuously being bombarded by meteoroids which, on encountering the increasing density of the atmosphere produce (if large enough), visible light and a trail of ionization. Typical sizes might be anything from as small as a grain of dusts or larger. Generally meteors enter the atmosphere at velocities ~ 12-72 km/s and quickly vapourize at heights between 80 and 100 km, forming long columns of ionized particles. Appleton in his early observations of the ionosphere, had suspected the sudden appearance of some type of ionization around the E-region to be due to meteors [e.g., Appleton and Barnett, 1925]. Whilst meteors had been studied by radio methods for astronomical interests before 1960 [e.g., McKinley and Millman, 1949] meteor trail movement became a subject of study for observing winds at meteor heights in the 1950s [e.g., Manning et al., 1953]. Since then radar observations of meteors have been carried out for the past 45 years.

7.1.1 The formation of the ionized column

Meteor trails are formed by the ablation of particles whose initial mass lies in the range 10^{-8} to tens of grams, and which orbit the Sun either in individual paths (sporadic meteors) or as members of streams with a common orbit (shower meteors).

When a meteoroid encounters air molecules in the upper atmosphere, the surface temperature of the impinging particle increases until fusion and vaporization begins. Evaporated meteoric atoms then collide with other air molecules, ionizing them and resulting in a neutral column of positive ions and electrons. Therefore, a meteor trail is a column of ionized particles. For radar purposes a trail is characterized by its maximum ionization line density q electrons/metre, which depends on the meteoroid velocity to approximately the power 3.5. If χ is the zenith angle of the meteoroid path then trails are commonly described in terms of the zenithal maximum ionization line density q_z, where:

$$q = q_z \cos \chi \tag{7.1}$$

[e.g., Thomas et al., 1988]. As an example, the value $q_z = 10^{10}\ \mathrm{m}^{-1}$ corresponds to a meteoroid mass of about 10^{-6} g for a velocity $V \sim 35$ km/s.

Once a column of electrons has been produced in the wake of the passage of the meteoroid, it forms an effective reflector to MF, HF and VHF electromagnetic radiation. All radio techniques applied in this field of study depend on the scattering of incident electromagnetic waves from the ionized matter in a meteor trail, and the free electrons in the plasma are important elements in the scattering process.

7.1.2 Underdense and Overdense meteor trails

Two distinct regimes exist in the detection of meteor trails by radar, these being the so-called underdense and overdense conditions. In the underdense regime the radio wave penetrates the trail with little attenuation and each electron acts as an independent scatterer. The echo from such a trail is characterized by a rapid initial rise in echo strength, followed by small amplitude fluctuations due to diffraction effects during the formation of the trail [e.g., Davies and Ellyett, 1949]. In an overdense trail the electron density is sufficiently high that the radio wave does not penetrate the trail, but is reflected by the trail as a whole. This overdense trail behaves more like a macroscopic conducting surface or a small scale ionosphere [e.g., Greenhow, 1952]. These echoes may also show the rapid initial rise in amplitude, followed by diffraction fluctuations. In contrast to underdense trail, the amplitudes remains fairly constant for some time and then rapidly fall to zero. It is usual to express the electron density as a line density, that is, the number of electrons per unit length of the trail. The transition from the underdense to the overdense condition occurs at $q = 2.4 \times 10^{14}$ electrons per metre [Bronsthen, 1983]. It is largely independent of the radio wavelength (for a detailed discussion of the above, see McKinley [1961]).

Booker [1956] showed that meteor trails at a mean height of 95 km reflecting 8 m wavelength (in our case, the wavelength is 7.375 m) waves for more than 0.4 s could be considered as overdense. Overdense echoes can be identified from echo duration exceeding 0.4 s and from the irregular fading of the echo amplitude produced by the interference between the discrete echoes received simultaneously from different parts of the trail with different Doppler frequency shifts (sample plots shown in Figures 7.4 and 7.5, see Section 7.2.2). Recently, Jones et al. [1990] showed that the trails can transgress from overdense to underdense due to dilution of the ionized cloud from reactions of that cloud with ozone (for trails near 80 km height).

For most radars the number of echoes from underdense trails greatly exceeds those from overdense trails, and the proportion increases with increasing radar sensitivity. Echoes from underdense trails are referred to as 'decay-type' echoes due to ambipolar diffusion and/or recombination and attachment, dependent upon the individual meteor's height. In the following sections we confine ourselves to echoes backscattered from underdense trails.

7.1.3 Radar detection of meteors

The ability of the meteor radar to detect underdense meteor trails depends on many factors. If the Gaussian radius of the ionized column is comparable with or larger than $\frac{\lambda}{2\pi}$ (λ = operating radio wavelength) then the radiation backscattered from electrons in the near and far parts of the trail will not be in phase, and these reflected wave components will interefere destructively. The resultant echo will therefore be severely attenuated [e.g., Manning, 1958; Poulter and Baggaley, 1977, 1978]. A long wavelength radar is therefore immediately seen to be preferable. However, there are many drawbacks such as: (1) the size of the antenna array necessary to achieve a high gain; (2) broadcast and natural interference; (3) ionospheric absorption; (4) confusion with ionospheric echoes. Because of these reasons the conventional meteor radars have normally been operated at wavelengths of around 5-15 m.

The factors which determine the amplitude of a radar echo from an underdense meteor trail during the formation and initial evolution of that train have been reviewed (amongst others) by Greenhow and Hall [1955], Greenhow and Newfeld [1955], Greenhow and Hall [1960], McKinley [1961], Olsson-Steel and Elford [1987], Thomas et al. [1988], and Steel and Elford [1991]. The main factors which cause the attenuation in echo amplitude are (1) the initial radius of the trail (2) the finite meteor velocity effect and (3) ambipolar diffusion. The attenuation factors given throughout in this section are those describing the attenuation in amplitude rather than in power.

The initial meteor trail with radius r_0, (usually defined as the half-amplitude half-width of the electron density distribution assumed to be Gaussian), will reduce the returned echo amplitude by a factor

$$\alpha_r = \exp(\frac{-4\pi^2 r_0^2}{\lambda^2}) \tag{7.2}$$

where λ is the radar wavelength [e.g., Baggaley, 1970]. This initial radius is thought to be due to the fact that the evaporating meteoric species initially have forward velocities close to the translational velocity of the meteor (which is in the 12-72 km/s range), this being about two orders of magnitude higher than the diffusive velocities of atmospheric species in the meteor region [Greenhow and Hall, 1960; McKinley, 1961]. The meteor trail is therefore formed with a certain radius and this arises essentially instantaneously. The initial radius of the meteor trial, r_0, in the 80-120 km height range is approximated by [Baggaley, 1980, 1981]:

$$\log_{10} r_0 = 0.019h - 1.92 + \log_{10}(\frac{V}{40}) \tag{7.3}$$

where h is the height in km and V is the meteor velocity in km/s; r_0 is then in m. As an example, if $V = 40$ km/s and $h = 88$ km (this height is taken as an example in this section because we shall see later that height distributions of the meteors peak around 88 km), then $r_0 = 0.56$ m and so for $\lambda = 7.375$ m (as in our case) the initial radius attenuation factor α_r is 0.8, while at $h = 110$ km, $\alpha_r = 0.2$. Considering only the initial radius effect, it can therefore be seen that a 7.375 m wavelength meteor radar has a very low probability of detecting any meteors forming above about 110 km.

The second factor to be considered is the effect of the finite meteor velocity [Kaiser, 1953]. The radio echo is dominated by the contribution of the first Fresnel zone of the trail, which the meteor takes a finite time to cross. If, by the time the meteor has reached the end of this zone, the trail has diffused to reach a width comparable to the wavelength, then the echo amplitude will be severely attenuated. Clearly this effect depends upon the length of this zone, $2\,(\frac{R\lambda}{2})^{\frac{1}{2}}$, where R is the meteor range from the observatory site [e.g., Greenhow and Hall, 1960]. Note that $(\frac{R\lambda}{2})^{\frac{1}{2}}$ is the radius of the first Fresnel zone. The attenuation in echo amplitude is then given by a factor

$$\alpha_V = \exp[-16\pi^2(\frac{D}{V})(\frac{R}{2\lambda^3})^{\frac{1}{2}}] \tag{7.4}$$

where D (m^2s^{-1}) is the ambipolar diffusion coefficient [McKinley, 1961]. Thus, although the first Fresnel zone increases in length with wavelength, in fact the finite velocity effect is reduced by using a longer wavelength. It should be noted that the finite velocity effect has the opposite trend to the initial radius effect; at any particular height the former is more severe for slower meteors. Note also that α_V approaches unity as V becomes very large. According to McDaniel and Mason [1973], the ambipolar diffusion is related to the zero field reduced mobility K by the expression:

$$D = 6.39 \times 10^{-2} \frac{T^2 K}{p} \tag{7.5}$$

where typically $K = 2.2 \times 10^{-4}$ m^{2}s$^{-1}V^{-1}$ and the temperature T (K) and pressure p (Pa) are functions of the height h (km). Using the U.S. Standard Atmosphere D is approximated over the height range 80-125 km by [Thomas et al., 1988]:

$$\log_{10} D = 0.0758h - 6.51 \tag{7.6}$$

As an example, if $h = 88$ km, then $D = 1.45$ m^{2}s^{-1} and so for $V = 40$ km/s, $\lambda = 7.375$ m and $R = 130$ km, we find $\alpha_V = 0.93$. At 110 km, λ_V is dramatically reduced to about 0.04. This shows that detectable echo amplitudes at 7.375 m radar wavelength are generally fairly unlikely above 100 km. It should be noted that, on occasions, larger temperature gradients are found in the meteor region and the relationship between $\log_{10} D$ and h is then no longer linear.

Another influence, (although of little importance here), is that meteors forming at heights of ≤ 78 km have a decreased probability of detection due to the rapid loss of ionization due to the transfer of charge from atomic oxygen ions, with molecular ions being formed [Jones, 1975; Baggaley, 1978, 1979]. At all heights, but especially in the lower regions, wind distortion of trails can lead to the non-observation of many meteors, or the multiple observation of some trails due to glinting as sections of the trail are blown into orientations which are orthogonal to the radar beam [McKinley, 1961; McIntosh, 1969].

The ionized trail dissipates by ambipolar diffusion, turbulence and chemical and ionic processes. Diffusion dominates for a few seconds while turbulence is the chief mechanism for trails lasting 30 s or more. Once the meteor trail has formed, the expansion of the column of ions and electrons due to radial diffusion causes the returned echo amplitude to decay exponentially with time in the manner

$$A = A_0 \exp(\frac{-t}{\tau_d}) \tag{7.7}$$

where A_0 is the initial amplitude and A is the amplitude after time t. The echo decay time constant τ_d is given by

$$\tau_d = \frac{\lambda^2}{16\pi^2 D} \tag{7.8}$$

which defines the duration to $1/e$ of the initial amplitude. Note that τ_d depends only upon the wavelength and diffusion coefficient [e.g., Herlofson, 1948]. Thus at a given λ and D the echoes from all underdense trails decay with the same time constant. Echoes from underdense trails are therefore referred to as 'decay-type-echoes' [Phillips, 1969]. As an example, if $h = 88$ km, $D = 1.45$ m^2s^{-1} and $\lambda = 7.375$ m the decay time constant is 0.24 s. Underdense trails at observable heights therefore have durations of about a few tenths of a second. In contrast to 88 km, at 110 km height the time decay constant is reduced to about 5 ms and trails become very difficult to detect unless the radar wavelength is increased. For example, at $\lambda = 50$ m and $h = 110$ km, the time decay constant has increased to about 0.24 s. It is noteworthy that for wavelengths below 15 m (or frequencies above 20 MHz) the decay time is short compared to the time taken for the wind to distort the trail from its initial straight line. However at long wavelengths (or low frequencies, e.g., 2 MHz) this is no longer the case and most trails are bent from a straight line (or deformed by wind shear) during the life time of the echo. Thus the exponential decay in strength of an echo has fluctuations due to focusing and defocusing superimposed on it, and it becomes difficult to determine the decay time constant.

It is interesting to note that if the pulse repetition frequency (PRF, number of pulses per second) of the radar is low, then it is possible that fast-decaying echoes are less likely to be seen by the radar. That is rapid diffusion of the trail occurs between pulses so that the first observed echo is attenuated by this effect, making meteor detection less likely [Steel and Elford, 1991]. In addition, if the PRF is low the long duration of the echoes (because of the long decay time constant) does lead to confusion between new meteor echoes, drifting meteor trails, and patches of sporadic E-region ionization. Thus an attenuation factor incorporating the effect of diffusion during the inter-pulse period is necessary. This factor is given by Steel and Elford [1991]:

$$\alpha_d = \exp(\frac{-16\pi^2 D}{\lambda^2(\mathrm{PRF})}) \tag{7.9}$$

where the PRF is in Hz. This assumes that the trail is formed just after the instant of passage of a transmitted pulse; a more precise expression for a particular experiment would be dependent upon the exact meteor recognition criteria used (e.g., single pulse return above some threshold, two successive pulses, a running average, etc.) [Steel and Elford, 1991] (also see Section 7.2.2).

The resultant effect of a trail's initial radius, finite velocity of formation and diffusion, is a significant attenuation of the radar echo so that an effective 'ceiling' of about 110 km occurs for observations at 40.68 MHz (corresponds to 7.375 m wavelength).

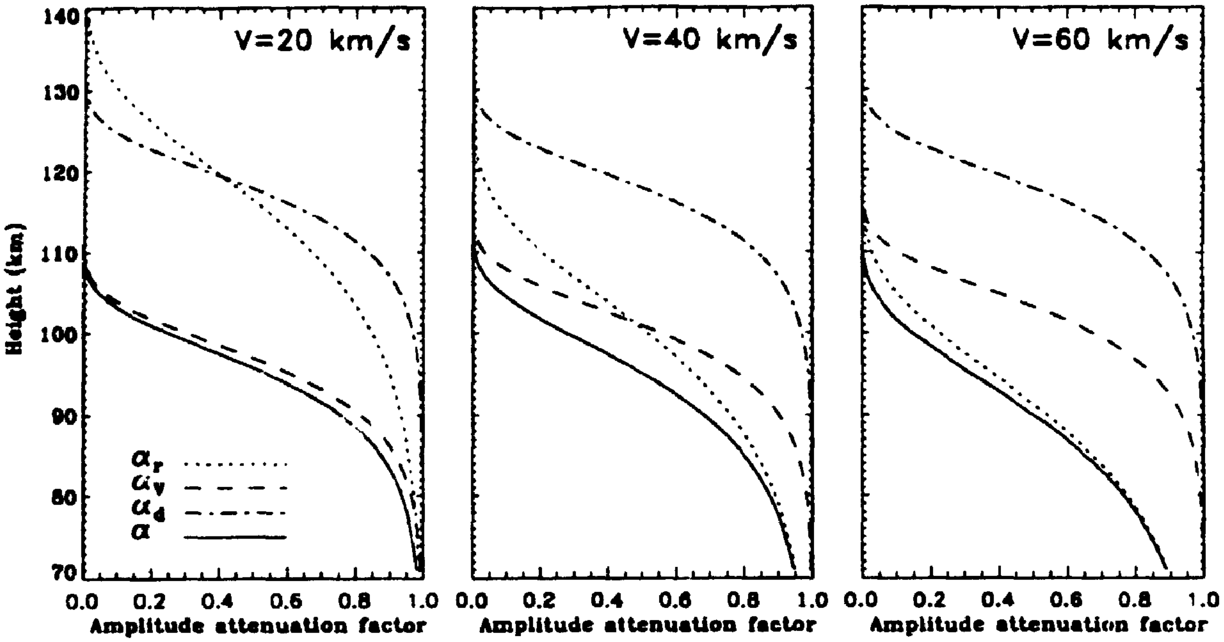

Figure 7.1: Amplitude attenuation factors at f = 40.86 MHz for three different velocities (V = 20, 40, 60 km/s). Input parameters are those used in our data collection at this frequency: PRF = 1100 Hz and range R = 130 km. The dotted line is for the initial radius effect (α_r from equation (7.2)); the dashes are for the finite velocity effect (α_V from equation (7.4)); the dash dotted are for the attenuation due to diffusion between radar pulses (α_d from equation (7.9)); and the solid line is the product of these three quantities (α from equation (7.11)). See the text for more details.

Thus, the average echo height of meteors becomes a function of frequency and can be described by [Greenhow and Hall, 1960; Thomas et al., 1988]

$$h = -17 \log_{10} f + 124 \qquad (7.10)$$

where h is in km and f is in MHz. At 40.68 MHz (as in our case), h = 96.6 km.

The individual attenuations from equations (7.2), (7.4), and (7.9) give a total attenuation in the returned amplitude from an underdense meteor trail of:

$$\alpha = \alpha_r \alpha_V \alpha_d \qquad (7.11)$$

[e.g., Steel and Elford, 1991]. Figure 7.1 shows the attenuation factors for our 40.68 MHz radar frequency. (The method of data collection is described in Section 7.2 of the current chapter.) The values of the four α's are plotted as functions of height at three velocities (20, 40, 60 km/s). The pulse repetition frequency used was 1100

Hz (sometimes we use 2143 Hz, see Section 7.2.1), as in the actual data collection. The range used in the computation was $R = 130$ km since data were collected in the 78-110 km height region; we have assumed $\theta = 53°$, where θ is the angle from zenith (this will be discussed shortly, see Section 7.2.4). At $V = 20$ km/s, the finite velocity effect α_V dominates the net attenuation and $\alpha = 0.5$ at $h \approx 96$ km; but at $V = 40$ km/s, the initial radius term α_r has taken control and $\alpha = 0.5$ at ~ 95 km; at $V = 60$ km/s, the initial radius term totally dominates and $\alpha = 0.5$ at ~ 90 km. This clearly indicates that the radar is insensitive to high velocity underdense meteors.

The initial echo power in watts, from underdense reflection, assuming the initial trail radius to be much smaller than the wavelength employed, is given by the radar equation [McKinley, 1961; Thomas et al., 1988; Steel and Elford, 1991]

$$P_r = 2.5 \times 10^{-32} (\frac{\lambda}{R})^3 P_t G_t G_r q^2 \tag{7.12}$$

where λ is the radar wavelength, R is the echo range, P_t is the transmitted power, G_t and G_r the gains with respect to an isotropic antenna of the transmitting and receiving systems respectively. The above attenuation factors mean that the expression (7.12) for the initial echo power must be modified to become:

$$P_r = 2.5 \times 10^{-32} (\frac{\lambda}{R})^3 P_t G_t G_r \alpha^2 q^2 \tag{7.13}$$

7.1.4 Radar detection of meteors at low frequency

Most meteor radars have customarily been operated at radio frequencies of around 20-60 MHz (5-15 m wavelengths) in order to avoid problems associated with reflection or absorption of the radio wave in the ionosphere. It is suggested that the 'missing mass' in the $10^{-6} - 10^{-2}$ g range of interplanetary material might be held in a faint, high velocity component which could be undetected since it ablates at high altitude [Hughes, 1978]. Hughes [1978] argued that only $3 - 4\%$ of the meteoric mass incident upon the upper atmosphere in the $10^{-6} - 10^{-2}$ g range is being detected by conventional radio meteor techniques. This would imply that the vast majority of meteoric material is deposited into the atmosphere above 100 km, having important ramifications for the aeronomy and other branches of the atmospheric sciences. The existence of such high velocity, low mass meteors would also be significant in relation to the origin and evolution of the meteoroidal complex in the solar system.

Conventional meteor radars, operating at wavelengths of around 5-15 m (20-60 MHz frequency), are unable to detect high altitude meteors due to the wavelength dependent echo ceiling (see Section 7.1.3). The diameter (or width) of an underdense ionized trail increases monotonically with height in the 80-140 km region due to the increase in the molecular mean free path with diminishing air density. Consequently, a rapid growth with height occurs both in the initial radius of a forming trail and also in its rate of expansion due to the mechanism of ambipolar diffusion during the finite time required for the meteor to traverse the central (first) Fresnel zone of the radar (so-called finite velocity effect, also see Section 7.1.3). The echo ceiling begins to act at heights for which the diameter of a trail approaches the dimensions of an appreciable fraction of the wavelength, when destructive interference between waves reflected from the front and back of the trail's cylindrical cross-section causes increasing attenuation of the backscattered signal.

However, recently there have been many observations of the meteors at frequencies below 20 MHz [e.g., Olsson-Steel and Elford, 1987; Elford and Olsson-Steel, 1988; Thomas et al., 1988]. Radars employing such frequencies are potentially able to detect many more underdense meteor echoes than the radars operating at the more conventional higher frequencies. This occurs as a consequence of the greater limiting height for the detection of echoes at longer wavelengths which is set by the so-called underdense ceiling [Greenhow and Hall, 1960; Olsson-Steel and Elford, 1987; Thomas et al., 1988]. Olsson-Steel and Elford [1987] studied the heights of radio meteors at a wavelength of 150 m (2 MHz frequency), for which the echo ceiling is above 140 km. Most observations were made between 0300 and 0700 h local time due to ionospheric activity, which gives rise to other echoes which could be confused with meteors. They found that the height distribution of radio meteors peaks at ~ 104 km. This is approximately 10 km higher than found from measurements at conventional wavelengths, due to the fact that these have a low probability of detecting high altitude meteors. They also found a substantial numbers of meteors above this peak (104 km), right up to the 140 km instrumental limit. Further, there is no sudden drop-off in numbers of meteors above the peak at 104 km. Therefore, they concluded that the 'missing mass', comprising the vast majority of the meteoric input to the atmosphere, ablates well above 100 km. It is noteworthy that the above results have a weakness of large uncertainty in the height determination; the uncertainty in individual meteor heights is ±7 km, due to the inaccuracy of phase measurements. These observations were further substantiated by Elford and Olsson-Steel [1988]. They have measured the height distribution of radio meteors at a frequency of 6 MHz which has the instrumental limitations of heights to $84 < h < 116$ km. In this case, the measurements were only made between 0800 and 1600 h local time, due to broadcast interference from a distant transmitter operating at almost exactly the same frequency as the radar. They found the peak at ~ 105 km, and in line with observations made at 2 MHz

[Olsson-Steel and Elford, 1987]. Unlike at 2 MHz, the 6 MHz height distribution of meteors appears to be symmetric about the peak with a quite rapid drop-off in the number of meteors detected above 105 km. The origin of this difference is probably due to the finite velocity of the meteors and diffusion effects [Elford and Olsson-Steel, 1988].

Steel and Elford [1991] compared the observed height distributions of underdense radio meteor echoes at frequencies of 2, 6, 26, and 54 MHz with a simple model based on the standard meteor echo theory which takes into account of the initial radius effect, the finite velocity effect, and diffusion effect [see Section 7.1.3]. The main features of the measured VHF (26 and 54 MHz frequencies) are predicted by this model, with peaks below 100 km and few meteors detected above 105 km. The main features of the measured MF-HF (2 and 6 MHz frequencies) distributions are also predicted, with peak about ~ 105 km. The model indicates few 6 MHz echoes above 116 km, in line with the observational data, although for the data used there is an instrumental cut-off just above this height [e.g., Elford and Olsson-steel, 1988]. The model suggested that even at 2 MHz possibly 50% of all meteor trails above 105 km remain undetected.

There are many factors influencing the observation of meteors at low radio frequencies (2-6 MHz). Whilst the neutral atmosphere has little effect upon the propagation of radio waves in the VHF band, in the MF-HF band it can cause significant retardation, refraction, absorption and reflection of the waves. Therefore, an experiment with the low frequency radar is not an easy task. The influences of the retardation and refraction could lead to the virtual height of the meteor trail being rather higher than its true height [e.g., Namboothiri et al., 1993]. The retardation arises whenever the background electron density approaches the critical density. Thus the transmitted pulse cannot be assumed to propagate with constant speed at the velocity of light in a vacuum. So the virtual height for a given frequency is always greater than the true height (see also Section 3.2.4). The refraction can also lead to the actual reflection point being displaced from that expected from linear geometry; that is the zenith angle of the ray path at the reflection point could differ from the zenith angle of the ray path at the ground.

Absorption can lead to attenuation of the returned echo signal in this frequency range (2-6 MHz), and hence leaving some meteors undetected. Severe ionospheric absorption sometimes occurs during the day, and also to a certain extent at night due to a substantial degree of ionization present above 80 km. During the daytime the large background electron density in the D- and E-regions make any observations unlikely. Sporadic E ionization could exist throughout some nights, making observations equally improbable. However, at night during the winter and spring months the ionization often falls to a level sufficiently low for meteor echoes to be detected [Brown, 1976]. Observations at a low radio frequency can be made at night if the amount of ionization below the E-region falls to a sufficiently low level, and using a right-hand circularly polarized transmitted beam for which absorption is very small [Steel and Elford, 1991]. For such observations the observational 'ceiling' would be raised so that the observed height distribution of the echoes should be much closer to the true height distribution of the trails.

Strong reflections from the meteor region generally occur until about 0200 h local time, and the morning development of the E-layer occurs quite rapidly after sunrise. Generally, no observations are possible after about 0800 h local time, and often an earlier cut-off is necessary. Even during the night time the background noise (for meteor-detection purposes) is not normally due to receiver or antenna noise, but rather to weak ionospheric reflections which fluctuate rapidly [Olsson-Steel and Elford, 1987]. The presence of F-region echoes, with multiple bounces lasting for 3-4 ms, can lead to confusion with meteor echoes. In this case, a low pulse repetition frequency (e.g., 20-25 Hz frequency or 0.04-0.05 s interval between pulses) is desirable in order to obviate confusion due to multiple bounce F-region/ground echoes. On the other hand, the low PRF pulses are unable to detect the fast decaying echoes so that the number of meteor echoes will be greatly reduced; at higher altitudes the reduction is even more severe (see Section 7.1.3).

7.1.5 Specular reflection and meteor trail drift

The radio echo from a meteor trail at the wavelengths used in drift studies is essentially of the diffraction type, where destructive interference reduces the returns from most parts of the trail so that only the first Fresnel zonal contributes effectively to the echo. In meteor studies the size of the first Fresnel zone is usually of the order of 1 km ($\approx 2(\frac{R\lambda}{2})^{\frac{1}{2}}$ near 88 km, as in our case) [McKinley, 1961], and the specular reflection point on a meteor is generally located within this zone. The specular reflection point (for a station or pair of stations) is the point on the trail at minimum distance from the station, or minimum sum of distances from a pair of stations [Grossi et al., 1972]. The process of detecting meteor trails with backscatter radar (as in our case) is a specular one, with the majority of the reflected energy coming from the first Fresnel zone about the specular reflection point. However, for overdense trails the radar echo lasts long enough to be deformed by wind shears, producing more than one specular reflection [Booker, 1956].

Does the column drift as the neutral wind, or does the presence of the Earth's magnetic field modify the motion ? It had always been assumed in the past that below 100 km or so the ionized matter in a meteor trail shares the motion of the atmosphere in which it is formed, so that the apparent drift of a meteor relative to a radar station may be interpreted as the sole effect of the upper atmospheric wind. That is, meteor trails, with a short life time (≤ 0.4 s), were expected to drift with the local neutral wind because of the high ion-neutral collision frequency (about $3 \times 10^5 s^{-1}$). It is questionable whether this assumption is justified in all cases since we must obviously consider the effect of the geomagnetic and electric field on the movement of a plasma at these heights. The situation has been reviewed by Kaiser et al. [1969] in a theoretical paper, and their results essentially confirm that below 95 km the effects of the geomagnetic field may be ignored because the collision frequency of the electrons (and ions) is much greater than their gyrofrequency, and the ionized medium will therefore behave in the upper atmosphere wind as part of the neutral gas. However, care must be taken when the meteor trail is closely aligned with the Earth's geomagnetic field (within a degree or two) [e.g., Kaiser et al., 1969], or possibly during periods of high geomagnetic activity when the ionized trail motions can be affected by very strong electric fields [e.g., Reid, 1982]. While theoretical discussion of this possibility continues, no concrete evidence has yet been forthcoming that other than the neutral wind is being measured over the height range 80 to 100 km. Thus under average conditions, the atmospheric motions at meteor heights should be deducible from the meteor radar returns. We may, therefore, assume with confidence that the general drifts studied in this chapter by the radio meteor method are representative of neutral air motions.

7.1.6 Continuous wave and pulse techniques

A number of techniques are used at present to investigate movements of neutral atmosphere between 80 and 100 km. The meteor winds radar technique has been generally recognized as being an extremely valuable method for studies of atmospheric wave dynamics in the 80-100 km height range of the atmosphere since the initial tidal motions by Greenhow [1954] and Elford and Robertson [1953].

Generally meteor radars operate at VHF frequencies of 20-60 MHz and employ either continuous wave (cw) or pulse techniques. Both cw and pulsed techniques have been favoured by individual research groups in the past, each stressing the particular merits of their chosen technique. It can be shown that the optimum theoretical sensitivity of a backscatter radar is independent of its mode, whether cw or pulsed, and only dependent on the mean power. For a cw system this is the actual output, whilst for a pulsed system it is the peak pulse power multiplied by the duty cycle (where duty cycle = pulse width × pulse rate, also see Section 3.2.4). The situation will be appreciated if we consider that although a pulsed radar can develop much greater instantaneous power levels than cw radar, a finite bandwidth has to be employed in order to resolve echo pulses without excessive distortion, and that bandwidth must be at least equal to the reciprocal of pulse length. The system noise power is proportional to its bandwidth, so that the signal-to-noise ratio, cannot be improved by increasing the peak transmitter power for a given mean power. In a cw system, on the other hand, the maximum bandwidth can be much smaller than in the pulsed system, with a resulting reduction in noise power so that a good signal-to-noise ratio may be achieved with comparatively low power levels.

In practice, the performance of a cw system is likely to be reduced owing to the presence of man-made (human) radio interference which is easily picked up by a low-noise receiver. There is increasing congestion of stations in the band of radio frequencies used for meteor wind studies. Because of the regular pulse spacing and wider receiver bandwidth, pulsed systems are able to distinguish positively between very small short duration meteor echoes and much larger unwanted interference signals. A further disadvantage of cw systems lies in the presence of short range echo signals due to reflection from aircraft, and these may at times obliterate echoes from the meteor trail. In a pulsed system such unwanted echoes can be easily discriminated or effectively suppressed. Another advantage of the pulsed system is that the range and range resolution (equivalent to pulse delay and pulse width) are easily discriminated compared to the cw system.

Perhaps the best way to compare the efficiency of one system to that of another is to look at the published figures for the hourly rates of meteor echoes. Such a comparison was carried out in the past by (amongst others) Greenhow [1954] and Spizzichino [1971]. Spizzichino [1971] showed that the peak hourly value in the diurnal rate curve is about 120, dropping to 26 at the time of minimum meteor activity for their 5 kW cw system. Greenhow [1954] observed a peak rate of 282/h at the same time of the year, decreasing to a minimum of 54 for a mean power of 150 W pulsed system. It thus appears that comparison of two systems, all operating, near frequencies of 30 MHz, comes out in favour of pulsed radar as far as the available meteor echo rate is concerned, on which the reliability of a wind measurement ultimately depends. A further advantage of a pulsed system is that the transmitter and the receiver may be located at the same place, and the same aerial may be used for transmission and reception, whereas a cw system has to be bistatic, i.e., transmitter and receiver must be well separated geographically, preferably utilizing topographical features such as hills or valleys in order to reduce the effect of the direct wave at the receiving end. Our meteor radar operates at VHF frequency and employs the pulsed technique. The experiment description and the method of data collection will be described in the following section.

7.2 Meteor wind analysis

7.2.1 Experiment description

The initial objective of a UWO VHF atmospheric radar was to study the winds and turbulence below 10 km in the troposphere. However, the idea that the new system might be extended to include a "meteor-mode" of operation evolved from earlier considerations of a general nature concerning the feasibility of using VHF radars for meteor work. With this in mind, the VHF radar was designed to study winds in the troposphere using clear air scatter as well as in the mesopause region using meteors. The system has proven an excellent tool for a variety of meteor experiments and is now used routinely to measure atmospheric winds at meteor heights. The operation time is distributed between the meteor-mode and the ST (Stratosphere-Troposphere) mode, so that continuous observation of meteor winds of a whole month is not generally achieved. However a minimum of five day data sets of meteor observations are long enough to study the mean winds and tides at a given station [Forbes, 1985]. In this section we describe the main features of the meteor mode system. The detailed description of the design strategy and the system implementation of the UWO VHF atmospheric radar can be found in Appendix 1 [Hocking, 1994].

The UWO VHF interferometer meteor radar described here is located at the Environmental Science Western Facility near the University of Western Ontario in London, Canada (43° N, 81° W). The radar operates at a frequency of 40.68 MHz which corresponds to 7.375 m wavelength. Peak power is 5 kW and the duty cycle is ~ 1.47%. Pulse length is 13.33 μs which is equivalent to 2 km range resolution. A pulse repetition frequency (PRF) of 1100 Hz was used in the beginning of the operation (from July 1994 to Dec 1994) and later (from Jan 1995) increased to 2143 Hz in order to increase the meteor echo rate. It is noteworthy here that the PRF of 2143

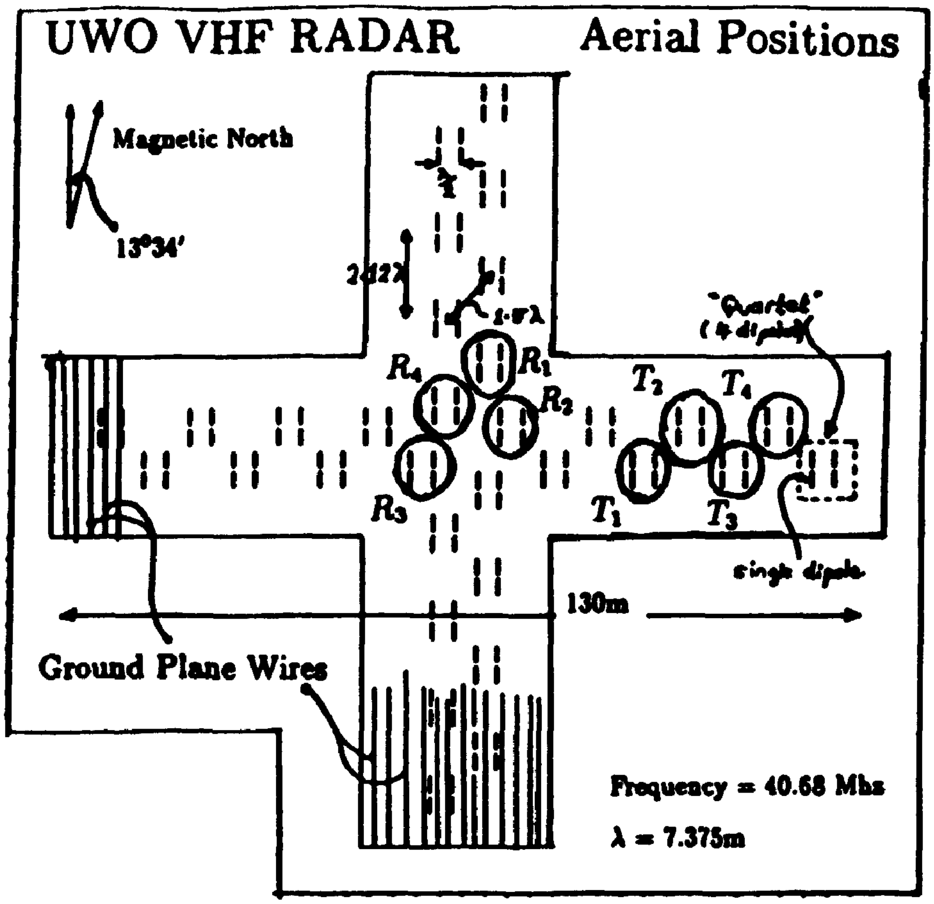

Figure 7.2: The configuration for the antenna system of the UWO VHF radar. In meteor mode, the T_1, T_2, T_3 and T_4 antennas are used simultaneously for transmission, and the R_1, R_2, R_3 and R_4 antennas are used for reception. A detailed description of the design strategy and the system implementation of the UWO VHF atmospheric radar can be found in Appendix 1 [Hocking, 1994].

Hz is carefully chosen so that there is no ambiguity in the ranging (for more details see Section 3.2.5 - range aliasing). A 16 point coherent smoothing was performed on the raw data to improve the signal to noise ratio. In meteor mode, we use a single receiver which has the ability to multiplex signals from 4 separate input receivers (see Appendix 1 for more details). Therefore we attain a sampling time interval of ~ 58 ms when using 1100 Hz PRF and ~ 30 ms when using 2143 Hz PRF.

Since July 1994 the radar has been used to measure horizontal winds. Vertical winds can also be calculated, but their reliability is unknown and these will not be discussed in this chapter. The meteor radar described here has been designed to provide near all-sky coverage and to measure any Doppler shift in the frequency of a meteor echo.

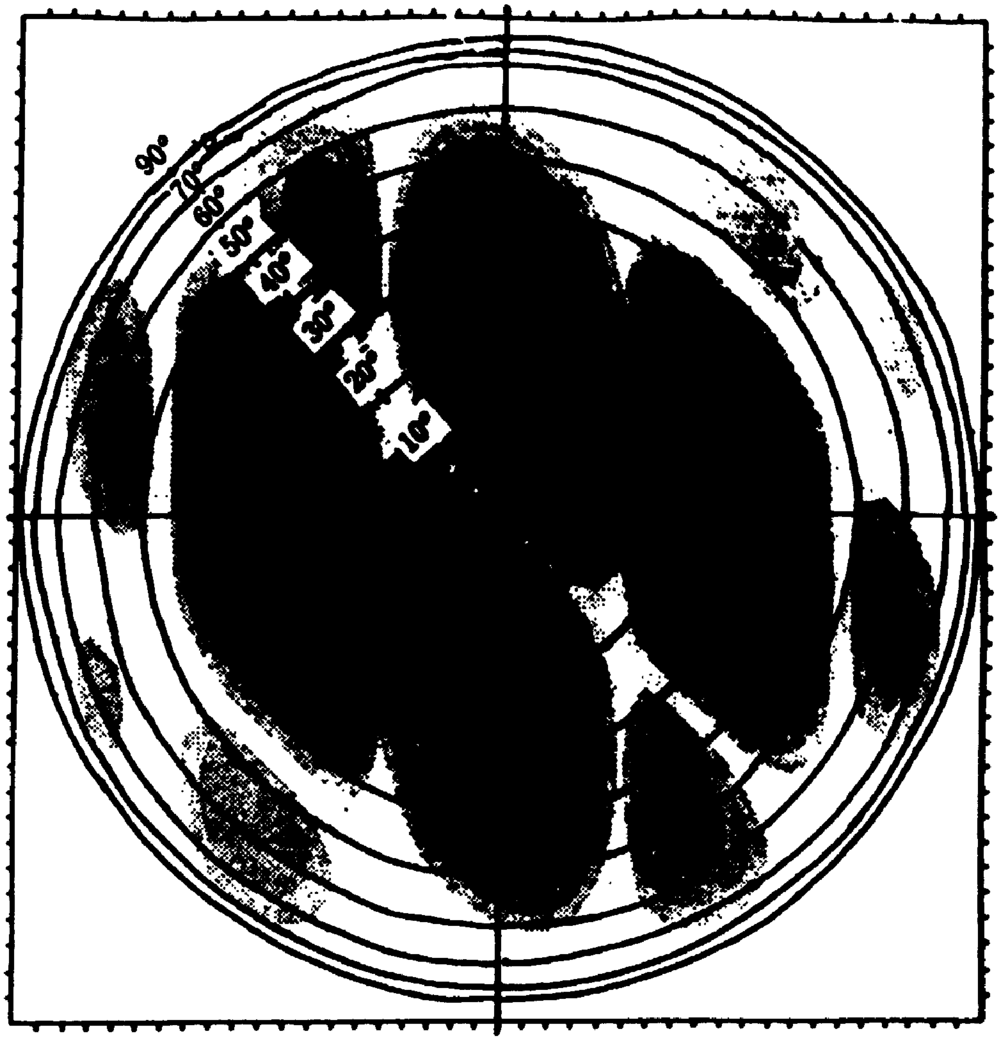

Figure 7.3: The polar diagram of the array. Contours are in 3 dB steps. This graph shows the polar diagram out to 90° from zenith, and clearly shows the significant reduction in signal at angles beyond 50° from vertical.

In addition, the radar operates in an interferometric mode on these occasions, so the meteor locations can easily be determined.

The configuration for the antenna system of the UWO VHF radar is sketched in Figure 7.2. Each antenna-group consists of 4 half-wave dipoles at the corners of a square. The dipoles are suspended $\frac{\lambda}{4}$ above the ground plane, where λ is the radar wavelength. The distance between each dipole of a "quartet" is $\frac{\lambda}{2}$. This arrangement ensured minimal radiation of RF (Radio Frequency) energy along directions parallel and perpendicular to the dipoles. Such "quartets" are configured in a staggered pattern as shown in Figure 2 [see Appendix 1, Hocking, 1994]. In meteor mode, the T_1, T_2, T_3 and T_4 antennas are used simultaneously for transmission, and the R_1, R_2, R_3 and R_4 antennas are used for reception. By phasing antennas T_2 and T_4 to be π out of phase with respect to T_1 and T_3, we force the transmitter polar diagram to look like 4 separate, broad beam pointing about 25° off-zenith to the north, south, east and west (see Figure 7.3). Each such beam has a half-width of about 25°. This arrangement ensures that maximum power is radiated in these 4 directions, but we emphasize that all meteor direction determinations are done by interferometry.

Another advantage of this configuration is that receiving antennas R_1 and R_2 are only 0.53 λ apart in the east-west direction, and R_2 and R_3 are only 0.53 λ apart in the north-south direction. The coordinates (in metres) of the receivers relative to (0,0) are: R_1 - (-7.82, -3.90); R_2 - (-3.91, 7.82); R_3 - (7.82, 3.91); R_4 - (3.91, 15.63) in meters. The more conventional spacing of $\frac{\lambda}{2}$ would have eliminated the region of ambiguity but coupling can be severe in this case. Our configuration turns out to produce reliable results and all quartets are at least 1.5 λ apart, thereby eliminating (almost) coupling effects between receiving antennas. This will be further discussed shortly.

In the following sections we describe the specific analysis algorithms that we used to measure the atmospheric winds at meteor heights. These are choices made after processing a number of synthetic and real data records.

7.2.2 Meteor detection algorithm

Meteor echoes are detected in the following manner. The meteor detection algorithm basically just searches for a place where two successive amplitude points exceed a threshold value compare to the mean noise level (fast-rising signals) of the time series. After several trial and error tests, it turns out that if the average amplitude of the pair of successive points exceeds 3σ, where σ is the root-mean-square amplitude over a length of 2.5 s of data, then amplitudes following these initial two larger successive peaks are examined, and if a large amplitude points last for long enough (i.e. not impulsive spikes), then the corresponding interval in the time series is identified as being a possible meteor. It is also required that no secondary peaks occur in a region up to 2.5 s after the original large amplitudes. There is evidence of overdense echoes which can last up to 10's of seconds, but it was decided to use the time interval of 2.5 s in order to eliminate false detections such as aircraft, random noise, etc. in the meteor detection procedure. Once the meteor is detected the algorithm also checks a few points back from the maximum amplitude of the location of the meteor trail to test whether the echo is characterized by a rapid initial rise in amplitude, followed by small amplitude fluctuations. This procedure successfully rejected the data if there was any beating (generally, overdense echoes have very long lifetimes and the trail can be distorted by the wind field, possibly producing multiple reflection points whose scattered signals beat with each other) present in the echo, or any other irregularities (e.g., two meteors observed within a short time interval) present due to trail distortion. After several tests, it turns out that the maximum amplitude is reached frequently within $\frac{1}{10}$ s, and it was decided to use this value as a reliable time limit in the meteor detection procedure. Any slowly rising echo is rejected by the program. This procedure successfully rejected the long meteors, aircraft, E-region echoes (e.g., sporadic E) and possible turbulence scatter. Studies of several hundred meteor observations using this algorithm show it is a reliable discriminator of meteors.

For comparison with the above time scales, a 40 km/s meteor at range 130 km (maximum range used in our case) takes $\sim$ 0.03 s ($\approx \frac{2\sqrt{R\lambda/2}}{V}$) to cross the first Fresnel zone, so that the rise of the echo is comparatively rapid. All rise times would be less than 0.1 s, corresponding to a meteor velocity of 12 km/s. The decay time constants for $\lambda = 7.374$ m are $\sim$ 1.36 s at 78 km, $\sim$ 0.24 s at 88 km, and $\sim$ 0.04 s at 110 km (see also Section 7.1.3). Therefore, the meteor echo must persist for $>$ 1.46 s to be recognized above 78 km. The data interval of 2.5 s is considered to be a good choice. The sampling time interval (time duration between successive points) is $\sim$ 0.058 s when using 1100 Hz PRF and $\sim$ 0.030 s when using 2143 Hz PRF. This indicates that some echoes above 110 km will be rejected by the processing; that is, the returned echo amplitude is sufficient for detection but the data processing scheme causes some of these high altitude meteors to not be recorded.

A typical underdense meteor echo is illustrated in Figure 7.4. The duration of the echo can be seen to be $\sim$ 200 ms. A typical overdense meteor echo is illustrated in Figure 7.5. The duration of the echo can be seen to be $\sim$ 800 ms. The cross-correlation

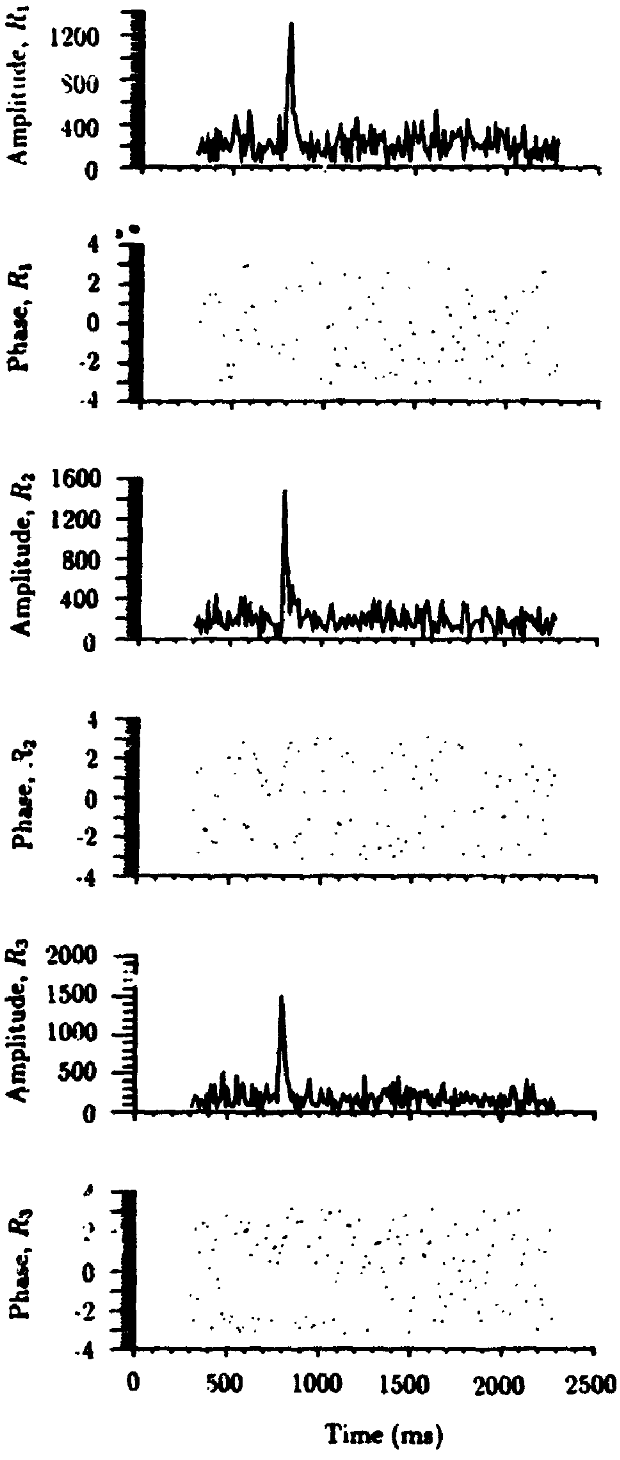

Figure 7.[illegible] The amplitude and phase of a typical underdense meteor echo detected with the VHF meteor radar.

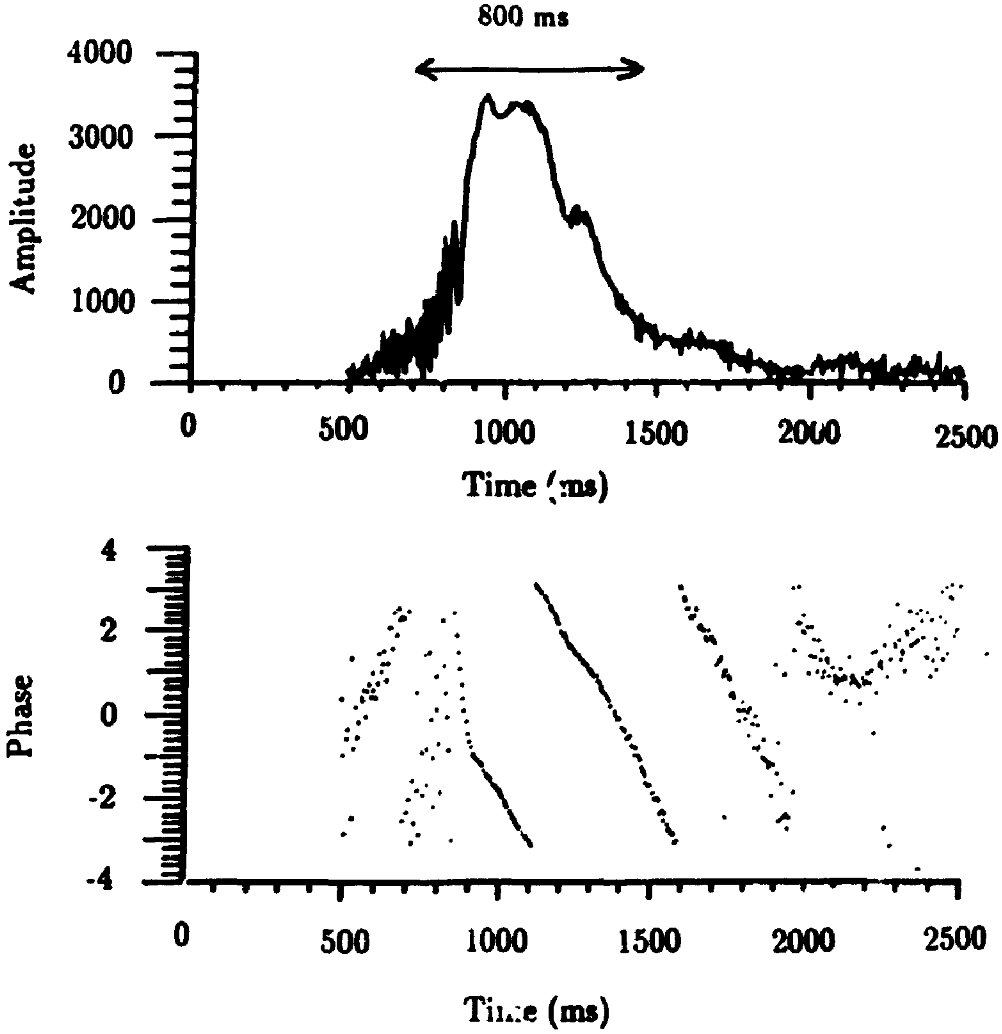

Figure 7.5: The amplitude and phase of a typical overdense meteor echo detected with the VHF meteor radar.

between the complex data recorded on each receiver is used along with the phase differences near zero lag to deduce the angle of arrival. The information which is of most interest for the calculation of wind velocities is the variation of the phase of the echo. It can be seen that once the trail is fully formed, the phase varies linearly with time (see Figure 7.5). The rate of change of phase is due to the trail drifting in the background wind, so that the slope of the phase gives us the Doppler shift of the signal and hence the radial velocity of the trail. When more than three receiver antennas are used consistency checks are possible which allow further validation that we truly have a meteor. The procedures used with our radar are described in Sections 7.2.7 and 7.2.8.

7.2.3 Measurement parameters

In order to determine the variation with height and time of the wind field in the meteor region, the following parameters of each echo must be determined.

1. The range of the echo.
2. The line-of-sight drift of the trail.
3. The echo arrival angle.
4. The wind components over the whole sky.

7.2.4 The range of the echo

Ranging, or measurement of the range to a target, is an important function of radar. In our case, the ranging is made by measuring the time delay of the received echo from the meteor trail with respect to the transmitted signal.

As long as the refractive index n satisfies the condition $\mid n-1 \mid \ll 1$ along all of the radio wave path, the speed of the radio wave can be well approximated by that in free space (see equation 3.3; the error in this approximation is given by equation 3.7). In the lower and middle atmosphere (below about 100 km) $\mid n-1 \mid < 10^{-3}$ as shown in Figure 3.1, so that the error is negligible for all practical applications.

Assuming $n = 1$, the range of a stationary meteor trail is given by

$$R = \frac{cT_R}{2} \tag{7.14}$$

where c is the speed of light in vacuum and T_R is the time interval between the pulse transmission and detection. The factor of 2 appears in the denominator of equation (7.14) because T_R corresponds to the round-trip time time interval for radio wave propagation over the range R. Once the range of the meteor trail is known, the height of the echo is given by

$$z = R \cos \theta \tag{7.15}$$

where θ is the angle from the zenith. With range and zenith angle available for each meteor, the echo height could be calculated. There is evidence that meteors seldom occur below 78 km and above 110 km (at the wavelength of 7.375 m). Therefore we used 130 km as the maximum range record in our analysis procedure. This determines the largest angle which a meteor can have is $\theta \approx \arccos(\frac{78}{130}) = 53°$. This limitation of the maximum range also helps to reduce the degree of ambiguity (the degree of ambiguity of the meteor detection will be further discussed in the following sections).

7.2.5 Radar interferometer

Interferometry can be defined as making use of phase differences between signals received at two or more spatial locations. In optics, phase differences are seen as bright and dark fringes, and have been studied since the work of Young and Fresnel early in the nineteenth century. At the radio frequencies used for atmospheric radar measurements (typically 2-1000 MHz), it is now possible to measure the phases of the received voltages on two or more antennas simultaneously.

The interferometer technique has been extensively used in radio astronomy [e.g., Kraus, 1966] and also for radar applications [e.g., Wohlleben and Mattes, 1973]. Under special conditions it was also employed in atmospheric investigations [e.g., Pfister, 1971; Woodman, 1971; Farley et al., 1981; Whitehead et al., 1983], although only Farley et al. [1981] use the name "radar interferometry". First attempts to apply it to VHF radar investigations of the lower and middle atmosphere were reported by Röttger and Vincent [1978], Vincent and Röttger [1980], Röttger [1983], Royrvik [1983], and Ierkic and Röttger [1984]. The interferometer method was also applied to investigation of the middle atmosphere with a MF radar [Adams et al., 1985].

In an idealized one-dimensional form, a radar interferometer consists of two separated receiving antennas, each with it's own receiver, and a single transmitting antenna, which could be either a third antenna or one of the two receiving antennas. Suppose all the antennas are pointed vertically and that there is a single small (e.g., a point) target located at some small angle θ from the zenith in the plane defined by the vertical and the line joining the centres of the two receiving antennas. If the range to the target is much greater than the separation, d, between the receiving antennas (as is always the case for meteors), then there will be a small time delay, given by $\frac{d\sin\theta}{c}$ (where c is the speed of light in free space), between signal reception at the two antennas. This delay translate into a phase difference of

$$\Delta\phi = (\frac{2\pi}{\lambda})d\sin\theta \tag{7.16}$$

where λ is the radar wavelength. In the absence of noise, this phase difference can be measured easily by forming the complex cross-correlation of the two signal voltages. The preceding discussion describes one-dimensional radar interferometry. How one applies these concepts depends on the experimental configuration used to collect the data. By extending this to four spaced-antenna systems (as in our case) and adding range-gating, we can derive the information needed to determine the scattering point locations in three dimensions.

7.2.6 Ambiguity of the meteor direction

The direction of arrival of the reflected wave is measured by a phase comparison method discussed in the previous section. The ambiguity of meteor direction (i.e. θ) arises whenever the spacing of the receiving antennas is more than $\frac{\lambda}{2}$ (see Figure 7.6). This may be explained in the following manner. Suppose that two receiving antennas R_1 and R_2 are separated by $\sim$ 1.68 λ (this values is taken as an example because we shall see later that R_1 and R_2 are 1.68 λ apart in our intended interferometer antenna configuration, see Figure 7.8; here we shall assume that meteor occurs at zero azimuth angle compared to the Figure 7.8), the phase difference $\Delta\phi$ is related to the zenith angle of the reflection point (θ) by equation (7.16)

$$\Delta\phi = (\frac{2\pi}{\lambda})(1.68\lambda)\sin\theta \tag{7.17}$$

or

$$\Delta\phi = 302.4^o \times \sin\theta \tag{7.18}$$

This relation does not allow an unambiguous determination of θ since the antenna separation is more than $\frac{\lambda}{2}$ wavelength. Thus there will be always a 2π or -2π ambiguity in the measurement of meteor arrival angle. For a measured phase difference of $\Delta\phi = 80^o$, the echo could be arriving at angle $\theta \approx 15^o$ from the zenith (meteor A), but it could also be coming from $\Delta\phi = 360^o - 80^o = 280^o$, corresponding $\theta \approx 68^o$ from the zenith (meteor B). It is not possible to say with certainty which angle is

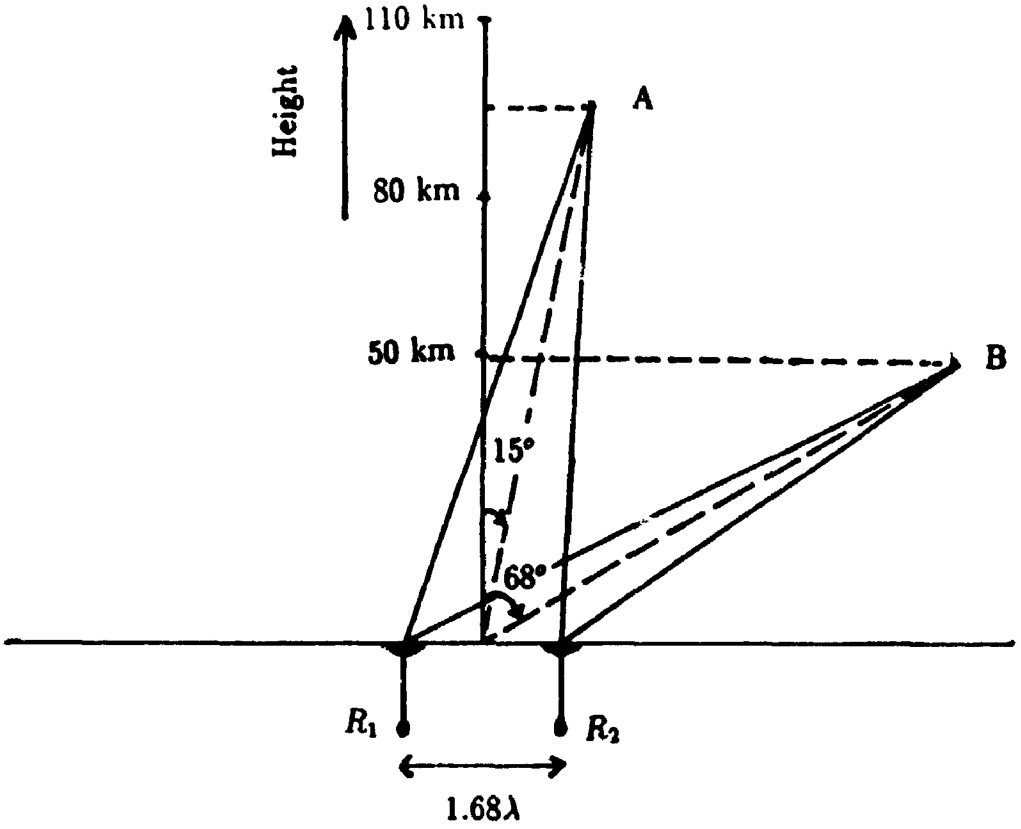

Figure 7.6: Diagram showing the method of determining the direction of meteor arrival (θ), from the receiving antennas R_1 and R_2 separated by more than $\frac{\lambda}{2}$. See the text for more details.

actually measured. This ambiguity was alleviated in the following manner. Taking 78 and 130 km (maximum range recorded in our analysis procedure) as being limits to the heights of meteors, unambiguous meteor echoes could be detected in this region. Therefore the echo arriving at angle $\theta \approx 68°$ (corresponding to $R\cos\theta \approx 49$ km) was rejected based on this height rejection criteria (see also Figure 7.6). These heights limit also alleviated problems due to other ionospheric echoes occurring around the times of observation. There are also a substantial zone in which ambiguous meteor echoes could be detected. The range of zenith angles from which meteors echoes could originate is therefore limited to $0° < \theta < 53°$ (see also Section (7.2.4)). It also later turns out that large errors of the velocity estimations are associated with echoes originating from overhead. After several tests, we decided to reject the echoes which originate from $\theta < 12°$. This place a quite a severe restriction on the number of acceptable echoes, but ensures that each echo accepted meets the requirements placed on echo arrival angle. We have used a four antenna interferometer to determine the zenith angle of the echoes. The fourth antenna is essentially used to check on the zenith angle and to resolve ambiguities in each arrival angle determination. With consideration of the above, the echo arrival angle is determined with high degree of unambiguity. The mathematical approach for the echo arrival angle will be presented in Section 7.2.9.

7.2.7 The Doppler principle

Meteor radars determine winds in the middle atmosphere by measuring the Doppler shift of the signal reflected from ionized meteor trails. These trails of ionization persist for sufficient time to enable a wind measurement to made (typically ≥ 0.1 s). The Doppler frequency shift of echoes from a moving meteor trail relative to the radar is given by

$$f_d = -\frac{2f_R}{c}V_R \tag{7.19}$$

where f_d is the Doppler frequency, f_R is a radar frequency, c is the speed of light, and V_R is the line-of-sight velocity away from the radar, which is the radial velocity in our case. A positive frequency shift denotes an approaching echo and a negative frequency shift denotes a receding echo. The Doppler frequency shift can also be written as:

$$f_d = \frac{1}{2\pi}\frac{d\phi}{dt} \tag{7.20}$$

where $\frac{d\phi}{dt}$ is the rate of change of phase. The rate of change of this phase is due to the trail drifting in the wind, so that the slope of the phase (Figure 7.7) gives us the Doppler shift of the signal and hence the radial velocity of the trail. Thus equations (7.19) and (7.20) yield

$$V_R = -\frac{\lambda}{4\pi}\frac{d\phi}{dt} \tag{7.21}$$

where $f = \frac{c}{\lambda}$. Therefore, the radial velocity can be determined if the rate of change of the relative phase is known.

7.2.8 Phase and radial velocity determination procedure

We have adapted the complex cross-correlation method to measure the phase differences between the receiving antennas in order to determine the echo arrival angle, and have used both the complex auto- and cross-correlation methods to measure the

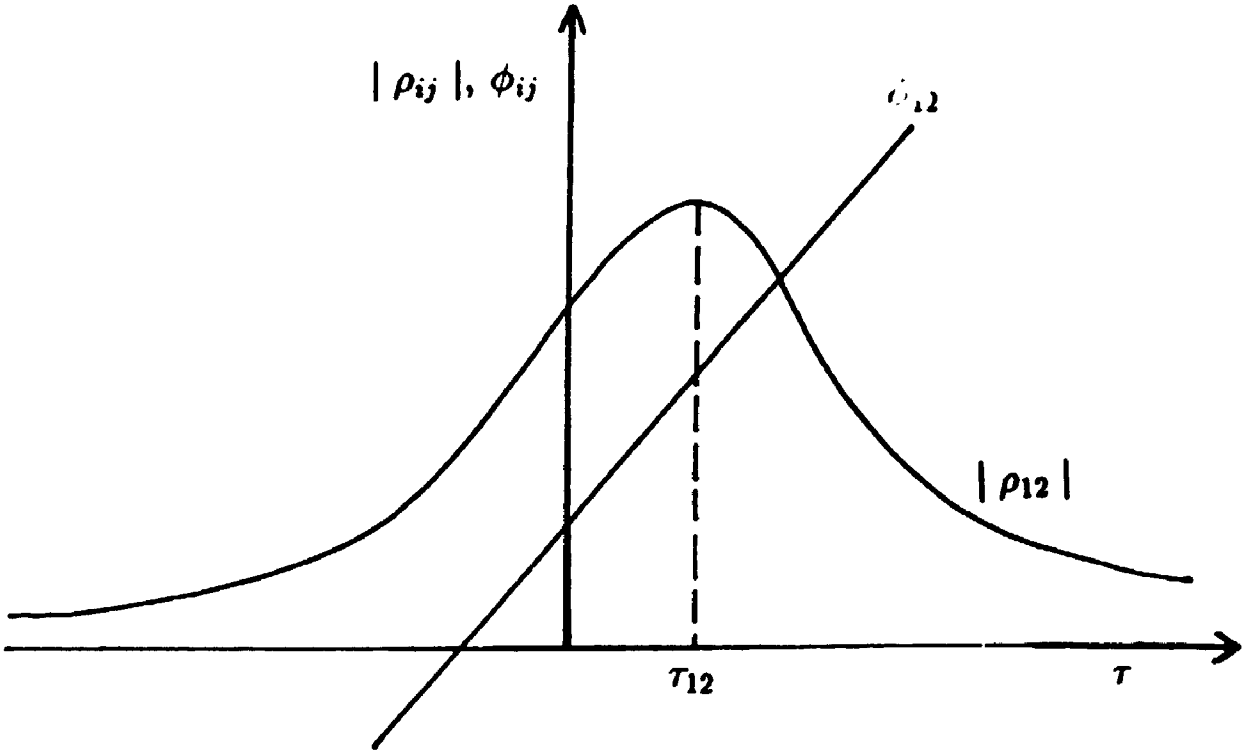

Figure 7.7: Cross-correlation of two complex signals measured at two spatially separated receiving antennas. The quantity $| \rho_{ij}(\tau) |$ is the amplitude, and $\phi_{ij}(\tau)$ is the phase of the cross correlation function. See the text for more details.

rate of change of the relative phase in order to determine the radial velocity of the meteor trail. This radar interferometer method is sketched in Figure 7.8. When we apply the interferometric technique with two receiving antennas R_1 and R_2, we can compute the complex cross-correlation function of the signals measured at R_1 and R_2 (Figure 7.7). The cross-correlation function of signals measured at one receiving antenna R_1 ($i = 1$) and the other receiving antenna R_2 ($j = 2$) is

$$\rho_{ij}(\tau) = | \rho_{ij}(\tau) | \, e^{i\phi_{ij}(\tau)} \tag{7.22}$$

where τ is the temporal displacement, $| \rho_{ij}(\tau) |$ is the amplitude, and $\phi_{ij}(\tau)$ is the phase of the cross-correlation function. The phase $\phi_{ij}(0)$ at zero lag ($\tau = 0$) yields the phase difference between the receiving antennas and can be related to the mean angle of arrival of the backscattered signal (see equation (7.16)). The radial velocity, V_R, is determined by measuring the time derivative of the phase near zero lag from both the auto- and cross-correlation functions. The equation (7.21) can be re-written as:

$$V_R = -\frac{\lambda}{4\pi}\frac{d\phi_{ij}}{d\tau} \tag{7.23}$$

We have used $\phi_{ij}(\tau)$ at $\tau = -1, 0, 1$ to measure the rate of change of phase. In order to measure the rate of change of phase, we used all combinations of i $(i = 1, 4)$ and j $(j = 1, 4)$. We avoided the duplicated combinations such as $\phi_{12}(1) = \phi_{21}(-1)$, $\phi_{11}(-1) = -\phi_{11}(1)$, etc. In all, there are 32 independent combinations of phase values to determine the rate of change of phase; as seen later, if there is too much variability between these various estimates then we reject the meteor.

7.2.9 The echo arrival angle

Our intended interferometer antenna configuration is given by Figure 7.8. The echo arrival angle is measured with a four antenna interferometer. The direction of the echo is obtained by comparison of the phase of the echo signal at four receiving antennas. A set of possible directions is obtained from the receiving antennas R_1, R_2, and R_3, while the antenna R_4 is sited for optimum resolution of the ambiguity. The point P represents the specular reflection point of a meteor trail which is drifting in the direction of (θ, ψ) with respect to (0,0) where θ and ψ represent the zenith and azimuth angles. The positive azimuth angle is measured in the anti-clockwise direction from eastward direction (x-axis).

The unit vector giving the direction of the specular reflection point can be written as

$$\vec{I_R} = \sin\theta\cos\psi\vec{i} + \sin\theta\sin\psi\vec{j} + \cos\theta\vec{k} \tag{7.24}$$

where $\vec{i}$, $\vec{j}$, and $\vec{k}$ unit vectors in the x, y, and z directions. The position vector of the receiving antenna R_1 is given by

$$\vec{R_1} = d_1\cos\psi_1\vec{i} + d_1\sin\psi_1\vec{j} + 0\vec{k} \tag{7.25}$$

Therefore, the phase of the signal received at R_1 with respect to (0,0) is given by:

$$\phi_1 = \frac{2\pi}{\lambda}(\vec{R_1}\cdot\vec{I_R}) \tag{7.26}$$

substituting (7.24) and (7.25) into (7.26), after some manipulations, one obtain

$$\phi_1 = (\frac{2\pi}{\lambda})d_1\cos(\psi - \psi_1)\sin\theta \tag{7.27}$$

Similarly, the phases of the signals received at R_2 and R_3 are:

$$\phi_2 = (\frac{2\pi}{\lambda})d_2\cos(\psi - \psi_2)\sin\theta \tag{7.28}$$

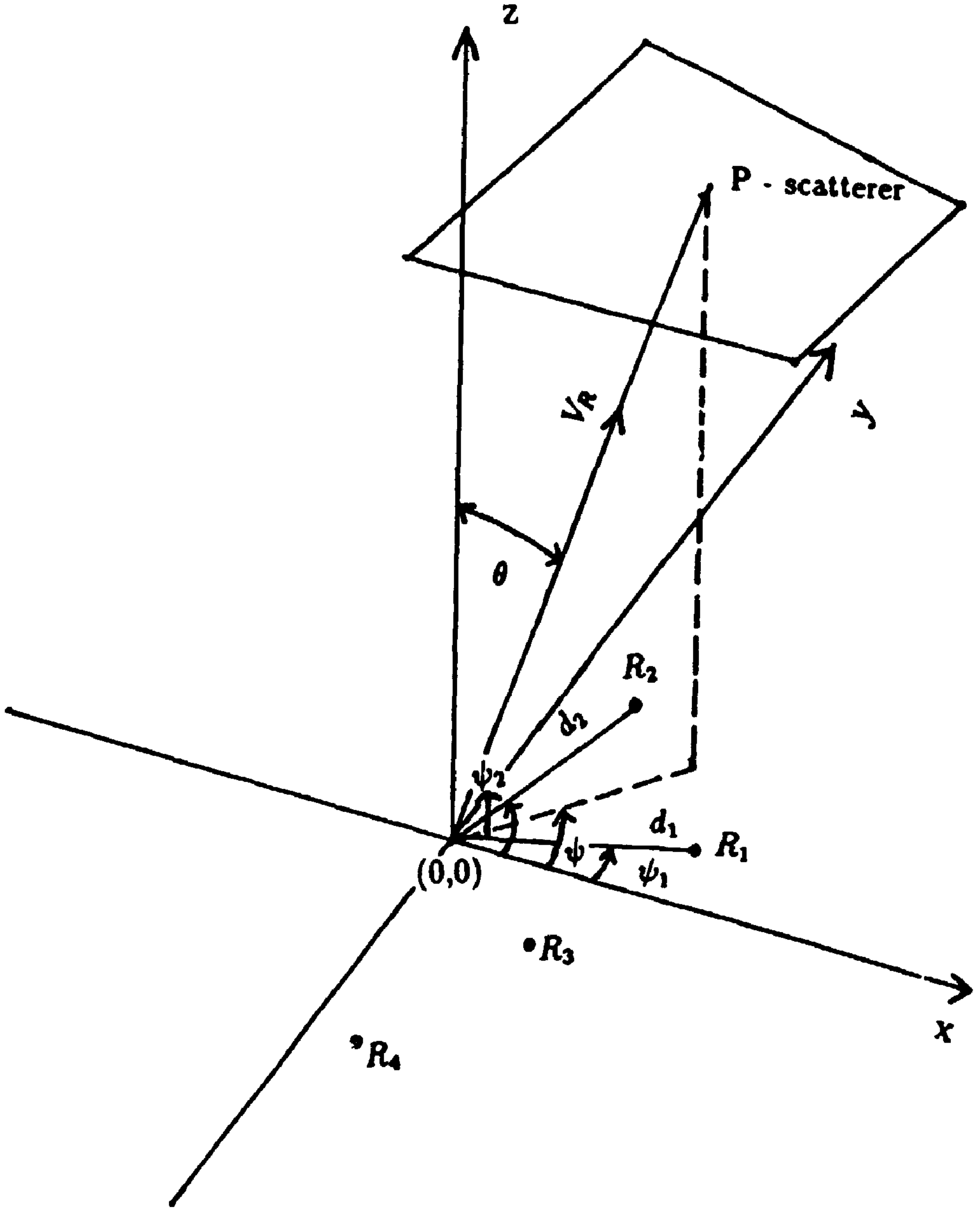

Figure 7.8: The geometry of the direction finding system. The point P represents the specular reflection point of a meteor trail which is drifting in the direction of (θ, ψ) with respect to (0,0); where θ and ψ represent the zenith and azimuth angles. See the text for more details.

$$\phi_3 = (\frac{2\pi}{\lambda})d_3 \cos(\psi - \psi_3) \sin\theta \tag{7.29}$$

where d_1, d_2, and d_3 are distances of the receivers R_1, R_2, and R_3 relative to (0,0). $\{\psi_{i=1,3}\}$ represent the azimuth angle, which are directly known, measured from the x-axis (east).

Now, consider 2 receivers at R_1 (d_1, ϕ_1) and R_2 (d_2, ϕ_2). Then the relevant phase difference between these receivers is:

$$\phi_{12} = \phi_2 - \phi_1 \tag{7.30}$$

i.e.

$$\phi_{12} = \frac{2\pi \sin\theta}{\lambda}[d_2 \cos(\psi - \psi_2) - d_1 \cos(\psi - \psi_1)] \tag{7.31}$$

Note that ϕ_{12} means the phase of the signal received at antenna 2 leads that received at antenna 1. However, it actually easier to use the expansion of the above equation in terms of the cosine of the angular differences. Therefore we get:

$$\phi_{12} = \frac{2\pi \sin\theta}{\lambda}[d_2 \cos\psi \cos\psi_2 + d_2 \sin\psi \sin\psi_2 - d_1 \cos\psi \cos\psi_1 - d_1 \sin\psi \sin\psi_1] \tag{7.32}$$

Similarly, the phase difference between receivers R_1 and R_3 is:

$$\phi_{13} = \frac{2\pi \sin\theta}{\lambda}[d_3 \cos\psi \cos\psi_3 + d_3 \sin\psi \sin\psi_3 - d_1 \cos\psi \cos\psi_1 - d_1 \sin\psi \sin\psi_1] \tag{7.33}$$

Note that

$$\phi_{12} + \phi_{23} + \phi_{31} = 0 \tag{7.34}$$

So, there is no useful extra information in the ϕ_{23} term except for subsequent error checking. ϕ_{12} and ϕ_{13} are determined by computing the complex cross-correlation of the signals measured at receivers (R_1, R_2) and (R_1, R_3) respectively, as described in Section 7.2.8. It is convenient to express the equations (7.32) and (7.33) in the matrix form. Thus we must solve the simple matrix equation

$$[A]\ \underline{x} = \underline{b} \tag{7.35}$$

i.e.

$$\left[\begin{array}{cc} \frac{2\pi}{\lambda}(d_2 \cos\psi_2 - d_1 \cos\psi_1) & \frac{2\pi}{\lambda}(d_2 \sin\psi_2 - d_1 \sin\psi_1) \\ \frac{2\pi}{\lambda}(d_3 \cos\psi_3 - d_2 \cos\psi_2) & \frac{2}{\lambda}(d_3 \sin\psi_3 - d_2 \sin\psi_2) \end{array} \right] \begin{pmatrix} \sin\theta \cos\psi \\ \sin\theta \sin\psi \end{pmatrix} = \begin{pmatrix} \phi_{12} \\ \phi_{13} \end{pmatrix} \tag{7.36}$$

where ϕ_{12}, ϕ_{13}, and $[A]$ are known, therefore we can solve for $\underline{x}$ using a matrix inversion method, i.e.

$$\underline{x} = [A]^{-1} \cdot \underline{b} \tag{7.37}$$

Thus, we obtain

$$\chi_1 = \sin\theta\cos\psi \tag{7.38}$$

$$\chi_2 = \sin\theta\sin\psi \tag{7.39}$$

and since

$$\sin^2\theta = \chi_1^2 + \chi_2^2 \tag{7.40}$$

$$\theta = \sin^{-1}\sqrt{\chi_1^2 + \chi_2^2} \tag{7.41}$$

We can determine ψ by substituting θ into equation (7.38) or (7.39)

$$\Longrightarrow \qquad \psi = \arccos(\frac{\chi_1}{\sin\theta}) \quad = \quad \arcsin(\frac{\chi_2}{\sin\theta}) \tag{7.42}$$

or dividing the equation (7.39) by (7.38) we can deduce

$$\psi = \arctan(\frac{\chi_2}{\chi_1}) \tag{7.43}$$

The arrival of the echo angle (θ, ψ) is thus readily determined. We determined such (θ, ψ) combinations for all measured phase differences ϕ_{ij}, and also for other combinations of ϕ_{ij} involving addition and substraction of 2π. This sometimes lead to two or more possible "acceptable" angles. We then turn to receiver R_4 to help resolve the ambiguity, and in 70% of all cases it was possible to produce an unambiguous meteor location.

The accuracy of the zenith angle determination is essentially depend upon the error in the phase determination. For each meteor the zenith angle of the reflection point was calculated from the mean phase difference between the receivers, averaged over 6 independent estimations (using the combinations of 4 receiving antennas). After several tests, we decided to limit the deviation in phase difference (i.e. $\phi_{ij(i\neq j)} - \phi(\bar{ave})$) to be $< 35^o$, which then turns out to be a reliable criteria. The experimental uncertainty in zenith angle is therefore $\leq 3^o$. The spread in possible zenith angles for each meteor was used in conjunction with the range to find the possible spread in heights. The average vertical spread was ± 3 km, due to the phase and range uncertainties. It is therefore not productive to bin the resultant individual meteor height values into divisions finer than ~ 3 km.

7.2.10 Wind components over the whole sky

The quantities R, θ, and ψ form a three dimensional coordinate system which we transform to a Cartesian system, where x-axis is east, y-axis is north, and z-axis is vertical. The scattering point parameters are then sorted by altitude and time bin.

Since an off-zenith point at 85 km height might be detected in the, say, 94 km range gate, a considerable regrouping of the points takes place at this point in the analysis. The main procedure for regrouping of the points in the analysis can be explained as follows.

Significant diurnal variation in the meteor echo rate is observed (see Section 7.3.2) with the largest echo rate occurring during the early mornings hours when the meteor fluxes were large and minimum values in the evening hours when the fluxes were small. When both the height distribution and hourly rates are considered, it is clear that it is difficult to make up a continuous time series of wind velocities for altitudes close to the top (about 100 km) and bottom (about 80 km) of the meteor region (see also Section 7.3.1). Therefore a weekly or monthly study of the mean winds and tidal oscillations using the vector average of the daily mean values (similar to chapter 4), irrespective of the time of the day, would be biased. To eliminate the possible bias due to the diurnal variation of the echo rate values in winds, we adapted the so-called "superposed epoch" analysis to estimate the mean winds and tidal oscillations. In such a case, recordings may be binned in the same hour of the day over several days. There are two options to perform the time-averaging of the data. We use either 1-hour or 2-hour bins of data. The basic procedure can be explained as follows for recording the data in 1-hour bins. The wind values during each hourly (local time) bins (2330-0030, 0030-0130, 0130-0230, ..., 2230-2330 LT) for all the days in each month are grouped together and a least-squares fitting procedure is applied to all these radial velocities to obtain the hourly mean values, and the resulting time series are taken to represent the 24 hourly mean values for the equivalent day of the month. In a similar fashion, the data can be grouped into 2-hour bins (2300-0100, 0100-0300, 0300-0500, ..., 2100-2300 LT), and the resulting time series are taken to represent the 12 two-hour mean values for the equivalent day of the month. It should be noted here that the 1-hour bins are allowed to overlap ±15 minutes on either end into adjacent intervals, and the 2-hour bins are allowed to overlap ±30 minutes. These "overlapping intervals" ensure that the winds are moderately smooth as a function of height and time. One of the main objectives of this study is to compare the winds and tides (i.e. long period oscillations) with the MF radar using the SA technique. Therefore it is not unreasonable to force a certain degree of continuity upon the data (this will be further discussed in the following chapter).

All echoes used in the analysis were distributed in heights between 77 and 130 km, with 85% of them lying between 80 and 100 km. The vertical structure of the winds and tides are established by dividing the recorded data into 6 height groups. The height groups used were 78-84 km, 83-87 km, 86-90 km, 89-93 km, 92-97 km, and 96-102.5 km for the central heights of 82 km, 85 km, 88 km, 91 km, 94 km, and 98 km respectively. Note that the winds are moderately smoothed as a function of height. We have grouped the echoes according to this sequence for two reasons. First, it increases the number of points to do the fitting and second, it gives a height resolution similar to the MF system. It should be noted that for the discussion of mean winds and tides, only the height region 82-98 km is considered (Chapter 8); for the discussion of echo rates and selection efficiency the height region 77-130 km is used (Section 7.3).

Next we want to calculate the mean apparent motion of the scattering points. For each scattering point we initially determined the Doppler frequency, so the scalar value of the radial velocity of each scatterer can be calculated from the equation (7.19) as

$$V_{Ri} = \frac{c}{2f} f_{di} \tag{7.44}$$

where $i = 1, 2, 3, ..., N$, where N is the number of scattering points identified at height z and the time bin Δt.

Having previously determined the location of each scattering point, we can now write the vector radial velocity as

$$\vec{V_{Ri}} = \mathrm{V_{Ri}} \vec{I_{Ri}} \tag{7.45}$$

where I_{Ri} is a unit vector in the radial direction passing through the i th point, and is given by

$$\vec{I_{Ri}} = l_i \vec{i} + m_i \vec{j} + n_i \vec{k} \tag{7.46}$$

where l_i, m_i, and n_i are the direction cosines of the i th scattering point, given by

$$l_i = \sin\theta_i \cos\psi_i \tag{7.47}$$

$$m_i = \sin\theta_i \sin\psi_i \tag{7.48}$$

$$n_i = \cos\theta_i \tag{7.49}$$

Now let the mean wind field vector is described by

$$\vec{V_m} = u\vec{i} + v\vec{j} + w\vec{k} \tag{7.50}$$

where u, v, and w are the zonal, meridional, and vertical components of the wind field, respectively. Three scattering points are sufficient (in principle !) to determine the three unknown components of the motion. With more than three points we can calculate a least-squares fit to the scattering point parameters as follows. V_{Ri} is simply the projection of the mean wind vector onto the radar's (unit) line-of-sight vector $\vec{I_{Ri}}$. Since

$$\mathrm{V_{Ri}} = \vec{V_m} \cdot \vec{I_{Ri}} \tag{7.51}$$

for all i if the least-squares fit is perfect, the residual is given by

$$\epsilon^2 = \sum_{i=1}^{N}[(ul_i + vm_i + wn_i) - \mathrm{V_{Ri}}]^2 \tag{7.52}$$

The best estimates for u, v, and w are those values for which ϵ^2 is smallest. Differentiating ϵ^2 with respect to u, v and w and setting these derivatives equal to zero, we obtain the three equations

$$\frac{\partial\epsilon^2}{\partial u} = \frac{\partial\epsilon^2}{\partial v} = \frac{\partial\epsilon^2}{\partial w} = 0 \tag{7.53}$$

which gives

$$u\sum l_i^2 + v\sum l_i m_i + w\sum l_i n_i = \sum \mathrm{V_{Ri}} l_i \tag{7.54}$$

$$u\sum l_i m_i + v\sum m_i^2 + w\sum m_i n_i = \sum \mathrm{V_{Ri}} m_i \tag{7.55}$$

$$u\sum l_i n_i + v\sum m_i n_i + w\sum n_i^2 = \sum \mathrm{V_{Ri}} n_i \tag{7.56}$$

For any set of measurements (l_i, m_i, n_i), these simultaneous equations for u, v, and w can be solved to find the best estimates for u, v, and w. These are then solved for u, v, and w.

When calculating apparent motions vector, we use two other selection criteria. First we reject points that lie within 12° of zenith, since errors in these points cause large errors in the calculated horizontal motion. Second we reject points when $\mid V_{Ri}(measured) - V_{Ri}(calculated) \mid > 30$ m/s. $V_{Ri}(calculated)$ is found in the following way. First, we do a first rough estimate of (u, v, w) without any rejection. Then we do a second run through, and use the previously calculated (u, v, w) as first guess to determine an estimation value for the radial velocity - which we call $V_{Ri}(calculated)$. If $\mid V_{Ri}(measured) - V_{Ri}(calculated) \mid > 30$ m/s then the measured value, $V_{Ri}(measured)$, is rejected as an outlier. After rejecting the worst outliers of $V_{Ri}(measured)$, a list of 'new' (u, v, w) estimates are determined, and subsequently used for the tidal analysis. Note that

$$V_\sigma = \sqrt{\left(\frac{\sum_{i=1}^{N}[V_{Ri}(measured) - V_{Ri}(calculated)]^2}{N}\right)} \tag{7.57}$$

represents a sort of a measure of the residuals. The residuals are typically ~ 5-20 m/s, which is to be expected, since they represent the effects of gravity wave fluctuations (see Chapter 5). The meteor region is characterized by a wide wave motion spectrum and is generally turbulent. Chapter 5 shows that gravity wave (GW) fluctuations are typically several times the fluctuation due to the tides, and $V_{rms} \sim 30$ m/s (V_{rms} = root-mean-square value). Bearing in mind that on the average the zenith angle is typically $\sim 30°$ off vertical, we expect the the residuals to be $\sim 0.5 \times V_{rms}(GW) \sim$ 15 m/s or so. Therefore, taking 30 m/s as a limit value is not unreasonable. It might be thought that the residuals would be largest for those time bins (1-hour or 2-hour bin) containing the smaller numbers of meteor echoes, but this is not so. In general the greatest scatter occurs for those time bins where the wind direction is changing most rapidly.

In our discussion of the statistical analysis of data, we have so far discussed only observations of three variables (eastward, northward, and vertical). However, we allow the following 3 options to deduce the wind field using the least-squares fitting procedure. (1) Do a fit to a 3-D wind field (eastward, northward, and vertical); the one discussed in the previous section. (2) Do a fit to a 2-D wind field; this wind analysis method assumes the vertical hourly average wind is zero (this is a valid assumption as the vertical wind velocity is on average 1-2 orders of magnitude less than the horizontal wind velocity), and simply project the line-of-sight component onto the horizontal plane. This problem is a special case of our three-variable method, i.e. a very straightforward generalization of our three-variable method discussed above, and can be solved in a similar way. Therefore, the mathematical details of this analysis will not further be discussed in this section. (3) Obtain the eastward wind using only the meteors to the east and west. After several trial tests, it turns out that options (1) and (2) work especially well if the meteors are symmetrically distributed about the sky, and (2) seems superior. The case (3) is a useful option when there are a majority of meteors in the east and west. The comparison of these different options will be further discussed in Chapter 8.

In the present study, the variation of wind velocity with height and time is also determined by a least-squares fitting analysis developed by Groves [1959]. This method allows variations in temporal bahaviour of the wind, with periods of 24, 12, and 8 hours. In addition, the amplitude and phase of each periodic component and amplitude and direction of the prevailing components are allowed a polynomial variation with height. Groves analysis has been used by several groups [e.g., Rossiter, 1971; Stubbs and Vincent, 1973; Roper, 1965, 1975, 1978; Aso et al., 1979, 1980; Tsuda et al., 1980]. This method will be further discussed, and will be compared with our analysis method in Chapter 8.

The following section presente the results of the meteor distribution versus the height, daily, seasonal, zenith, and azimuth angles based on observations made with VHF meteor system, comprising in total over 45,000 usable echoes observed for the period from July 1994 to May 1995. The results of the mean winds and tides are discussed separately and compared with the MF radar in Chapter 8.

7.3 Results

The VHF interferometer meteor radar was active and observations were made at London during the following periods:

- July 7-31, 1994
- August 1-30, 1994
- September 9-30, 1994
- October 1-25, 1994
- December 25-31, 1994
- January 1-17, 1995
- March 1-21, 1995
- April 2-23, 1995
- May 2-9, 1995

On the basis of our stringent rejection criteria, meteor echoes were selected from the data set for the period July 1994 to March 1995. Of all the meteors detected, about 35% were rejected due to the reasons previously mentioned. Histograms of the mean daily as well as the seasonal variation of meteor echo rates were determined for this period, along with the height distribution of average meteors echoes. The distribution of the average meteor echoes versus the zenith and azimuth angles were also determined during this period. (Note these plots are biased by our unusual transmitter polar diagram pattern, See Figure 7.3). We show the height profiles of average meteor echoes for each month in Figures 7.9. The mean daily and seasonal variation of meteor echo rates for the representative months are shown in Figures 7.10 and 7.11 respectively. Figures 7.12 and 7.13 show the distribution of average meteor echoes versus zenith (angle from vertical) and azimuth (measured in the anti-clockwise direction from east) angles for the representative months. It should be noted that effects of the major showers were recognized and removed from the observational data to yield a mean distribution of the normal nonshower meteor rates. However, we plot the January Quadrantids shower, as an example, in each figure (dotted lines in Figures 7.9, 7.10, 7.12 and 7.13) to show how the recognized meteor showers can affect the normal nonshower distribution.

7.3.1 Meteor Heights

The height distribution of average daily (i.e. average number of meteors per day) meteor echoes observed for each month is shown in Figure 7.9. The height distribution is typical of VHF meteor radars, with the maximum number of meteor echoes occurring near 88-91 km and the number of echoes falling off rapidly above this peak height. It is noteworthy that above this height peak the diffusion reduces the echo duration, while below it attachment and wind turbulence become increasingly important. The observed height of maximum echo rate is consistent with other similar meteor radar observations [e.g., Hess and Geller, 1977; Tetenbaum et al., 1986; Wang et al., 1988; Reddi et al., 1993]. Note that the height of maximum echo rate predicted by the empirical formula based on linear relationship between the height h and radar frequency f (equation (7.10), see Section 7.1.3) is 96.6 km. This indicates an overestimation of the height by the empirical relationship. An average meteor echo rate of 15-20 per day was observed near 88-91 km from May to October and a low echo rate of 10 per day was observed from December to March. This was partly affected by some local variation in noise levels especially due to signal from a nearby transmitter which occasionally contaminated the signal. It is interesting to note that the height distribution of meteors belonging to the January Quadrantids shower maximizes at the same height that is observed from the nonshower meteor height distribution (see Figure 7.9f). It should be noted that we have set the lowest height limit of meteors to 77 km because there are only a few meteors detected below this height. This height limitation also helps to reduce the degree of ambiguity of the meteor detection (see Section 7.2.6), which reflects the sudden drop off of meteors to zero below 77 km (artificial cut-off) in the figure. The choice of 40.68 MHz for the radar frequency reduces the ceiling altitude (about 110 km) from which useful underdense echoes are received (see Sections 7.1.3 and 7.1.4).

It is seen that a pronounced peak in the number distribution occurs near an altitude of 88-91 km, an effect which is associated with the physics of meteor flights and is well documented in the literature [McKinley, 1961]. The height at which a meteor appears depends on its mass, velocity, and path inclination as well as on the density

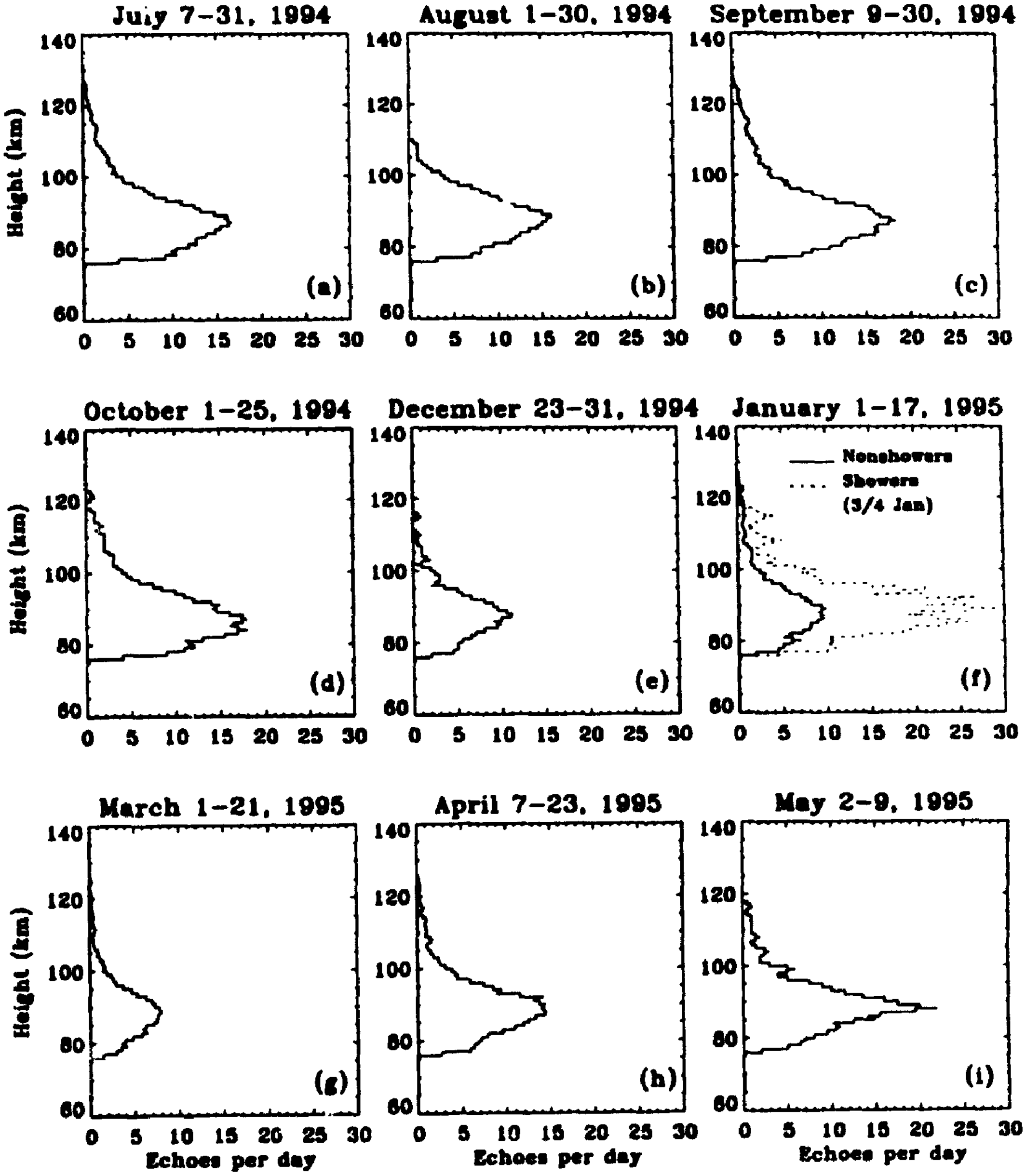

Figure 7.9: The height distribution of average meteor echoes observed for each month from July 1994 to May 1995. The dotted lines in the figure illustrate the Quadrantids shower observed during 3/4 january 1995.

of the atmosphere. The height profile of meteor echoes observed with our system agrees well with that expected from the ablation process of meteors entering the atmosphere. This can be explained in terms of the physical characteristics of meteors as follows [McKinley, 1961; Sugar, 1964]: As a meteor enters the atmosphere, heating and ablation begins. Depending on the mass and velocity of the incoming meteors, these processes begin between 100 and 120 km where the air density is large enough to generate friction. As a meteor penetrates further, the exponentially increasing air density leads to an increase in ablation and ionization thus produced reaches a maximum at about 88 km. At lower altitudes, the ionization falls off rapidly, since only a few of the larger meteors penetrate to these levels. Thus the small thickness of the meteor region (80-100 km) is the result of the rapid change in air density and the size distribution of the incoming meteors [Avery et al., 1983].

7.3.2 Daily variation of meteor rates

The incidence of various meteor showers during the 9 months and the diurnal variation of the rate of sporadic meteors cause the number of echoes per hour to vary markedly during each day and from day to day. In general the activity is a maximum in the early morning hours and a minimum in the late afternoon hours.

Figure 7.10 shows the distribution of average meteor echoes for the entire height range versus the local time of day. Figure 7.10 shows a predominant diurnal variation in hourly echo rate particularly for the period from July to December in 1994 and during May in 1995. If no appreciable shower activity is present, the hourly rate of arrival of meteors varies from a minimum (4-6 meteors) around 1800 LT to a maximum (15-25 meteors) in the early morning hours around 0600 LT. Normally the daily ratio of maximum to minimum hourly rate is in the range 2 to 4. The observed diurnal variation is the result of the relative motion between the Earth and the meteors recorded by the radar [Whipple, 1954; Lovell, 1954]. The morning maximum and evening minimum are a natural consequence of the Earth's motion in its orbit. Because the Earth is moving in its orbit at ~ 30 km/s, we will encounter more meteors when we are on the "forward side" of the Earth, around 0600 LT, than we will 12 hour later. The late afternoon meteors will have to catch up with the Earth; hence there will be fewer of them and their resultant velocities will be lower [McKinley, 1961].

At times of meteor showers, the hourly rate may go up considerably. During the January Quadrantids shower, for example (see Figure 7.10f), the London hourly rate

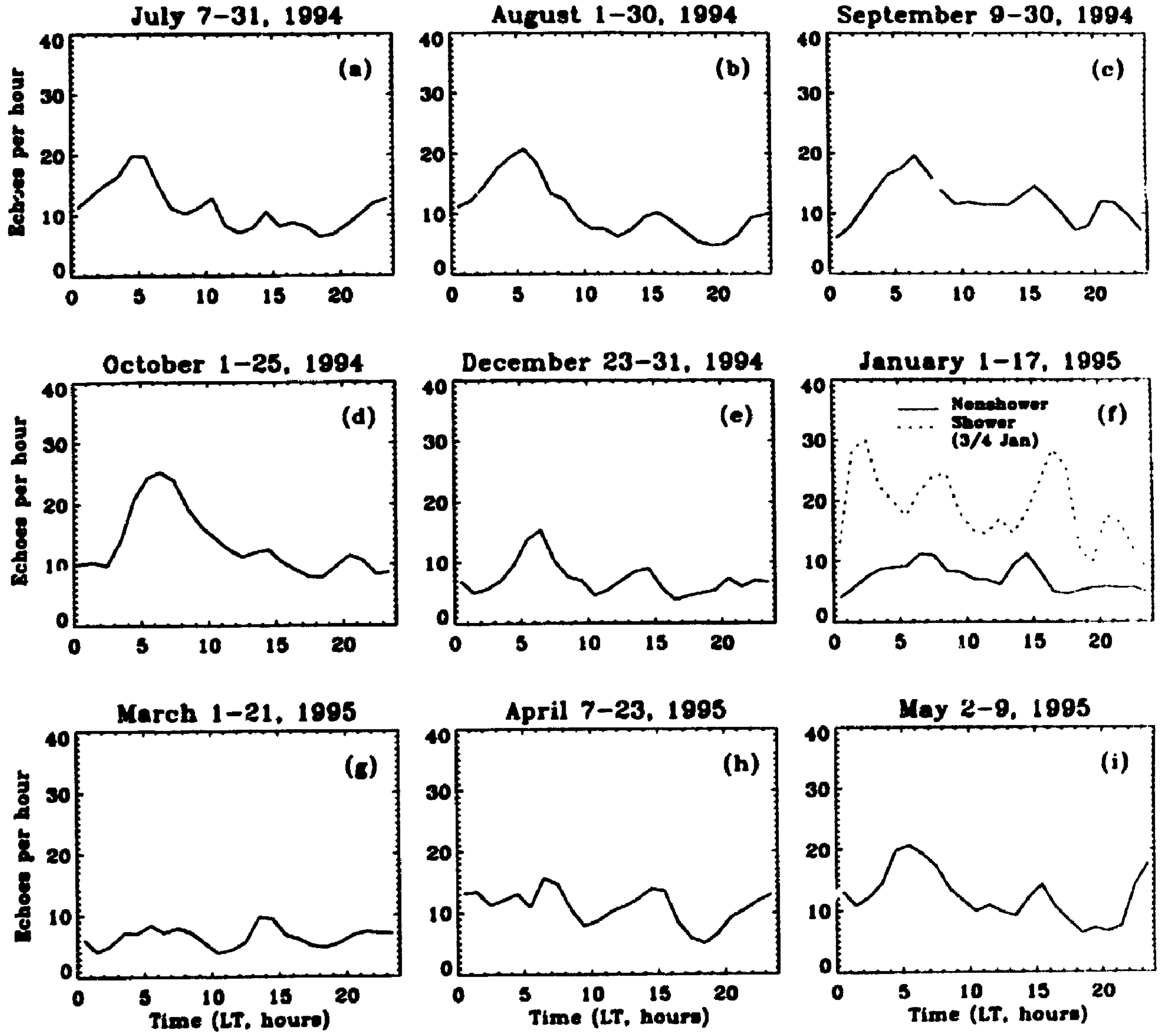

Figure 7.10: The mean daily variation of meteor rates observed for each month from July 1994 to May 1995. The dotted lines in the figure illustrate the Quadrantids shower observed during 3/4 january 1995.

goes up to 30 and peaked at around 0200, 0800 and 1600 LT hours. A considerable number of meteors are detected in the afternoon during the Quandrantids shower.

The general trend of the Figure 7.10 is quite similar to other observations [e.g., McKinley, 1961; Avery et al., 1983]. However, it is interesting to note that there is an indication of secondary maxima of the echo rate during the afternoon at about 1500 LT. The afternoon maximum is not so well defined, depending on the particular month, while the morning maximum is fairly stable. Similar secondary afternoon maxima were also observed by other meteor radar stations [e.g., Avery et al., 1983; Tetenbaum et al., 1986; Wang et al., 1988; Valentic, 1994; Cervera, 1995]. The daily variation of echo rates so obtained can be explained by the geometry of the Earth's path intersecting the meteor trajectories, the geometry of the antenna pointing direction relative to the ecliptic plane [Tetenbaum et al., 1986; Wang et al., 1988] and the statistics of the meteor arrival [Avery et al., 1983]. A large number of meteors over London ($\sim$ 70% of the total meteors) are detected at angles of 20° to 45° (see Section 7.3.4 and Figure 7.12). This can be related to the Earth's rotation axis, and therefore could introduce a detection efficiency which has two peaks per day. But recent research has shown that the observed daily variation is the result of the sporadic sources belong to (very ancient and spread-out) meteor streams, presumably due to very old comets or asteroids which broke up a long time ago. Indeed this also can accounts for the secondary maximum in the mid afternoon (e.g., Jones and Brown, 1994; Cervera, 1995].

7.3.3 Monthly variation of meteor rates

The mean monthly variation of meteor rates at London is shown in Figure 7.11. The observed monthly variation is the result of the sporadic radiant sources, namely apex, helion, antihelion and toroidal sources, changing their strengths significantly during the year [e.g., Stohl, 1968; Mawrey and Broadhurst, 1993; Jones and Brown, 1994]; this leads to nonuniform spatial density of meteors along the Earth's orbit. The shape of the curve is in agreement with observations reported in both Northern and Southern Hemispheres [McKinley, 1961; Avery et al., 1983]. One can note that the maximum influx (330-350 meteors per day) occurs in September-October (during the fall), and the minimum influx (140-170 meteors per day) occurs in January-March (spring). The apex of the Earth's way is above the horizon of the observer in the Northern Hemisphere for more hours each day during September than it is during March [McKinley, 1961]. One would thus expect that the monthly rates in the Northern Hemisphere would show a maximum around September and a minimum

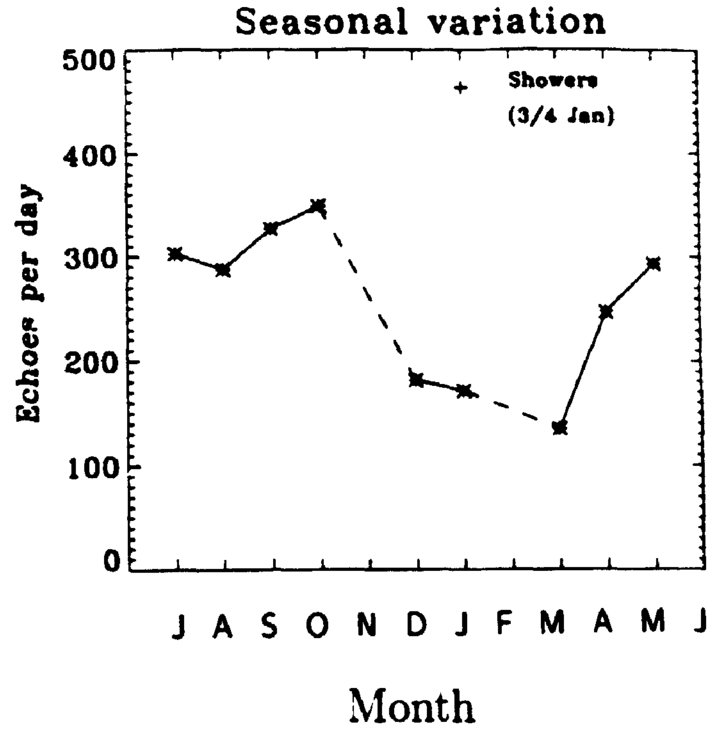

Figure 7.11: The mean monthly variation of meteor rates observed for each month from July 1994 to May 1995. The dotted lines indicate that no data were taken during that month (e.g., November and February). The meteor rate for the Quadrantids shower observed during 3/4 January 1995 is illustrated by the symbol "+".

around March. That this is indeed the case is shown in Figure 7.11. The meteor rate for the Quadrantids shower observed during 3/4 january 1995 is illustrated by the symbol "+" in Figure 7.11: an average of 464 meteors per day was observed.

It is noteworthy that some of these changes are not due to variation in count rate but variations in local noise levels. Note that the seasonal variations may also be involved with system modifications which were periodically applied to improve the system.

7.3.4 Meteor arrival angle distribution

Figures 7.12 and 7.13 show the distribution of mean meteor echoes for the entire height range versus the zenith and azimuth angles respectively. Figure 7.12 shows that on the average a large number of meteors (~ 70% of the total meteors) over London are detected at angles of 20° to 45° for our instrument, due to the radar polar diagram (see also Figure 7.3). The January Quadrantids shower also illustrates a similar behaviour (see Figure 7.12f). Another reason for this can be seen by inspection of the

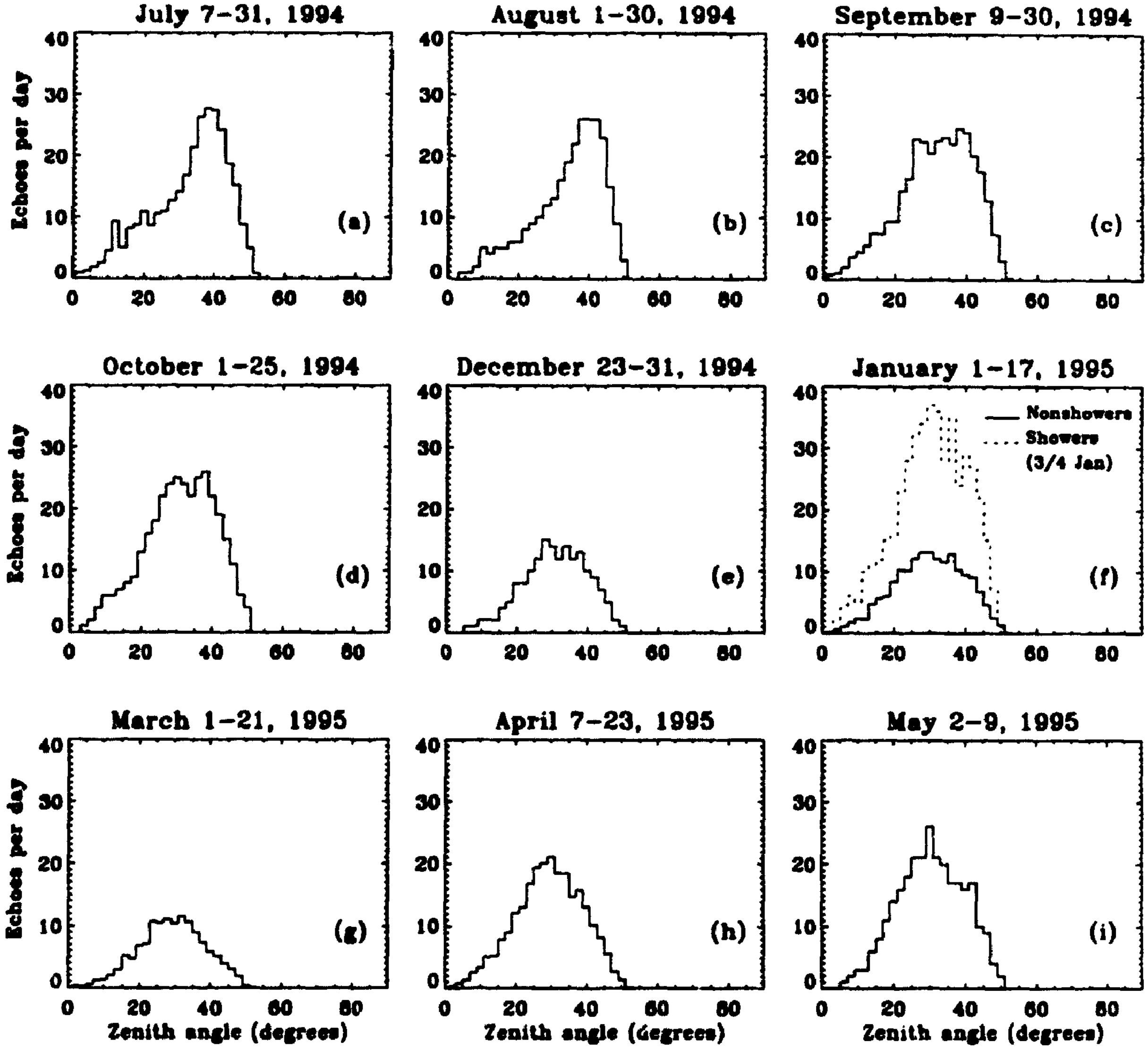

Figure 7.12: The distribution of mean meteor echoes for the entire height range versus the zenith angle for each month from July 1994 to May 1995. The dotted lines in the figure illustrate the Quadrantids shower observed during 3/4 january 1995.

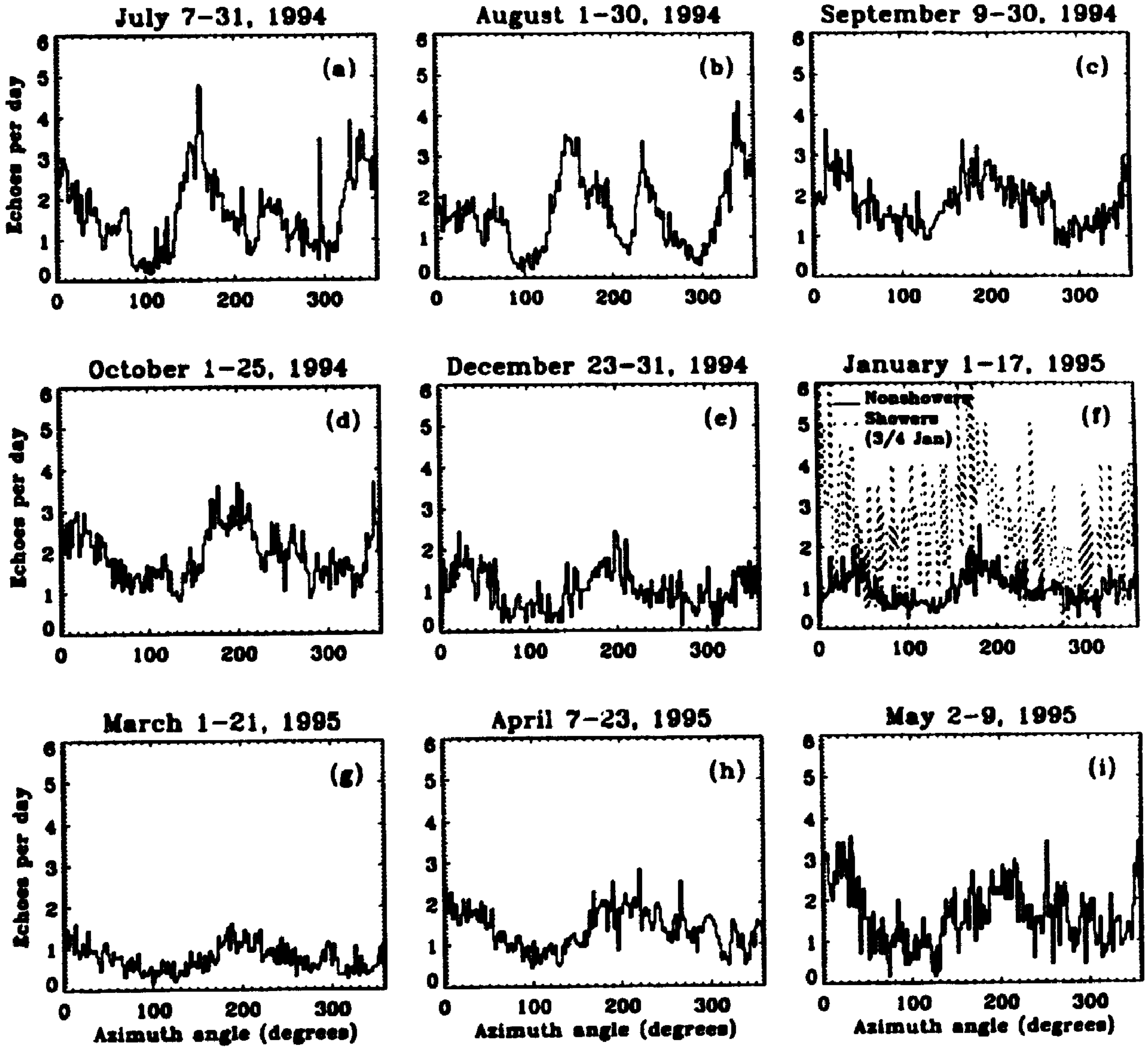

Figure 7.13: The distribution of mean meteor echoes for the entire height range versus the azimuth angle for each month from July 1994 to May 1995. Note that azimuth angle is measured in the anti-clockwise direction from true eastward direction. The dotted lines in the figure illustrate the Quadrantids shower observed during 3/4 january 1995.

meteor response function [e.g., Thomas et al., 1988], a discussion of which will not be reproduced here. However, briefly, the meteor count rates drop off as the zenith angle approaches to zero because the meteor collecting volume decreases. It should be noted that we have set the maximum limit for the zenith angle which a meteor can have to 53°, because there are only a few meteors detected from greater zenith angles. This limitation of the zenith angle also helps to reduce the degree of ambiguity of the meteor detection (see Section 7.2.6), which reflects the sudden drop off of meteors to zero above 53° (artificial cut-off) in the figure. Note also that we have not set the minimum limit for the zenith angle (i.e. 12°, see Section 7.2.6) which a meteor can have in this figure.

The mean meteor echoes versus the azimuth angle (measured in the anti-clockwise direction from east) in Figure 7.13 generally shows that on the average a large number of meteors ($\sim$ 70% of the total meteors) are detected from the eastward (0°) and westward (180°) directions. The January Quadrantids shower also illustrates the similar behaviour (see Figure 7.13f).

7.4 Conclusion

The new UWO VHF interferometer meteor radar has been in operation since July 1994 at the Environmental Science Western Facility near the University of Western Ontario in London, Canada (43° N, 81° W). The system has proven an excellent tool for a variety of meteor experiments and is now used to measure atmospheric winds at meteor heights by means of radio reflection from meteor trails.

The UWO meteor radar system has been described, and the data processing algorithms have been presented and their performance has been discussed. Some preliminary results of the meteor distribution versus the height, daily, seasonal, zenith and azimuth angles are presented in this chapter based on observations made at London, numbering in total over 45,000 usable echoes observed from July 1994 to May 1995. The results of the mean winds and tides are discussed separately and compared with the MF radar in the following chapter.

It is seen that a pronounced peak in the number distribution occurs near an altitude of 88-91 km, and the number of echoes drops off rapidly above and below this peak height. The height profile of meteor echoes ob[illegible]ed using our meteor technique agrees well with that expected from the ablation process of meteors entering the atmosphere. It is interesting to note that the height distribution of meteors belonging to the January Quadrantids shower maximize at the same height that is observed from the nonshower meteor height distribution.

The meteor echo rate varies diurnally and in this present investigation the peak rates of usable meteor echoes are found to be about ~ 15-25 per hour in the early hours of the morning (0600 LT) dropping to ~ 4-6 per hour at the time of the diurnal minimum (1800 LT). The ratio of maximum to minimum number of meteors per hour for the present data was between 2 and 4. The observed predominant diurnal variation in the number of meteors recorded per hour by meteor radar is due to the relative motion between the Earth and the meteors. We also note that there is a hint of secondary peak of the echo rate during the afternoon at about 1500 LT. A considerable number of meteors are detected in the afternoon during the January Quandrantids shower, and the corresponding hourly rate goes up to 30 and peaked at around 0200, 0800 and 1600 LT hours.

The meteor echo rate varies monthly and in this present investigation the peak rates of usable meteor echoes are found to be ~ 330-350 per day in September-October (fall) dropping to ~ 140-170 per day in January-March (spring). The meteor rate for the January Quadrantids shower is ~ 464 per day. Some of these changes are not due to variation in count rate but variations in local noise levels.

A large number of meteors ($\geq$ 70% of the total meteors) over London are detected at zenith angles between 20° and 45° for our instrument, due to the radar's polar diagram. It is also noted that on the average most of the meteors ($\geq$ 70% of the total meteors) are detected from eastward and westward directions. The January Quadrantids shower also reflects a similar behaviour.

Chapter 8

Simultaneous observation of winds and tides by MF and Meteor radars

8.1 Introduction

Atmospheric winds in the mesosphere and lower thermosphere have been observed routinely for many years with MF radars using the spaced antenna technique. The spaced antenna technique (hereafter referred to as the SA technique) was originally used for total reflection experiment and was subsequently modified for D-region work using partial reflections [e.g., Awe, 1961; Fraser, 1965, 1968; Fraser and Kochanski, 1970; Briggs, 1977, 1984; Hocking et al., 1989], and later still used for tropospheric and stratospheric wind measurements with VHF radars [e.g., Röttger and Vincent, 1978; Röttger, 1981]. Extensive observational studies of winds, waves and turbulence have been made with this technique, but doubts have been expressed in the past as to the type of motion actually measured in such experiments, which might be the motion or turbulence carried along by the wind, atmospheric wave motions or ionization drifts of electromagnetic origin [e.g., Hines, 1968, 1993]. The best way to test the possible biases in wind estimates by a SA technique is by comparisons with other different techniques at the same place and time. Extensive comparisons and tests of the SA technique have been carried out with rocket, satellite, and radar measurements. Several comparisons suggest that the SA technique can give a reliable means of estimation of the motion of the neutral air in the mesosphere (at MF and HF) and in the troposphere and stratosphere (at VHF), when using weak partial reflections. In the mesosphere, the reflections are from weakly ionized irregularities, and in the troposphere and stratosphere are from irregularities in the neutral air.

Several comparisons of meteor winds with ionospheric drifts using totally reflected radio waves have shown good agreement between the two methods with respect to monthly and seasonal averages, and in a comparison of hourly observations during one day [e.g., Sprenger and Schminder, 1967, 1968; Wright, 1968; Muller, 1968; Lysenko et al., 1972; Sprenger and Lysenko 1972]. Several comparisons have been made using the technique of partial reflections from time to time. Fraser and Kochanski [1970] and Gregory and Rees [1971] initially showed that SA measurements at MF and HF in the D-region produced reliable winds. Fraser and Kochanski [1970] compared the SA drift data (Birdlings Flat, 44° S, 173° E), with meteor wind measurements (Adelaide, 35° S, 138° E), chemical release trails, and with general circulation models. It should be noted that comparisons were made during the winter months (from May to September) in different years (1964 and 1961) and the separation between the Birdlings Flat and Adelaide sites was about 1,900 miles. Gregory and Rees [1971] compared the SA drift data (52° N, 107° W) with rocketsonde measurements (53° N, 110° W) for the months of May and June in 1969. In many such comparisons, the two sets of data were separated in space and time.

Felgate et al. [1975] and Wright et al. [1976] compared the SA winds with neutral winds measured by meteor radars in a common volume of the atmosphere. These workers reported comparisons involving SA drift measurements made using totally reflected radio waves in the lower E-region (90-120 km). Felgate et al. [1975] performed detailed comparisons between the SA drifts with neutral winds measured by meteor radar in 1972 and 1973 and found very good general agreement. Wright et al. [1976] conducted comparison between SA drifts and meteor wind measurements during January-April in 1970 and also found close agreement between the two techniques.

Stubbs [1973] and Stubbs and Vincent [1973] compared the SA wind with the meteor measurement of the neutral wind, where the two sets of equipment were at nearby locations. Stubbs [1973] compared the results obtained during the summer and fall months (February-May) in 1972, whereas Stubbs and Vincent [1973] compared the results obtained in the midwinter month of July for the years 1970-72. They showed that SA wind agreed well with meteor measurements of winds in the 80-100 km region and concluded that the partial reflection experiment was capable of measuring the neutral air motion in the D-region. It has been shown that over the height range where the observations overlap (~ 85-95 km) and over the time intervals of the order of an hour or longer the results agree well. Comparisons with shorter time resolutions are not possible because of the relatively small number of meteors usually observed in one hour with the meteor system. Recently, Cervera and Reid [1995] compared the MF SA wind velocities in the 80-98 km height range with meteor measurements. The agreement between the two techniques was generally good below 90 km, while above 90 km they found that the SA technique yields smaller wind speeds than the meteor drift technique.

Vincent et al. [1977] compared the neutral wind measurements in the D-region made by rocket technique with drift observations made by SA technique, and again good agreement was obtained. Labitzke el al. [1987] made a comparison between direct wind observations based on the MF SA technique and geotropic winds based on satellite derived height fields (approximately 78-80 km) in 1979-1982, and found very good agreement for most of the year. Lloyd et al. [1990] compared the winds measured by the optical Fabry-Perot interferometer system and by the MF SA radar system during the autumn and early winter in 1987. When data were available, the results from the two instruments were consistent with each other, both in wind direction and amplitude. Similar investigation was later carried out by Phillips et al. [1994]; this study is similar to earlier comparison of Lloyd et al. [1990] except it draws on 4 years of simultaneous observations. Once again, strong similarities in the MF SA radar and Fabry-Perot interferometer Doppler wind fields are observed, although there are some differences (possibly due to auroral contamination).

In the troposphere and stratosphere, several sets of SA measurements have been compared with wind measurements made by more conventional meteorological means. Röttger and Vincent [1978] first showed that SA winds are in good agreement with balloon measurements. Likewise, Vincent and Röttger [1980] found good agreement between SA winds and balloon measured winds. More comparisons were made by Röttger and Czechowsky [1980] who reported results from an experiment showing that aircraft and radar data were in excellent agreement. Vincent et al. [1987] carried out a detailed intercomparison of winds measured with the SA and Doppler techniques, and also made comparisons with 80 radiosonde profiles. There are no clear systematic differences among different techniques. They concluded that their statistical analysis showed excellent agreement, although the SA winds tended to be 1-2 m/s smaller than the radiosonde measurements. Overall, the rms differences between the sets of measurements were only 3-4 m/s, which they found to be consistent with random errors inherent in each technique, as well as the spatial separation between radar and balloon observations. Röttger 1981 [a,b] also shown the reliability of the SA technique.

The above extensive comparisons, which include a large body of data at a variety of locations, strongly suggest close agreement between winds measured by SA technique and neutral air motions. While there is much accumulating evidence that the SA technique yields a reliable means of estimation of the motion of the neutral air, nevertheless a few report disagreements including Wright [1968], Rossiter [1970], and Hines et al. [1993]. Most of the disagreements, for example Wright [1968] and Rossiter [1970], are understandable as defects of the experimental arrangement and as the consequence of spatial or temporal sampling distinctions in the measurements compared. Rossiter [1970] made a common volume comparison of meteor radar measurements with lower ionospheric drifts (total and partial reflections), and found better agreement with total reflection drifts than his partial reflection data. These results were taken over a small part of the day and the scatter of the individual comparisons indicated that there was a basic lack of reliability in individual drift determinations. There was also a tendency for the drifts to be systematically too small, a fact which may well have resulted from the use of a triangle of size 91 m. However, these discrepancies did not reappear when Stubbs [1973] and Stubbs and Vincent [1973] undertook similar observations with an improved experimental arrangement and a modified method of data analysis.

Recently, Hines et al. [1993] conducted intercomparisons among wind measurements using MF radar, incoherent scatter radar, and meteor radar during the AIDA'89 (Arecibo Initiative in Dynamics of the Atmosphere) campaign in April 1989 with the fundamental objective of testing the wind interpretation of MF/HF partial reflection drift measurements in the lower ionosphere. Based on comparisons of the different sets of observations they concluded that MF/HF partial reflections systems are capable of measuring the neutral air motion below 80 km, and above 80 km they fail to give consistently reliable measurements of the neutral winds. It is important to pointed out here that these results are limited to a single site over a limited period (7 days) of observations. Hines el al. [1993] suggested that the discrepancies revealed during the AIDA'89 experiments may be a result of the contamination of wind estimates by the phase velocity of the internal gravity waves if the MF scattering process is modulated by the passage of such waves through the scattering volume. This is a recurring suggestion put forward by Hines [1968] and hard to sustain based on extensive observational evidences which have been generally favourable to the wind interpretation.

A very different explanation for the AIDA'89 campaign results was given by Kudeki et al. [1993]. These authors pointed out that SA wind estimation errors due to wind field inhomogeneities within the scattering volume may account for the discrepancies observed in the AIDA campaign. Kudeki et al. [1993] proposed a wave-induced fluctuations model and showed that systematic wind estimation errors should be expected to result from spatial variation in the vertical component of the perturbation wind field associated with gravity waves. The fluctuation biases may be large in instantaneous velocity estimates but will average to zero mean in a long-term temporal average suggesting that estimates of tidal and longer period waves should be relatively accurate. This explanation was further substantiated and supported by a more detailed numerical simulation results presented by Sürücü et al. [1995]. Only isotropic scattering was considered by Kudeki et al. [1993], but the numerical simulations were carried out for both isotropic and specular scatterers with different sets of gravity wave parameters by Sürücü et al. [1995]. The numerical results of Sürücü et al. [1995] are summarized as follows. First, the individual horizontal SA wind estimates are very well predicted by the model of Kudeki et al. [1993] as long as the gravity wave has a long horizontal wavelength larger than the horizontal dimension of the MF radar scattering volume. When the scatterers are highly anisotropic ('specular') the estimated winds averaged over one period of the perturbing gravity wave exhibit statistically significant biases from the model of Kudeki et al. [1993], but the bias is not necessarily towards the phase speed of the gravity wave. The largest biases were obtained for large amplitude ($\sim$ 10 m/s) waves with small horizontal wavelengths ($<$ 40 km) and were on the order of 15 m/s. Based on these results, Sürücü et al. [1995] concluded that wind estimation biases of the magnitude observed in AIDA campaign results are unlikely to result from the mechanism suggested by Hines et al. [1993] but are more likely to result from the systematic measurement errors described by Kudeki et al. [1993]. Hocking [1989] has suggested that extended specular reflectors are unlikely, and probably broken up into short sections, thereby reducing further any biases produced by this "specular reflection" model.

The question about what motions were being detected by the SA type of experiment was not completely resolved by previous observations. Hence further studies of a similar type have been carried out over London, Ontario and the results are presented in the following sections. Our study contributes additional simultaneous comparison and includes continuous observations over fairly long collection periods. Our radars were located about 400 metres apart.

Intercomparison of different experimental techniques is essential, because this is the only way their suitability and limitations for particular applications may be rigorously determined. The two techniques that we consider here are the MF SA and the VHF meteor interferometer radar techniques. These are of particular interest because they

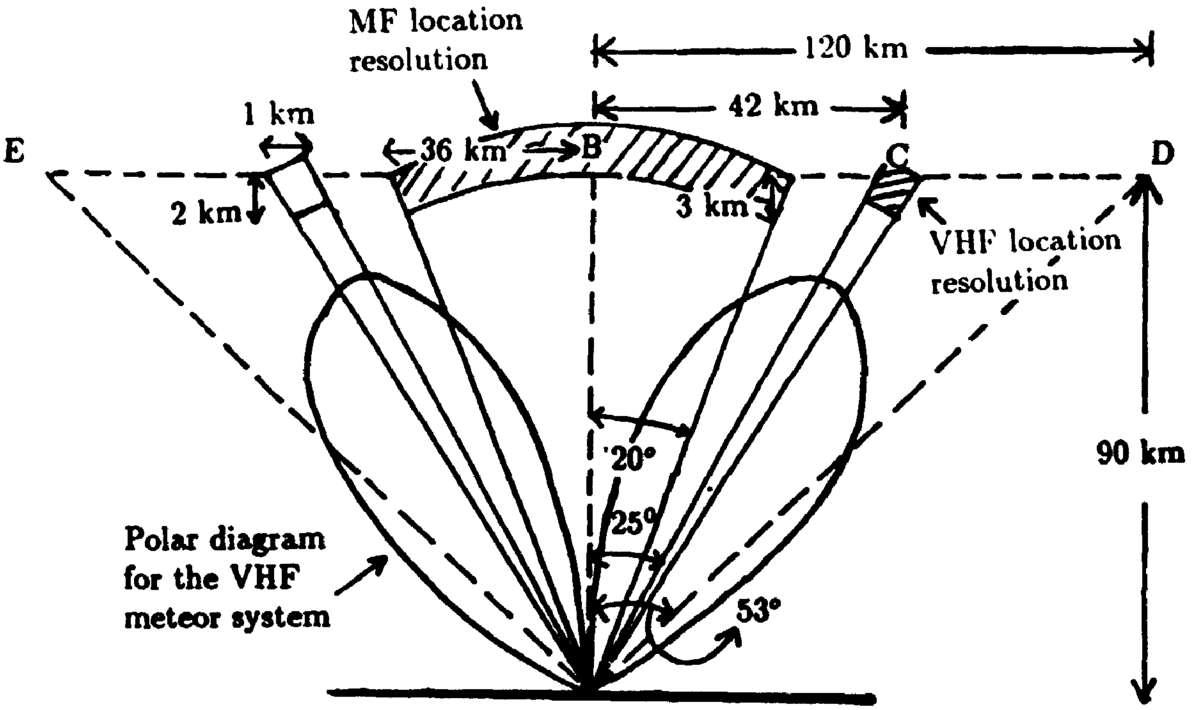

Figure 8.1: Geometrical overview of the experiment and the regions covered by the MF SA radar in relation to the VHF meteor system. See the text for more details.

are both used to measure winds and tides in the mesosphere and lower thermosphere (80-100 km). In the following section the comparison of the two experimental techniques are described. Section 8.3 describes two different data analysis methods used to analyze the meteor data, together with the method of analyzing the MF data and its statistical uncertainties. Following this, a comparison of winds and tides measured by the two techniques is described in Section 8.4, and the overall results are summarized in Section 8.5. The discussions and conclusions of this study are presented in Sections 8.6 and 8.7 respectively.

8.2 Comparison of the experimental techniques

Before we can make a useful comparison between the results obtained with two different techniques, we must recognize that the two techniques are strongly influenced by many factors unique to each particular system, such as location, antenna system, radar parameters and especially temporal and spatial distinctions between the two techniques.

A VHF interferometer meteor radar and a MF radar have been used to produce simultaneous observations of the horizontal winds in the mesosphere and lower thermosphere (81-98 km) above London, Ontario. The two sets of equipment were at locations about 400 meters apart. The MF (2.219 MHz) system has been used to measure the horizontal winds with the SA method in the 70-100 km height range. The VHF (40.68 MHz) system determines the horizontal wind velocity by means of radio reflections from meteor trails. The meteors are located to an accuracy of ±3 degrees in zenith and azimuth and their radial velocities recorded. All-sky least-squares fitting algorithms are then used to determine the 2D and 3D wind fields. A more detailed description of the MF and VHF radar systems can be found in Chapters 4 and 7 respectively. The VHF and MF systems have been operating simultaneously since July 1994. These provide a unique opportunity to check the consistency of parameters measured by the two different experimental techniques. The comparison between the two observations can be used to calibrate the techniques and to determine the importance of various assumptions that must be made in order to apply either method. Results of these comparisons are presented and discussed in the following sections.

Figure 8.1 illustrates the geometry of the experiment and the regions covered by the two techniques. The volume from which information is received by the MF SA system can be approximately determined from the effective pulse width (equivalent to height resolution) and the beam width of the polar diagram of the radar. The half-power half-width of the polar diagram is $\sim 20^o$ and the effective pulse width is $\sim$ 3 km. This implies that measurements at a nominal height of 90 km must be an average result for a horizontal area $\sim$ 72 km in diameter, with an 3 km uncertainty in height. Therefore, for the MF partial reflection experiment, the bulk of the returned power comes from within the volume of $\sim$ 10,100 km^3 ($\sim \pi r^2 h$, where $r \approx 36$ km at $h = 3$ km) centered at 90 km and the wind fields are probably more homogeneous over this region. Because the partial reflection process often involves scattering from a considerable volume, the wind field obtained by the SA technique is effectively a spatial smoothing (or averaging) over the volume from which information is obtained. Additionally, the 5 min record time length may result in some degree of smoothing (or averaging) of the drift motion.

In contrast, for the VHF meteor wind technique, because of the short lifetime of a meteor trail (typically ≤ 0.4 s) the radial component of the wind velocity obtained is essentially an instantaneous measurement and the wind measurement is made at time intervals of 2.5 s. The pulse width (equivalent to range resolution) of the VHF meteor radar is ~ 2 km. In meteor studies the radio reflection from a meteor trail is specular, with the majority of the reflected power coming from the first Fresnel zone. The size of the first Fresnel zone is of the order of 1 km ($\approx 2\ (\frac{R\lambda}{2})^{\frac{1}{2}}$, where R is the meteor range from the observatory site and λ is the operating radio wavelength) near 90 km at $\lambda = 7.375$ [McKinley, 1961]. Therefore, the majority of the returned power comes from relatively small volume of ~ 2.5 km^3. However, the need to combine data from many meteors to make useful estimates of the mean wind in fact means that the meteor winds produced are determined over a longer time period and larger effective volume than the SA method.

The VHF meteor radar described here has been designed to provide near all-sky coverage, but we have set the maximum limit for the zenith angle which a meteor can have to 53° in our data analysis procedure because there are only a few meteors detected from greater zenith angles. This limitation of the zenith angle also helps to reduce the degree of ambiguity of the meteor detection (see also Section 7.2.6). Figure 7.12 clearly shows that a large number of meteors ($\geq 70\%$ of the total meteors) over London are detected at zenith angles between 20° and 45°. In addition, the maximum power is radiated in the direction 25° off-zenith to the north, south, east and west (see the transmitter polar diagram in Figure 7.3). That is why the VHF radar beam is tilted 25° off zenith (on average) in Figure 8.1. It turns out that on average the collecting volumes of the two techniques are separated by ~ 50 km (distance between points B and C in Figure 8.1). Note that on occasions it is also possible for the two reflection points to differ horizontally more than 100 km (distance between points B and D in Figure 8.1) although the two techniques basically probe a very similar volume. Hence it is noteworthy that comparison was actually made using simultaneous MF and meteor measurements from the same height rather than the same volume. Therefore fluctuations possibly due to turbulence or gravity waves would be recorded by one technique before the other. It is also important to note that the successive trails observed with the meteor radar may be separated by horizontal distances up to 250 km (distance between points E and D in Figure 8.1). Since it is therefore possible that the line-of-sight velocities measured from successive meteor trails occurring at the same height but separated by large horizontal distances will be inconsistent, any meteor wind determinations from only a few widely spaced meteors within a given time interval should be suspect.

Finally, it is important to bear these points in mind when comparing the results obtained with two different techniques in these regions. When attention is given to short-period averages or instantaneous comparison (see Section 8.4.3), effects of temporal and spatial sampling distinctions between the two techniques become more evident and extreme care must be taken to interpret the data.

8.3 Data analysis methods

Different ways of procedures were applied and tested to make sophisticated analysis techniques to estimate the mean winds and tides between 82 and 98 km with MF and meteor radars. The probable uncertainty of the mean winds and tides has also been studied. Two types of analysis are in general use at London at present. The first analysis procedure was developed by the atmospheric dynamics group of the UWO (University of Western Ontario), and the second one was those of Groves [1959]. These two types of analysis will be discussed in the following sections.

8.3.1 UWO analysis method

The meteor data have been analyzed for the mean winds and tides using a standard UWO analysis procedure. In our analysis procedure, we have used both the 1-hour and 2-hour averaged mean winds at each height of observation, making the assumption that the wind is constant within the data interval. Information from other intervals is ignored. It should be noted here that each 1-hour or 2-hour averaged mean wind was obtained by using both the 2-D and 3-D least-squares fitting procedures (see Section 7.2.10 for more details). Different ways to deduce the wind field are denoted by Me_{12}, Me_{13}, Me_{22}, and Me_{23}, where the first subscript denotes the time bin (either 1-hour or 2-hour) and the second subscript denotes the type of least-squares fitting procedure (either 2-D or 3-D). This allows us to perform 4 different optional ways to estimate the mean winds and tides. Because of the presence of a low echo rate at certain times (see Figure 7.10), we adopted the superposed epoch analysis to estimate the mean winds and tidal oscillation. For a given height and time bins, all echoes occurring during a given month are superimposed onto either 24×1 hour bins period or 12×2 hour bins period for the equivalent day of the month (see Section 7.2.10 for more details).

There is considerable theoretical and experimental evidence that the wind variations in the mesosphere and lower thermosphere result from the superposition of a prevailing wind, and various tidal components (plus gravity waves). Therefore, we routinely fit and analyze the data using the classical harmonic techniques with mean, 24, 12, and 8 hour components [Manson and Meek, 1985; Manson et al., 1989]. The zonal (u)

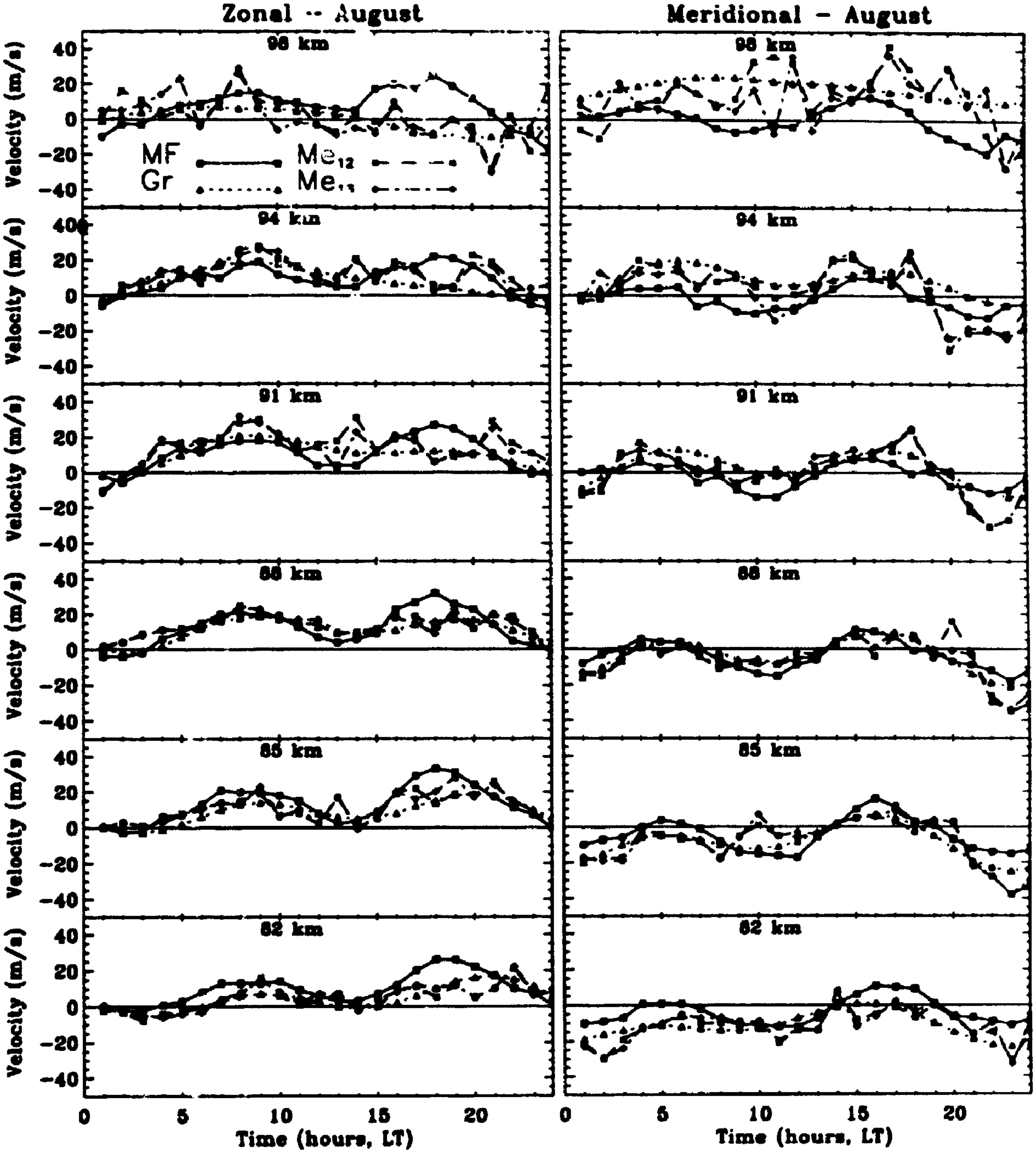

Figure 8.2: Hourly means and tidal fits for the zonal and meridional winds between 82 and 98 km in August 1994. See the text for more details.

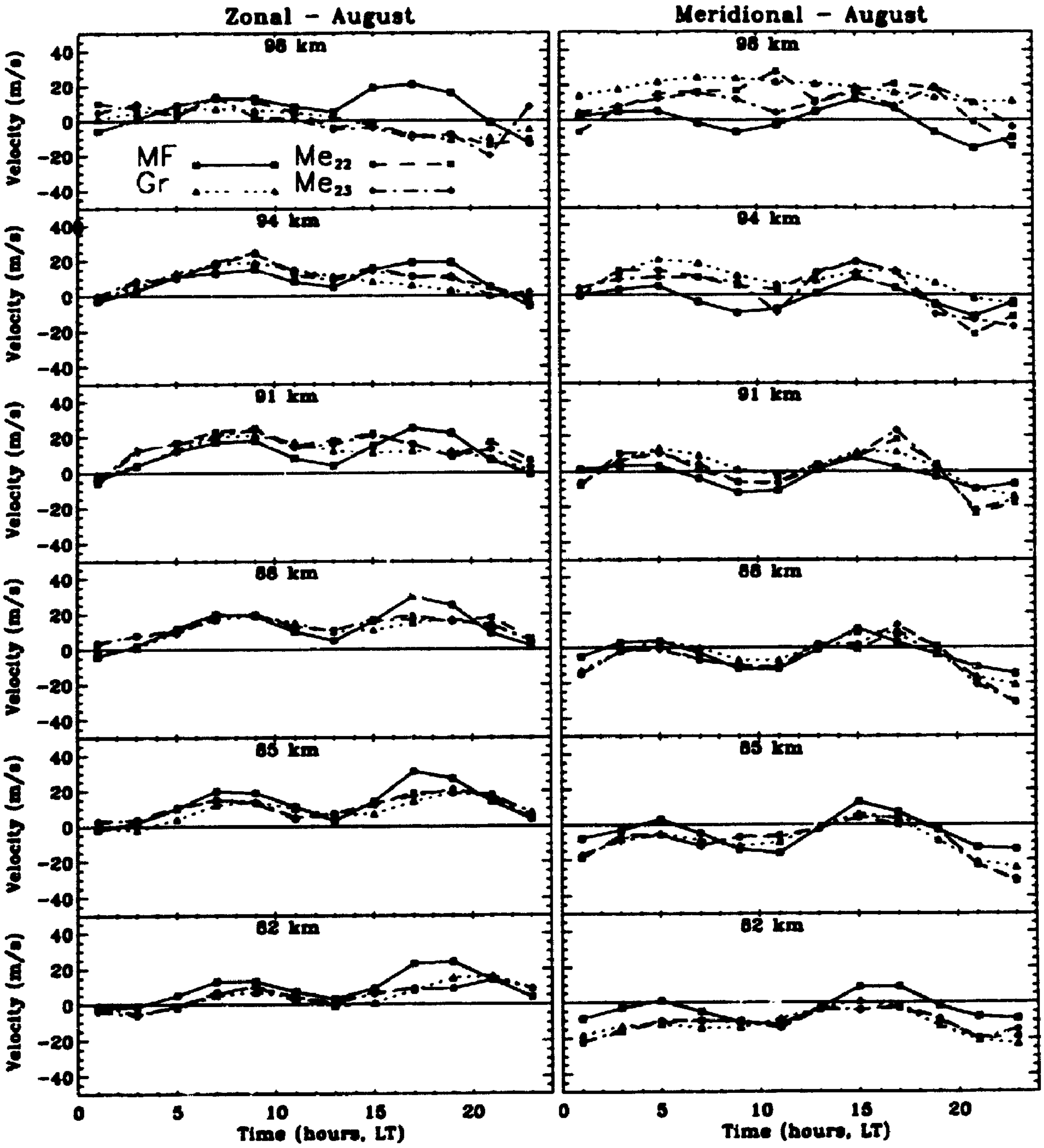

Figure 8.3: 2-hourly means and tidal fits for the zonal and meridional winds between 82 and 98 km in August 1994. See the text for more details.

and meridional (v) components were represented as a function of time (t) by

$$u(t), v(t) = a_0 + \sum_{i=1}^{i=3} a_i \sin(\frac{2\pi}{T_i} t + \Phi_i) \qquad (8.1)$$

where a_0 is the prevailing mean wind and a_i and Φ_i give the mean amplitude and phase for the 8 h ($i = 1$), 12 h ($i = 2$), and 24 h ($i = 3$) tidal components (in fact, any number of higher order harmonics could be included by simply continuing the Fourier series). The analysis was carried out separately for the Me_{12}, Me_{13}, Me_{22}, and Me_{23} wind fields at each height. Figures 8.2 and 8.3 show a typical least-squares sinusoidal fit (plus a fit by Grove's analysis, this will be discussed shortly) performed to the winds determined from meteor echoes. When there were short breaks in the data, these were simply omitted from the least-squares fitting routine without seriously affecting the results. A fit is only performed if at least 20 (10) different hours are represented in the 24 hourly (12 × 2 hour bins) data set for a given height. Note that there was no data gaps in the 24 hourly (12 × 2 hour bins) data set at all heights from July 1994 to May 1995.

In a similar fashion, the MF data have been analyzed during the same time period of observation for the mean winds and tides using a standard UWO analysis procedure (see Chapter 4). We also adopted the superposed epoch analysis for the MF data (similar to the meteor data). The time series of data is averaged into 1-hour or 2-hour bins and then a least-squares fit to the mean, 24, 12, and 8 hour periodicities is performed; i.e. a common method of data analysis was used for both the MF and meteor data.

8.3.2 Groves analysis method

An alternative meteor analysis procedure is due to Groves [1959]. Groves [1959] applied a statistical method to all the meteor wind data from a given observing period to determine specified parameters, characterizing the tidal structure. This consists of a parameter estimation on the basis of the least-squares theory. The data are usually analyzed in 24 hour periods and a prevailing wind plus 24, 12, and 8 hour harmonic components are fitted. The mean value and the amplitude and phase of each components are allowed to have polynomial variations with height. Several methods of wind analysis assume the vertical wind to be zero, and simply project the line-of-sight component onto the horizontal plane. This approximation is not serious (because the vertical velocity components for the tides are generally very small compared to the horizontal components), but is not made in the analysis method of Groves [1959].

Grove's analysis has been used by several groups [e.g., Rossiter, 1970; Stubbs and Vincent, 1973; Roper, 1965, 1975, 1978; Aso et al., 1979, 1980; Tsuda et al., 1980].

The accuracy of these profiles depends on the number of data points available, the distribution of echoes in space and time, and the number of degrees of freedom allowed in the polynomial height profiles. In our routine analysis, cubic (or third degree) polynomial variations with height in the zonal and meridional components were used. The Groves analysis can accommodate gaps of up to 4 hour in the data, although best results are obtained when echoes are evenly distributed throughout the day. The wind profiles are least reliable near the limits of the height range, where the echoes occur less frequently; often the velocities derived from the Groves analysis then tend to be very large. It is important to bear this in mind when comparing magnitudes in these regions. The best results are likely to be obtained near 88-91 km. The Groves analysis will not detect changes in the wind with periods less than 8 hour. No attempt has been made in the analysis to extract periodicities greater than diurnal.

Groves analysis produces mean vertical winds that can be of the order of meters per second, much larger than expected. Nevertheless, we will not use this in any of our analysis.

8.3.3 Comparisons of different methods

There are 4 different ways (Me_{12}, Me_{13}, Me_{22}, and Me_{23}) to estimate the winds and tides from the meteor data using the UWO analysis method. These four different ways, were applied and used for the estimation of winds and tides and their uncertainty. All these analysis methods were performed at each height. This leads to a better feel for the accuracy of our fits of winds and tides with the meteor radar.

The graphs in Figures 8.2 and 8.3 illustrate the accuracy of our fitting procedure between 82 and 98 km in August 1994 by showing the tidal fits performed on the 1-hour and 2-hour bins of MF and meteor data. Statistical analysis of uncertainty in winds and tides showed that the UWO harmonic fit performed on the 2-hour bins of data deduced by the 2-D least-squares fitting procedure (i.e. Me_{22}) agrees well with the harmonic fit of the Groves analysis (i.e. Gr in the figure). This may be due to relatively large number of meteors usually observed in 2-hour bins of data. Therefore, the mean wind and the amplitude and phase of the tidal oscillation for each month are finally estimated by taking a vector average of the two methods (i.e. vector average of Me_{22} and Gr, see Figure 8.3). From this type of data analysis, the tidal amplitude and phase structure are calculated for the meteor data, and then subsequently compared with the MF data.

8.3.4 Statistical analysis of uncertainty

In the following sections, a comparison between the MF SA winds and meteor winds is discussed. The MF data are displayed by solid lines and the meteor data are displayed by dotted lines. In general the error of any measurement system depends on non-ideal characteristics, e.g., non-linearity, environment and statistical effects of elements [Taylor, 1982]; i.e. uncertainty is a function of several variables.

In discussing the measurement accuracy, one needs consider the statistical uncertainties associated with the measurement. Not all types of experimental uncertainties can be assessed by statistical analysis based on repeated measurements. For this reason uncertainties are classified into two groups; the random uncertainty and the systematic uncertainty. Almost all derived wind measurements are subject to both random and systematic uncertainties. The systematic uncertainties are associated with imperfect knowledge of the radar system measurement inaccuracies. Systematic errors may arise for the MF system if the aerial separation is too small relative to the scale of the diffraction pattern; the calculated "true" velocity is often too small [e.g., Golley and Rossiter, 1970; also see Section 3.5.4]. Care must therefore be taken to ensure that the triangle used is sufficiently large, but if it is too large the analysis frequently breaks down. The aerial separation for our work is 225 metre and it turns out to produce reliable results. As another example, in our analysis (e.g., 2-D least-squares fit), a non-uniform distribution of scatterers in the volume, together with a strong vertical wind, could contaminate the measurement of the horizontal wind and lead to a systematic error in horizontal wind speed. This effect would always bias our result in the same direction. There is no definite method to tell us what to do about systematic uncertainties. Even then, other biases may be introduced by echoes from nearby transmitters, weak ground clutter echoes, etc. within a range gate. Also meteors might have a bias to certain days and the MF might have a bias to other different days. In fact, the only way of minimizing systematic errors is that they should be identified and reduced until they are much less than the required precision. Great care has been taken for the MF and meteor radars in system calibrations and processing to reduce the systematic errors as far as possible.

The random errors can be estimated by comparing results obtained simultaneously by quasi-independent methods. We can obtain a good feel for the uncertainties associated with the meteor wind velocities by comparing independently deduced quantities derived using the UWO and Groves analysis methods. The (random) uncertainties in the mean wind in our data analysis are found from the wind differences measured by the two different analysis procedures. Thus, provided the various quantities involved are independent, we can estimate the uncertainty in the resultant mean wind by taking a 95% confidence limits for the standard deviation for the differences measured by the two different analysis procedures between July 1994 and May 1995; i.e. we record statistics of the differences in amplitudes, phases, etc. and consider the data sets collectively to find typical distributions and thence standard deviations. The vertical structure of the uncertainties are established by dividing the recorded data into 3 height groups; i.e. 82-85, 88-91 and 94-98 km.

The uncertainties associated with the MF SA mean wind velocities were calculated in the following way. The data for each month were divided into two groups of data (e.g., 1-15 and 16-30 of August, 1994). Each group of data was then folded into a single 12 × 2-hour record (i.e. a superposed epoch). A fit was performed to each superposed epoch and the errors associated with the wind velocities were calculated from the differences in amplitudes, phases, etc. measured by the two groups of data. Again, data from all months were considered as a collective in order to determine standard deviations, etc. Thus, the resultant uncertainties of the MF data are estimated by taking a 95% confidence limits for the standard deviation for the differences measured by the two groups of data over all heights between July 1994 and May 1995.

8.4 Comparison of winds and tides measured by the two techniques

In the present section results obtained by two different techniques at the same time and place are compared, with a view to investigating whether the measured velocities detected by the partial reflection SA type of experiment are truly indicators of neutral air motions. Simultaneous MF and meteor measurements were made during the periods: 7-31 July, 1-30 August, 9-30 September, 1-25 October, and 23-31 December in 1994; 1-17 January, 1-21 March, 7-23 April, and 2-9 May in 1995.

It must be emphasized here that we have greatest confidence in our data for heights between 85 and 94 km (both MF and meteor radars), but show the data between 82 and 98 km for completeness. When both the height distribution (see Figure 7.9) and diurnal variations (see Figure 7.10) are considered, it is clear in the previous chapter that there is a general decrease of available meteor numbers detected below 82 km and above 98 km. Therefore, the profiles are most reliable between 85 and 94 km as far as the available meteor rate is concerned, on which the reliability of a wind measurement ultimately depends (see also Section 7.2.10). Furthermore, it should be also noted, as discussed in the previous chapters, that the summer MF radar echoes received above 95 km are contaminated by some degree of group retardation (see also Sections 3.2.4, 4.2 and 7.1.4). Therefore both techniques are most reliable in the 85-94 km height range.

It must also be emphasized here that we will only focus and discuss the comparison of the mean winds and tides by the two techniques - the characteristics of the mean winds and tides have already been discussed in Chapter 4.

8.4.1 Mean winds

Many studies have been made of neutral upper atmospheric movements using a variety of techniques. Reflection of electromagnetic waves from the ionized trails left by meteor ablation has long been used to determine the neutral wind motions in the upper mesosphere (80-100 km) [e.g., Greenhow, 1954; Elford and Robertson 1953; Robertson et al., 1953; Elford, 1959; Greenhow and Neufeld, 1956, 1961; Muller, 1966, 1968, 1970; Clark, 1974, 1978; Fellous et al., 1975; Glass et al., 1975; Roper, 1975, 1978; Kingsley et al., 1978; Poulter, 1980; Tsuda et al., 1980, 1981, 1887; Aso et al., 1980; Massebeuf et al., 1981; Poole, 1988, 1990; Reddi at al., 1993]. We are aware that our argument is very much based on the assumption that the meteor measurements provide accurate wind data in the 85-94 km height region, except where very strong alignment of the meteor trail with the direction of the Earth's magnetic field exists [Kaiser et al., 1969]; i.e. meteor trails follow very closely the movement of the neutral atmosphere at these heights. The degree of alignment required decreases with height and is about two degrees at 114 km. It can therefore be assumed with confidence that the large majority of meteor trials observed move with the neutral wind [see Section 7.1.5 for more details].

This section presents a comparison between the monthly mean winds measured by the MF and meteor radar systems for both the zonal and meridional components from July 1994 to May 1995 (Figures 8.4 and 8.5). The MF winds are displayed by squares connected by a solid line and the corresponding meteor winds are displayed by asterisks connected by a dashed line. We begin by drawing attention to the relatively excellent agreement between the two techniques observed for the zonal component in the 85-94 km height region. In particular, both techniques show excellent agreement below 94 km during July (exactly overlaying each other), below 94 km during August

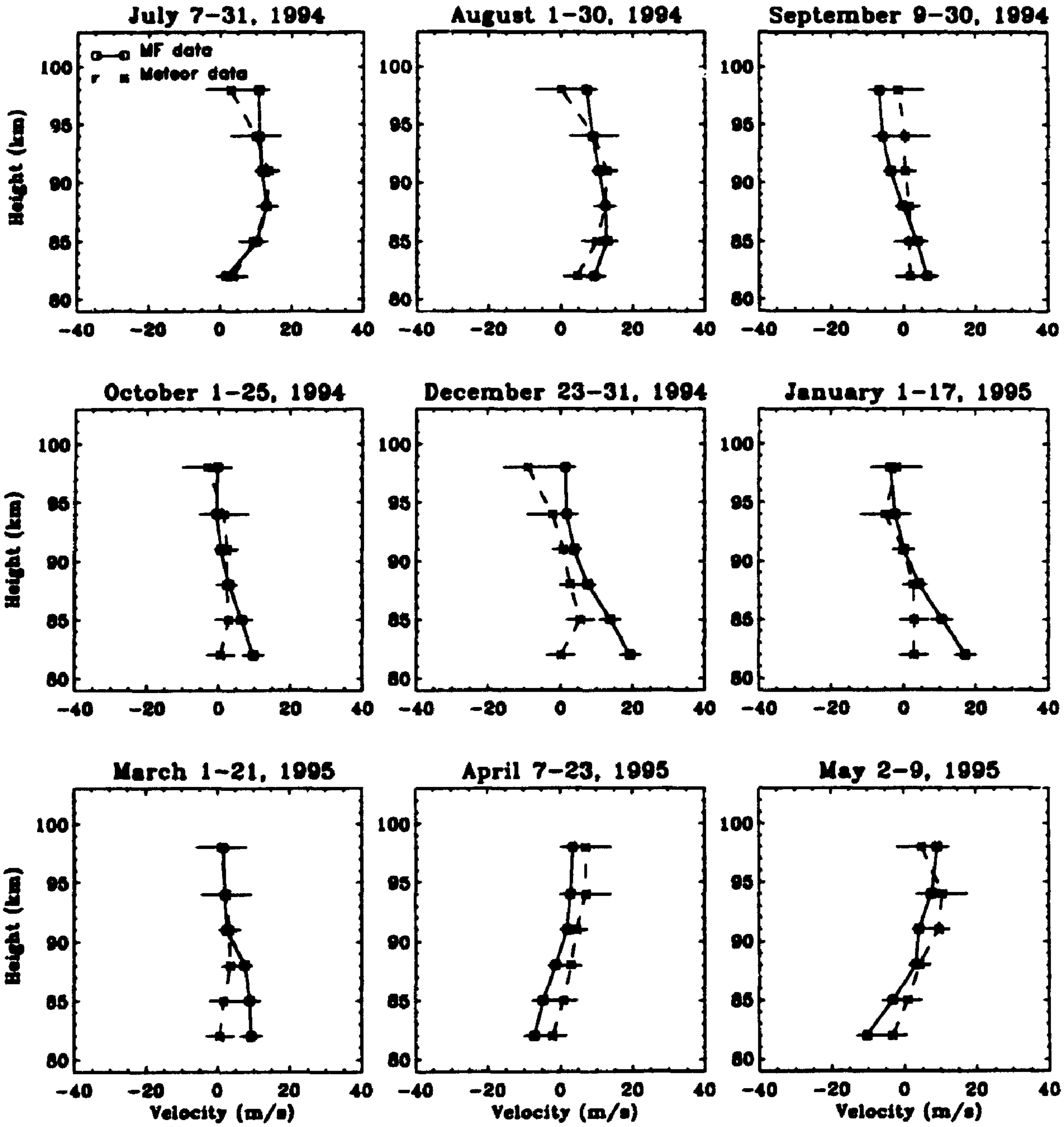

Figure 8.4: A comparison between the monthly mean winds measured by the MF and meteor radar systems for the zonal component from July 1994 to May 1995. The MF winds are displayed by squares connected by a solid line and the corresponding meteor winds are displayed by asterisks connected by a dashed line.

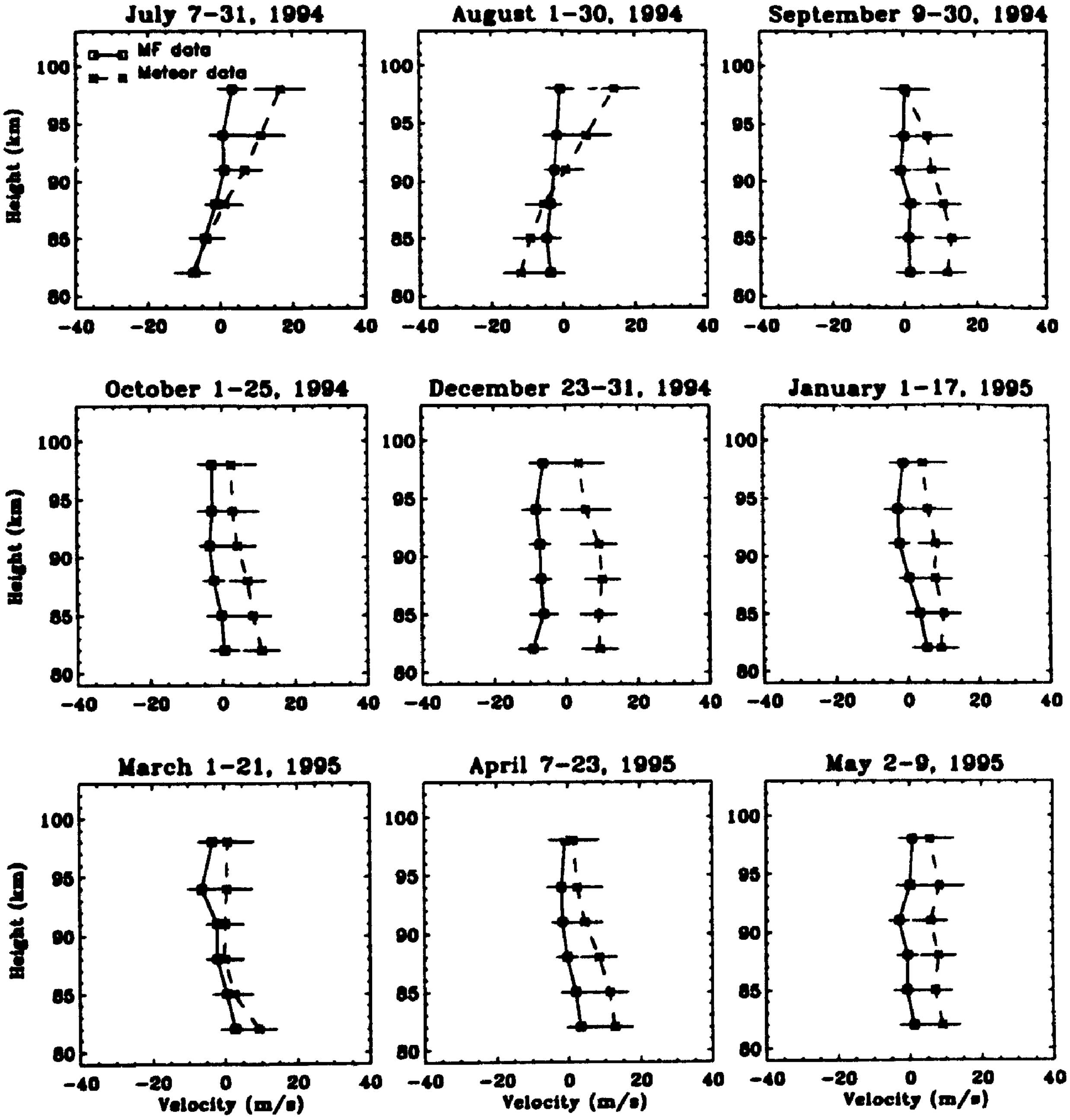

Figure 8.5: A comparison between the monthly mean winds measured by the MF and meteor radar systems for the meridional component from July 1994 to May 1995. The MF winds are displayed by squares connected by a solid line and the corresponding meteor winds are displayed by asterisks connected by a dashed line.

(just overlaying each other), above 85 km during October (just overlaying each other), above 88 km during January (exactly overlaying each other), and above 88 km during March (exactly overlaying each other). The agreements are not perfect, but very good agreements are observed during September, December, April and May. Overall, comparisons show remarkable agreement between the MF and meteor winds during all months of observation, and there are only a few instances of disagreement (> 5 m/s; *e.g*, December and March) is observed at certain heights.

Despite excellent agreement for the zonal component, as noted above, there are some discrepancies between the two techniques for the meridional component. There is a tendency for the meteor winds in the meridional component to be larger (> 8 m/s) than the SA winds at certain months (e.g., September, December, May). However, the agreement is generally good below 94 km during July, August, October, January, March and April. It is interesting to note here that the agreement seems a bit better after January 1995; this is when we increased the PRF from 1100 Hz to 2143 Hz in order to increase the meteor echo rate, on which the reliability of a wind measurement ultimately depends. In general, the meridional winds are relatively much more variable than the zonal winds over London (see Figure 4.5, Chapter 4). Also recall from Figure 7.13 that there was a higher percentage of meteors in the east-west vertical plane, which is also explain why the zonal agreement is better.

In order to arrive at a quantitative measure of the quality of agreement between the two sets of data, we have created scatter plots between the 2-hour averaged wind velocities deduced by the MF and meteor techniques for both the zonal and meridional components (Figure 8.6). Here, all 9 months of data were taken for heights between 85 and 94 km. The solid lines show the least-squares best fit. The linear correlation coefficient is 0.74 and the 95% confidence limits are 0.54 and 0.86 for the zonal component. For the meridional component the correlation coefficient is 0.42 and the 95% confidence limits are 0.11 and 0.66. The results reveal that the zonal mean winds are measured with a higher degree of consistency by the two techniques than the meridional mean winds during this period of observation.

Figure 8.7 shows histograms of the mean wind difference between the two techniques, MF minus meteor measurements, for all heights between 85 and 94 km from July 1994 to May 1995. In order to estimate the rough departure from symmetry (about zero value) of a distribution, we fit the data with Gaussian, mean, linear, and quadratic terms (i.e. least-squares fit to the histogram). That is, a functional form of the equation

$$F(x) = a_0 \exp(-z^2/2) + a_3 + a_4 x + a_5 x^2 \tag{8.2}$$

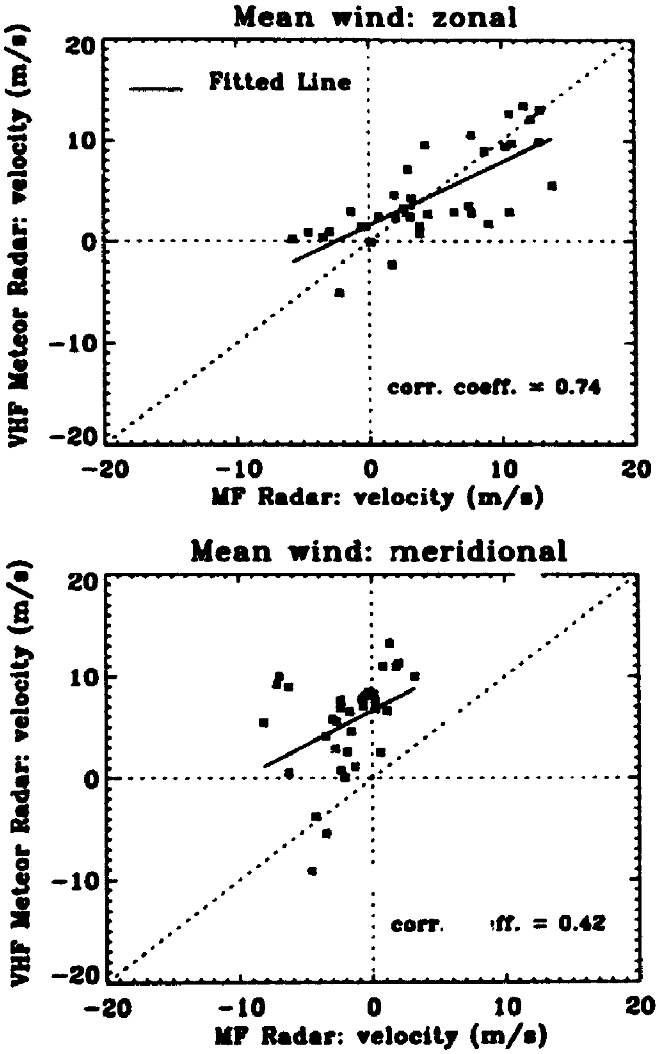

Figure 8.6: Scatter plots between the 2-hour averaged wind velocities measured by the MF and meteor radar systems for the zonal and meridional components. Here, all 9 months (from July 1994 to May 1995) of data were taken for heights between 85 and 94 km. The solid lines show the least-squares best fit.

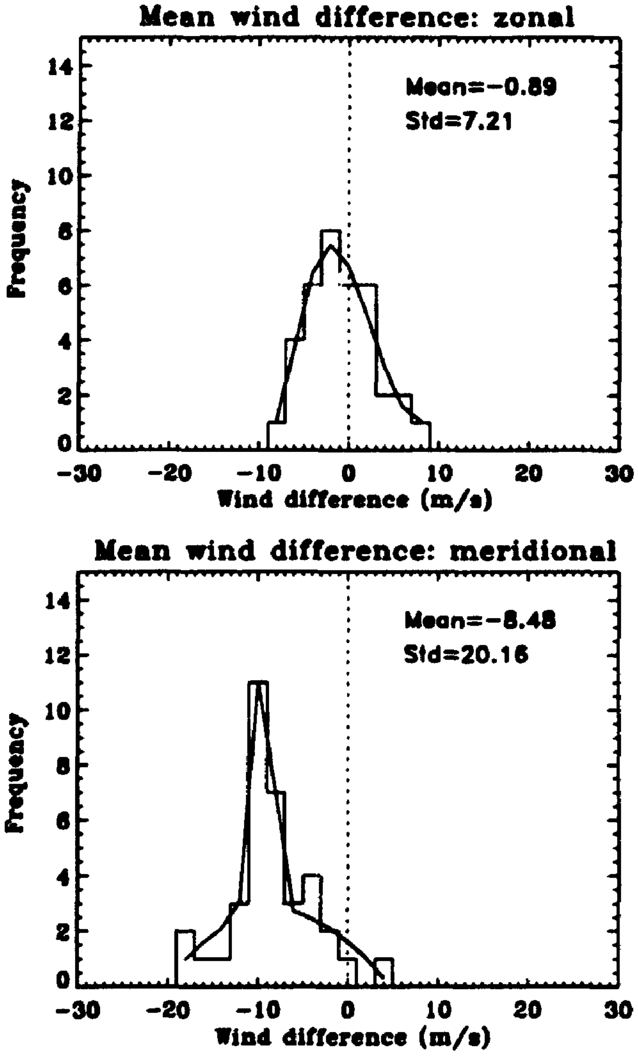

Figure 8.7: Histograms of the mean wind differences between the two techniques, MF minus meteor measurements, for the zonal and meridional components. Here, all 9 months (from July 1994 to May 1995) of data were taken for heights between 85 and 94 km. The fitted frequency curves are displayed by solid lines. The solid curve is a Gaussian with mean, linear and quadratic terms fitted to the distributions.

where

$$z = (x - a_1)/a_2 \qquad (8.3)$$

was fitted to the histograms of the zonal and meridional components, where a_0 = height of exp, a_1 = center of exp, a_2 = sigma (the width), a_3 = constant term, a_4 = linear term, a_5 = quadratic term. The fitted frequency curves are displayed by solid curves. If the central maximun of the frequency curve is to the right of the central origin (0,0), the distribution is said to have a larger MF wind velocity than the meteor wind velocity and vice versa. Figure 8.7 shows that the frequency curve for the zonal component is approximately evenly distributed to either side of the histogram. The mean of the fit is -0.89 m/s. Looking at a histogram of the meridional component, we see that most often the meteor wind is larger than the MF wind. The mean of the fit is about -8 m/s. This shows an underestimation of the meteor winds by the MF technique or an overestimation by the meteor method (possibly due to smaller percentage of meteors in north-south direction).

8.4.2 Tides

The meteor method has shown diurnal and semidiurnal tidal components to be present in the winds in the 80-100 km height range [e.g., Elford and Roberton, 1953; Greenhow, 1954; Muller, 1966; Fellous et al., 1975; Roper, 1966, 1975, 1978; Clark, 1978, 1983; Bernard, 1981; Aso et al., 1987; Reddi et al., 1993]. These should also be present in the drift results, if the latter reveal the neutral air motion. Therefore a comparison of the phases and amplitudes of tidal components would provide another method for testing the agreement of results obtained by two methods.

It should be noted here that the phases of the tidal oscillation were only taken into account when the amplitudes of the tidal oscillation are greater than 3 m/s, which is considered as a reasonable cut-off value after several tests. This is because the highest reliability of the phase estimates are associated with reasonably large tidal amplitudes. When amplitudes are small, the phase determinations are of dubious quality, reflecting more random phases. Therefore we ignore the phase estimates when the amplitudes are small ($<$ 3 m/s) for the tidal oscillation in the following sections.

In this section, the comparison of the amplitude and phase of the monthly tidal oscillation is made by the MF and meteor radar systems for both the zonal and meridional components from July 1994 to May 1995. We found that the influence of the terdiurnal tide is very small during this period of observation, and therefore will not be discussed in this chapter. The phase of the zonal component is defined as the local time in hours after midnight at which the maximum eastward wind velocity occurs and the phase of the meridional component is defined as the time of maximum northward wind velocity.

Semidiurnal tide

This section and the following subsection present the comparison of the tidal winds by the MF and meteor radars over London. The diurnal and the semidiurnal tides are separately compared and discussed. Figures 8.8-8.10 illustrate the mean behaviour as a function of height of the amplitude and phase of the semidiurnal tide observed by the two techniques from July 1994 to May 1995. The squares with the connecting solid line indicate the MF SA wind profile, the asterisks with the dashed line indicate the meteor wind profile. We see a relatively very good overall agreement in phase by the two techniques for the semidiurnal tide. Both techniques show excellent agreement particularly between 85 and 94 km in all months for the zonal component. Remarkably excellent agreement is clearly apparent for the zonal component during August, March and April; both measurements are just overlaying each other. Similar excellent agreements between the two techniques are also observed for the meridional component during August and April, and relatively good agreements are observed in all months except during May and July. A large difference of the phase is observed between the two techniques during May and July for the meridional component. It is important to point out that despite poor agreement of phase during July for the meridional component, excellent agreement is distinctly evident in amplitude during that month.

In general both techniques show clear tidal rotations with good agreement in amplitude (amplitude will be discussed shortly) and phase. Distinct tidal rotations are evident in both techniques during most of the months. The phases of the zonal and meridional of the semidiurnal tide generally show the form of a propagating tide, with the meridional component leading the zonal by ~ 3 h. This behaviour is consistent with the expected clockwise rotation of the wind vector in the Northern Hemisphere. In general downward phase progression (as inferred by the negative phase gradients i.e. earlier phases at upper height) of the semidiurnal tides are observed during most of the months. During the summer months (e.g., July and August) the phase profiles tend towards constant with height suggesting the presence of evanescent or long vertical wavelength behaviour. These structures are simultaneously observed by both techniques, and these characteristics are typical over London (see also Chapter 4).

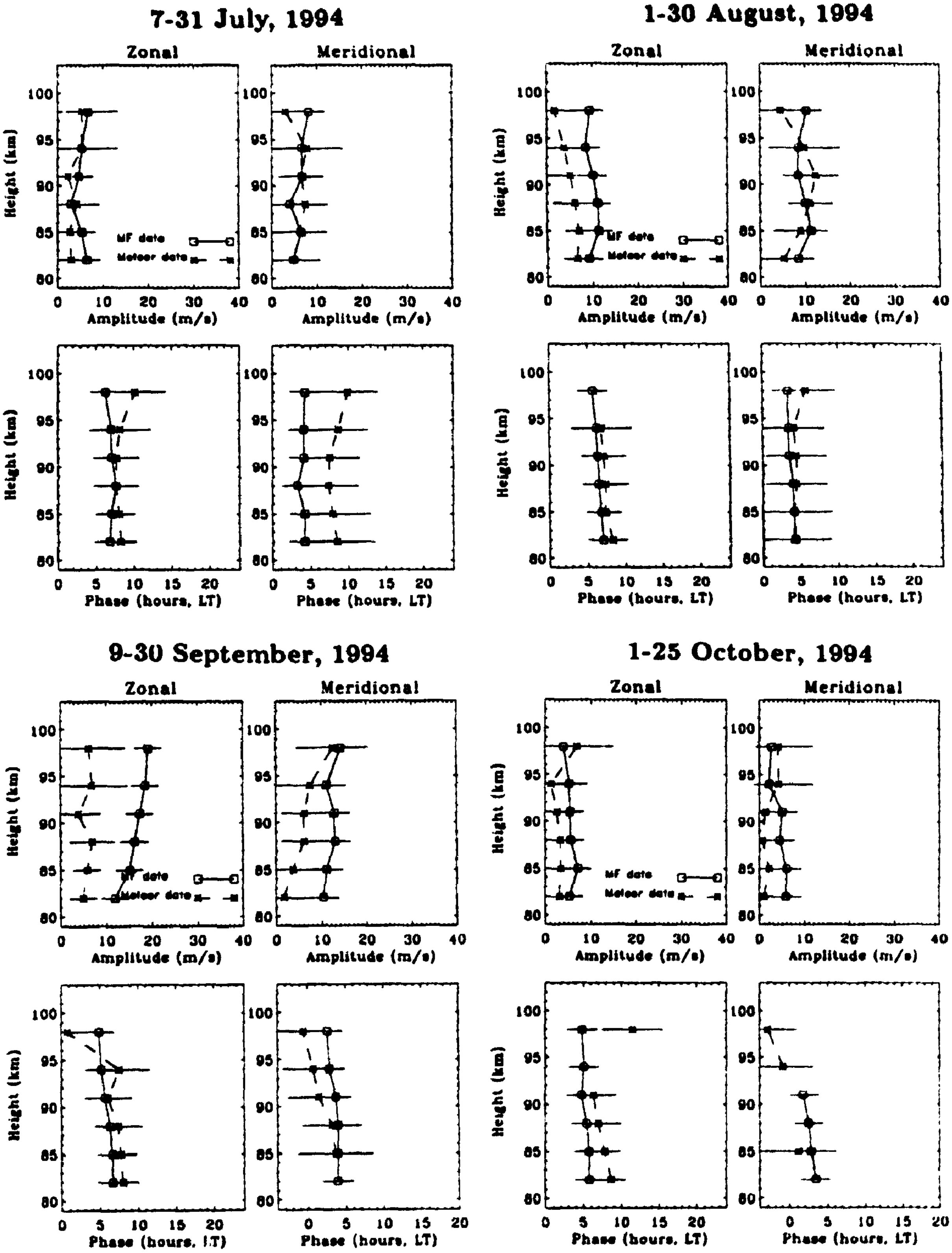

Figure 8.8: Height profiles of the amplitude and phase of the zonal and meridional components for the semidiurnal tide observed by the two techniques from July 1994 to October 1994. The squares with the connecting solid line indicate the MF SA wind profile, the asterisks with the dashed line indicate the meteor wind profile. Note that we ignore the phase estimates when the amplitudes are small (< 3 m/s). See the text for more details.

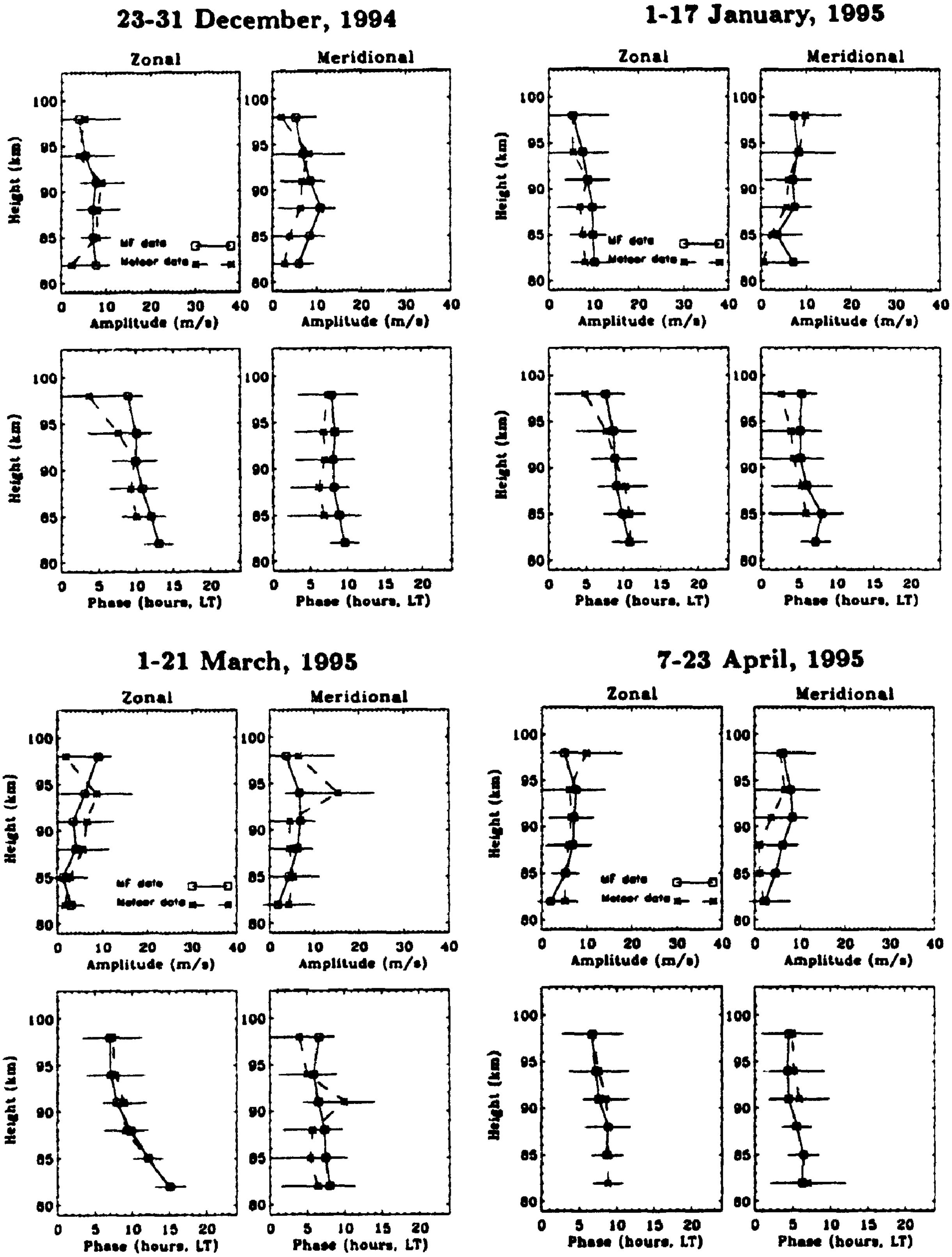

Figure 8.9: Height profiles of the amplitude and phase of the zonal and meridional components for the semidiurnal tide observed by the two techniques from December 1994 to April 1995. The squares with the connecting solid line indicate the MF SA wind profile, the asterisks with the dashed line indicate the meteor wind profile. Note that we ignore the phase estimates when the amplitudes are small (< 3 m/s). See the text for more details.

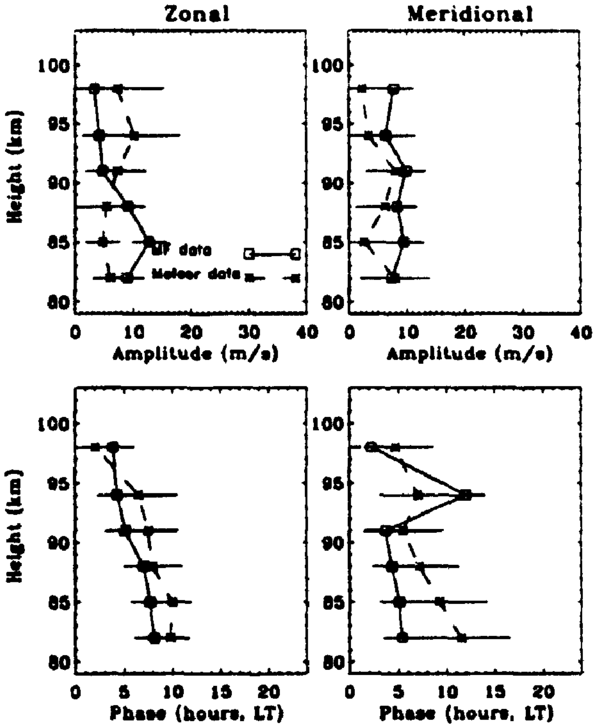

2-9 May, 1995

Figure 8.10: Height profiles of the amplitude and phase of the zonal and meridional components for the semidiurnal tide observed by the two techniques during May 1995. The squares with the connecting solid line indicate the MF SA wind profile, the asterisks with the dashed line indicate the meteor wind profile. Note that we ignore the phase estimates when the amplitudes are small (< 3 m/s). See the text for more details.

The comparison of the amplitude of the semidiurnal tide by the two techniques often show good agreement. In particular, both techniques show excellent agreement above 85 km during July, above 85 km during December, during January, below 91 km during March, and below 94 km during April for the zonal component. This excellent agreement is also observed for the meridional component below 94 km during July, above 85 km during January, below 91 km during March, and at certain heights during August and April. It is also clear that there is a tendency for the MF winds to be larger (> 5 m/s) than the meteor winds in both the zonal and meridional components during September. In contrast, the meteor winds show larger values than the MF winds in the zonal (e.g., between 88-94 km during March and above 91 km during May) and meridional (e.g., above 91 km during March and at certain height during August and October) components during certain months. One point which is

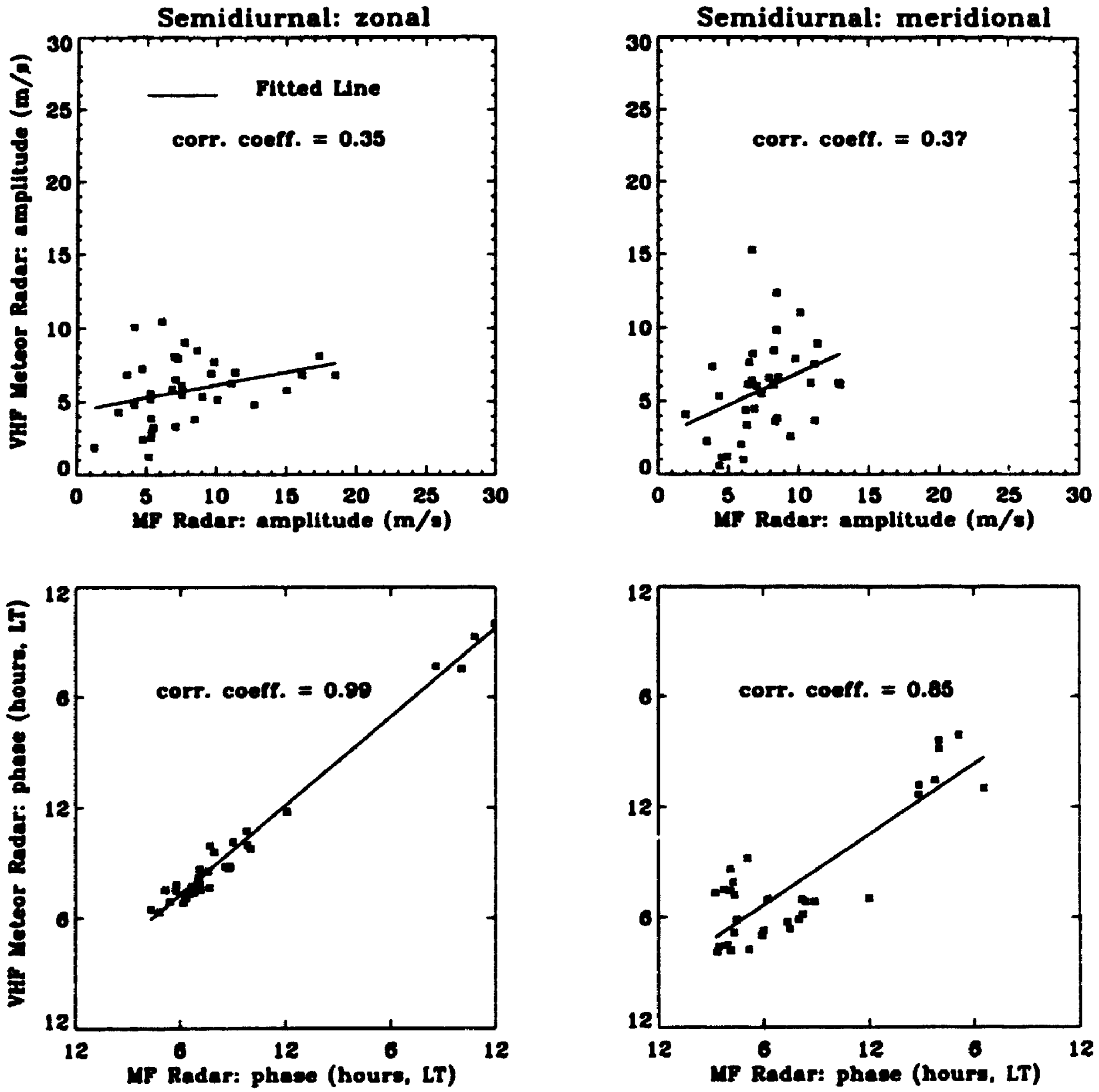

Figure 8.11: Scatter plots of the amplitude and phase (2-hourly average values) of the semidiurnal oscillation for the zonal and meridional components measured by the two techniques. Here, all 9 months (from July 1994 to May 1995) of data were taken for heights between 85 and 94 km. The solid lines show the least-squares best fit.

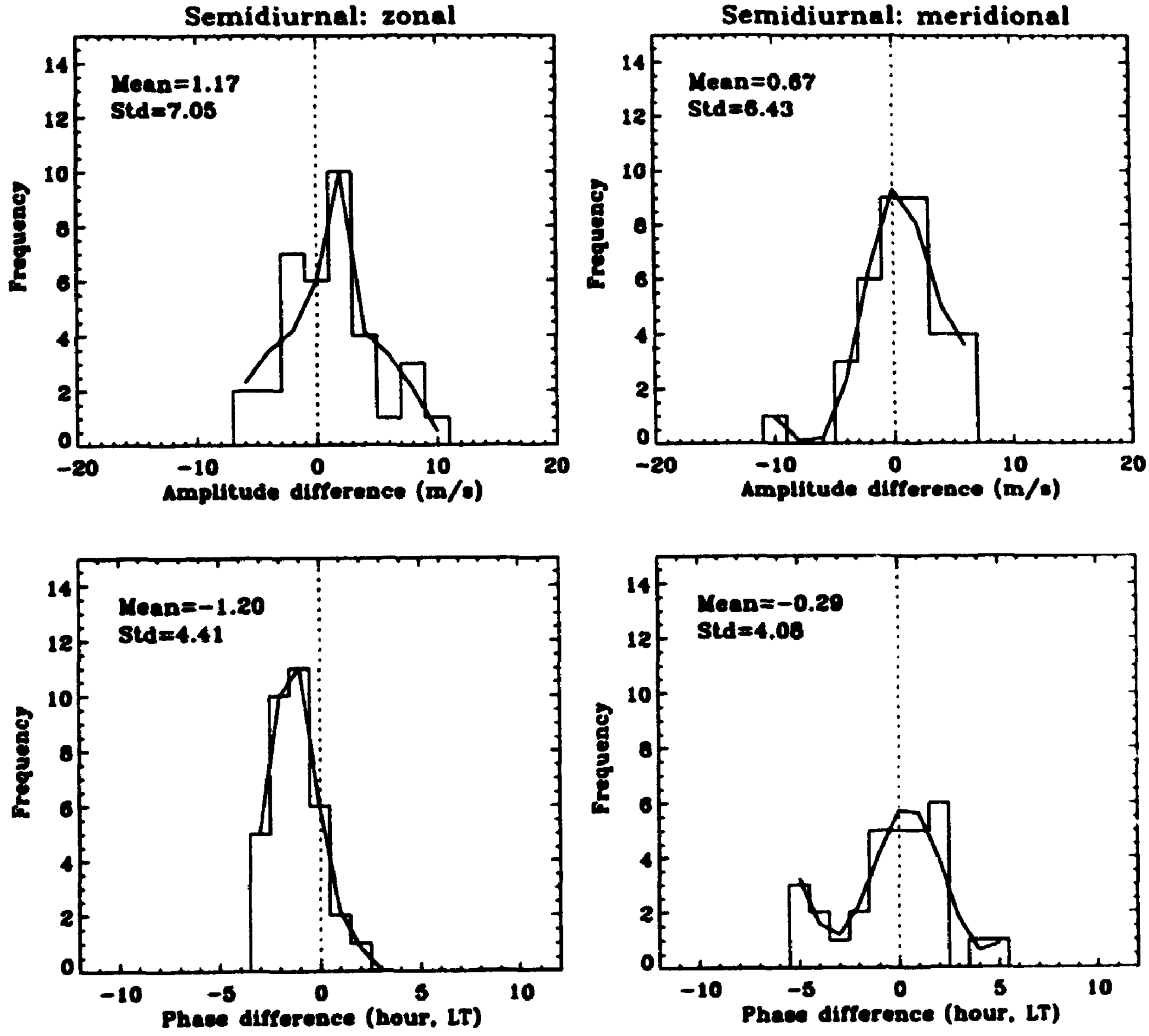

Figure 8.12: Histograms of the amplitude and phase differences between the two techniques, MF minus meteor measurements, of the semidiurnal oscillation for the zonal and meridional components. Here, all 9 months (from July 1994 to May 1995) of data were taken for heights between 85 and 94 km. The fitted frequency curves are displayed by solid lines. The solid curve is a Gaussian with mean, linear and quadratic terms fitted to the distributions.

worth making is that despite the poor agreement in amplitude during September, the phase does show relatively good agreement for the two techniques.

We also have created scatter plots of the amplitude and phase (2-hour average values) of the semidiurnal oscillation for both the zonal and meridional components measured by the two techniques, and these are illustrated in Figure 8.11. The solid lines show the least-squares best fit. Here, all 9 months of data were taken for heights between 85 and 94 km. The linear correlation coefficient for the amplitude is 0.35 and the 95% confidence limits are 0.02 and 0.61 for the zonal component. For the meridional component the correlation coefficient is 0.37 and the 95% confidence limits are 0.05 and 0.62. Similarly, the correlation coefficient for the phase is 0.99 and the 95% confidence limits are 0.98 and 0.99 for the zonal component. For the meridional component the correlation coefficient is 0.85 and the 95% confidence limits are 0.71 and 0.92. A remarkably excellent correlation between the two techniques for the phase is clearly apparent from these results for both the zonal and meridional components. In particular, the high degree of consistency between the two techniques are more striking for the zonal component (99%) than the meridional component. On the other hand, the low correlation valu flect the greater variability of the amplitude for the two techniques.

Figure 8.12 shows histograms of the amplitude and phase difference between the two techniques, MF minus Meteor measurements, for all heights between 85 and 94 km from July 1994 to May 1995. The solid curve is a least-squares fit to the histogram. For the amplitude the means of the fits are 1.17 m/s and 0.69 m/s for the zonal and meridional components respectively. This shows clearly that the MF amplitudes of the semidiurnal tide are on average comparable (within 1 m/s) with the meteor measurements. For the phase the means of the fits are -1.20 h and -0.29 h for the zonal and meridional components respectively. Again this shows that both techniques measure the same phase of the semidiurnal tide but on average phases occur (marginally) earlier in the MF observation than the meteor observation at higher heights.

The fact that there is overall good agreement in amplitude and an excellent agreement in phase for the two techniques clearly show that the two techniques are measuring the same phenomenon, i.e. the 12-hour tide.

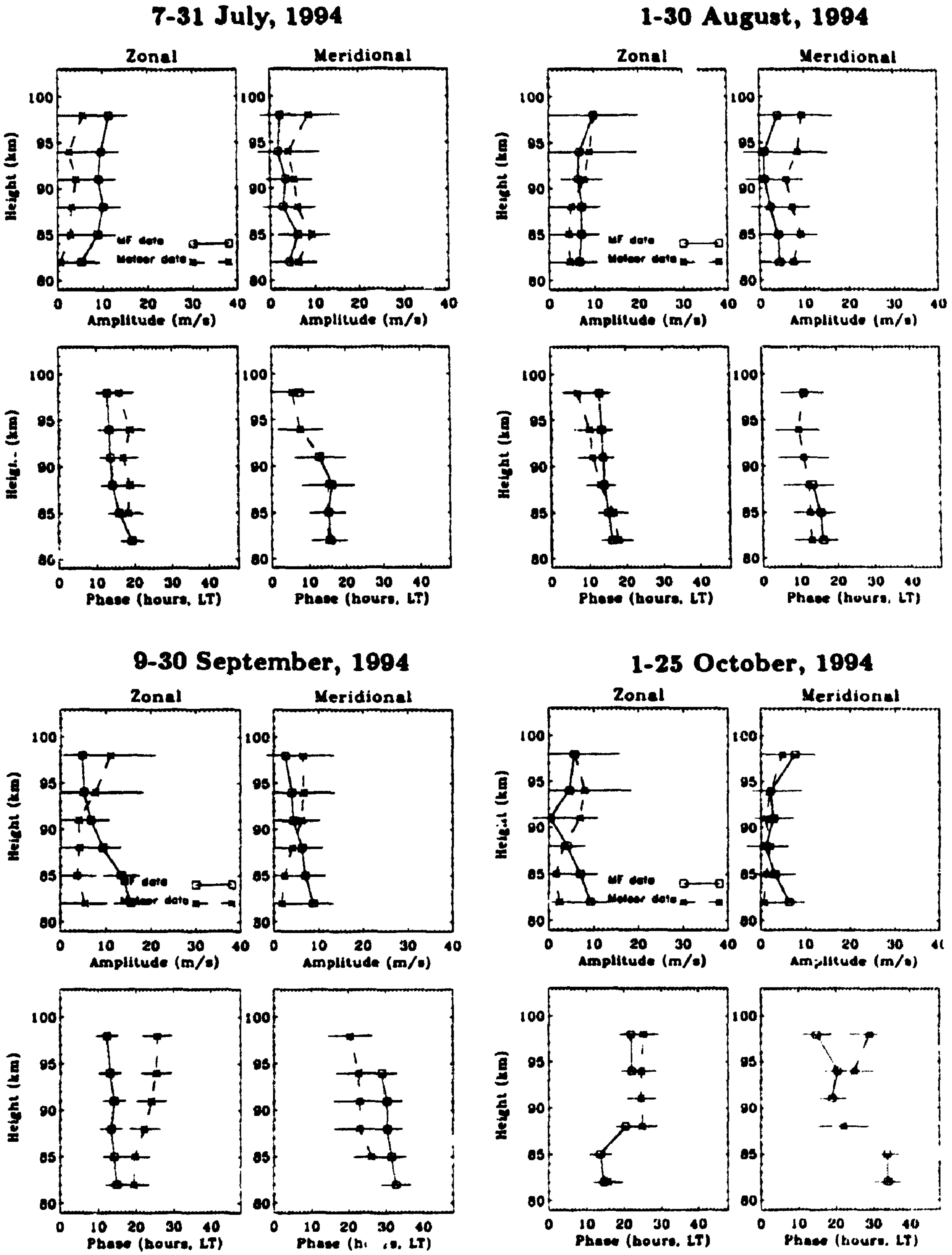

Figure 8.13: Height profiles of the amplitude and phase of the zonal and meridional components for the diurnal tide observed by the two techniques from July 1994 to October 1994. The squares with the connecting solid line indicate the MF SA wind profile, the asterisks with the dashed line indicate the meteor wind profile. Note that we ignore the phase estimates when the amplitudes are small (< 3 m/s). See the text for more details.

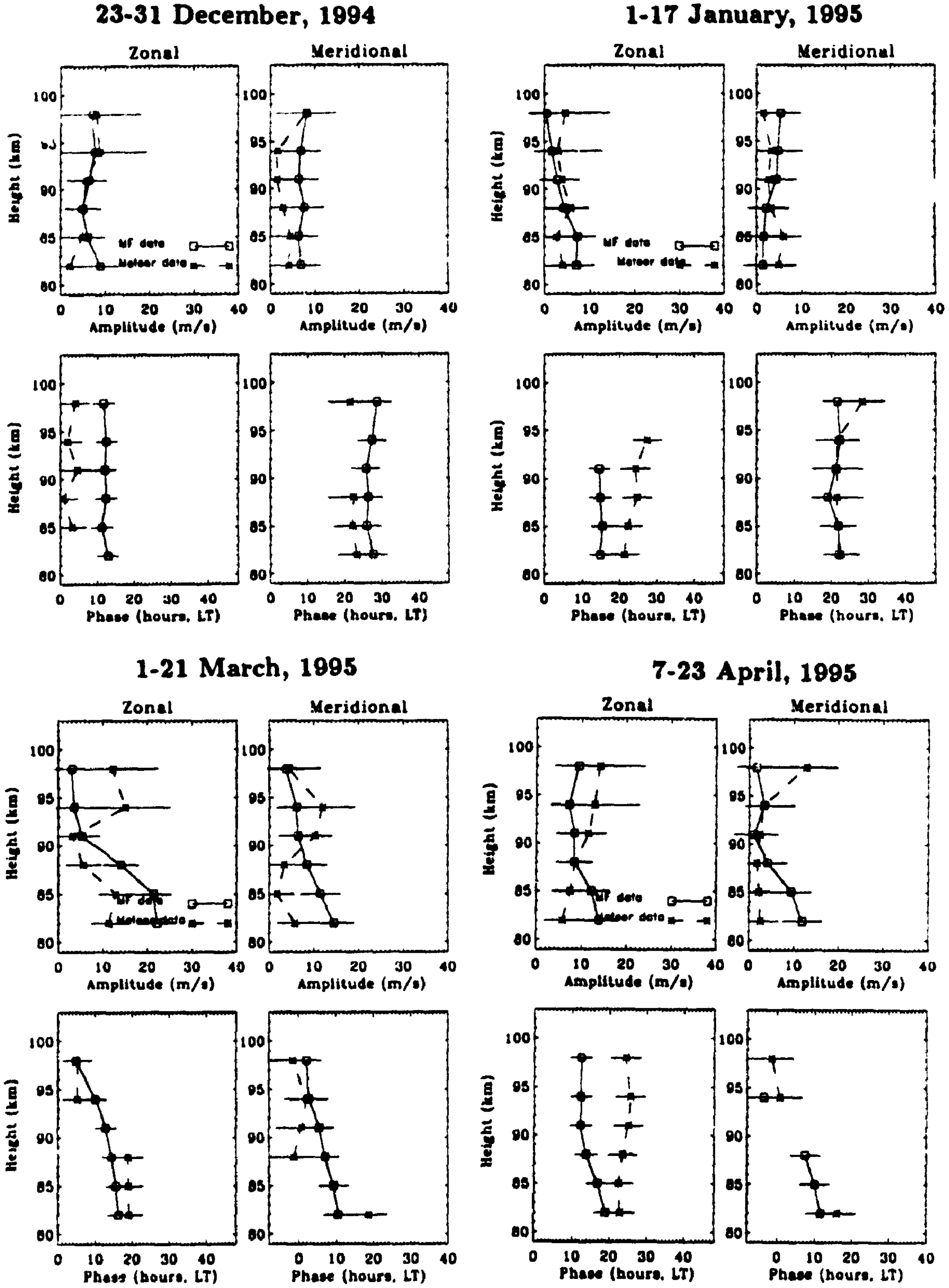

Figure 8.14: Height profiles of the amplitude and phase of the zonal and meridional components for the diurnal tide observed by the two techniques from December 1994 to April 1995. The squares with the connecting solid line indicate the MF SA wind profile, the asterisks with the dashed line indicate the meteor wind profile. Note that we ignore the phase estimates when the amplitudes are small (< 3 m/s). See the text for more details.

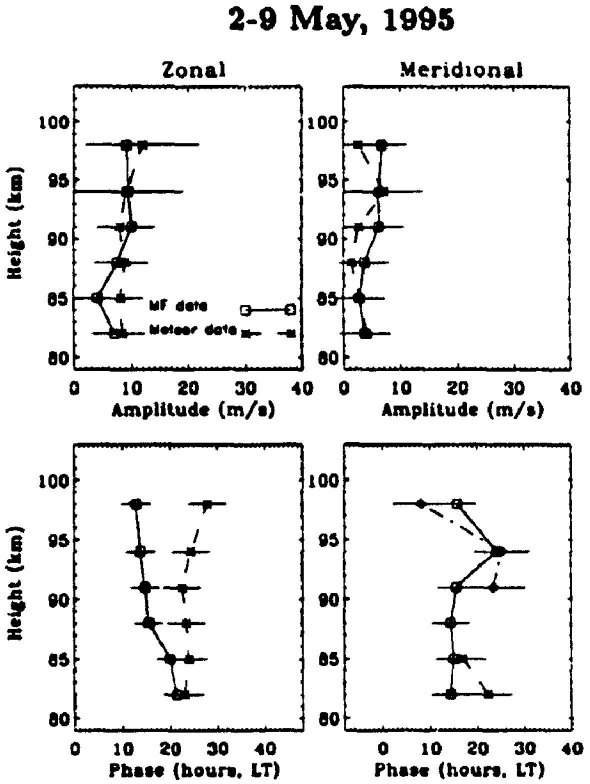

Figure 8.15: Height profiles of the amplitude and phase of the zonal and meridional components for the diurnal tide observed by the two techniques during May 1995. The squares with the connecting solid line indicate the MF SA wind profile, the asterisks with the dashed line indicate the meteor wind profile. Note that we ignore the phase estimates when the amplitudes are small ($<$ 3 m/s). See the text for more details.

Diurnal tide

Figures 8.13-8.15 present the mean behaviour as a function of height of the amplitude and phase of the diurnal tide observed by the two techniques from July 1994 to May 1995. The squares with the connecting solid line indicate the MF SA wind profile, the asterisks with the dashed line indicate the meteor wind profile. We again begin by drawing to the relatively good overall agreement in phase by the two techniques for the diurnal tide. Both techniques show good agreement particularly during July, August, September, and March for the zonal component. For the meridional component both techniques show excellent agreement during July, August and January, and show good agreement during September, October, December, March, April and May. Although the preceding comparisons have shown that on the average there is good overall agreement between the two techniques, it is nevertheless true that there are some disagreement in phase. The disagreement is apparently evident during October, December, January, April and May for the zonal component. Despite poor agreement in phase during December, January and May for the zonal component, it is interesting to note that both techniques show remarkably excellent agreement in amplitude during December, and good agreement during January and May.

The phases of the diurnal tides are generally less organized and show greater variability than the semidiurnal tide. In general downward phase progression of the diurnal tides are observed during most of the months, but on occasions the phase profiles of the diurnal tide show evanescent or long vertical wavelength behaviour (e.g., during July and December for the zonal, and during December and January for the meridional).

Comparison of the diurnal amplitude by the two techniques show reasonable agreement, but again some disparities are also observed. It is interesting to note that both techniques show excellent agreement in amplitude above 85 km during December, January and May for the zonal component; both measurements exactly overlaying each other particularly during December. Good agreements for the zonal component are apparent during August, September, and April. For the meridional component excellent agreement is clearly apparent for the two techniques above 85 km during September, May, and at certain heights during other months (e.g., between 88-91 km during October and January, between 88-94 km during April, and 82-88 km during May). Good agreement is also noted during July, above 88 km during October, December, below 94 km during January, between 85-94 during April. Despite overall good agreement, significant differences in amplitude of the diurnal tide are observed by the two techniques. The disagreements are clearly seen during July, October and March for the zonal component. For the meridional component the disagreements are apparent during August and March. It is important to point out that despite poor agreement in amplitude during July and March by the two techniques, good agreements are noted in phase during those months for the zonal component. Similarly, for the meridional component, in spite of the poor agreement in amplitude during August and March, the excellent agreement in phase during August and good agreement during March are observed.

Like the semidiurnal tide, we also have created the scatter plots of the amplitude and phase (2-hour average values) of the diurnal oscillation measured by the two techniques for both the zonal and meridional components. These are illustrated in Figure 8.16. The linear correlation coefficients for the amplitude are 0.21 and -0.16 for the zonal and meridional components. For the phase the correlation coefficient is

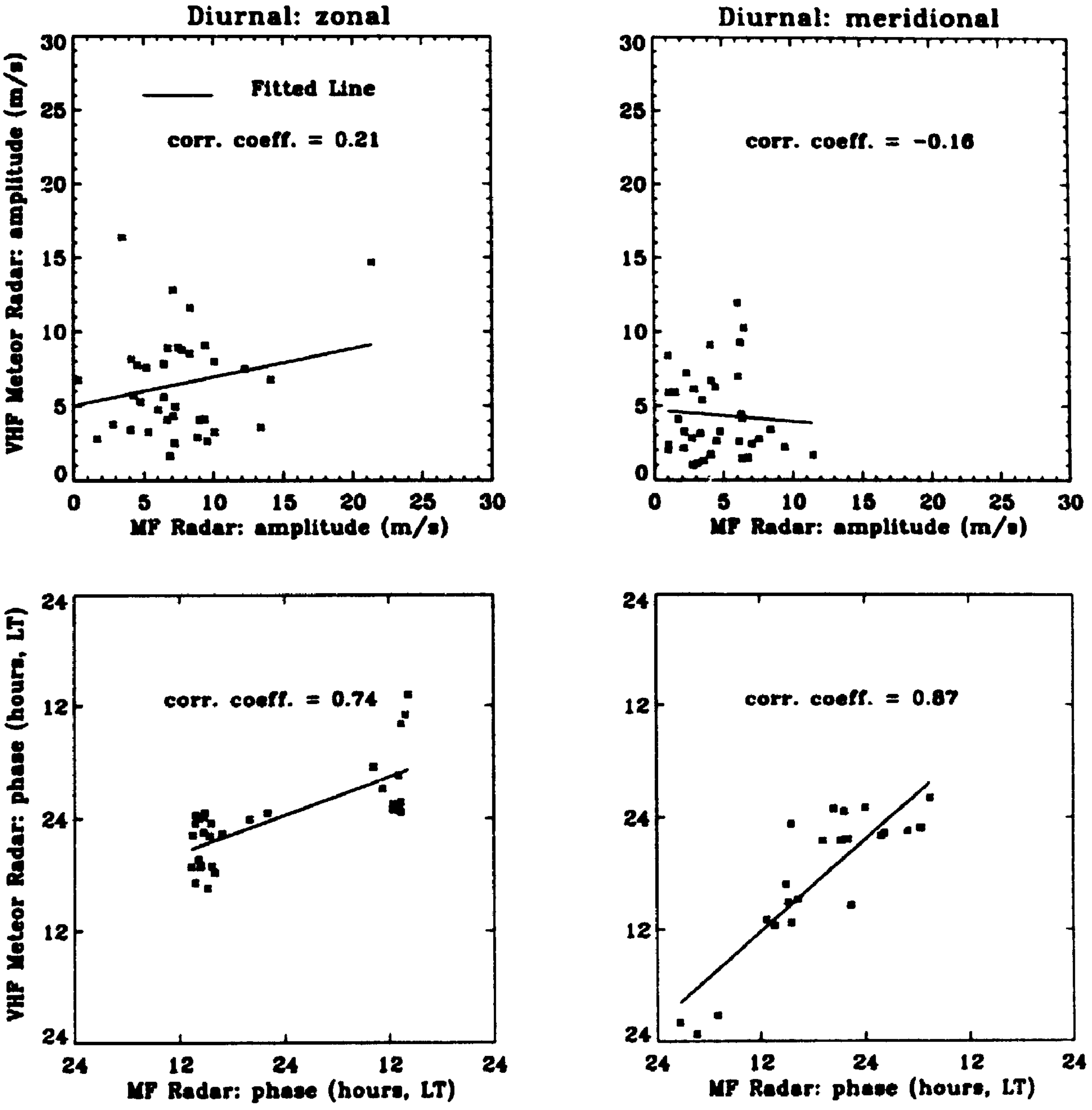

Figure 8.16: Scatter plots of the amplitude and phase (2-hourly average values) of the diurnal oscillation for the zonal and meridional components measured by the two techniques. Here, all 9 months (from July 1994 to May 1995) of data were taken for heights between 85 and 94 km. The solid lines show the least-squares best fit.

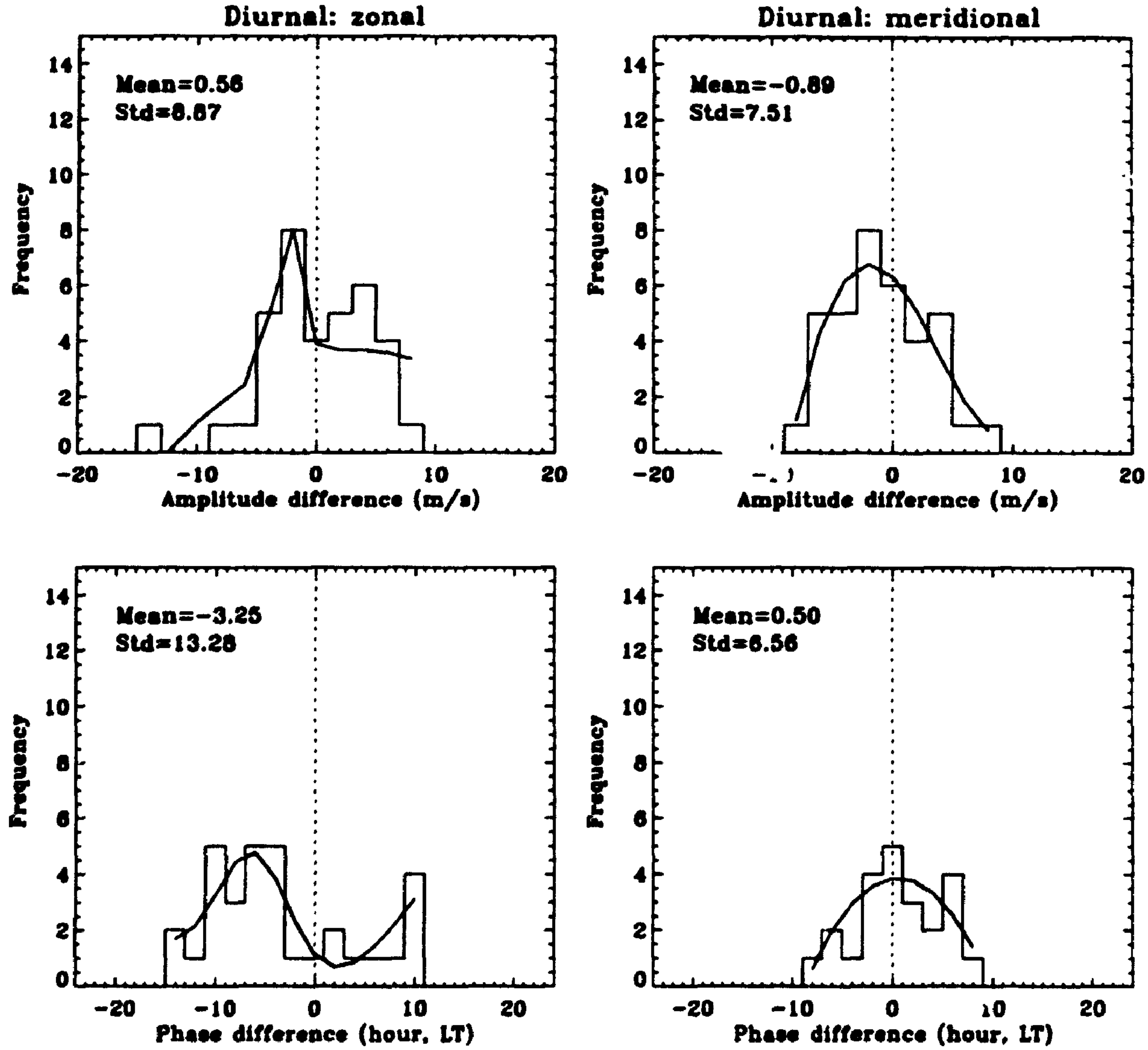

Figure 8.17: Histograms of the amplitude and phase differences between the two techniques, MF minus meteor measurements, of the diurnal oscillation for the zonal and meridional components. Here, all 9 months (from July 1994 to May 1995) of data were taken for heights between 85 and 94 km. The fitted frequency curves are displayed by solid lines. The solid curve is a Gaussian with mean, linear and quadratic terms fitted to the distributions.

0.74 and the 95% confidence limits are 0.53 and 0.87 for the zonal component. For the meridional component the correlation coefficient is 0.87 and the 95% confidence limits are 0.71 and 0.94. A significant correlation between the two techniques for the phase is clearly apparent from these results for both the zonal and meridional components. However, we also note that correlation values are not satisfactory in amplitude. This may be due to the general decrease of available meteor numbers for about 12 hours centered at 1800 LT (also see Figure 7.10), and this could lead to a poor harmonic fits. Groves analysis also depends on the number of points available, and the best results are obtained when echoes are evenly distributed throughout the day. Similar behaviour is also noted by other stations [e.g., Cervera et al., 1995].

Like the semidiurnal tide, Figure 8.17 shows histograms of the amplitude and phase difference between the two techniques, MF minus meteor measurements, for the diurnal tide from all heights between 85 and 94 km from July 1994 to May 1995. For the amplitude the means of the fits are -0.56 m/s and -0.89 m/s for the zonal and meridional components respectively. This shows that the MF amplitudes of the diurnal tide are on average comparable (within 1 m/s) with the meteor measurements. In contrast to the semidiurnal tide (mildly skewed to the left, $\sim$ 1 m/s), the frequency curve for the diurnal tide is mildly skewed to the right, $\sim$ 1 m/s). For the phase the means of the fits are -3.24 h and 0.50 h for the zonal and meridional components respectively. This shows that both techniques measure the same phase of the diurnal tide but on average phases occur earlier (skewed to the left) in the MF than the meteor observation at higher heights for the zonal component. In contrast, on average phases occur earlier in the meteor observation than the MF observation at higher heights for the meridional component.

8.4.3 Instantaneous wind comparison

The velocity determined from an individual meteor is only a component of the true wind, so the comparison must be made by projecting the individual MF wind velocities onto the meteor line-of-sight relating the reflection point to the receiving station. In this manner, a direct comparison was made with the line-of-sight velocity determined from individual meteors. In practice, records obtained within 5 minutes of each other were compared. If there were more than one meteor measurement detected within a 5 minute time interval then the average value was calculated and compared with the MF measurement. Figure 8.18 shows the results of more than 700 such comparisons randomly selected from different days throughout the 9 months period. The line-of-sight velocity, determined from the motion of the meteor trail, is

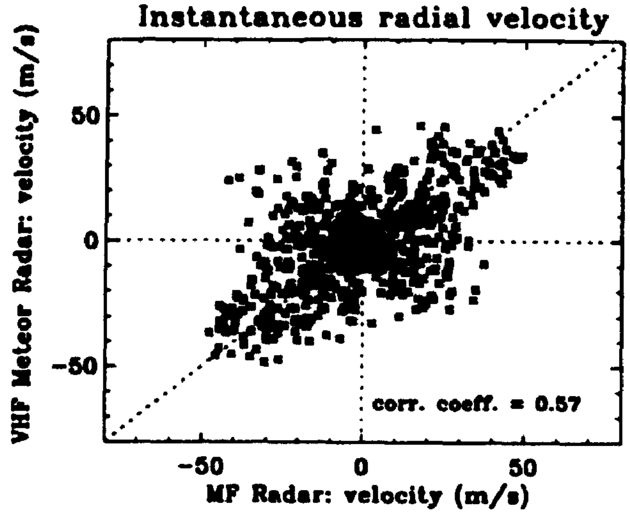

Figure 8.18: Projection of instantaneous horizontal MF drift velocities on the meteor line of sight compared with the line-of-sight velocity derived from meteor trails occurring simultaneously at the same height. See the text for more details.

plotted along the vertical axis, and the projection of the MF wind velocity is plotted along the horizontal axis. The line-of-sight velocities are regarded as positive if they were approaching the station.

Figure 8.18 shows a scatter plot of the instantaneous meteor wind velocities versus the MF SA winds. If there were perfect agreement between the two techniques, all points would lie along the straight dotted line bisecting the angle between the axes. In fact the agreement is not perfect. However, a statistical relationship does exists between the two sets of data, as the correlation coefficients have the values of 0.57, and the points tend to lie in the correct quadrants. The 95% confidence limits are 0.53 and 0.62. Figure 8.19 shows the histogram, for all heights, of the differences between the two techniques. A positive value for the difference indicates a greater MF wind velocity. This suggests that the agreement between the two techniques is better on some days than on others, and that on some days there is no agreement at all.

If the partial reflection experiment were always measuring the true wind alone, the scatter evident in Figures 8.18 could arise for a variety of reasons. The major part of the differences are explainable, as discussed in previously, due to geometry of the experiment, the wave-induced fluctuations model due to Kudeki el at. [1993], temporal and spatial distinctions between the two techniques. These may be recalled from Section 8.1 (pages 4 and 5) and Section 8.2. It is possible for the two reflection

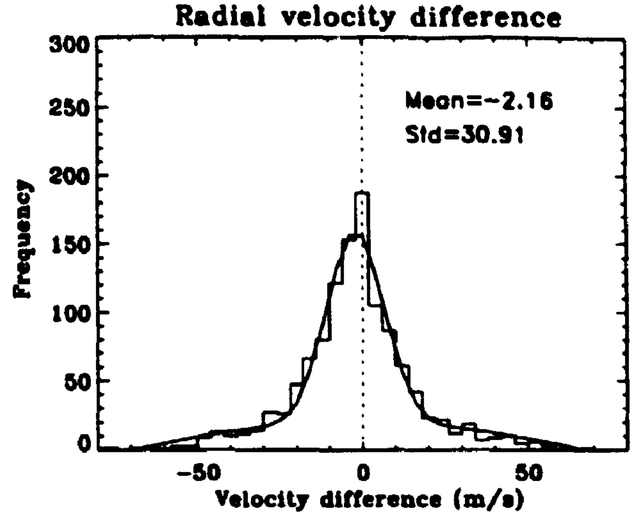

Figure 8.19: Histograms of the instantaneous radial velocity differences between the two techniques, MF minus meteor measurements. The fitted frequency curves are displayed by solid lines. The solid curve is a Gaussian with mean, linear and quadratic terms fitted to the distributions.

points to be separated horizontally by up to 100 km and vertically by 3 km. Obviously differences in the winds at these points could lead to differences in the velocities.

We have also performed instantaneous wind comparison between MF radar and WINDII (WIND imaging interferometer) instrument on the Upper Atmosphere Research Satellite (UARS) from January 20 to 30, 1993 during orbits of the spacecraft over London [Shepherd et al., 1993]. The kind of comparisons which have been accomplished are coincidences, where we look for WINDII observations which are within a certain radius of the ground radar station. A coincidence is defined as occurring when the ground radar station and the satellite measurement location differ by less than 500 km [Ward, 1995]. Preliminary comparisons were not encouraging (not shown) largely because of a paucity of WINDII data close enough to London, but we intend to pursue more intensive studies in the future. It is worth noting that wind measurements by WINDII at each height are essentially average over a layer 2-3 km thickness and 400 by 400 km horizontally.

8.5 Statistical summary of the MF and meteor comparisons

Finally, Tables 8.1 and 8.2 summarize the monthly behaviour of the simultaneous comparison of the mean winds and tides measured by the two techniques from July 1994 to May 1995. The behaviour of the comparison for each month on which comparison between the two techniques is possible has been classified into one of the three types as follows; based on associated error bars of the measurements (see Section 8.3.4).

The comparison is classified as "excellent" (denoted by "E") if wind difference measured by the two techniques is ≤ 2 m/s or if the amplitude difference of the tidal (semidiurnal or diurnal) oscillation measured by the two techniques is ≤ 2 m/s or if the phase difference of the semidiurnal (diurnal) oscillation measured by the two techniques is $\leq 1(2)$ hour (hours). The comparison is classified as "good" (denoted by "G") if wind difference measured by the two techniques is between 2 and 8 m/s or if the amplitude difference of the tidal (semidiurnal or diurnal) oscillation measured by the two techniques is between 2 and 5 m/s or if the phase difference of the semidiurnal (diurnal) oscillation measured by the two techniques is between 1 and 3 (between 2 and 6) hours. The comparison is classified as "poor" (denoted "P") if wind difference measured by the two techniques is > 8 m/s or if the amplitude difference of the tidal (semidiurnal or diurnal) oscillation measured by the two techniques is > 5 m/s or if the phase difference of the semidiurnal (diurnal) oscillation measured by the two techniques is $> 3(6)$ hours. It should be noted that the behaviour for each month is classified according to the average behaviour of the profile between 85 and 94 km: i.e. average value $\bar{x}$ of the difference (between the two techniques) for each profile is calculated as follows; $\bar{x} = \sum_{i=1}^{i=4} \mid \mathrm{MF} - \mathrm{meteor} \mid$, where, $i = 1$ (85 km), $i = 2$ (88 km), $i = 3$ (91 km), and $i = 4$ (94 km). The results of this type of comparison may therefore be summarized in the following way.

The general agreement between the MF and the meteor results is striking. It is to be seen from Tables 8.1 and 8.2 that in the majority of the cases there is a satisfactory agreement between the results of the two different techniques. It is distinctly evident that the zonal mean winds are measured with a higher degree of consistency by the two techniques than the meridional mean winds. Tables 8.1 and 8.2 show that all 9 comparisons for the zonal component correspond to either E or G type, while only 5 comparisons correspond to G type for the meridional component. In general, the semidiurnal tide shows relatively quite good agreement for the two techniques

Month	Mean wind	Semidiurnal		diurnal	
		Amplitude	Phase	Amplitude	Phase
July 7-31	E	E	E	P	G
August 1-30	E	G	E	G	G
September 9-30	G	P	G	G	G
October 1-25	E	G	G	P	P
December 23-31	G	E	G	E	P
January 1-17	E	E	E	E	P
March 1-21	G	G	E	P	G
April 7-23	G	E	E	G	P
May 2-9	G	P	G	E	P

Table 8.1: Monthly behaviour of the simultaneous comparison of the mean winds and tides measured by the two techniques for the zonal component from July 1994 to May 1995. The behaviour for each month on which comparison between the two techniques is possible has been classified into one of the three types, excellent (E), good (G), and poor (P) (see the text for more details).

Month	Mean wind	Semidiurnal		diurnal	
		Amplitude	Phase	Amplitude	Phase
July 7-31	G	E	P	G	E
August 1-30	G	G	E	P	E
September 9-30	P	P	G	E	G
October 1-25	G	G	G	G	G
December 23-31	P	G	G	G	G
January 1-17	G	E	C	G	E
March 1-21	G	G	G	P	G
April 7-23	P	G	E	G	G
May 2-9	P	G	P	E	G

Table 8.2: Monthly behaviour of the simultaneous comparison of the mean winds and tides measured by the two techniques for the meridional component from July 1994 to May 1995. The behaviour for each month on which comparison between the two techniques is possible has been classified into one of the three types, excellent (E), good (G), and poor (P) (see the text for more details).

than the diurnal tide. Out of 36 comparisons (combining amplitude and phase), only 5 comparisons correspond to P type for the semidiurnal tide, while there are 10 comparisons correspond to P type for the diurnal tide. It is interesting to note from Tables 8.1 and 8.2 that the semidiurnal phase for the zonal component and the diurnal phase for the meridional component correspond to either E or G type for all months. Thus we can say that both techniques measure these quantities with high degree of consistency. We also note that the worst agreement occurs in the diurnal amplitude for the zonal component; out of 9 comparisons, only 5 comparisons correspond to G type.

Furthermore, it must be noted from Tables 8.1 and 8.2, that out of 45 comparisons for the zonal component (9 comparisons for the mean wind plus 18 comparisons for the semidiurnal tide plus 18 comparisons for the diurnal tide), there are 16 comparisons correspond to E type, 19 comparisons correspond to G type, and 10 comparisons correspond to P type. For the meridional component, there are 9 comparisons correspond to E type, 27 comparisons correspond to G type, and 9 comparisons correspond to P type. Combining the results of the zonal and meridional components, it is equivalent to say that we are 80% confident that both techniques measure the same motion of the winds and tides. Therefore, it is concluded that when using weak partial reflections in the height range 85-94 km, the SA technique provide reliable estimates of the neutral air motion.

Differences and discrepancies are as likely to be due to errors in the meteor method as in the SA method. Figure 8.20 illustrates the mean behaviour as a function of height of the amplitude and phase of the semidiurnal tide during July and August obtained by UWO (i.e. Me_{22}) and Groves (i.e. Gr) least-squares fitting analysis procedures performed on the meteor data, and these are compared with the MF data (see Section 8.3). Generally the UWO least-squares fitting procedure agrees well with the harmonic polynomial fit of the Groves analysis, and these are illustrated for the zonal component during July and August in Figure 8.20. However, it is important to note that on occasions there are differences between these two types of analysis methods. These are illustrated for the meridional component during July and August in Figure 8.20. Note also that the UWO method agrees better with the MF data than the Groves method during July, and the Groves analysis method agrees better with the MF data than the UWO method during August. These comparisons suggest that on occasions differences can be significant just between these two analysis methods; that is, UWO-Groves comparison is no better than MF-meteor comparison. Therefore it is important to bear this point in mind when comparing the results obtained with

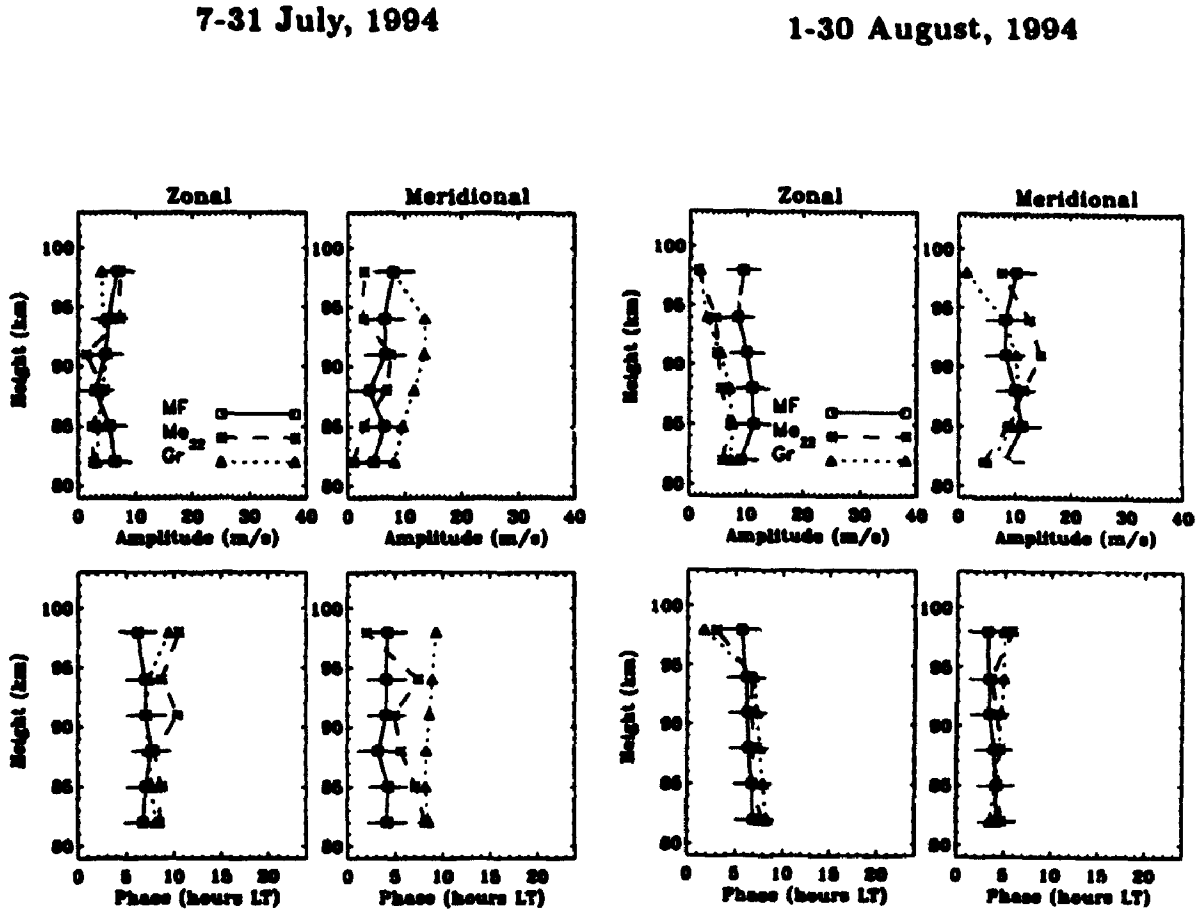

Figure 8.20: This figure illustrates the mean behaviour as a function of height of the amplitude and phase of the semidiurnal tide during July and August obtained by UWO (i.e. Me_{22}) and Groves (i.e. Gr) least-squares fitting procedures performed on the meteor data, and these are compared with the MF data.

the two techniques.

In order to arrive at a quantitative measure of the quality of agreement between the two techniques, the 9 months of the data from July 1994 to May 1995 were classified into summer (July and August), fall (September and October), winter (December and January), and spring (March, April and May). Tables 8.1 and 8.2 show that, out of 20 comparisons during the winter, there are 17 comparisons correspond to E or G type. It is equivalent to say that we are 85% confident that both techniques measure the same motion of the winds and tides. In the fall, out of 20 comparisons, there are 15 comparisons (75% confident) correspond to either E or G type. Similarly in the winter, out of 20 comparisons, there are 17 comparisons (85% confident) correspond to either E or G type. Finally in the spring, out of 30 comparisons, there are 22 comparisons (73% confident) corresponding to either E or G type. These results reveal that the agreement is often better during the summer and winter periods than the fall and spring periods. It is noteworthy that the seasonal changes occurs during the fall (summer to winter circulation) and spring (winter to summer circulation) periods, and consequently the wind fields in the upper atmosphere are considerably more variable during these periods than other seasons. In summary, during all season the amplitude and phase of both the semidiurnal and diurnal tides estimated from partial reflections from the meteor region show a good agreement with meteor winds.

8.6 Discussion

The MF SA partial reflection experiment has been shown to be capable of measuring the neutral air motion in the 85-94 height region at least as well as the meteor winds. Both methods are susceptible to errors and biases, but we cannot determine if one is worse than the other. A comparison has been made with winds and tides determined by the VHF interferometer meteor radar technique and very good agreement has often been found in most of the months. A comparison of the two sets of winds and tides measurements shows very good overall agreement between the two techniques. These comparisons confirm the overall impression created by the MF SA technique that the technique reliability indicates the principal features of the neutral air circulation.

At the same time, however, we note in particular that while the spaced antenna method using partial reflection is capable of measuring the neutral wind, on occasions there are some differences between the results of the two measuring techniques, which are too large to be explained by the random and systematic errors of the two methods and will have to be studied further. It should be remembered that almost all derived wind measurements by different techniques are subject to their own inherent limitations, assumptions and uncertainties, such as environment, geometry, statistical effects, spatial and time resolution, etc. Therefore, the two determinations might be expected to differ for several reasons.

Although the principles of measuring and expressing the velocities are quite different for the two techniques, each experiment purports to detect individual motions of small (temporal and/or spatial) scale and to summarize these statistically. If the estimated mean values were found to differ in a systematic manner, (and if the spatial and temporal sampling were more nearly identical) then we might expect to explain this as a difference in the quantity actually measured. For example, the SA technique might respond to the phase velocity of gravity wave motions differ systematically from the winds revealed by the meteor radar, as has been asserted in the past. However the converse is generally observed. The sampling intervals of the two experiments, although similar in many respects, differ significantly in others, and despite this they yield nearly excellent estimates of mean wind velocities (particularly for zonal) and tides (both amplitude and phase) in many cases (Tables 8.1 and 8.2).

However, we also see that most often the meteor wind is larger than the MF wind for the meridional component. This may be due to smaller percentage of meteors observed in the north-south vertical plane. On the other hand, it is interesting to note that on average the amplitude of the semidiurnal tide for both the zonal and meridional components measured by the meteor technique is larger than measured by the SA technique, while the amplitude measured by the SA technique is larger than measured by the meteor technique for the diurnal tide for both the zonal and meridional components. One point which is worth making here is that whenever there is a significant difference occurs between the two techniques in amplitude for tides (either semidiurnal or diurnal), we see good or excellent agreement in phase most of the times, and the reverse is also true (i.e. for the phase).

Previous observations in the past showed that the quality of agreement between the MF and meteor measurements varied seasonally, the greatest discrepancies occurring in winter [e.g., Rossiter, 1970]. Rossiter [1970] suggested that the MF drift results may be influenced by eastward propagating internal gravity waves. However, our results do not support his observation but clearly reveal that the agreement is relatively often better during the summer and winter periods than the fall and spring periods. As has been shown in a previous chapter (see Chapter 4), strong variations of the phase of the diurnal tide are usually observed during changes of the circulation in the mesosphere and lower thermosphere. Thus, it may be quite natural that the agreement between the two techniques is not as good during such times than during times of stable circulation. In addition, the meteor rate and the MF echo strength undergo seasonal and diurnal variations which limit the occasions when drifts can be obtained simultaneously. These also play a role in the quality of agreement between the two techniques.

Furthermore, it must be noted that there are many other possible causes for the differences sometimes observed between the results of the MF and meteor techniques. Different influences upon the electron concentration and the neutral gas of the mesosphere and lower thermosphere, for instance by geomagnetic disturbances, sudden warming of the upper atmosphere and other disturbances, may cause the differences. Existence of diverse wave processes and turbulent motions in the mesosphere and lower thermosphere which may sometimes affect the motions of the neutral gas and of the irregularities of electron concentration in different ways, thereby causing variations in the occurrence of useful MF echoes.

Our long period observational results strongly suggest that interaction between the diurnal tide and gravity waves occurs over London, at certain times of the year (Chapter 5). Such interactions may be an important source of short-term tidal variability in the mesosphere and lower thermosphere. These observations showed that propagating gravity waves with periods less than 2 hours can significantly modulate the tidal amplitudes, and the reverse is also true. Furthermore, our observations show that the tidal amplitudes are reduced by 2-6 m/s and the phase differences are less than one hour compared to the mean of the month, when mutual interaction between the tides and the gravity waves exists in the 85-94 km height range. Therefore it is possible that differences between the tidal amplitudes determined by the two techniques are also affected by spatial variations related to such phenomena. However more observations and comparisons of this kind should be done in order to study these causes; in particular an increase in the number of meteors is needed, e.g., increase transmitter power.

The results of the instantaneous comparison between the two techniques show that on the average the MF radar using the SA technique provides moderate agreement with winds determined by the VHF interferometer meteor radar technique. The majority of the differences are explainable, as discussed in previously, in terms of geometry of the experiment, the wave-induced fluctuations model due to Kudeki et al. [1993], temporal and spatial distinctions between the two techniques. These may again be recalled from Sections 8.1 and 8.2. It should be remembered that although we have used a common method of data analysis for both the MF and meteor data, the fundamental principles of measuring and determining the velocities are quite different. We noted previously that the MF SA wind velocities are essentially a spatial and temporal average, while in contrast, the meteor wind velocities are essentially instantaneous measurements from a relatively small region combined together over a larger time and larger spatial area. (It is also important to note that on occasions the collecting regions of the two techniques could be separated horizontally by up to 50-100 km and vertically 3 km.) Obviously differences in the sizes and locations of the MF and meteor observing volumes may be partially responsible for differences in the winds near these regions and subsequently may lead to differences in the velocities. Differences in the winds could possibly be due to turbulence and gravity waves. Hines [1968, 1993] suggested that the results of the SA technique might be influenced by the phase velocity of internal gravity waves propagating through the atmosphere. He suggested that the waves could create the irregularities in the ionosphere seen by the SA technique and that the measured drift would then be result of the combination of the horizontal phase velocity of the wave and the background motion.

In contrast to Hines [1993], Kudeki [1993] and Sürücü et al. [1995] showed that there exists unavoidable systematic error sources to SA horizontal wind estimation technique and demonstrated that such systematic wind estimation errors can be explained in terms of inhomogeneous flow field conditions which arises in conjunction with gravity wave fluctuations (see also Section 8.1 - pages 266-267 for more details). These authors showed that the fluctuation-induced error magnitudes can be as large as several tens of meteor per second. It is important to point out here that the single-viewing direction line-of-sight wind speeds determined by the VHF meteor radar would not be affected by the fluctuating biases, whereas MF radar vector winds projected along the single viewing direction of the VHF meteor radar will carry the systematic errors along in the projection (see also Section 8.4.3). Therefore, we believe that some and possibly a substantial fraction of the wind discrepancies observed for the instantaneous comparison may be a manifestation of such fluctuation-induced errors in MF wind measurements. The average of fluctuation-induced errors over independent wind estimates, however, should converge to zero, so long-term wind statistics should be unaffected by fluctuation-induced wind measurement errors.

At present, the observational material obtained in this experiment is not yet sufficient in order to decide on the relative importance of the diverse possibilities mentioned above. A detailed clarification of the occasional differences between the results of meteor wind measurements and MF SA measurements in the same height region must, therefore, be the object of special investigations and will require more observations through longer periods of time.

8.7 Conclusion

Simultaneous comparisons between winds and tides measured by the MF SA radar and those by VHF interferometer meteor radar have been made in the 85-94 km height range from July 1994 and May 1995 over London, Ontario. From the results of this comparison it is concluded that in general the MF SA technique provides a reliable means for synoptic studies of neutral air motions in the height range 85-94 km. This conclusion is particularly well illustrated by Tables 8.1 and 8.2, showing results averaged over several days. Overall, our statistical analysis showed that the agreement is remarkably good for the two techniques. It is equivalent to say, based on statistical analysis, that we are 80% confident that both techniques measure the same motion of winds and tides. Errors in the SA method with respect to tides and mean winds do not seem substantially worse than errors associated with meteor measurements.

It is distinctly evident from our observation that the zonal mean winds are measured with a higher degree of consistency by the two techniques than the meridional mean winds. In general, the phase of the tides (both the semidiurnal and diurnal) shows relatively better agreement for the two techniques than the amplitude. Overall, the semidiurnal tide shows relatively better agreement for the two techniques than the diurnal tide, possibly due to biases introduced by the diurnal variation in meteor count rate. Furthermore, it is also noteworthy that there is less differences between the two techniques in the summer and winter periods than the fall and spring periods, and consequently better agreement between the winds and tides deduced by the two techniques in the summer and winter periods than the fall and spring months. This may be due to the fact that the seasonal changes occurs during the fall (summer to winter circulation) and spring (winter to summer circulation) periods, and consequently the wind fields in the upper atmosphere are considerably more variable during these periods than other seasons.

In detail, however, there are some differences between the results of the two measuring techniques which will have to be studied further. It may be that there are occasions when partial reflection results are influenced by other than the neutral air motion, but the present results indicate that these cases are not as common as has been suggested. While there is now more confidence that SA winds can provide reliable estimates of the neutral air motion, closer attention must be given to an understanding of why, and under what circumstances, they don't. Clearly, additional observations over a longer periods of time are needed to clarify the measurement biases and errors associated with each technique.

The most important conclusion, however, of this chapter may be repeated once more: That in general and on the average and with relatively few exceptions the technique of MF SA drift measurements approximately reflects the real motions of the neutral air in the 85-94 km region for periods of greater than a few hours, and therefore is a valuable tool in middle atmospheric research.

Chapter 9

Conclusions and Suggestions for future work

The principle objective of this thesis has been the experimental investigation of large- and medium-scale dynamics in the 70-100 km height range above ground level at mid-latitude location. For this study, a MF (2.219 MHz) radar and a VHF (40.68 MHz) meteor radar have been used to make measurements of the horizontal winds in the 70-100 km height range. The main body of this study can be divided into five parts; (1) investigation of the reliability of the full correlation analysis method (2) studies of the spatial and temporal characteristics of atmospheric tides, (3) observational evidence of tidal-gravity wave interactions, (4) studies of the spatial and temporal characteristics of the quasi 2-wave, and (5) investigation of the reliability of the spaced antenna drift measurement. The principle conclusions of this study are summarized in this chapter.

9.1 Reliability of the full correlation analysis method

In Chapter 3 the data analysis technique used with the UWO MF radar system was discussed and a simple numerical model of the spaced antenna method assumed by the full correlation analysis (FCA) was given. The numerical model simulates the volume scatter (in our case, point scatterers) condition. The results show that a spaced antenna system using the full correlation analysis does extract relatively accurate velocities of the atmosphere under various degrees of turbulence, antenna spacing and different radar polar diagrams.

It is noted that there is a slight tendency for the true velocity to overestimate the model velocity for larger value of turbulent motion (> 6 m/s) but the errors are usually less than 5%. On the other hand, the magnitude of the apparent velocity increases with increasing model turbulent motions. Both apparent and true directions accurately estimate the model direction although there is a slight tendency for a small directional error in the model direction for larger values of turbulent motion (> 6 m/s). Our results also suggest that the true velocity gets larger with increasing antenna spacing, i.e. triangle size effect, and an optimum spacing must be chosen before applying the method.

In general, it can be concluded that although individual SA wind measurements yield values very similar to the original input model wind velocities, it should be interpreted with care. True wind velocity and direction are better when the turbulent motions are small (less than 6 m/s). However, long term averages (*e.g.*, hourly values) of data collected by the spaced antenna system should provide excellent measurements of mean winds and tides and other full correlation parameters. This work therefore validated the use of the spaced antenna derived results which are subsequently used in this thesis.

For future work, the spaced antenna numerical model should be used to determine the impact of other variables on the accuracy of the full correlation analysis. This includes such things as introducing the effects of aspect sensitivity (anisotropic scatterers), tilts in the scatterers, finite scatterer lifetimes, and gravity wave perturbations through the scattering field.

9.2 Mean winds and tides

Chapter 4 provides the middle atmospheric winds and tides over London, Canada during 1992-1993. Using a two year continuous set of data, the mean winds are compared with a recent empirical model. The diurnal tides are discussed, and these are compared with results from other similar latitude ground-based radars.

9.2.1 Mean winds

In general, the amplitude of the zonal component of the prevailing wind is much larger than the meridional component. The mesospheric circulation pattern for the zonal component is predominantly westward in summer and eastward in winter, at heights below 86 km, which is characteristics of a mesospheric monsoonal type circulation. The zonal component of the prevailing wind is particularly weak during the equinoxes as is expected due to the zonal flow reversal in equinoctial months. Above 91 km, the zonal component of the prevailing wind is predominantly eastward in all seasons. The mesospheric circulation pattern for the meridional component is northward in all seasons below 80 km. Above 94 km, there is evidence of northward flow in summer and southward flow in winter.

Our mean winds show generally good agreement with the CIRA-86 empirical model below 86 km. Significant differences above 86 km have been noted in comparisons between the CIRA-86 empirical model and other similar mid-latitude radars, and the same is true for our results.

9.2.2 Semidiurnal and diurnal tides

The zonal and meridional semidiurnal tides have similar amplitudes at most heights in all seasons. The semidiurnal tide generally exhibits evanescent or long vertical wavelength structure during the summer and fall. We also note that there is a hint of short wavelengths below 85 km during the summer. During the winter and spring, strong phase gradients equivalent to wavelengths of 30-50 km are observed. The comparisons of semidiurnal tides with the tidal model of Forbes and Vial [1989] show excellent agreement in phase, although some differences do exist in amplitude.

The amplitude of the observed zonal diurnal tide is generally larger than the meridional component. The vertical wavelengths are generally short ($\sim$ 35-50 km) during the winter and long ($\sim$ 90-∞ km) during the summer, but this is not always true. The evanescent or long vertical wavelength structure is also observed above 91 km during the winter for the meridional component and relatively short wavelengths are observed during the summer below 88 km. A qualitative comparisons of diurnal tides with the numerical model due to Forbes and Hagan [1988] also show excellent agreement. The only difference is that the model predicts an amplitude peak in the vicinity of 90 km, but our observations show that the amplitude peak does not occur during the summer, although it certainly exists in other seasons.

9.2.3 Comparison of tides with other MF radars

Comparisons of tidal data with sites at similar latitudes show reasonable agreement, but again some disparities are also noted. We have shown that these differences are of a geophysical nature, and illustrated that a great deal still needs to be learned about atmospheric tides. Tidal-gravity wave interactions may well be at the heart of this variability. The proximity of London to the 'Great Lakes' region, which is an area prone to intense convection and therefore a possibly important source of gravity waves, may be a significant factor. The observed variability of the tides among similar mid-latitude radars sets forth the motivation to investigate tidal-gravity wave interactions over London.

9.3 Tidal-gravity wave interactions

Our long period observational results strongly suggest that tidal (diurnal)-gravity wave interactions can occur over London, Canada at certain times of the year (Chapter 5). Such tidal-gravity wave interactions may be an important source of short-term tidal variability in the mesosphere and lower thermosphere. These observations showed that propagating gravity waves with periods of less than 2 hours can significantly modulate the tidal amplitudes, and the reverse is also true. Numerical studies of such phenomena [*e.g.*, Walterscheid, 1981] have also shown such interactions.

We surmise that such mutual interactions may explain at least some of the differences observed in tidal amplitudes and phases from mid-latitude ground based radars. The previous chapter has shown that the zonal tidal amplitudes over London at times are suppressed compared with other sites, and we believe that this is an indication of tidal variability and may relate to tidal-gravity wave interactions. Numerical models also show that the zonal tidal amplitude can be significantly reduced (~ 8 ms^{-1} at 43° N) by momentum deposition due to gravity waves and the phase differences are less than one hour when the mutual interaction between the tides and the gravity waves exists at altitudes greater than 80 km [Miyahara and Forbes, 1991, 1992]. Our observations show that the zonal diurnal amplitude is reduced by ~ 3-6 ms^{-1} compared to the mean value of that month in the 88-94 km height range during 15-18 July. For the February data the amplitude is reduced by ~ 2 ms^{-1} in the 85-94 km height range. Overall phase differences are less than one hour compared to the mean of the month, in accord with these modeling studies.

As a result of our observations, a simple tidal-gravity wave interaction model has been proposed and the major features of the observed data are found to be consistent with the model. The nature of the interaction which varies with time of year supports the model.

The observational evidence presented here indicates that tidal-gravity wave interactions play a major role in middle atmosphere large and small scale variability and also provides some important insights into the dynamics in the mesosphere and lower thermosphere. The observations of these interactions are important, regardless of the frequency of occurrence, and will stimulate further observations and modelling work in this area. More detailed analysis of such interactions are essential in order to improve our understanding of the dynamics on these regions. In order to study the complete nature of atmospheric tides at mid-latitudes, it is necessary to continue these investigations. Coordination and intercomparisons on an international scale are particularly important.

9.4 The quasi 2-day wave

Chapter 6 provides the spatial and temporal characteristics of the quasi 2-day wave over London during 1992-1994, and the observed results are simultaneously compared with results from a similar MF radar system located at Saskatoon (52° N, 107° W).

9.4.1 London

The observations at London show very clearly the existence of the 2-day wave during the late June-early August months, and the presence of the 2-day wave at other times of the year in 1993 and 1994 is also evident, although with lesser amplitudes. A subsidiary maximum of about 70 % of the summer peak, appears during the late April-May months. The amplitudes of the meridional components (20-30 m/s) are generally larger than the zonal component (15-18 m/s), and maximize between 88-91 km in both years. Strong year-to-year variation was found for both the zonal and meridional components, but it is clear that the summer amplification is generally confined to a duration of about 48 days.

The period of the 2-day wave was determined at all heights by the complex demodulation method. The mean periods are found to be $\sim 47.1 \pm 1.3$ h for the zonal component and $\sim 46.2 \pm 1.4$ h for the meridional component in 1993. These values are $\sim 46.2 \pm 1.4$ h and $\sim 46.7 \pm 1.3$ h for the zonal meridional components respectively in 1994. Variations with height were of the order of ± 1 h. These values are shown to be consistent with the values obtained from the harmonic analysis method. The periods determined from the present study are found to be smaller than the 51-52 h period generally suggested by the northern hemisphere results.

The mean phases during intervals of larger amplitudes tend to have phases in the afternoon quadrant between 1000 h LT and 1700 h LT for both the zonal and meridional components for the years 1993 and 1994, although the number of occurrences of larger amplitudes are fewer in the zonal component. The mean phase (i.e time of maximum) over all heights were found to be ~ 12.5 ± 1.4 h and ~ 12.3 ± 1.3 h for the zonal and meridional components respectively in 1993 (assuming the 2-day wave period was exactly 48 h). In 1994 the respective values are ~ 12.1 ± 1.6 h and ~ 12.2 ± 1.2 h for the zonal and meridional components. These values are estimated when the amplitudes are greater than 8 m/s. These results strongly indicate that the 2-day wave prefers to peak near 1200 h LT during intervals of large wave amplitude, suggesting some solar influence on the 2-day wave, possibly through interaction with the solar tides. No obvious phase locking was apparent for small amplitudes in both components. Generally the meridional component leads the zonal component by 1-14 h most of the time. But it was frequently found that the phase relationship between the wind components are nearly 12-14 h during the time intervals of strong 2-day wave activity in the 88-94 km height range, suggesting the wave components are close to in-quadrature.

The estimated vertical wavelengths are generally greater than 150 km when the wave amplitudes are larger, but smaller vertical wavelengths of 60-80 km are also estimated at certain times of the observation.

The temporal relationship between the 2-day wave and the diurnal tide shows that the amplitude of the diurnal tide diminish in the meridional component and increase in the zonal component during time periods of strong 2-day wave activity. On the other hand, the semidiurnal amplitude maximizes whenever the 2-day wave attains its peak amplitude. The observations indicate that a 16 h component appears to maximize just after the peak of the 2-day wave amplitude, and a weak 9.6 h component may also be present during the same time. No correspondence can be seen between the 2-day wave and the terdiurnal tide.

9.4.2 Comparison with Saskatoon

Simultaneous observations between the London and Saskatoon sites have shown the existence of the 2-day wave during the late June-early August months, although these observations indicate the presence of the 2-day wave at other times of the year in 1993 and 1994. A subsidiary maximum of about 70% of the summer peak, appears during the late April-May months. The amplitudes of the meridional components (20-30 m/s) are generally larger than the zonal component (15-18 m/s) at the London site in both years. In contrast, at the Saskatoon site the amplitudes of the zonal components (~ 30 m/s) are larger than the meridional component (~ 25 m/s) in 1993, but in 1994 both the zonal and meridional components have somewhat comparable amplitudes (25-30 m/s). The amplitude variations with latitude suggest that the amplitude maximizes at low latitudes. It is still not clear whether the meridional amplitude is larger at London than at Saskatoon, although the zonal amplitudes at Saskatoon is larger by a factor of 2-3 than at London. Amplitudes vary from year to year but it is clear that the summer amplification is generally confined to a duration of about 50 days.

The period of the 2-day wave was determined by the complex demodulation method. The period of the wave is found to change with time. The mean periods during the bursts of the 2-day activity are 47.1 ± 1.3 h and 47.3 ± 1.2 h for the zonal component at the London and Saskatoon sites respectively, while the respective mean periods are 46.2 ± 1.4 h and 46.8 ± 1.6 h for the meridional component at the London and Saskatoon sites in 1993. In 1994 the mean period values are 47.2 ± 0.9 h and 47.0 ± 1.2 h for the zonal component at the London and Saskatoon sites respectively, and the respective values are 46.7 ± 1.2 h and 46.1 ± 1.7 h for the meridional component at the London and Saskatoon sites. It should be noted that the period of the 2-day wave was only taken into account when the wave had a demodulated amplitude greater than 8 m/s. These values are shown to be consistent with the values obtained from the cross-correlation method. The periods determined from the present study are found to be smaller than the 51-52 h period generally suggested by other northern hemisphere results.

A striking similarity appears between the 2-day waves at London and Saskatoon. Our observations show significant correlation between the two sites of the 2-day wave during time periods of strong 2-day activity. The cross-correlation coefficient values are found to be between 0.7 and 0.8, particularly in the meridional component in 1993 and 1994.

Our results strongly suggest that the 2-day wave is a westward propagating Rossby-gravity wave of zonal wavenumber 3, assuming the phase difference to be due solely to the difference in longitude. A possible connection with the zonal wavenumber 5 is suggested at certain time (early August) in 1994. These results are independently determined by the cross-spectrum and cross-correlation methods. More comparisons should be done in order to study these waves, and also to confirm our observation.

The phase relationship between the zonal and meridional components was studied at the London and Saskatoon sites using the cross-spectrum method. It was found that the meridional component leads the zonal component by ~ 12-13 h, strongly suggesting the wave components are nearly in quadrature.

Finally, in order to study the complete nature of the 2-day wave at mid-latitudes, it is imperative to continue these investigations. Coordination and intercomparisons are required in order to resolve questions about the generating mechanism as well as to understand better the role of the wave in the middle atmosphere.

9.5 Meteor distribution

Chapter 7 provides the data analysis technique used with the VHF interferometer meteor radar system, and also provides the observed results of the meteor distribution as a function of height, time, month, zenith and azimuth angles. The system has proven an excellent tool for a variety of meteor experiments and is now used to measure atmospheric winds at meteor heights by means of radio reflection from meteor trails. It is seen that a pronounced peak in the number distribution occurs near an altitude of 88-91 km, and the number of echoes drops off rapidly above and below this peak height. The meteor echo rate varies diurnally and in this present investigation the peak rates of usable meteor echoes are found to be about ~ 15-25 per hour in the early hours of the morning (0600 LT) dropping to ~ 4-6 per hour at the time of the diurnal minimum (1800 LT). The ratio of maximum to minimum number of meteors per hour for the present data was between 2 and 4. We also note that there is a hint of secondary peak of the echo rate during the afternoon at about 1500 LT. The meteor echo rate varies monthly and in this present investigation the peak rates of usable meteor echoes are found to be ~ 330-350 per day in September-October (fall) dropping to ~ 140-170 per day in January-March (spring). Some of these changes are not due to variation in count rate but variations in local noise levels. It is observed that on the average a large number of meteors ($\geq$ 70% of the total meteors) over London are detected at zenith angles between 20° and 45° for our instrument, but this is a result of the radar polar diagram. It is also observed that on the average most of the meteors ($\geq$ 70% of the total meteors) are detected from eastward and westward directions.

9.6 Reliability of the spaced antenna drift measurement by comparison with meteor drift

Simultaneous comparisons between winds and tides measured by the MF SA radar and those by VHF interferometer meteor radar have been made in the 85-94 km height range from July 1994 and May 1995 over London, Ontario, and the results are discussed in Chapter 8. From the results of this comparison it is concluded that in general the MF SA technique provides a reliable means for synoptic studies of neutral air motions in the height range 85-94 km (Tables 8.1 and 8.2). Overall, our statistical analysis showed that the agreement is remarkably good for the two techniques. Based on statistical analysis, that we are 80% confident that both techniques measure the same motion of winds and tides. Errors in the SA method with respect to tides and mean winds do not seem substantially worse than errors associated with meteor measurements.

It is evident from our observation that the zonal mean winds are measured with a higher degree of consistency by the two techniques than the meridional mean winds. In general, the phase of the tides (both the semidiurnal and diurnal) shows relatively better agreement for the two techniques than the amplitude. Overall, the semidiurnal tide shows better agreement for the two techniques than the diurnal tide, possibly due to biases introduced by the diurnal variation in meteor count rate. Furthermore, It is also noteworthy that there is less differences between the two techniques in the summer and winter periods than the fall and spring periods, and consequently better agreement between the winds and tides deduced by the two techniques in the summer and winter periods than the fall and spring months. This may be due to the fact the seasonal changes occurs during the fall (summer to winter circulation) and spring (winter to summer circulation) periods, and consequently the wind fields in the upper atmosphere are considerably more variable during these periods than other seasons.

In detail, however, there are some differences between the results of the two measuring techniques which will have to be studied further. It may be that there are occasions when partial reflection results are influenced by other than the neutral air motion but the present results indicate that these cases are not as common as has been suggested. While there is now more confidence that SA winds can provide reliable estimates of the neutral air motion, closer attention must be given to an understanding of why, and under what circumstances, it can't do so. Clearly, additional observations over a longer periods of time are needed to clarify the measurement biases and errors associated with each technique.

The most important conclusion, however, of this chapter may be repeated once more: That in general and on the average and with relatively few exceptions the technique of MF SA drift measurements is no worse at approximately real tides and mean winds than the meteor method, and therefore is a valuable tool in middle atmospheric research, at least for periods of greater than a few hours.

Appendix 1

The University of Western Ontario VHF atmospheric radar

This is a reprint of the paper,

Hocking, W. K., The University of Western Ontario VHF atmospheric radar, *STEP handbook,* Proceedings of the sixth workshop on technical and scientific aspects of MST radar, Edwards, B. (Ed.), 349-356, 1993.

THE UNIVERSITY OF WESTERN ONTARIO
VHF ATMOSPHERIC RADAR

W.K. Hocking,
Department of Physics, University of Western Ontario,
London, Ontario, N6A 3K7, Canada

Abstract

A VHF atmospheric wind-profiler radar has recently begun operation near the University of Western Ontario in London, Canada (43°N, 81°W). The system operates at a frequency of 40.68 MHz, and has some unique new features. The basic design of the system is described, and its newer and more interesting features are elucidated.

1. Introduction

There are now several tens of VHF radars world-wide which are used for lower atmospheric research. However, there have to date been none in Canada. Furthermore, new technology has allowed some potential for improving the effectiveness of such instruments, which can enable cost-savings. The objective of construction of a VHF-ST radar in Canada was to make an effective, low-maintenance VHF atmospheric radar for about US $120,000, but nevertheless one with a large degree of flexibility and adaptability.

2. Design Strategy

In designing this system, several features needed to be considered. First, for turbulence studies it is necessary to have a relatively narrow main lobe of the polar diagram [Hocking, 1986]. Secondly, London lies under a major flight path out of Detroit (U.S.A.) so rejection of aircraft clutter was a major consideration. Thirdly, it was necessary to reduce radiation along the ground to a minimal amount to avoid interference. Fourthly, it was decided that the system should be able to act in an interferometric mode if necessary. Fifthly, a large degree of steerability of the main beam was desired. Pulse lengths as short as 150 m were also required, necessitating moderately wide bandwidths. It was also necessary for the system to have up to 8 receivers in order to allow interferometric applications, and to permit application of spaced antenna techniques.

An additional complication also arose. The site of the radar was an agricultural site, and it was not possible to substantially disturb the soil. In particular, it was not permitted to grade the site flat, so it became difficult to lay a ground plane. Indeed, even if the land could have been graded, the ground plane would not have functioned properly for at least part of the year when covered in snow and partly melted ice.

All these features had to be addressed for a cost of just over US $120,000 and this included the antenna system, transmitter, receivers, and digitization system.

3. System Implementation

The following solutions were adopted in order to meet the various objectives outlined above.

Firstly, the antenna system was designed as a cross, as shown in Fig. 1. This enabled a relatively narrow half-power-half-width of 2° for the main beam, whilst at the same time reducing costs. The trade-off was of course the existence of significant side-lobes. Nevertheless, it was felt that the trade-off was worthwhile. Within the cross, dipoles were used as the basic transmitting elements. The dipoles were arranged in groups of 4 at the corners of a square, with sides of length $\lambda/2$, where λ is the radar wavelength. This arrangement ensured minimal radiation of RF energy along directions parallel to the edges of the square. Such "quartets" were then configured in a staggered pattern, as shown in Fig. 1. Fig. 2 shows a schematic of a typical quartet. The diagonal spacing between successive quartets was chosen to be 1.5λ, thereby almost eliminating radiation at angles of 45° to the to the edges of the quartets. This design therefore achieves the objective of producing a narrow main lobe for the polar diagram, while at the same time minimizing radiation along the ground (and therby also minimizing noise pick-up from nearby radio wave sources).

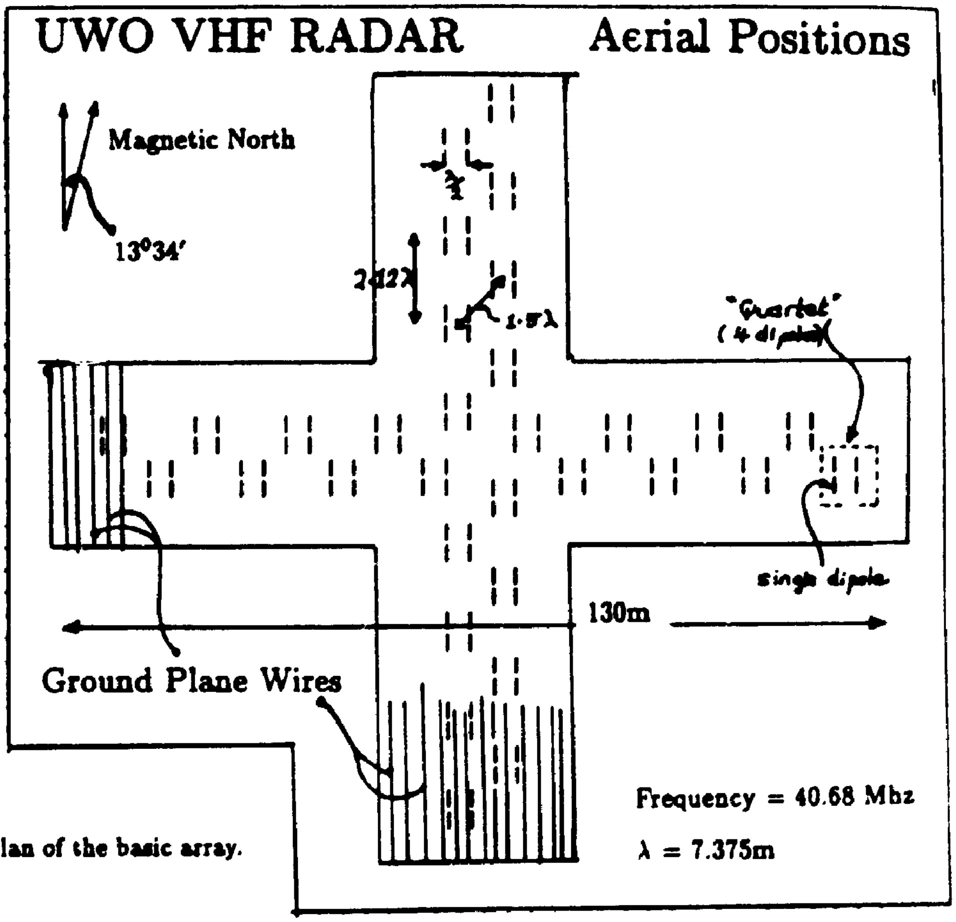

Fig. 1 Plan of the basic array.

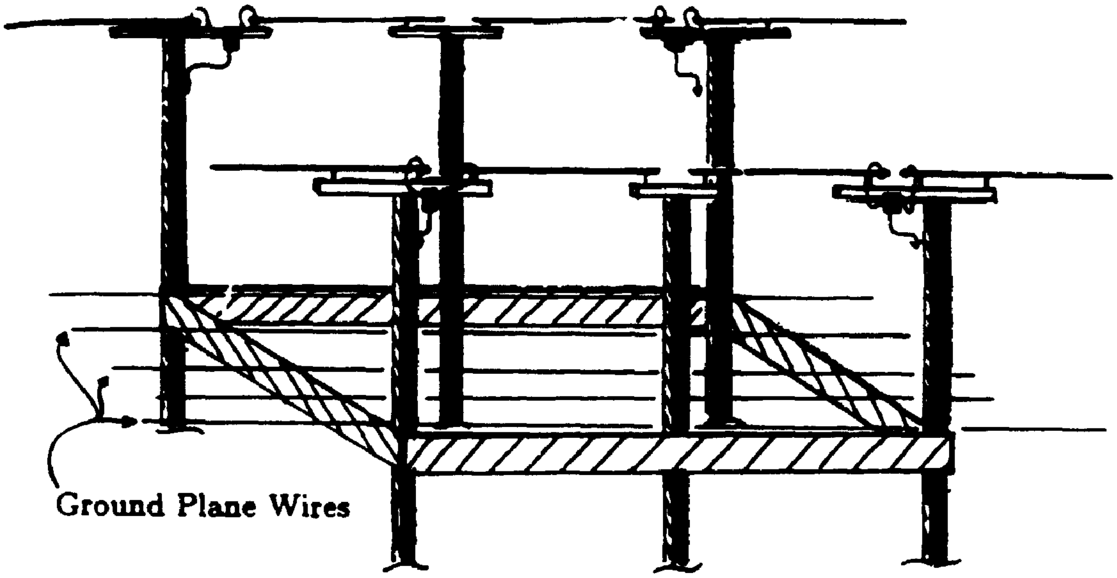

Fig. 2 Schematic diagram of a typical "quartet". The ground plane is supported by the cross-beams, and the dipoles are suspended $\lambda/4$ above the ground plane.

In order to resolve the problem concerning a suitable ground plane it was decided to suspend the ground plane above the earth. The height of the ground plane varied from 30 cm to 150 cm above the true ground, so that the radar ground plane remained flat to within ± 5 cms, despite the undulating nature of the land underneath. It later proved necessary to partially earth the ground plane, but the design has proved to work well. The ground plane comprises lengths of parallel wire with a $\lambda/10$ spacing.

In order to achieve interferometric capabilities, each quartet was separately connected to the transmit-receive system by an independent co- axial cable, each of length $12\lambda_c$, where λ_c is the wave-length of the radio waves in the cable. Low loss cable was used, with a loss factor of 1dB per 30m. Thus the cable attenuated the transmitted power by 2dB, and the received power by a further 2dB. However, the 2dB reduction on reception is unimportant for signal-to-noise considerations, since the sky-noise is also reduced by a similar factor upon reception. Thus the cables introduce only a 2dB loss. However, interferometric applications are simple because each quartet has an identical phase delay between the quartet and the transmit-receive system. The use of equal length cables to each quartet also enables use of short radar pulses.

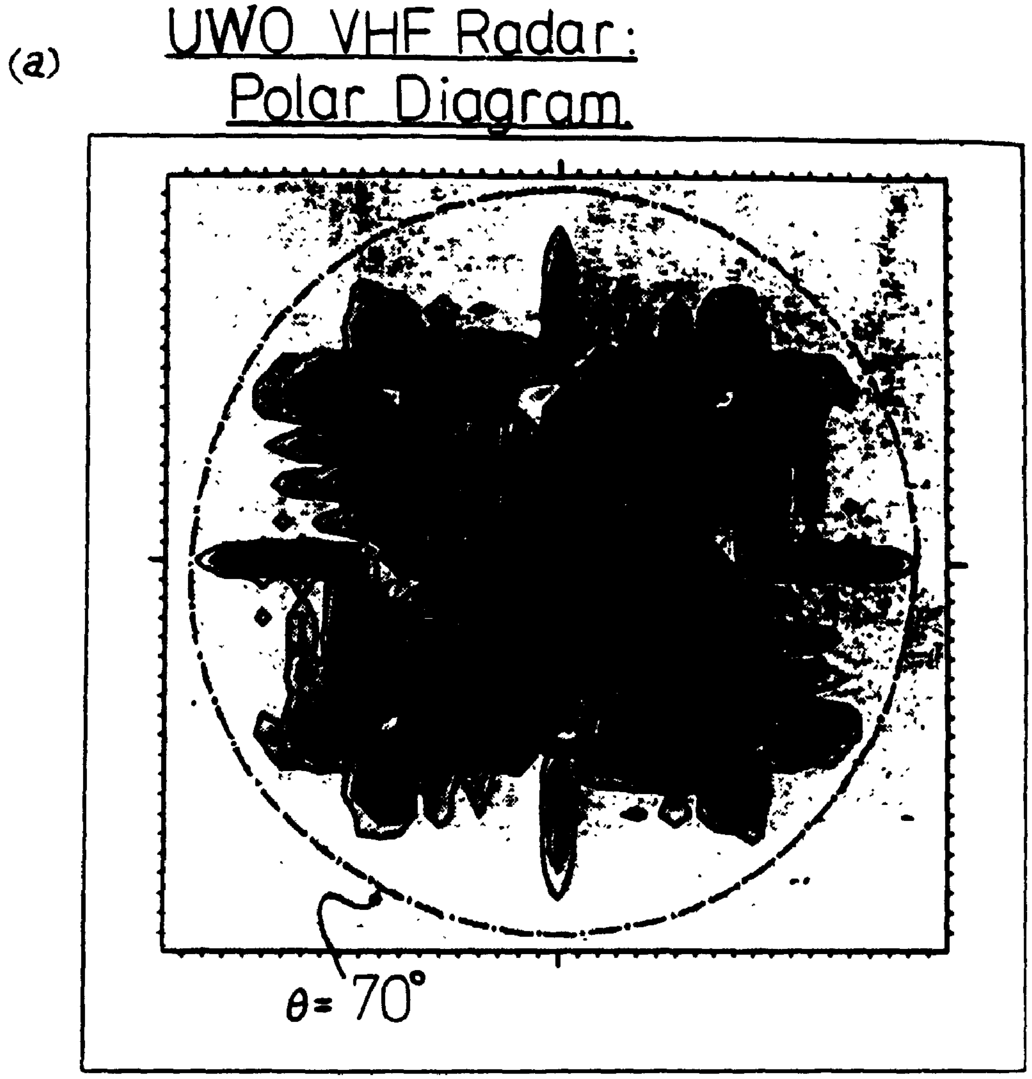

Fig. 3. Two representations of the polar diagram of the array. Contours are in 3 dB steps.

The first graph *(a)* shows the polar diagram out to 90° from zenith, and clearly shows the significant reduction in signal at angles beyond 70° from vertical.

The second graph *(b)* is an expanded view of the central region of the polar diagram. The half-power half-width of the one-way polar diagram is 2.0°, and the first sidelobe occurs at 7.7° from the centre

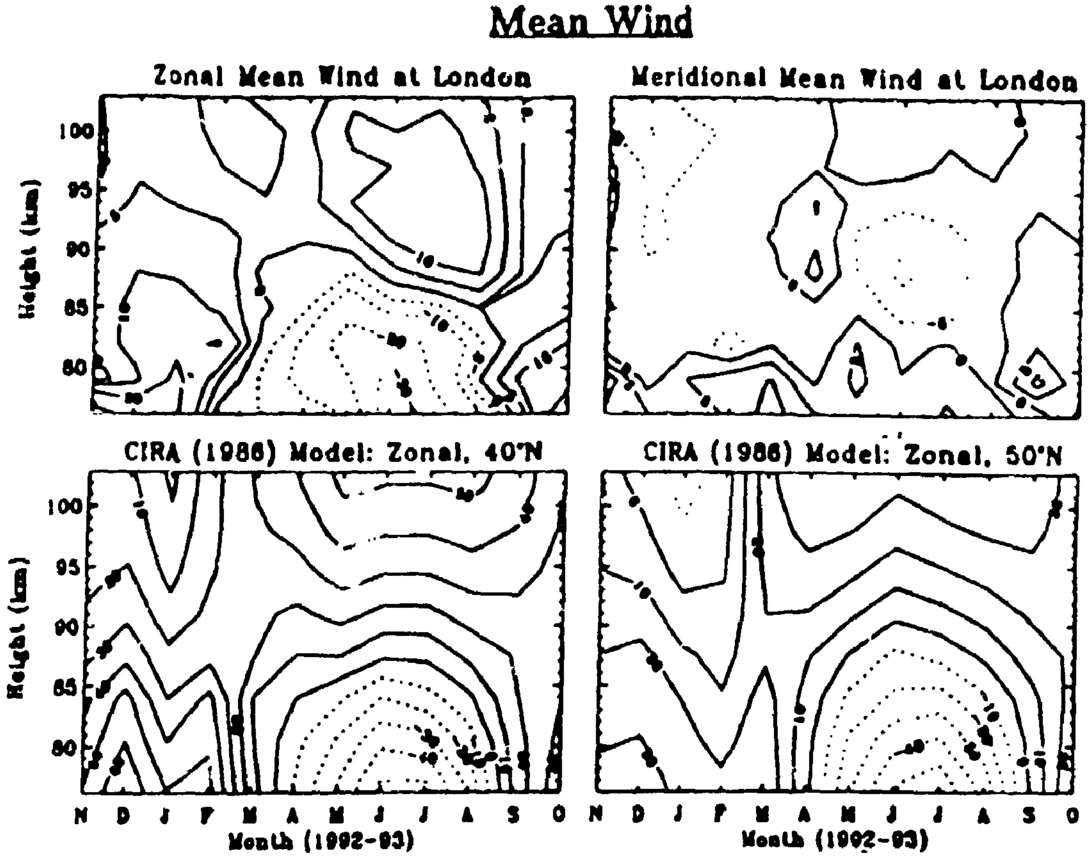

Figure 5. Contours of zonal and meridional mean winds at London in m/s constructed from a year of continuous data, and zonally averaged zonal monthly mean winds from the empirical model of *Fleming et al.* [1988] over a comparable time period. Periods of westward and southward flows are denoted by dashed lines. Note that time marks on the abscissa indicate the middle of the month. Data above 95 km will suffer group retardation and should be treated with caution; see section 2.

3. Mean Winds

This section presents measurements of the mean circulation in the mesosphere and compares them with the CIRA (1986) empirical zonal wind model for the northern hemisphere for 40° N and 50° N. Note that the comparison may not be ideal because our latitude (43° N) is neither 40° N nor 50° N. Figure 5 illustrates time-height contours representing average prevailing zonal and meridional wind patterns for the first 12 months of observations at London, Ontario. The general form of the plots are somewhat similar, but there are also significant differences. In general, the meridional winds are relatively much more variable than the zonal winds, and the magnitude of the zonal component of the prevailing wind in the upper mesosphere is larger than the meridional component.

In the late spring and summer months, from March to mid-August, the zonal flow over London is westward at heights below 86 km, reversing to an eastward flow above this height. The change-over from the winter to summer circulation commences during February-March, and the summer to winter circulation commences during August-September. However, in the model the zero wind line during the spring occurs in mid-March. Note that the seasonal changes show a sudden transition during the fall and a more gradual transition during the spring. Meridional flow is essentially northward below 80 km, but reversing to southward flow above this height during the May-August months. It

Figs. 3a & b shows the polar diagrams of the radar when phased to transmit vertically. The main lobe is moderately narrow, (one-way half width = 2°) and the first side-lobes are 14dB below maximum when the system is used in transmit-receive mode.

In order to allow the system to be able to receive with multiple receivers, and also to help eliminate aircraft echoes, a special new feature was implemented. Rather than using large amounts of coherent integration, as is traditionally done in most radars, it was decided to minimize coherent integration and digitize large amounts of raw data. Then these long data streams are Fourier transformed using an array processor card. At the same time, a single receiver is used, but it has the ability to multiplex signals from up to 8 separate inputs. Because data are acquired at a high data rate, the time delay between signals on successive inputs can be minimized. It is in fact possible to multiplex at up to 16kHz. A commercial digization card has been used to allow digitization at these high PRFs without any need for coherent integration, and also permit digitization to 12 bits accuracy. Whilst coherent integration is not necessary, it is available and is sometimes used, but the system has been configured so that it can transfer up to 65,000 points per height and per record. This use of large data streams with small time steps between successive points enables efficient detection of aircraft and meteors. Aircraft in particular are easily removed from the signal because as a rule they have large velocities and therefore are shifted out in the spectrum to frequencies which are of no interest for atmospheric work. Of course another advantage of this procedure is that the system can successfully measure all atmospheric winds - even hurricane strength - without fear of frequency aliasing. The technical details of the data acquisition system were designed and implemented by Genesis software.

The successful application of these strategies is illustrated in Fig. 4. This shows a spectrum including atmospheric echoes, a meteor (range aliased) and aircraft signals. The bottom graph shows the full spectrum, and has a width of ±100Hz, whilst the upper spectrum shows an expanded view of the centre part of the spectrum. Note that the spectrum due to the aircraft is shifted well away from O Hz, and this is normal. In a more traditional VHF system, similar aircraft signals would often render the data useless.

The detection of meteors is commonplace with this system, and because high digitization rates are used, it is simple to analyze and interpret them. It is intended to both ignore and utilize these signals. In ST mode, when PRFs of ~ 10,000 Hz are often used, the meteors are ignored by detecting and eliminating them in the time domain. In meteor mode, when PRFs of ~100 Hz are used, the meteors are detected and used to determine meteor drifts at 80-100 km altitude. The radar is operated in an interferometric mode on these occasions, so the meteor locations can easily be determined.

The transmitter has been chosen to be a solid state system comprising 12 modules, each of ~ 400 W peak power, and was built by Tomco Inc. The system uses a distributed network, with groups of modules feeding separate antenna quartets. The system is air-cooled, capable of operating at 10 % duty cycle, and is designed to require only minimal maintenance. The effective pulse-width can be adjusted under computer control, and can very between ~200 m and 1 km. Two different RF filters (500 kHz & 1 MHz) can be introduced into the receiver, again under computer control, so as best to optimize the signal-to-noise ratio.

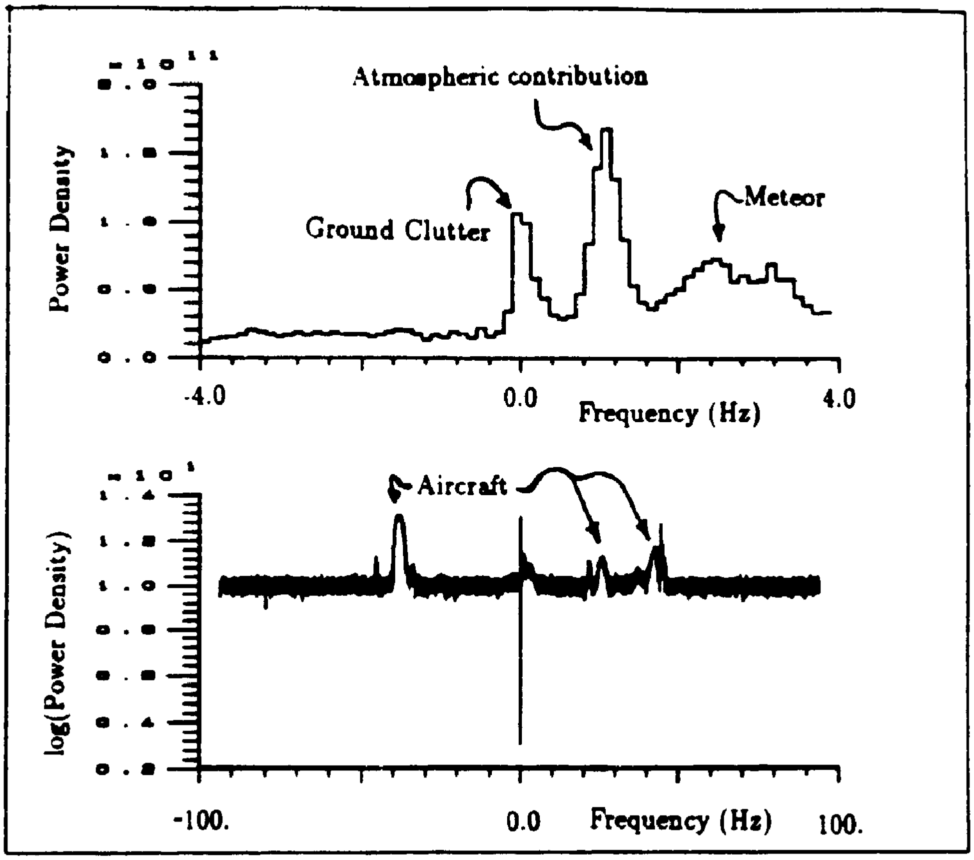

Fig. 4 A spectrum received by the radar, illustrating the existence of aircraft, meteors, atmospheric signals and ground clutter recorded with an off-vertical beam. The lower graph shows the full spectrum of the whole data series, whilst the upper one shows only the central +/- 4 Hz of this spectrum.

Despite the relatively low peak power of this system, it is possible to routinely obtain atmospheric echoes from 1.0 up to 8.5 km altitude. For example, Fig. 4 shows spectra recorded from 7 km altitude and the signal-to-noise is clearly still good. At the same time, when used in meteor-mode, winds in the height region 80-100 km can also be regularly measured.

Finally, the issue of steerability needs to be discussed. Beam tilting is achieved by using cables introduced in series with the antenna cables, and these can be switched in and out by RF relays. Fig. 1 shows that the antenna configuration is rotationally symmetric, so it is possible to simply switch cables in one arm to another. A switching box has already been designed and is currently under construction, which enables such switching. With this sytem, it will be possible to rotate the main lobe of the radar from vertical to off-vertical directions towards the north, east, west and south, all under computer control. The switching unit has also been designed to allow azimuthal beam-point directions in the NE, SE, SW & NW direction, again under computer control. Thus the system has excellent beam-pointing steerability with up to 9 different directions being accessible.

To date, the system has proven to satisfy all conditions which were required of it. There was some initial difficulty in designing the quartets to have a 50Ω output when coupled together, but after some initial experimentation this has proven not only to be relatively simple but also extraordinarily repeatable. All quartets have impedances of 50 Ω to within ±3Ω.

The only real surprise has been the ground plane, which exhibited some after-pulse ringing, due to standing waves being set up on the long stretches of ground plane wire. This problem has been largely eliminated by earthing the ground plane (as it would be if it had been laid directly on the ground), and by adding more wires running perpendicular to the main elements.

4. Conclusion

The University of Western Ontario VHF radar is operational, and has proven to satisfy all the requirements made of it. It is able to record atmospheric echoes up to 8.5 km altitude at .5 km resolution, and 150 m resolution is possible in the lowest few km. The system is also an excellent meteor radar and will be used to measure winds in the mesopause region as well as in the troposphere.

References

Hocking, W.K., "Observation and measurement of turbulence in the middle atmosphere with a VHF radar". *J. Atmos. Terr. Phys.*, **48**, 655-670 (1986).

Appendix 2

Middle atmospheric winds and tides over London, Canada (43° N, 81° W) during 1992-1993

This is a reprint of the paper.

Thayaparan, T., W. K. Hocking, and J. MacDougall, Middle atmospheric winds and tides over London, Canada (43° N, 81° W) during 1992-1993, *Radio Sci.*, 30, 1293-1309, 1995.

Radio Science, Volume 30, Number 4, Pages 1293-1309, July-August 1995

Middle atmospheric winds and tides over London, Canada (43° N, 81° W) during 1992-1993

T. Thayaparan, W. K. Hocking and J. MacDougall

Department of Physics, The University of Western Ontario, London, Ontario, Canada

Abstract. Mean winds and tides have been measured with the new MF radar at London, Ontario. Using a 1-year continuous set of data, the mean winds are compared with a recent empirical model. The diurnal and semidiurnal tides are discussed, and these are compared with results from other similar midlatitude ground-based radars. There are interesting similarities and discrepancies, although we note that some of the initial comparisons use data from different years. The diurnal and semidiurnal tides are also compared with recent tidal models. Tidal characteristics are generally consistent with the models, but again some differences are also noted.

1. Introduction

Atmospheric solar tides in the atmosphere have been observed routinely for many years and have been the subject of many experimental and theoretical investigations. The theoretical understanding and historical resume of advances in atmospheric tidal theory are given by (amongst others) *Chapman and Lindzen* [1970], *Lindzen and Hong* [1974], and *Vial* [1989]. In the middle atmosphere, tides are among the most regular conspicuous dynamical phenomena and play an important role in the dynamics and energy budget of the lower thermosphere [*Teitelbaum and Vial*, 1991; *Groves and Forbes*, 1984, 1985]. Atmospheric tides are global-scale oscillations in temperature, wind, density, and pressure at periods which are harmonics of a solar or lunar day. Here we will mainly be concerned with solar or thermally forced tides, which are excited by the periodic absorption of solar radiation connected with the apparent motion of the Sun around the Earth. Absorption of infrared radiation by water vapor in the troposphere and absorption of ultraviolet radiation by ozone in the atmosphere are known to provide most of the forcing for the solar atmospheric tides. The tidal amplitude grows with height due to the effect of decreasing background atmospheric density with height and becomes a significant wave component in observations by radar and optical probing in the middle atmosphere. Extensive observational studies of the winds and tides in the mesosphere and lower thermosphere have been made with MF (medium frequency) radars using the SA (spaced antenna) technique [e.g., *Manson and Meek*, 1985, 1986; *Fleming et al.*, 1988]. Tidal components observed in this region sometimes indicate inherent variability from day-to-day as well as variation on seasonal and yearly timescales. Atmospheric tides are also observed to be nonuniform with longitude and latitude [*Kato*, 1989].

We report measurements of climatologies of the tides and mean winds made with a new MF radar located near London, Ontario, Canada. In the following section the MF radar system and data analysis methods are described. Section 3 gives the monthly mean winds, and these are compared with the empirical CIRA (1986) model [*Fleming et al.*, 1988]. Sections 4 and 5 present the mean seasonal behavior of the amplitude and phase of the semidiurnal and diurnal tides over London as a function of height. The semidiurnal tides are compared with a model of *Forbes and Vial* [1989], and the diurnal tides are qualitatively compared with a model of *Forbes and Hagan* [1988]. In Section 6 we compare our tidal results with three other ground-based radars. These radars are the MF radars using the SA technique at Saskatoon (52° N, 107° W)

Paper number 95RS00803.
0048-6604/95/95RS-00803$08.00

and Urbana (40° N, 88° W) and the meteor wind radar at Durham (43° N, 71° W). Our comparisons will be based to some extent on the data presented by *Manson et al.* [1989]. The conclusions of this study are presented in Section 7.

The Saskatoon data used for our comparisons were recorded in the same time period (A. H. Manson, private communication, 1994), whilst the Urbana data were recorded in 1991-1992 [*Franke and Thorsen*, 1993] and the Durham data in 1978-84 [*Manson et al.*, 1989], so these comparisons may not be ideal. More detailed comparisons using data from the same time period have yet to be performed, but nevertheless the current comparisons are sufficient to validate our system and at the same time make some interesting comparisons between the different sites.

2. The London MF Radar System and Data Analysis Methods

A new MF radar which uses the SA technique was established at London, Ontario, (43° N, 81° W), in November 1992. The MF radar operates at a frequency of 2.219 MHz and transmits 20 kW of peak power at a duty cycle of 0.12%. Table 1 gives the radar system parameters. Since November 1992 the radar has been used to measure horizontal winds with the spaced antenna method in the 49-142 km height range. Vertical winds are also measured but will not be discussed in this paper. Wind measurements are made at time intervals of 5 min and at 3-km height intervals, although the vertical pulse length is closer to 4-5 km. The configuration for the three antennas is an equilateral triangle with a spacing of 225 m. The complex auto- and cross-correlations functions obtained with 512-point time series are parameterized to obtain true velocity estimates using full correlation analysis (FCA) [*Briggs et al.*, 1950; *Meek*, 1980; *Briggs*, 1984; *Hocking et al.*, *1989*]. Records are 4.55 min in length and start at 5-min intervals. Using a 12-month continuous set of data from November 1992 to October 1993, studies of the mean winds, atmospheric tides, and tidal-gravity wave coupling have been made. We will concentrate on the region 79-103 km, because we believe the data to be most reliable in this height region. This point will be elaborated upon shortly.

Table 1. Radar System Parameters

Radar characteristic	Value
Operating frequency	2.219 MHz
Half-power half-beamwidth	20°
Antenna spacing	225 m
Pulse repetition frequency	60 Hz
Coherent integration	32
Peak power output	20 kW
Duty cycle	0.12%
Height resolution	3 km
Height range	49-142 km

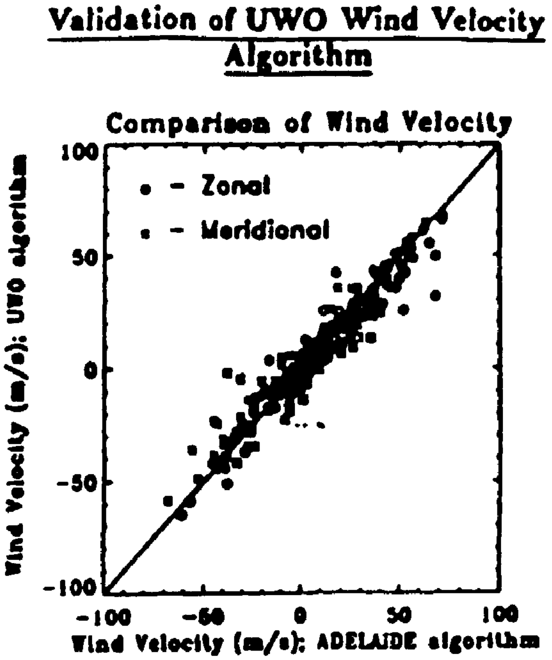

Figure 1. A scatter plot between the wind velocities deduced by the UWO spaced antenna FCA algorithm and by the spaced antenna FCA algorithm used in Adelaide, Australia, where each program has been applied to the same data sets.

As part of our system development, a new software code was developed so that the FCA analysis could be applied in real time on the Zenith 386 personal computer which controls the system (this has subsequently been upgraded to a DX 66-MHz 486 system). Therefore our first procedure was to validate the new code. The best way to test for possible biases in wind estimates by a given spaced antenna FCA algorithm is by comparisons with other commonly used and accepted algorithms. We collected a series of sets of raw data at different times of the year and deduced the wind velocities by two different spaced antenna FCA algorithms. Figure 1 shows a scatter plot between the wind velocities deduced by the UWO (University of Western Ontario) spaced antenna FCA algorithm and by the spaced antenna FCA algorithm used in Adelaide, Australia [e.g., *Ball*, 1981; *Briggs*, 1984], which is in its third decade of operation. The best fit line suggests good agreement, and it is concluded that the UWO spaced antenna FCA algorithm provides reliable estimates of the neutral air motion. Figure 2 shows one example of velocity histograms which was produced from 1-month of observation, in this case February. These histograms were generally approximately normally distributed (as seen in Figure 2), but visual inspection showed that there were on occasion some unacceptably large velocities which fell outside the bell shape of the histogram; they are usually referred to as "outlier." Nevertheless, these were not large in number and could easily be rejected in any subsequent analysis procedures; in general, the majority of data points show a very acceptable distribution..

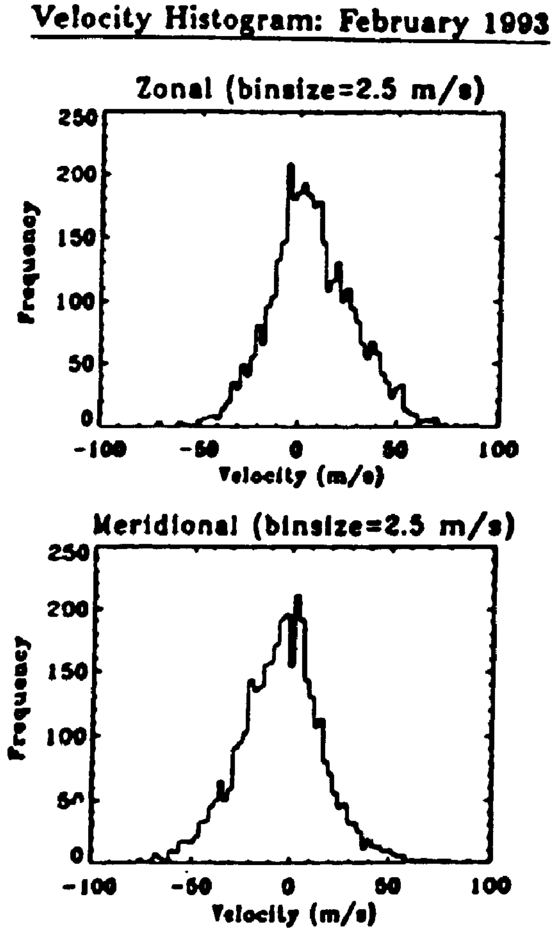

Figure 2. The upper panel shows the velocity histogram of the zonal wind, and the lower panel shows the velocity histogram of the meridional wind at 91 km in February 1993.

In our analysis procedure we have used the hourly averaged mean winds (centered about the half hour) at each height of observation in the analysis. There is considerable theoretical and experimental evidence that wind variations in the mesosphere and lower thermosphere result from the superposition of a prevailing wind, possibly 2-day oscillations, and various tidal components (plus gravity waves). Therefore, we used 2 day groups of data, stepped by 1 day (e.g., 1-2, 2-3, 3-4, ...). We then routinely fit and analyzed the data using classical harmonic analysis techniques with mean, 48, 24, 12, and 8 hour components [e.g., *Manson and Meek*, 1985; *Manson et al.*, 1989]. A typical comparison of the original measurements and the tidal fit for the zonal wind is given in Figure 3. When there were short breaks in the data, these were simply omitted from the least squares fitting routine without seriously affecting the results. A fit is only performed if at least 16 different hours are represented in the 2-day data set for a given height. Note that less than 10% of all available data have less than 30 hours per 2-day data set. Data were also rejected if the errors in the parameters produced by the fitting procedure were unacceptably larger. Thus a substantial proportion of these 10% is reliable. We therefore believe that we have suitably rejected any data which might bias our conclusions. We also compared our fitting procedure for the tides with the Saskatoon fitting procedure (C. E. Meek, private communication, 1994) performed on the London data set. Both amplitudes and phases have shown excellent agreement: the correlation coefficients for the amplitudes and phases are ~ 0.94 and ~ 0.98, respectively. Fitting procedures have also been applied to 24-hour data sets, with 24- and 12-hour components; in general, the overall results were the same as for the 2-day fits, but in this paper we will only use the 48-hour data sets.

The graphs in Figure 3 illustrate the accuracy of our fitting procedures by showing the tidal fits over 8 successive days at 91 km in February 1993. In Figure 4 we also illustrate

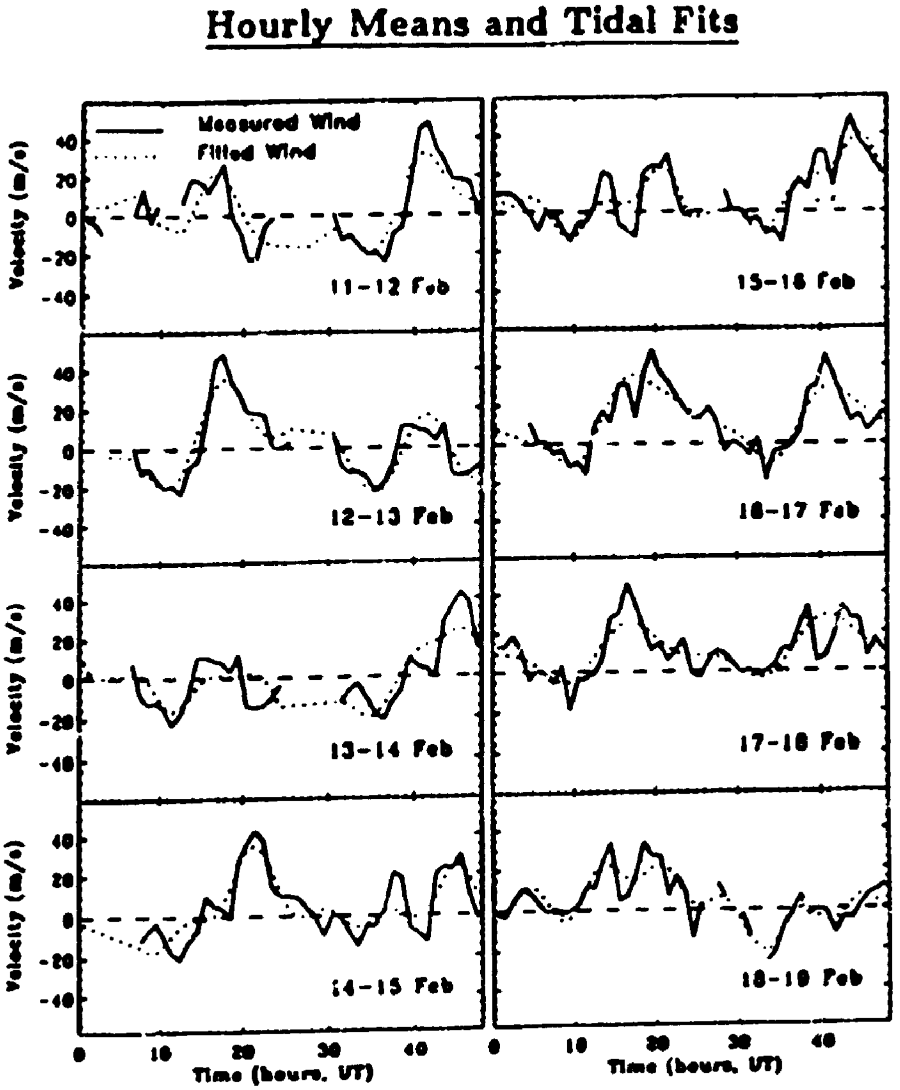

Figure 3. Hourly means and tidal fits for the zonal wind at 91 km, 8 successive days from February 11 to 18, 1993.

the phase variations of the diurnal and semidiurnal components by using both phase plots and a phasor diagram-type format. The phase and phasor diagram of the meridional semidiurnal tide in July (an example) shows moderate day-to-day variability of the [illegible] components and indicates that the phase [illegible] tide does not remain constant over a month. However, it does show a tendency to fluctuate around a fairly well-defined mean phase. On the other hand, the phase and phasor diagram of the meridional diurnal tide shows substantial day-to-day variability. Observations made at London often show large changes in both amplitude and phase of the diurnal tide from one day to the next. While the day-to-day variability of the diurnal tide at midlatitude is a prevalent feature of the mesospheric winds observed in London, the semidiurnal tide, by comparison, exhibits relatively more constant phase, although amplitudes can be variable. The causes of the observed short-term variations (of the order of 3 days) in tidal amplitudes and phases are not well understood, although a number of plausible explanations have been proposed by *Forbes* [1985], *Bernard* [1981], and *Vial et al.* [1985].

Throughout the discussion of the results the following convention is used to describe the wind components. When a wind vector is resolved into geographic coordinates, a positive wind am-

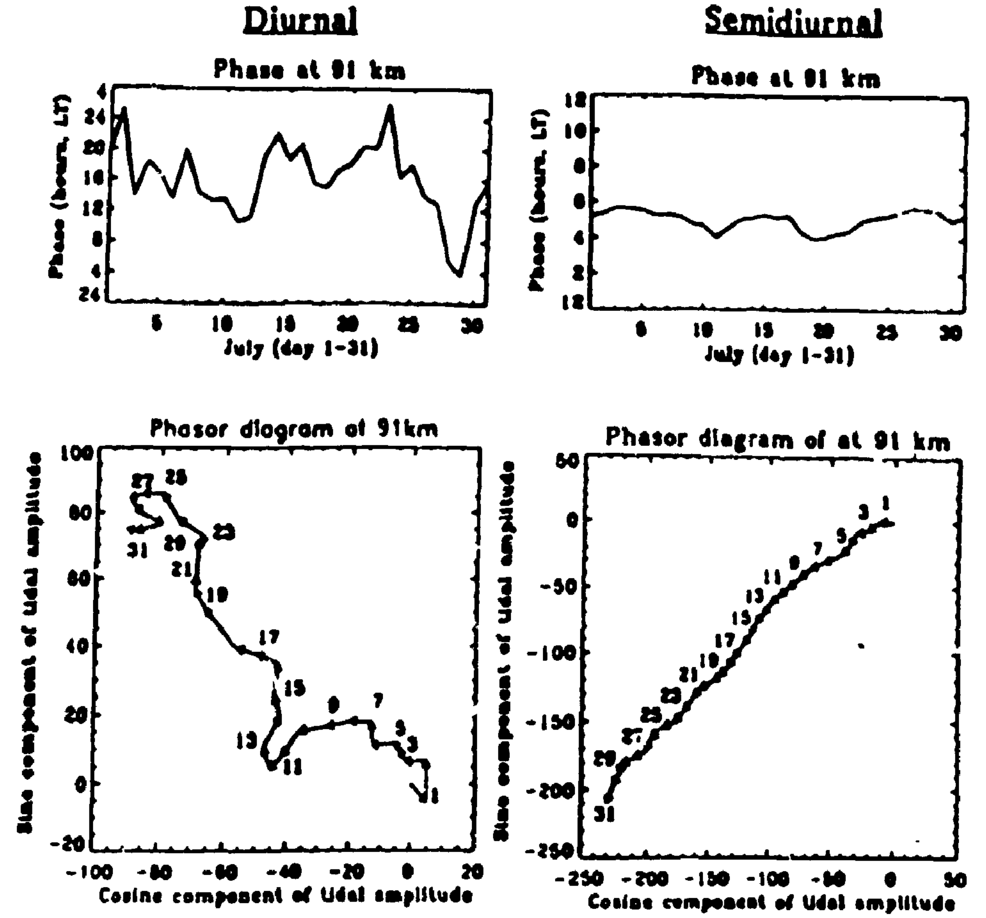

Figure 4. Phase and phasor diagrams of the meridional component of the diurnal and semidiurnal tides at 91 km in July 1993.

plitude refers to a wind directed towards the east or north (eastward or northward) for zonal or meridional components, respectively. The phase of the zonal component is defined as the local time in hours after midnight at which the maximum eastward wind velocity occurs, and the phase of the meridional component is defined as the time of maximum northward wind velocity. Throughout this work we used vector averaging of the daily means for the diurnal and semidiurnal tides. It should be also noted that the results presented here are plotted in terms of virtual heights. Generally the virtual height and the true height are similar up to about 95 km, but there is evidence that the radar echoes received near and above 100 km are affected by some degree of group retardation. *Namboothiri et al.* [1993] demonstrated the effects of group retardation on 2.2-MHz received echoes at Saskatoon, and suggested that the summer noon time virtual heights are similar to the international reference ionosphere (IRI) model, but during the wintertime the IRI virtual heights are considerably lower than the observed heights. It was also demonstrated that during the winter for both solar maximum and minimum the tidal and wind data are valid up to 111 km without any correction, but in the solar minimum summer season heights falls to 97 km, and the corresponding solar maximum height falls as low as 95 km. The period 1992-93 was one of transition from solar maximum to minimum. In order to ensure that our data are not seriously affected by group retardation and *E* region effects, we have limited our data to heights below 103 km. We have greatest confidence in our data for heights below 95 km, but show the data between 95 km and 103 km for completeness.

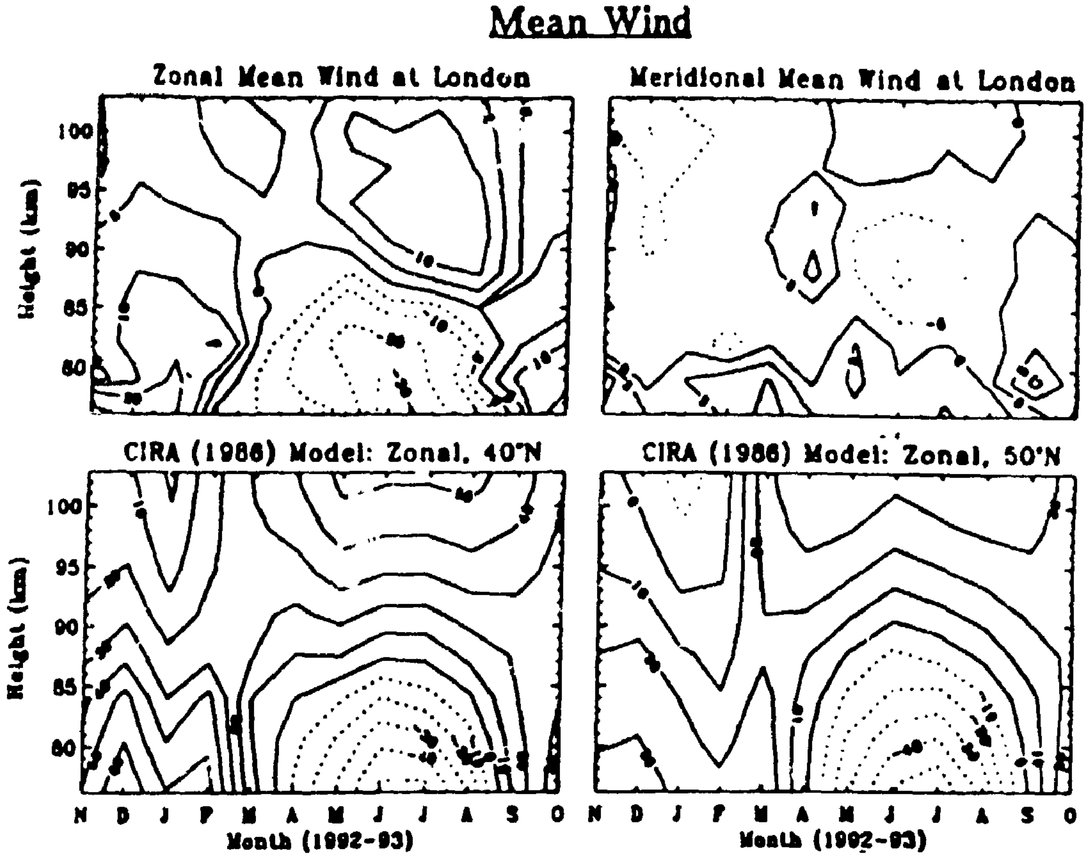

Figure 5. Contours of zonal and meridional mean winds at London in m/s constructed from a year of continuous data, and zonally averaged zonal monthly mean winds from the empirical model of *Fleming et al.* [1988] over a comparable time period. Periods of westward and southward flows are denoted by dashed lines. Note that time marks on the abscissa indicate the middle of the month. Data above 95 km will suffer group retardation and should be treated with caution; see section 2.

3. Mean Winds

This section presents measurements of the mean circulation in the mesosphere and compares them with the CIRA (1986) empirical zonal wind model for the northern hemisphere for 40° N and 50° N. Note that the comparison may not be ideal because our latitude (43° N) is neither 40° N nor 50° N. Figure 5 illustrates time-height contours representing average prevailing zonal and meridional wind patterns for the first 12 months of observations at London, Ontario. The general form of the plots are somewhat similar, but there are also significant differences. In general, the meridional winds are relatively much more variable than the zonal winds, and the magnitude of the zonal component of the prevailing wind in the upper mesosphere is larger than the meridional component.

In the late spring and summer months, from March to mid-August, the zonal flow over London is westward at heights below 86 km, reversing to an eastward flow above this height. The change-over from the winter to summer circulation commences during February-March, and the summer to winter circulation commences during August-September. However, in the model the zero wind line during the spring occurs in mid-March. Note that the seasonal changes show a sudden transition during the fall and a more gradual transition during the spring. Meridional flow is essentially northward below 80 km, but reversing to southward flow above this height during the May-August months. It is interesting to note that the largest meridional winds were observed during March below 80 km, when speeds of 10 m/s were measured.

In the fall and winter, from September to February, the zonal flow is strongly eastward at most heights, being of maximum amplitude in the 76-88 km height range and decreasing with increasing height. The meridional flow is northward below 80 km, but there is evidence of reversal at heights above 80 km during the winter time (November-February).

The amplitudes of the zonal winds are in good agreement with the model below 85 km during the summer and early fall months (April-October). However, during the winter and early spring months (December-March) the model winds are typically 2-3 times as large as the observed values over virtually the entire height range. The model values appear to be consistently larger than those actually observed. Significant differences above 85 km have also been noted in comparisons between the CIRA (1986) empirical model and the other similar radars [e.g., *Manson et al.*, 1991; *Franke and Thorsen*, 1993]. *Manson et al.* [1991] compared meteor and MF radar zonal winds with CIRA (1986) and found the model values to be flawed, especially in the 90-95 km height range during the spring. It should be also noted that the summer comparisons may be somewhat contaminated by daytime group retardation above 95 km.

4. Semidiurnal Tide

This and the following section present observations of the tidal winds over London during 1992-1993. The diurnal and semidiurnal tides are discussed separately and compared with recent tidal wind models. The semidiurnal tides are compared with the recent tidal wind model of *Forbes and Vial* [1989] and the diurnal tides are qualitatively compared with the *Forbes and Hagan* [1988] numerical model. General tidal characteristics are briefly compared with other midlatitude radar observations [*Manson et al.*, 1989]. More detailed comparisons are further presented in Section 6. The data from 1992-93 were classified into winter (December, January, and February), spring (March, April, and May), summer (June, July, and August), and fall (September, October, and November). The seasonal tidal averages and associated error bars of the London data and the model data are estimated by taking a vector average of the monthly mean tides. The model results are sampled at heights corresponding to those of the radar data.

4.1. Semidiurnal Amplitudes

Figures 6-9 present the mean behavior as a function of height of the amplitude and phase profiles of the semidiurnal tides over London, together with the results of a tidal numerical computer model. To begin, we will discuss only our data; comparison with the model and other midlatitude stations will be left until later in the text.

The zonal and the meridional semidiurnal tides have similar amplitudes at most of the

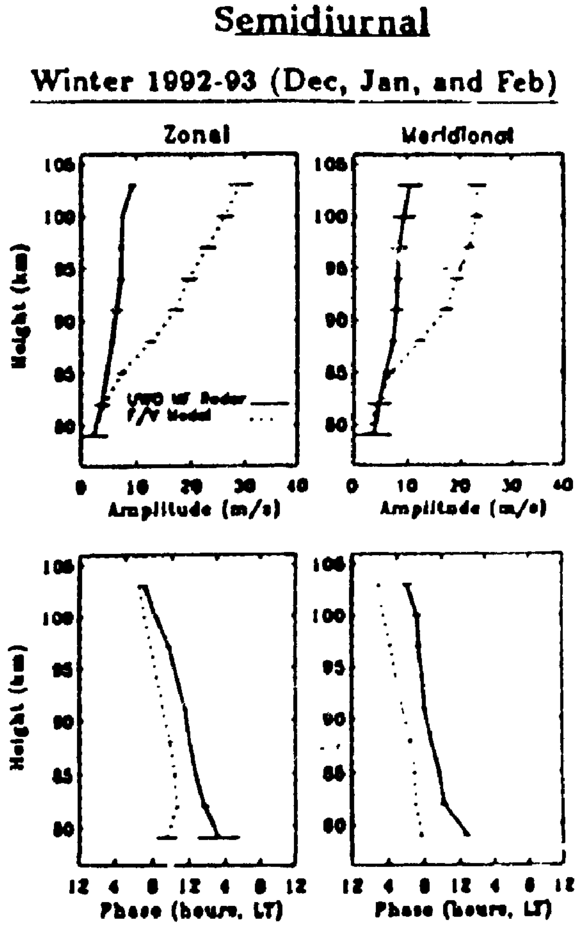
Semidiurnal

Winter 1992-93 (Dec, Jan, and Feb)

Figure 6. Height profiles of the amplitude and phase of the zonal and meridional wind components for the semidiurnal tide during the winter in 1992-93 at London compared with the *Forbes and Vial* [1989] model data. Data are averaged over 3 months (December, January, and February) and the horizontal lines show the monthly variability within the season.

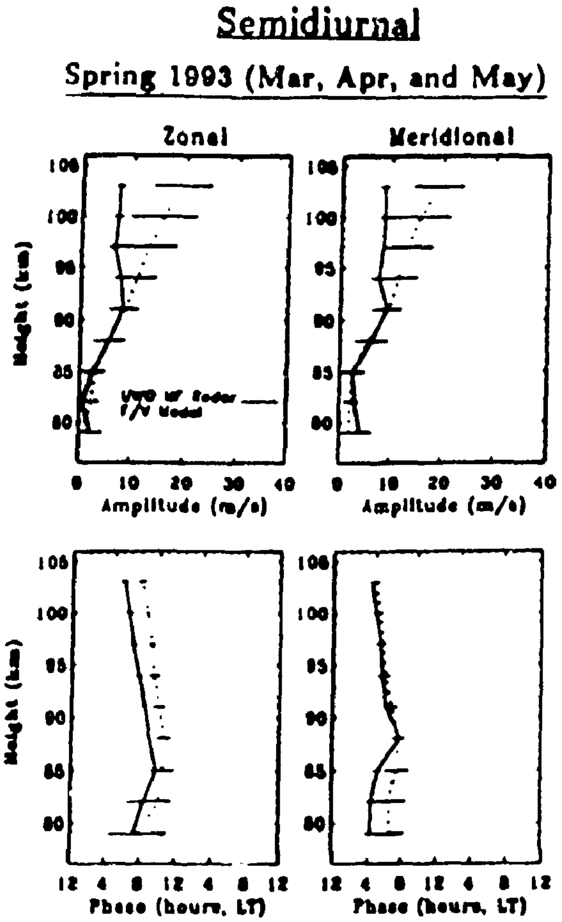

Figure 7. Height profiles of the amplitude and phase of the zonal and meridional wind components for the semidiurnal tide during the spring in 1993 at London compared with the *Forbes and Vial* [1989] model data. Data are averaged over 3 months (March, April, and May) and the horizontal lines show the monthly variability within the season. Data above 95 km will suffer group retardation and should be treated with caution; see section 2.

heights in all seasons. In general the amplitudes are < 10 m/s; the amplitudes are seldom more than 10 m/s and show gradual change with season. The winter and fall amplitudes show very moderate increase with height, whilst in summer the amplitudes of both the meridional and zonal tides seem to decrease in the 79-85 km height range and then reach a broad maximum at about 94 km (± 5 km). In spring above 82 km the amplitudes of the semidiurnal tides show an approximately linear increase with height and become constant above 91 km.

4.2. Semidiurnal Phases

The phases of the zonal and meridional components of the semidiurnal tide generally show the form of a propagating tide, with the meridional component leading the zonal by ~ 3 h and phase propagating downwards. This suggests that the directions of the tidal winds at London (as is true generally in the northern hemisphere) rotate clockwise with the meridional component leading the zonal by approximately 90°.

Figure 6 demonstrates that the semidiurnal phase profiles are very linear in the 79-103 km height range during the winter. This linearity

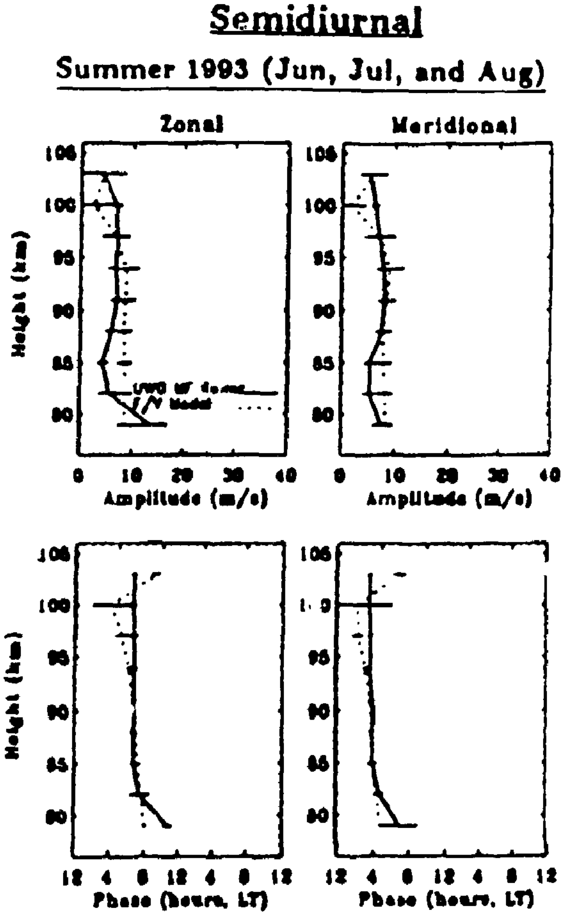

Figure 8. Height profiles of the amplitude and phase of the zonal and meridional wind components for the semidiurnal tide during the summer in 1993 at London compared with the *Forbes and Vial* [1989] model data. Data are averaged over 3 months (June, July, and August) and the horizontal lines show the monthly variability within the season. Data above 95 km will suffer group retardation and should be treated with caution; see section 2.

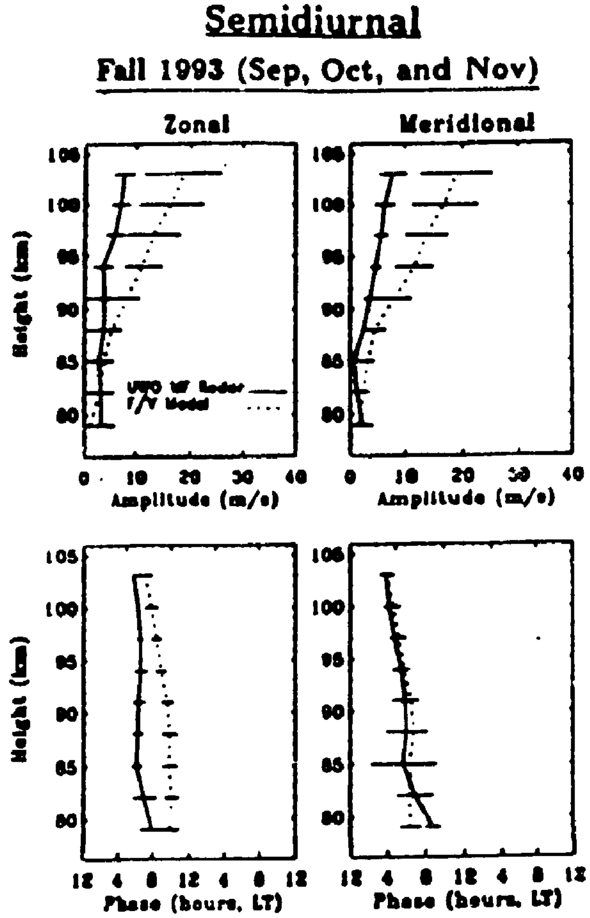

Figure 9. Height profiles of the amplitude and phase of the zonal and meridional wind components for the semidiurnal tide during the fall in 1993 at London compared with the *Forbes and Vial* [1989] model data. Data are averaged over 3 months (September, October, and November) and the horizontal lines show the monthly variability within the season. Data above 95 km will suffer group retardation and should be treated with caution; see section 2.

can also be observed during the spring (Figure 7) in the 85-103 km height range. The stability of this phase structure is indicated by the very small error bars on the seasonal averages. There is an annual variation of vertical wavelength with the shortest values being estimated to be ~ 30-50 km during the winter and spring, whilst the longest values tend towards infinite during the summer (above 85 km) and are ~ 70-100 km during the fall. The seasonal mean vertical wavelength values (λ_z) are given for each season in Table 2. It is possible that the shorter wavelengths may be due to the joint presence of the (2,4), (2,5), and (2,6) modes and the longer wavelengths due to the (2,2) and (2,3) modes [*Forbes*, 1982b]. We note in particular that there is a hint of very short summer wavelengths (~ 25-30 km) below 85 km and then a sudden transition to near evanescence (probably due to the (2,2) symmetric mode) of both the zonal and meridional components above this height. Because of its long vertical wavelength the (2,2) mode is considerably less attenuated and may penetrate into the thermosphere [*Groves*, 1983]. The large amplitude and normalization factors for the (2,2) eigenfunctions also suggest this mode should be strong over London. It is also noted that during the solstitial months of June and December the amplitudes and phases appear to be much the same as the seasonal averages.

Manson et al. [1989] summarized and compared semidiurnal and diurnal tidal characteristics observed from midlatitude (40° – 55°) radar measurements and we briefly compare the general characteristics with the London observation. General characteristics are short vertical wavelengths during the winter (≤ 50 km), long wavelengths above 80 km (≥ 100 km), and short wavelengths below 80 km (≤ 50 km) during the summer, rapid phase transitions between these states, small amplitudes during the summer (~ 5-10 m/s); and large amplitudes during the winter (~ 10-35 m/s). It is clear that these characteristics are observed over London except the winter amplitudes, which are generally small over London.

4.3. Comparisons With a Numerical Model

Recent semidiurnal tidal model predictions from *Forbes and Vial* [1989] are also shown in Figures 6-9, and these are compared with tidal wind data from London. We begin by drawing attention to the relatively excellent agreement in phase between the observation and the model and also the excellent overall agreement in amplitude and phase in some periods of the year. In particular, both amplitude and phase profiles show excellent agreement with the model during the summer time although the sudden phase transition seen in the model at around 100 km is not observed in the data. It is worthwhile to note here that the summer differences

Table 2. Seasonal Mean Vertical Wavelengths λ_z for the Semidiurnal Tide

Season	Zonal, km	Meridional, km
Winter	35 ± 4	40 ± 4
Spring	29 ± 1 (below 85 km)	30 ± 5 (below 88 km)
	54 ± 2 (above 85 km)	50 ± 3 (above 88 km)
Summer	24 ± 4 (below 85 km)	28 ± 4 (below 85 km)
	evanescent (above 85 km)	evanescent (above 85 km)
Fall	100 ± 13	72 ± 25

might be because the radar echoes received near and above 100 km may be affected by daytime group retardation. In spring, summer and fall the agreement for the amplitude profiles below 91 km is also excellent, and in summer the good agreement extends up to 103 km (Figure 8).

Despite some excellent agreement, as noted above, there are also some discrepancies between the model and the data. For example, although the observed amplitudes below 85 km approximate the generally small model tidal amplitudes, the approximately linear increase in amplitude which takes place above 85 km in the model is not observed in the data. Comparisons between model results and observations show that model amplitudes are significantly stronger than observed amplitudes at the higher altitudes except during the summer, probably because dissipation is not adequately accounted for in the high-order modes of the model (F. Vial, private communication, 1994). It should be also noted that the large error bars for the model during the fall and spring are due to very rapid transitions between summerlike and winterlike months. This behavior is generally not seen at London, where the changes in the semidiurnal tidal phase tend to be gradual throughout the year. This will be discussed further in relation to Figures 13 and 14 later in the text.

5. Diurnal Tide

5.1. Diurnal Amplitudes

Figures 10 and 11 present the mean behavior as a function of height of the amplitude and phase of the diurnal tides over London during 1992-93. Unlike the semidiurnal tide, the amplitude of the zonal diurnal tide is in general larger (often up to 100%) than the meridional diurnal tide at most heights during all seasons, although this may not be true above 97 km during the winter. The dominance of the zonal diurnal tide can be anticipated from the Hough velocity expansion functions and their normalizing factors

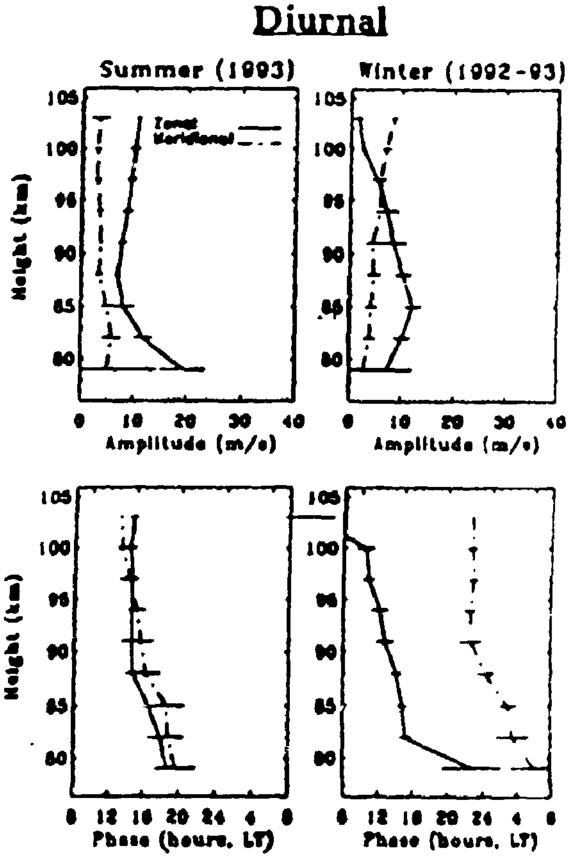

Figure 10. Height profiles of the amplitude and phase of the zonal and meridional wind components for the diurnal tide during the summer (June, July, and August) in 1993 and during the winter (December, January, and February) in 1992-93 at London. Data are averaged over 3 months and the horizontal lines show the monthly variability within the season. Data above 95 km will suffer group retardation and should be treated with caution; see section 2.

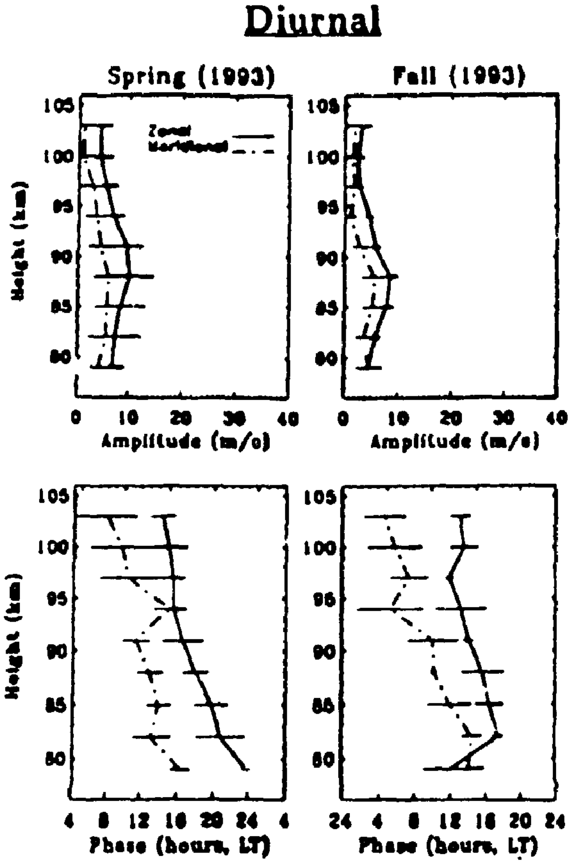

Figure 11. Height profiles of the amplitude and phase of the zonal and meridional wind components for the diurnal tide during the spring (March, April, and May) and fall (September, October, and November) in 1992-93 at London. Data are averaged over 3 months and the horizontal lines show the monthly variability within the season. Data above 95 km will suffer group retardation and should be treated with caution; see section 2.

[*Forbes*, 1982a]. The zonal-meridional difference is especially pronounced during the summer at many heights and during the winter below 88 km.

Generally the amplitudes of the zonal tides during the summer are greater than those in the winter except between 85-88 km. In summer the amplitudes of the zonal tides are ~ 10 m/s except below 82 km, and the amplitudes of the meridional tides are ~ 3-4 m/s. The amplitudes of the meridional tides during the winter are ~ 5-8 m/s, 70 – 100% greater than summer. One noticeable feature of the zonal tide during the winter is that the amplitudes show an approximately linear decay with height above 88 km: in the 88-103 km height range the amplitude decreases from ~ 13 m/s to ~ 2 m/s. Another interesting feature is that the zonal amplitudes reach a broad minimum during the summer and peak during the winter at about 88 km.

In spring and fall the amplitudes of both the zonal and meridional diurnal tides increase with height and reach a broad maximum at around 88 km and then decrease with height. The maximum amplitudes of the zonal tides during the spring and fall are ~ 10 m/s and ~ 8 m/s, respectively, while the amplitudes of the meridional tides are ~ 6 m/s and ~ 5 m/s, respectively. Above 95 km the amplitudes are generally small (less than 5 m/s) during the spring and fall.

5.2. Diurnal Phases

The phases of the diurnal tides are generally less organized and show larger variability than the semidiurnal tides, but some characteristics can be observed. Unlike the semidiurnal tide, the large error bars on the seasonal averages demonstrate instability of the phase structure. In general, downward phase propagation of the tides (as inferred by the negative phase gradients, i.e., earlier phases at upper heights) are observed during all seasons. On occasions the phase profiles of the diurnal tide are almost constant with height, suggesting the presence of evanescent or long vertical wavelength behavior. Figure 10 highlights the phase transition at 88 km from propagating wave structure to near evanescent behavior in the zonal component during the summer. This tendency can also be seen in the meridional phase profiles during the winter. The meridional phase profiles typically undergo a smooth change of ~ 6 h between 79 and 103 km with the earlier phase occurring at greater heights during the summer Similar behavior is also apparent for the zonal phase profiles during the winter, where a change in phase of ~ 12 h occurs. The vertical wavelengths are generally short (~ 40-50 km) during the winter and long (90 – ∞ km) during the summer. A summary of the seasonal mean vertical wavelength (λ_z) values are given in Table 3. It is also interesting to note that the phase of the zonal component leads that of the meridional component by ~ 8-12 h at many heights, indicating anticlockwise rotation of the wind vector during

Table 3. Seasonal Mean Vertical Wavelengths λ_z for the Diurnal Tide

Season	Zonal, km	Meridional, km
Winter	46 ± 8	40 ± 6 (below 91 km) evanescent (above 91 km)
Spring	60 ± 10	68 ± 15
Summer	54 ± 5 (below 88 km) evanescent (above 88 km)	90 ± 8
Fall	100 ± 10 (above 82 km)	60 ± 17

the winter. However, in summer the rotation of the wind vector is clockwise with the meridional component leading the zonal component by ~ 0-2 h above 97 km and anticlockwise with the zonal leading the meridional component below 97 km.

In spring and fall abrupt changes with height in the phase of the meridional component are clearly apparent and suggest that mode superposition or interference may be occurring: the strong phase gradients which suggest vertical wavelengths of less than 10 km are probably not to be interpreted as a wave. These may be caused by the joint presence of two or more modes or by tidal reflections taking place d[illegible] to large temperature or density gradients [*Vi*[illegible] *et al.*, 19[illegible]3]. The vertical wavelengths are ~ 60-100 km. The phase of the meridional component generally leads that of the zonal component by ~ 4-8 h at many heights, indicating anticlockwise rotation of the wind vector during the spring. A similar change of rotation of the wind vector with height is also apparent during the fall.

Most vertical structure variations of the diurnal tide at midlatitudes are due to superposition of the (1,1) and (1,-2) modes [*Forbes*, 1982a, 1984; *Forbes and Hagan*, 1988]. The propagation characteristics of the first symmetric or (1,1) tidal mode have been investigated numerically by *Forbes and Hagan* [1988] for a background atmosphere characterized by zonally averaged mean winds, meridional temperature gradients, and mechanical and thermal dissipation. That numerical model predicts a well-defined amplitude peak in the vicinity of 90 km, an increase in the vertical wavelengths with height from 80 to 100 km, small amplitudes (≤ 10 m/s) near 43° in latitude and larger amplitudes during the summer than during the winter. It also predicts that the winter phases tend to lead the summer phases for the zonal component and the summer phases tend to lead the winter phases for the meridional component. These model characteristics are remarkably consistent with the behavior of the diurnal tide over London observation. Despite this excellent agreement the model fails to predict the observed amplitude minimum during the summer near 88 km.

Like the semidiurnal tide, we briefly compare the behavior of the diurnal tide over London with work by *Manson et al.* [1989]. General characteristics are weaker seasonal variations, a tendency for longer vertical wavelengths during the summer, a tendency for shorter wavelengths during the winter, and generally small amplitudes with summer amplitudes often exceeding winter values. These characteristics are generally evident and observed over London, except for the long wavelengths which are observed for the meridional component in the data during the winter above 91 km.

6. Comparison of Tides With Other MF Radars

In this section we will compare our data with measurements from stations at Saskatoon (A. H. Manson, private communication, 1994), Urbana, and Durham [*Manson et al.*, 1989]. The geographical locations of these sites are illustrated in Figure 12. Figure 13 illustrates the monthly averages of the semidiurnal amplitude and phase at 91 km, and Figure 14 illustrates the monthly averages of the diurnal amplitude and phase at 91 km over London, and these are compared with results from the three other similar midlatitude radars. Monthly tidal averages are estimated by taking a vector average of the daily mean fits at the London site. As noted earlier, it should be borne in mind that the overall comparison of results during different years may not

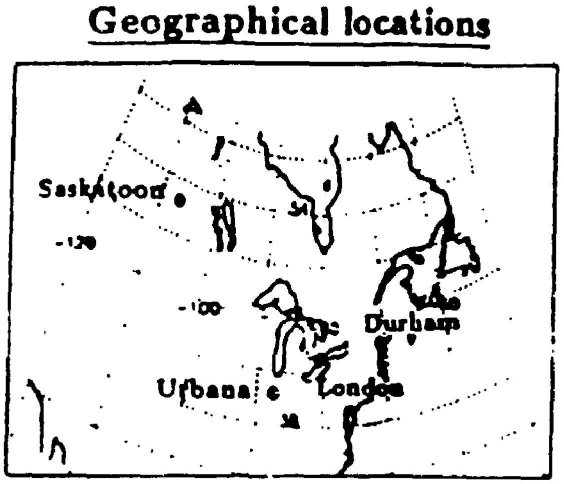

Figure 12. Geographical locations of London (43° N, 81° W), Urbana (40° N, 88° W), Saskatoon (52° N, 107° W), and Durham (43° N, 71° W).

be ideal because of the interannual variability of the tide. However, note that the Saskatoon data are observed during the same time period of observation, so that in some ways the comparisons with the Saskatoon data are the most interesting. In addition, different methods of data reduction (e.g., Durham site) and data analysis (e.g., Urbana site) have been used at different sites. It is desirable that a common method of data reduction be used when the results from two or more sites are compared. We intend to perform such comparisons in the future, but, nevertheless, for the time being we still feel that the comparisons shown here make useful contributions to a description of the morphology of atmospheric tides.

6.1. Semidiurnal Tide

6.1.1. Semidiurnal phase comparisons.

We begin by drawing attention to the relatively good overall agreement in phase between all sites for the semidiurnal component. An especially notable feature of the London and Saskatoon sites is that both the zonal and meridional semidiurnal tidal components show good agreement in phase at the two sites during the solstitial months of June and December, although the amplitudes are generally larger at Saskatoon. In

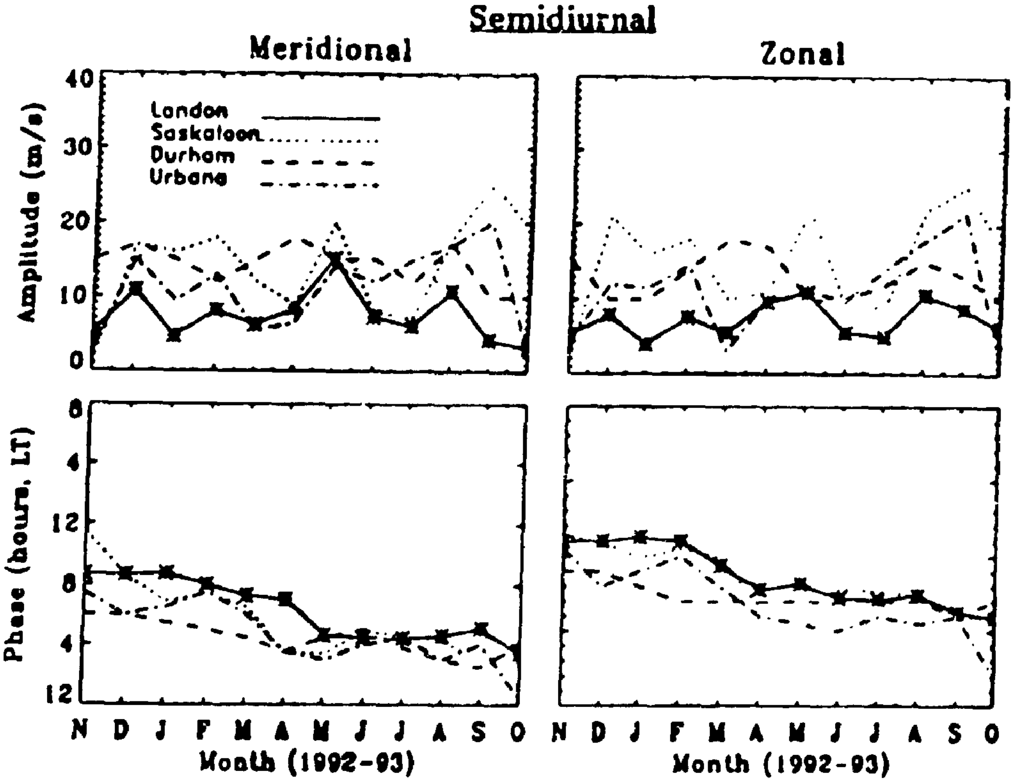

Figure 13. Comparison of monthly averages of amplitude and phase at 91 km of the meridional and zonal semidiurnal tides at London, Saskatoon, Urbana, and Durham. Note that time marks on the abscissa indicate the middle of a month.

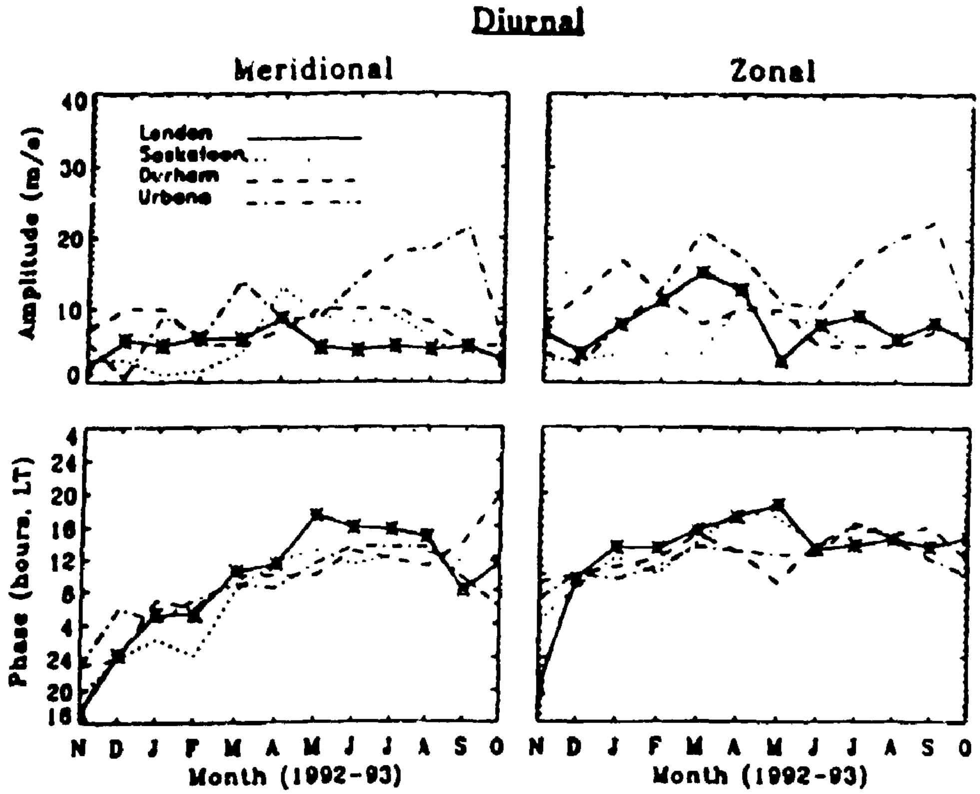

Figure 14. Comparison of monthly averages of amplitude and phase at 91 km of the meridional and zonal diurnal tides at London, Saskatoon, Urbana, and Durham. Note that time marks on the abscissa indicate the middle of a month.

addition, the meridional components have the same amplitude at the June solstice. Generally, the phases for the semidiurnal tide are seen to be constant for several months around the solstices, and the change from one state to another takes place around the equinoxes. The period of almost constant phase around June lasts longer than the period of constant phases around December for the meridional component, whilst for the zonal component the December phases are constant for a longer period than the phases around June. We also note that there is a dramatic change in phase of the zonal component from October to November, and this is evident at London, Urbana, and Saskatoon.

As noted, the phases of the meridional and zonal semidiurnal tides are broadly similar at the four sites, although agreement is clearly not perfect in some months. The meridional component at London in April is one example. Differences in phase are typically 0-4 h, and there is no consistent phase relationship apparent among the sites. These second-order differences may be due to mode superposition or tidal-gravity wave interactions, which differ at different sites. This point will be discussed in more detail shortly. At all four sites the meridional component leads the zonal component by ~ 3 h, indicating clockwise rotation of the wind vector (looking from above).

6.1.2. Semidiurnal amplitude comparisons. The amplitudes of the semidiurnal tides at London (both meridional and zonal) appear to be significantly smaller (50 – 100%) than those of the other three sites during the same month of the year. We note however that our values (below 91 km) show excellent agreement with the model data of *Forbes and Vial* [1989], as already discussed. The amplitude is seldom more than 10 m/s and shows gradual change with season. Whilst these amplitudes are small throughout much of the year when compared with other sites, the amplitudes observed in March-May and October-November coincide remarkably with similar values at the Urbana site. This excellent agreement was observed for both meridional and zonal components. Amplitude values of the meridional component in April-July and the zonal component in certain months also coincide with similar values at the Saskatoon site (same time period of observation). Relatively great day-to-day variability of the amplitudes and phases were observed in these months (March-July) and this may be important; tidal variations on timescales substantially less than 1 month may be important to consider when making these comparisons. London and Urbana are separated by only 3° in latitude and 7° in longitude, so simultaneous observations made at London and Urbana may in the future be possible and allow us to resolve some of the causes of these variations. Nevertheless, the good agreement of phase, and the excellent agreement of amplitudes with Urbana in March, April, May, October, and November makes us feel that the instrument is operating properly, and any differences with other sites are of true geophysical origin.

Interactions between gravity waves and tides have received considerable attention during recent years. This problem is particularly important with regard to tidal variability and has been discussed by (for example) *Fritts and Vincent* [1987]; we surmise that such interactions may explain at least some of the differences between the tides at the four sites under discussion. The variability due to this effect may well be substantially local and random. *Walterscheid* [1981] proposed a possible connection with gravity waves and thus demonstrated theoretically how tides can modulate the momentum deposited by gravity waves in the course of their interactions with the mean wind. Our preliminary observations show significant correlation between gravity waves and tides at certain times of the year, but detailed studies still need to be done. We will address such coupling in a future publication. It is possible that the reduced tidal amplitudes at London may relate to such interactions. The rather unique location of the London radar, in a region surrounded by the "Great Lakes," may in some way explain some of the pecularities found there. We note that the *Forbes and Vial* [1989] numerical model does not predict a reduction in amplitudes near 43° N in latitude.

6.2. Diurnal Tide

6.2.1. Diurnal phase comparisons. Figure 14 shows the monthly averages of the diurnal amplitude and phase at 91 km at the four radars. One outstanding feature seen from the Figure is that for the London and Saskatoon sites, the zonal diurnal tidal components show good agreement in phase during the solstitial months, and good agreement is also found between the meridional components during the December solstice. There is also excellent agreement in amplitudes for the zonal component at the December and June solstices, and this will be discussed in more detail shortly.

The good agreement for the solsticial months has been noted above, but in fact it is clear that the phase of the zonal component generally shows good agreement at all sites in most months. Remarkably good agreement is clearly apparent between the London and Saskatoon sites throughout the year, and this agreement is no doubt helped by the fact that observations were made at the same time. Unlike the semidiurnal phase, the phase of the diurnal tide shows substantial changes with season, particularly for the meridional component. The phases of meridional component at all four sites differ by ~ 0-4 h from January to April and differ by ~ 6-9 h from October to December. However, we note in Figure 10 that the summer diurnal tide shows a sudden phase transition, and an amplitude minimum near 88 km, which may well be due to reflection of a tide. This makes the phase very sensitive to height. Indeed, if similar reflection occur at other locations from marginally different heights, the phase at one height could show considerable sensitivity and therefore variability. We intend to address this further.

Another interesting observation is the clear differences in the phase in May-August at the London site relative to the other sites, but again we note that these observations were made in different years except for the Saskatoon data. We also wish to note that London is a region close to the Great Lakes area and is often subject to strong tropospheric convective activity in these months. Although speculation at this stage we note that this area could be a strong source of gravity waves which may propagate up and interact with the tide in these months. It is also possible that nonmigrating tides play a role to produce such variabilities at these heights [*Kato*, 1989]. We intend to pursue this further, but we do generally feel that all the differences discussed are geophysical or temporal in origin.

Like the semidiurnal tide, there is no apparent uniform phase variation as a function of longitude across the sites. At all four sites the meridional component leads the zonal component, indicating clockwise rotation of the wind vector.

6.2.2. Diurnal amplitude comparisons. It is significant to note that the amplitude time series of the zonal diurnal tides are almost similar in shape and magnitude at London and Urbana in October-February. Good agreement can also be observed between London and Saskatoon in certain months. However, large variation of the amplitude (~ 10 m/s) is also apparent among the sites during other months. Similar large variation also applies to the meridional components. The amplitudes of the meridional component during October-April are comparable (variations are 0-5 m/s) among the sites. The amplitudes remain constant at ~ 5 m/s during May-September at the London site, and this constant amplitude behavior is also observed during May-July at the Saskatoon and Durham sites. Very large amplitudes (~ 20 m/s) are observed over Urbana in the same months. Constant amplitudes are also observed in December-March at London with amplitudes of ~ 6 m/s. The comparisons between the London and Sakatoon sites show that the zonal diurnal tide is considerably stronger in London than in Saskatoon, except in May. Furthermore, the meridional diurnal tide is significantly weaker in April-August at London than at Saskatoon, whilst the converse is true from December to March.

7. Conclusion

We have begun analysis of data recorded with a 2 MHz MF radar at London, Ontario. Our mean winds show generally good agreement with the empirical model of CIRA (1986) below 85 km. Significant differences above 85 km have been noted in comparisons between the CIRA (1986) empirical model and other similar midlatitude radars.

The zonal and meridional semidiurnal tides have similar amplitudes at most of the heights in all seasons. The semidiurnal tide generally exhibits evanescent or long vertical wavelength structure during the summer and fall. We also note that there is a hint of short wavelengths below 85 km during the summer. During the winter and spring, strong phase gradients equivalent to wavelengths of 30-50 km are observed. The comparisons of semidiurnal tides with the tidal model of *Forbes and Vial* [1989] show excellent agreement in phase, although some differences do exist in amplitude.

The amplitude of the observed zonal diurnal tide is larger than the meridional component. The vertical wavelengths are generally short (~ 40-50 km) during the winter and long (~ 90 – ∞ km) during the summer, but this is not always true. The evanescent or long vertical wavelength structure is also observed above 91 km during the winter for the meridional component, and relatively short wavelengths are observed during the summer below 68 km. A qualitative comparison of diurnal tides with the numerical model due to *Forbes and Hagan* [1988] also shows excellent agreement. The only difference is that the model predicts an amplitude peak in the vicinity of 90 km, but our observations show that the amplitude peak does not occur during the summer, although it certainly exists in other seasons.

Comparisons of tidal data with sites at similar latitudes show reasonable agreement, but again some disparities are also noted. We have shown that these differences are of a geophysical nature, and illustrated that a great deal still needs to be learnt about atmospheric tides. We feel that gravity wave-tidal interaction may well be at the heart of this variability. The proximity of London to the Great Lakes area, which is an area prone to intense convection and therefore a possibly important source of gravity waves, may be a significant factor. These results are preliminary, and we intend to pursue more intensive studies as more data accumulates. Future studies will also examine gravity waves and planetary waves.

Finally, in order to study the complete nature of atmospheric tides at midlatitudes, it is necessary to continue these investigations. Coordination and intercomparisons on a international scale are particularly important.

Acknowledgments. We warmly acknowledge the provision of tidal data from Saskatoon by A. H. Manson and C. E. Meek for comparison purposes. Their helpful suggestions and comments are acknowledged with pleasure. The helpful comments of F. Vial are also gratefully acknowledged. The role played by John Dubois in developing the new FCA PC-based software is gratefully acknowledged.

References

Ball, S. M., Upper atmosphere tide and gravity waves at mid- and low-latitudes, Ph.D. thesis, Univ. of Adelaide, Adelaide, Aust., 1981.

Bernard, R., Variability of the semi-diurnal tide in the upper mesosphere, *J. Atmos. Terr. Phys.*, *43*, 663-674, 1981.

Briggs, B. H., G. J. Phillips, and D. H. Shinn, The analysis of observations on spaced receivers of the fading of radio signals, *Proc. Phys. Soc.*, *63B*, 106-121, 1950.

Briggs, B. H., The analysis of spaced sensor records by correlation techniques, *Handbook for MAP*, Vol. 13, pp. 166-186, SCOSTEP Secr., Univ. of Ill., Urbana, Ill., 1984.

Chapman, S., and R. S. Lindzen, Atmospheric tide, pp. 106-171, D. Reidel, Norwell, Mass., 1970.

Fleming, E. L., S. Chandra, M. R. Schoeberl, and J. J. Bernett, Monthly mean global climatology of temperature, wind, geopotential height and pressure from 0-120 km, *NASA Tech. Memo. 100697*, 85 pp., 1988.

Forbes, J. M., Atmospheric tides, 1, Model description and results for the solar diurnal tide, *J. Geophys. Res.*, *87*, 5222-5240, 1982a.

Forbes, J. M., Atmospheric tides, 2, The solar and lunar semidiurnal components, *J. Geophys. Res.*, *87*, 5241-5252, 1982b.

Forbes, J. M., Middle atmospheric tides, *J. Atmos. Terr. Phys.*, *46*, 1049-1967, 1984.

Forbes, J. M., Middle atmospheric tides between 80 and 120 *km*, *Handbook for MAP*, Vol 16, pp. 278-279, SCOSTEP Secr., Univ. of Ill., Urbana, Ill., 1985.

Forbes, J. M., and M. E. Hagan, Diurnal propagating tide in the presence of mean winds and dissipation, *Planet. Space Sci.*, *36*(6), 579-590, 1988.

Forbes, J. M., and F. Vial, Monthly simulations of the solar semidiurnal tide in the mesosphere and lower thermosphere, *J. Atmos. Terr. Phys.*, *51*(7/8), 649-661, 1989.

Franke, S. J., and D. Thorsen, Mean winds and tides in the upper middle atmosphere at Urbana (40° *N* 88° *W*) during 1991-1992, *J. Geophys. Res.*, *98*, 18,607- ,615, 1993.

Fritts, D. C., and R. A. Vincent, Mesospheric momentum flux studies at Adelaide, Australia: Observations and a Gravity wave-tidal interaction model, *J. Atmos. Sci.*, *44*, 605-619, 1987.

Groves, G. V., Thermospheric energy flux of the semidiurnal tide, *Planet. Space Sci.*, *31*, 1183-1186, 1983.

Groves, G. V., and J. M. Forbes, Equinox tidal heating of the upper atmosphere, *Planet. Space Sci.*, *32*, 447-456, 1984.

Groves, G. V., and J. M. Forbes, Mean zonal and meridional accelerations and mean heating induced by solar tides for equinox and solstice conditions, *Planet. Space Sci.*, *33*, 283-293, 1985.

Hocking, W. K., P. May, and J. Röttger, Interpretation, reliability and accuracies of parameters deduced by the spaced antenna method in middle atmosphere applications, *Pure Appl. Geophys.*, *130*, 571-604, 1989.

Kato, S., Non-migrating tides, *J. Atmos. Terr. Phys.*, *51*, 673-682, 1989.

Lindzen, R. S., and S. S. Hong, Effects of mean winds and horizontal temperature gradients on solar and lunar semidiurnal tides in the atmosphere, *J. Atmos. Sci.*, *31*, 1421-1446, 1974.

Manson, A. H., and C. E. Meek, Middle atmosphere (60-110 km) tidal oscillations at Saskatoon, Canada (52° N 107° W) during 1983-1984, *Radio Sci.*, *20*, 1441-1451, 1985.

Manson, A. H., and C. E. Meek, Dynamics of the middle atmosphere at Saskatoon (52° *N* 107°. W) a spectral study during 1981, 1982. *J. Atmos. Terr. Phys.*, *48*, 1029-1055, 1986.

Manson, A. H., C. E. Meek, H. Teitelbaum, F. Vial, R. Schminder, D. Kurschner, M. J. Smith, J. Fraser, and R. R. Clark, Climatologies of semidiurnal and diurnal tides in the middle atmosphere (70-110 km) at middle latitudes (40-55), *J. Atmos. Terr. Phys.*, *51*, 579-593, 1989.

Manson, A. H., C. E. Meek, E. Fleming, S. Chandra, R. A. Vincent, A. Phillips, S. K. Avery, G. J. Fraser, M. J. Smith, J. L. Fellous, and M. Massebeuf, Comparisons between satellite-derived gradient winds and radar-derived winds from the CIRA-86, *J. Atmos. Sci.*, *48*, 411-428, 1991.

Meek, C. E., An efficient method for analysing ionospheric drifts data, *J. Atmos. Terr. Phys.*, *42*, 835-839, 1980.

Namboothiri, S. P., A. H. Manson, and C. E. Meek, E region real heights and their implications for MF radar-derived wind and tidal climatologies, *Radio Sci.*, *28*(2), 187-202, 1993.

Teitelbaum, H., and F. Vial, On tidal variability induced by nonlinear interaction with planetary waves, *J. Geophys. Res.*, *96*, 14,169-14,178, 1991.

Vial, F., J. L. Fellous, and H. Teitelbaum, Tidal vertical structure and temperature profiles in the lower thermosphere, *Ann. Geophys.*, *3*, 313-318, 1985.

Vial, F., Tides in the middle atmosphere, *J. Atmos. Terr. Phys.*, *51*, 3-17, 1989.

Walterscheid, R. L., Inertio-gravity wave induced accelerations of mean flow having an imposed periodic component: Implications for tidal observations in the meteor region, *J. Geophys. Res.*, *86* 9698-9706, 1981.

W. K. Hocking, J. MacDougall, and T. Thayaparan, Department of Physics, The University of Western Ontario, London, Ontario N6A 3K7, Canada. (e-mail whocking@canlon.physics.uwo.ca)

(Received May 9, 1994; revised November 28, 1994, accepted December 1, 1994 .)

Appendix 3

Observational evidence of tidal/gravity wave interactions using the UWO 2 MHz radar

This is a reprint of the paper,

Thayaparan, T., W. K. Hocking, and J. MacDougall, Observational evidence of tidal/gravity wave interactions using the UWO 2 MHz radar, *Geophys. Res. Lett.*, 22, 381-384, 1995.

GEOPHYSICAL RESEARCH LETTERS, VOL 22, NO 4, PAGES 373-376, FEBRUARY 15, 1995

Observational evidence of tidal/gravity wave interactions using the UWO 2 MHz radar

T. Thayaparan, W. K. Hocking and J. MacDougall

Department of Physics, The University of Western Ontario, London, Ontario, Canada

Abstract. The degree of interaction between atmospheric gravity waves and tides is an issue which is of great importance in middle atmosphere studies. It is especially important with regard to tidal variability which is frequently observed in the mesosphere and lower thermosphere, but as yet has not been subject to adequate study. In this paper, we present some strong observational evidence of such interactions made with the *UWO* 2 MHz radar near London, Canada. Our observations show significant correlation between gravity waves and tides (diurnal) at certain times of the year, and the nature of the correlation is intermittent and varies with time of year. It is possible that differences between tidal amplitudes at sites with mesoscale separations may be explained in terms of such phenomena. We also propose a simple model which is found to be consistent with the major features of the observed data.

1. Introduction

It is well known that atmospheric solar tides and gravity waves play a significant role in the dynamics of the middle atmosphere [*Lindzen*, 1981; *Geller*, 1983]. Tidal and gravity wave amplitudes grow with height due to the effect of decreasing background atmospheric density, and eventually can become large enough to induce nonlinear interactions and breaking in the mesosphere and lower thermosphere.

However, our understanding of the complex interactions among atmospheric waves (e.g., gravity/tidal/planetary waves) remains limited. Tidal/gravity wave coupling represents one such interaction which has received considerable attention, and which can be moderately easily studied with modern radars. These studies are particularly important with regard to short-term tidal variability, which is frequently observed in the mesosphere and lower thermosphere [*Bernard*, 1981; *Lu and Fritts*, 1993].

Walterscheid [1981] was the first to propose a possible connection of this modulation with gravity waves and thus demonstrated theoretically how tidal/gravity wave interactions can significantly modulate the tidal amplitudes. Such interactions can produce some wave-stress contribution to the zonal mean circulation [*Miyahara et al.*, 1993; *McLandress and Ward*, 1994] and affect the spatial/temporal distribution of turbulent intensity. It should be noted that such a mutual interaction might also produce a local time variation in eddy diffusivity, which in turn may possibly impact the distributions of long-lived species (e.g., O, O_3, OH and NO) in the mesosphere and lower thermosphere. The potential importance of this problem has not yet received adequate study [*Forbes et al.*, 1991]. It has also been shown theoretically that gravity wave stresses modified by the diurnal tide can produce significant tides having other frequencies than the primary (e.g., the semidiurnal and terdiurnal tides) in this region [*Forbes et al.*, 1991; *Miyahara and Forbes*, 1991].

Recently, observational evidence of tidal/gravity wave interactions has been found by *Fritts and Vincent* [1987] over Adelaide, and is further substantiated by *Wang and Fritts* [1991] on the basis of winds measured by the Poker Flat radar system. These studies showed that the tidal amplitudes may be modulated by upward propagating gravity waves. Such tidal/gravity wave interactions were also noted by *Reid et al.* [1988] and *Fritts and Yuan* [1989], but were not addressed in detail.

In this paper, we present analysis of radar data for different seasons which indicate that tidal/gravity wave interactions do occur and furthermore suggests that the nature of the interaction varies with time of year. As such this study is an advancement of previous work in which only a single time period was examined [*Fritts and Vincent*, 1987, *Wang and Fritts*, 1991]. Our study contributes additional geographic and seasonal data and includes continuous observations over fairly long collection periods. In the following section, data collection methods are briefly described. *Section* 3 discusses the data analysis procedures and results. A proposed model of this tidal/gravity wave interaction is presented in *Section* 4. The discussions and conclusions of this study are presented in *Sections* 5 & 6 respectively.

2. Data collection

A new MF (2.219 MHz) radar which uses the SA technique was established at London (43°N, 81°W), Canada in November 1992. Peak power is 20 kW and the duty cycle is 0.12 %. The pulse repetition frequency is 60 Hz with 32 point coherent integration. Since November 1992 the radar has been used to measure horizontal winds with the spaced antenna method in the height range 60-100 km, with wind measurements being made at time intervals of 5 min and at 3 km height intervals. The configuration for the three antennas is an equilateral triangle with a spacing of 225 m, and the complex auto and cross correlations functions obtained with 512 point time series are parameterized to obtain true velocity estimates using Full Correlation Analysis (FCA) [*Briggs*, 1984; *Hocking et al*, 1989]. We will concentrate on the 85-94 km height range.

3. Data analysis and results

We have examined 4 day data sets from November 1992 to October 1993, and three examples of tidal/gravity wave interactions observed during different times of the year are presented - specifically data collected in 1993 from 26 February to 1 March (winter), 15-18 July (summer) and 12-15 August (summer). We have adopted a 4 day fit because this is long enough to give reasonable significance to our results yet short enough to give reasonable sensitivity during periods of large tidal activity. It should be noted that 53-63 % of the total available wind data were accepted in the 85-94 km height range using FCA acceptance criteria during these periods of time [*Briggs*, 1984; *Hocking et al*, 1989]. The other data were rejected due to either poor signal to noise ratio or various stringent rejection criteria. Generally the data were

Paper number 94GL03270
0094-8534/95/94GL-03270$03.00

distributed fairly evenly throughout each period, ensuring no bias due to sampling problems. The average number of wind estimates during daytime (0700-1800 *hrs*) and nighttime (1800-0700 *hrs*) hours in the 85-94 *km* height range are 51 % and 49 % of the total possible number of records which could have been recorded from 26 February to 1 March respectively. These values are 54 % (0600-2100 *hrs*) and 46 % (2100-0600 *hrs*) during 15-18 July, and are 52 % (0630-2030 *hrs*) and 48 % (2030-0630 *hrs*) during 12-15 August.

In our analysis procedure, the data for 4 days in each month were analyzed using classical harmonic analysis techniques with mean, 48, 24, 12 and 8 *hour* components. We then obtained means and variances of wind fluctuations in 2 – *hour* intervals, and compared these to the tidal oscillations. We will assume, as is normally done, that these residual oscillations are due to gravity waves. The graphs in *Figure* 1 illustrate our fitting and analysis procedures at 94 *km* from 26 February to 1 March (winter). A median filter has been applied to the data, so that outlier points lying outside of the 95 % significance level were rejected in each 2 *hour* interval when estimating gravity wave variance.

The sequence of diagram shown in *Figure* 1 are ordered in the following way. First, the raw data, two hourly means with a 3 point running mean, and tidal fits for the zonal component are shown on the left side of the panel. The 48 and 8 *hour* components are not shown in *Figure* 1c due to their comparatively small amplitudes. The non-tidal component, gravity wave variance of the residuals (zonal component only), and its 3 point running mean are shown on the right side of the panel. A similar example showing gravity wave variances as a function of time at 91 *km* during 15-18 July (summer) is illustrated in *Figure* 2 (similar to *Figures* 1c and 1*f*).

Figure 3*a* illustrates the cross correlation between the zonal diurnal tides and gravity waves during February-March. A significant correlation between the gravity wave variance and the amplitude of the diurnal tidal motion is clearly apparent for the zonal component. It occurs in phase at all four adjacent heights between 85-94 *km*, with similar correlation values. The correlation values are ~ 0.55 and the time lags for maximum correlation are found to occur between 0 and 2 *hours*. These data reveal that the diurnal variability of the gravity wave variance occurred with a high degree of consistency over a number of heights on this occasion. *Figure* 3*b* illustrates the cross correlation between zonal diurnal tides and gravity waves during 15-18 July. A clear tendency for good correlations is also evident for the zonal component in these data. The phase of the correlation shows good agreement at all four adjacent heights between 85-94 *km* with correlation values of ~ 0.4-0.6. The time lags for maximum correlation occur in this case between 8 and 14 *hours*. This remarkable occurrence of diurnal variations shows up particularly well in the mean square velocities, and the plots of this parameter as a function of time are shown in *Figures* 1*f* and 2*b*. These features of the data strongly suggest that gravity wave motions may affect, and/or be affected by, daily variations of diurnal tides in that region at certain times of the year.

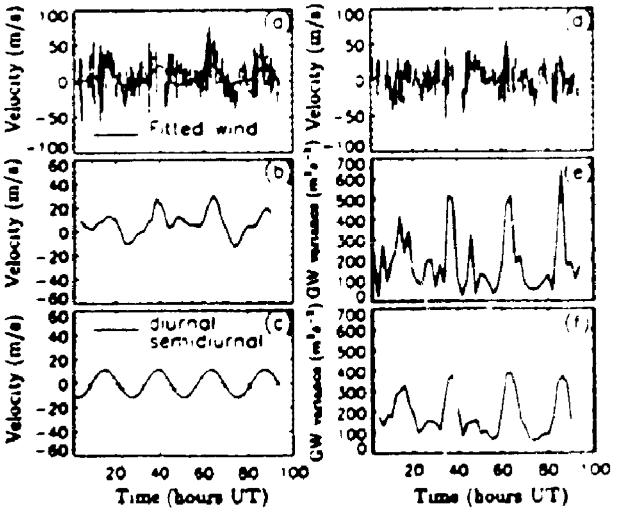

Figure 1. Tidal fitting and analysis procedures: The raw data, two hourly means with a 3 point running mean and tidal fits for the zonal component at 94 *km* from 26 February to 1 March (winter) are shown on the panels *a*, *b*, *c*. The non-tidal component, the gravity wave variance and its 3 point running mean are shown on the panels *d*, *e*, *f*.

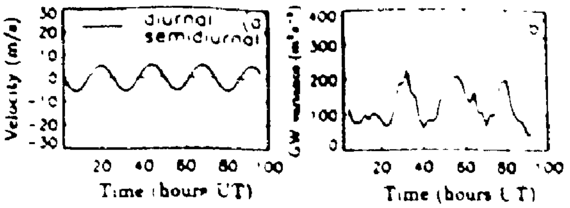

Figure 2. As in Figures 1c and 1f, but during 15-18 July (summer) at 91 *km*.

On the other hand, the correlation values for the meridional component were smaller at all heights and the maximum values did not show the same time lag at different heights (not shown). We emphasize that in this study we will concentrate on only the clearest examples of tidal/gravity wave coupling; other, more tentative cases will be ignored, although we may return and re-analyze these less clear examples in future publication. Our purpose here is to use our most convincing data to demonstrate that these interactions do occur.

We have also created scatter plots between the smoothed gravity wave variances and the zonal tides, and these are illustrated in *Figures* 4*a* and 4*b*. The solid lines show the least-squares best fit. The linear correlation coefficient at 94 *km* for the February data is positive with a value of 0.73 and the 95 % confidence limits are 0.46 and 0.87. The average value of the correlation coefficient in the 85-94 *km* height range is 0.62 and the confidence limits are 0.29 and 0.82. For the July data the linear correlation coefficient at 91 *km* alone is negative with the value of - 0.62 and the confidence limits are - 0.29 and - 0.82. The average value of the correlation coefficient in the 85-94 *km* range is - 0.50 and the confidence limits are - 0.12 and - 0.75. It can be seen that especially for the February data (winter), the zonal component of the gravity wave variance shows a clear tendency for larger values to occur when the zonal diurnal tidal wind is largest. In contrast, the July data (summer) shows the

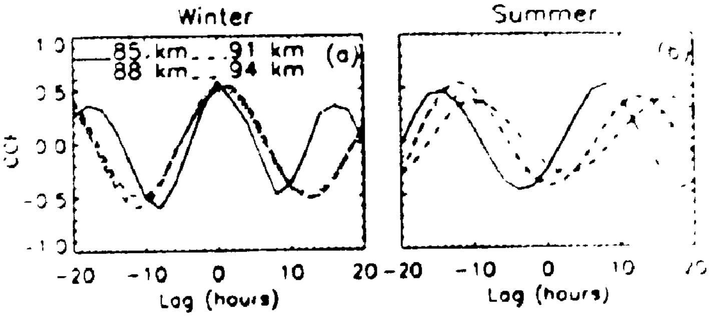

Figure 3. Cross-correlation between zonal diurnal tides and gravity wave variances in the 85-94 *km* height region a) from 26 February to 1 March 1993 (winter) and b) during 15-18 July (summer).

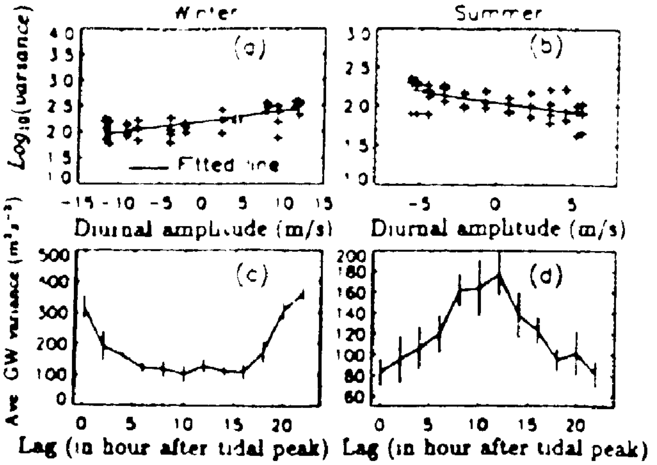

Figure 4. Scatter plots between the amplitude of the zonal diurnal tidal motion and the smoothed gravity wave variance a) from 26 February to 1 March and b) during 15-18 July 1993. Using the diurnal tide as a reference, superposed epochs of the gravity wave variance are shown in *c* and *d*.

opposite tendency with largest values associated with most negative tidal winds. These differences are discussed in our model below. Using the diurnal tide as a reference, superposed epoch analysis of the variance is presented in *Figures* 4c and 4*d*. Note that the zero time lag is taken to be the maximum amplitude of the zonal diurnal tidal motion. The maximum values of the gravity wave variances occur around 11.00 *a.m.* local time (daytime) for the February data but for the July data the maximum values occur around 3.00 *a.m.* local time (nighttime). This behaviour is also seen to be present in *Figures* 1*f* and 2*b* as well. It is noteworthy that the average acceptance rates of wind estimates within ± 4 *hours* of the maximum of the gravity wave variance in the 85-94 *km* height range are 58 % and 59 % for the February and July data respectively. This again shows that the observed correlation is not biased towards decreasing number of data points.

The tidal/gravity wave interactions identified here are not observed at all times of the year, and an example in which there is no significant correlation is shown in *Figure* 5 (during 12-15 August). We also found no apparent correlation between semidiurnal tides and gravity waves over London during our observation period (not shown). This may be due to the larger amplitude of the diurnal tide as compared with the semidiurnal tide (see *Figures* 1c and 2*a*).

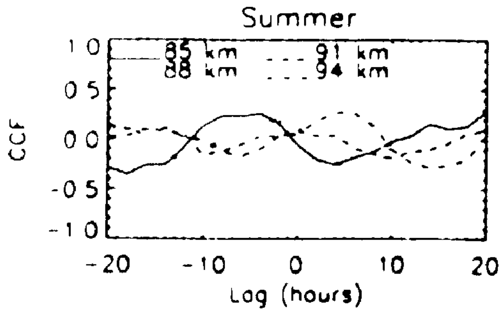

Figure 5. As in Figure 3, but during 12-15 August.

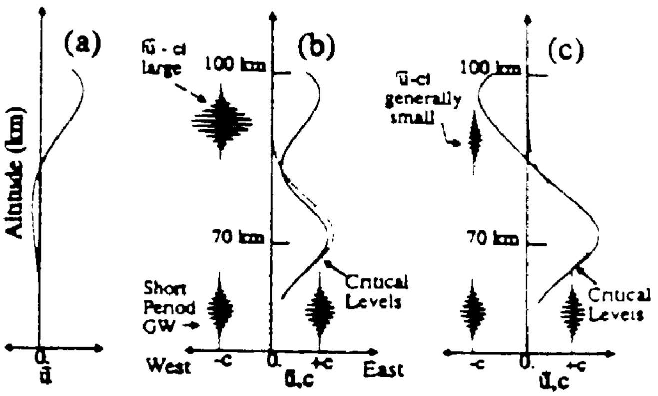

Figure 6. (a) Illustration of a typical height profile of the diurnal tide at one particular time of day. (b) The mean wind for a typical winter situation (broken line) is shown superposed with the tide, giving the solid line, where the phase of the tide is the same as that given in (a). Eastward propagating waves strike a critical level below 70 *km*, whilst westward propagating ones may grow uninhibited (at least until instability is achieved), since $|\bar{u}-c|$ is large. (c) As for part (b), but this time 12 hours later, when the phase of the tide has changed by 180°. Eastward propagating waves still strike critical levels, but westward propagating ones are severely damped because $|\bar{u}-c|$ is generally small, thus restricting the amplitudes to which the gravity waves can reach at 90 *km* altitude.

4. Proposed explanation of observations

Figure 6 illustrates one proposal to explain these observations. It is based on the work of *Fritts and Vincent* [1987] and *Walterscheid* [1981]. The essential fact which forms the basis of the model is that gravity wave amplitudes cannot exceed $u' = |\bar{u} - c|$, where $\bar{u}$ is the background wind (means + tidal components) and c is the horizontal phase speed of the gravity waves. Waves with greater amplitudes than $|\bar{u}-c|$ are convectively unstable and begin to dissipate.

Then, as described in the figure caption, when the wind profile (mean + tide) is as shown in (b) (winter situation), westward propagating gravity waves can propagate up to 90 *km* with little dissipation. However, 12 *hours* later the situation is like (c), and the mean wind at 90 *km* is substantially westward. Thus $|\bar{u} - c|$ is generally small, and the waves are forced to dissipate below 90 *km*, reducing the wave energy which reaches the higher altitudes.

Note that this scenario predicts that gravity waves in winter will be strongest when the 90 *km* tidal winds are eastward. In summer, the mean winds are opposite in direction so that the reverse is true, and gravity waves will be strongest at 90 *km* when the tidal winds are westward. Both these predictions are borne out in the observations. It is also important to note that large amplitude waves can act to accelerate the flow as they break, so that the breaking gravity waves will also alter the tidal amplitudes.

The interaction model described here represents an interaction between the bulk flow (where the bulk flow is assumed to be the sum of steady and tidal components) and waves, rather than a true non-linear interaction. Therefore one might expect an even better correlation if a scatter plot is performed between the 2 *hour* mean winds and the gravity wave variances. However, tests of this hypothesis showed in fact much worse correlation (see *Figure* 7). Note, however, that the fitted lines have a similar tendency to those in *Figures* 4*a* and 4*b*. We do not yet understand why these plots show poorer correlation than do those for just the 24 hour tide. A more elaborate theoretical analysis is obviously required in order to understand what factors other than those discussed above are important in the interaction of gravity waves and tidal components, although we

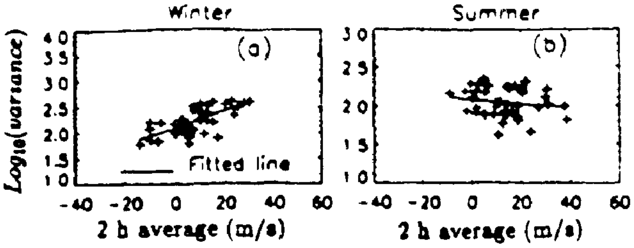

Figure 7. Scatter plots between the smoothed two hourly mean and the smoothed gravity wave variance a) from 26 February to 1 March and b) during 15-18 July.

can make some suggestions. The importance of other long period waves with short vertical wavelengths in the process is one possible candidate to explain this worsened correlation, as is the relative importance of local and non-local effects on the tide. We recognise that our model may not be complete, and more detailed studies of a theoretical nature are needed to investigate other likely causes, but these are beyond the scope of this letter.

5. Discussion

Our long period observational results strongly suggest that tidal (diurnal)/gravity wave interactions can occur over London, Canada at certain times of the year. The observed intermittency is an expected feature, given the day-to-day variability in the gravity wave sources and background wind fields. Such interactions may be an important source of short-term tidal variability in the mesosphere and lower thermosphere. These observations showed that propagating gravity waves with periods less than 2 *hours* can significantly modulate the tidal amplitudes, and the reverse is also true. Numerical studies of such phenomena [e.g., *Walterscheid*, 1981] have also shown suggestion of such interactions.

We surmise that such mutual interactions may explain at least some of the differences observed in tidal amplitudes and phases from mid-latitude ground based radars. Previous studies have shown that zonal tidal amplitudes over London at times are suppressed compared with other sites [*Thayaparan et al.*, 1994], and we believe that this is an indication of tidal variability and may relate to tidal/gravity wave interactions. Numerical models also show that the zonal tidal amplitude can be significantly reduced ($\sim 8\ ms^{-1}$ at $43^{\circ}N$) by momentum deposition due to gravity waves and the phase differences are less than one hour when the mutual interaction between the tides and the gravity waves exists at altitudes greater than 80 *km* [*Miyahara and Forbes*, 1991, 1992]. Our observations show that the zonal diurnal amplitude is reduced by $\sim 3\text{-}6\ ms^{-1}$ compared to the mean value of that month in the 88-94 *km* height range during 15-18 July. For the February data the amplitude is reduced by $\sim 2\ ms^{-1}$ in the 85-94 *km* height range. Overall phase differences are less than one hour compared to the mean of the month, in accord with these modeling studies.

6. Conclusion

As a result of our observations, a simple tidal/gravity wave interaction model has been proposed and the major features of the observed data are found to be consistent with the model. The nature of the interaction which varies with time of year supports the model quite nicely.

The observational evidence presented here indicates that tidal/gravity wave interactions play a major role in middle atmosphere large and small scale variability and also provides some important insights into the dynamics in the mesosphere and lower thermosphere. The observations of these interactions are important, regardless of the frequency of occurrence, and will stimulate further observations and modelling work in this area. More detailed analysis of such interactions are essential in order to improve our understanding of the dynamics on these regions.

References

Bernard, R, Variability of the semi-diurnal tide in the upper mesosphere, *J. Atmos. Terr. Phys.*, 43, 663-674, 1981

Briggs, B. H , The analysis of spaced sensor records by correlation techniques, *Handbook for MAP*, 13, 166-186, 1984.

Forbes, J. M., J. Gu and S. Miyahara, On the interactions between gravity waves and the diurnal propagating tide, *Planet. Space Sci.*, 39, 1249-1257, 1991.

Fritts, D. C. and R. A. Vincent, Mesospheric momentum flux studies at Adelaide, Australia: Observations and a Gravity wave-tidal interaction model, *J. Atmos Sci*, 44, 605-619, 1987.

Fritts D. C. and L. Yuan, Measurement of momentum fluxes near the summer mesopause at Poker Flat, Alaska, *J. Atmos. Sci.*, 46, 2569-2579, 1989.

Geller, M. A., Dynamics of the middle atmosphere, *Space Science Reviews.*, 34, 359-375, 1983.

Hocking, W. K., P. May and J. Röttger, Interpretation, reliability and accuracies of parameters deduced by the spaced antenna method in middle atmosphere applications, *Pure Appl. Geophys.*, 130, 571-604, 1989.

Lindzen, R. S., Turbulence and stress owing to gravity wave and tidal breakdown, *J. Geophys. Res.*, 86, 9707-9714, 1981.

Lu, W. and D. C. Fritts, Spectral estimates of gravity wave energy and momemtum fluxes. Part 3: Gravity wave-tidal interactions, *J. Atmos. Sci.*, 50, 3714-3727, 1993.

McLandress, C. and W. E. Ward, Tidal/gravity wave interactions and their influence on the large-scale dynamics of the middle atmosphere: Model results, *J. Geophys Res.*, 99, 8139-8155, 1994.

Miyahara, S. and J. M. Forbes, Interactions between gravity waves and the diurnal tide in the mesosphere and lower thermosphere, *J. Meteorol. Soc. Jpn.*, 69, 523-531, 1991

Miyahara, S. and J. M. Forbes, Tide/gravity-wave/mean flow interactions in the mesosphere and lower thermosphere, *Adv. Space Res.*, 12, 10(7)- 10(16), 1992

Miyahara, S., Y. Yoshida and Y. Miyoshi, Dynamical coupling between the lower and upper atmosphere by tides and gravity waves, *J. Atmos. Terr. Phys.*, 55, 1039-1053, 1993.

Reid, I. M., R. Rüster, P. Czechowsky and G Schmidt, VHF radar measurements of momemtum flux in the summer polar mesosphere over Andenes (69°*N*, 16°*S*), Norway, *Geophys. Res. lett.*, 15, 1263-1266, 1988.

Thayaparan, T., W. K. Hocking and J. MacDougall, Middle atmospheric winds and tides over London, Canada (43°*N* 81°*W*) during 1992-1993, in press, *Radio Science*, 1994

Wang, D. Y. and D. C. Fritts, Evidence of Gravity wave-tidal interaction observed near the summer mesopause at Poker Flat, Alaska, *J. Atmos. Sci.*, 48, 572-583, 1991

Walterscheid, R. L., Inertio-gravity wave induced accelerations of mean flow having an imposed periodic component Implications for tidal observations in the meteor region, *J. Geophys. Res.*, 86, 9698-9706, 1981.

W. K. Hocking, J. MacDougall and T. Thayaparan, Department of Physics, The University of Western Ontario, London, Ontario, Canada, N6A 3K7.

(received August 10, 1994;
accepted November 2, 1994.)

References

Adams, G. W., J. W. Brosnahan, and D. P. Edwards, The imaging Doppler interferometer: data analysis, *Radio Sci.*, 20, 1481-1492, 1985.

Amayenc, P., and C. A. Reddy, Height structure of tidal winds as inferred from incoherent scatter observations, *Planet. Space Sci.*, 20, 1269-1270.

Andrews, D. G., J. R. Holton, and C. B. Leovy, Middle atmospheric dynamics, *International geophysics series*, Vol. 40, Academic press, New York, U.S.A., 1987.

Appleton, E. V., and M. A. F. Barnett, On some direct evidence for downward atmospheric reflection of electric rays, *Proc. Roy. Sco.*, A 109, 621-641, 1925.

Aso, T., T. Tsuda, and S. Kato, Meteor radar observations at Kyoto university, *J. Atmos. Terr. Phys.*, 41, 517-525, 1979.

Aso, T. and S. Kato, Simulation of atmospheric tides, *J. Met. Soc. Japan*, 58, 286-291, 1980.

Aso, T., T. Tsuda, Y. Takashima, R. Ito, and S. Kato, Observations of lower ionospheric wind by the Kyoto meteor radar, *J. Geophys. Res., 85, 177-184, 1980.*

Aso, T., and R. A. Vincent, Some direct comparisons of mesospheric winds observed at Kyoto and Adelaide, *J. Atmos. Terr. Phys.*, 44, 267-280, 1982.

Aso, T., S. Ito, and S. Kato, *J. Geomagn. Geoelect.*, 39, 287, 1987.

Avery, S. K., A. C. Riddle, and B. B. Balsley, The Poker Flat, Alaska, MST radar as a meteor radar, *Radio, Sci.*, 18, 1021-1027, 1983.

Awe, O., The fading of radio waves weakly scattered at vertical incidence from heights near 90 km, *J. Atmos. Terr. Phys.*, 21, 142-156, 1961.

Baggaley, W. J., On the variation of the ambipolar diffusion coefficient with height, *Planet. Space Sci.*, 18, 1836-1842, 1970.

Baggaley, W. J., and E. M. Poulter, The radio meteor wind facility at Christchurch, New Zealand, *J. Atmos. Terr. Phys.*, 40, 941-943, 1978.

Ball, S. M., Upper atmosphere tide and gravity waves at mid- and low-latitudes, *Ph.D. thesis*, University of Adelaide, Adelaide, Australia, 1981.

Balsley, B. B., and K. S. Gage, The MST radar technique: potential for middle atmospheric studies, K. S., and B. B. Balsley, *Pure Appl. Geophys.*, 118, 453-493, 1980.

Barnett, J. J., and M. Corney, Middle atmosphere reference model derived from satellite data, *Handbook for MAP*, 16, 47-85, 1985.

Bartels, J., Gezeitenschwingungen der atmosphere, *Handbuch der experimentalphysik*, 25, Geophysik 1, 163-210, 1928.

Berggren, R., and K. Labitzke, The distribution of ozone on pressure surfaces, *Tellus*, 20, 88, 1968.

Beer, T., Atmospheric waves, Halsted press, A division of John Wiley and Sons, Inc., New York, U.S.A., 1974.

Bernard, R., Variability of the semi-diurnal tide in the upper mesosphere, *J. Atmos. Terr. Phys.*, 43, 663-674, 1981.

Bills, R. E., C. S. Gardner, and S. J. Franke, Na Doppler/ Temperature Lidar: Initial mesopause region observations and comparison with the Urbana medium frequency radar, *J. Geophys. Res.*, 90, D12, 22701-22707, 1991.

Blamont, J. E., and H. Teitelbaum, La rotation Du vector vitesse horizontal dans les marees atmospheriques, *Ann. Geophys.*, 24, 287-391, 1968.

Bloomfield, P., Fourier analysis of time series: an introduction, *Willey and Sons*, New York, USA.

Booker, H. G., Turbulence in the ionosphere with applications to meteor trails, radio star, scintillations, auroral radar echoes, and other phenomena, *J. Geophys. Res.*, 61, 673-705, 1956.

Brasseur, G., and S. Solomon, Aeronomy of the middle atmosphere, Chemistry and physics of stratosphere and mesosphere, *2nd. ed.*, *Reidel*, Dordrecht, Holland, 1986.

Bretherton, F. P., Waves and turbulence in stably stratified fluids, *Radio Sci.*, 4, 1279, 1969.

Briggs, B. H., G. J. Phillips, and D. H. Shinn, The analysis of observations on spaced receivers of the fading of radio signals, *Proc. Phys. Soc. London*, B 63 (2), 106-121,1950.

Briggs, B. H., On the analysis of moving in geophysics, I, Correlation analysis, *J. Atmos. Terr. Phys.*, 30, 1777-1788, 1968.

Briggs, B. H., Ionospheric drifts, *J. Atmos. Terr. Phys.*, 39, 1023-1033, 1977.

Briggs, B. H., Radar observations of atmospheric winds and turbulence: A comparison technique, *J. Atmos. Terr. Phys.*, 42, 823-833, 1980.

Briggs, B. H., The analysis of spaced sensor records by correlation techniques, *Handbook for MAP* 13, 166-186, 1984.

Bronshten, V. A., Physics of meteoric phenomena, *Reidel*, Dordrecht, 1983.

Brown, N., Radio echoes from meteor trains at a frequency of 1.98 MHz, *J. Atmos. Terr. Phys.*, 38, 83-87, 1976.

Brown, G. M., and J. I. John, Vertical penetration of planetary waves into the lower ionosphere, *J. Atmos. Terr. Phys.*, 41, 379-386, 1979.

Butler, S. T., and K. A. Small, The excitation of atmospheric oscillations, *Proc. Roy. Soc.*, A 274, 91-121, 1963.

Burks, D. and C. Leovy, Planetary waves near the mesospheric easterly jet, Geophys. Res. Lett., 13, 193-196, 1986.

Casson, L., The ancient mariners, Gollancz, London, United Kingtom, 1959.

Cervera, M. A., and Reid, I. M., Comparison of simultaneous wind measurements using colocated VHF meteor radar and MF spaced antenna radar systems, *Radio Sci.*, 30, 1245-1261, 1995.

Cervera, *private communication*, 1995.

Cevolani, G., S. P. Kingsley, and G. Muller, Three-station meteor wind observations in northern Europe during summer 1980, *J. Atmos. Terr. Phys.*, 45, 275-280, 1983.

Cevolani, G. and S. P. Kingsley, Non-linear effects on tidal and planetary waves in the lower thermosphere: preliminary results, *Adv. Space Res.*, 12, (10)77-(10)80, 1992.

Chamberlain, M. T., and F. Jacka, Optical evidence for midlatitude charged particle precipitation, *J. Atmos. Terr. Phys.*, 41, 111, 1979.

Chapman, S., The semidiurnal oscillation of the atmosphere, *Quart. J. Roy. Met. Soc.*, 50, 165-195, 1924.

Chapman, S., Atmospheric tides and oscillations, *Contendium of Meteorology,* Boston, 1951.

Chapman, S. and R. S. Lindzen. Atmospheric tide, *D. Reidel Publishing Company, Dordrecht, Holland,* 106-171, 1970.

Chapman, W. A., and P. G. Peckham, Spectral analyses of wave motions in the middle atmosphere, *Phil. Trans. R. Soc. London,* A 296, 59, 1980.

Charney, J. G., and P. G. Drazin, Propagation of planetary-scale disturbances from the lower into the upper atmosphere, *J. Atmos. Sci.*, 66, 83-100, 1961.

Chelton, D. B., K. J. Hussey, and M. F. Parke, *Science,* 294, 1981.

Clark, R. R., Meteor wind measurements at Durham, New Hampshire (43° N, 71° W), *J. Atmos. Sci.*, 32, 1689-1693, 1975.

Clark, R. R., Meteor wind data for global comparisons, *J. Atmos. Terr. Phys.*, 40, 905-911, 1978.

Clark, R. R., Upper atmosphere wind observations of waves and tides with the UNH meteor radar system at Durham 43° N (1977, 1978 and 1979), *J. Atmos. Terr. Phys.*, 45 621-627, 1983.

Clark, R. R., The quasi 2-day wave at Durham (43° N); solar and magnetic effects, *J. Atmos. Terr. Phys.*, 51, 617-622, 1989.

Clark, R. R., A. C. Current, A. H. Manson, C. E. Meek, S. K. Avery, S. E. Palo, and T. Aso, Global properties of the 2-day wave from mesosphere-lower thermosphere radar observations, *J. Atmos. Terr. Phys.*, 43, 1279-1288, 1993.

Covez, L., On the theory of the atmospheric tides, *J. Atmos. Terr. Phys.*, 33, 1273, 1971.

Coy, L., A possible 2-day oscillation near the tropical stratopause, *J. Atmos. Sci.*, 36, 1615-1618, 1979.

Craig, R. A., The upper atmosphere, *Academic press*, New York, U.S.A., 1965.

Craig, R. L., R. A. Vincent, G. J. Fraser, and M. J. Smith, The quasi 2-day wave near 90 km altitude at Adelaide (35° S), *Nature,* 287, 319-302, 1980.

Craig, R. L., and W. G. Elford, Observations of the quasi 2-day wave in the southern hemisphere mesosphere, *J. Atmos. Terr. Phys.*, 43, 1051-1056, 1981.

Craig, R. L., R. A. Vincent, S.P. Kingley, and H. G. Muller, Simultaneous observations of the quasi 2-day wave in the northern and southern hemispheres, *J. Atmos. Terr. Phys*, 45, 539-541, 1983.

Davies, J. G., and C. D. Ellyett, The diffraction of radio waves from meteor trials and the measurement of meteor velocities, Phil. Mag., (7) 40, 614-626, 1949.

Davies, K., and J. E. Jones, Ionospheric disturbances produced by severe thunderstorms. *NOAA Professional Paper 6,* U.S Government printing office, Washington, D.C., 1972.

Doviak, R. J., and D. S. Zrnic, Doppler radar and weather observations, *Academic Press*

Inc., New York, 1984.

Dunkerton, T. J., Theory of the mesopause semiannual oscillation, *J. Atmos. Sci.*, 39, 2681-2690, 1982.

Eckermann, S. D., and R. A. Vincent, Falling sphere observations of anisotropic gravity wave motions in the upper stratosphere over Australia, *Pure Appl. Geophys.*, 130, 509-532, 1989.

Egeland, A., O. Holter, and A. Omholt, Cosmical geophysics, *Scandinavian university books*, Oslo, Norway, 1973.

Elford, W. G., and D. S. Robertson, Measurements of winds in the upper atmosphere by means of drifting meteor trails, *J. Atmos. Terr. Phys.*, 4, 271-284, 1953.

Elford, W. G., A Study of winds between 80 and 100 km in medium latitudes, *Planet. Space Sci.*, 1, 94-101, 1959.

Elford, W. G., and D. Olsson-Steel, The height distribution of radio meteors: observations at 6 MHz *J. Atmos. Terr. Phys.*, 50, 811-818, 1988.

Farley, D. T., H. M. Ierkic, and B. G. Fejer, Radar interferometry: A new technique for studying plasma turbulence in the ionosphere, *J. Geophys. Res.*, 86, 1467-1472, 1981.

Fedor, L. S., A statistical approach to the determination of three dimensional ionospheric drifts, *J. Geophys. Res.*, 72, 5401-5415, 1967.

Felgate, D. G., On the point source effect in the measurement of ionospheric drifts, *J. Atmos. Terr. Phys.*, 32, 241-245, 1970.

Felgate, D. G., A. N. Hunter, S. P. Kingsley, and H. G. Muller, Comparative studies of E-region ionospheric drifts and meteor winds, *Planet. Space Sci.*, 23, 389-400, 1975.

Fellous, J. M., M. Glass, and A. Spizzichino, Meteor study of tides in the 80 to 100 km altitude range, *Proc. of the COSPAR Symp. held in Constance*, 383-387, 1974.

Fellous, J. L., R. Bernard, M. Glass, M. Massebeuf, and A. Spizzichino, A study of the variations of atmospheric tides in the meteor zone, *J. Atmos. Terr. Phys.*, 37, 1511-1524, 1975.

Fellous, J. M., A. Spizzichino, M. Glass, and M. Massebeuf, Vertical propagation of tides at meteor heights, *J. Atmos. Terr. Phys.* 36, 385-396, 1975.

Flattery, T. W., Hough functions, Technical report No. 21. *Dept. of Geophysical sciences*, University of Chicago, 1967.

Fleming, E. L., S. Chandra, M. R. Schoeberl and J. J. Bernett, Monthly mean global climatology of temperature, wind, geopotential height and pressure from 0-120 km, *NASA Technical Memorandum 100697*, 85 pp, 1988.

Forbes, J. M. and H. B. Garrett, Thermal excitation of atmospheric tides due to insolation absorption by H_2O and O_3, *Geophys. Res. Lett.*, 5, 1013-1016, 1978.

Forbes, J. M., and M. E. Hagan, Tides in the joint presence of friction and rotation, An f-plane approximation. *J. Geophys. Res.*, 84, 803-810, 1979.

Forbes, J. M. and H. B. Garrett, Theoretical studies of atmospheric tides, *Rev. Geophys. Space Phys.*, 17, 1951-1981, 1979.

Forbes, J. M., Mesospheric and thermospheric tides, *J. Met. Soc. Japan*, 58, 298-301, 1980.

Forbes, J. M., Atmospheric tides 1. Model description and results for the solar diurnal tide, *J. Geophys. Res.*, 87, 5222-5240, 1982.

Forbes, J. M., Atmospheric tides 2. The solar and lunar semidiurnal components, *J. Geophys. Res.*, 87, 5241-5252, 1982.

Forbes, J. M. and M. E. Hagan, Thermospheric extensions of the classical expansion functions for semidiurnal tides, *J. Geophys. Res.*, 87, 5253-5259, 1982.

Forbes, J. M., Middle atmospheric tides, *J. Atmos. Terr. Phys.*, 46, 1049-1967, 1984.

Forbes, J. M., Middle atmospheric tides between 80 and 120 km, *Handbook for MAP*, 16, 278-279, 1985.

Forbes, J. M. and G. V. Groves, Diurnal propagating tides in the low-latitude middle atmosphere, *J. Atmos. Terr. Phys.*, 49, 153-164, 1987.

Forbes, J. M. and M. E. Hagan, Diurnal propagating tide in the presence of mean winds and dissipation, *Planet. Space. Sci.*, 36(6), 579-590, 1988.

Forbes, J. M. and F. Vial, Monthly simulations of the solar semidiurnal tide in the mesosphere and lower thermosphere, *J. Atmos. Terr. Phys.*, 51(7/8), 649-661, 1989.

Forbes, J. M. and R. A. Vincent, Effects of mean winds and dissipation on the diurnal propagating tide: an analytic approach, *Planet. Space Sci.*, 37 197-209, 1989.

Forbes, J. M., J. Gu, and S. Miyahara, On the interactions between gravity waves and the diurnal propagating tide, *Planet. Space Sci.*, 39, 1249-1257, 1991.

Forbes, Tidal and Planetary waves, A tutorial lecture *The CEDAR workshop*, June, 1993.

Franke, S. J. and D. Thorsen, Mean winds and tides in the upper middle atmosphere at Urbana (40^oN 88^oW) during 1991-1992, *J. Geophys. Res.*, 98, 18607-18615, 1993.

Fraser, G. J., The measurement of atmospheric winds at altitudes of 64-120 km using ground-based radio equipment, *J. Atmos. Sci.*, 22, 217-218 , 1965.

Fraser, G. J., Seasonal variation of southern hemisphere mid-latitude winds at altitudes 70-100 km, *J. Atmos. Terr. Phys.*, 30, 707-719, 1968.

Fraser, G. J., and A. Kochanski, Ionospheric drifts from 64-108 km altitudes at Birdlings Flat, *J. Geophys. Res.*, 26, 675-687, 1970.

Fritts, D. C., and R. A. Vincent, Mesospheric momentum flux studies at Adelaide, Australia: Observations and a Gravity wave-tidal interaction model, *J. Atmos. Sci.*, 44, 605-619. 1987.

Fritts, D. C., and L. Yuan, Measurement of momentum fluxes near the summer mesopause at Poker Flat, Alaska, *J. Atmos. Sci.*, 46, 2569-2579, 1989

Fritts, D. C., and J. R. Isler, Mean motions and tidal and two-day structure and variability in the mesosphere and lower thermosphere over Hawaii, *J. Atmos. Sci.*, 51, 2145-2164, 1994.

Fukao, S., S. Kato, S. Yokoi, R. M. Harper, R. F. Woodman, and W. E. Gordon, One full-year radar measurement of lower stratosphere winds over Jicamarca, *J. Atmos. Terr. Phys*, 40, 1331-1337, 1978.

Fukao, S., T. Sato, S. Kato, R. M. Harper, R. F. Woodman, and W. E. Gordon, One full-year radar measurement of lower stratosphere winds over Jicamarca, *J. Geophys. Res*, 40.

133-139, 1979.

Fukao, S., T. Sato, N. Yamasaki, R. M. Harper, and S. Kato, Radar measurement of tidal winds at stratospheric heights over Arecibo, *J. Atmos. Sci.*, 37, 2540-2544, 1980.

Gage, K. S., and J. L. Green, Evidence for specular reflection from monostatic VHF radar observations of the stratosphere, *Radio Sci.*, 13, 991-1001, 1978.

Gage, K. S., and B. B. Balsley, On the scattering and reflection mechanisms contributing to clear air radar echoes from the troposphere, stratosphere, and mesosphere, *Radio Sci.*, 15, 243-257, 1980.

Gage, K. S., W. L. Ecklund, and B. B. Balsley, A modified Fresnel scattering model for the parameterization of Fresnel returns, *Radio Sci.*, 20, 1493-1501, 1985.

Gage, K. S., Radar observations of the free atmosphere: structure and dynamics, Radar in meteorology edited by David Atlas, *American meteorological society,* Boston, 235-281, 1990.

Geller, M. A., S. A. Bowhill, and G. C. Hess, A description of the university of Illinois meteor radar system and some first results, *J. Atmos. Terr. Phys.*, 39, 15-24, 1977.

Geller, M. A., Dynamics of the middle atmosphere, *Space Science Reviews.*, 34, 359-375, 1983

Garcia, R. R., and S. Solomon, The effects of breaking gravity waves on the dynamical and chemical composition of the mesosphere and lower thermosphere, *J. Geophy. Res.*, 90, 3850-3858, 1985.

Glass, M., J. L. Fellous, M. Massebeuf, A. Spizzichino, I. A. Lysenko, and Y. I. Portnyagin, Comparison and interpretation of the results of simultaneous wind measurements in the lower thermosphere at Garchy (France) and Obninsk (USSR) by meteor radar technique, *J. Atmos. Terr, Phys.*, 37, 10771087, 1975.

Glass, M., J. L. Fellous, M. Massebeuf, A. Spizzichino, I. A. Lysenko, and Y. I. Portniagin *J. Atmos. Terr. Phys.*, 37, 1077, 1975.

Glass, M., R. Bernard, J. L. Fellous, and M. Massebeuf, The French meteor radar facility, *J. Atmos. Terr. Phys.*, 40, 923-931, 1978.

Gnanalingam, S., and J. A. Kane, Shortcomings in our understandings of the lower atmosphere as revealed by an analysis of radio wave absorption measurements, *J. Atmos. Terr. Phys.*, 40, 629, 1978.

Golley, M. G., and Rossiter, D. E., Some tests of methods of analysis of ionospheric drift records using an array for 89 aerials, *J. Atmos. Terr. Phys.*, 32, 1215-1233, 1970.

Gossard, E. E., Vertical flux of energy into the lower ionosphere from internal gravity waves generated in the troposphere, *J. Geophys. Res.*, 67, 745-757, 1962.

Gossard, E. E., and W. H. Hooke, Waves in the atmosphere, Elsevier, New York, 1975.

Green, J. L., and K. S. Gage, A reexamination of the range resolution dependence of backscattered power observed by VHF radars at vertical incidence, *Radio Sci.*, 20, 1001-1005, 1985.

Greenhow, J. S., Characteristics of radio echoes from meteor trails: the behaviour of the electron trails after formation, *Proc. Phys. Sco.*, 65, 169-181, 1952.

Greenhow, J. S., Systematic wind measurements at altitudes of 80-100 km using radio echoes from meteor trails, *Philos. Mag.*, 45, 471-490, 1954.

Greenhow, J. S., and E. L. Neufeld, The diffusion of ionized meteor trails in the upper atmosphere, *J. Atmos. Terr. Phys.*, 6, 133-140, 1955.

Greenhow, J. S., and J. E. Hall, *J. Atmos. Terr. Phys.*, 5, 109, 1955.

Greenhow, J. S., and E. L. Neufeld, Height variation of upper atmospheric winds, *Philos. Mag. Ser.*, 8, 1, 1157-1171, 1956.

Greenhow, J. S., and J. E. Hall, The importance of initial trail radius on the apparent height and number distributions of meteor echoes, *Mon. Not. R. Astr. Soc.*, 121, 183-196, 1960.

Greenhow, J. S., and E. L. Neufeld, Winds in the upper atmosphere, *Quart. J. Roy. Meteorol. Soc.*, 87, 472-489, 1961.

Gregory, J. B., and A. H. Manson, Seasonal variations of electron densities below 100 km at mid-latitudes-III. Stratospheric-ionospheric coupling, *J. Atmos. Terr. Phys.*, 32, 837-852, 1970.

Gregory, J. B., and D. T. Rees, Wind profiles to 100 km near 53 N during 1969, *J. Atmos. Sci.*, 1079-1082, 1971.

Grossi, M. D., R. B. Southworth, S. K. Rosenthal, Radar observations of meteor winds above Illinois, Thermospheric circulation, *Willis L. Webb, ed., Mass. Institute of technology*, 205-248, 1972.

Groves, G. V., A theory for determining upper atmosphere winds from radio observations on meteor trails, *J. Atmos. Terr. Phys.*, 16, 344-356, 1959.

Groves, G. V., Rocket studies of atmospheric tides: review lecture, *Proc. R. Soc. Lond.*, A, 351, 437-469, 1976.

Groves, G. V., Thermospheric energy flux of the semidiurnal tide, *Planet Space Sci.*, 31, 1183-1186, 1983.

Groves, G. V. and J. M. Forbes, Equinox tidal heating of the upper atmosphere, *Planet. Space Sci.*, 32, 447-456, 1984.

Groves, G. V. and J. M. Forbes, Mean zonal and meridional accelerations and mean heating induced by solar tides for equinox and solstice conditions, *Planet. Space. Sci.*, 33, 283-293, 1985.

Hagan, M. E., J. M. Forbes, and F. Vial, Numerical investigation of the propagation of the quasi 2-day wave into the lower thermosphere, *J. Geophys. Res.*, 98, 23,193-23,205, 1993.

Hargreaves, J. K., The solar terrestrial environment, *Cambridge university press*, New York, 1992.

Harris, M. F., F. G. Finger, and S. Teweles, Diurnal variations of winds, pressure, and temperature in the troposphere and stratosphere over the Azores, *J. Atmos. Sci.*, 19, 136-149, 1962.

Harris, T. J., A long-term study of the quasi 2-day wave in the middle atmosphere, *J. Atmos. Terr. Phys.*, 55, 1993.

Harris, T. J., and R. A. Vincent, The quasi 2-day wave observed in the equatorial middle atmosphere, *J.Geophys. Res.*, 98, 10,481-10,490, 1993.

Haurwitz, B., The diurnal surface pressure oscillation, *Arch. Met. Geophys. Bioklim.*, A 14, 361-379, 1965.

Haurwitz, B., and A. D. Cowley, The diurnal and semidiurnal barometric oscillations, global distribution and annual variation, *Pure Appl. Geophys.*, 102, 193-222, 1973.

Herlofson, N., The theory of meteor ionization, *Phys. Soc. Rep. Prog. Phys.*, 11, 444-454, 1948.

Hines, C. O., Internal gravity waves at ionospheric heights, *Canadian Journal of Physics*, 38, 1441-1481, 1960.

Hines, C. O., I. Paghis, T. R. Hartz, and J. A. Fejer, Physics of the earth's upper atmosphere, *Prentice-Hall*, Inc, Englewood Cliffs, New York, 1965.

Hines, C. O., and C. A. Reddy, On the propagation of atmospheric gravity waves through regions of wind shear, *J. Geophys. Res.*, 72, 1015-1034, 1967.

Hines, C. O., Motions in the ionospheric D and E regions, *Phil. Trans. R. Soc. London*, A 271, 457-471, 1972.

Hines, C. O., G. W. Adams, J. W. Brosnahan, F. T. Djuth, M. P. Sulzer, C. A. Tepley, and J. S. Van Baelen, Multi-instrument observations of mesospheric motions over Arecibo: comparisons and interpretations, *J. Atmos. Terr. Phys.*, 55, 241-287, 1993.

Hirota, I., Y. Maekawa, S. Fukao, K. Fukuyama, M. P. Sulzer, J. L. Fellous, and S. Kato, *J. Geophys. Res.*, 88, 6835, 1983.

Hocking, W. K., and J. Röttger, Pulse length dependence of radar signal strengths for Fresnel backscatter, *Radio Sci.*, 18, 1312-1324, 1983.

Hocking, W. K., Measurement of turbulent energy dissipation rates in the middle atmosphere by radar techniques: a review, *Radio Sci.*, 20, 1403-1422, 1985.

Hocking, W. K., Target parameter estimation, *Handbook for MAP*, 30, 228-268, 1989.

Hocking, W. K., P. May and Röttger, J., Interpretation, reliability and accuracies of parameters deduced by the spaced antenna method in middle atmosphere applications, *Pure Appl. Geophys.*, 130, 571-604, 1989.

Hocking, W. K., The effects of middle atmosphere turbulence on coupling between atmospheric regions, *J. Geomag. Geoelectr.*, 43, 621-636, 1991.

Hocking, W. K., The University of Western Ontario VHF atmospheric radar, Solar-terrestrial energy program, Proceedings of the sixth workshop on technical and scientific aspects of MST radar, SCOSTEP Secretariat NOAA, Boulder, Colorado, 349-356, 1993.

Holdsworth, D. A., and I. M. Reid, A simple model of atmospheric radar backscatter: Description and application to the full correlation analysis of spaced antenna data, *Radio Sci.*, 30, 1263-1280, 1995.

Holton, J. R., The dynamic meteorology of the stratosphere and mesosphere, Metor. Monog 15(37), *Ame. Met. Soc.*, Mass., U.S.A., 1975.

Holton, J. R., An introduction to dynamic meteorology, *International geophysical series*, 2 nd edition, Academic press, New York, 1979.

Holton, J. R., The role of gravity wave-induced drag and diffusion in the momentum budget of the mesosphere, *J. Atmos. Sci.*, 39, 791-799, 1982.

Hough, S. S., On the application of harmonic analysis to the dynamical theory of tides, Part I. On Laplace's 'oscillations of the first species', and on the dynamics of ocean currents, *Phil. Trans. Roy. Soc.*, A 189, 201-257, 1897.

Hough, S. S., On the application of harmonic analysis to the dynamical theory of tides, Part II. On the general integration of Laplace's dynamical equations, *Phil. Trans. Roy. Soc.*, A 189, 201-257, 1898.

Houghton, J. T., The physics of atmospheres, *Cambridge university press*, Cambridge England, 1977.

Houghton, J. T., The stratosphere and mesosphere, *Quarterly journal of the Royal Meteorological Society*, 104, 1-29, 1978.

Houghton, J. T., The physics of the atmosphere, *Cambridge university press*, Cambridge, England, 1986.

Hughes, D. W., Cosmic dust, McDonnell, J. A. M., ed., Willey, Chichester, 123, 1978.

Hung, R. J., Observations of upper atmospheric disturbances caused by hurricanes and tropical storms, *Space Research*, 17, 205, 1977.

Hung, R. J., T. Phan, and R. E. Smith, Observation of gravity waves during the extreme tornado outbreak of 3 April, 1974, *J. Atmos. Terr. Phys.*, 40, 831, 1978.

Hyde, W. W., Ancient Greek mariners, Oxford university press, New York, U.S.A., 1947.

Ito, R., S. Kato, and T. Tsuda, Consideration of an ionospheric wind dynamo driven by a planetary wave with a two-day period, *J. Atmos. Terr. Phys.*, 48, 1-13, 1986.

Ierkic, H. M., and J. Röttger, Mesospheric measurements of irregularity patches using a 3 antenna interferometer, *Handbook for MAP*, Vol. 14, Scostep Secretariat, University of Illinois, Urbana, 174-178, 1984.

Jacchia, L. G., and Kopal, Z., Atmospheric oscillations and the temperature profile of the upper atmosphere, *J. Meteorol.*, 9, 13-23, 1951.

Jones, J., On the decay of underdense radio meteor echoes, *Mon. Not. R. Astr. Soc.*, 173, 637-646, 1975.

Jones, J., B. A. McIntosh, M. Scmek, Ozone and the duration of overdense radio meteors, *J. Atmos. Terr. Phys.*, 52, 253-258, 1990.

Jones, J., and P. Brown, The radiant distribution of sporadic meteors., *Planet. Space Sci.*, 42, 123-126, 1994.

Kaiser, T. R., Radio echo studies of meteor ionization, *Adv. Phys. (Phil. Mag. Supp.,)* 2, 495-544, 1953.

Kaiser, T. R., W. M. Pickering, and C. D. Watkins, Ambipolar diffusion and motion of ion clouds in the earth's magnetic field, *Planet. Space Sci.*, 17, 519-552, 1969.

Kalchanko, B., and S. Bulgakov, Study of periodic components of wind velocity in the lower thermosphere above the equator, *Geomagn. Aeron.*, 13, 955-956, 1973.

Kato, S., Diurnal atmospheric oscillation, 1, eigenvalues and Hough functions, *J. Geophys. Res.*, 71, 3201-3209, 1966.

Kato, S., Dynamics of the upper atmosphere, Developments earth and planetary sciences, *D. Reidel*, Tokyo, Japan, 1980.

Kato, S., T. Tsuda and F. Watanabe, Thermal excitation of non-migrating tides, *J. Atmos. Terr. Phys.*, 44, 131-146, 1982.

Kato, S., Non-migrating tides, *J. Atmos. Terr. Phys.*, 51, 673-682, 1989.

Kawahira, K., An observational study of the D-region winter anomaly and sudden stratospheric warmings, *J. Atmos. Terr. Phys.*, 44, 947-955, 1982.

Kelley, M. C., The earth's ionosphere, *Academic press inc.*, New York, 1989.

Kelley, M. C., and J. C. Ulwick, Large- and small-scale organization of electrons in the high latitude mesosphere, *J. Geophys. Res.*, 93, D6, 7001-7008, 1988.

Kertz, W., Components of the semidiurnal pressure oscillation, *New York university*, Dept of meteor. and Ocean., Sci. Rep. 4, 1956.

Kingsley, S., H. Muller, L. Nelson, and A. Scholefield, Meteor winds over Sheffield, *J. Atmos. Terr. Phys.*, 40, 917-922, 1978.

Koshelev, V. V., Variations of transport conditions and winter anomaly in the D-ionospheric region, *J. Atmos. Terr. Phys.*, 41, 431, 1979.

Koshelkov, V. V., The winter anomaly in the ionospheric D-region - some numerical calculations, *J. Atmos. Terr. Phys.*, 49, 81-97, 1987.

Kraus, J. D., Radio astronomy, *McGill-Hill*, New York, 1966.

Kudeki, E., P. K. Rastogi, and F. Sürücü, Systematic errors in radar wind estimation: Implications for comparative measurements, *Radio Sci.*, 28, 169-179, 1992.

Labitzke, K., A. H. Manson, J. J. Barnett, and M. Corney, Comparison of geostrophic and observed winds in the upper mesosphere over Saskatoon, Canada, *J. Atmos. Terr. Phys.*, 49, 987-997, 1987.

Lamb, H., On atmospheric oscillation, *Proc. Roy. Soc.*, A 84, 551-572, 1910.

Lamb, H., Hydrodynamics, 4 th edition, Cambridge, *Cambridge university press*, United Kingtom, 1916.

Laplace, P. S. (later Marquis De La Place), *Mecanique celeste*, Paris (a) 2 (iv), 294-298, 1799.

Laplace, P. S. (later Marquis De La Place), *Mecanique celeste*, Paris (a) 5 (xiii), 145-167, 1825.

Lesicar, D., and W. K. Hocking, Studies of seasonal behaviour of the shape of mesospheric scatterers using 1.98 MHz radar, *J. Atmos. Terr. Phys.*, 54, 295-309, 1992.

Lieberman, R. S., Nonmigrating diurnal tides in the equatorial middle atmosphere, *J. Atmos. Sci.*, 48, 1112-1123, 1991.

Lindzen, L. S., On the theory of the diurnal tide, *Mon. Wea. Rev.*, 94, 295-301, 1966.

Lindzen, L. S., and D. J. McKenzie, Tidal theory with Newtonian cooling, *Pageoph.*, 66, 90-96, 1967.

Lindzen, L. S., Thermally driven diurnal tide in the atmosphere, *Q. J. Roy. Met. Soc.*, 93, 18-42, 1967.

Lindzen, L. S., The application of classical atmospheric tidal theory, *Proc. Roy. Soc.*, A 303, 299-316, 1968.

Lindzen, L. S., Internal gravity waves in atmospheres with realistic dissipation and temperature, I. Mathematical development and propagation of waves into the thermosphere, *Geophys. Fl. Dyn*, 1, 303-355, 1970.

Lindzen, R. S. and D. Blake, Lamb waves in the presence of realistic distributions of temperature and dissipation, *J. Geophys. Res.*, 77, 2166-2176, 1972.

Lindzen, R. S., Tides and internal gravity waves in the atmosphere, from Developments in atmospheric science, I. - Structure and dynamics of the upper atmosphere, ed. F. Vernieni, *Elsevier Sci. Pub. co.*, New York, U.S.A., 1974.

Lindzen, R. S. and S. S. Hong, Effects of mean winds and horizontal temperature gradients on solar and lunar semidiurnal tides in the atmosphere, *J. Atmos. Sci.*, 31, 1421-1446, 1974.

Lindzen, R. S., Theory of atmospheric tides, *J. Met. Soc. Japan*, 58, 273-276, 1980.

Lindzen, R. S., Turbulence and stress owing to gravity waves and tidal breakdown, *J. Geophys. Res.*, 86, 9707-9714, 1981.

Lindzen, R. S., Dynamics in atmospheric physics, *Cambridge university press*, New York, U.S.A., 1990.

Liu, C. H., and K. C. Yeh, Scattering of VHF and UHF radar signals from the turbulent air, *Radio Sci.*, 15, 277-282, 1980.

Lloyd, N., A. H. Manson, D. J. McEwen, and C. E. Meek, A comparison of middle atmospheric dynamics at Saskatoon (52° N, 107° W)as measured by a medium-frequency radar and a Fabry-Perot interferometer, *J. Geophys. Res.*, 95, D6, 7653-7660, 1990.

Longuet-Higgins, M. S., The eigenfunctions of the Laplace's tidal equations over a sphere. *Phil. Trans. Roy. Soc.*, London, A 262, 511-607, 1968.

Lord Kelvin (before Thomson, W.), On the thermodynamic acceleration of the earth's rotation, *Proc. Roy. Soc. Edinb.*, 11, 396-405, 1882.

Lu, W., and D. C. Fritts, Spectral estimates of gravity wave energy and momentum fluxes. Part 3: Gravity wave-tidal interactions, *J. Atmos. Sci.*, 50, 3714-3727, 1993

Lysenko, I. A., A. D. Orlyansky, and Yu. I. Portnyagin, A study of the wind regime at an altitude of about 100 km by the meteor radar method, *Phil. Trans. R. Sco. Lond.*, A 271, 601-610, 1972.

Lysenko, I. A., Yu. I. Portnyagin, K. Sprenger, K. M. Greisiger, and R. Schminder, Results of a comparison between radar meteor wind measurements and simultaneous lower ionosphere drifts measurements in the same area, *J. Atmos. Terr. Phys.*, 34, 1453-1444, 1972.

Maekawa, Y., T. Aso, J. Röttger, P. Czechowsky, R. Rüster, G. Schmidt, I. Hirota, R. F. Woodman, and S. Kato, A cooperative synchronous observation of winds and tides in the tropical lower stratosphere and mesosphere using VHF radars at Jicamarca and Arecibo, *J. Geomag. Geoelectr.*, 38, 81-97, 1986.

Manning, L. A. O., O. G. Villard, and A. M. Peterson, Meteoric echo study of upper atmospheric winds, Proc. *Inst. Radio. Engrs.*, 38, 877-883, 1953.

Manning, L. A. O., The initial radius of meteoric ionization, *J. Geophys. Res.*, 63, 81-196, 1958.

Manson, A. H., J. B. Gregory, and D. G. Stephenson, Winds and wave motions to 110 km at mid-latitudes, I, Partial reflection radiowave soundings, 1972-1973, *J. Atmos. Sci*., 31, 2207, 1974.

Manson, A. H., J. B. Gregory, and D. G. Stephenson, Winds and wave motions to 110 km at mid-latitudes, Coupling between internal gravity waves and the mean flow, *J. Atmos. Sci.*, 31, 1682, 1975.

Manson. A. H., J. B. Gregory, C. E. Meek, and D. G. Stephenson, Winds and wave motions to 110 km at mid-latitudes, *J. Atmos. Sci.*, 35, 592-599, 1978.

Manson. A. H., C. E. Meek, J. B. Gregory, and D. K. Chakrabarty, Fluctuations in tidal (24-, 12-h) characteristics and oscillations (8-h-5-d) in the mesosphere and lower thermosphere (70-110 km): Saskatoon (52° N, 107° W), 1979-1981, *Planet Space Sci.*, 30, 1283-1294, 1982.

Manson, A. H., and C. E. Meek, Winds and the tidal oscillations in the upper middle atmosphere at Saskatoon (52° N, 107° W, L=4.3) during the year June 1982-May 1983, *Planet Space Sci.*, 32, 1087-1099, 1984.

Manson, A. H. and C. E. Meek, Middle atmosphere (60-110 km) tidal oscillations at Saskatoon, Canada (52° N 107° W) during 1983-1984, *Radio Science*, Vol. 20, 1441-1451, 1985.

Manson, A. H. and C. E. Meek, Dynamics of the middle atmosphere at Saskatoon (52° N 107° W) a spectral study during 1981, 1982, *J. Atmos. Terr. Phys.*, 48, 1029-1055, 1986.

Manson, A. H., C. E. Meek, H. Teitelbaum, F. Vial, R. Schminder, D. Kurschner, M. J. Smith, G. J. Fraser and R. R. Clark, Climatologies of semidiurnal and diurnal tides in the middle atmosphere (70-110 km) at middle latitudes (40-55), *J. Atmos. Terr. Phys.*, 51, 579-593, 1989.

Manson, A. H., and C. E. Meek, Long period (~ 8-20 h) wind oscillations in the upper middle atmosphere at Saskatoon (52° N): evidence for non-linear tidal effects, *Planet Space Sci.*, 38, 1431-1441, 1990.

Manson, A. H., C. E. Meek, E. Fleming, S. Chandra, R. A. Vincent, A. Phillips, S. K. Avery, G. J. Fraser, M. J. Smith, J. L. Fellous and M. Massebeuf, Comparisons between satellite-derived gradient winds and radar-derived winds from the CIRA-86, *J. Atmos. Sci.*, 48, 411-428, 1991.

Margules, M., Uber die Schwingungen periodisch erwarmter luft, *Sitzber. Akad. Wiss. Wien.*, Abt. IIa, 99, 204-227, 1890.

Margules, M., Luftbewegungen in einer rotierenden Scharoidschale, *Sitzber. Akad. Wiss. Wien.*, Abt. IIa, 101, 597-626, 1892.

Margules, M., *Sitzber. Akad. Wiss. Wien.*, Abt. IIa, 102, 11-56, 1893.

Martyn, D. F., and Pulley, O. O., The temperature and constituents of the atmosphere, *Proc. Roy. Soc.*, A 154, 455-486, 1936.

Massebeuf, M., R. Bernard, J. L. Fellous, and M. Glass, Simultaneous meteor radar observations at Monpazier (France, 44° N) and Punta Borinquen (Puerto Rico, 18° N) - mean zonal wind and long period waves, *J. Atmos. Terr. Phys.*, 43, 535-542, 1981.

Mastrantonio, G., F. Einaudi, and D. Fua, Generation of gravity waves by jet streams in the atmosphere, *J. Atmos. sci.*, 33, 1730, 1976.

Mathews, J. D., *J. Geophys. Res.*, 81, 4671, 1976.

Matsuno, T., A dynamical model of the stratospheric warming *J. Atmos. Sci.*, 28, 1479-1494, 1971.

Matsuno, T., A trial search for minor components of lunar tides and short period free oscillations of the atmosphere in surface pressure data, *J. Met. Soc. Japan*, 58, 281-285, 1980.

Matsuno, T., A quasi one-dimensional model of the middle atmosphere circulation interacting with internal gravity waves, *Journal of the Meteorological Society of Japan*, 60, 215-226, 1982.

Mawrey, R. S., and A. D. Broadhurst, Comparison of predicted and measured detection rates of meteor signals, *Radio Sci.*, 28, 415-427, 1993.

May, P. T., Statistical errors in the determination of wind velocities by the spaced antenna technique, *J. Atmos. Terr. Phys.*, 50, 21-32, 1988.

McDaniel, E. W., and E. A. Mason, Mobility and diffusion of ions in gases, *John Willey*, New York, 1973.

McEwan, M. J., and L. F. Phillips, Chemistry of the atmosphere, *Edward Arnold*, London, England, 1975.

McIntosh, B. A., The effect of wind shear on the decay constant of meteor echoes, *Can. J. Phys.*, 47, 1337-1341, 1969.

McKinley, D. W. R., and P. M. Millman, A phenomenological theory of radar echoes from meteors, *Proc. Inst. Radio Engrs.*, 37, 364-375, 1949.

McKinley, D. W. R., Meteor science and engineering, *McGraw-Hill*, New York, 1961.

McLandress, C., and W. E. Ward, Tidal/gravity wave interactions and their influence on the large-scale dynamics of the middle atmosphere: Model results, *J. Geophys. Res.*. 99, 8139-8155, 1994.

Meek, C. E., A. H. Manson, and J. B. Gregory, Internal consistency analysis tor partial and total reflection drifts data, *J. Atmos. Terr. Phys.*, 41, 251-258, 1979.

Meek, C. E., An efficient method for analysing ionospheric drifts data, *J. Atmos. Terr. Phys.*, 42, 835-839, 1980.

Meek, C. E., and I. M. Reid, A simple model for testing the effects of gravity wave produced vertical oscillations of scattering irregularities on spaced antenna horizontal drift measurements, *Handbook for MAP*, SCOSTEP Secr., Univ. of Illinois, Urbana, 1984.

Miller, D. A., S. A. Bowhill, K. P. Gibbs, and I. D. Countryman, First measurements of mesospheric vertical velocities by VHF radar at temperature latitudes, *Geophys. Re. Lett.*, 5, 939-942, 1978.

Miyahara, S, Zonal mean winds induced by vertically propagating atmospheric tidal waves in the lower thermosphere, *J. Met. Soc. Japan*, 56, 548-558, 1978.

Miyahara, S, Solar diurnal tides and the induced zonal mean flows, *J. Met. Soc. Japan*, 58. 302-306, 1980.

Miyahara, S, Zonal mean winds induced by solar diurnal tides in the lower thermosphere, *J.*

Met. Soc. Japan, 59, 303-319, 1981.

Miyahara, S, Dynamics of the middle atmosphere, *D. Reidel*, MA, U.S.A, 1984.

Miyahara, S., Y. Hayashi, and J. D. Mahlman, Interactions between gravity waves and the planetary scale flow simulated by the GFDL "SKYHI" general circulation model, *J. Atmos. Sci.*, 43, 1844-1861, 1986.

Miyahara, S. and D. H. Wu., Effects of solar tides on the zonal mean circulation in the lower thermosphere:solstice condition, *J. Atmos. Terr. Phys.*, 51, 635-647, 1989.

Miyahara, S., and J. M. Forbes, Interactions between gravity waves and the diurnal tide in the mesosphere and lower thermosphere, *J. Meteorol. Soc. Jpn.*, 69, 523-531, 1991.

Miyahara, S., and J. M. Forbes, Tide/gravity-wave/mean-flow interactions in the mesosphere and lower thermosphere, *Adv. Space Res.*, 12, 10(7)- 10(16), 1992

Miyahara, S., Y. Yoshida, and Y. Miyoshi, Dynamical coupling between the lower and upper atmosphere by tides and gravity waves, *J. Atmos. Terr. Phys.*, 55, 1039-1053, 1993.

Mitra, S. N., A radio method of measuring winds in the ionosphere, *Proc. Inst. Electr. Eng.*, 43, 441-446, 1949.

Montbriand, L. E., and J. S. Belrose, Changes in electron precipitation inferred from spectra deduced from D-region electron densities during a post-magnetic storm effect, *J. Geophys. Res.*, 81, 2213, 1976.

Muller, H. G., Atmospheric tides in the Meteor zone, *Planet. Space Sci.*, 14, 1253-1272, 1966.

Muller, H. G., Wind shears in the meteor zone, *Planet. Space Sci.*, 16, 61-90, 1968.

Muller, H. G., Simultaneous observations of meteor winds and ionospheric drifts, *J. Atmos. Terr. Phys.*, 30, 701-706, 1968.

Muller, H. G., The Sheffield meteor wind experiment, *Quart. J. R. Met. Soc.*, 96, 195-213, 1970.

Muller, H. G., Long-period meteor wind oscillations, *Phil. Trans. R. Soc. London*, Ser. A, 271, 585-598, 1972.

Muller, H. G., and S. P. Kingsley, Long period meteor wind oscillations, *J. Atmos. Terr. Phys.*, 36, 1933-1943, 1974.

Muller, H. G., and S. P. Kingsley, On the scale sizes of wind in the meteor region, *J. Atmos. Terr. Phys.*, 40, 761-766, 1978.

Muller, H. G., and L. Nelson, A travelling quasi-2-day in the meteor region, *J. Terr. Atmos. Phyc.*, 40, 761-766, 1978.

Muller, H. G., R. L. Havill, V. E. Comley, and P. C. J. Hill, A study of meteor winds from two locations in the British Isles, *J. Atmos. Terr, Phys.*, 57, 979-993, 1995.

Murphy, C. H., Seasonal variation of ionospheric winds over Barbados, West Indies, *J, Geophys. Res.*, 74, 339, 1969.

Namboothiri, S. P., A. H. Manson and C. E. Meek, E region real heights and their implications for MF radar-derived wind and tidal climatologies, *Radio Science*, Vol. 28, no. 2, 187-202, 1993.

Newell, R. E., J. W. Kidson, D. G. Vincent, and G. J. Boer, The general circulation of the tropical atmosphere and interactions with extratropical latitudes, Vol 1. *M.I.T. press*, Cambridge, MA, U.S.A, 1972.

Newton, I., Philosophiae naturalis principia mathematica, (a) Bk. 1, prop. 66, Cor. 19, 20; Bk. 3, Prop. 24, 36 37, (b) Bk. 2, Prop. 48-50, 1687.

Olsson-Steel, D., and W. G. Elford, The height distribution of radio meteors: observations at 2 MHz, *J. Atmos. Terr. Phys.*, 49, 243-258, 1987.

Offermann, D., Recent advances in the study of the D-region winter anomaly, *J. Atmos. Terr. Phys.*, 41, 735-752, 1979.

Pekeris, C. L., Atmospheric oscillation, *Proc. Roy. Soc.*, A 158, 650-671, 1937.

Phillips, G. J., M. Spencer, The effects of anisometric amplitude patterns on the measurement of ionospheric drifts, *Proc. Phys. Soc. London*, B 68 (8), 481-492, 1955.

Phillips, N. A., Simplification of the equations of motion, *J. Atmos. Sci.*, 25, 1155-1157, 1968.

Phillips, E., Wind structure from the amplitude fluctuations in persistent radio meteor echoes, *Planet. Space Sci.*, 17, 553-559, 1969.

Phillips, A., Simultaneous observations of the quasi 2-day wave at Mawson, Antarctica, and Adelaide, South Australia, *J. Atmos. Terr. Phys.*, 51, 119-124, 1989.

Phillips, A., A. H. Manson, C. E. Meek, and E. J. Llewellyn, A long-term comparison of middle atmosphere winds measured at Saskatoon (52° N, 107° W) by a medium-frequency radar and a Fabry-Perot interferometer, *J. Geophys. Res.*, 99, D6, 12923-12935, 1994.

Pfister, W., The wave-like nature of inhomogeneities in the E-region, *J, Atmos. Terr. Phys.*, 33, 999-1025, 1971.

Pfister, L., Baroclinic instability of easterly jets with application to the summer mesosphere, *J. Atmos. Sci.*, 42, 313-330, 1985.

Plumb, R. A., Baroclinic instability of the summer mesosphere: A mechanism for the quasi 2-day wave ?, *J. Atmos. Sci.*, 40, 262-270, 1983.

Plumb, R. A., R. A. Vincent, and R. L. Craig, The quasi 2-day wave event of January 1984 and its impact on the mean mesospheric circulation, *J. Atmos. Sci.*, 44, 3030-3036, 1987.

Poole, L. M. G., The Grahamstown all-sky meteor radar, *J. Atmos. Terr. Phys.*, 50, 585-590, 1988.

Poole, L. M. G., Characteristics of the mesospheric two day wave as observed at Grahamstown (33.3° S, 26.5° E), *J. Atmos. Terr. Phys.*, 52, 259-268, 1990.

Poulder, E. M., - d W. J. Baggaley, Radiowave scattering from meteor in ionization, *J. Atmos. Terr. Phys.*, 39, 757-768, 1977.

Poulder, E. M., and W. J. Baggaley, The application of radio-wave scattering theory to radio-meteor observations, *Planet. Space sci.*, 26, 969-977, 1978.

Poulder, E. M., Winter motions in the southern hemisphere meteor region, *J. Atmos. Terr. Phys.*, 42, 661-672, 1980.

Randel, W. J., Observations of the 2-day wave in NMC stratospheric analyses, J. Atmos. Sci., 51, 306-313, 1993.

Ranta, H., and A. Ranta, Daily variation of absorption in the D-region using riometer data at high latitudes, *J. Atmos. Terr. Phys.*, 39, 309-312, 1977.

Rayleigh, 3rd Baron (Strutt, J. W.), On the vibration of an atmosphere, Phil. Mag. 5, 29, 173-180, 1890.

Reddi, C. R., K. Rajeev, and R. Ramkumar, Annual and semiannual temperature oscillations at the mesopause levels over Trivandrum (8.5° N, 78° E), *J. Geophys. Res.*, D5, 8925-8931, 1993.

Reed, R. J., Semidiurnal tidal motions between 30 and 60 km, *J. Atmos. Sci.*, 24, 315-317, 1967.

Rees, D., H. G. Muller, and S. P. Kingsley, Comparative wind measurements in the lower thermosphere using rocket trail and meteor radar techniques, *J. Atmos. Terr. Phys.*, 38, 365-370, 1976.

Reid, G. C., The influence of electric fields on radar measurements of winds in the upper mesosphere, *paper presented at URSI Symposium*, Fairbanks, Alaska, August 1982.

Reid, G. C., The production of water-cluster positive ions in the quiet day-time D region, *Planet. Space Sci.*, 25, 275, 1977.

Reid, I. M., and R. A. Vincent, Measurements of mesospheric gravity wave momentum fluxes and mean flow accelerations at Adelaide, *J. Atmos. Terr, Phys.*, 49, 443-460, 1987.

Reid, I. M., MF Doppler and spaced antenna radar measurements of upper middle atmospheric winds, *J Atmos. Terr. Phys.*, 50, 117-134, 1988.

Reid, I. M., R. Rüster, P. Czechowsky, and G. Schmidt, VHF radar measurements of momentum flux in the summer polar mesosphere over Andenes (69° N, 16° S), Norway, *Geophys. Res. lett.*, 15, 1263-1266, 1988.

Robert-Jones, J. R., The radar equation in meteorology, *Quarterly Journal of the Royal Meteorological Society*, 88, 485, 1962.

Robertson, D. S., D. T. Liddy, and W. G. Elford, Measurement of winds in the upper atmosphere by means of drifting meteor trails, *J. Atmos. Terr. Phys.*, 4, 255-270, 1953.

Roble, R. G., and R. E. Dickinson, How will changes in carbon dioxide and methane modify the mean structure of the mesosphere and thermosphere ?, *Geophys. Res. Lett.*, 16, 1441-1444, 1989.

Rodgers, C. D., and A. Prata, Evidence for a travelling 2-day wave in the middle atmosphere, *J. Geophys. Res.*, 86, 9661-9664, 1981.

Roper, R. G., The semidiurnal tide in the lower thermosphere, *J. Geophys. Res.*, 71, 5746-5748, 1966.

Roper, R. G., The measurement of meteor winds over Atlanda (34° N, 84° W), *Radio Sci.*, 10, 363-369, 1975.

Roper, R. G., Winds from the Atlanda (34° N, 84° W) radio meteor wind facility, *J. Atmos. Terr. Phys.*, 40, 891-894, 1978.

Rosenlof, K. H., and R. J. Thomas, Five-day mesospheric waves observed in solar mesosphere explorer ozone, *J. Geophys. Res.*, 95 (D1), 895-899, 1990.

Rossiter, D. E., A comparison of ionospheric drifts with radio meteor measurement of the

neutral wind, *Aus. J. Phys.*, 23, 103-117, 1970.

Royrvik, O., VHF radar signals scattered from the equatorial mesosphere, *Radio Sci.*, 18, 1325-1335, 1983.

Röttger, J., and R. A. Vincent, VHF radar studies of tropospheric velocities and irregularities using spaced antenna techniques, *Geophys. Res. Lett.*, 5, 917-920, 1978.

Röttger, J., and C. H. Liu, Partial reflection and scattering of VHF radar signals from the clear atmosphere, *Geophys. Res. Lett.*, 5, 357-360, 1978.

Röttger, J., and P. Czechowsky, Tropospheric and stratospheric wind measurements with the spaced antenna drifts technique and the Doppler beam swinging technique using a VHF radar, Preprint, *19th Conf. on radar meteorology of Am. Met. Soc.*, Miami, FL, USA, 15-18 Apr., 577-584, 1980.

Röttger, J., Structure and dynamics of the stratosphere and mesosphere revealed by VHF radar investigations, *Pageoph*, 118, 494, 1980.

Röttger, J., Reflection and scattering of VHF radar signals from atmospheric refractivity structures, *Radio Sci.*, 15, 259-276, 1980.

Röttger, J., Investigations of lower and middle atmosphere dynamics with spaced antenna drift radars, *J. Atmos. Terr. Phys.*, 43, 277-292, 1981.

Röttger, J., The capabilities of VHF radar for meteorological observations, Preprint of Nowcasting Symposium, *Third scientific assembly of international association of meteorology and atmospheric physics*, Hamburg, Germany, 17-21 Aug. 1981.

Röttger, J., Techniques for measurements of horizontal and vertical velocities: Determination of horizontal and vertical wavelengths of gravity waves, *Handbook for MAP*, Vol. 9, SCOSTEP Secretariat, Dep. Elec. Computer Eng., Univ. of Il. Urbana, 150-163, 1983.

Röttger, J., and M. F. Larsen, UHF/VHF radar techniques for atmospheric research and wind profiler applications, Radar in meteorology edited by David Atlas, *American meteorological society*, Boston, 235-281, 1990.

Salby, M. L., and Roper, R. G., Long-period oscillation in the meteor region, *J. Atmos. Sci.*, 37, 237-244, 1980.

Salby, M. L., The 2-day wave in the middle atmosphere: observations and theory, *J. Geophys. Res.*, 86, 9654-9660, 1981.

Salby, M. L., Survey of planetary-scale travelling waves: theory and observations, *Rev. Geophys.*, 22, 209-236, 1984.

Sato, T., Radar principles, *Handbook for MAP*, 30, 19-53, 1989.

Sawada, R., A note on altitude effect on the atmospheric lunar tides in the lower thermosphere, *J. Met. Soc. Japan*, 58, 279-280, 1980.

Sawada, R. and M. Ueno, Possible effect on ocean with variable depth on the atmospheric lunar tides, *J. Met. Soc. Japan*, 58, 277-278, 1980.

Schmidt, M., The influence of large scale advection on the vertical distribution of stratospheric source gases in 44° and 41° north, *J. Geophys. Res.*, 87, 11239-11246, 1982.

Scientific assessment of stratospheric ozone, *World meteorological report*, No. 20, Vol 1, pp 486, 1989.

She, C. Y., J. R. Yu, and H. Chen, Observed thermal structure of a midlatitude mesopause, *Geophys. Res. Lett.*, 20, 567-570, 1993.

She, C. Y., J. R. Yu, and D. A. Krueger, Vertical structure of the midlatitude temperature from stratosphere to mesopause (30-105 km), *Geophys. Res. Lett.*, 22, 377-380, 1995.

Shepherd, G. G., G. Thuillier, W. A. Gault, B. H. Solheim, C. Hersom, J. M. Alunni, J. -F. Brun, P. Charlot, L. L. Cogger, D. -L. Desaulniers, W. F. J. Evans, R. L. Gattinger, F. Girod, D. Harvie, R. H. Hum, D. J W. Kendall, E. L. Llewellyn, R. P. Lowe, J. Ohrt, F. Pasternak, O. Peillet, I. Powell, Y. Rochon, W. E. Ward, R. H. Wiens, and J. Wimperis, "WINDII, the Wind Imaging Interferometer on the Upper Atmosphere Research Satellite", *J. Geophys. Res.*, 98, 10,725-10,750, 1993.

Sidi, C., and H. Teitelbaum, Thin shear turbulent layers within the lower thermosphere induced by nonlinear interaction between tides and gravity waves, *J. Atmos. Terr. Phys.*, 40, 529, 1978.

Siebert, M., Atmospheric tides, *Advances in Geophysics*, 7, 105-182, 1961.

Smith, A. K., Wave transience and wave-mean flow interaction caused by the interference of stationary and travelling wave, *J. Atmos. Sci.*, 42, 529-535, 1985.

Solomon, S., and R. R. Garcia, Simulation of NO_x partitioning along isobaric parcel trajectories, *J. Geophys. Res.*, 88, 5497, 1983.

Spizzichino, A., Meteor trail radar winds over Europe, Thermospheric circulation, *The MIT Press*, Massachusetts, 205-248, 1972.

Spizzichino, A., Meteor trail winds over Europe, Thermospheric circulation, Progress in astronautics and aeronautics, W. Webb, Ed., Vol. 27, it The MIT press, 117-180, 1973.

Sprenger, K., and Schminder, R., Results of ten years ionospheric drift measurements in the L.F. range, *J. Atmos. Terr. Phys.*, 30, 183-199, 1967.

Sprenger, K., and Schminder, R., On the significance of ionospheric drift measurements in the L. F. range, *J. Atmos. Terr. Phys.*, 30, 693-700, 1968.

Sprenger, K., and Lysenko, I. A., The significance and interpretation of ionospheric drift measurements in the low frequency range, *Phil. Trans. R. Soc.*, A271, 473-484, 1972.

Steel, D. I., and W. G. Elford, The height distribution of radio meteors: comparison of observations at different frequencies on the basis of standard echo theory, *J. Atmos. Terr. Phys.*, 53, 409-417, 1991.

Stenning, R., C. E. Meek, A. H. Manson, and D. Stephensen, Winds and wave motions to 110 km at mid-latitudes, *J. Atmos. Sci.*, 35, 2194-2204, 1978.

Stix, T. H., The theory of plasma waves, *McGraw-Hill*, New York, 1962.

Stohl, J., Seasonal variation in the radiant distribution of meteors, Physics and dynamics of meteors, *Physics and dynamics of meteors (edited by L. Kresak and P. M. Millman)*, Reidel, Dordrecht, 298-303, 1968.

Stubbs, T. J., The measurement of winds in the D-region of the ionosphere by the use of partially reflected radio waves, *J. Atmos. Terr. Phys.*, 35, 909-919, 1973.

Stubbs, T. J., and R. A. Vincent, Studies of D-region drifts during the winters of 1970-72, *Aus. J. Phys.*, 26, 645-660, 1973.

Sugar, G. R., Radio propagation by reflection from meteor trails, *proc. IEEE,* 52, 116-136, 1964.

Sürücü, F., S. J. Franke, and E. Kudeki, On the influence of specular reflections in MF radar wind measurements, *Radio Sci.*, 30, 1229-1244, 1995.

Tatarski, V. I., Wave propagation in a turbulent medium, *McGraw-Hill,* New York, 1961.

Taylor, G. I., The resonance theory of semidiurnal atmosphere oscillation, *Mem. Roy. Meteorol. Soc.*, 4, 41-52, 1932.

Taylor, G. I., The oscillation of the atmosphere, *Proc. Roy. Soc.*, A 156, 318-338, 1936.

Taylor, J. R, An introduction to error analysis, *University science books,* Mill valley, California, USA.

Tetenbaum, D., S. K. Avery, and A. C. Riddle, Observations of mean winds and tides in the upper mesosphere during 1980-1984, using the Poker Flat, Alaska, MST radar as a meteor radar, *J. Geophys. Res.*, 91, D13, 14539-14555, 1986.

Teitelbaum, H., F. Vial, A. H. Manson, R. Giraldez and M. Massebeuf, Non-linear interaction between the diurnal and semidiurnal tides: terdiurnal and diurnal secondary waves, *J. Atmos. Terr. Phys.*, 51, 627-634, 1989.

Teitelbaum, H., and F. Vial, On tidal variability induced by non-linear interaction with planetary waves, *J. Geophys. Res.* 96, 14169-14178, 1991.

Thomas, L., The lower ionosphere, *J. Atmos. Terr. Phys.*, 33, 157, 1971.

Thomas, L., Recent developments and outstanding problems in the theory of the D-region, *Radio Sci.*, 9, 121, 1974.

Thomas, L., The composition of the mesosphere and lower thermosphere *Phil. Trans. Roy. Soc. London,* A 296, 243, 1980.

Thomas, R. J., and C. A. Barth, Seasonal variation of ozone in the upper mesosphere and gravity waves, *Geophys. Res. Lett.*, 11, 673-676, 1984.

Thomas, R. M., P. S. Whitham, and W. G. Elford, Response of high frequency radar to meteor backscatter, *J. Atmos. Terr. Phys.*, 50, 703-724, 1988.

Thomas, R. M., Detection by HF radar of the Eta Aquarid meteor shower, *Planet. Space Sci.*, 37, 837-846, 1989.

Tokioka T., and I. Yagai, Atmospheric tides appearing in a global atmospheric general circulation model, *J. Meteor. Soc. Japan,* 65, 423-437, 1987.

Torr, F. G., and M. R. Torr, Chemistry of the thermosphere and ionosphere, *J. Atmos. Terr. Phys.*, 41, 797, 1979.

Tsuda, T., T. Aso, Y. Takashima, R. Ito, and S. Kato, Meteor radar observations at Kyoto in two C.T.O.P. periods, *J. Atmos. Terr. Phys.*, 42, 461-469, 1980.

Tsuda, T. and S. Kato, Seasonal variation of diurnal tide due to ozone heating, *J. Met. Soc. Japan,* 58, 292-297, 1980.

Tsuda, T., J. Tanil, T. Aso, and S. Kato, Lunar tides at meteor heights, *Geophys. Res. Lett.*, 8, 191-194, 1981.

Tsuda, T., T. Aso, and S. Kato, Seasonal variation of solar atmospheric tides at meteor heights, *J. Geomag. Geoelectr.*, 35, 65-86, 1983.

Tsuda, T., and S. Kato, Diurnal non-migrating tides excited by a differential heating due to land-sea distribution, *J. Meteor. Soc. Japan*, 67, 43-54, 1987.

Tsuda, T., S. Kato, and R. A. Vincent, Long period oscillations observed by the Kyoto meteor radar and comparison of the quasi-2-day wave with Adelaide HF radar observations, *J. Atmos. Terr. Phys.*, 50, 225-230, 1988.

Vial, F., and H. Teitelbaum, *Planet. Space Sci.*, 32, 1559, 1984.

Vial, F., J. L. Fellous and H. Teitelbaum, Tidal vertical structure and temperature profiles in the lower thermosphere, *Annales Geophysicae*, 3, 313-318, 1985.

Vial, F., Numerical simulations of atmospheric tides for solstice conditions, *J. Geophys. Res.*, 91, 8955-8969, 1986.

Vial, F., Tides in the middle atmosphere, *J. Atmos. Terr. Phys.*, 51, 3-17, 1989.

Vial, F., and J. Forbes, Recent progress in tidal modelling, *J. Atmos. Terr. Phys.*, 51, 663-671, 1989.

Vial, F. and J. M. Forbes, Monthly simulations of the lunar semidiurnal tide, *J. Atmos. Terr. Phys.*, 56, 1591-1607, 1993.

Vial, F., private communication, 1994.

Vincent, R. A., T. J. Stubbs, R. H. O. Pearson, K. H. Lloyd, and C. H. Low, A comparison of partial reflection drifts with winds determined by rocket techniques - I, *J. Atmos. Terr. Phys.*, 39, 813-821, 1977. Vincent, R. A., and S. M. Ball, Tides and gravity waves in the mesosphere at low- and mid-latitudes, *J. Atmos. Terr. Phys.*, 39, 965-970, 1977.

Vincent, R. A., and Röttger, Spaced antenna radar observations of tropospheric velocities and irregularities, *Radio Sci.*, 15, 319-335, 1980.

Vincent, R. A., P. T. May, W. K. Hocking, W. K. Elford, W. G. Candy, and B. H. Briggs, First results with the Adelaide VHF radar: Spaced antenna studies of tropospheric winds, *J. Atmos. Terr. Phys.*, 49, 353-366, 1987.

Vincent, R. A., MF/HF radar measurements of the dynamics of the mesopause region - A review, *J. Atmos. Terr. Phys.*, *46*, 961-974, 1984.

Vincent, R. A., T. Tsuda, and S. Kato, A comparative study of mesospheric solar tides observed at Adelaide and Kyoto, *J. Geophys. Res.*, 699-708, 1988.

Volland, H., Atmospheric tidal and planetary waves, *Kluwer academic publishers*, Boston, U.S.A., 1988.

Wallace, J. M., and R. F. Tadd, Some further results concerning the vertical structure of atmospheric tidal motions within the lowest 30 kilometers, *Mon. Wea. Rev.*, 102, 795-803, 1974.

Wallace, J. M., and P. V. Hobbs, Atmospheric science, *Academic Press*, New York, 1977.

Williams, C. R., Analysis of deep convective clouds and their association with non-migrating atmospheric diurnal tides in the tropical troposphere, *Aeronomy laboratory*, Boulder, Colorado, U.S.A., 1994.

Walterscheid, R. L. and S. V. Venkateswaran, Influence of mean zonal motion and meridional temperature gradients on the solar semidiurnal atmospheric tide: A spectral study. Part

1: Theory, *J. Atmos. Sci.*, 36, 1623-1635, 1979.

Walterscheid, R. L. and S. V. Venkateswaran, Influence of mean zonal motion and meridional temperature gradients on the solar semidiurnal atmospheric tide: A spectral study. Part 2: Numerical results, *J. Atmos. Sci.*, 36, 1636-1662, 1979.

Walterscheid, R. L., J. G. DeVore and S. V. Venkateswaran, Influence of mean zonal motion and meridional temperature gradients on the solar semidiurnal atmospheric tide: A revised spectral study with improved heating rates, *J. Atmos. Sci.*, 37, 455-470, 1980.

Walterscheid, R. L., Inertio-gravity wave induced accelerations of mean flow having an imposed periodic component: Implications for tidal observations in the meteor region, *J. Geophys. Res.*, 86 9698-9706, 1981.

Walterscheid, R. L., V. V. Sivjee, G. Schubert and R. M. Hamwey, Large-amplitude semidiurnal temperature variations in the polar mesopause: evidence of a pseudotide, *Nature*, 324, 347.

Wang, D. Y., and D. C. Fritts, Evidence of Gravity wave-tidal interaction observed near the summer mesopause at Poker Flat, Alaska, *J. Atmos. Sci.*, 48, 572-583, 1991.

Wang, S. T., D. Tetenbaum, B. B. Balsley, R. L. Obert, S. K. Avery, and J. P. Avery, A meteor echo detection and collection system for use on VHF radars,*Radio Sci.*, 23, 46-54, 1988.

Ward, W., *Private communication,* 1995.

Watson, R. T. and the ozone trends panel, Present state of the upper atmosphere 1988: an assessment, *NASA Ref. Pub.*, 1208, pp 200, 1988.

Wayne, R. P., Chemistry of atmospheres, *Clarendon press*, Oxford, England, 1991.

Weekes, K., and Wilkes, M. V., Atmospheric oscillations and the resonance theory, *Proc. Roy. Soc.*, A 192, 80-99, 1947.

Whipple, F. J. W., A note on the propagation of the semidiurnal pressure wave, *Quart. J. Roy. Meteorol. Soc.*, 44, 20-23, 1918.

Whitehead, J. D., W. R. From, K. L. Jones, and P. E. Monro, Measurements of movements in the ionosphere using radio reflections, *J. Atmos. Terr. Phys.*, 45, 345-351, 1983.

Wilkes, M. V., Oscillations of the Earth's atmosphere, *Cambridge University press,* United Kingtom, 1949.

Williams, C. R., and S. K., Avery, Analysis of long-period waves using the MST radar at Poker Flat, Alaska, *J. Geophys. Res.*, 97 (D18), 20,855-20,861, 1992.

Williams, C. R., Analysis of deep convective clouds and their association with non-migrating atmospheric diurnal tides in the tropical troposphere, *Aeronomy laboratory,* Boulder, Colorado, U.S.A., 1994.

Witt, G., Height, structure, and displacements of noctilucent clouds, *Tellus,* 14, 1-18, 1962.

Wohlleben, R., and H. Mattes, Interferometrie in radioastronomie und radartechnik, *Vogel-Verlag,* Wurzburg.

Woodman, R. F., Inclination of the geomagnetic field measured by an incoherent scatter technique, *J. Geophys. Res.*, 76, 178-184, 1971.

Woodman, R. F., and A. Guillen, Radar observations of winds and turbulence in the stratosphere and mesosphere, *J. Atmos. Sci.*, 31, 493-505, 1974.

Wright, J. W., The interpretation of ionospheric radio drift measurements - I. Some results of experimental comparisons with neutral wind profiles, *J. Atmos. Terr. Phys.*, 30, 919-930, 1968.

Wright, J. W., M. Glass, and A. Spizzichino, The interpretation of ionospheric radio drift measurements - VII. Direct comparisons of meteor radar winds and kinesonde measurements: mean and random motions, *J Atmos. Terr. Phys.*, 38, 713-729, 1976.

Wu D. H., S. Miyahara, and Y. Miyoshi, A nonlinear simulation of the thermal diurnal tide, *J. Atmos. Terr. Phys.*, 51, 1017-1030, 1989.

Yagai, I., Nonmigrating thermal tides detected in data analysis and a general circulation model simulation, *J. Geophys. Res.*, 94, 6341-6356, 1989.

Yanowitch, M., A remark on the hydrostatic approximation, *Pure appl. Geophys.*, 64, 169-172, 1966.